

UNIVERSITY OF OKLAHOMA
GRADUATE COLLEGE

INTEGRATED RESERVOIR CHARACTERIZATION OF A MIXED SILICICLASTIC-
CARBONATE SYSTEM, MISSISSIPPIAN STRATA OF NORTHERN AND CENTRAL
OKLAHOMA

A DISSERTATION
SUBMITTED TO THE GRADUATE FACULTY
In partial fulfillment of the requirement for the
Degree of
DOCTOR OF PHILOSOPHY

By
FNU SURIAMIN
Norman, Oklahoma
2020

INTEGRATED RESERVOIR CHARACTERIZATION OF A MIXED SILICICLASTIC-
CARBONATE SYSTEM, MISSISSIPPIAN STRATA OF NORTHERN AND CENTRAL
OKLAHOMA

A DISSERTATION APPROVED FOR THE
SCHOOL OF GEOSCIENCES

BY THE COMMITTEE CONSISTING OF

Dr. Matthew J. Pranter, Chair

Dr. Kurt J. Marfurt

Dr. Deepak Devegowda

Dr. John D. Pigott

To my family and my late dad

ACKNOWLEDGEMENTS

I would like to express my sincerest gratitude to Dr. Matthew J. Pranter, my Ph.D. advisor as well as life mentor. This dissertation profited greatly from his advice, support, and guidance, and I am indebted to him for his continuous financial support throughout my stay at OU.

I wish to thank all of the members of my dissertation committee: Drs. Kurt J. Marfurt, Deepak Devegowda, and John D. Pigott for their critical comments and thoughtful discussions. I also want to thank Dr. Doug Elmore, Dr. Kyle E. Murray, and Dr. Roger M. Slatt (Late) for their guidance and time.

Over my six years at OU, it has been a great experience to be part of the RCML research group. I wish to thank all former and present students of RCML for their stimulating discussion, creative support, and continuing friendship. I am especially grateful to Rebecca Fay for her kindness and resourcefulness ever since my arrival at OU.

I wish to thank all of the OGS staffs, especially Brian J. Cardott, for his time to review part of this dissertation. I wish to thank David P. Brown for his support and opportunity to work on my dissertation while working for Oklahoma Geological Survey.

I would like to thank my mother Ong A Tjuan for her motivation and encouragement in my study at OU. Now, she can stop asking me “are you graduated yet?” every time I call her. I also would like to thank my late dad who always tell me the important of high education.

Finally, my special thank go to Lily Lim, my wife, not only for her moral support, but also for her sacrifice. Special thank also go to Annika D. Huang, my daughter, because of her innocent laugh and sweet face has enriched my daily life. We did this together.

TABLE OF CONTENTS

ACKNOWLEDGEMENTS	v
TABLE OF CONTENTS	vi
LIST OF FIGURES	x
LIST OF TABLES	xxi
ABSTRACT.....	xxii
1. STRATIGRAPHIC AND LITHOFACIES CONTROL ON PORE	
CHARACTERISTICS OF MISSISSIPPIAN LIMESTONE AND CHERT	
RESERVOIRS OF NORTH-CENTRAL OKLAHOMA.....	1
ABSTRACT.....	1
INTRODUCTION	2
GEOLOGICAL SETTING.....	5
METHODOLOGY	8
Lithofacies and sequence-stratigraphic framework	8
Pore-architecture characterization	9
RESULTS AND DISCUSSION.....	13
Lithofacies and sequence-stratigraphic framework	13
Depositional model.....	22
Pore-system characteristics.....	27
Porosity, permeability, and lithofacies.....	45
Porosity, permeability, and sequence-stratigraphic framework.....	48
CONCLUSIONS.....	48

REFERENCES	52
2. VARIABILITY OF MISSISSIPPIAN LITHOFACIES, DEPOSITIONAL ENVIRONMENTS, DIAGENETIC PROCESSES, AND RESERVOIR QUALITY WITHIN A MIXED SILICICLASTIC-CARBONATE SYSTEM, EASTERN ANADARKO BASIN, OKLAHOMA, USA.	57
ABSTRACT.....	57
INTRODUCTION	58
GEOLOGICAL SETTING.....	59
METHODOLOGY	64
RESULTS	66
Well-log response	66
Lithofacies.....	67
Diagenesis.....	67
INTERPRETATION AND DISCUSSION	77
Depositional environment.....	77
General Diagenetic Characteristics.....	81
Paragenesis.....	94
Reservoir Inferences	97
CONCLUSIONS.....	103
REFERENCES	105
3. PETROPHYSICAL ANALYSIS OF MISSISSIPPIAN ROCK TYPES AND RESERVOIR PROPERTIES WITHIN A SEQUENCE-STRATIGRAPHIC FRAMEWORK, EASTERN ANADARKO BASIN, OKLAHOMA, USA	110

ABSTRACT.....	110
INTRODUCTION	111
GEOLOGICAL SETTING.....	114
DATA AND METHODOLOGY.....	117
Petrophysical Properties Calculation.....	120
Sequence Stratigraphy	121
Rock Typing.....	121
K-means Clustering Method.....	122
Random Forests Classification	122
Reservoir Modeling	124
RESULTS	127
Mineral Volumes	127
Mineral-based Rock Types.....	132
Extending Mineral-based Rock Types to Well Logs.....	132
Mississippian Sequence Stratigraphy.....	135
Reservoir Modeling	143
DISCUSSION.....	150
Spatial Distribution of Rock Types within Sequence Stratigraphy Framework.....	150
Sequence-Stratigraphic Control of Porosity Distribution.....	153
Sweet Spot Identification.....	154
CONCLUSIONS.....	154
REFERENCES	157
APPENDIX A: THIN SECTION AND SEM PHOTOMICROGRAPHS	161

APPENDIX A1: Whole Thin Section Photo (Devon Energy 1–7 SWD Frieouf).....	162
APPENDIX A2: SCANNING ELECTRON MICROSCOPE PHOTOMICROGRAPHS	
.....	188
APPENDIX B: CORE DESCRIPTION	339

LIST OF FIGURES

- Figure 1.1. Regional base map showing the major tectonic and basinal features of Oklahoma and northwestern part of Texas (modified after Dutton, 1984; Campbell et al., 1988; McConnell, et al. 1989; Northcutt and Campbell, 1995; Johnson and Luza, 2008; LoCricchio, 2012). The Devon Energy 1-7 SWD Frieouf well (star) is located on the Anadarko Shelf and on the western side of the Nemaha uplift. 4
- Figure 1.2. Stratigraphic column for the Ordovician to Mississippian-age deposits in the north-central Oklahoma. (Modified after Mazzullo, 2011; Mazzullo et al., 2011; Mazzullo et al., 2016). 7
- Figure 1.3. A schematic illustration of a pore showing measured pore parameters. The measured parameters include pore area (shaded gray area), perimeter (black solid line), length (black dashed line), and width (black dotted line). The pore area is calculated as the sum of the areas of each individual pixel within the borders of the pore. The pore perimeter is the total length of the pore boundary. The length and width of a pore are the maximum distance between any two points on the perimeter of the pore parallel to the major axis and minor axis, respectively. 11
- Figure 1.4. Pore-size classification used in this study. The classification is based on pore width following Loucks (2012) pore-size classification for mudrock. 12
- Figure 1.5. Photographs of core-based lithofacies in the Mississippian interval of Devon Energy 1-7 SWD Frieouf well. a) Chert breccia in greenish shale matrix. b) Chert breccia showing severely compacted clasts. c) Skeletal mudstone-wackestone showing lenticular/flaser features (possibly spicule) and cross bedding. d) Skeletal grainstone. Note the presence of fracture filled by possibly calcite and pressure solution feature. e) Splotchy packstone-grainstone. f) Bedded skeletal packstone-grainstone. Note the presence of scour surface, stylolite, and possibly hardgrounds. g) Nodular packstone-grainstone showing common silica-replacement nodules. Note the nodule shapes are irregular. h) Skeletal peloidal packstone-grainstone. Scale Bar = 5 cm. 14
- Figure 1.6. Photographs of core-based lithofacies in the Mississippian interval of Devon Energy 1-7 SWD Frieouf well (continued). a) Bioturbated skeletal-peloidal packstone-grainstone. Note centimeter-size skolithos (black line). b) Bioturbated mudstone-wackestone and Brecciated spiculitic mudstone where most clasts are intact suggesting in-situ deformation. c) Intraclast mudstone-wackestone. d) Spiculitic mudstone-wackestone with deformed lenticular/flaser features. e) Argillaceous spiculitic mudstone-wackestone. Note moderate fracture associated with this lithofacies. f) Glauconitic sandstone deposited on top of a scour surface. g) Shale. h) Shaly claystone showing very faintly fissile. Scale Bar = 5 cm. 15
- Figure 1.7. Thin-section photomicrographs of lithofacies: a) Chert breccia in greenish shale matrix showing microcrystalline quartz replacing grains and matrix and creating vuggy porosity. b) Chert breccia showing calcite and microcrystalline quartz; c) Skeletal mudstone-wackestone showing predominant microcrystalline-quartz replacing grain and matrix. Cross-cutting relationship indicates silica replacement took place before fracturing and calcite filling. d)

Skeletal grainstone showing bryozoan with moldic pores after skeletal, calcite (cal), and dolomite (dol). e) Splotchy packstone-grainstone showing extensive alteration of grains and matrix into microcrystalline quartz (white color). f) Bedded skeletal peloidal packstone-grainstone showing microcrystalline quartz, vuggy pores, peloids, and unidentified skeletal grains. 16

Figure 1.8. Thin-section photomicrographs of identified lithofacies (continued): a) Bedded skeletal peloidal packstone-grainstone. Note oil filling vuggy pores and microcrystalline quartz. b) Nodular packstone-grainstone with predominantly calcite cement (cal) and dolomite rhombic crystals (black arrow). Note the presence of oil filling fracture. c) Bioturbated skeletal peloidal packstone-grainstone. Note the presence of vuggy pore due to dissolution of grains. d) Bioturbated mudstone-wackestone with mainly lime-mud, quartz grains (white-color grains), and glauconite grains (yellow arrow). e) Spiculitic mudstone-wackestone. Note the bioturbations show textural contrast between the filling (darker color) and surrounding sediment; and the presence of isolated bright area with sponge spicules. f) Argillaceous spiculitic mudstone-wackestone. Note the presence of glauconite grain and monaxon sponge spicules. 17

Figure 1.9. Devon Energy 1-7 SWD Frieouf well core lithofacies, properties, and cycles. The Mississippian strata in this well consists of 3 sequences. The high-order sequence-stratigraphic framework is based on lithofacies stacking patterns. See Figure 10 for lithofacies key. Note that higher reservoir quality is associated with the upper intervals of upward-shoaling high-order cycles (black arrows on porosity and permeability tracks). TVDSS = True Vertical Depth Subsea. BI = Bioturbation Index, Phi (DIA) = Digital-Image Analysis calculated porosity, Phi (Core) = Laboratory-measured core porosity, K = Permeability, RT10 = shallow resistivity, RT90 = deep resistivity, NPHI = Neutron porosity, RHOB = bulk density, GR = Gamma Ray, DTC = Compressional wave travel time. 18

Figure 1.10. Core legend, idealized shallowing-upward lithofacies succession for the sequence 2 and sequence 3 in the Mississippian strata, and lithofacies color codes. The sequences are identified based on the presence of erosional surface or interval of brecciated lithofacies. Note that there is no idealized stacking pattern for sequence 1 due to the limited presence of lithofacies (only shale and shaly claystone lithofacies are observed within sequence 1). The blue triangle represents relative sea level rise (transgressive - T) and the red triangle represents relative sea level fall (regressive - R)..... 19

Figure 1.11. Example of observed sequence boundary (SB) in the Devon Energy 1-7 SWD Frieouf well. The SB features including erosional surface (a and b) (black dash line) and brecciation (c). 20

Figure 1.12. Schematic diagram showing a generic carbonate ramp depositional model for the Mississippian strata in the Grant County, Oklahoma, especially during deposition of sequences 1-3. Sequence 1 contains shaly claystone (17) and shale (16). Sequence 2 consists of glauconitic sandstone (15), argillaceous spiculitic mudstone-wackestone (14), spiculitic mudstone-wackestone (13), intraclast spiculitic mudstone (12), and brecciated spiculitic mudstone (11). Sequence 3 consists of bioturbated mudstone-wackestone (10), bioturbated skeletal peloidal packstone-grainstone (9), skeletal peloidal packstone-grainstone (8), nodular packstone-grainstone (7), bedded skeletal peloidal packstone-grainstone (6), splotchy packstone-grainstone

(5), skeletal grainstone (4), skeletal mudstone-wackestone (3), chert breccia (2), and chert breccia in greenish shale matrix (1). Note that breccia lithofacies (1, 2, and 11) are not placed in the model as breccia can occur in inner- to outer-ramps depending on relative sea-level change. Lithofacies are spatially distributed within their sequences based on grain size, texture, sedimentary structure, degree and type of bioturbation..... 24

Figure 1.13. Histogram of measured pores from >3100 SEM and 57 thin section photomicrographs. Noted that the pores are primarily nanopores (1 nm < width < 1 μm) with secondary mesopores (1 μm < width < 62.5 μm) and minor mesopore (62.5 μm < width < 4 mm)..... 28

Figure 1.14. Schematic diagram of carbonate pore types observed in this study. Intraparticle pores including: a) Intercrystalline pores within pyrite framboid vuggy pore; b) Crystal-form pore channel pore; c) Particle-rim pore; d) Moldic pores after crystals/skeletals; e) Pores within crystals; and f) Microfracture within crystals. Intraparticle pores including: g) Pore between crystals and h) Pore between grains. Non-fabric-selective pores including: i) Vuggy; j) Channel; and k) Microfracture. 30

Figure 1.15. Example SEM photomicrographs of common pore types. a) Interparticle pore between dolomite crystals, channel, vuggy, and intraparticle pores (crystal-form pores and intercrystalline within pyrite framboid). Note the dolomite crystals have a variety polygon shapes. b) Interparticle (pore within dolomite crystals), intraparticle (microfracture within crystals), and vuggy pores. c) Microfracture and intraparticle pores (pore within crystals). d) Vuggy pores in bedded skeletal peloidal packstone-grainstone. The vuggy pores have a large range in size (nano- to mesopore sizes). e) Intraparticle (moldic pore after crystal) and interparticle pores (pore between crystals). f) Skeletal mudstone-packstone with predominantly intraparticle (particle-rim pores)..... 33

Figure 1.16. SEM photomicrographs showing two examples of extracted pores and their parameters. a) A sample with crystal-form pore, vuggy, and interparticle. Extracted pore 1 has more circular shape (circularity 0.4) as compared to pore 2 (circularity 0.1). a) A sample showing predominantly vuggy and interparticle pores. Pore 3 is also an example of pore with circularity of 0.1. Note, pores with relatively lower circularity can have variety of shapes (from elongated to amorphous shapes)..... 34

Figure 1.17. Comparison of porosity values obtained from core-plug helium porosimetry (Laboratory-Measured Core Porosity) and digital-image analysis (DIA Porosity). A positive relationship ($R^2 = 0.94$) is apparent. Data are from thin sections for 12 lithofacies: 1. Chert breccia in greenish shale matrix, 2. Chert breccia, 3. Skeletal mudstone-wackestone, 4. Skeletal grainstone, 5. Splotchy packstone-grainstone, 6. Bedded skeletal peloidal packstone-grainstone, 7. Nodular packstone-grainstone, 8. Skeletal peloidal packstone-grainstone, 9. Bioturbated skeletal peloidal packstone-grainstone, 10. Bioturbated mudstone-wackestone, 13. Spiculitic mudstone-wackestone, 14. Argillaceous spiculitic mudstone-wackestone. Note fine-grained dominated lithofacies 13 (spiculitic mudstone-wackestone) and 14 (Argillaceous spiculitic mudstone-wackestone) tend to deviate from ideal correlation. The variation might be attributed to the difference between effective porosity from core-based laboratory measurements and total

porosity from digital-image analysis; where in laboratory-measured core porosity, the dominant nanopores in mud-dominated lithofacies are not accessible to helium..... 36

Figure 1.18. a). Cross plot of average pore circularity versus laboratory-measured core permeability. Circularity is defined as the degree to which the pore is similar to a circle. Data are color coded based on lithofacies including 1. Chert breccia in greenish shale matrix, 2. Chert breccia, 3. Skeletal mudstone-wackestone, 4. Skeletal grainstone, 5. Splotchy packstone-grainstone, 6. Bedded skeletal peloidal packstone-grainstone, 7. Nodular packstone-grainstone, 8. Skeletal peloidal packstone-grainstone, 9. Bioturbated skeletal peloidal packstone-grainstone, 10. Bioturbated mudstone-wackestone, 13. Spiculitic mudstone-wackestone, 14. Argillaceous spiculitic mudstone-wackestone. Note that the data show an indeterminate relationship. b). Cross plot of mode pore circularity versus laboratory-measured core permeability. Data are color coded based on lithofacies including 1. Chert breccia in greenish shale matrix, 2. Chert breccia, 3. Skeletal mudstone-wackestone, 4. Skeletal grainstone, 5. Splotchy packstone-grainstone, 6. Bedded skeletal peloidal packstone-grainstone, 7. Nodular packstone-grainstone, 8. Skeletal peloidal packstone-grainstone, 9. Bioturbated skeletal peloidal packstone-grainstone, 10. Bioturbated mudstone-wackestone, 13. Spiculitic mudstone-wackestone, 14. Argillaceous spiculitic mudstone-wackestone. c). Cross plot of mode pore circularity versus laboratory-measured core permeability for lithofacies 6. d). Cross plot of mode pore circularity versus laboratory-measured core permeability for lithofacies 9 shows a weak positive correlation. e). Cross plot of mode pore circularity versus laboratory-measured core permeability for lithofacies 13 shows a weak positive correlation. f). Cross plot of mode pore circularity versus laboratory-measured core permeability for lithofacies 14 shows a weak negative correlation.. The poor relationship is possibly due to complex internal pore network, cemented pore throats, or the presence of isolated pores. 39

Figure 1.19. Example of pore-size distribution plot for samples A and B. Pore-size distribution is plotted as a probability percentage in which pore width (micron) (in x-axis) is compared to the percentage of pores in the sample that has a width greater than a given width (%) (in y-axis). Straight-line segments (e.g. solid black, solid orange, dash black, and dash orange lines) represent each pore-size class. The plot provides simple identification of pore-size classes, dominant pore-size class, quantitative percentage of a pore class, and approximate minimum and maximum pore size (black arrows). Data (red line of part a) are divided into pore-size classes (colored regions on plot) with each pore-size class represented by straight-line segments (black line in part a and black and orange lines in part b). For each straight-line segment, the A) slope and B) probability range (range in y-values, %) are obtained. In part a, the data show that the probability range for nanopores is 60-100% or ~40% of measured pores are nanopores with porosity of 2.50% (purple and green lines in part a). b) The line-segment slopes for pore-size classes of two samples are compared in part b. For example, the straight-line segment representing nanopores of sample B (orange solid line) has a steeper slope as compared to sample A (black solid line). This indicates that sample B has a greater quantity of nanopores as compared to sample A and a greater number of smaller nanopores than in sample A. Therefore, sample B has lower nano-porosity ($\phi_{\text{nano}} = 2.32\%$) as compared to sample A ($\phi_{\text{nano}} = 2.50\%$). Additionally, the line segment representing mesopores of sample A (black dashed line) has a similar slope to sample B (orange dashed line) but a higher probability (y-value) indicating that sample A has a greater quantity of mesopores and higher mesoporosity ($\phi_{\text{meso}} = 6.22\%$) as compared to sample B ($\phi_{\text{meso}} = 0.17\%$)..... 41

Figure 1.20. Pore-size distribution plots for 12 lithofacies including: 1. Chert breccia in greenish shale matrix, 2. Chert breccia, 3. Skeletal mudstone-wackestone, 4. Skeletal grainstone, 5. Splotchy packstone-grainstone, 6. Bedded skeletal peloidal packstone- grainstone, 7. Nodular packstone-grainstone, 8. Skeletal peloidal packstone-grainstone, 9. Bioturbated skeletal peloidal packstone-grainstone, 10. Bioturbated mudstone-wackestone, 13. Spiculitic mudstone-wackestone, 14. Argillaceous spiculitic mudstone-wackestone. Note that fine-grained lithofacies 3, 10, 13 and 14 have predominantly nanopores and micropores while coarse-grained lithofacies 1, 2, 4, 5, 6, 7, 8, 9 have a variable pore-size distribution ranging from nanopores to mesopores. 44

Figure 1.21. Plot of laboratory-measured core porosity versus laboratory-measured core permeability for 12 lithofacies including: 1. Chert breccia in greenish shale matrix, 2. Chert breccia, 3. Skeletal mudstone-wackestone, 4. Skeletal grainstone, 5. packstone grainstone, 6. Bedded skeletal peloidal packstone-grainstone, 7. Nodular packstone-grainstone, 8. Skeletal peloidal packstone-grainstone, 9. Bioturbated skeletal peloidal packstone-grainstone, 10. Bioturbated mudstone-wackestone, 13. Spiculitic mudstone-wackestone, 14. Argillaceous spiculitic mudstone-wackestone. Exponential trend lines of lithofacies 6, 9, 13, and 14 show a reasonable positive correlation between laboratory-measured core porosity and permeability. Lithofacies 13 and 15 are fine-grained lithofacies while lithofacies 5 and 9 are coarse-grained lithofacies. Note the poor relationship between porosity and permeability of lithofacies 14 ($R^2 = 0.46$). This might be attributed to the presence of clay as indicated by relatively high gamma-ray responses (Figure 2.9). 46

Figure 2.1. Regional base map showing the major tectonic and basinal features of Oklahoma and Texas Panhandle (modified after Dutton, 1984; Campbell et al., 1988; McConnell, et al. 1989; Northcutt and Campbell, 1995; Johnson and Luza, 2008; LoCricchio, 2012). The Humble Oil & Refining Company 1 Van Horn Unit (1), Gulf Oil Corporation 1 Musselman (2), Gulf Oil Corporation 1-23 Shaffer (3), Humble Oil & Refining Company 1 Lloyd L Hawkins (4), and Petrolia Drilling Corporation 1 Payne (5) are located on the Anadarko Basin (labelled as black dot). 60

Figure 2.2. Generalized Stratigraphic summary of Mississippian strata in the Anadarko Shelf and Anadarko Basin at the north and central Oklahoma (Modified after Mazzullo, 2011; Mazzullo et al., 2011; Mazzullo et al., 2016; Stuke, 2018). 62

Figure 2.3. Well logs correlation of five wells in this study from north to south (Annotated as A – A' red line in Figure 1). If available, each wells have gamma-ray (GR), bulk density (RHOB), shallow resistivity (RESS), medium resistivity (RESM), and deep resistivity (RESD). This correlation is based on flooding surfaces observed using gamma ray (GR) logs. The gamma-ray log become relatively flat to the north which pose a challenge to the correlation. Noted the top of the Mississippian strata (Miss 13) is represented by increasing bulk density value (RHOB). The cross section was flattened on top of Woodford Shale. The core interval for each wells are represented by black bar. 65

Figure 2.4. Eight lithofacies of the Mississippian strata in the Anadarko Basin, central Oklahoma: (a) skeletal wackestone-packstone, noted the presence of abundant crinoids (yellow arrow); (b) chert - cherty breccia, noted the presence of fractures filled by quartz cement and in-

situ brecciation (red arrow); (c) structureless siltstone, noted a horizontal fracture filled by calcite cement (yellow arrow); (d) cross-laminated siltstone, noted the presence of wavy, planar, cross lamination, and possibly Bergaueria (bioturbation – yellow arrow); (e) laminated siltstone, noted many of the laminations are faded (yellow dashed lines); (f) bioturbated siltstone, noted the presence of abundant *Phycosiphon* (red arrow) and rare skeletal grain (black arrow). (g) glauconitic siltstone/sandstone, and (h) structureless sandstone, noted a vertical fracture filled by calcite cement (yellow arrow) and man-made saw marks (red arrow)..... 71

Figure 2.5. Photomicrographs of the 8 lithofacies. (a) skeletal wackestone-packstone shows the presence of peloids, sponge spicules, crinoids, brachiopod, blocky calcite cement replacing skeletal grains, and silt-size quartz grains. (b) chert – cherty breccia shows silicified matrix with rhombic dolomite crystals, calcite cement, and possible pollens and spores. (c) structureless siltstone reveals the presence of abundant angular to sub-angular silt-size quartz grains and calcite cement. (d) cross-laminated siltstone demonstrates the presence of quartz-rich and clay-rich angular lamination. (e) laminated siltstone with clay-rich and calcite-rich parallel lamination. (f) Various sizes of oncoids and aggregate grains (grapestone) floating on quartz grains. Some oncoids and aggregate grains have multiple types of nuclei including quartz grains, calcite grains, peloids, or combination of them. (g) bioturbated siltstone shows burrow filled by dark fine-grained material surrounded by silt-size quartz grains. (h) bioturbated siltstone with a spicule’s central body cavity filled by micrite and microcrystalline quartz. (i) glauconitic siltstone - sandstone shows abundant glauconite with turbid rhombic dolomite crystals. The ductile deformation of the glauconite is caused by mechanical compaction. Note the presence of abundant opaque minerals (e.g. pyrite), organic matter, and possibly oil. (j) structureless sandstone with abundant very fine sand-size quartz grains. Calcite cement has filled intergranular pores. Noted the presence of organic matter, dissolution, vacuole inclusion (black arrow) indicating boundary between detrital quartz and quartz overgrowth, and calcite cement that grading from non-ferroan calcite cement to diagenetically later ferroan calcite cement (white arrow)..... 73

Figure 2.6. North-South (A - A’) stratigraphic cross section through the Mississippian strata in the Anadarko Basin, central Oklahoma. Location of the wells used in the construction of this cross-sections are presented in Figure 1. The correlations were guided using subsurface core observation combined with gamma-ray logs in Figure 3. The black lines represent interpreted flooding surfaces (parasequence boundaries) and the red line is the datum (Woodford Shale). Noted that the lithofacies distribution within the Mississippian strata appears extremely variable laterally and vertically..... 75

Figure 2.7. Typical type of fractures associated with the Mississippian strata in the Anadarko basin, central Oklahoma. (a) vertical fracture within relatively lighter calcite-rich bed and bounded by argillaceous beds/laminae. (b) ptygmatic fractures show folded fracture grew within argillaceous bed. Noted that both fractures were filled by calcite cement (red arrow). 76

Figure 2.8. Cartoon highlighting the proposed depositional environment model (near-shore wave dominated setting) for this study. This model is interpreted based on integration of ichnotaxa, grains composition, and sedimentary structures. The 5 wells location are placed arbitrarily closed to their interpreted deposition settings (labelled as (1) The Humble Oil & Refining Company 1 Van Horn Unit, (2) Gulf Oil Corporation 1 Musselman, (3) Gulf Oil Corporation 1-23 Shaffer,

(4) Humble Oil & Refining Company 1 Lloyd L Hawkins, and (5) Petrolia Drilling Corporation 1 Payne). 80

Figure 2.9. Photomicrographs showing diagenetic features observed in the Mississippian strata of the Anadarko Basin, central Oklahoma. (a) Calcite cementation as pore filling (blue arrows). (b) Calcite rhombic crystals (black arrows) as well as rhombic dolomite crystals (red arrows) floating within microcrystalline quartz. (c) Calcite cement replacing compacted skeletal grains (possibly bivalve). (d) Blocky calcite cement filling fracture. (e) Calcite cement grading from non-ferroan cement to ferroan calcite cement (pink to purple stained color) under plane-polarized light, noted silicified rock with calcite rhombic crystal. (f) Calcite cement grading from non-ferroan cement to ferroan calcite cement (pink to purple stained color) under cross-polarized light, noted diagenetic microcrystalline quartz replacing calcite cement (yellow arrow). (g) SEM photomicrograph showing quartz overgrowth was inhibited by the presence of clay minerals. (h) Photomicrograph showing angular to sub-angular quartz grains under scanning electron microscope (SEM). (i) Photomicrograph of Cathodoluminescence analysis reveal that in fact the detrital quartz grain in the photomicrograph 9h has rounded to sub-rounded shape before quartz cementation. Noted the detrital quartz grains shape and size before quartz cementation (yellow dash line). (j) Photomicrograph showing angular to sub-angular quartz grains under scanning electron microscope (SEM). (k) Photomicrograph of Cathodoluminescence analysis reveal that in fact the detrital quartz grain in the photomicrograph 9j has sub-angular to sub-rounded shape before quartz cementation. Noted the detrital quartz grains shape and size prior to quartz cementation (yellow dash line). (l) Fractured dolomite crystal (red arrow) due to mechanical compaction. (m) Baroque (saddle) dolomite with curved-face grew in silicified rock. (n) SEM photomicrograph showing the presence of detrital dolomite (broken and pitted) and Fe-dolomite overgrowth templating the detrital dolomite. (o) Fe-dolomite replacing some precursor rhombic dolomite crystals. (p) Fe-dolomite (blueish in color) replacement of preexisting mineral or grew as cement filling intragranular pores. (q) Fe-dolomite as cement and replacement of calcite cement. Noted that diagenetic microcrystalline quartz replacing diagenetic calcite and dolomite. (r) Albite grain under SEM indicating albitization process. Noted that the albite was replaced by calcite cement in the center. (s) SEM photomicrograph showing the presence of framboidal pyrite and titanium oxide minerals. (t) A photomicrograph of Energy Dispersive X-ray (EDX) map confirming the presence of calcite cement, quartz cement, titanium oxide, and pyrite. (u) Moldic pore resulted from dissolution of probably a sponge spicule. (v) Dissolution of calcite cement and peloid. Noted the presence of poikilotopic cement. (w) Dissolution of silica (microcrystalline quartz). Noted that in the pore area (indicated by blue epoxy) some quartz remains undissolved. (x) SEM photomicrograph showing dissolution of calcite cement and resulted in the formation of micropores..... 83

Figure 2.10. Energy Dispersive X-ray spectrum of a sample (9999.9 ft) from the Gulf Oil Corporation 1 Musselman suggests the presence of Chlorite mineral as indicated by the major elements Si and Al, with a minor amount of Mg, K, and Fe. 93

Figure 2.11. Paragenetic sequence inferred for the diagenesis of the Mississippian strata in the Anadarko Basin, central Oklahoma. This analysis is based on cross-cutting relationship and in the context of temperature dependency. Glauconite and chlorite, and pyrite could be formed in the earlier stage of diagenesis at near surface under reduction condition. Quartz cementation, albitization, dolomitization, and Fe-dolomite cementation commonly associated with late

diagenesis in the deep burial setting above 60⁰C. Pyrite formation, silicification, calcite cementation, and compaction appear to take place throughout early to late stage of diagenesis. 95

Figure 2.12. Cross-plot of main composition XRD data (n = 48) such as clay, calcite, and quartz against laboratory measured porosity. (a) cross-plot of clay versus porosity. Noted that the porosity decreases as the clay content increases. (b) cross-plot shows scattered data point and lack of relationships between calcite and porosity. (c) cross-plot shows scattered quartz versus porosity data points and no simple linear relationship..... 99

Figure 2.13. Porosity and permeability cross-plot and its relationship with lithofacies and diagenesis. Good reservoir quality rocks, which have relatively higher porosity and permeability values mainly associated with structureless sandstone with minor amount of calcite cement and clay content, and have considerable dissolution (labelled as red square). Noted the presence of Fe-dolomite and quartz cements decreasing reservoir quality. Relatively poor and moderate reservoir quality rocks, which have relatively low to moderate porosity but relatively low permeability, typically associated with structureless siltstone, laminated siltstone, and bioturbated siltstone (labelled as yellow triangle, purple circle, and green square respectively) with considerable amount of clay, calcite composition, and minor to no dissolution. 102

Figure 3.1. Regional base map showing the major tectonic and basinal features of Oklahoma and Texas Panhandle (modified after Dutton, 1984; Campbell et al., 1988; McConnell et al., 1989; Northcutt and Campbell, 1995; Johnson and Luza, 2008; LoCricchio, 2012). Cored well were located on the Anadarko Basin: Humble Oil & Refining Company 1 Van Horn Unit (1), Gulf Oil Corporation 1 Musselman (2), Gulf Oil Corporation 1-23 Shaffer (3), Humble Oil & Refining Company 1 Lloyd L Hawkins (4), and Petrolia Drilling Corporation 1 Payne (5) (labelled as red dots). STACK Play area is annotated as green polygon. The modeling study area is annotated as red polygon. 112

Figure 3.2. Generalized stratigraphic summary of Mississippian strata in the Anadarko Shelf and Anadarko Basin at the north and central Oklahoma (Modified after Mazzullo, 2011; Mazzullo et al., 2011; Mazzullo et al., 2016; Stuke et al., 2018). 115

Figure 3.3. Random Forests classification schematic. This supervised classification algorithm creates a model based on a training dataset with features (gamma-ray, neutron porosity, and bulk density) and targets (rock types). The model is applied to another dataset where Random Forests will create an n number of decision trees that evaluate the data and predict a rock type based on the input data. The rock type outcomes from all of the decision trees are then counted to determine majority votes. The majority vote is used as the final rock type for that data point.. 123

Figure 3.4. A basemap showing the location of 19 wells used in a 3D modeling area (red polygon). Note all of the wells outside the red polygon were perpendicularly projected into the center of modeling area. The wells are 1). Humble Oil and Refining Company 1 Van Horn Unit. 2). Pan American 1 Effie B York. 3). OFS-Tulsa Corp 4-31 Moshe. 4). The Rodman Corporation 1 Maxwell 4. 5). Kaiser Francis Oil Company 1 State of Oklahoma. 6). Magic Circle Energy Corporation 2 Kunneman. 7). Gulf Oil Exploration and Production Company 1-14 Musselman. 8). Gulf Oil Exploration and Production Company 1-23 Shaffer. 9). BRG Petroleum LLC 1-3 Benson. 10). Humble Oil and Refining Company 1 Lloyd L Hawkins. 11). Range Production

Company 1-5 Unity. 12). L G Williams Oil Company 29-1 Girard. 13). Bristol Resources Corporation 9-1A Siegrist. 14). Mack Oil Company 3 Merveldt. 15). Andover Oil Company 7-3 Adams Park. 16). Texas Oil and Gas Corporation 1 Matthies C. 17). Western Oil and Gas Corp. 2-14 Guth. 18). Kaiser Francis Oil Company 1 Estes. 19). Petrolia Drilling Corporation 1 Payne. 126

Figure 3.5. Well-log data of Gulf Oil Exploration and Production Company 1-23 Shaffer. Track 7 – 9 show the result of dominant mineral volumes using a matrix algebra inversion method. Track 7 is the calculated volume of carbonate minerals compared with volume of carbonate measured using X-Ray Diffraction method (black dot). Track 8 is the calculated volume of quartz mineral compared with volume of quartz measured using X-Ray Diffraction method (black dot). Track 9 is the calculated volume of clay minerals compared with volume of clay minerals measured using X-Ray Diffraction method (black dot). (TVD= True Vertical Depth, GR = Gamma-Ray, RESS = shallow depth resistivity, RESM= intermediate depth resistivity, RESD = true deep resistivity, PE = photoelectric effect, RHOB = bulk density, DRHO = bulk density correction, NPHI = neutron porosity, PHIE = log-based effective porosity, Core PHIE = effective porosity measured from core plugs, SW EFF = log-based effective water saturation, CALC CARBONATE = calculated volume of carbonate minerals, XRD CARBONATE = volume of carbonate minerals measured using XRD, CALC QUARTZ = calculated volume of quartz minerals, XRD QUARTZ = volume of quartz mineral measured using XRD, CALC CLAY = calculated volume of clay minerals, XRD CLAYS = volume of clay minerals measured using XRD). 129

Figure 3.6. Comparison of mineral volumes obtained from XRD measurement and log-derived using matrix algebra inversion method in the Gulf Oil Exploration and Production Company 1-23 Shaffer well. a). Comparison of carbonate mineral volume obtained from XRD measurement and log-derived. b). Comparison of clay mineral volume obtained by XRD measurement and log-derived. c) Comparison of quartz mineral volume obtained from XRD measurement and log-derived. Note all three comparisons showing R^2 values of ~ 0.7 suggesting a relatively good predictive accuracy. 131

Figure 3.7. An elbow method showing the optimum clusters of 3 at a point where the sum of square between (SSB - blue line) intersect with the sum of square within (SSW - red line). SSW refers to the variance between data points in the same cluster and SSB line refers to the variance between data points of different clusters. 133

Figure 3.8. Boxplots showing the result summary of K-means clustering based on mineral volumes and effective porosity as the input. a). A boxplot showing statistical measures of volume carbonate minerals for 3 clusters. b). A boxplot showing statistical measures of volume of quartz mineral for 3 clusters. c). A boxplot showing statistical measures of volume of clays minerals for 3 clusters. d). A boxplot showing statistical measures of effective porosity for 3 clusters. Each cluster represent 1 rock type. Noted that rock type 1 has relatively moderate clays, quartz, carbonates contents, and lower effective porosity (<2 %). Rock type 2 has relatively higher quartz, moderate carbonates and clays contents, and higher effective porosity (4% – 7%). Rock type 3 has relatively higher percentage of carbonates, lower clays and quartz contents, and moderate effective porosity (2% – 4%). In terms of reservoir quality, rock type 1 is the worst

reservoir rocks and rock type 2 is the best reservoir rocks with high storage capacity and brittleness. 134

Figure 3.9. a) A stratigraphic cross-section of Mississippian strata from northwest (A) to southeast (A') with proportionally spaced gamma-ray log (2nd track). The cross-section was flattened at Woodford Shale (datum) and displayed with 1:600 ft scale. The cross section shows that the Mississippian strata in the study area of Anadarko Basin has at least 13 parasequences (represented by colors) that were bounded by flooding surfaces picked based on gamma-ray log responses.. The cross-section shows that the Mississippian strata thins to the southeast. Noted the rock types of each wells are plotted in track 3. Four wells (Humble Oil and Refining Company 1 Van Horn Unit, Pan American 1 Effie B York, and Humble Oil and Refining Company 1 Lloyd L Hawkins) have incomplete dataset to predict rock type. Track 1 is depth, track 2 is gamma-ray log, track 3 is rock type, track 4 is core interval (black bar), and track 5 is parasequences. b). A stratigraphic cross section of Mississippian strata from northwest (A) to south east (A') showing the interpreted systems tract that correlate to intermediate sea-level changes. The parasequence Miss 1 to Miss 7 represent highstand systems tract. Parasequence Miss 8 represent a lowstand systems tract deposit, parasequence Miss 9 to Miss 10 are interpreted to be transgressive systems tract, parasequence Miss 11 and Miss 12 correlate to highstand systems tract, and finally parasequence Miss 13 is a lowstand systems tract..... 138

Figure 3.10. Biozones based on study of conodonts from Pan American D-2 Barnes Unit well that is located at Major County. The Biozones were associated to the well's gamma-ray log and correlated to Pan American 1 Effie B York well that is used in this study. The correlation shows the Mississippian strata in the study area is Meramecian in age. (Modified from Stukey et al., 2018). 139

Figure 3.11. a). Interpreted systems tract of the Mississippian strata. Parasequence Miss 1 through Miss 7 were interpreted as highstand systems tract. Parasequence Miss 8 represented a lowstand systems tract deposits. Parasequences Miss 9 and 10 were part of transgressive systems tract. The subsequence Miss 11 and 12 were interpreted as highstand systems tract, and the uppermost parasequence Miss 13 represented another lowstand systems tract. b). Core photo showing a brecciated chert lithofacies associated with subaerial exposure (sequence boundary) in the updip well. c). Core photo showing a platy black shale interval associated with a condensed section (maximum flooding surface) in the updip well. d). Core photo showing a blocky black shale associated with a condensed section in a deeper water well. Noted the moderate amount of skeletal grains, probably reworked from shallow water deposits. E). Core photo showing an erosional surface associated with abrupt landward lithofacies shift (a channel eroded into deeper water bioturbated siltstone lithofacies) at the basin margin well (east of the Anadarko Basin). Noted the presence of possible boring features at the erosional surface. F). Core photo showing glauconitic siltstone to sandstone that associated with sequence boundary between parasequence Miss 12 and Miss 13 that occurs at a basin margin well (southeast of the Anadarko Basin). LST = Lowstand Systems Tract, TST = Transgressive Systems Tract, and HST = Highstand Systems Tract, SB = Sequence Boundary, TS = Transgressive Surface, MFS = Maximum Flooding Surface. Noted the threefold order cycles are shown at L G Williams Oil Company 29-1 Girard well (high order), Range Production Company 1-5 Unity well (intermediate order), and Humble Oil and Refining Company 2 Lloyd L Hawkins (low order). Blue triangle represents transgression and green triangle represents regression)..... 142

Figure 3.12. A dip-oriented models flattened on top of Woodford Shale. The models were displayed with 125X vertical exaggeration. Both cored and un-cored wells were displayed along the cross-section of the model. a). Zones index model showing the stratigraphic zones through which rock types, effective porosity, and effective water saturations were modeled within. The zones were defined by the parasequences of Miss 1 through Miss 13 that were picked using gamma-ray log. The threefold stratigraphy order (low, intermediate, and high orders) as indicated by transgression and regression arrow b). A zone model populated with rock types showing Miss 1 - 8 has predominantly carbonate-rich rock type 3 ranging from 55% - 91%, Miss 9 – 12 are richer in clay-rich rock type 1 ranging from 43% – 52%, and Miss 13 has 77% of clay-rich rock type 1. Noted that the interval suggests an overall deepening-upward with the increase of clay-rich rock type 1 and decrease of carbonate rich-rock type 3. 146

Figure 3.13. A dip-oriented models flattened on top of Woodford Shale. The models were displayed with 125X vertical exaggeration. Both cored and un-cored wells were displayed along the cross-section of the model. a). A total porosity model shows the increase of total porosity upward following the increase of clay-rich rock type 1. b). An effective porosity model shows indeterminate relationship between effective porosity distribution within parasequences. c) A total water saturation model show that total water saturation decreases along with the carbonate-rich rock type 3 from parasequence Miss 1 to Miss 6. total water saturation is relatively high in the parasequence Miss 7 to Miss 8 during the late highstand systems tract and lowstand systems tract following the increase of clay-rich rock type 1, moderate in parasequence Miss 10 and Miss 11, and relatively high in the parasequence Miss 12 and Miss 13 following the increase of clay-rich rock type 1 (early highstand systems tract and lowstand system tract). Noted that the total porosity and total water saturation typically increase with the increase of clay-rich rock type 1. This is most likely associated with the clay-bound-water (CBW) 148

LIST OF TABLES

Table 1.1. Summary of key characteristics that distinguish each identified lithofacies in the core used in this study.....	25
Table 1.2. Summary of data obtained from digital-image analysis and laboratory measured properties including porosity and permeability for all 57 samples in the Mississippian interval of the Devon Energy 1-7 SWD Frieouf well.....	29
Table 1.3. Pore types identified in 12 lithofacies that have their thin section and SEM photomicrographs available in this study.	31
Table 2.1. Summary of key characteristics that distinguish each identified lithofacies in the core used in this study.....	68
Table 2.2. XRD data of the Mississippian strata from 5 cored wells.	87
Table 3.1. Summary of available well data.....	118
Table 3.2. The confusion matrices of Random Forests classification for testing dataset.	136
Table 3.3. Rock type percentage per stratigraphic zones.....	149

ABSTRACT

The Mississippian strata have been a long sought-after reservoir objective in Oklahoma. These reservoirs have produced several million barrels of oil since early in the 20th century. Despite hundreds of thousands of wells have been drilled into these reservoirs throughout the state of Oklahoma, their stratigraphy and fundamental controls on reservoir quality and occurrence have remain elusive and enigmatic. Studies, documented in this dissertation, have resulted in the generation of lithofacies variations, depositional environment, and sequence-stratigraphic models that are applicable to the exploration of these reservoirs.

Study of Mississippian strata in the Mississippian Limestone play area reveals the presence of 17 lithofacies and 29 high-frequency cycles. The lithofacies are predominantly skeletal-rich limestones. The good reservoir quality is typically associated with the upper intervals of these high-frequency shallowing-upward cycles. Pore characterization using digital-image analysis of 58 thin-sections photomicrographs exhibits unique correlations among core porosity, permeability, and lithofacies within a sequence-stratigraphic framework. These correlations are: 1). porosity from digital-image analysis (DIA) and laboratory core measurements has a strong positive relationship ($R^2 = 0.94$). However, some values from DIA porosity yield relatively higher values, specifically in fine-grained lithofacies. The difference is due to the present of isolated nanopores that are not accessible by helium during measurement of core porosity. 2). The relationship between pore circularity and permeability is indeterminate. The indeterminate relationship is related to a complex internal pore network, intensive diagenetic alteration, an unconnected microfracture network, and isolated pores. 3). Coarse-grained lithofacies within the uppermost depositional sequence of the Mississippian interval have a

heterogeneous pore-size distribution while fine-grained lithofacies tend to exhibit a homogenous pore-size distribution.

In the STACK Play area, eastern Anadarko Basin of central Oklahoma, the Mississippian strata consists of 8 lithofacies and are dominated by detrital-rich lithofacies. Study on 5 cores (260 m; 850 ft) suggests these lithofacies were deposited in wave-dominated nearshore with a restricted embayment (lagoon) and channels or lobes. Analysis of 34 thin sections indicates the lithofacies have undergone diagenetic alteration including calcite cementation, mechanical compaction, albitization, quartz cementation, silicification, dolomitization, Fe-dolomite cementation, pyritization, and dissolution. A paragenesis scheme suggests that quartz cementation occurred earlier compared to albitization and Fe-dolomite cementation. The Fe-dolomite is the latest authigenic mineral formed whereas the quartz and calcite cement can be attributed to earlier diagenesis. The reservoir quality is significantly reduced by compaction, calcite and quartz cements, as well as amount of clay minerals. However, the dissolution of cement and detrital grains tends to improve reservoir quality by forming secondary pores.

The 8 lithofacies in the STACK play area can be grouped into 3 rock types based on their dominant minerals composition. Rock type 1 is characterized by relatively moderate clay (22% - 39%), quartz (26% - 43%), and carbonate (25% - 47%) contents and lower effective porosity (<2%). Rock type 2 has relatively higher quartz (43% - 48%), moderate carbonate (20% - 45%) and clay (6% - 18%) contents and higher effective porosity (4% - 7%). Rock type 3 has relatively higher percentage of carbonates (61% - 85%), lower clay (<11%) and quartz (8% - 30%) contents and moderate effective porosity (2% - 4%). In terms of reservoir quality, rock type 2 is the best reservoir rocks with high storage capacity and brittleness.

Stratigraphically, The Mississippian strata of the STACK play area consist of 1 low stratigraphic order with overall upward-deepening profile. The intermediate stratigraphic order correlates to multiple depositional episodes consisting of lowstand-, transgressive-, and highstand systems tract. Clay-rich rock type 1 typically increases during late highstand systems tract and lowstand system tract and quartz-rich rock type 2 typically increases during transgressive systems tract and early highstand systems tract. The higher stratigraphic order exhibits an ideal upward-shallowing succession within parasequences that consists of bioturbated siltstone, laminated-siltstone, structureless siltstone, and cross-laminated siltstone. Proximally, individual cycles are often capped by skeletal wackestone-packstone. A sequence boundary is characterized by a subaerial exposure with brecciated chert or an erosional surface; and glauconitic siltstone-sandstone is typically present atop of this boundary.

The threefold (low, intermediate, and high) stratigraphic orders combined with a dip-oriented 3D model indicate that the reservoir sweet spots containing higher percentage of quartz-rich rock type 2 occur during deepening in the transgressive and highstand systems tract (parasequence Miss 9 to Miss 12). These stratigraphic orders provide a predictive framework that aids in reservoir characterization for optimal development of the Mississippian reservoirs.

This manuscript was published at Journal of Interpretation, on November 2018:

Fnu Suriamin and Matthew J. Pranter, 2018, Stratigraphic and lithofacies control on pore characteristics of Mississippian limestone and chert reservoirs of north-central Oklahoma: Interpretation, 6 – 4, T1001–T1022. doi: <https://doi.org/10.1190/INT-2017-0204.1>

**1. STRATIGRAPHIC AND LITHOFACIES CONTROL ON PORE
CHARACTERISTICS OF MISSISSIPPIAN LIMESTONE AND CHERT RESERVOIRS
OF NORTH-CENTRAL OKLAHOMA**

ABSTRACT

This study shows how stratigraphic and lithofacies control pore structures in the Mississippian limestone and chert reservoir of north-central Oklahoma. There are 17 lithofacies and 29 high-frequency cycles documented in the Mississippian interval of this study. The high-frequency cycles have thickness ranging from 1-100 ft (0.3-30.5 m) and are mainly asymmetric regressive phases.

The pore characteristics, measured through digital-image analysis of thin-sections photomicrographs (N>3,100), exhibit unique correlations with core porosity, permeability, and lithofacies within a sequence-stratigraphic framework. There are five fundamental correlations observed. First, porosity from digital-image analysis (DIA) and laboratory core measurements has a strong positive relationship ($R^2 = 0.94$). However, some values from DIA porosity yield relatively higher values, specifically in spiculitic mudstone-wackestones and argillaceous spiculitic mudstone-wackestones. The difference is hypothesized due to the present of isolated nanopores that are not accessible by helium during measurement of core porosity. Second, the relationship between pore circularity and permeability is indeterminate. The indeterminate relationship is related to a complex internal pore network, intensive diagenetic alteration, an unconnected microfracture network, and isolated pores. Third, positive moderate to strong correlations ($R^2 = 0.46$ to 0.85) between porosity and permeability are observed only in 4 lithofacies. Fourth, coarse-grained lithofacies within the uppermost depositional sequence of the

Mississippian interval have a heterogeneous pore-size distribution while fine-grained lithofacies tend to exhibit a homogenous pore-size distribution. Fifth, higher reservoir quality is associated with the upper intervals of high-frequency shallowing-upward cycles. This confirms the sequence-stratigraphic variability of lithofacies is important to predict reservoir quality and its distribution.

An alternative graphical method of pore-size distribution is also developed. To be a useful “technique”, examples of the plot were demonstrated using samples in this study. The plot successfully provides simple identification of pore-size classes, quantitative percentage of pore-size class, dominant pore class, and approximate minimum and maximum pore size.

INTRODUCTION

Mississippian limestone and chert deposits of the Mid-continent form important petroleum reservoirs despite their generally low porosity (<10 %), low permeability (< 1 mD), and highly variable pore systems. The limestone and chert reservoirs have been informally referred to as the “Mississippi Lime” or “Mississippi Chat”. The chert-rich intervals were coined “chat” by drillers because of the chattering noise and bit-bounce during drilling (Rogers, 2001). As described herein, the Mississippian Limestone refers to the Mississippian-age limestone and chert deposits that are present above the Woodford Shale.

Previous research on the Mississippian Limestone of the U.S. Mid-continent has focused on carbonate sequences and architecture (Fritz and Medlock, 1994; Mazzullo et al., 2013; Wittman, 2013; Price, 2014; Leblanc, 2014; Childress and Grammer 2015; Mazzullo et al., 2016; Jaeckel, 2016; Wethington, 2017), structural features (Gay, 2003), reservoir characteristics (Parham and Northcutt, 1993; Rogers et al., 1995; Montgomery et al., 1998; Watney et al., 2001;

Franseen, 2006; Mazzullo et al., 2009; Costello et al., 2014; Turnini, 2015; Lindzey et al. 2017; Turnini et al., 2017), deposition and diagenesis of chert deposits (Rogers, 2001), and pore characteristics (Vanden Berg and Grammer, 2016). Vanden Berg and Grammer (2016) show there is a positive correlation between porosity and permeability in carbonate mudrocks, similar to those observed in conventional carbonates. However, they found no clear relationship between pore shape and laboratory-measured porosity or permeability (Vanden Berg and Grammer, 2016). This is possibly due to the complex pore architecture, extensive diagenetic alterations, and the presence of a multiscale fracture network. However, for various carbonate deposits in general, several studies have illustrated how digital-image analysis is a useful approach for characterize carbonate pores and predict petrophysical properties (Anselmetti et al., 1998; Bauget et al., 2005; Al-Kharusi, 2007; Sok et al., 2009; Norbistrath et al., 2015). The studies document a predicable correlation between pore-scale structure and petrophysical properties, especially permeability.

To investigate this further for the Mississippian Limestone, using core and well-log data, pore parameters including circularity and pore-size distribution as well as porosity and permeability are related to lithofacies. This study provides an example of how lithofacies, reservoir quality, and pore characteristics can vary within the Mississippian Limestone sequence-stratigraphic framework. Moreover, this study proposes an improved method to plot pore-size distribution to 1) identify dominant pore-size classes, 2) investigate pore-size contribution or percentage to pore volume, and 3) compare pore-size distribution by samples or lithofacies.

The study focuses on the Devon Energy 1-7 SWD Frieouf well in Grant County, Oklahoma on the western side of the Nemaha uplift (Figure 1.1). The cored well was selected because of the relatively thick interval of Mississippian strata (527 ft; 160 m) that consist of

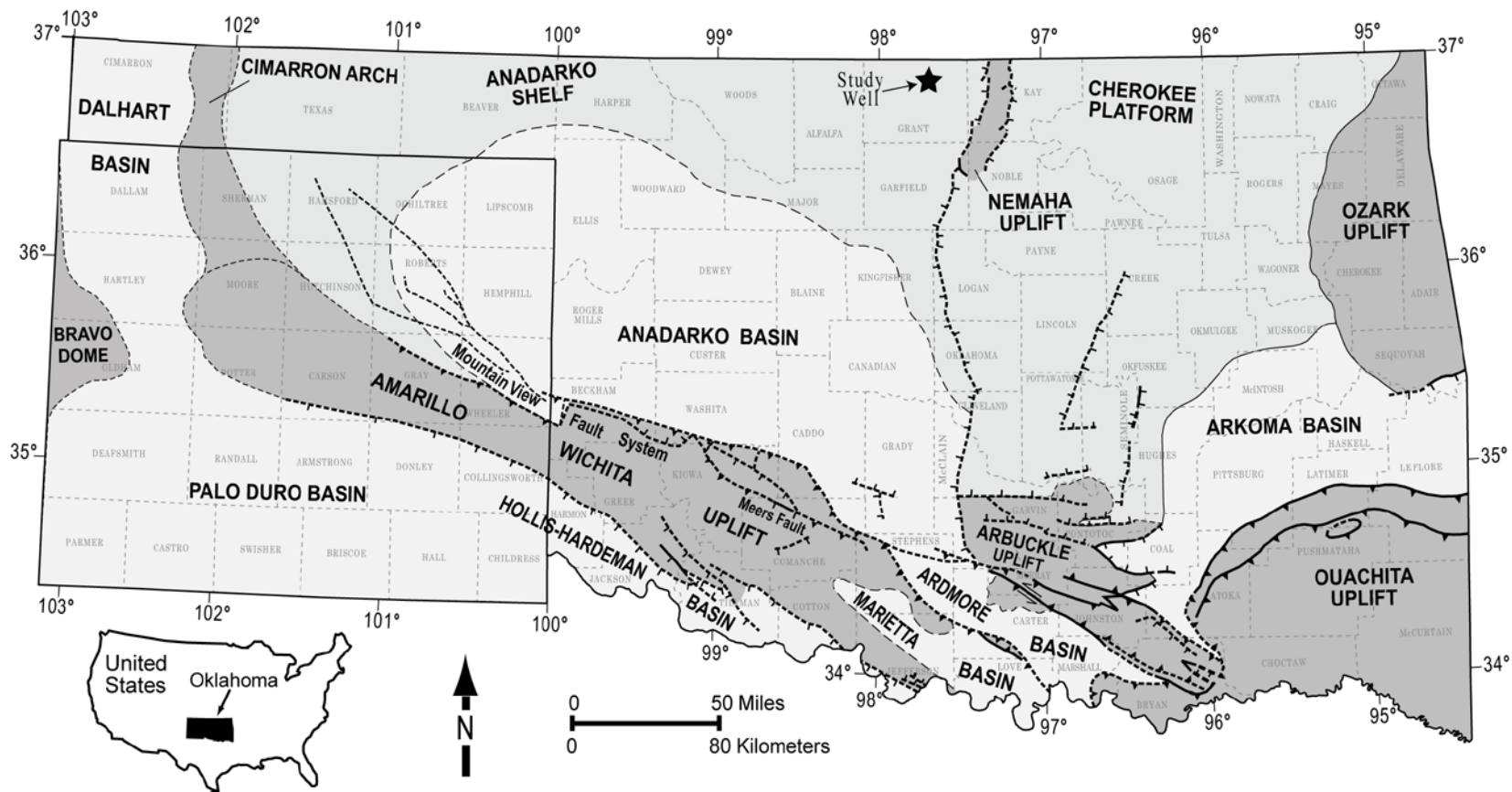


Figure 1.1. Regional base map showing the major tectonic and basinal features of Oklahoma and northwestern part of Texas (modified after Dutton, 1984; Campbell et al., 1988; McConnell, et al. 1989; Northcutt and Campbell, 1995; Johnson and Luza, 2008; LoCricchio, 2012). The Devon Energy 1-7 SWD Frieouf well (star) is located on the Anadarko Shelf and on the western side of the Nemaha uplift.

high-energy grainstones to low-energy mudstones with pores ranging in size from macro- to nanopores. This study provides an example of Mississippian lithofacies and pore types from north-central Oklahoma and serves as an analog to investigate Mississippian reservoirs that have similar pore characteristics including pore dimensions across several orders of magnitude.

GEOLOGICAL SETTING

During the Mississippian Period, the North America Mid-continent was occupied by a shallow, tropical, epeiric sea with a broad carbonate platform ([Gutschick and Sandberg, 1983](#)). The period represents a transitional time from the greenhouse to icehouse conditions with associated deposits that reflect an overall regression during this span of time ([Buggisch et al., 2008](#); [Haq and Schutter, 2008](#)). The Mississippian Limestone of the Mid-continent was deposited as a series of high-frequency transgressive-regressive, shallowing-upward cycles ([Watney et al., 2001](#); [Mazzullo et al., 2009](#)).

The core used in this study was deposited on the Anadarko Shelf located 10 - 15° south of the paleoequator in the Early Mississippian Period (~359-347 Ma) ([Gutschick and Sandberg, 1983](#); [Blakey, 2013](#)). [Lane and DeKeyser \(1980\)](#) and [Gutschick and Sandberg \(1983\)](#) conclude that the Mississippian strata were deposited on a carbonate shelf. Additionally, [Gutschick and Sandberg \(1983\)](#) suggest that the depositional conditions along the Anadarko shelf south and west of the Ozark Uplift, produced a gentle foreslope with an undefined shelf edge.

The Mississippian strata at the base of the Pennsylvanian become younger in a southwestward and westward direction away from Central Kansas and Nemaha uplifts, respectively ([Nissen et al., 2004](#); [Franseen, 2006](#)). Uplift resulted in subaerial exposure and extensive erosion of the Mississippian rocks forms a regional unconformity that separates the

Mississippian strata from the overlying Pennsylvanian rocks ([Parham and Northcutt, 1993](#); [Rogers, 2001](#); [Nissen et al., 2004](#); [Franseen 2006](#)).

Mississippian strata in Oklahoma comprise several groups and members including, from oldest to youngest, the Kinderhookian Shale, St. Joe Group, Reeds Spring Limestone, Pineville Tripolite, Bentonville Limestone, Cowley Formation, Ritchey Limestone, and undivided Meramecian unit ([Figure 1.2](#)) ([Mazzullo 2011](#); [Mazzullo et al., 2011](#); [Mazzullo et al., 2016](#)). The St. Joe Group is Kinderhookian - Osagean in age and lies conformably on the Kinderhookian Shale. The St. Joe Group is subdivided, in ascending order, into the Compton Limestone, Northview Formation, and Pierson Limestone. The upper St. Joe Group has a conformable contact with the Bentonville Limestone and is conformable to unconformable with the Reeds Spring Limestone depending on location.

The Osagean Reeds Spring and Bentonville Limestones are coeval shelf and slope deposits with distinct lithologic characters. The Reeds Spring Limestone is conformably capped by the bioturbated or brecciated Pineville Tripolite. In contrast, the Bentonville Limestone is unconformably overlain by the Cowley Formation. The Cowley Formation, early Meramecian in age, is strictly a subsurface unit with spicule-rich shale and bedded spiculites. [Mazzullo et al. \(2009\)](#) suggests that the Cowley Formation represents a time when the carbonate factory of the Anadarko shelf was suppressed due to silica poisoning of sea water and upwelling within a geographically restricted area.

In an ideal scenario, the Osagean limestones (the Reeds Spring, Pineville Tripolite, and Bentonville) are overlain by the Cowley Formation. However, [Mazzullo et al. \(2016\)](#) interpreted that the Osagean limestones, particularly in Grant County, Oklahoma, have been completely eroded due to Kanoka Ridge uplift during the late Osagean stage. Therefore, the Osagean

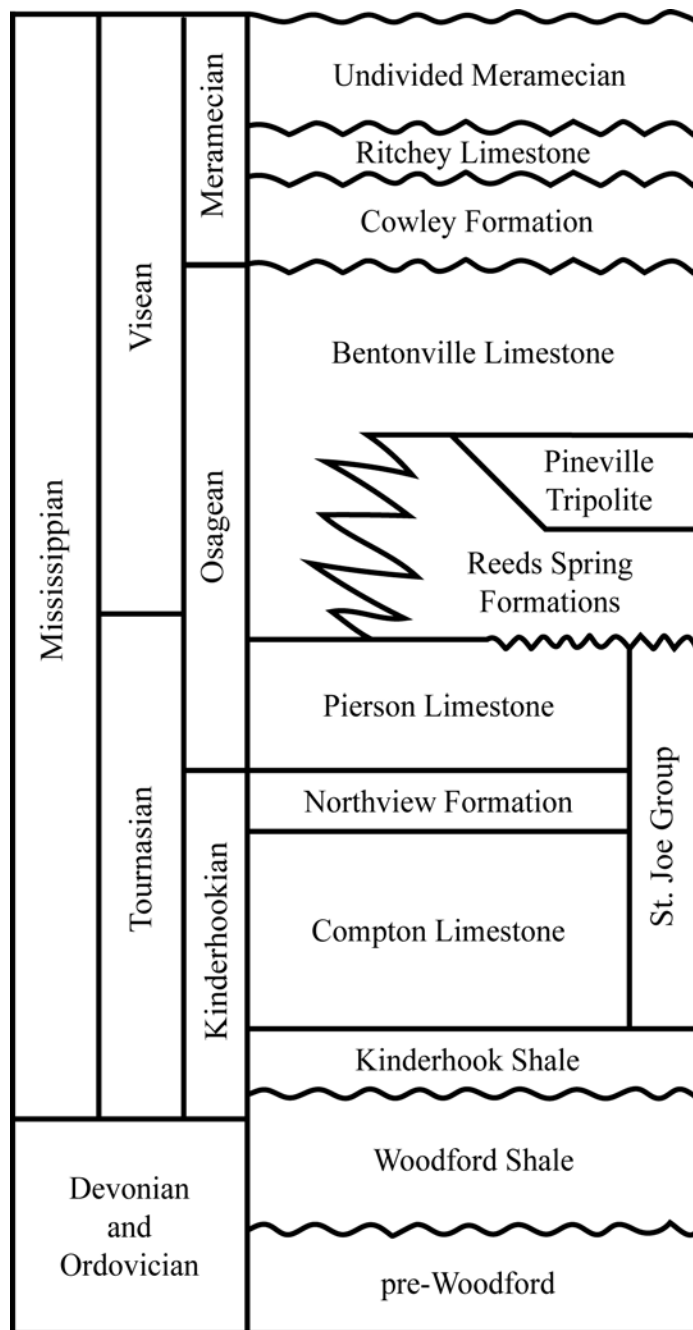


Figure 1.2. Stratigraphic column for the Ordovician to Mississippian-age deposits in the north-central Oklahoma. (Modified after [Mazzullo, 2011](#); [Mazzullo et al., 2011](#); [Mazzullo et al., 2016](#)).

limestones are not present in this study area, and the Cowley Formation is bounded unconformably by the underlying St. Joe Group and overlying undivided Meramecian or possibly Ritchey Limestone (Mazzullo et al., 2016). The Ritchey Limestone is predominantly light-colored cherty limestone with some dolomite and dolomitic limestone (Mazzullo et al., 2016). These limestones are mainly undivided and their formal formational subdivisions are not recognized in the subsurface of north-central Oklahoma.

METHODOLOGY

Lithofacies and sequence-stratigraphic framework

Lithofacies were identified from visual observation of (527 ft; 160 m) of slabbed core and associated thin sections (N = 57). Lithofacies were defined following the Dunham classification (Dunham, 1962) based on differences in composition, texture, and bioturbation. Lithofacies color was determined using a Munsell rock-color chart (Munsell, 2009). Level of bioturbation was estimated using the bioturbation index proposed by Miller and Smail (1997) with values ranging from 1 to 6; where level 1 indicates no visible bioturbation, and level 6 indicated completely homogenized beds.

Due to the lack of biostratigraphic data, the sequence-stratigraphic analysis is solely based on the vertical succession of lithofacies and recognition of key stratigraphic surfaces. Lithofacies are assigned to their relative spatial distribution using a generic depositional model. The model was used to develop an idealized vertical stacking pattern and to establish the sequence-stratigraphic framework.

Pore-architecture characterization

Digital-image analysis provides quantitative characteristics of pore parameters identified using color segmentation of thin-section and SEM photomicrographs (Anselmetti et al., 1998). Fifty-seven (57) thin sections were made from their core plugs. Photomicrographs of whole thin sections were acquired using a QImaging Retiga 2000R camera mounted on an Olympus BX41 Optical Microscope with 10x magnification to capture pores ranging from macropores ($4 \text{ mm} < \text{Pore Width} < 256 \text{ mm}$) to mesopores ($62.5 \text{ }\mu\text{m} < \text{Pore Width} < 4 \text{ mm}$). To image pores ranging from micropores ($1 \text{ }\mu\text{m} < \text{Pore Width} < 62.5 \text{ }\mu\text{m}$) to nanopores ($1 \text{ nm} < \text{Pore Width} < 1\mu\text{m}$), thin sections were placed under an electron beam in a FEI Quanta 250 field-emission scanning electron microscope for analysis and SEM photomicrographs acquisition. The SEM photomicrographs were obtained from 6 - 8 random areas for each sample to reduce sampling bias. More than 3,000 SEM images were captured from the 57 thin sections. The thin sections and SEM photomicrographs are shown in [Appendix A](#).

The Optical Microscope and SEM photomicrographs were segmented with a color or gray-intensity-threshold technique to differentiate matrix (the solid) and pore using a standard image-analysis software (JMicroVision). The software requires the appropriate blue-color threshold to represent blue-epoxy-filled pore space and a pixel-size limit for scaling. Single pixel size ($1 \text{ pixel} = 1.4814 \text{ }\mu\text{m}$; $\sim 5.83 \times 10^{-5} \text{ in}$) was applied to all Optical Microscope photomicrographs based on 10x magnification. In contrast, a gray-intensity threshold with black pixels representing pore space and various pixel sizes were used for SEM photomicrographs depending on the magnification.

The segmented pores in each photomicrograph were measured for their pore parameters and classified into pore-size classes. The measured pore parameters include pore area, perimeter,

length, and width (Figure 1.3). The pore area is calculated as the sum of the areas of individual pixels within the pore boundary. The pore perimeter is the total length of the pore boundary. The length and width of a pore are the maximum distance between any two points on the pore perimeter parallel to the major axis and minor axis respectively. Circularity is calculated separately. Davis (1986) and Olson (2011) defines circularity (C) as the degree to which the pore is like a circle and calculates it as:

$$C = \sqrt{\frac{4\pi A}{P^2}} \quad (1)$$

Where C = Circularity (dimensionless)

A = Area (L²)

P = Perimeter (L)

Circularity ranges from 0 for an elongate pore and 1 for a perfectly circular pore. Anselmetti et al. (1998) showed that pore shape, in this study, called circularity, in conventional carbonates has a strong relationship with pore connectivity (permeability). In general, rocks with more elongate (circularity near 0) pores tend to have higher permeability than rocks with circular pores (circularity near 1).

Pore size is a key parameter for determining pore characteristics in a rock sample. In this study, the pores measured from each photomicrograph were classified into macro-, meso-, micro-, nano-, and picopore based on their pore width following pore-size classification for mudrock proposed by Loucks et al. (2012) (Figure 1.4).

Two-dimensional (2D) pore morphology (e.g., interparticle, intraparticle, and moldic) was also described based on visual observation from Optical Microscope and SEM

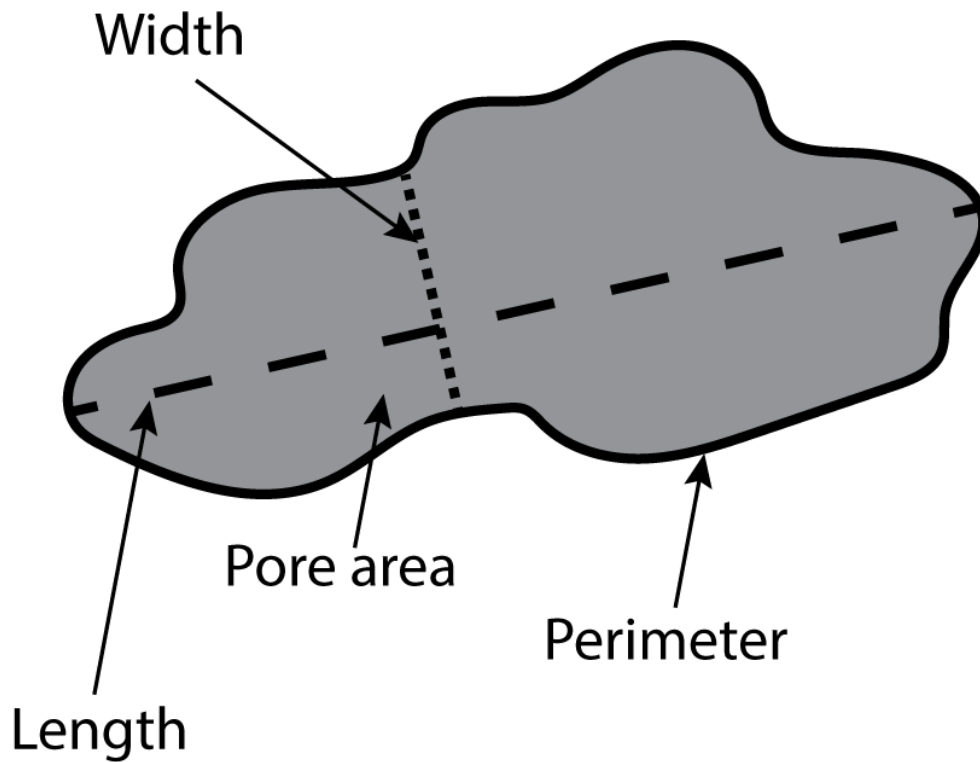


Figure 1.3. A schematic illustration of a pore showing measured pore parameters. The measured parameters include pore area (shaded gray area), perimeter (black solid line), length (black dashed line), and width (black dotted line). The pore area is calculated as the sum of the areas of each individual pixel within the borders of the pore. The pore perimeter is the total length of the pore boundary. The length and width of a pore are the maximum distance between any two points on the perimeter of the pore parallel to the major axis and minor axis, respectively.

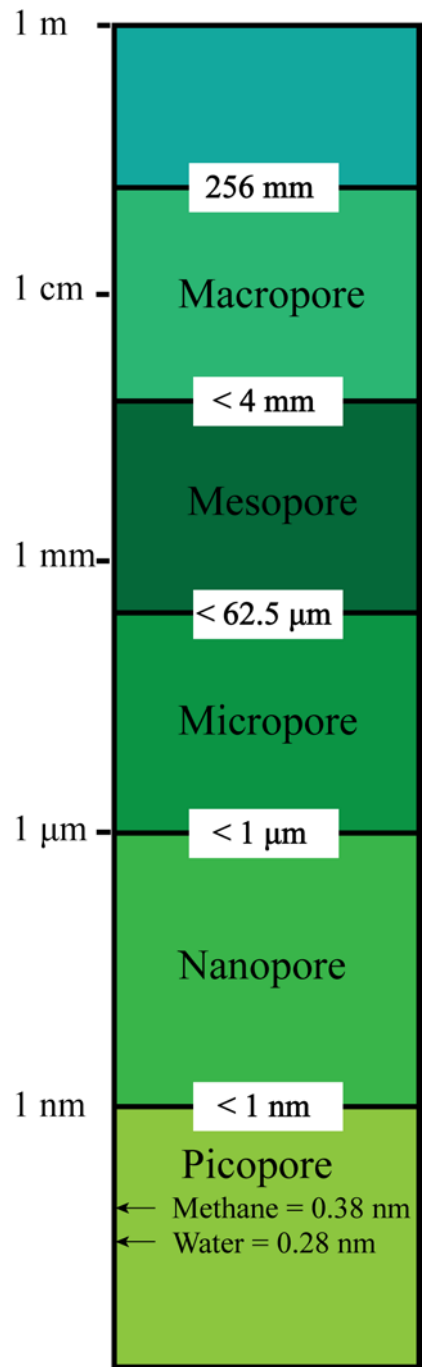


Figure 1.4. Pore-size classification used in this study. The classification is based on pore width following Loucks (2012) pore-size classification for mudrock.

photomicrographs. This visual observation is an attempt to build a catalogue of pore types observed in the Mid-continent Mississippian Limestone.

RESULTS AND DISCUSSION

Lithofacies and sequence-stratigraphic framework

Seventeen lithofacies (Figures 1.5-1.8) were identified based on their grain types, texture, and bioturbation (Table 1.1). Based on the vertical succession of lithofacies, the interval consists of 29 relatively high-frequency cycles that are 1 to 100 ft (0.3 to 30.5 m) thick (Figure 1.9), and 24 of 29 cycles are asymmetric with thicker regressive phases than transgressive phases. The relatively high-frequency cycles stack to form three lower order depositional sequences (Figures 1.9 - 1.10) that are bounded by erosional surfaces, intervals of brecciated lithofacies, or both. The sequence-stratigraphic framework of the Mississippian interval was established by using the interpreted idealized vertical stacking of lithofacies. The exact time intervals (orders) for the sequence-stratigraphic framework cannot be determined because biostratigraphic data are not available.

Sequence 1 contains approximately 22 ft (6.7 m) of shale (lithofacies 16) and 38 ft (~12 m) of shaly claystone (lithofacies 17) (Figure 1.9). The basal sequence boundary was not observed in core. It is interpreted as the contact with the underlying Woodford Shale and exhibits a relatively high gamma-ray response (>150 API). The upper boundary of sequence 1 is an erosional surface (Figure 1.11A).

Sequence 2 has a total thickness of 268 ft (~81 m) and consists of glauconitic sandstone (lithofacies 15), argillaceous spiculitic mudstone-wackestone (lithofacies 14), spiculitic mudstone-wackestone (lithofacies 13), intraclast spiculitic mudstone (lithofacies 12), and

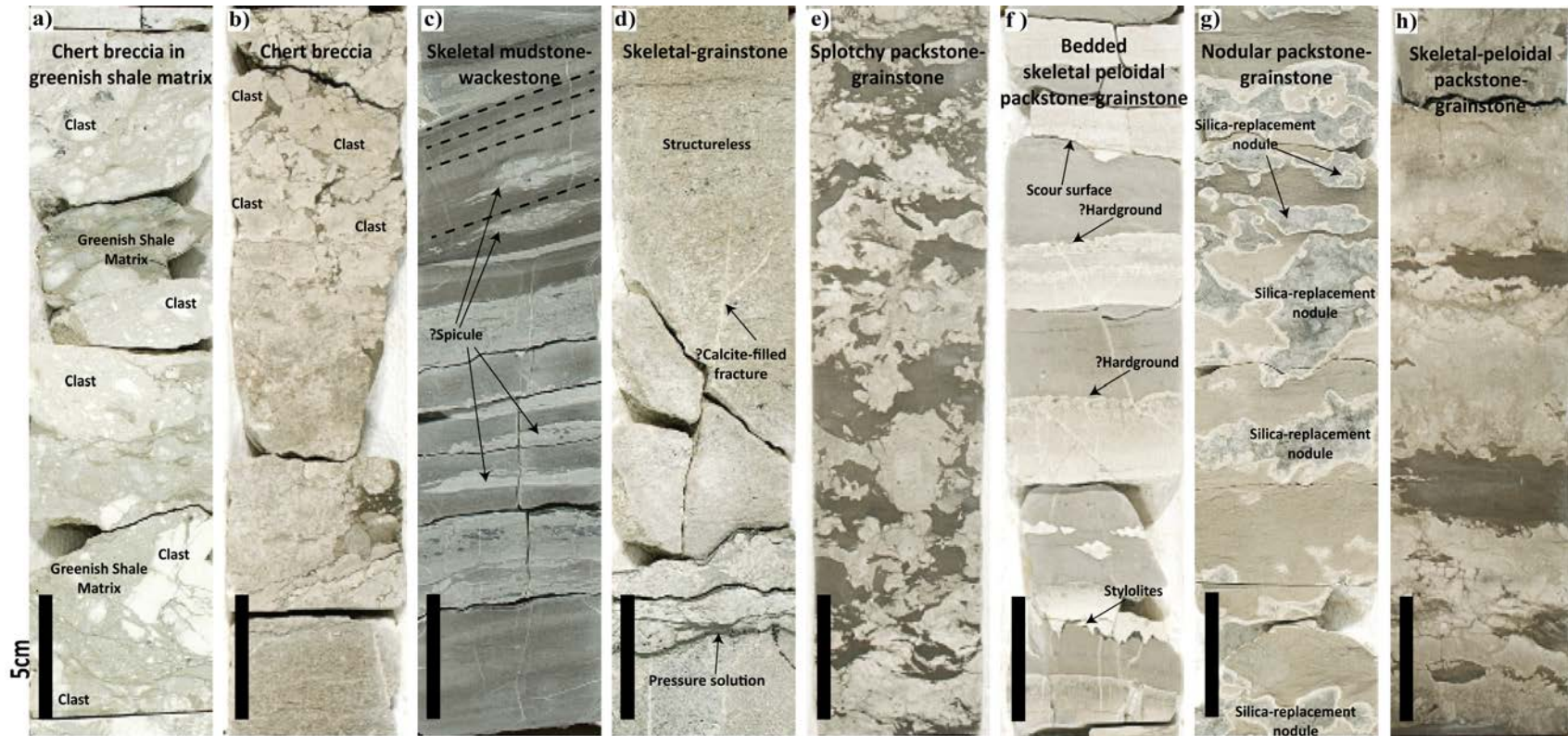


Figure 1.5. Photographs of core-based lithofacies in the Mississippian interval of Devon Energy 1-7 SWD Frieouf well. a) Chert breccia in greenish shale matrix. b) Chert breccia showing severely compacted clasts. c) Skeletal mudstone-wackestone showing lenticular/flaser features (possibly spicule) and cross bedding. d) Skeletal grainstone. Note the presence of fracture filled by possibly calcite and pressure solution feature. e) Splotchy packstone-grainstone. f) Bedded skeletal packstone-grainstone. Note the presence of scour surface, stylolite, and possibly hardgrounds. g) Nodular packstone-grainstone showing common silica-replacement nodules. Note the nodule shapes are irregular. h) Skeletal peloidal packstone-grainstone. Scale Bar = 5 cm.

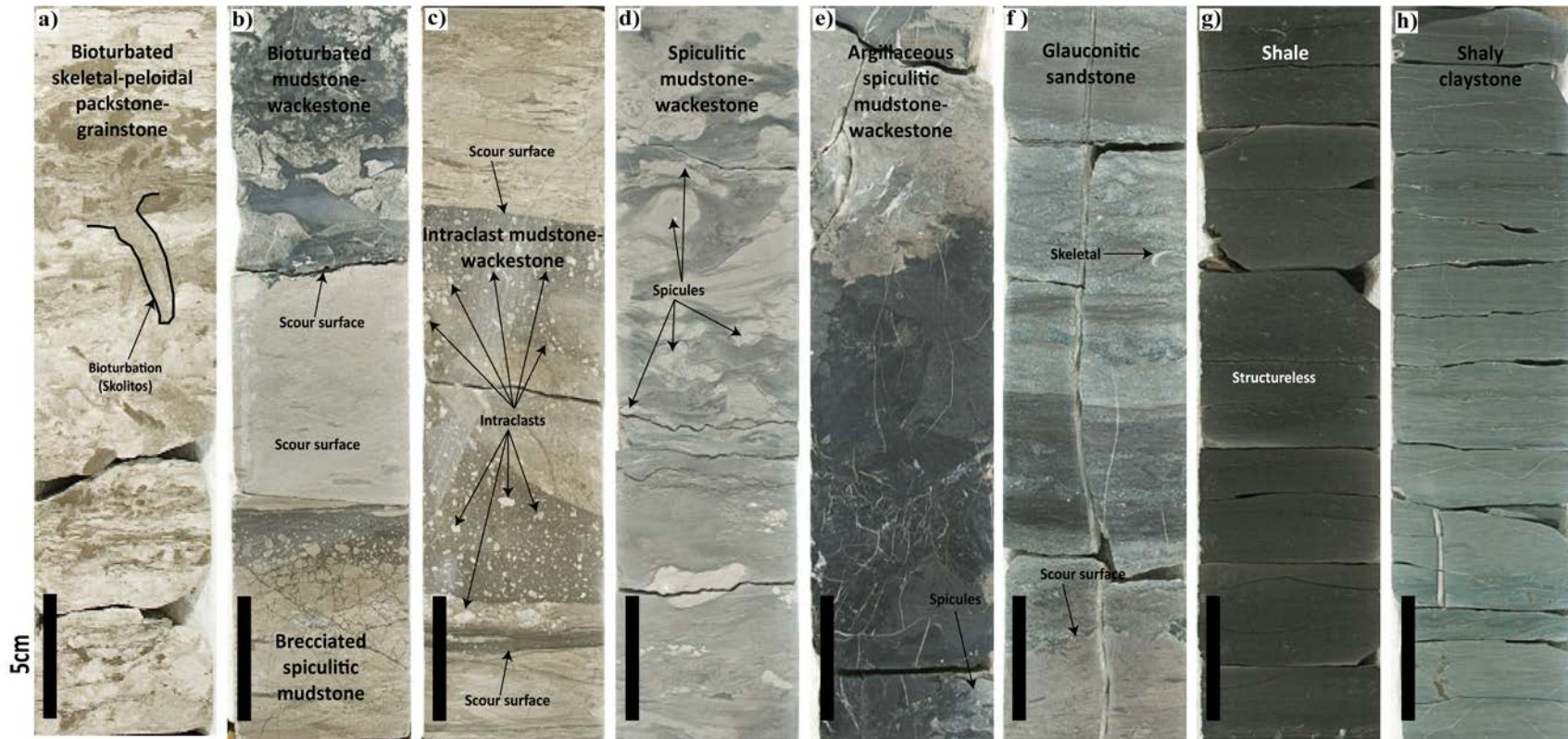


Figure 1.6. Photographs of core-based lithofacies in the Mississippian interval of Devon Energy 1-7 SWD Frieouf well (continued). a) Bioturbated skeletal-peloidal packstone-grainstone. Note centimeter-size skolithos (black line). b) Bioturbated mudstone-wackestone and Brecciated spiculitic mudstone where most clasts are intact suggesting in-situ deformation. c) Intraclast mudstone-wackestone. d) Spiculitic mudstone-wackestone with deformed lenticular/flaser features. e) Argillaceous spiculitic mudstone-wackestone. Note moderate fracture associated with this lithofacies. f) Glauconitic sandstone deposited on top of a scour surface. g) Shale. h) Shaly claystone showing very faintly fissile. Scale Bar = 5 cm.

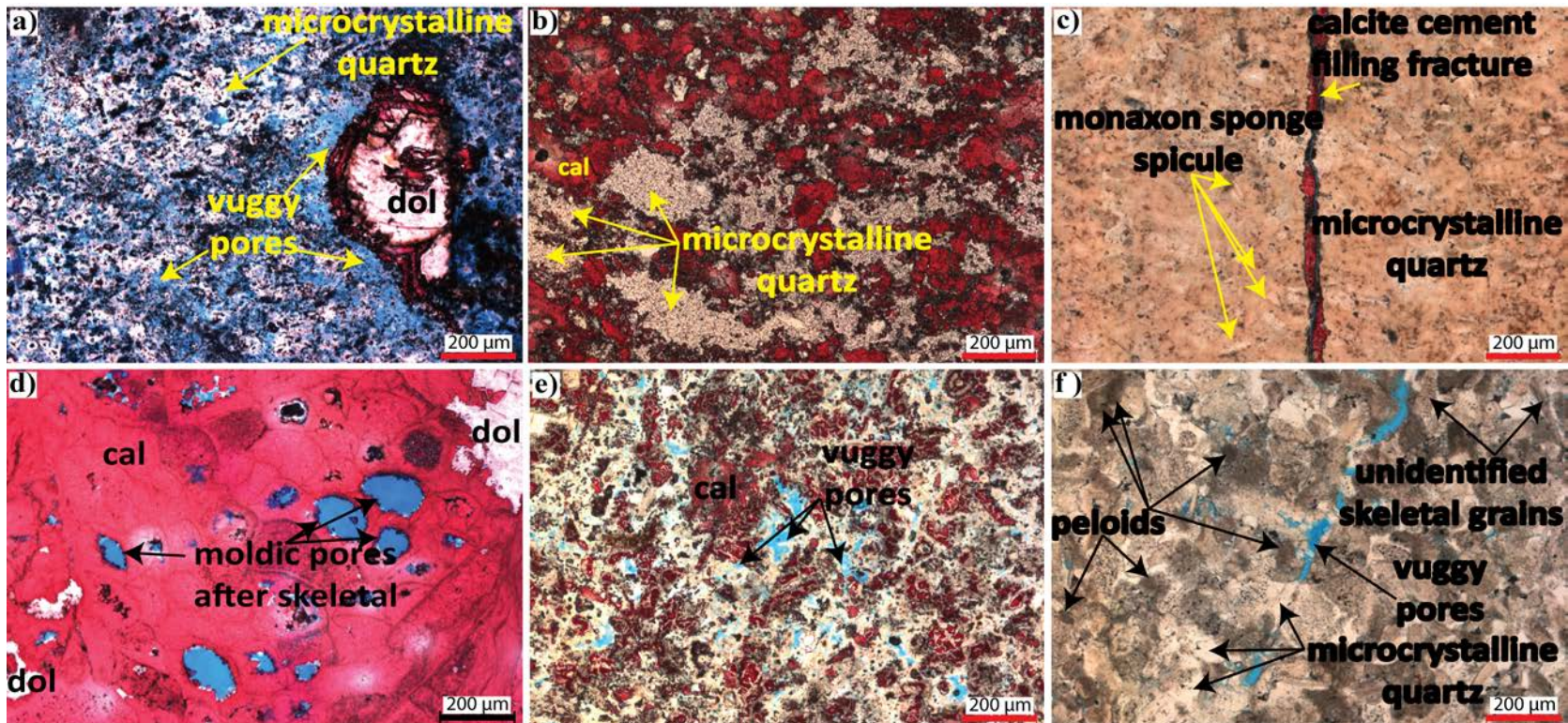


Figure 1.7. Thin-section photomicrographs of lithofacies: a) Chert breccia in greenish shale matrix showing microcrystalline quartz replacing grains and matrix and creating vuggy porosity. b) Chert breccia showing calcite and microcrystalline quartz; c) Skeletal mudstone-wackestone showing predominant microcrystalline-quartz replacing grain and matrix. Cross-cutting relationship indicates silica replacement took place before fracturing and calcite filling. d) Skeletal grainstone showing bryozoan with moldic pores after skeletal, calcite (cal), and dolomite (dol). e) Splotchy packstone-grainstone showing extensive alteration of grains and matrix into microcrystalline quartz (white color). f) Bedded skeletal peloidal packstone-grainstone showing microcrystalline quartz, vuggy pores, peloids, and unidentified skeletal grains.

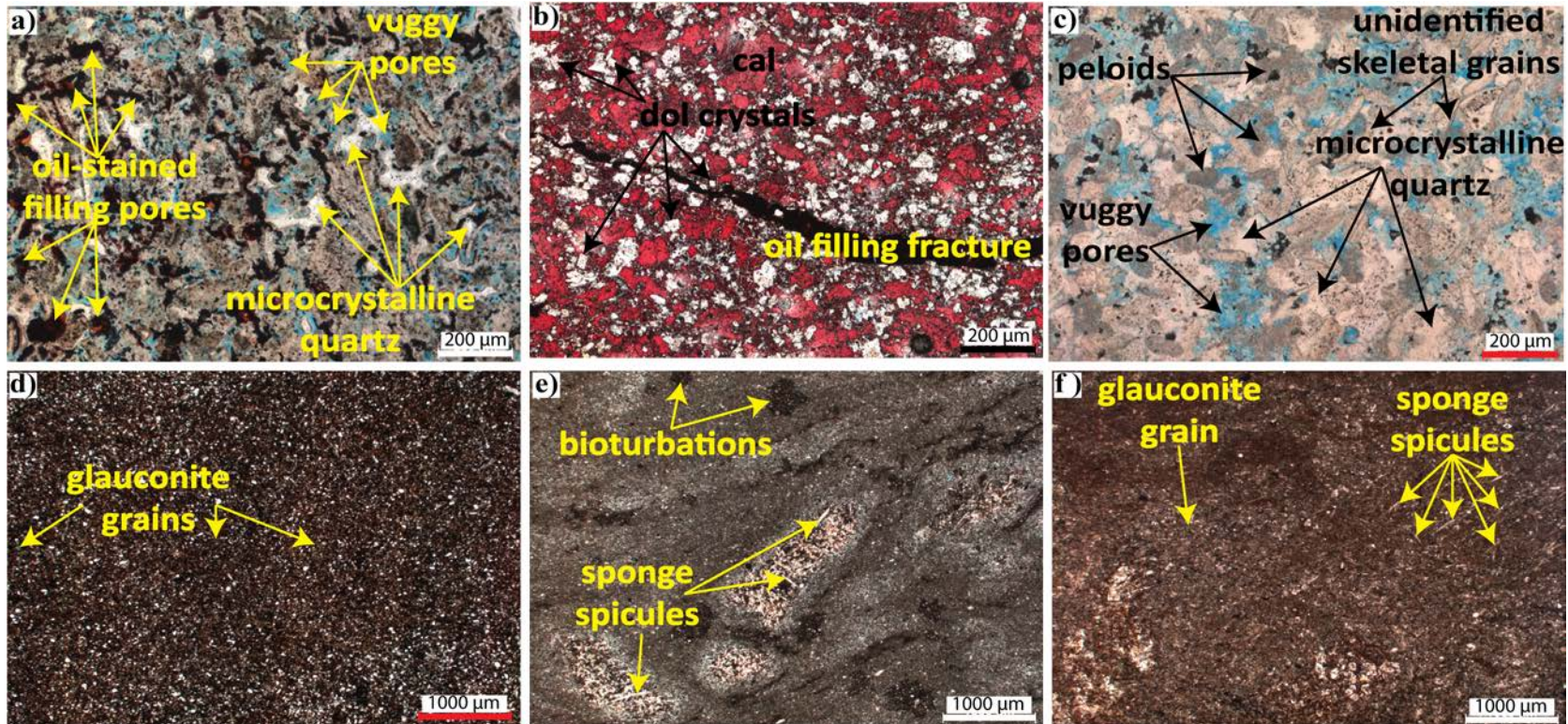


Figure 1.8. Thin-section photomicrographs of identified lithofacies (continued): a) Bedded skeletal peloidal packstone-grainstone. Note oil filling vuggy pores and microcrystalline quartz. b) Nodular packstone-grainstone with predominantly calcite cement (cal) and dolomite rhombic crystals (black arrow). Note the presence of oil filling fracture. c) Bioturbated skeletal peloidal packstone-grainstone. Note the presence of vuggy pore due to dissolution of grains. d) Bioturbated mudstone-wackestone with mainly lime-mud, quartz grains (white-color grains), and glauconite grains (yellow arrow). e) Spiculitic mudstone-wackestone. Note the bioturbations show textural contrast between the filling (darker color) and surrounding sediment; and the presence of isolated bright area with sponge spicules. f) Argillaceous spiculitic mudstone-wackestone. Note the presence of glauconite grain and monaxon sponge spicules.

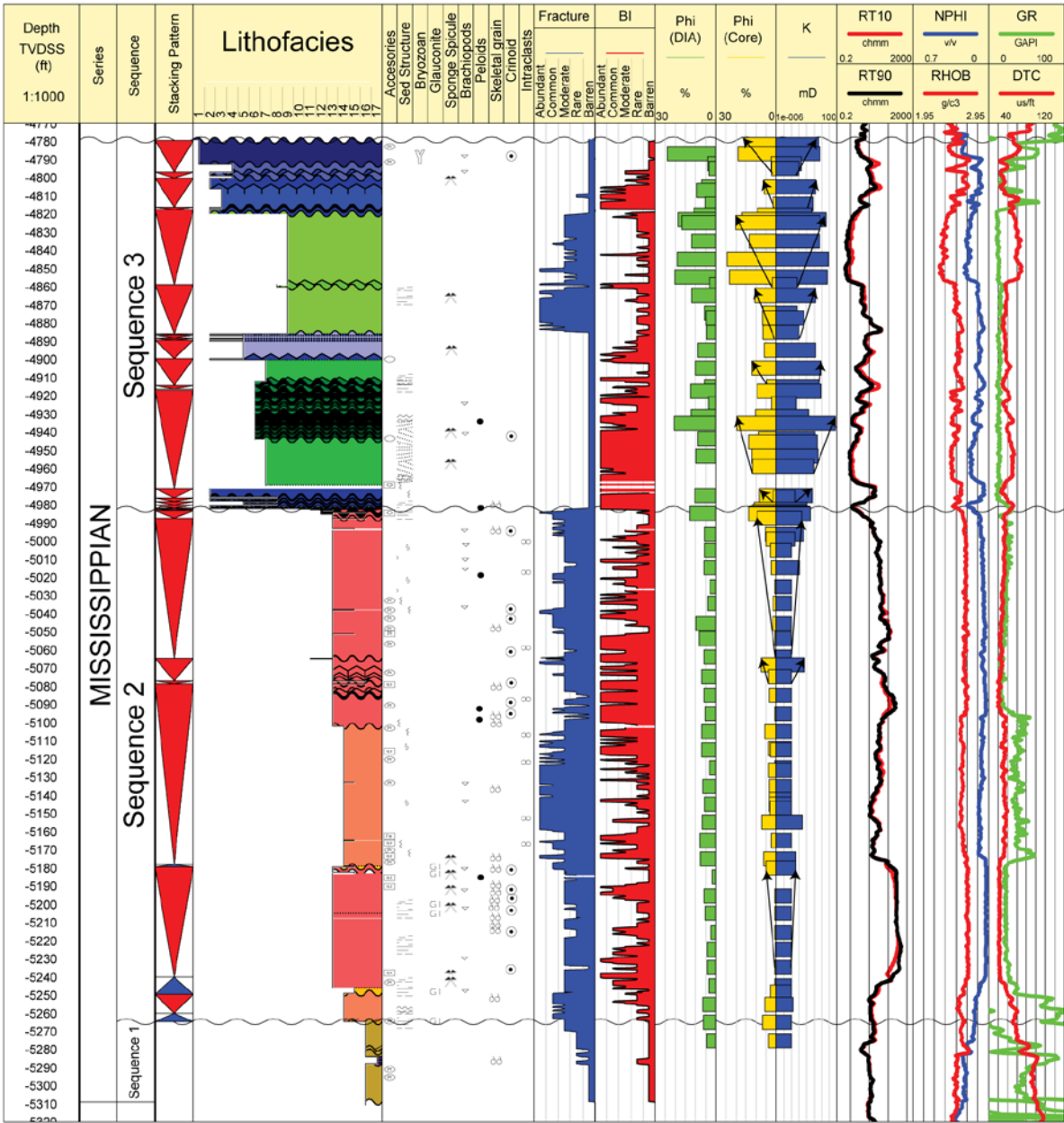



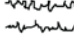

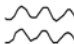




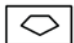

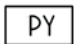

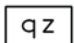



Figure 1.9. Devon Energy 1-7 SWD Friouf well core lithofacies, properties, and cycles. The Mississippian strata in this well consists of 3 sequences. The high-order sequence-stratigraphic framework is based on lithofacies stacking patterns. See Figure 10 for lithofacies key. Note that higher reservoir quality is associated with the upper intervals of upward-shoaling high-order cycles (black arrows on porosity and permeability tracks). TVDSS = True Vertical Depth Subsea. BI = Bioturbation Index, Phi (DIA) = Digital-Image Analysis calculated porosity, Phi (Core) = Laboratory-measured core porosity, K = Permeability, RT10 = shallow resistivity, RT90 = deep resistivity, NPHI = Neutron porosity, RHOB = bulk density, GR = Gamma Ray, DTC = Compressional wave travel time.

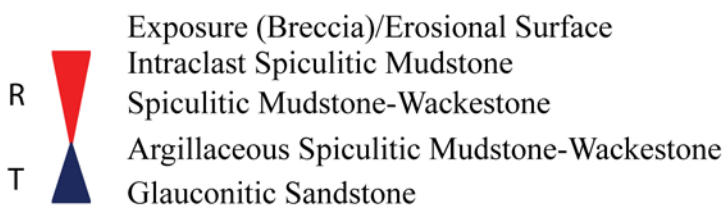
Legend:

	Cherty Limestone		Pyrite Concretion
	Brecciated Chert		Irregular Lamination
	Shale		Parallel wavy lamination
	Limestone		Mottled
	Nodule		Crossbedded
	Cherty Cement		Parallel lamination
	Disseminated Pyrite		Non-parallel wavy lamination
	Quartz Cement		Rubble

Idealized Vertical Succession (Sequence 3):



Idealized Vertical Succession (Sequence 2):



Lithofacies:



Figure 1.10. Core legend, idealized shallowing-upward lithofacies succession for the sequence 2 and sequence 3 in the Mississippian strata, and lithofacies color codes. The sequences are identified based on the presence of erosional surface or interval of brecciated lithofacies. Note that there is no idealized stacking pattern for sequence 1 due to the limited presence of lithofacies (only shale and shaly claystone lithofacies are observed within sequence 1). The blue triangle represents relative sea level rise (transgressive - T) and the red triangle represents relative sea level fall (regressive - R).

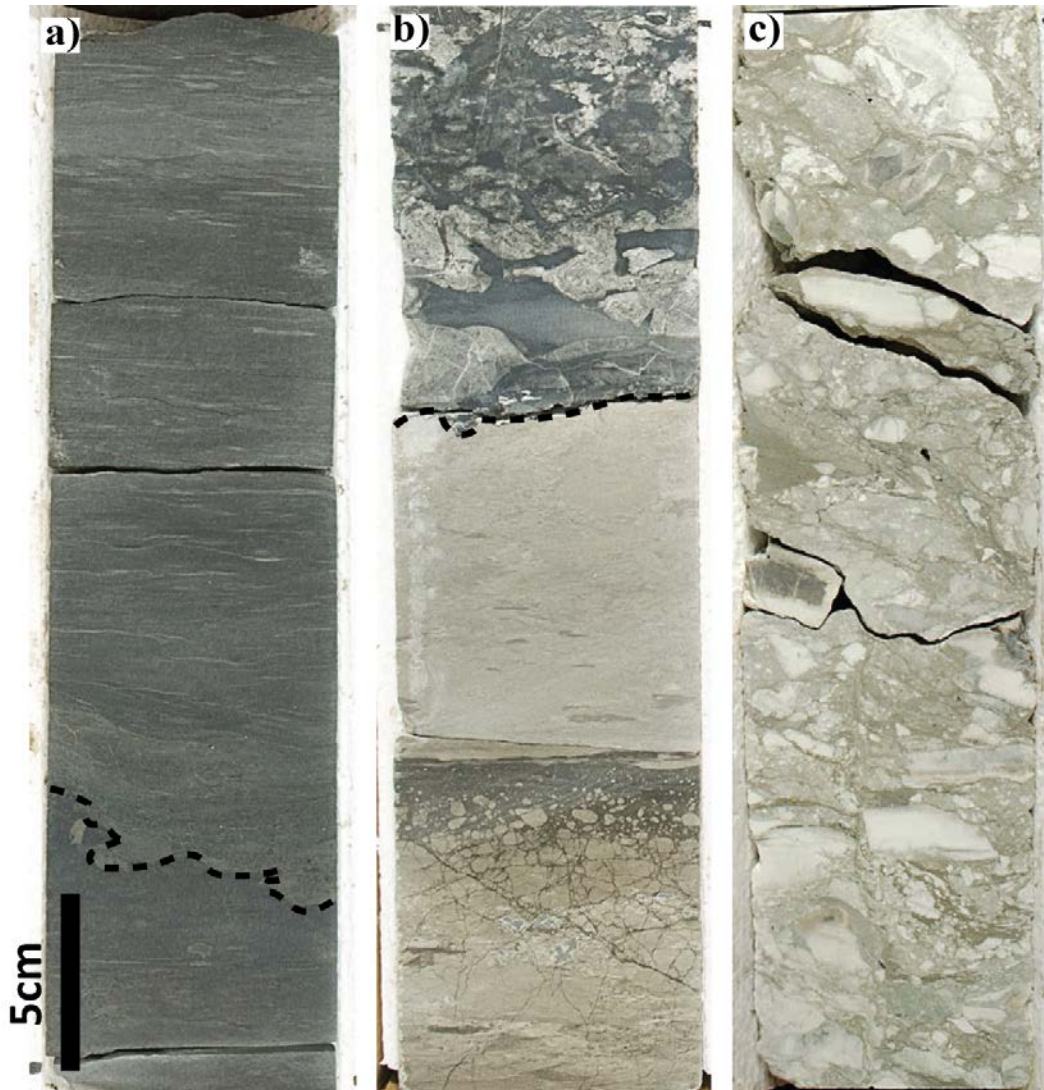


Figure 1.11. Example of observed sequence boundary (SB) in the Devon Energy 1-7 SWD Frieouf well. The SB features including erosional surface (a and b) (black dash line) and brecciation (c).

brecciated spiculitic mudstone (lithofacies 11). The basal unit of sequence 2 is glauconite sandstone that was deposited on top of the sequence 1 erosional surface. The sequence is capped by erosional surface (Figure 1.11B).

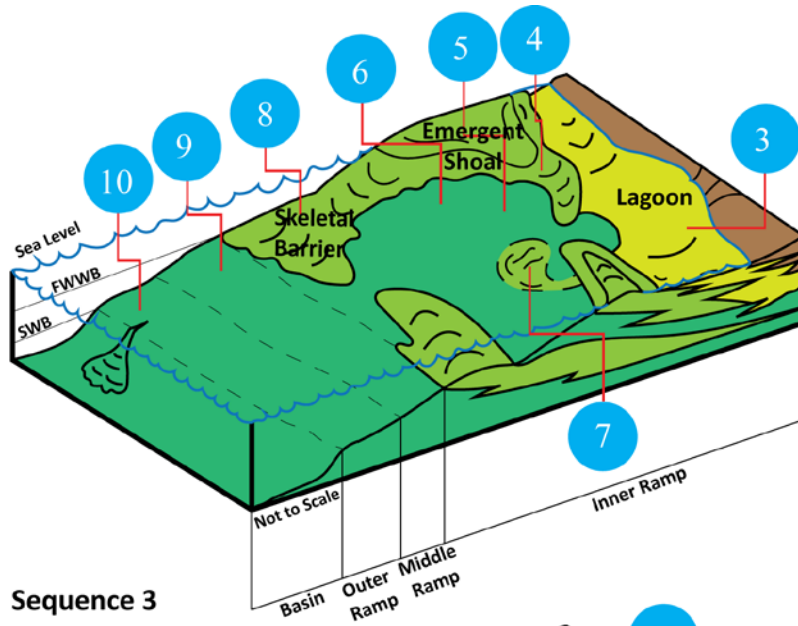
Sequence 3 is 200 ft (~ 62 m) thick and consists of consists of bioturbated mudstone-wackestone (lithofacies 10), bioturbated skeletal peloidal packstone-grainstone (lithofacies 9), skeletal peloidal packstone-grainstone (lithofacies 8), nodular packstone-grainstone (lithofacies 7), bedded skeletal peloidal packstone-grainstone (lithofacies 6), splotchy packstone-grainstone (lithofacies 5), skeletal grainstone (lithofacies 4), skeletal mudstone-wackestone (lithofacies 3), chert breccia (lithofacies 2), and chert breccia in greenish shale matrix (lithofacies 1). Trace fossils (e.g. skolithos, planolites, chondrites, thalassinoides, and teichichnus) are commonly observed in bioturbated and splotchy lithofacies. The upper interval of sequence 3 consists of mudstone to packstone and grainstone with abundant skeletal grains (e.g. crinoids and bryozoans). The uppermost part of this sequence is chert breccia in greenish shale matrix (Figures 1.5A and 1.11C); a weathered chert breccia that possibly marks the major unconformity between the Mississippian and Pennsylvanian periods.

The sequence 1 has only two basinal lithofacies that were eroded. Therefore, an idealized stacking pattern for the sequence 1 cannot be established. The idealized vertical stacking pattern for sequences 2 and 3 were established based on the relative spatial distribution of lithofacies observed within the sequences. Both sequences 1 and 2 represent an overall shallowing-upward interval (Figure 1.10). Sequence 2 has 11 higher frequency cycles with three thick regressive cycles exceeding 60 ft (18.2 m) each. The thick cycles suggest a relatively moderate to high-amplitude relative sea-level oscillation in sequence 2. Sequence 3 has 18 higher frequency cycles with boundaries that are mainly minor unconformities with associated thin in-situ breccias.

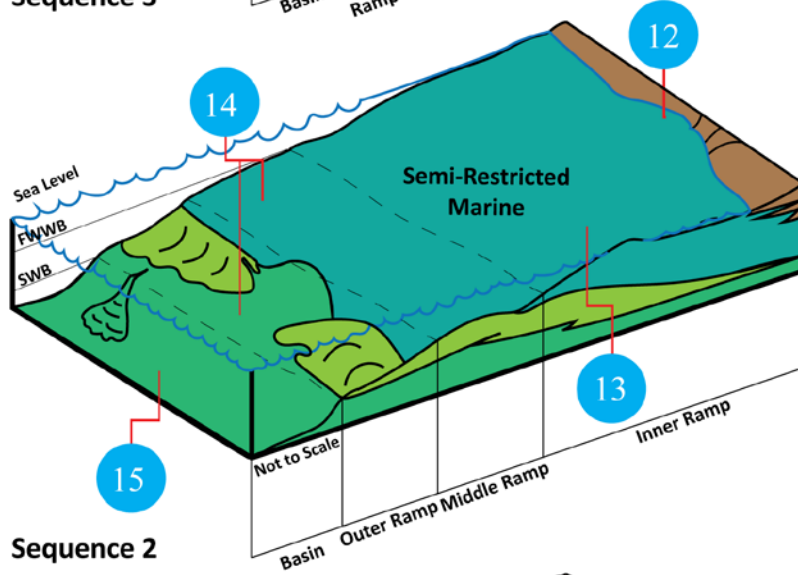
Depositional model

For each sequence, a generic carbonate ramp model is assumed to place lithofacies in their relative spatial positions (i.e., inner-, middle-, outer-ramp, and basinal environments; [Figure 1.12](#)). Placement of lithofacies is guided by their grain size, texture, sedimentary structure, skeletal content, and degree and type of bioturbation (see [Table 1.1](#) and [Figure 1.12](#)). Lithofacies 16 (shale) and 17 (shaly claystone) of sequence 1 are interpreted to have been deposited under quiet-water conditions below the fair-weather wave base in a basinal environment. The relatively low bioturbation and abundance of sponge spicules in lithofacies 13 (spiculitic mudstone-wackestone) and 14 (argillaceous spiculitic mudstone-wackestone) within sequence 2 suggest that deposition occurred under more restricted conditions. [Franseen \(2006\)](#) suggested that the abundance of sponge spicules may also reflect in-place accumulation where sponges thrived due to conditions inhibiting other biota (e.g., salinity, elevated silica and nutrients, cooler water temperatures). Similarly, [Mazzullo et al. \(2009\)](#) suggested the spiculitic-rich rocks represent a time when the Anadarko shelf was suppressed due to silica poisoning of sea water and upwelling within a geographically restricted area.

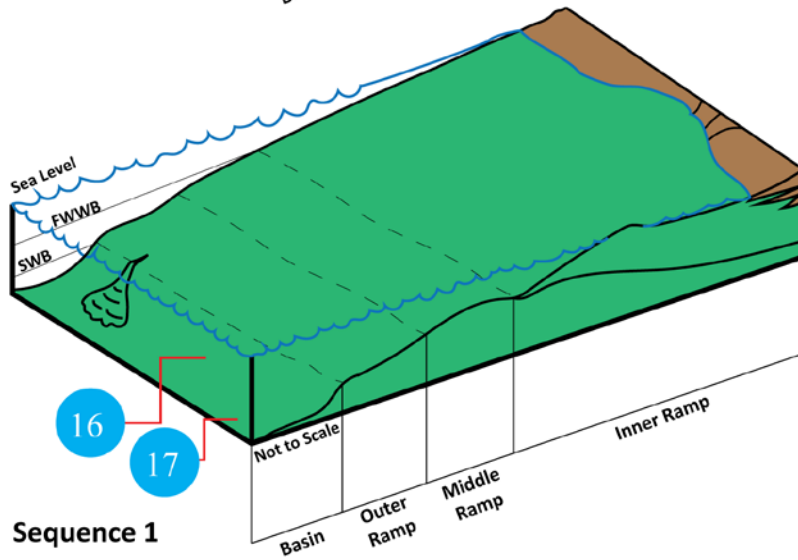
The abundance of skeletal grains and high degree of bioturbation in the sequence 3 suggests that deposition occurred in relatively shallow water under a normal-marine condition. Sedimentary structures including cross bedding, parallel laminations, and wavy laminations are rare. The presence of scoured surfaces, locally preserved cross bedding, and skeletal fragments is indicative of fluctuating energy conditions.



Sequence 3



Sequence 2



Sequence 1

Figure 1.12. Schematic diagram showing a generic carbonate ramp depositional model for the Mississippian strata in the Grant County, Oklahoma, especially during deposition of sequences 1-3. Sequence 1 contains shaly claystone (17) and shale (16). Sequence 2 consists of glauconitic sandstone (15), argillaceous spiculitic mudstone-wackestone (14), spiculitic mudstone-wackestone (13), intraclast spiculitic mudstone (12), and brecciated spiculitic mudstone (11). Sequence 3 consists of bioturbated mudstone-wackestone (10), bioturbated skeletal peloidal packstone-grainstone (9), skeletal peloidal packstone-grainstone (8), nodular packstone-grainstone (7), bedded skeletal peloidal packstone-grainstone (6), splotchy packstone-grainstone (5), skeletal grainstone (4), skeletal mudstone-wackestone (3), chert breccia (2), and chert breccia in greenish shale matrix (1). Note that breccia lithofacies (1, 2, and 11) are not placed in the model as breccia can occur in inner- to outer-ramps depending on relative sea-level change. Lithofacies are spatially distributed within their sequences based on grain size, texture, sedimentary structure, degree and type of bioturbation.

Table 1.1. Summary of key characteristics that distinguish each identified lithofacies in the core used in this study.

No.	Lithofacies	Texture/Grain Types	Characteristics and Associated Features	Color	Depositional Environment
1	Chert Breccia in greenish shale matrix	Bryozoan, brachiopod, crinoid, sponge spicules, microcrystalline quartz, pyrite, Fe-rich nodules.	Matrix- and clast-supported. Clasts with partial alteration. Stylolite. Grain-suture contact. Poikilotopic calcite cement. Saddle dolomite, Dedolomitization.	Very Light Gray, White, Light Gray, Yellowish Gray, Greenish Gray.	Inner Ramp
2	Chert Breccia	Bryozoan, brachiopod, peloids, microcrystalline quartz, dolomite crystals, pyrite.	Grain-supported. Grain suture contacts. Stylolite. Clasts with partial alteration. Fractured clasts. Poikilotopic calcite cements. Saddle dolomite. Calcite-filled fractures. Oil-filled fractures.	Light Gray, Very Light Gray, White, Dark Gray.	Inner Ramp
3	Skeletal Mudstone-Wackestone	Brachiopods, crinoids, sponge spicules, microcrystalline quartz, nodules.	Massive, cross-bedding, parallel lamination, flaser/lenticular. Dolomite and calcite cements. Dedolomitization.	Medium Gray, Dark Gray, Yellowish Gray, Nodule: White, Dark Gray.	Lagoon
4	Skeletal Grainstone	Bryozoan, brachiopod, crinoid, pyrite, nodules.	Massive, laminated, or wavy to wispy laminated. Saddle dolomite.	Light Olive Gray, Yellowish Gray, White, Medium Gray, Dark Gray.	Inner Ramp
5	Spotchy Packstone-Grainstone	Blotchy texture. Peloids, skeletal grains, microcrystalline quartz, dolomite rhombic crystals, pyrite.	Cross lamination.	Light Gray, Medium Gray.	Inner Ramp
6	Bedded Skeletal Peloidal Packstone-Grainstone	Local spotchy texture. Peloids, skeletal grains (brachiopods, crinoids), chalcedony, microcrystalline quartz, quartz grains, dolomite crystals,	Parallel lamination, cross bedding, wavy bedded to wispy laminated, and ragged or wavy to convoluted boundaries. Shrinkage crack feature. Calcite cement and saddle dolomite. Grains suture contact. Saddle-dolomite-filled fractures. Oil-filled fractures. oil- or microcrystalline-quartz - filled vuggy porosity. Microcrystalline dolomite rimming vuggy pores	Dusky Yellowish Brown, Light Olive Gray.	Inner Ramp
7	Nodular Packstone-Grainstone	Irregular shape nodules, dolomite crystals, Disintegrated skeletal grains (?brachiopod), pyrite .	Wispy laminated to draped around nodules. Anastomosing bedded (following terminology of Nolte and Benson, 1998). Convoluted nodules. Nodules with partial alteration. Shrinkage crack feature on nodules. Nodular suture contact. Quartz-filled vuggy porosity. Oil-stained. Calcite cement.	Medium Gray, Light Olive Gray, Dusky Yellowish Brown, White, Very Light Gray.	Inner Ramp
8	Skeletal Peloidal Packstone-Grainstone	Local mottled texture. Peloids, ?brachiopods, quartz grains.	Convoluted bedded to wavy bedded. Micritization. Calcite cements. Grain-suture contact. Calcite-filled fractures. Oil stained.	Medium Gray, Light Gray, Light Olive Gray, Bluish White, Light Olive Gray.	Inner Ramp

9	Bioturbated Skeletal Peloidal Packstone-Grainstone	Blotchy texture. Peloids, ?brachiopod, nodules, quartz, microcrystalline quartz, glauconite, pyrite.	Milli- to centimeters glossifungites and skolithos. Irregular to discontinuous wavy lamination. Calcite-filled fractures. Open fractures. Oil stained. Calcite and poikilotopic cements.	Yellowish Gray, Light Gray, Medium Gray, Dark Gray.	Middle Ramp
10	Bioturbated Mudstone-Wackestone	Flecky texture.	Local silica replacement. Closed fracture. Silica-filled vuggy pores.	Medium Gray, Dark Gray, White	Outer ramp
11	Brecciated Spiculitic Mudstone	In situ-deformed clasts	Structureless. Matrix to grain supported. Uniformly fragmented and disrupted nature of the clasts.	Light Olive Gray	Inner Ramp
12	Intraclast Spiculitic Mudstone	Intraclasts (irregularly non-skeletal grains or broken down chert clasts)	Structureless. Poorly Sorted. Matrix supported. Oil stained.	Light Olive Gray	Inner Ramp
13	Spiculitic Mudstone-Wackestone	Monaxon sponge spicules, brachiopod, crinoids, glauconite, pyrite, dolomite crystals, microcrystalline quartz, chalcedony.	Lenticular/Flaser spicules. Parallel laminations and wispy laminations. Millimeters bioturbation (planolites, thalassinoides, cruziana, chondrites, and zoophycos). Glauconite-filled burrow. Diagenetic fronts. Closed fractures, some are filled by microcrystalline quartz, chalcedony, or calcite cement. Stylolite. Saddle dolomite and Poikilotopic calcite cement.	Light Gray, Light Olive Gray.	Inner Ramp
14	Argillaceous Spiculitic Mudstone-Wackestone	Monaxon sponge spicules, brachiopod, crinoids, glauconite, pyrite, dolomite crystals, microcrystalline quartz, chalcedony.	Differentiated from facies 13 by diversity and quantity of trace fossil, and gamma-ray response. Lenticular/Flaser spicules. Parallel laminations and wispy laminations. Bioturbation (planolites, thalassinoides, cruziana, chondrites, and zoophycos). Glauconite-filled burrow. Diagenetic fronts. Closed fracture, some are filled by microcrystalline quartz, chalcedony, or calcite cement. Stylolite. Saddle dolomite and Poikilotopic calcite cement.	Light Gray, Light Olive Gray.	Outer to Middle Ramp
15	Glauconitic Sandstone	Glauconite, quartz.	Structureless. Glauconite-filled burrow.	Greenish Gray.	Basinal
16	Shale	Unidentifiable grains rare	Structureless, local very thin parallel lamination. Fissile.	Dark Gray, Black.	Basinal
17	Shaly Claystone	Intraclasts, pyrite	Structureless to locally laminated. Local darker blebs (?bioturbation).	Dark Gray, Light Gray, Greenish Gray, Light Brownish Gray	Basinal

Pore-system characteristics

Image analysis was performed using 57 optical microscope photomicrographs and 3,171 SEM photomicrographs where a total of 913,327 pores were identified, measured, and analyzed. The types of pores consisted of 682,143 nanopores, 188,535 micropores, and 42,649 mesopores (Figure 1.13). In addition to pore type, the key parameters that were measured included pore area, perimeter, length, width, and circularity. Table 1.2 shows laboratory measured properties (porosity, permeability) and a statistical summary of data obtained from digital-image analysis organized by lithofacies.

Pore types

Pore types in Mississippian carbonate and chert deposits range from simple to complex shapes and origin. Pores were formed by a combination of depositional and diagenetic processes such as compaction, dissolution, shrinkage, or dolomitization. Pore types for each lithofacies are summarized in Table 1.3. Most of the pores observed in this study (Figures 1.14, 1.15, and 1.16) are intraparticle (Figures 1.14A – 1.14F) and interparticle (Figures 1.14G and 1.14H) pores with some non-fabric selective pores including vuggy (Figure 1.14I), channel (Figure 1.14J), and microfractures (Figure 1.14K). Most pores appear to have been enlarged through dissolution.

The crystal-form pore is similar to the dissolution-rim pore of Loucks et al. (2012) and the shrinkage pore of Vanden Berg and Grammer (2016). The pores within crystals are defined as void spaces within a well-defined crystal. A microfracture within a crystal pore is defined as a highly elongated void space within a well-defined crystal. The microfracture within a crystal is possibly associated with fractures and/or dissolution along dolomite-crystal cleavage. The intercrystalline pores within pyrite framboid, crystal-form pores, pores within crystal, microfracture within crystal, particle-rim pores, and moldic pores as observed in the 2-D SEM

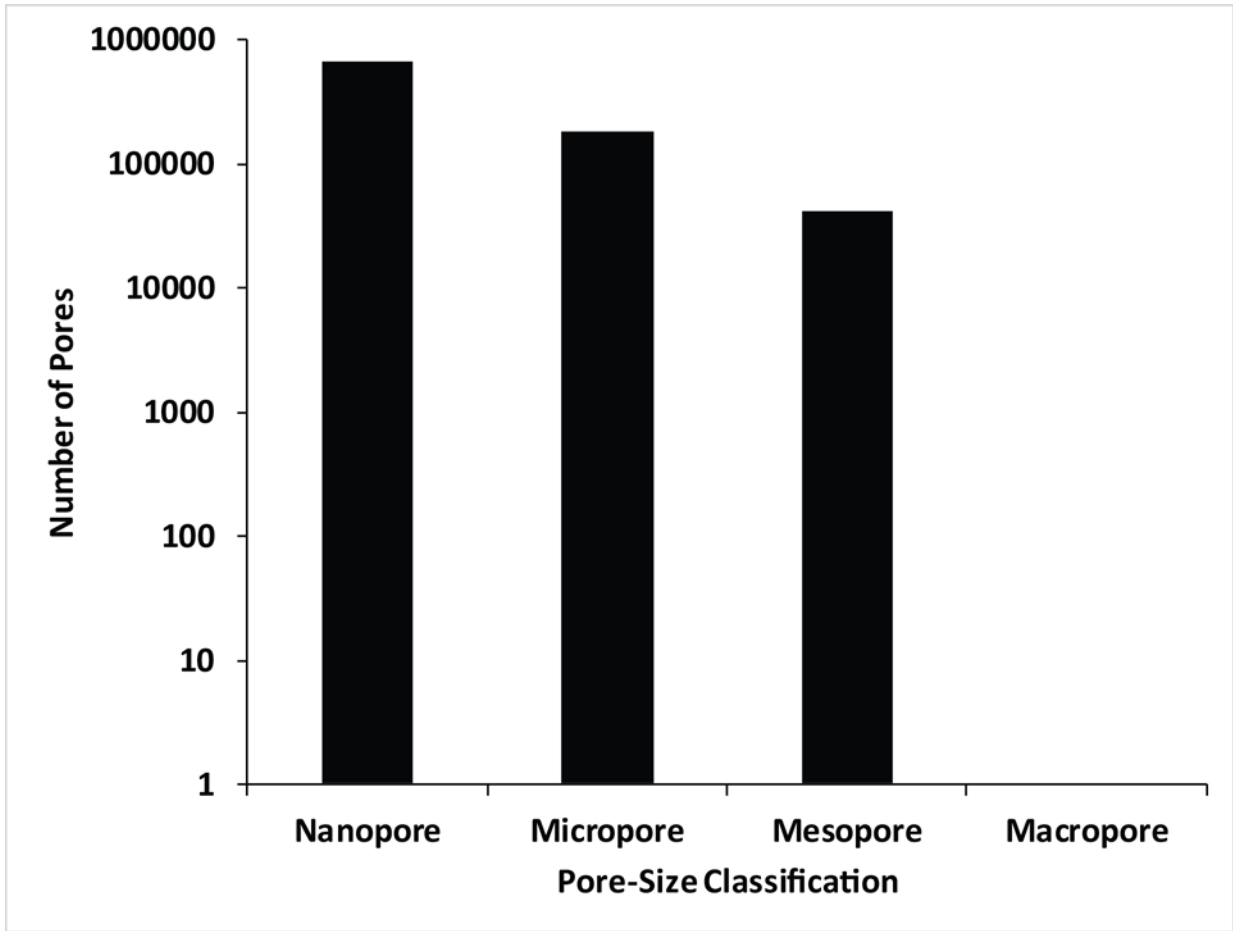


Figure 1.13. Histogram of measured pores from >3100 SEM and 57 thin section photomicrographs. Noted that the pores are primarily nanopores ($1 \text{ nm} < \text{width} < 1 \text{ }\mu\text{m}$) with secondary mesopores ($1 \text{ }\mu\text{m} < \text{width} < 62.5 \text{ }\mu\text{m}$) and minor mesopore ($62.5 \text{ }\mu\text{m} < \text{width} < 4 \text{ mm}$).

Table 1.2. Summary of data obtained from digital-image analysis and laboratory measured properties including porosity and permeability for all 57 samples in the Mississippian interval of the Devon Energy 1-7 SWD Frieouf well.

No	Sample Depth (ft)	Macropore (%)	Mesopore (%)	Micropore (%)	Nanopore (%)	Number of Macropore	Number of Mesopore	Number of Micropore	Number of Nanopore	Total Number of Pores	DIA Porosity	Core Porosity	Permeability - Air (mD)	Lithofacies
1	4786.75	0.00	6.22	12.55	2.50	0	7890	20393	21456	49739	21.27	19.30	0.766	1
2	4792.4	0.00	0.17	1.29	2.32	0	163	1168	28349	29680	3.78	2.70	0.0064	1
3	4794.95	0.00	0.13	1.78	1.79	0	164	1231	29235	30630	3.70	2.34	0.0037	4
4	4804.95	0.00	0.08	4.11	2.29	0	47	2262	41689	43998	6.48	6.15	0.218	2
5	4807.1	0.00	0.00	7.53	1.40	0	0	499	13624	14123	8.93	3.36	N/A	3
6	4814.75	0.00	0.12	2.04	0.65	0	1	190	10495	10686	2.81	1.67	0.122	3
7	4820.4	0.00	0.00	9.21	0.96	0	0	320	94391	94711	10.17	9.42	0.086	9
8	4823.1	0.00	7.15	9.95	0.81	0	9855	31320	25784	66959	17.91	17.00	4.44	9
9	4824.85	0.00	3.14	14.49	1.96	0	6379	20786	23619	50784	19.59	20.38	0.85	9
10	4834.8	0.00	0.17	11.01	1.70	0	502	4728	40780	46010	12.88	13.66	0.689	9
11	4844.75	0.00	0.93	21.51	1.00	0	1926	13614	49149	64689	23.44	24.50	9.41	9
12	4854.8	0.00	0.07	21.83	0.93	0	201	4325	19323	23849	22.83	23.26	7.2	9
13	4858.9	0.00	0.06	2.77	0.41	0	176	1748	506	2430	3.24	2.16	0.0027	8
14	4864.85	0.00	0.05	13.25	0.89	0	216	5724	10864	16804	14.19	10.94	0.214	9
15	4874.8	0.00	0.00	4.72	1.12	0	3	578	2676	3257	5.84	6.60	0.0026	9
16	4877.15	0.00	0.00	4.98	1.78	0	7	668	3311	3986	6.76	6.94	0.012	9
17	4885.15	0.00	0.00	5.05	0.72	0	19	1472	4478	5969	5.77	6.74	0.0035	9
18	4894.95	0.00	0.06	7.54	2.01	0	58	1163	9156	10377	9.61	6.14	0.245	5
19	4904.95	0.00	0.51	9.83	1.72	0	988	5834	8958	15780	12.06	12.45	1.38	7
20	4914.85	0.00	0.14	5.80	0.50	0	269	2158	2232	4659	6.44	5.03	0.59	6
21	4917.7	0.00	0.77	10.22	1.37	0	1713	9423	3755	14891	12.36	9.77	1.23	6
22	4924.65	0.00	0.00	1.74	1.83	0	1	321	5982	6304	3.57	2.66	0.0023	6
23	4931.35	0.00	1.92	8.47	0.61	0	5538	29490	1911	36939	11.00	10.38	0.04	6
24	4935.25	0.00	12.52	7.30	0.62	0	2779	374	2509	5662	20.44	19.60	80.2	6
25	4943.95	0.00	0.00	7.90	1.11	0	0	146	13964	14110	9.01	8.64	0.185	6
26	4953.55	0.00	0.00	9.23	1.63	0	0	4440	35608	40048	10.86	12.48	0.416	7
27	4975	0.00	3.31	6.37	0.64	0	3592	9507	1618	14717	10.32	8.54	0.11	2
28	4984.95	0.00	0.06	11.27	1.74	0	192	1697	4287	6176	13.07	13.53	0.049	13
29	4996.4	0.00	0.00	5.39	1.29	0	0	592	4495	5087	6.68	5.44	0.012	13
30	5005.3	0.00	0.00	3.27	0.47	0	0	203	2512	2715	3.74	3.20	0.0004	13
31	5014.9	0.00	0.00	3.22	2.47	0	0	1100	11146	12246	5.69	2.77	0.0042	13
32	5025.35	0.00	0.00	1.33	1.28	0	0	210	2838	3048	2.61	0.84	0.0004	13
33	5034.45	0.00	0.00	1.90	1.37	0	0	260	1974	2234	3.27	1.49	0.0002	13
34	5045.5	0.00	0.00	3.45	1.65	0	0	219	5625	5844	5.10	2.06	0.0005	13
35	5053.9	0.00	0.00	3.49	1.74	0	0	468	8666	9134	5.23	0.61	0.0003	13
36	5063.8	0.00	0.00	2.45	1.18	0	0	263	2810	3073	3.63	0.52	0.0002	13
37	5074.9	0.00	0.00	4.96	0.83	0	0	336	6543	6879	5.79	3.87	0.0007	13
38	5084.95	0.00	0.00	3.98	1.37	0	0	494	8109	8603	5.35	3.83	0.0006	13
39	5095	0.00	0.00	5.14	0.73	0	0	712	37253	37965	5.87	0.59	0.0001	13
40	5105	0.00	0.00	5.48	0.69	0	0	351	2753	3104	6.17	5.68	0.0008	14
41	5115.2	0.00	1.93	3.03	1.04	0	2	1056	11037	12095	6.00	3.17	0.0003	14
42	5125	0.00	0.00	1.09	0.20	0	0	879	9313	10192	1.29	0.63	0.0005	14
43	5135.2	0.00	0.00	5.12	0.62	0	0	290	1599	1889	5.74	3.84	0.0002	14
44	5144.85	0.00	0.00	4.71	0.65	0	0	330	2141	2471	5.36	3.69	0.0001	14
45	5154.75	0.00	0.00	6.41	0.82	0	0	245	1300	1545	7.23	7.29	0.0083	14
46	5165.15	0.00	0.00	4.25	0.48	0	0	407	1866	2273	4.73	2.71	N/A	14
47	5175.1	0.00	0.00	5.85	1.15	0	0	1145	7519	8664	7.00	6.20	0.0018	14
48	5185	0.00	0.00	0.41	0.98	0	0	91	2042	2133	1.39	0.75	N/A	13
49	5195.6	0.00	0.00	1.50	1.61	0	0	185	4687	4872	3.11	0.77	0.0001	13
50	5205.15	0.00	0.00	2.76	1.45	0	0	270	2486	2756	4.21	0.64	0.0001	13
51	5215.5	0.00	0.00	1.10	1.17	0	0	124	1827	1951	2.27	0.74	0.0002	13
52	5225.15	0.00	0.00	1.40	1.80	0	0	653	10492	11145	3.20	0.57	0.0002	13
53	5234.75	0.00	0.00	1.21	1.25	0	0	268	3461	3729	2.46	0.67	0.0002	13
54	5245.15	0.00	0.00	2.13	1.51	0	0	199	2143	2342	3.64	0.72	0.0002	13
55	5255.2	0.00	0.00	5.44	1.49	0	0	402	4748	5150	6.93	5.60	0.0009	14
56	5265.15	0.00	0.00	4.74	2.06	0	0	496	4050	4546	6.80	7.05	0.0003	10
57	5275.15	0.00	0.00	5.19	1.81	0	0	708	6999	7707	7.00	3.98	0.0007	10

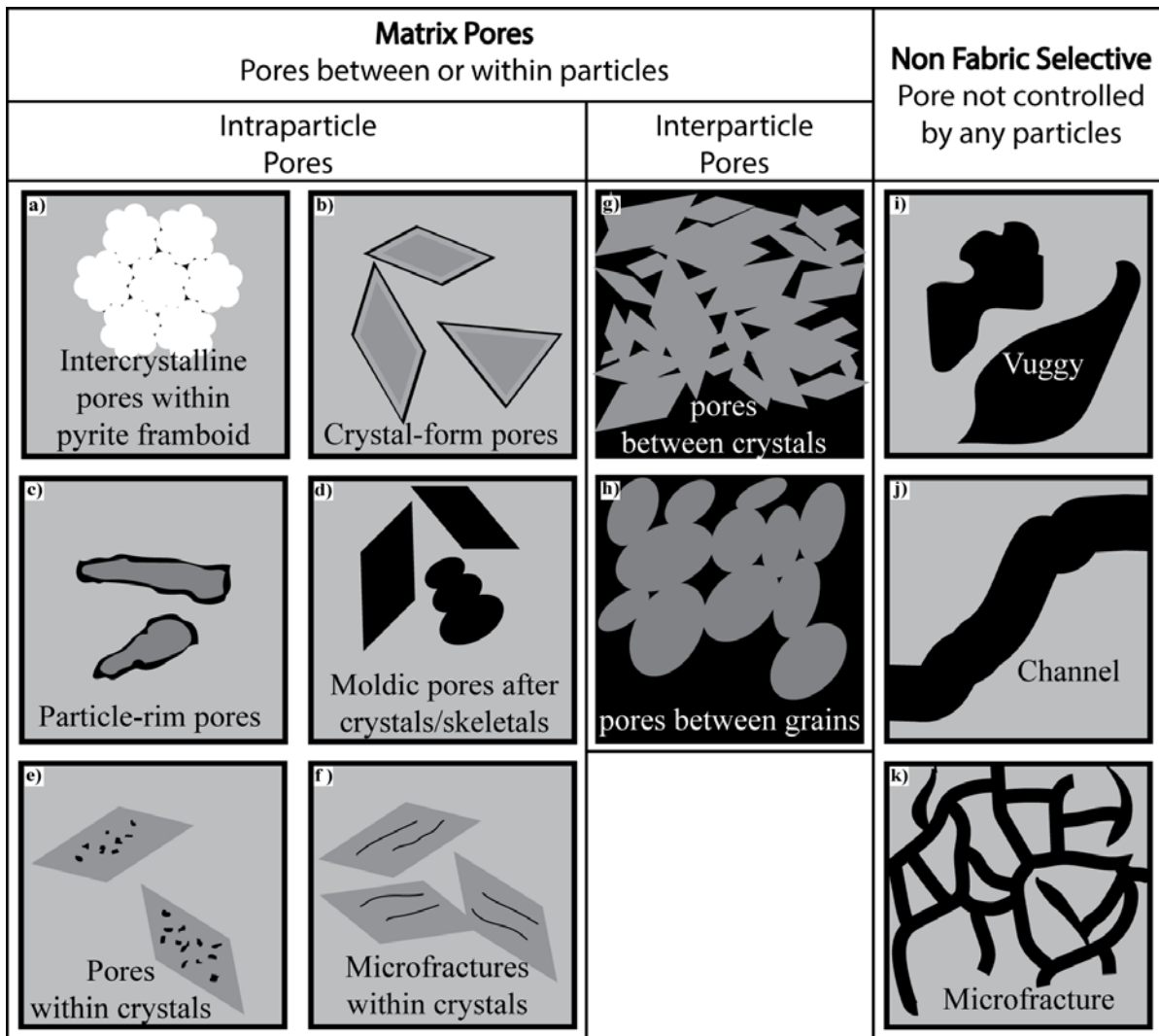


Figure 1.14. Schematic diagram of carbonate pore types observed in this study. Intraparticle pores including: a) Intercrystalline pores within pyrite framboid vuggy pore; b) Crystal-form pore channel pore; c) Particle-rim pore; d) Moldic pores after crystals/skeletal; e) Pores within crystals; and f) Microfracture within crystals. Intraparticle pores including: g) Pore between crystals; and h) Pore between grains. Non-fabric-selective pores including: i) Vuggy; j) Channel; and k) Microfracture.

Table 1.3. Pore types identified in 12 lithofacies that have their thin section and SEM photomicrographs available in this study.

Lithofacies No.	Lithofacies	Pore Types
1	Chert Breccia in greenish shale matrix	Interparticle (pores between grains or crystals), microfracture, intraparticle (pore within crystals, particle-rim pores), vuggy, channel.
2	Chert Breccia	Fracture, microfracture, vuggy , intraparticle (pores within crystals), interparticle.
3	Skeletal Mudstone-Wackestone	Microfracture, interparticle, vuggy, intraparticle (pores within crystals, moldic after crystals, particle-rim pores).
4	Skeletal Grainstone	Vuggy , moldic, microfracture, intraparticle (particle-rim pore), interparticle (pores between grains).
5	Spotty Packstone-Grainstone	Interparticle (pore between crystals or grains), vuggy , intraparticle (particle-rim pores), microfracture.
6	Bedded Skeletal Peloidal Packstone-Grainstone	Interparticle (crystal between grains or crystals), intraparticle (pore within crystals, crystal-form pores), vuggy, microfracture.
7	Nodular Packstone-Grainstone	Microfracture, intraparticle (pore within crystals), vuggy, interparticle (pore between crystals or grains)
8	Skeletal Peloidal Packstone-Grainstone	Intraparticle (crystal-form pores), microfracture, vuggy, interparticle (pore between crystals).
9	Bioturbated Skeletal Peloidal Packstone-Grainstone	Intraparticle (crystal-form pores, particle-rim pores), microfracture, vuggy, interparticle.
10	Bioturbated Mudstone-Wackestone	Intraparticle (intercrystalline pore within pyrite framboid, pore within grains, crystal-form pores), vuggy, interparticle (pores between crystals or grains).
13	Spiculitic Mudstone-Wackestone	Microfracture, channel, intraparticle (intercrystalline pore within pyrite framboid, crystal-form pores, particle-rim pore, microfractures within crystals, moldic pores after crystals,), vuggy, interparticle (pores between crystals or grains)
14	Argillaceous Spiculitic Mudstone-Wackestone	Microfracture, vuggy, intraparticle (pore within crystals, moldic pores after crystals), interparticle (pore between grains or crystals).

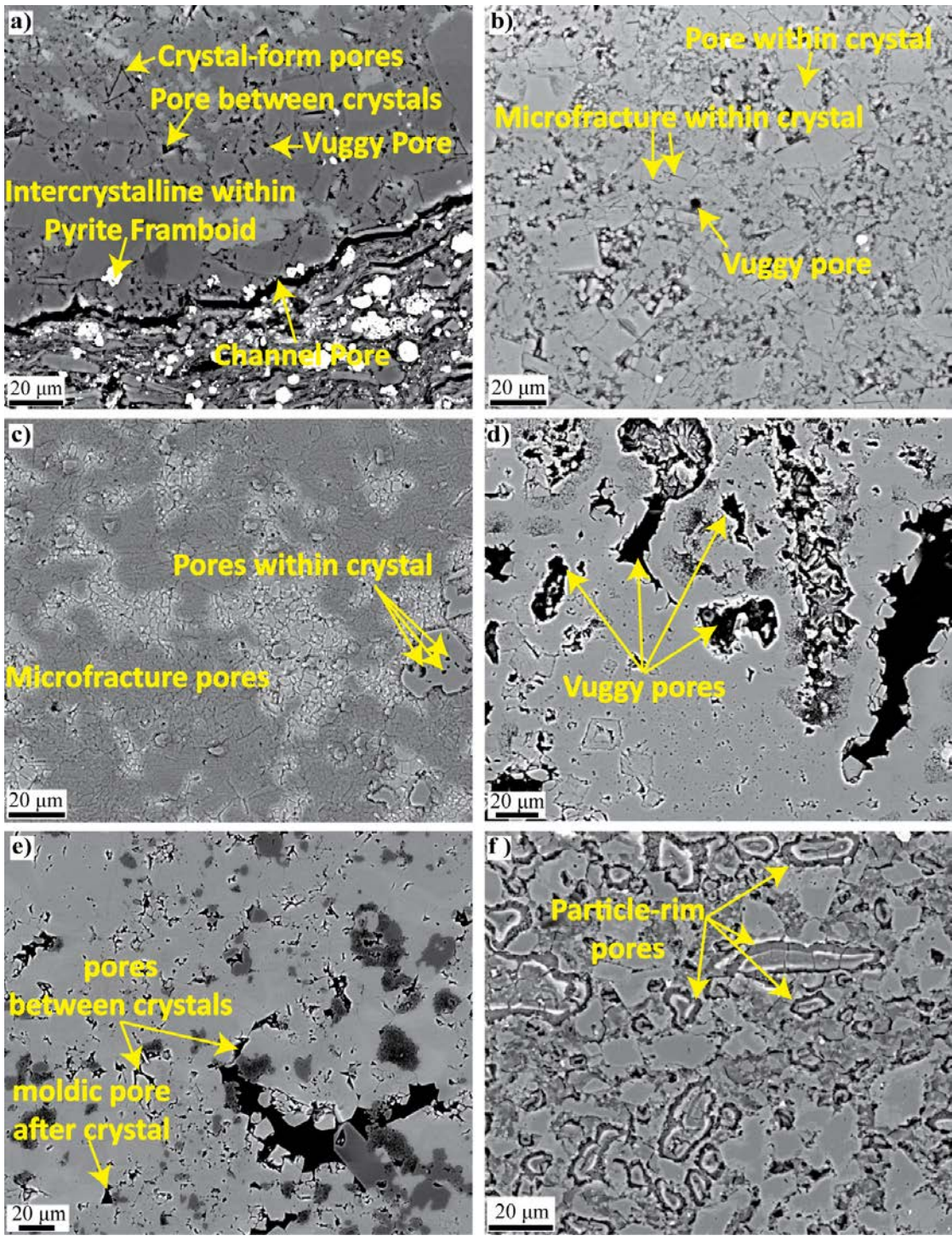


Figure 1.15. Example SEM photomicrographs of common pore types. a) Interparticle pore between dolomite crystals, channel, vuggy, and intraparticle pores (crystal-form pores and intercrystalline within pyrite framboid). Note the dolomite crystals have a variety polygon shapes. b) Interparticle (pore within dolomite crystals), intraparticle (microfracture within crystals), and vuggy pores. c) Microfracture and intraparticle pores (pore within crystals). d) Vuggy pores in bedded skeletal peloidal packstone-grainstone. The vuggy pores have a large range in size (nano- to mesopore sizes). e) Intraparticle (moldic pore after crystal) and interparticle pores (pore between crystals). f) Skeletal mudstone-packstone with predominantly intraparticle (particle-rim pores).

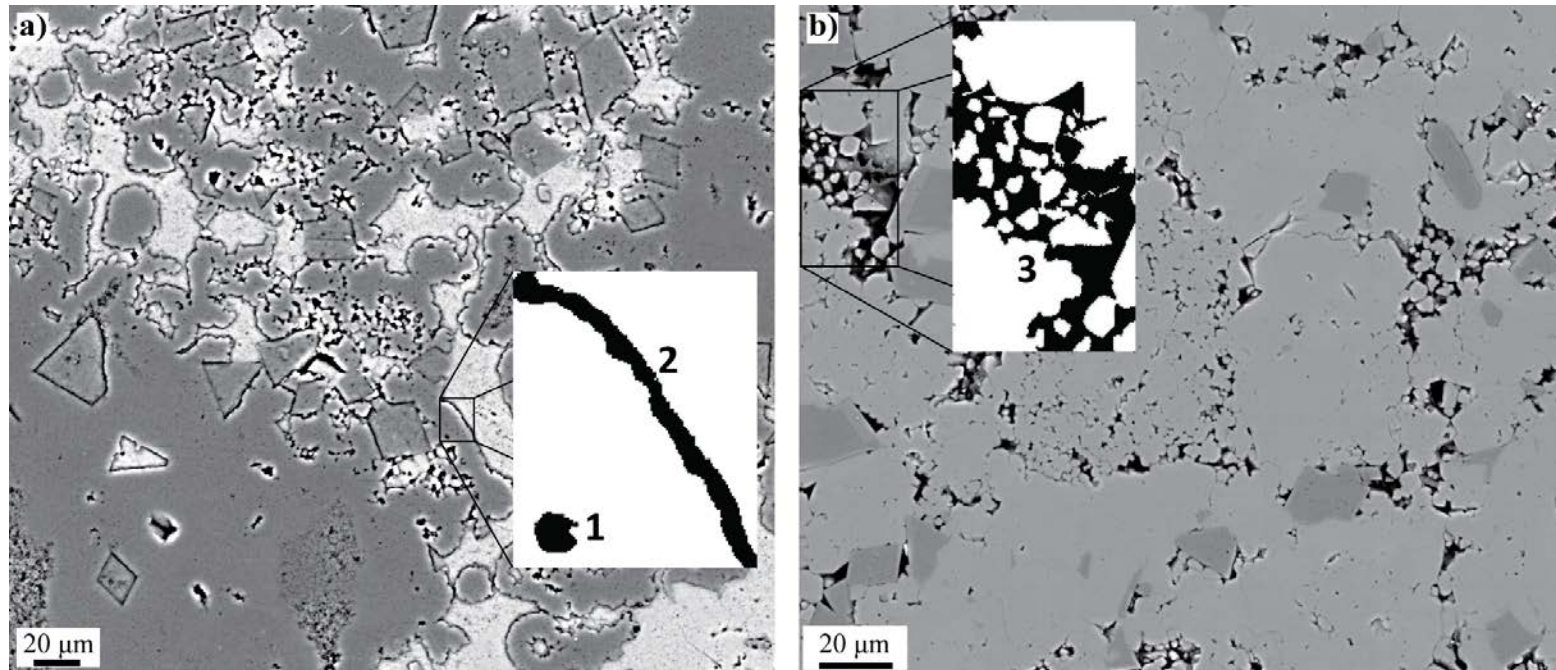


Figure 1.16. SEM photomicrographs showing two examples of extracted pores and their parameters. a) A sample with crystal-form pore, vuggy, and interparticle. Extracted pore 1 has more circular shape (circularity 0.4) as compared to pore 2 (circularity 0.1). a) A sample showing predominantly vuggy and interparticle pores. Pore 3 is also an example of pore with circularity of 0.1. Note, pores with relatively lower circularity can have variety of shapes (from elongated to amorphous shapes).

photomicrographs appear to be open. However, [Vanden Berg and Grammer \(2016\)](#) observed a complex internal architecture in many of the interparticle pores caused by calcite or dolomite crystals growth from the pore wall into pore space and/or precipitation of clay minerals on the pore wall or filling the pore space. This complexity of the internal complex architecture might occlude the connectivity of the pore. Therefore, their contribution to permeability and fluid flow is assumed to be negligible.

Image-based porosity measurement

Porosity based on digital-image analysis (DIA), measured as the sum of all pore areas divided by total image area, reveals that lithofacies 13 (spiculitic mudstone-wackestone) and 1 (chert breccia in greenish shale matrix) have the lowest and highest porosity (for a single sample) at 1.86% and 24.20%, respectively. The smallest pore area is $0.0004 \mu\text{m}^2$ (nanopore) in lithofacies 9 (bioturbated skeletal peloidal packstone-grainstone), and the largest pore area is $2,261,479 \mu\text{m}^2$ (macropore) in lithofacies 1 (chert breccia in greenish shale matrix).

Although, overall comparison of DIA and laboratory-measured core porosity ([Figure 1.17](#)) reveals a positive correlation ($R^2 = 0.94$), it was observed that DIA porosity of lithofacies 13 (spiculitic mudstone-wackestone) and 14 (argillaceous spiculitic mudstone-wackestone) tends to have values somewhat greater than laboratory-measured porosity. The greater DIA porosity values might be due to 1) image-analysis statistical bias, 2) subjectivity in selecting color or gray intensity threshold, 3) plucking of grains during thin-section polishing, and 4) helium porosimetry measurements of effective porosity as compared to total porosity from DIA. In this study, the later reason is hypothesized as the cause. The difference between DIA and laboratory-measured porosity suggests that 3-20% of the pores were possibly inaccessible to helium during

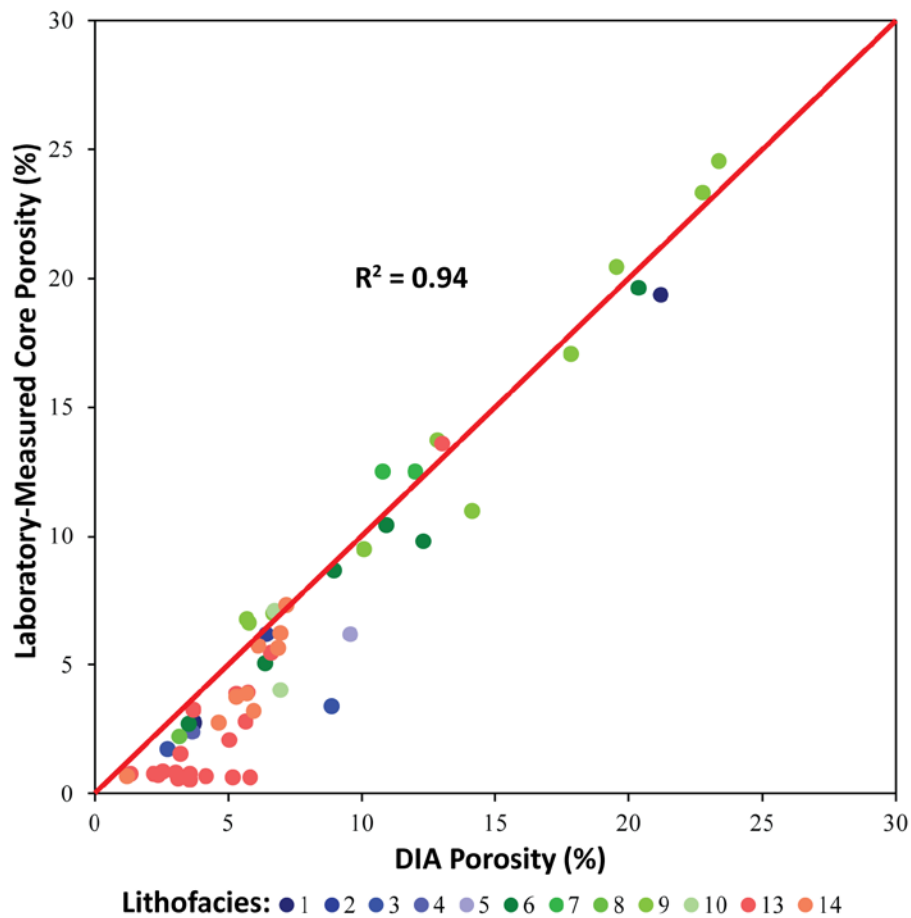


Figure 1.17. Comparison of porosity values obtained from core-plug helium porosimetry (Laboratory-Measured Core Porosity) and digital-image analysis (DIA Porosity). A positive relationship ($R^2 = 0.94$) is apparent. Data are from thin sections for 12 lithofacies: 1. Chert breccia in greenish shale matrix, 2. Chert breccia, 3. Skeletal mudstone-wackestone, 4. Skeletal grainstone, 5. Splotchy packstone-grainstone, 6. Bedded skeletal peloidal packstone-grainstone, 7. Nodular packstone-grainstone, 8. Skeletal peloidal packstone-grainstone, 9. Bioturbated skeletal peloidal packstone-grainstone, 10. Bioturbated mudstone-wackestone, 13. Spiculitic mudstone-wackestone, 14. Argillaceous spiculitic mudstone-wackestone. Note fine-grained dominated lithofacies 13 (spiculitic mudstone-wackestone) and 14 (Argillaceous spiculitic mudstone-wackestone) tend to deviate from ideal correlation. The variation might be attributed to the difference between effective porosity from core-based laboratory measurements and total porosity from digital-image analysis; where in laboratory-measured core porosity, the dominant nanopores in mud-dominated lithofacies are not accessible to helium.

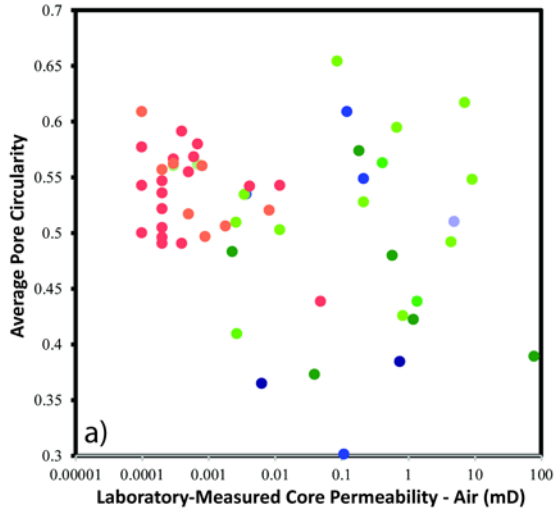
the laboratory measurement and indicates the presence of predominantly isolated nanopores, particularly in lithofacies 13 (spiculitic mudstone-wackestone) and 14 (argillaceous spiculitic mudstone-wackestone).

Pore circularity and its relationship to permeability

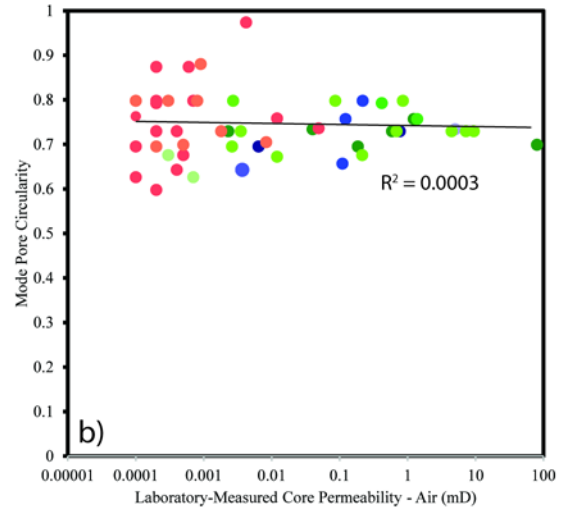
Pore circularity of 57 samples is highly variable, ranging from 0.30-0.65 with an average of 0.52, indicating that the Mississippian rocks have variable pore shapes that range from slightly elongated to slightly circular. The relationship between average pore circularity and laboratory-measured core permeability is indeterminate based on the scattered data (Figure 1.18a). The mode pore circularity shows weak correlation with the laboratory-measured core permeability (Figures 1.18b to 1.18f). These results contrast with previous study in conventional carbonates by Anselmetti et al. (1998) in which pore circularity is an indication of pore connectivity and more elongated pores tend to have better permeability than more circular pores. The real reasons of the poor relationship between average pore circularity and permeability are unknown and required further investigation using other analysis methods (e.g. 3-D image analysis, MICP, or NMR). Vanden Berg and Grammar (2016) proposed that it might be attributed to the complex internal pore network, unconnected microfracture network, and the presence of pore-throat cementation or isolated pores that hinder fluid-flow pathways.

Pore-size distribution

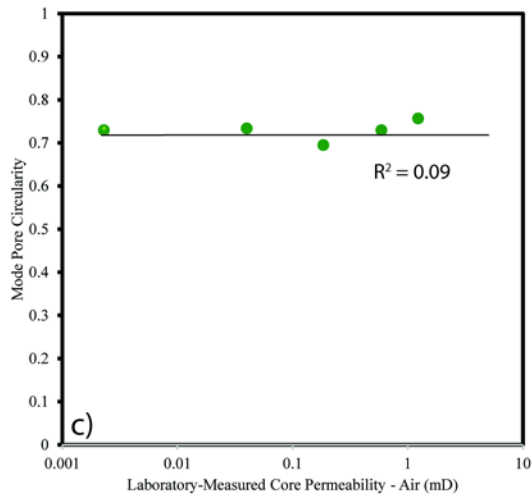
Pore-size distribution can be depicted using a variety of graphical methods. In this study, pore-size distribution of each sample is alternatively plotted as a probability percentage in which pore width (x-axis) is compared to the percentage of pores in the sample that has a width greater than a given width (y-axis) (Figure 1.19). The plot provides simple identification of pore-size classes, dominant pore-size class, quantitative percentage of a pore size class, and approximate



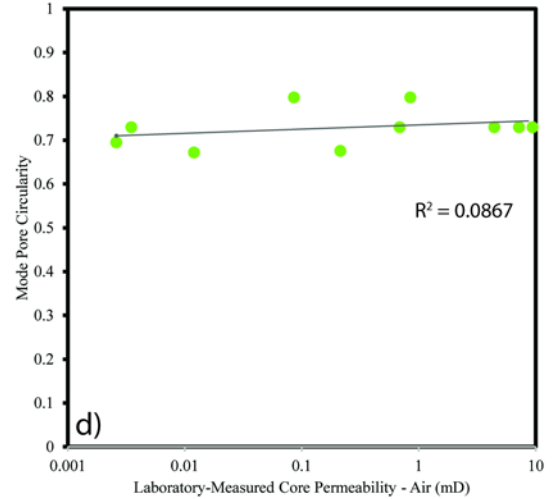
Lithofacies: ● 1 ● 2 ● 3 ● 4 ● 5 ● 6 ● 7 ● 8 ● 9 ● 10 ● 13 ● 14



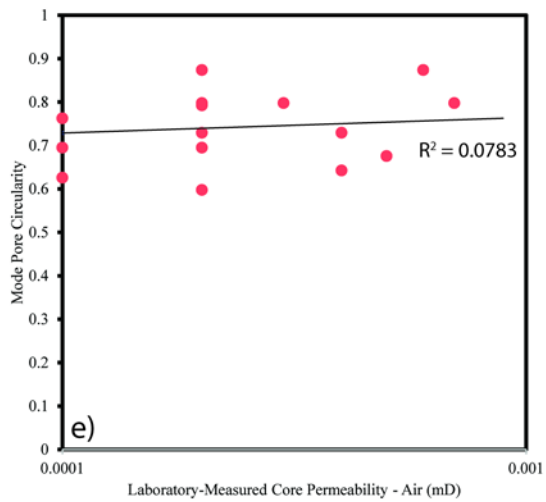
Lithofacies: ● 1 ● 2 ● 3 ● 4 ● 5 ● 6 ● 7 ● 8 ● 9 ● 10 ● 13 ● 14



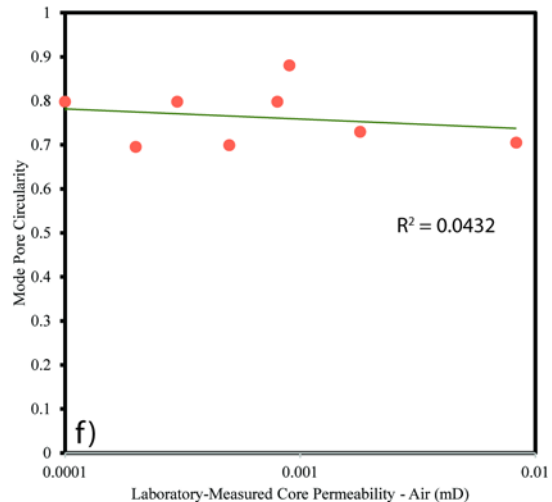
Lithofacies: ● 6



Lithofacies: ● 9



Lithofacies: ● 13



Lithofacies: ● 14

Figure 1.18. a). Cross plot of average pore circularity versus laboratory-measured core permeability. Circularity is defined as the degree to which the pore is similar to a circle. Data are color coded based on lithofacies including 1. Chert breccia in greenish shale matrix, 2. Chert breccia, 3. Skeletal mudstone-wackestone, 4. Skeletal grainstone, 5. Splotchy packstone-grainstone, 6. Bedded skeletal peloidal packstone-grainstone, 7. Nodular packstone-grainstone, 8. Skeletal peloidal packstone-grainstone, 9. Bioturbated skeletal peloidal packstone-grainstone, 10. Bioturbated mudstone-wackestone, 13. Spiculitic mudstone-wackestone, 14. Argillaceous spiculitic mudstone-wackestone. Note that the data show an indeterminate relationship. b). Cross plot of mode pore circularity versus laboratory-measured core permeability. Data are color coded based on lithofacies including 1. Chert breccia in greenish shale matrix, 2. Chert breccia, 3. Skeletal mudstone-wackestone, 4. Skeletal grainstone, 5. Splotchy packstone-grainstone, 6. Bedded skeletal peloidal packstone-grainstone, 7. Nodular packstone-grainstone, 8. Skeletal peloidal packstone-grainstone, 9. Bioturbated skeletal peloidal packstone-grainstone, 10. Bioturbated mudstone-wackestone, 13. Spiculitic mudstone-wackestone, 14. Argillaceous spiculitic mudstone-wackestone. c). Cross plot of mode pore circularity versus laboratory-measured core permeability for lithofacies 6. d). Cross plot of mode pore circularity versus laboratory-measured core permeability for lithofacies 9 shows a weak positive correlation. e). Cross plot of mode pore circularity versus laboratory-measured core permeability for lithofacies 13 shows a weak positive correlation. f). Cross plot of mode pore circularity versus laboratory-measured core permeability for lithofacies 14 shows a weak negative correlation. The poor relationship is possibly due to complex internal pore network, cemented pore throats, or the presence of isolated pores.

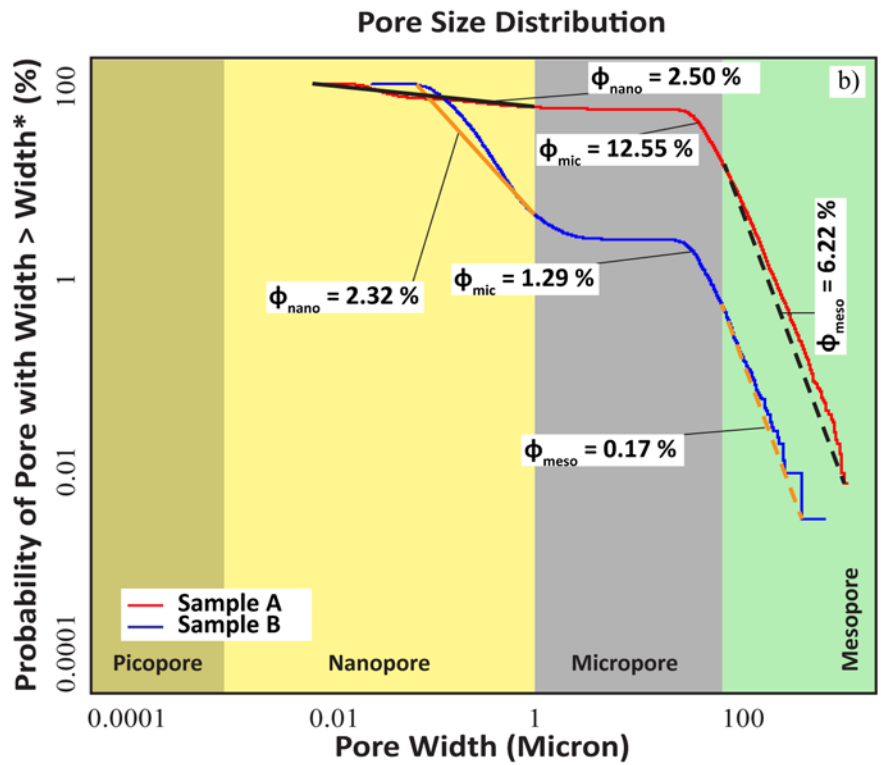
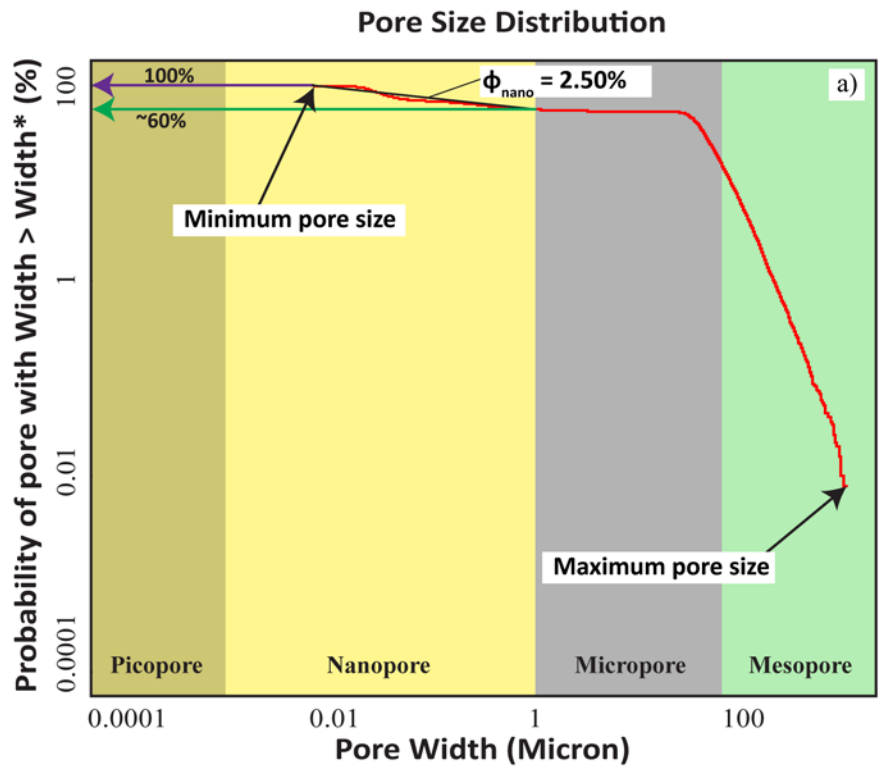


Figure 1.19. Example of pore-size distribution plot for samples A and B. Pore-size distribution is plotted as a probability percentage in which pore width (micron) (in x-axis) is compared to the percentage of pores in the sample that has a width greater than a given width (%) (in y-axis). Straight-line segments (e.g. solid black, solid orange, dash black, and dash orange lines) represent each pore-size class. The plot provides simple identification of pore-size classes, dominant pore-size class, quantitative percentage of a pore class, and approximate minimum and maximum pore size (black arrows). Data (red line of part a) are divided into pore-size classes (colored regions on plot) with each pore-size class represented by straight-line segments (black line in part a and black and orange lines in part b). For each straight-line segment, the A) slope and B) probability range (range in y-values, %) are obtained. In part a, the data show that the probability range for nanopores is 60-100% or ~40% of measured pores are nanopores with porosity of 2.50% (purple and green lines in part a). b) The line-segment slopes for pore-size classes of two samples are compared in part b. For example, the straight-line segment representing nanopores of sample B (orange solid line) has a steeper slope as compared to sample A (black solid line). This indicates that sample B has a greater quantity of nanopores as compared to sample A and a greater number of smaller nanopores than in sample A. Therefore, sample B has lower nano-porosity ($\phi_{\text{nano}} = 2.32\%$) as compared to sample A ($\phi_{\text{nano}} = 2.50\%$). Additionally, the line segment representing mesopores of sample A (black dashed line) has a similar slope to sample B (orange dashed line) but a higher probability (y-value) indicating that sample A has a greater quantity of mesopores and higher mesoporosity ($\phi_{\text{meso}} = 6.22\%$) as compared to sample B ($\phi_{\text{meso}} = 0.17\%$).

minimum and maximum pore size (see black arrows in [Figure 1.19A](#)). On the pore-size distribution plot, the data (red line) are divided into pore-size classes (colored regions on plot) with each pore-size class represented by straight-line segments (black line in [Figure 1.19A](#) and black and orange lines in [Figure 1.19B](#)). For each straight-line segment, the A) slope and B) probability range (range in y-values, %) are obtained. In [Figure 19A](#), the data show that the probability range for nanopores is 60-100% or ~40% of measured pores are nanopores with porosity of 2.50% (see purple and green lines in [Figure 1.19A](#)).

The line-segment slopes for pore-size classes of two samples are compared in [Figure 19B](#). For example, the straight-line segment representing nanopores of sample B (orange solid line) has a steeper slope as compared to sample A (black solid line). This indicates that sample B has a greater quantity of nanopores as compared to sample A and a greater number of smaller nanopores than in sample A. Therefore, sample B has lower nano-porosity ($\phi_{\text{nano}} = 2.32\%$) as compared to sample A ($\phi_{\text{nano}} = 2.50\%$). Additionally, the line segment representing mesopores of sample A (black dashed line) has a similar slope to sample B (orange dashed line) but a higher probability (y-value) indicating that sample A has a greater quantity of mesopores and higher mesoporosity ($\phi_{\text{meso}} = 6.22\%$) as compared to sample B ($\phi_{\text{meso}} = 0.17\%$).

Pore-size class slope and probability range (y-values) for samples can be compared and analyzed as follows: 1) an equal slope and greater probability indicates higher porosity, 2) an equal slope but lower probability indicated lower porosity, 3) a steeper slope and greater probability indicates a greater quantity of smaller pores and lower porosity, 4) a gentler slope and lower probability indicates a greater quantity of larger pores and higher porosity, and 5) a slope near zero indicates there are few pores for that pore-size class.

Pore-size distributions from 57 samples for each lithofacies ([Figure 1.20](#)) show complex pore-size distributions with a minimum pore size $<0.02 \mu\text{m}$ and predominantly nanopores and micropores.

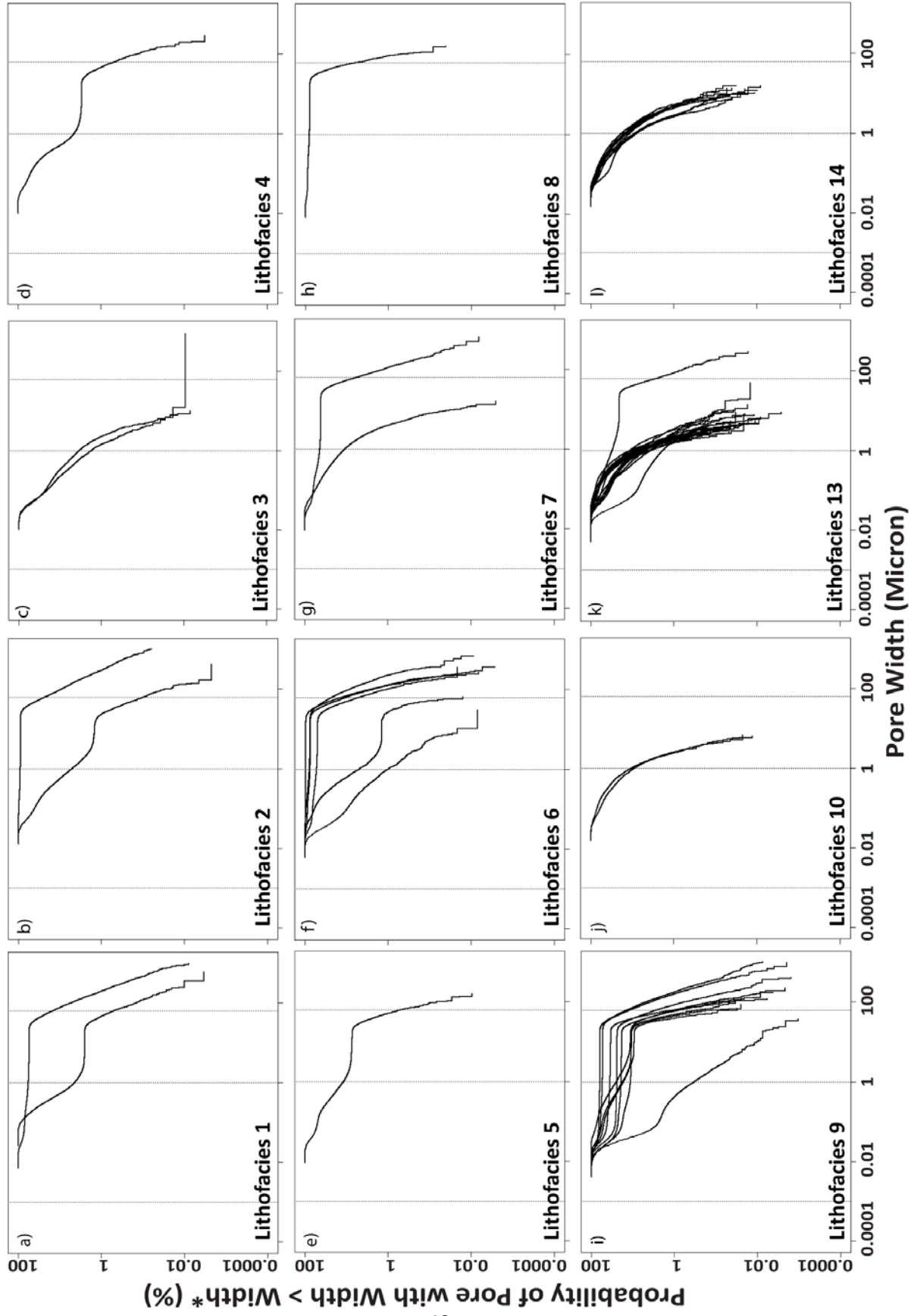


Figure 1.20. Pore-size distribution plots for 12 lithofacies including: 1. Chert breccia in greenish shale matrix, 2. Chert breccia, 3. Skeletal mudstone-wackestone, 4. Skeletal grainstone, 5. Splotchy packstone-grainstone, 6. Bedded skeletal peloidal packstone- grainstone, 7. Nodular packstone-grainstone, 8. Skeletal peloidal packstone-grainstone, 9. Bioturbated skeletal peloidal packstone-grainstone, 10. Bioturbated mudstone-wackestone, 13. Spiculitic mudstone-wackestone, 14. Argillaceous spiculitic mudstone-wackestone. Note that fine-grained lithofacies 3, 10, 13 and 14 have predominantly nanopores and micropores while coarse-grained lithofacies 1, 2, 4, 5, 6, 7, 8, 9 have a variable pore-size distribution ranging from nanopores to mesopores.

The quantitative data shows most samples of lithofacies 1, 2, 4, 5, 6, 7, 8, 9, which are coarse-grained lithofacies, generally exhibit a wider spectrum of pore sizes ranging from nano- to mesopores. These variable pore-size distributions could be the result of the complex diagenetic history of the Mississippian strata. Lithofacies 3, 10, 13, and 14, fine-grained lithofacies, mainly have bimodal pore-size distributions with a significant proportion of nanopores and therefore have a relatively lower DIA total porosity.

These observations suggest that there is a clear primary textural control on pore-size distribution of two lithofacies groups; coarse-grained lithofacies that occur mainly within sequence 3 have a more variable pore-size distribution, and the fine-grained lithofacies of sequences 2 and 3 are more uniform in terms of pore-size distribution.

Porosity, permeability, and lithofacies

Based on laboratory-measured core porosity and permeability, only lithofacies 6, 9, 13, and 14 have well-defined porosity-permeability relationships (Figure 1.21). The highest core-measured porosity and permeability is in lithofacies 6 (bedded skeletal peloidal packstone-grainstone) at 19.60% porosity and 80.2 mD air-permeability. The second highest core-measured porosity and permeability is in lithofacies 9 at 24.50 % porosity and 9.41 mD air-permeability. Lithofacies 13 (spiculitic mudstone-wackestone) and 14 (argillaceous spiculitic mudstone-wackestone) have the lowest and consistent air-permeability ranging from 0.0001 – 0.049 mD with porosity vary from 0.52 – 13.53 %. A comparison of lithofacies 6, 9, 13, and 14 supports a typical porosity-permeability relationship that coarse-grained lithofacies (lithofacies 6 and 9)

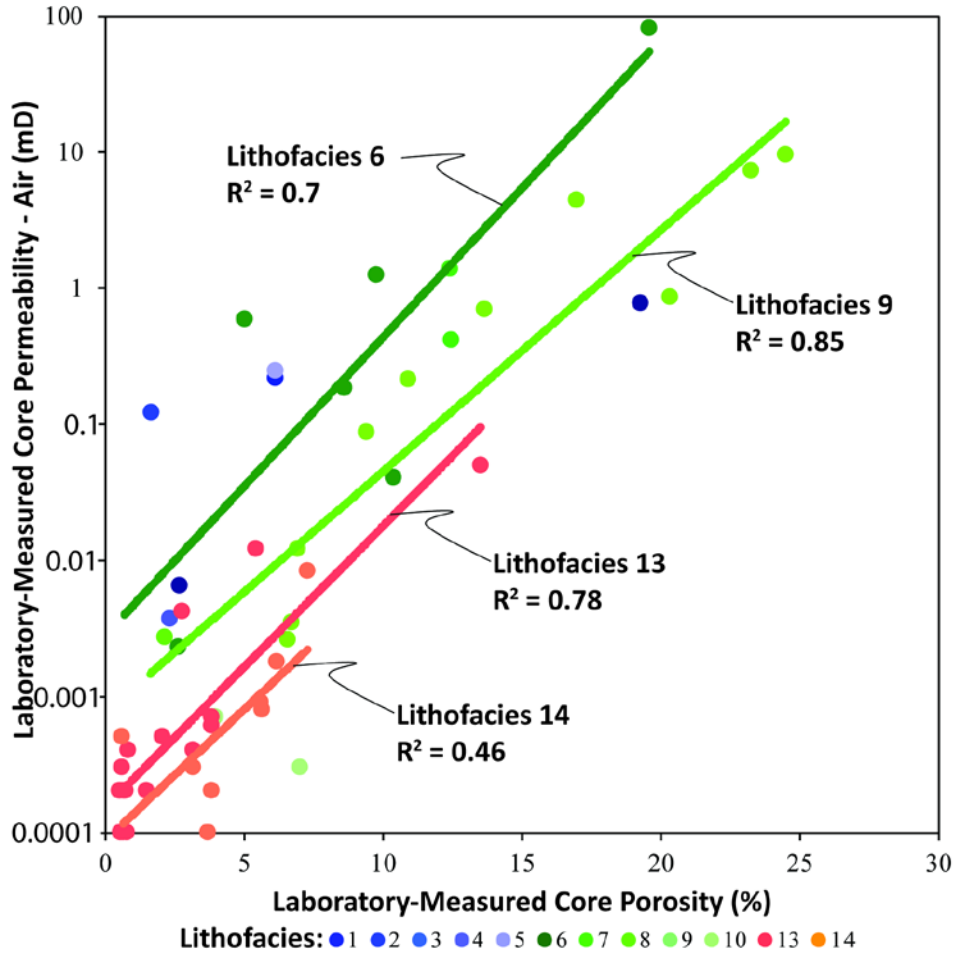


Figure 1.21. Plot of laboratory-measured core porosity versus laboratory-measured core permeability for 12 lithofacies including: 1. Chert breccia in greenish shale matrix, 2. Chert breccia, 3. Skeletal mudstone-wackestone, 4. Skeletal grainstone, 5. packstone grainstone, 6. Bedded skeletal peloidal packstone-grainstone, 7. Nodular packstone-grainstone, 8. Skeletal peloidal packstone-grainstone, 9. Bioturbated skeletal peloidal packstone-grainstone, 10. Bioturbated mudstone-wackestone, 13. Spiculitic mudstone-wackestone, 14. Argillaceous spiculitic mudstone-wackestone. Exponential trend lines of lithofacies 6, 9, 13, and 14 show a reasonable positive correlation between laboratory-measured core porosity and permeability. Lithofacies 13 and 15 are fine-grained lithofacies while lithofacies 5 and 9 are coarse-grained lithofacies. Note the poor relationship between porosity and permeability of lithofacies 14 ($R^2 = 0.46$). This might be attributed to the presence of clay as indicated by relatively high gamma-ray responses (Figure 2.9).

tend to be more permeable for a given porosity than fine-grained lithofacies (lithofacies 13 and 14). The porosity-permeability transforms for these 4 (four) lithofacies can be written as:

Lithofacies 6 (Bedded skeletal peloidal packstone-grainstone):

$$k = 0.0028 e^{0.5041\phi} \quad R^2 = 0.70$$

Lithofacies 9 (Bioturbated skeletal peloidal packstone-grainstone):

$$k = 0.0005 e^{0.4918\phi} \quad R^2 = 0.94$$

Lithofacies 13 (Spiculitic mudstone-wackestone):

$$k = 0.0002 e^{0.4762\phi} \quad R^2 = 0.78$$

Lithofacies 14 (Argillaceous spiculitic mudstone-wackestone):

$$k = 0.00009 e^{0.4332\phi} \quad R^2 = 0.46$$

where k = permeability (mD) and ϕ = laboratory-measured core porosity (effective porosity) (%). The poor relationship between porosity and permeability of lithofacies 14 (argillaceous spiculitic mudstone-wackestone) is likely due to clay particles as indicated by the relatively high gamma-ray response (Figure 9).

Lithofacies 1, 2, 3, 4, 5, 7, 8, and 10 have undefined relationships between porosity and permeability. This indeterminate correlation is due to limited data. Hypothetically, if there are Mercury Injection Capillary Pressure (MICP), sonic velocity (V_p and V_s), and more core porosity and permeability data available, one can calculate pore structure index (γ_μ) and integrate it with core data to improve accuracy of permeability prediction using porosity. This integration approach has been proven successful to work in conventional carbonate (e.g. [Dou et al., 2011](#); [Huang et al., 2017](#))

Porosity, permeability, and sequence-stratigraphic framework

The Mid-continent Mississippian interval of this study contains 29 relatively high-frequency cycles that are 1 to 100 ft (0.3 to 30.5 m) thick and stack to form three lower order depositional sequences (Figure 9-10). Predicting reservoir-quality distribution in this stratum is challenging due to the complexity of the pore systems and diagenesis. There are no clear relationships between reservoir quality (porosity and permeability) and fracture density or percentage of specific minerals such as quartz, calcite and dolomite. Detail examination shows porosity and permeability are most predictively controlled by stratigraphic cycles and lithofacies; therefore, the sequence stratigraphy could be used as a predictable model for reservoir quality and distribution. A predictable vertical distribution of porosity and permeability is identified in the cycles and reveals that high reservoir quality in the Mid-continent Mississippian strata appears to be associated with high-frequency upward-shoaling regressive cycles (Figure 2.9). This finding agrees with previous studies (Wittman, 2013; Birch, 2015; and Vanden Berg and Grammer, 2016) which also observed that the highest reservoir quality occurs at the tops of upward-shoaling regressive cycles. However, unlike the Mississippian-age rocks in the Osage County, east of the Nemaha Ridge (e.g. Vanden Berg and Grammer 2016) there is no evidence of hydrothermal brecciation increasing porosity and permeability value in the core of this study.

CONCLUSIONS

The Mississippian limestone and chert reservoirs of north-central Oklahoma in the core of this study exhibit pore characteristics that vary considerably with lithofacies and stratigraphy. The observed pore characteristics including pore area, circularity, and pore-size distribution show unique relationships with core porosity, permeability, and lithofacies within a sequence-stratigraphic framework.

There are at least 17 lithofacies and 29 relatively high-frequency cycles (and 3 lower order depositional sequences) documented for the Mississippian Limestone of this study. The high-frequency cycles range in thickness from 1-100 ft (0.3-30.5 m) and are primarily represented as asymmetric regressive phases.

A generic carbonate ramp model is used to place identified lithofacies in their relative depositional positions spatially. The result shows sequence 1 was deposited under quiet-water conditions below the fair-weather wave base in the basinal environment. The relatively low bioturbation and abundance of sponge spicules within sequence 2 are consistent with deposition under more restricted conditions. The abundance of skeletal grains and high degree of bioturbation in the sequence 3 correlate to deposition in relatively shallow water under a normal-marine condition. The presence of scoured surfaces, locally preserved cross bedding, and skeletal fragments indicate fluctuating energy conditions.

A positive correlation ($R^2 = 0.94$) is observed between porosity from digital-image analysis (DIA) and laboratory core measurements with values from DIA yielding relatively higher values, specifically in fine-grained lithofacies. The porosity value discrepancy in the fine-grained lithofacies (bioturbated mudstone-wackestone, spiculitic mudstone-wackestone, and argillaceous spiculitic mudstone-wackestone) is hypothesized as a result of the presence of isolated nanopores that are not accessible by helium during laboratory measurement of core effective porosity. Additionally, unlike the conventional carbonates, there is an insignificant correlation between pore circularity and permeability. This low correlation is hypothesized to be related to a complex internal pore network that is not revealed by DIA using 2-D optical and SEM photomicrographs. To prove these hypotheses of intensive diagenetic alteration that occluded pore-throat flow paths, an unconnected microfracture network, and isolated pores requires 3-D image analysis or other analytical methods (e.g. MICP, NMR).

Also, unlike the conventional carbonate, there is no general correlation between porosity and permeability in the Mid-continent Mississippian interval of the core in this study. Only 4 identified lithofacies including skeletal peloidal packstone-grainstone, bedded skeletal peloidal packstone-grainstone, spiculitic mudstone-wackestone, and argillaceous spiculitic mudstone-wackestone have a positive strong correlation between porosity and permeability. The Mississippian-aged rocks in this study is also different than Mississippian Lime in the east of the Nemaha Ridge (e.g. Rottmann, 2014) as there are only a few streaks of high porosity and high permeability rocks in the core of this study. These rocks are often occurred at the upper intervals of relatively high-frequency shallowing-upward cycles. This finding agrees with previous studies which also observed the occurrence of highest reservoir quality at the tops of upward-shoaling regressive cycles; and confirmed that the sequence-stratigraphic variability of lithofacies is important to predict reservoir quality and its distribution.

This study proposed an alternative graphical method to represent and analyze pore-size distribution. The pore-size distribution is plotted as a probability percentage in which pore width (x-axis) is compared to the percentage of pores in the sample that has a width greater than a given width (y-axis). The plot offers simple identification of pore-size classes, quantitative percentage of a pore-size class, dominant pore class, and approximate minimum and maximum pore size. The line-segment slopes and probability range for pore-size classes of each samples in a plot also provide an unique opportunity to compare pore-size distribution as follows: 1) an equal slope and greater probability indicates higher porosity, 2) an equal slope but lower probability indicated lower porosity, 3) a steeper slope and greater probability indicates a greater quantity of smaller pores and lower porosity, 4) a gentler slope and lower probability indicates a greater quantity of larger pores and higher porosity, and 5) a slope near zero indicates there are few pores for that pore-size class. The plot of pore-size distributions from 57 samples show coarse-grained lithofacies within the uppermost depositional sequence of the Mississippian have a

more variable pore-size distribution while fine-grained lithofacies tend to exhibit a more uniform pore-size distribution. These observations show that there is a clear primary textural control on pore-size distribution of two lithofacies groups; coarse-grained lithofacies that occur mainly within sequence 3, and the fine-grained lithofacies within sequences 2.

REFERENCES

- Al-Kharusi, A. S., and M. J. Blunt, 2007, Network extraction from sandstone and carbonate pore space images: *Journal of Petroleum Science and Engineering* **56**, 219 – 231.
- Anselmetti, F. S., S. M. Luthi, and G. P. Eberli, 1998, Quantitative characterization of carbonate pore systems by digital image analysis: *AAPG Bulletin*, **82**, 1815-1836.
- Bauget, F., C.H. Arns, A. Sheppard, R. Sok, V. Pinczewski, and M. Knackstedt, 2005, Rock Typing and Petrophysical property estimation via direct analysis on microtomographic image: *Proceeding of the Annual Symposium of the Society of Core Analysts, SCA2005-81*, Toronto, Canada.
- Birch, C. B., 2015, Reservoir-scale stratigraphy, sedimentology, and porosity characteristics of Mississippian reservoirs, northeastern Anadarko Shelf, Oklahoma, Master's thesis, University of Oklahoma, Norman, Oklahoma, 81.
- Blakey, R., 2013, Paleogeography and Geologic Evolution of North America, <http://www2.nau.edu/rcb7/nam.html>. Accessed October 2013.
- Buggisch, W., M. M. Joachimski, G. Sevastopulo, and J. R. Morrow, 2008, Mississippian $\delta^{13}\text{C}_{\text{carb}}$ and Conodont Apatite $\delta^{18}\text{O}$ Records – Their Relation to the Late Palaeozoic Glaciation: *Palaeogeography, Palaeoclimatology, Palaeoecology*, **268**, 273-292.
- Campbell, J. A., C. J. Mankin, A. B. Schwarzkopf, and J. J. Raymer, 1988, Habitat of petroleum in Permian rocks of the midcontinent region, in W. A. Morgan and J. A. Babcock, eds., *Permian Rocks of the Midcontinent: Midcontinent Society of Economic Paleontologists and Mineralogists (SEPM) Special Publication* **1**, 13-35.
- Childress, M., and G.M. Grammer, 2015, High resolution sequence stratigraphic architecture of a Mid-Continent Mississippian outcrop in southwest Missouri: *The Shale Shake*, **66**, 206-234.
- Choquette, P. W., and L. C. Pray, 1970, Geologic nomenclature and classification of porosity in sedimentary carbonates: *AAPG Bulletin*, **54**, 207–250.
- Costello, D., M. Dubois, and R. Dayton, 2014, Core to characterization and modeling of the Mississippian, North Alva Area: 2014 Mid-Continent Section AAPG Core Workshop, 165-174.
- Davis, J. C., 1986, *Statistics and data analysis in geology*: New York, Wiley, 646.
- Dou, Q., Y. Sun, and C. Sullivan, 2011, Rock-physic-based carbonate pore type characterization and reservoir permeability heterogeneity evaluation, Upper San Andres reservoir, Permian Basin, west Texas: *Journal of Applied Geophysics*, **74**, 8-18.
- Dunham, R. J., 1962, Classification of carbonate rocks according to depositional texture: *AAPG Memoir* **1**: *Classification of Carbonate Rocks – A Symposium*, 108–121.

- Dutton, S. P., 1984, Fan-delta Granite Wash of the Texas Panhandle: Oklahoma City Geological Society Short Course, 1–144.
- Franseen, E. K., 2006, Mississippian (Osagean) shallow-water, mid-latitude siliceous sponge spicule and heterozoan carbonate facies: An example from Kansas with implications for regional controls and distribution of potential reservoir facies: *Current Research in Earth Sciences Bulletin*, **252**, 1–23: <http://www.kgs.ku.edu/Current/2006/franseen/index.html>
- Fritz, R. D., and P. L. Medlock, 1994, Sequence stratigraphy of the Hunton Group as defined by core, outcrop, and log data in K.S. Johnson, eds., Hunton Group core workshop and field trip: Oklahoma Geological Survey Special Publication **93-4**, 161-180.
- Gay, P. S. Jr., 2003, The Nemaha Trend – A System of Compressional Thrust-Fold, Strike-Slip Structural Features in Kansas and Oklahoma Part 1: Shale Shaker, July-August, 9-49.
- Gutschick, C. R., and C.A. Sandberg, 1983, Mississippian continental margins of the conterminous United States: in Stanley, D. J., and Moore, G. T., eds., *The Shelfbreak: Critical Interface on Continental Margins: Society of Economic Paleontologists and Mineralogists (SEPM) Special Publication* **33**, 79-96.
- Haq, B. U., and S. R. Schutter, 2008, A chronology of Paleozoic sea-level changes: *Science*, **322**, 64-68.
- Huang, Q., Q. Dou, Y. Jiang, Q. Zhang, and Y. Sun, 2017, An integrated approach to quantify geologic controls on carbonate pore types and permeability, Puguang gas field, China: *Interpretation*, **5-4**, T545-T561.
- Jaekel, L., 2016, High-resolution sequence stratigraphy and reservoir characterization of midcontinent Mississippian carbonates in north-central Oklahoma and south-central Kansas, Master's thesis, Oklahoma State University, Stillwater, Oklahoma, 356.
- Johnson, K. S., and K. V. Luza, 2008, Earth sciences and mineral resources of Oklahoma: Educational Publication **9**, Oklahoma Geological Survey, 22.
- Lane, H. R., and T. L. De Keyser, 1980, Paleogeography of the late Early Mississippian (Tournaisian 3) in the central and southwestern United States, in T. D. Fouch and E. R. Magathan, eds., *Paleozoic Paleogeography of west-central United States: Rocky Mountain Section SEPM*, 149-159.
- LeBlanc, S., 2014, High resolution sequence stratigraphy and reservoir characterization of the “Mississippian Limestone” in North-Central Oklahoma, Master's thesis, Oklahoma State University, Stillwater, Oklahoma, 443.
- Lindzey, K. M., M. J. Pranter, and K. J. Marfurt, 2017, Lithological and petrophysical controls on production of the Mississippian Limestone, northeastern Woods County, Oklahoma, in G. M. Grammer, J. M. Gregg, J. O. Puckette, P. Jaiswal, S. J. Mazzullo, M. J. Pranter, and R. H. Goldstein, eds., *Mississippian Reservoir of the Midcontinent, AAPG Memoir* **116**.

- LoCricchio, E., 2012, Granite Wash play overview, Anadarko Basin: Stratigraphic framework and controls on Pennsylvanian Granite Wash production, Anadarko Basin, Texas and Oklahoma, AAPG Annual Convention and Exhibition: Long Beach, California, 1-17.
- Loucks, R. G., R. M. Reed, S. C. Ruppel, and U. Hammes, 2012, Spectrum of pore types and networks in mudrocks and a descriptive classification for matrix-related mudrock pores: AAPG Bulletin, **96**, 1071-1098.
- Mazzullo, S. J., 2011, Mississippian oil reservoirs in the Southern Midcontinent: New exploration concepts for a mature reservoir objective: AAPG Search and Discovery #10373.
- Mazzullo, S. J., B. W. Wilhite, and D. R. Boardman, 2011, Lithostratigraphic architecture of the Mississippian Reeds Spring Formation (Middle Osagean) in S. W. Missouri, N. W. Arkansas, and N. E. Oklahoma: Outcrop analog of subsurface petroleum reservoirs: Shale Shaker, **61**, 254-269.
- Mazzullo, S. J., B. W. Wilhite, D. R. Boardman, B. T. Morris, and C. J. Godwin, 2016, Stratigraphic architecture and petroleum reservoirs in lower to middle Mississippian strata (Kinderhookian to basal Meramecian in subsurface central to southern Kansas and northern Oklahoma: Shale Shaker, **67**, 20-49.
- Mazzullo, S. J., B. W. Wilhite, and W. Woolsey, 2009, Rhythmic carbonate versus spiculite deposition in Mississippian hydrocarbon reservoirs in the Midcontinent USA: Causative factors and resulting reservoir petrophysical attributes, AAPG Search and Discovery #10209.
- Mazzullo, S. J., D. R. Boardman, B. W. Wilhite, C. Godwin, and B. T. Morris, 2013, Revisions of Outcrop Lithostratigraphic Nomenclature in the Lower to Middle Mississippian Subsystem (Kinderhookian to Basal Meramecian Series) Along the Shelf-Edge in Southwest Missouri, Northwest Arkansas, and Northeast Oklahoma, Shale Shaker, **63-6**, 414-454.
- McConnell, D. A., M. J. Goydas, G. N. Smith, and J. P. Chitwood, 1989, Morphology of the frontal fault zone, southwest Oklahoma: Implications for deformation and deposition in the Wichita uplift and Anadarko basin: Geology, **18-7**, 634-637.
- Miller, M. F., and S. E. Smail, 1997, A semi-quantitative field method for evaluation bioturbation on bedding planes: PALAIOS, **12**, 391-396.
- Montgomery, S.L., J. C. Mullarkey, M. W. Longman, W. M. Colleary, and J. P. Rogers, 1998, Mississippian chat reservoirs, south Kansas: Low-resistivity pay in a complex chert reservoir: AAPG Bulletin, **82-2**, 187-205.
- Munsell, 2009, Geological Rock-Color with genuine Munsell color chips, 2009 Year Revised, Grand Rapids, Michigan, 11.

- Nissen, S. E., K. J. Marfurt, and T. R. Carr, 2004, Identifying subtle fracture trends in the Mississippian saline aquifer unit using new 3-D seismic attributes, KGS Open File Report, **56**.
- Norbisrath, J. A., G. P. Eberli, B. Laurich, G. Desbois, R. J. Weger, and J. L. Urai, 2015, Electrical and fluid flow properties of carbonate microporosity types from multiscale digital image analysis and mercury injection; AAPG Bulletin, **99-11**, 2077-2098.
- Northcutt, R. A., and J. A. Campbell., 1995, Geologic provinces of Oklahoma: Oklahoma Geological Survey Open-File Report **5-95**, 1 sheet, scale 1:750,000, 6-page explanation and bibliography.
- Olson, E., 2011, Particle shape factors and their use in image analysis – Part 1: Theory: Journal of GXP Compliance, **15-3**, 85-96.
- Parham, K. D., and R. A. Northcutt, 1993, Mississippian chert and carbonate and basal Pennsylvanian sandstone – central Kansas uplift and northern Oklahoma, in D. Bebout, W. White, and T. Hentz, eds., Atlas of Major Midcontinent Gas Reservoirs: Gas Research Institute, 57-59.
- Price, B., 2014, Identification of high-frequency cyclicity in the Mississippian (Osagean) Bentonville Formation, northwestern Arkansas, Master's thesis, Oklahoma State University, Stillwater, Oklahoma, 226.
- Rogers, S. M., 2001, Deposition and diagenesis of Mississippian chat reservoirs, north central Oklahoma: AAPG bulletin, **85**, 115-129.
- Rogers, J. P., M. W. Longman, and R. M. Lloyd, 1995, Spiculitic chert reservoir in Glick Field, south-central Kansas: The Mountain Geologist, **32**, 1-22.
- Rottmann, K., 2014, Stratigraphic architecture of the Kinderhookian to Meramecian Series: Mississippian Play Workshop, Oklahoma Geological Survey, Norman, Oklahoma, 41.
- Sok R. M., T. Varslot, A. Chous, S. Latham, A. P. Sheppard, and M. A. Knackstedt, 2009, Pore scale characterization of carbonates at multiple scale: Integration of Micro-CT, BSEM, and FIBSEM: Petrophysics, **51-6**, 379-387.
- Turnini, A.M., 2015, Stratigraphic and structural controls on Mississippian limestone and tripolitic chert reservoir distribution using seismic-constrained reservoir characterization and modeling, northern Oklahoma, Master's thesis, University of Oklahoma, Norman, Oklahoma, 83.
- Turnini, A.M., M. J. Pranter, and K. J. Marfurt, 2017, Mississippian limestone and chert reservoirs, Tonkawa Field, north-central Oklahoma, in G. M. Grammer, J. M. Gregg, J. O. Puckette, P. Jaiswal, S. J. Mazzullo, M. J. Pranter, and R. H. Goldstein, eds., Mississippian Reservoir of the Midcontinent, AAPG Memoir **116**.
- Vanden Berg, B., G.M. Grammer, 2016, 2-D pore architecture characterization of a carbonate mudrock reservoir: insight from the Mid-Continent “Mississippi Lime”, in T. Olson, ed., Imaging unconventional reservoir pore systems: AAPG Memoir **112**, 185-232.

- Watney, W. L., W. J. Guy, and A. P. Byrnes, 2001, Characterization of the Mississippian chat in south-central Kansas: AAPG Bulletin, **85**, 85–113.
- Wethington, N., 2017, Stratigraphic architecture of the Mississippian limestone through integrated electrofacies classification, Hardtner field area, Kansas and Oklahoma, Master's thesis, University of Oklahoma, Norman, Oklahoma, 103.
- Wittman, B. R., 2013, Subsurface stratigraphy and characterization of Mississippian (Osagean to Meramecian) carbonate reservoir of the Northern Anadarko Shelf, North-Central Oklahoma, Master's thesis, University of Arkansas, Fayetteville, Arkansas, 76.

2. VARIABILITY OF MISSISSIPPIAN LITHOFACIES, DEPOSITIONAL ENVIRONMENTS, DIAGENETIC PROCESSES, AND RESERVOIR QUALITY WITHIN A MIXED SILICICLASTIC-CARBONATE SYSTEM, EASTERN ANADARKO BASIN, OKLAHOMA, USA.

ABSTRACT

In the eastern Anadarko Basin of central Oklahoma, the variability of Mississippian lithofacies, diagenetic products, and reservoir quality are poorly understood but critical for reservoir development. This study investigates lithofacies variability based on sedimentological characteristics and diagenetic alteration through integration of core and thin sections by using optical microscope, scanning electron microscope (SEM), energy dispersive x-ray diffraction spectroscopy (EDX), and electron probe micro-analyzer (EPMA)-cathodoluminescence (CL) analyses.

Based on detailed descriptions of 5 cores (260 m; 850 ft) and analysis of 34 thin sections, the Mississippian strata consists of 8 lithofacies that represent wave-dominated nearshore, restricted embayment (lagoon), and channel or lobe deposits. Lithofacies have undergone diagenetic alteration including calcite cementation, mechanical compaction, albitization, quartz cementation, silicification, dolomitization, Fe-dolomite cementation, pyritization, and dissolution. A paragenesis scheme suggests that quartz cementation occurred earlier compared to albitization and Fe-dolomite cementation. The Fe-dolomite is the latest authigenic mineral formed whereas the quartz and calcite cement can be attributed to earlier diagenesis. Reservoir quality is relatively good in the channel or lobe deposits and is generally poor in the upper shoreface to upper offshore environments. The reservoir quality is significantly reduced by compaction, calcite and quartz cements, as well as amount of clay minerals. However, the dissolution of cement and detrital grains tends to improve reservoir quality by forming secondary pores.

INTRODUCTION

Mississippian strata form unconventional reservoirs of the STACK (Sooner Trend in the Anadarko [Basin] in Canadian and Kingfisher counties) play, central Oklahoma. The reservoirs primarily consist of regionally extensive low permeability ($k < 0.1$ mD) siltstones. Economic production from such low-permeability but volumetrically large reservoirs relies not only on locating the intervals within the reservoirs that exhibit mechanical properties that facilitate hydraulic fracture stimulation, but also on the understanding of sedimentological and diagenetic characteristics of the reservoirs and the way in which these characteristics control reservoir quality. Several recent studies of the Mississippian-age rocks in the Anadarko Basin have focused on the control of stratigraphy on fracture growth and completion optimization (Price et al., 2017); stratigraphic variability of lithology (Drummond, 2018; Hickman, 2018; Miller, 2018); understanding of the regional distribution of fluid composition and properties (Welker et al., 2016); regional diagenesis of Mississippian strata of the southern Midcontinent (Dehcheshmehi, 2016); and modeling the spatial distribution of reservoir properties and organic content (Shelley et al., 2017; Hickman, 2018; Miller, 2018). However, there have been fewer studies on Mississippian lithofacies and diagenetic characteristics and how they influence reservoir quality (e.g., Hardwick, 2018). Important geologic controls on reservoir quality including provenance and depositional environment have not been adequately investigated. This study presents the results of detailed core and thin section analyses of the Mississippian-age rocks in the STACK play area and addresses lithofacies and their sedimentological and diagenetic characteristics as identified in 5 cores (total length ~260 m or 850 ft) that are located in Kingfisher, Blaine, and Canadian Counties (Figure 2.1). A depositional model is generated based on the lithofacies and their sedimentological characteristics. The impact of lithofacies and diagenetic alterations on reservoir quality is also investigated and discussed.

Reservoir quality, when linked to petrological analysis, is the realistic basis for understanding fluid flow paths within these fine-grained siliciclastic lithofacies. [Price et al. \(2017\)](#) suggested that the reservoir quality of the STACK play is controlled by the percentage of calcite cement. Primary porosity is typically preserved when clays are present to inhibit cementation. In order to investigate how diagenetic processes and mineral composition influence the reservoir quality, 34 thin-sections were analyzed using the combination of optical microscope, scanning electron microscope (SEM), energy dispersive x-ray diffraction spectroscopy (EDX), and electron probe micro analyzer (EPMA)-cathodoluminescence.

The improved understanding of the proximal to distal lithofacies variation and sedimentological characteristics allow for the production of an accurate depositional model, an understanding of the influence of sedimentological and diagenetic characteristics on reservoir quality, and potentially improved exploration and development strategies.

GEOLOGICAL SETTING

The Anadarko Basin ([Figure 2.1](#)) was a relatively stable basin during the deposition of the Cambrian-Ordovician Arbuckle dolomite, the Ordovician Simpson sandstone, Viola limestone, and Sylvan shale, and the Silurian-Devonian Hunton carbonates. A major unconformity was developed as the Hunton carbonates were eroded into canyons wherein the Late Devonian Woodford Shale was later deposited ([Harris, 1975](#); [Rottmann, 2018](#)). The Woodford Shale is overlain by the Early Mississippian Kinderhook Shale either conformably ([Harris, 1975](#)) or unconformably ([Curtis and Champlin, 1959](#); [Rowland, 1961](#)) depending on the location. These shales have gone through compaction and formed drape folds that affected the deposition of younger Mississippian strata such as Osagean, Meramecian,

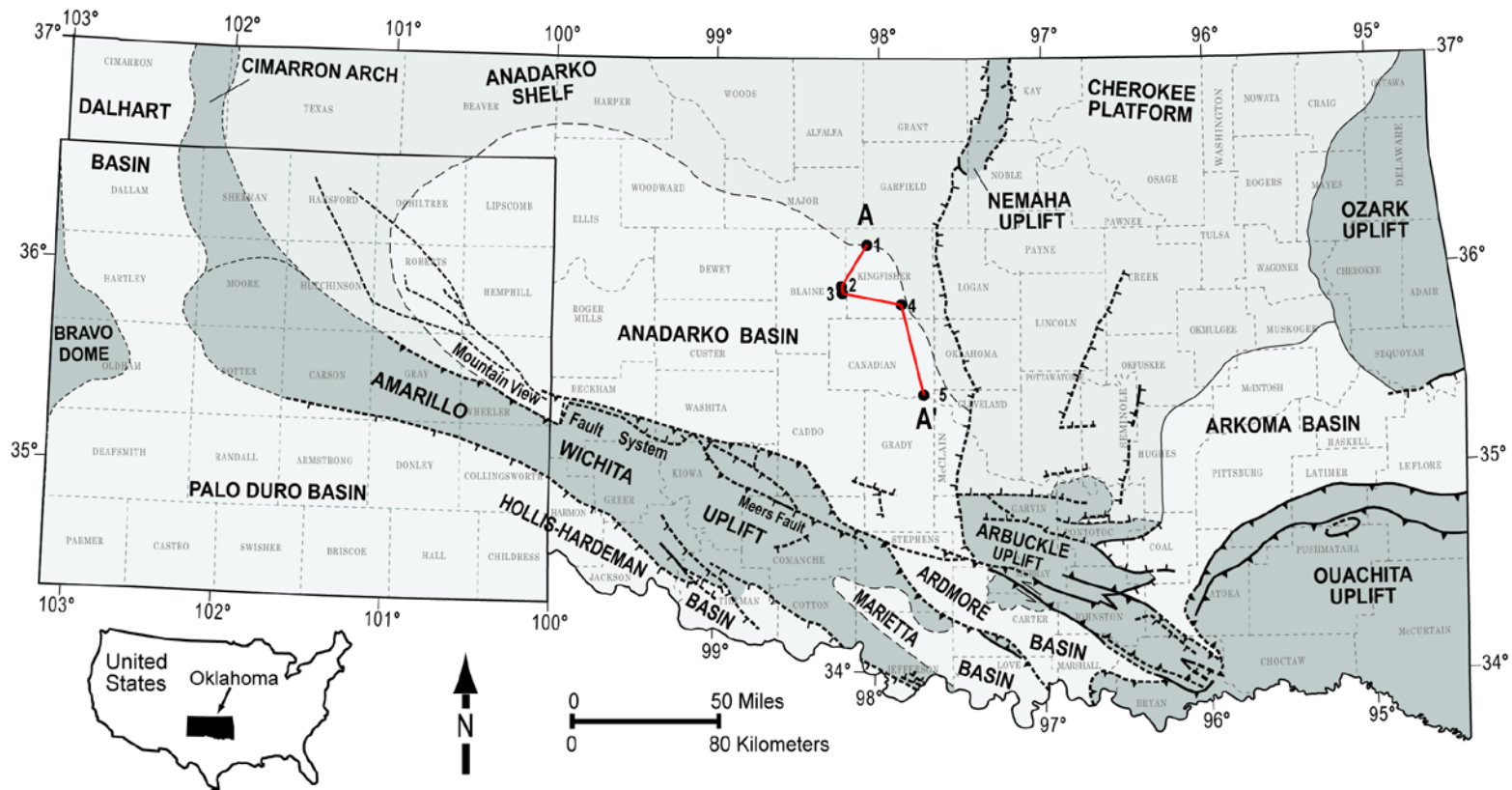


Figure 2.1. Regional base map showing the major tectonic and basinal features of Oklahoma and Texas Panhandle (modified after Dutton, 1984; Campbell et al., 1988; McConnell, et al. 1989; Northcutt and Campbell, 1995; Johnson and Luza, 2008; LoCricchio, 2012). The Humble Oil & Refining Company 1 Van Horn Unit (1), Gulf Oil Corporation 1 Musselman (2), Gulf Oil Corporation 1-23 Shaffer (3), Humble Oil & Refining Company 1 Lloyd L Hawkins (4), and Petrolia Drilling Corporation 1 Payne (5) are located on the Anadarko Basin (labelled as black dot).

and Chesterian series (ascending order). The generalized stratigraphic column of Mississippian strata of the Anadarko Shelf and Anadarko Basin is shown in [Figure 2.2](#).

The Osagean was described as carbonate units by [Curtis and Champlin \(1959\)](#), [Harris \(1975\)](#), and [Boyd \(2008\)](#). These carbonate rocks occur throughout the area as brown, dolomitic, fine crystalline limestone to off white limestone and interbedded brownish gray, finely crystalline, cherty limestone; however, there are a few occurrences of chert, shale, siltstone, and sandstone.

The Osagean-Meramecian contact is unconformable ([Rowland, 1961](#)); yet it is challenging to determine because of the lithology similarity of the Osagean to the overlying rocks. [Stukey et al. \(2018\)](#) also revealed that the Osagean and Meramecian boundary is unresolved based on conodont biostratigraphy from wells in Major County. Despite this, integration of biozonation and cross-section correlations from Major to Kingfisher counties show that most of the Mississippian strata in the Anadarko Basin of central Oklahoma is Meramecian and Lower Chesterian in age.

[Ulrich \(1904\)](#) first studied Meramecian rocks from outcrops in Missouri. The Meramecian rocks comprise light to dark, coarse to fine-crystalline limestone with the presence of oolite, dolomite, and chert ([Ulrich, 1904](#); [Clair, 1949](#); [McDuffie, 1959](#)). Even though the Meramecian has long been attributed as carbonate units ([Ulrich, 1904](#); [Clair, 1949](#); [McDuffie, 1959](#); [Curtis and Champlin, 1959](#); [Harris, 1975](#); [Boyd, 2008](#)), current investigations suggested Meramecian rocks of the Anadarko Basin in central Oklahoma primarily represent a siliciclastic system consisting of argillaceous to calcareous siltstones or very fine sandstones or a mixed siliciclastic-carbonate system (e.g., [Price et al., 2017](#); [Miller, 2018](#)).

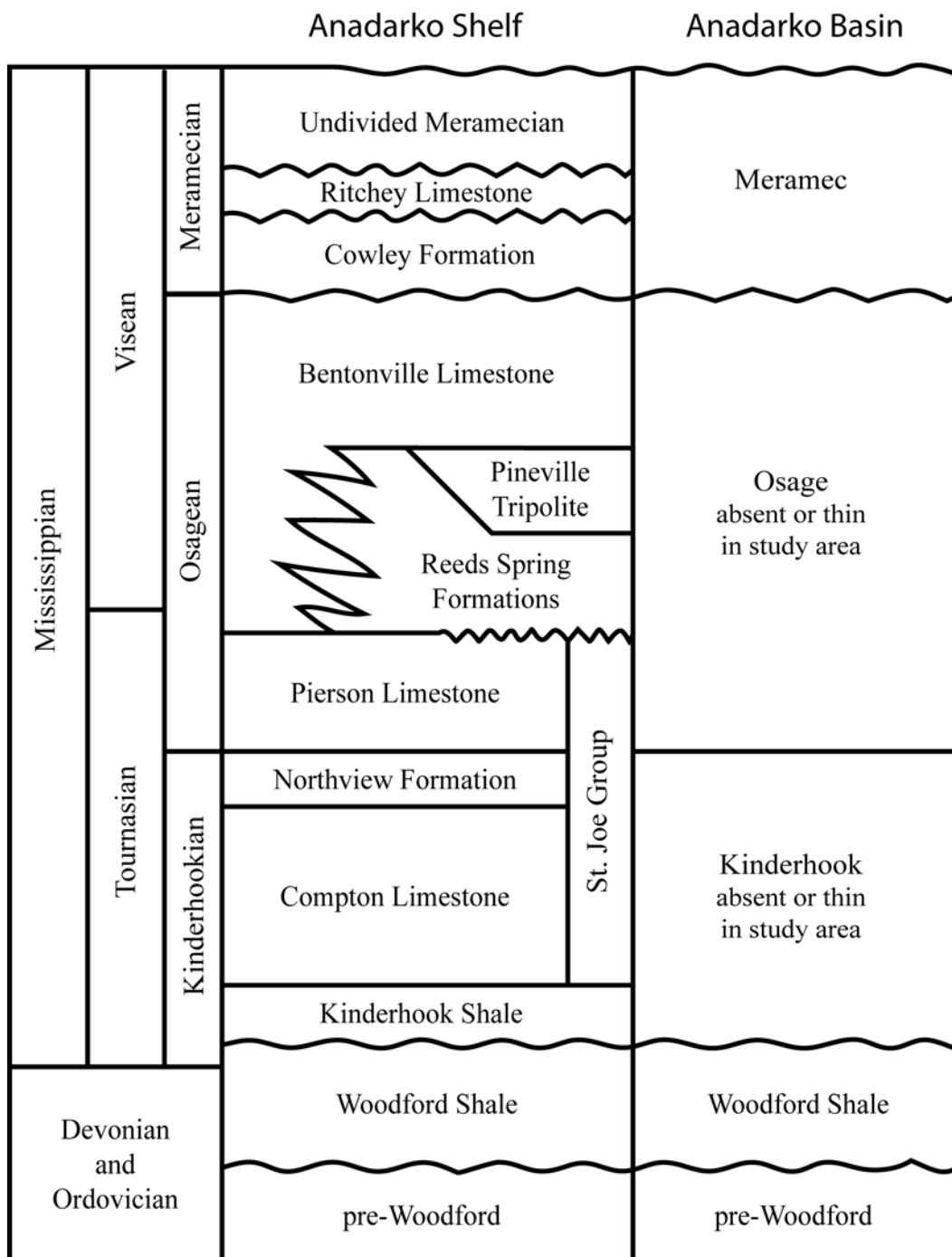


Figure 2.2. Generalized Stratigraphic summary of Mississippian strata in the Anadarko Shelf and Anadarko Basin at the north and central Oklahoma (Modified after [Mazzullo, 2011](#); [Mazzullo et al., 2011](#); [Mazzullo et al., 2016](#); [Stukey, 2018](#)).

Chesterian strata unconformably overly the Meramecian. [Curtis and Champlin \(1959\)](#) described the Chesterian rocks as oolitic to fossiliferous limestone in northern Oklahoma to interbedded sandstone, shale, and fossiliferous fragmental limestones in southern Oklahoma.

Since the Osagean, Meramecian, and Chesterian series were first named, differences have existed among researchers as to their boundaries and age. For this study, the interval of interest (possibly post-Woodford Shale and pre-Chesterian) is arbitrarily assigned as the Mississippian strata in the Anadarko Basin, central Oklahoma.

Besides the stratigraphic age uncertainty, the depositional environments of Mississippian deposits in the Anadarko Basin, central Oklahoma are also poorly understood and there have been limited studies. Previous studies of proximal counterpart regions of “Anadarko Shelf” areas have interpreted the Mississippian strata (also known as the Mississippian limestone) as having been deposited on a carbonate ramp with a very low gradient ([Rogers, 2001](#); [Watney et al., 2001](#); [Mazzullo et al., 2011](#); [Leblanc, 2014](#); [Birch, 2015](#); [Childress and Grammer, 2015](#); [Vanden Berg and Grammer, 2016](#); [Suriamin and Pranter, 2018](#)). Based on a study on the Meramecian-Chesterian Moorefield Formation within a quarry near Pryor Creek, Oklahoma (correlative to the Mississippian strata in the Anadarko Basin, central Oklahoma), [Shelley et al. \(2017\)](#) also interpreted that these rocks are associated with a carbonate ramp system. [They](#) also revealed the presence of eolian, fluvial, and deltaic inputs into the carbonate ramp system.

According to [Price et al. \(2017\)](#), the depositional environment changes to a subaqueous delta complex fed by fine-grained riverine input at the distal regions of the Anadarko Basin, central Oklahoma. This interpretation was generally based on internal mapping geometries that show a system of low angle, shore-parallel prograding clinoforms. In contrast, [Leavitt \(2018\)](#) suggested that deposition occurred from storm or turbidite flows transporting eolian-sourced silt and detrital carbonates.

METHODOLOGY

Detailed lithofacies analysis of the Mississippian strata is based on visual observations of 5 cores and associated thin sections from the Humble Oil & Refining Company 1 Van Horn Unit, Gulf Oil Corporation 1 Musselman, Gulf Oil Corporation 1-23 Shaffer, Humble Oil & Refining Company 1 Lloyd L Hawkins, and Petrolia Drilling Corporation 1 Payne wells. The cores are located in Kingfisher, Blaine, and Canadian Counties (Figure 2.1). The cores have a total length of ~260 m (~850 ft). The interval of interest is arbitrarily assigned to the time-stratigraphic unit of Mississippian age based on well-log responses. The cores and well logs were used to construct a north-south oriented stratigraphic cross section (Woodford Shale as the datum) (Figure 2.3).

The lithofacies were defined based on differences in lithology, texture, primary sedimentary structures, composition, and bioturbation. Changes in grain size are very subtle and not easily inferred from macroscopic visual observation or even gamma-ray log response. Therefore, 34 thin sections were described using a Zeiss Axio Imager Polarizing Microscope at 5X, 10X and 20X magnification to determine grain texture, porosity characteristics, cements, and insight on sedimentary structures and

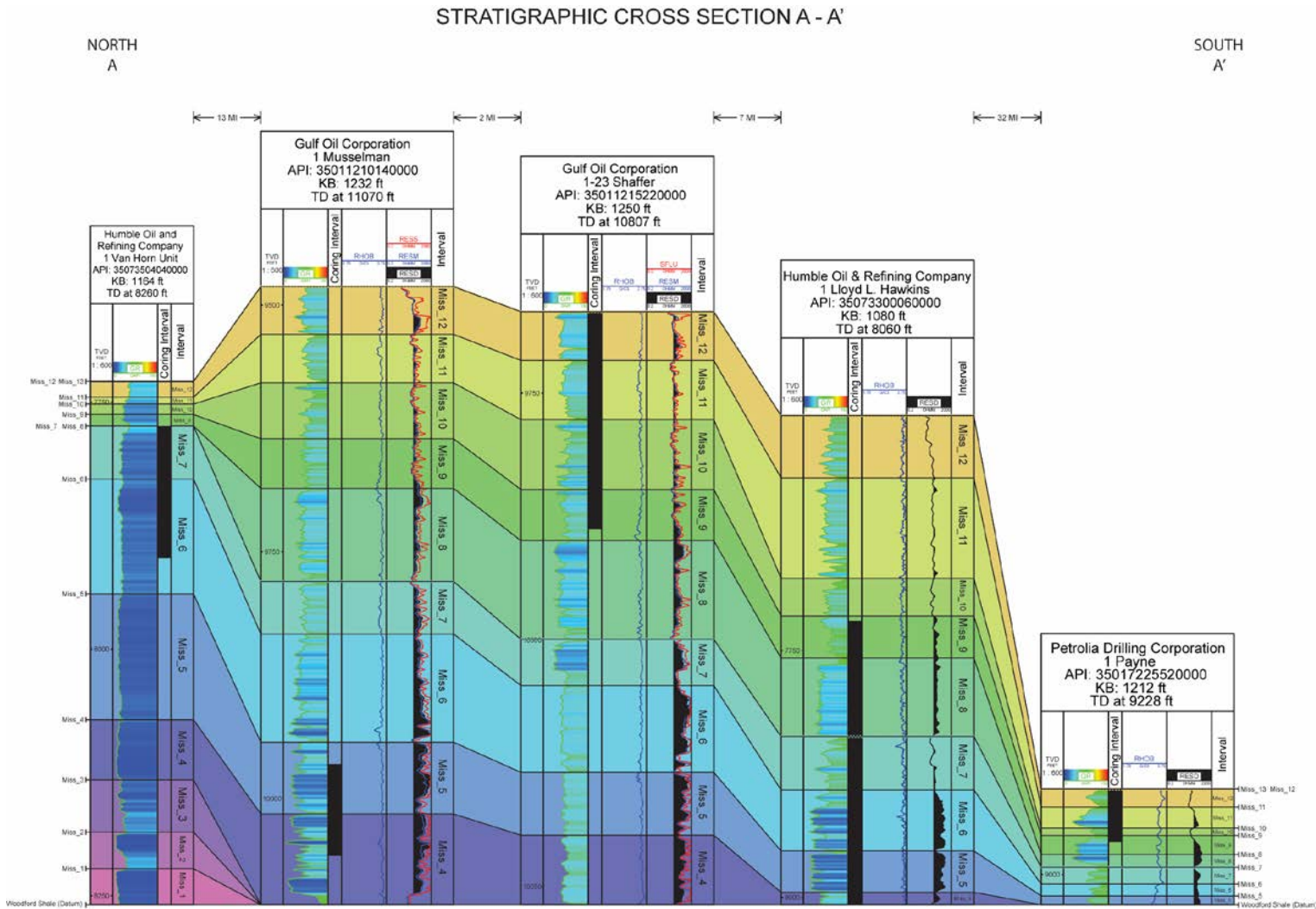


Figure 2.3. Well logs correlation of five wells in this study from north to south (Annotated as A –A’ red line in Figure 1). If available, each wells have gamma-ray (GR), bulk density (RHOB), shallow resistivity (RESS), medium resistivity (RESM), and deep resistivity (RESA). This correlation is based on flooding surfaces observed using gamma ray (GR) logs. The gamma-ray log become relatively flat to the north which pose a challenge to the correlation. Noted the top of the Mississippian strata (Miss 13) is represented by increasing bulk density value (RHOB). The cross section was flattened on top of Woodford Shale. The core interval for each wells are represented by black bar.

ichnotaxon. Thin sections were stained with Alizarin Red S and Potassium Ferricyanide to differentiate calcite from dolomite and Fe-calcite from Fe-dolomite, respectively. A few polished thin sections from selected samples were prepared and analyzed using a Field Electron and Ion (FEI) Quanta 250 field-emission scanning electron microscope combined with a built-in Bruker Quantax energy dispersive x-ray spectroscope. The thin sections were also examined using a CAMECA SX100 electron probe microanalyzer (EPMA) that is equipped with an energy dispersive x-ray spectroscope and a GATAN PanaCL/F cathodoluminescence detector to investigate compositional variations in calcite or dolomite and to differentiate quartz cement from detrital quartz grains. Quartz cement that typically occurs as an overgrowth on detrital quartz grains may be difficult to recognize using an optical microscope. However, it can be easily differentiated from detrital quartz in CL images by their less intense luminescence (Boggs and Krinsley, 2006). Thin sections for EPMA and cathodoluminescence examinations were thinly coated with carbon. Similarly, thin sections for SEM and EDX analysis were coated with gold-palladium to avoid electron charging and increase signal-to-noise ratio.

RESULTS

Well-log response

A stratigraphic cross-section through the five studied wells illustrates key characteristics of the Mississippian strata and shows the core coverage (Figure 2.3). The detailed description of cores are shown in Appendix B. The top of the interval of interest (Miss 13) corresponds to an abrupt bulk density increase, and the base of the interval of interest corresponds to a distinctive gamma-ray value above 150 API which is associated with the top of Woodford Shale. The Mississippian tops (Miss 1 to Miss 12) were picked based on a relatively high gamma-ray response which are interpreted as flooding surfaces.

The gamma-ray log of each wells shows a significant change in trend; from relatively low values and flat updip (e.g., Humble Oil and Refining Company 1 Van Horn Unit well) to relatively higher values with slightly serrated and blocky patterns (e.g., Gulf Oil Corporation 1 Musselman, Gulf Oil Corporation 1-23 Shaffer, and Humble Oil & Refining Company 1 Lloyd L Hawkins wells) and relatively high values with bell patterns at the downdip (e.g., Petrolia Drilling Corporation 1 Payne well). The flat and low gamma-ray response in the Humble Oil & Refining Company 1 Van Horn Unit well corresponds to the abundance of carbonate and chert as identified in the core.

Lithofacies

Eight lithofacies are defined for the Mississippian based on grain types, bioturbation, sedimentary structures, and composition (Table 2.1; Figures 2.4, 2.5, and 2.6). Lithofacies include 1) skeletal wackestone-packstone, 2) chert - cherty breccia, 3) structureless siltstone, 4) cross-laminated siltstone, 5) laminated siltstone, 6) bioturbated siltstone, 7) glauconitic siltstone and sandstone, and 8) structureless sandstone.

Diagenesis

Based on thin-section analysis using an optical microscope, scanning electron microscope (SEM), energy dispersive x-ray diffraction spectroscopy (EDX), and electron probe micro analyzer (EPMA)-cathodoluminescence (CL), diagenetic products observed in the eight lithofacies include calcite cements (non-ferroan to ferroan calcite cement), mechanical compaction, albite grains, quartz cement, diagenetic silica, dolomite crystals, Fe-dolomite, pyrite, and secondary porosity

Table 2.1. Summary of key characteristics that distinguish each identified lithofacies in the core used in this study.

No.	Lithofacies	Characteristics, Associated Features, Grain Types, and Mineral Composition	Color
1*	Skeletal wackestone-packstone (Figure 2.4a), occasionally grainstone	Variable bed thickness (2 - 238 cm [1 - 94 in.]). Skeletal grains are moderately to poorly sorted and range in size from less than 1 to 2 mm (0.02 to 0.04 in). Vuggy pores are rare. Rare wispy laminations. Abundant peloids and moderate angular to sub-angular silt-size quartz. Calcified skeletal grains (crinoids, brachiopods, bryozoan, monoaxon sponge spicule) and peloids (Figure 2.5a). Grains are well cemented by calcite with either blocky or poikilotopic fabrics. Calcite cement significantly occluded pores. Dolomite, fluid inclusion, and quartz overgrowths are present but rare. No observed porosity.	White to very light gray
2*	Chert - cherty breccia (Figure 2.4b)	About 0.5 - 13 cm (0.2 - 5 in.) thick chert or in-situ cherty breccia beds with wispy laminations and bioturbation. The breccia is monomictic with silicified components. Microcrystalline quartz is dominant. Fractures are present in chert beds and filled by silica cement. Calcite cement, sponge spicules, organic materials, and possible spores and pollen are moderately present (Figure 2.5b). Rhombic dolomite crystals, baroque dolomite, ferroan dolomites, detrital quartz, and opaque minerals are rare. The ferroan dolomite is observed as overgrowth zones on precursor dolomite crystals.	Grayish black to dark gray
3	Structureless siltstone (Figure 2.4c)	Well sorted quartz-rich siltstone with varying amount of peloids. Quartz grains are angular to sub-angular in shape. The thickness vary from ~0.02 – 2.7 m (~0.08 – 9 ft). Occasionally faint laminations exist. Predominantly detrital monocrystalline quartz and calcite cement (Figure 2.5c). Crinoids and brachiopods are irregularly distributed. Bioturbation is rarely present. Pyrite, vertical and ptigmatic fractures, organic-rich clasts, oxidized surfaces as the result of probably chemical weathering are observed particularly in the Gulf Oil Exploration and Production Company 1-14 Musselman core. Most, if not all, silt-size quartz grains are cemented by quartz overgrowth. Calcite occurs pervasively either as intragranular cement or grain replacement. Anhedra and euhedral dolomite, ferroan dolomite, potassium feldspar with twinning, and greenish clay clasts are also observed. The Fe-dolomites appears to form overgrowths on rhombic dolomite crystals. Pore is not visible.	Light to medium gray
4	Cross-laminated siltstone (Figure 2.4d)	Mm-to-cm-scale low-angle planar laminations, ripple laminations, or hummocky cross-stratification. Bed thickness varies from 0.02 – 0.6 m (0.08 – 2 ft). Angular to sub-angular silt-size detrital quartz grains are abundant (Figure 2.5d). Quartz exists as both monocrystalline grains and microcrystalline texture. Most quartz grains are rich in vacuoles inclusion and cemented by authigenic quartz overgrowth; some grains show a diffuse boundary; and others appear to be thinly coated by clay mineral. Ptygmatic fractures occasionally occur in hummocky beds. Thalassinoides and horizontal sprite burrows are rare. Calcite cement are locally common to abundant, while peloids and clay minerals are moderate in abundance. Ferroan dolomite replaces rhombic dolomite crystals. Crinoids, feldspar with twinning, opaque minerals, and possibly greenish clay clasts and muscovite are rare. No pore is observed.	Light to medium gray

5	Laminated siltstone (Figure 2.4e)	<p>Parallel to occasionally discontinuous, wavy, or wispy laminations and consist of silt-sized quartz grains and calcite cement. Relatively small phycosiphon-like burrows are rare and calcite-filled vertical fractures are common. It can be divided into calcite-rich and argillaceous (Figure 2.5e). The calcite-rich laminated siltstone consists of coarse calcite cement and carbonate grains with a moderate amount of peloids and silt-sized detrital quartz grains. Greenish clay clasts and disintegrated skeletal grains (brachiopods and sponge spicules). The spicules often have a polycrystalline quartz wall with their center filled by calcite cement. The argillaceous-rich laminated siltstone consists of silt-sized detrital quartz grains floating within a clay matrix. The quartz grains have overgrowth cement and many have fluid inclusions. Oncoids and aggregate grains (grapestone) are locally present and have rounded to elongated shapes (Figure 2.5f). Oncoid and grapestone nuclei are either quartz grains, rhombic dolomite crystals, calcite cement, greenish clay clasts, or a combination. Ferroan dolomite and pyrite are also present but rare. No pore is observed.</p>	Light to medium gray
6	Bioturbated siltstone (Figure 2.4f)	<p>Bed thickness varies from 0.003 – 11 m (~0.01 – 36 ft). Common Phycosiphon-like burrows which appear as darker U-shape lobes or a fish-hook shapes surrounded by lighter grains. Uncommon ichnofabrics include Chondrites, Skolithos, Thalassinoides, Teichicnus, Planolites, vertical and horizontal sprites, and possibly Bergaueria. Crinoid and brachiopods grains are occasionally present. Wavy and wispy lamination, disseminated pyrite, and vertical and pygmatic fractures occur locally. Most vertical fractures are observed within lighter colored calcite-rich beds that are bounded by thin darker colored argillaceous-rich beds (Figure 2.7a). In contrast, the pygmatic fractures are always associated with clay-rich intervals (Figure 2.7b). All fractures are filled by cement and are occasionally associated with disseminated pyrite. This lithofacies can be divided into argillaceous bioturbated siltstone, calcareous bioturbated siltstone, and quartz siliceous bioturbated siltstone. All varieties have mainly lenticular-shaped burrows with textural contrast between the burrow fills and surrounding sediments (Figure 2.5g); none have visible porosity. The argillaceous bioturbated siltstone appears to be primarily clay-rich; however, a moderate amount of silt-size detrital monocrystalline quartz grains is present. Some grains show microinclusion minerals or fluid inclusions that appear like bubbles (vacuoles). Calcite grains, pyrite, dolomite, ferroan dolomite, greenish clay clasts, and rock fragments are also observed. Some of the rhombic dolomite crystals have ferroan dolomite overgrowths. The calcareous bioturbated siltstone is rich in calcite grains, calcite cements, or microcrystalline calcite (micrite). Monoaxon sponge spicules floating in a micrite matrix are common. Most siliceous spicules are either fully or partially calcified, some have a well-defined central body cavity that is filled by micrite or microcrystalline quartz (Figure 2.5h). Some calcite crystals are partially or fully silicified into microcrystalline quartz (late silicification). Organic materials are present but uncommon. The siliceous bioturbated siltstone has abundant silt-sized detrital quartz grains. The monocrystalline quartz grains are mainly angular to sub-angular in shape. Grains show rusty quartz overgrowths around the rims. Calcite grains and ferroan dolomite are observed but not common. Greenish clay clasts and opaque minerals including pyrite and titanium oxide minerals are rare.</p>	Dark gray to black
7**	Glauconitic siltstone and sandstone (Figure 2.4g)	<p>Structureless. Glauconite is silt to very-fine sand in size. Horizontal spreiten rarely occurs and is typically filled by light-colored minerals. Rhombic dolomite crystals, detrital angular to sub-angular silt-sized quartz grains, organic materials, opaque minerals, and clay are also present (Figure 2.5i). Grains are mainly well compacted, and glauconite grains are deformed plastically. Many glauconite grain contacts are sutured; however, grain boundaries are clearly visible due to trapped clay (see Figure 2.5i). Some rhombic dolomite crystals are cracked and sheared. Baroque dolomite and possible phosphatic debris are present but rare. No pore is observed.</p>	Greenish gray

8	Structureless sandstone (Figure 2.4h)	<p>Very-fine grained, well-cemented quartz-rich sandstone with varying amounts of cement. Filled vertical fractures are common. Skeletal grains including crinoids and brachiopods are occasionally present. Bioturbation represented by skolithos and planolites are rare. Thin section analysis shows abundant angular to sub-angular detrital sand-sized quartz grains that are moderate to well sorted. Some quartz grains have a diffuse boundary and show authigenic quartz overgrowths. Some grains appear to have fluid inclusions (vacuoles); and the fluid inclusions occasionally form a pseudo line along the grain-overgrowth contact (Figure 2.5j). Calcite grains, calcite cement, ferroan dolomite, plagioclase feldspar with twinning, and clay are observed but rare. Ferroan dolomite commonly exhibits a pore-filling habit. Intragranular pores are observed if not occluded by ferroan dolomite.</p>	Light to medium gray
---	---------------------------------------	--	----------------------

*Only observed in the Humble Oil 1 Van Horn Well

** Only observed in Humble Oil and Refining Company 1 Lloyd L. Hawkins and Petrolia Drilling Corporation 1 Payne wells

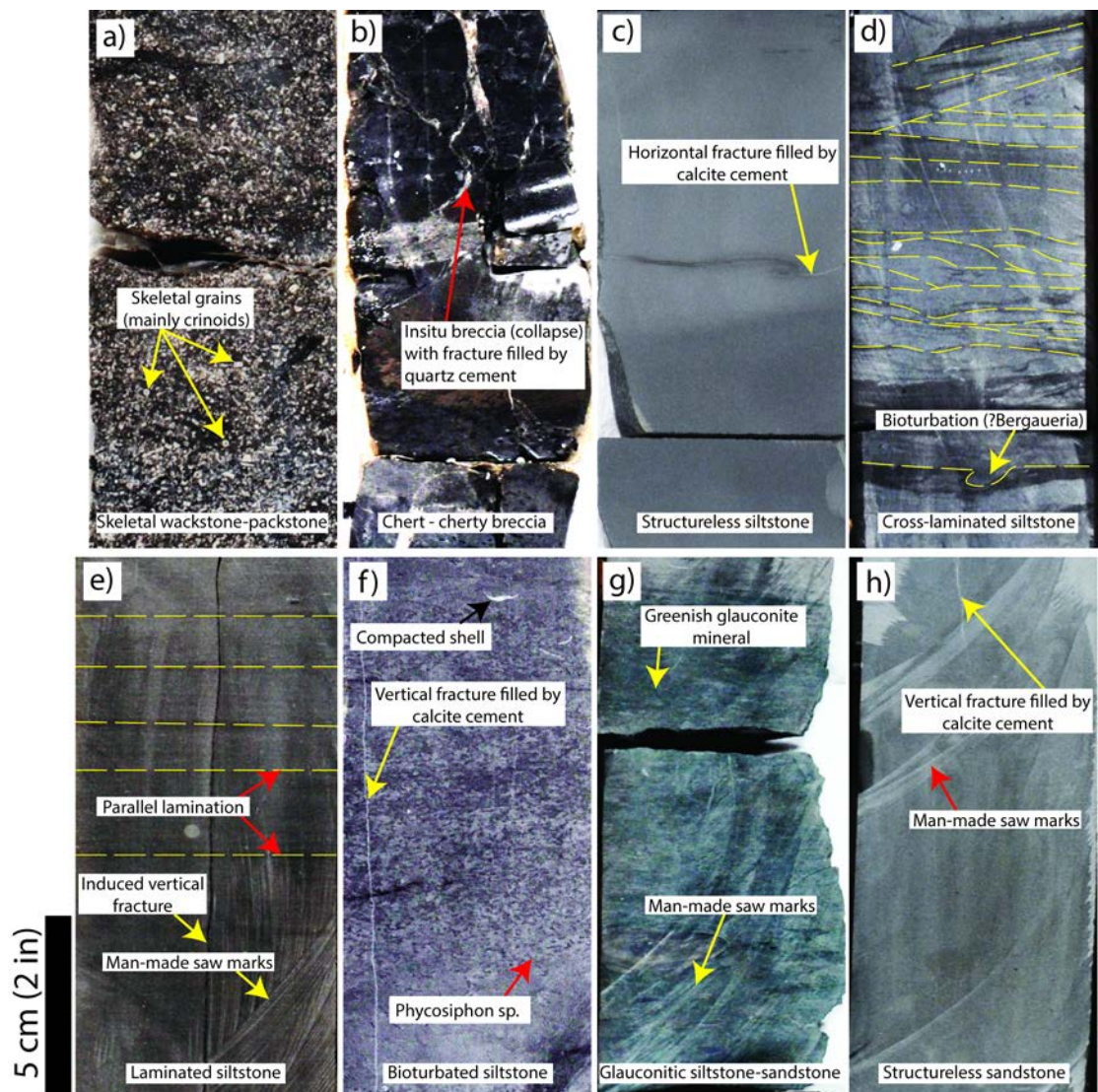


Figure 2.4. Eight lithofacies of the Mississippian strata in the Anadarko Basin, central Oklahoma: (a) skeletal wackestone-packstone, noted the presence of abundant crinoids (yellow arrow); (b) chert - cherty breccia, noted the presence of fractures filled by quartz cement and in-situ brecciation (red arrow); (c) structureless siltstone, noted a horizontal fracture filled by calcite cement (yellow arrow); (d) cross-laminated siltstone, noted the presence of wavy, planar, cross lamination, and possibly Bergaueria (bioturbation – yellow arrow); (e) laminated siltstone, noted many of the laminations are faded (yellow dashed lines); (f) bioturbated siltstone, noted the presence of abundant Phycosiphon (red arrow) and rare skeletal grain (black arrow). (g) glauconitic siltstone/sandstone, and (h) structureless sandstone, noted a vertical fracture filled by calcite cement (yellow arrow) and man-made saw marks (red arrow).

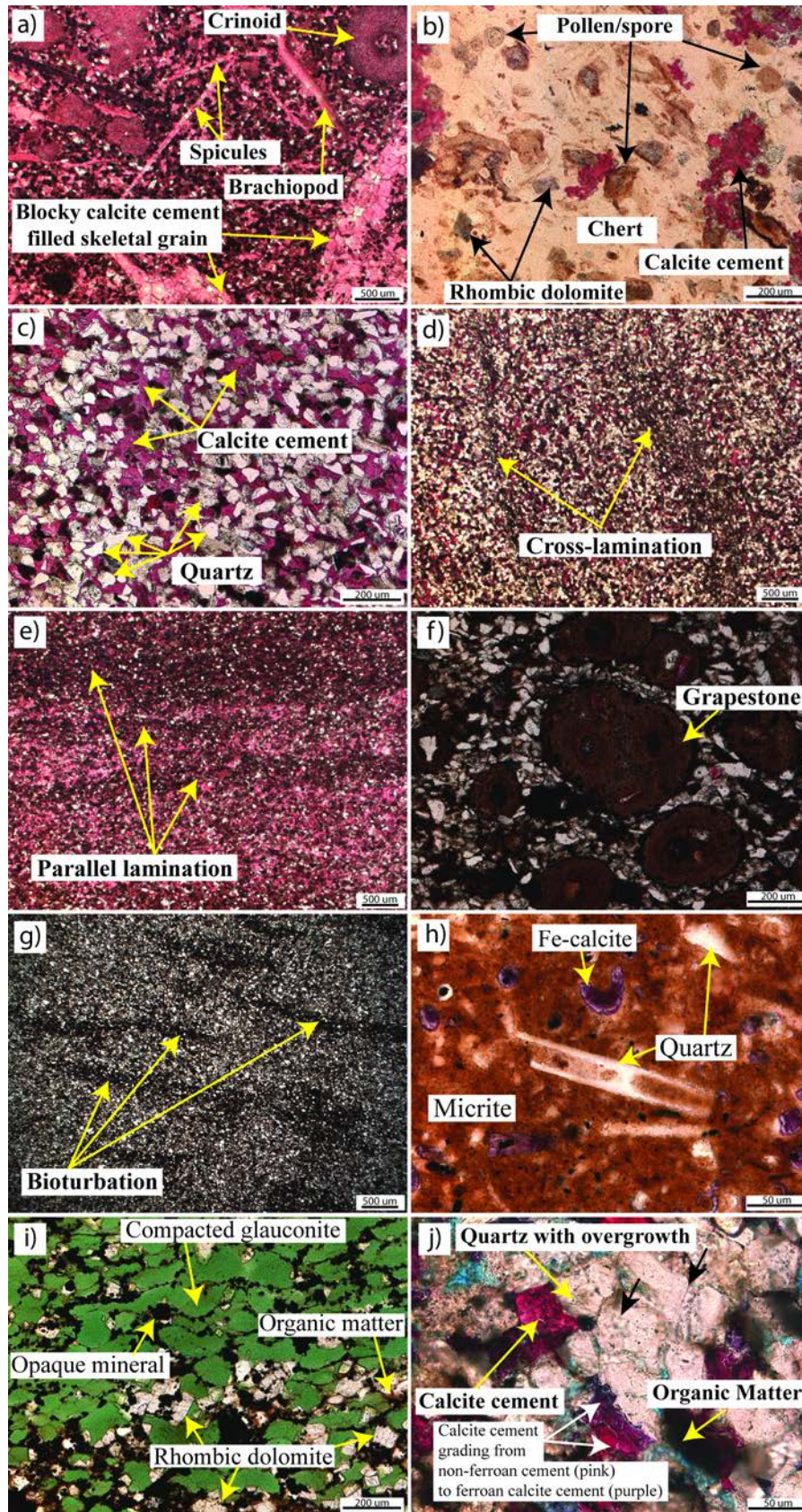


Figure 2.5. Photomicrographs of the 8 lithofacies. (a) skeletal wackestone-packstone shows the presence of peloids, sponge spicules, crinoids, brachiopod, blocky calcite cement replacing skeletal grains, and silt-size quartz grains. (b) chert – cherty breccia shows silicified matrix with rhombic dolomite crystals, calcite cement, and possible pollens and spores. (c) structureless siltstone reveals the presence of abundant angular to sub-angular silt-size quartz grains and calcite cement. (d) cross-laminated siltstone demonstrates the presence of quartz-rich and clay-rich angular lamination. (e) laminated siltstone with clay-rich and calcite-rich parallel lamination. (f) Various sizes of oncoids and aggregate grains (grapestone) floating on quartz grains. Some oncoids and aggregate grains have multiple types of nuclei including quartz grains, calcite grains, peloids, or combination of them. (g) bioturbated siltstone shows burrow filled by dark fine-grained material surrounded by silt-size quartz grains. (h) bioturbated siltstone with a spicule's central body cavity filled by micrite and microcrystalline quartz. (i) glauconitic siltstone - sandstone shows abundant glauconite with turbid rhombic dolomite crystals. The ductile deformation of the glauconite is caused by mechanical compaction. Note the presence of abundant opaque minerals (e.g. pyrite), organic matter, and possibly oil. (j) structureless sandstone with abundant very fine sand-size quartz grains. Calcite cement has filled intergranular pores. Noted the presence of organic matter, dissolution, vacuole inclusion (black arrow) indicating boundary between detrital quartz and quartz overgrowth, and calcite cement that grading from non-ferroan calcite cement to diagenetically later ferroan calcite cement (white arrow).

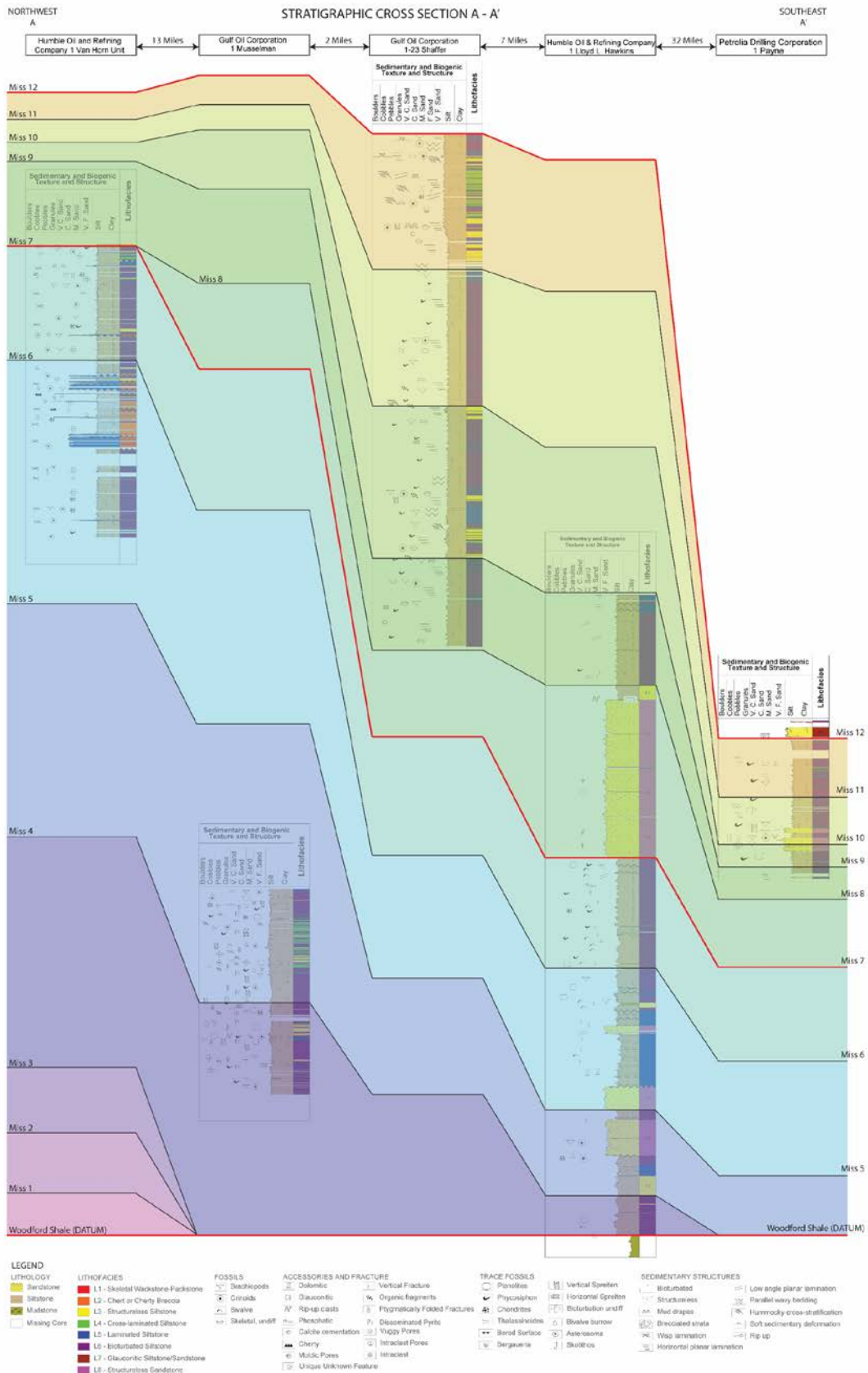


Figure 2.6. North-South (A - A') stratigraphic cross section through the Mississippian strata in the Anadarko Basin, central Oklahoma. Location of the wells used in the construction of this cross-sections are presented in Figure 1. The correlations were guided using subsurface core observation combined with gamma-ray logs in Figure 3. The black lines represent interpreted flooding surfaces (parasequence boundaries) and the red line is the datum (Woodford Shale). Noted that the lithofacies distribution within the Mississippian strata appears extremely variable laterally and vertically.

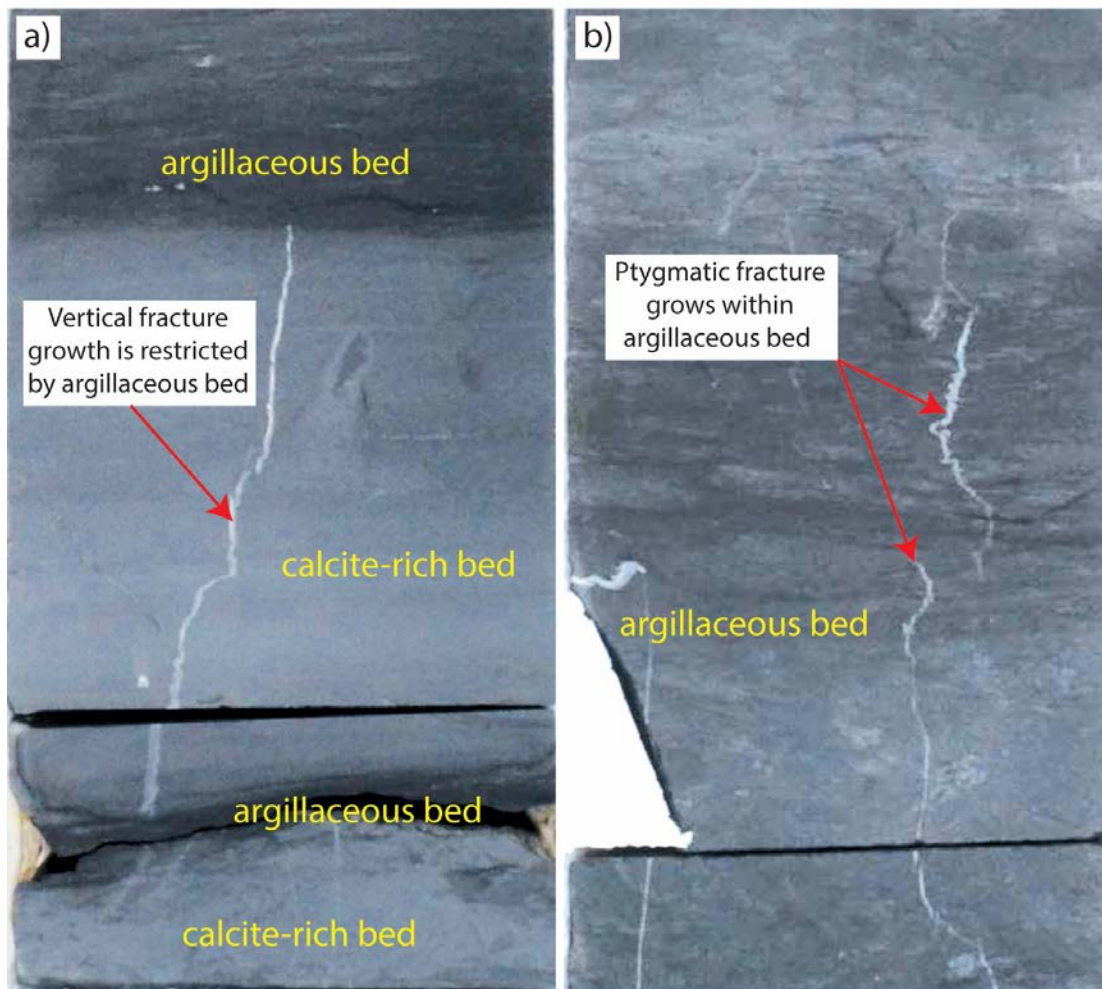


Figure 2.7. Typical type of fractures associated with the Mississippian strata in the Anadarko basin, central Oklahoma. (a) vertical fracture within relatively lighter calcite-rich bed and bounded by argillaceous beds/laminae. (b) ptygmatic fractures show folded fracture grew within argillaceous bed. Noted that both fractures were filled by calcite cement (red arrow).

INTERPRETATION AND DISCUSSION

Depositional environment

The upper section deposits of the Gulf Oil Exploration and Production Company 1-14 Musselman and Gulf Oil Corporation 1-23 Shaffer commonly have hummocky cross stratification (HCS). This HCS sedimentary structure was once considered to be ubiquitous to shallow marine storm deposits. However, [Morsilli and Pomar \(2012\)](#) suggested that internal waves that break on a shelf may also initiate hummocky cross-stratification by creating episodic high-turbulence events, inducing upslope- and downslope currents and producing oscillatory flow at the depth where the pycnocline intersects the sea floor. At similar water depths, wave or current low-angle planar laminations (ripples) may occur as well. Other dominant sedimentary structures observed within these 5 cores are parallel lamination which correlate to quiet-fluid deposition of particles by settling. Parallel laminations mainly occur at the ocean bottom where low-velocity currents carrying a supply of fine-grained suspended sediment from upcurrent. In the Humble Oil & Refining Company 1 Van Horn Unit well, the presence of wispy laminations is significant and indicates alternating periods of high- and low-energy conditions with deposition of a mixture of mud and silt-size materials. These wispy laminations are interpreted to be deposited during “the stand of the tide” condition, resulting in the suspension settling of clay from the water column. Within this context, the parallel lamination is interpreted to occur in deeper water compared to that of hummocky cross-stratification, while wispy laminations in updip areas are affected more by tides.

In the eastern and southern parts of the Anadarko Basin, some siltstone and sandstone beds in the Humble Oil & Refining Company 1 Lloyd L Hawkins and Petrolia Drilling Corporation 1 Payne wells are very thick (0.3 – 21 m; 1 – 71 ft) and structureless. These deposits possibly represent a channel or

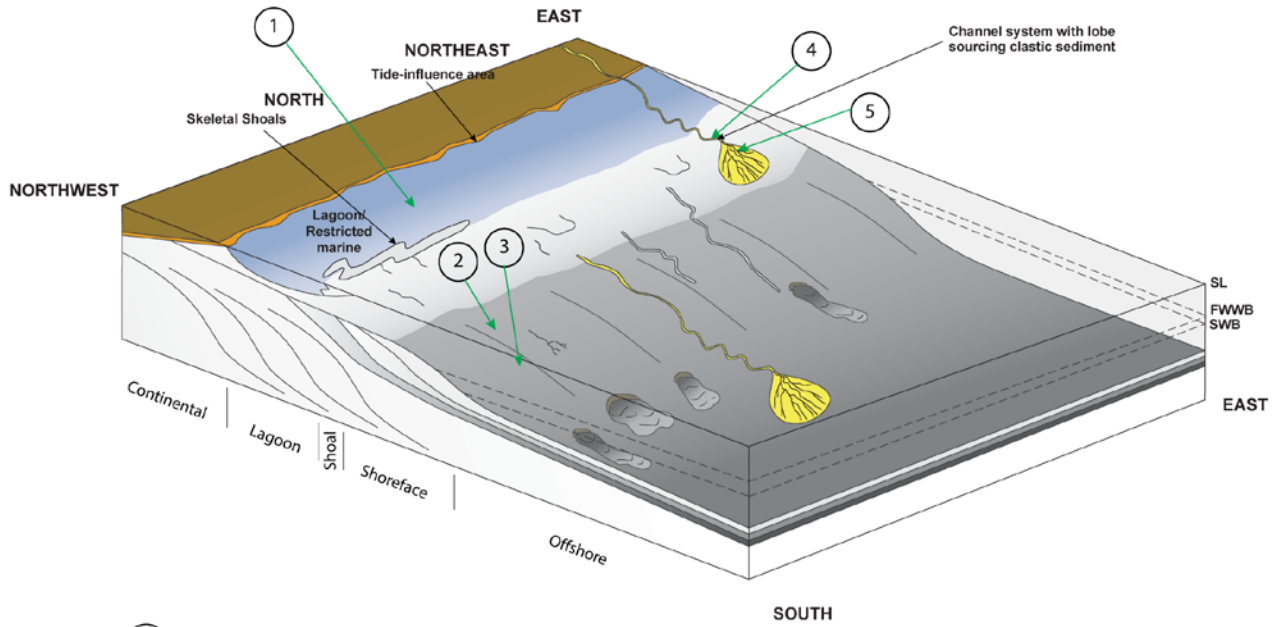
lobe (sand sheet) deposit. They also support the interpretation of [Cullen \(2017\)](#) that a specific interval of the Mississippian sediments were fan-lobe deposits.

In terms of grain textures, most thin sections reveal angular-sub-angular silt-size quartz grains with poor to moderate sorting. Due to quartz overgrowth, the shape and size properties of quartz grains have been altered, and therefore they do not represent the condition during deposition when analyzed under an optical microscope. Moderate sorting is commonly associated with relatively quartz-rich structureless and laminated siltstone. This suggests reworking and sorting of the grains by wave energy. On the contrary, the relatively poorly sorted lithofacies is predominantly associated with either argillaceous-rich or bioturbated rocks. Bioturbation can significantly alter primary sediment fabrics; thus bioturbation can enhance or destroy reservoir quality. In the study area, ichnotaxa such as *Chondrites*, *Skolithos*, *Thalassinoides*, *Teichicnus*, *Planolites*, vertical and horizontal *Sprites*, and probably *Bergaueria* are rarely to moderately present. The most abundant ichnotaxa is *Phycosiphon*. Due to its shape, the *Phycosiphon* has been documented to have a significant role in a reservoir as it can improve storage capacity, particularly in gas reservoirs (e.g., [Lemiski et al., 2011](#)). Based on their distribution along an ideal depositional profile, the ichnotaxa strongly correlate to deposition on upper shoreface to upper offshore areas.

Other important indicators of the environment of deposition are oncoids and aggregate grains. These unique grains which commonly form within a protected shallow-marine setting or lagoon ([Flügel, 2004](#); [Strasser, 1986](#)) are exclusively present in the Gulf Oil Corporation 1-23 Shaffer well. The presence of sponge spicules also supported the deposition under a restricted-marine (lagoonal) setting.

The information from the sedimentological and ichnofacies observations of the 5 cores suggests that the Mississippian strata in the eastern Anadarko Basin represents most likely a wave-dominated near-shore environment with lagoon (restricted shallow marine) and channels or lobes ([Figure 2.8](#)).

Proposed Depositional Model



① *well location in the interpreted depositional setting.

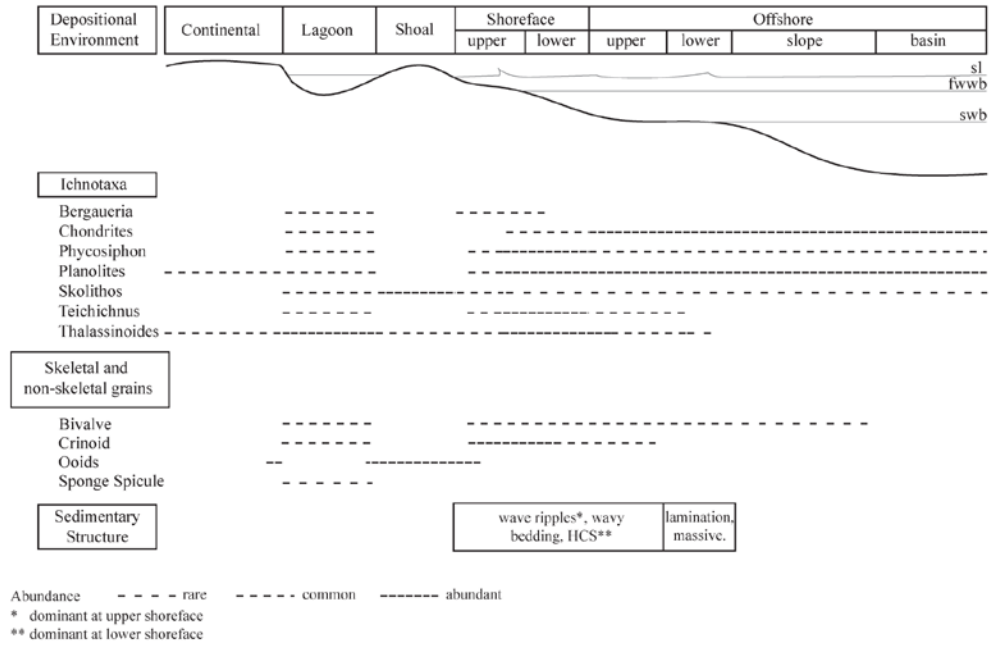


Figure 2.8. Cartoon highlighting the proposed depositional environment model (near-shore wave dominated setting) for this study. This model is interpreted based on integration of ichnotaxa, grains composition, and sedimentary structures. The 5 wells location are placed arbitrarily closed to their interpreted deposition settings (labelled as (1) The Humble Oil & Refining Company 1 Van Horn Unit, (2) Gulf Oil Corporation 1 Musselman, (3) Gulf Oil Corporation 1-23 Shaffer, (4) Humble Oil & Refining Company 1 Lloyd L Hawkins, and (5) Petrolia Drilling Corporation 1 Payne).

General Diagenetic Characteristics

A variety of authigenic minerals were recognized, including calcite cements (non-ferroan to ferroan calcite cement), mechanical compaction, albite grains, quartz cement, diagenetic silica, dolomite crystals, Fe-dolomite, pyrite, and titanium oxide (Figure 2.9). Compaction and formation of secondary porosity due to dissolution are the other important diagenetic parameters identified.

Calcite Cement

Calcite cement appears to be one of the main diagenetic minerals in the system. Although possible, calcite cement normally cannot be derived from external sources such as associated carbonate rocks, evaporites, and mudstone owing to a lack of transport mechanisms for significant amounts of dissolved calcium carbonate (Walderhaug and Bjorkum, 1998). The main source of calcium carbonate was likely biogenic carbonate such as skeletal grains, oncoids, aggregate grains, peloids, and other carbonate grains. Albitization is another possible source of calcium. Albite grains occur in the Mississippian strata but in insignificant quantities. The amount of calcium introduced during albitization, therefore, was probably minor compared with biogenic-derived calcium. Most of the calcite cements are either pore-filling cement forming a calcite mosaic with blocky crystals (Figures 2.5a and 2.9a) or rhombic calcite crystals (Figure 2.9b). Besides the replacement of calcite cement in skeletal remnants (Figure 2.5a and 2.9c), calcite-filled fractures are also common (Figure 2.9d). The calcite cement occasionally replaced by Fe-calcite (Figure 2.9e and 2.9f). Calcite cement can precipitate under meteoric to deep-burial environments and stable isotope study is necessary to confirm the time of

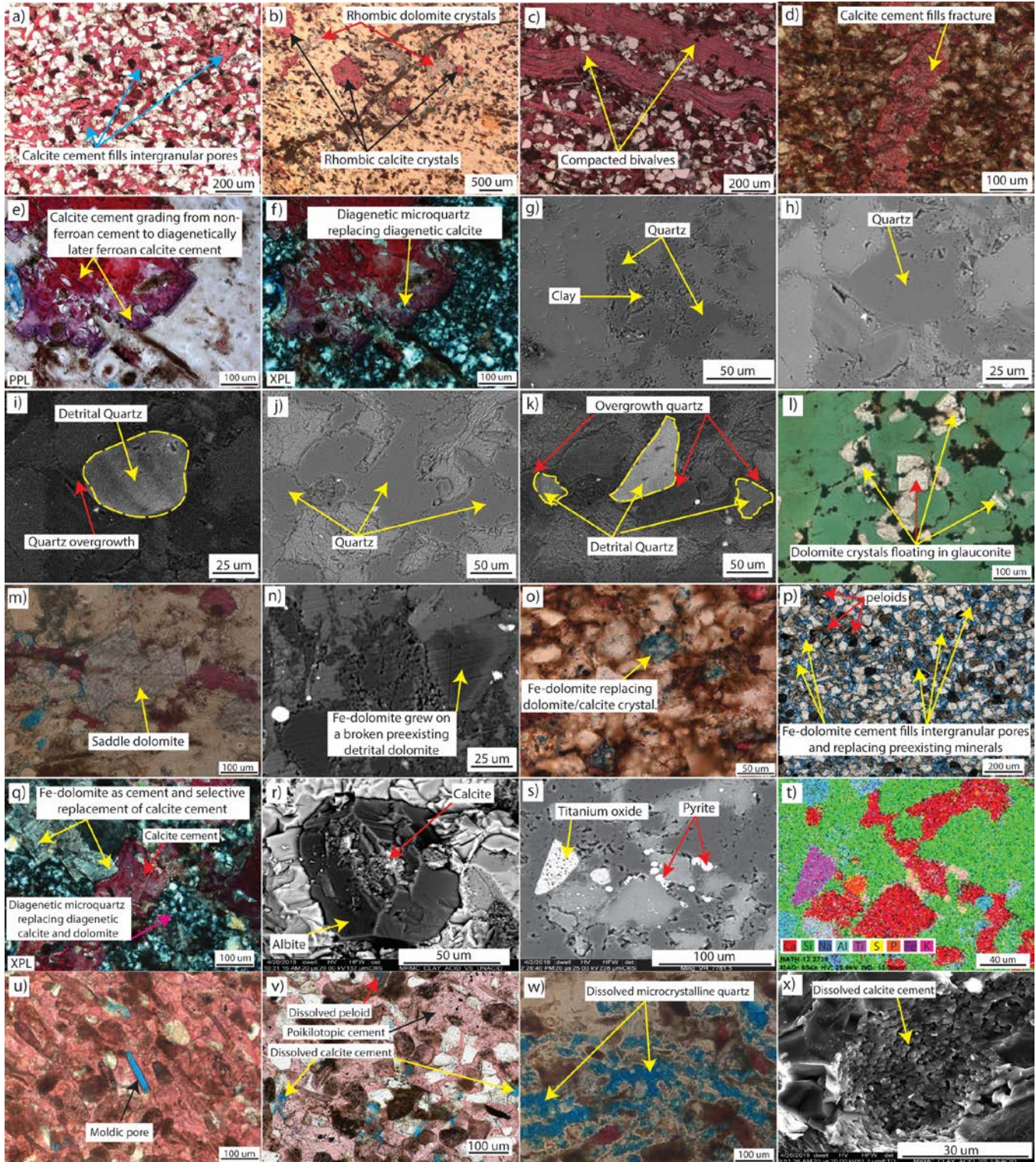


Figure 2.9. Photomicrographs showing diagenetic features observed in the Mississippian strata of the Anadarko Basin, central Oklahoma. (a) Calcite cementation as pore filling (blue arrows). (b) Calcite rhombic crystals (black arrows) as well as rhombic dolomite crystals (red arrows) floating within microcrystalline quartz. (c) Calcite cement replacing compacted skeletal grains (possibly bivalve). (d) Blocky calcite cement filling fracture. (e) Calcite cement grading from non-ferroan cement to ferroan calcite cement (pink to purple stained color) under plane-polarized light, noted silicified rock with calcite rhombic crystal. (f) Calcite cement grading from non-ferroan cement to ferroan calcite cement (pink to purple stained color) under cross-polarized light, noted diagenetic microcrystalline quartz replacing calcite cement (yellow arrow). (g) SEM photomicrograph showing quartz overgrowth was inhibited by the presence of clay minerals. (h) Photomicrograph showing angular to sub-angular quartz grains under scanning electron microscope (SEM). (i) Photomicrograph of Cathodoluminescence analysis reveal that in fact the detrital quartz grain in the photomicrograph 9h has rounded to sub-rounded shape before quartz cementation. Noted the detrital quartz grains shape and size before quartz cementation (yellow dash line). (j) Photomicrograph showing angular to sub-angular quartz grains under scanning electron microscope (SEM). (k) Photomicrograph of Cathodoluminescence analysis reveal that in fact the detrital quartz grain in the photomicrograph 9j has sub-angular to sub-rounded shape before quartz cementation. Noted the detrital quartz grains shape and size prior to quartz cementation (yellow dash line). (l) Fractured dolomite crystal (red arrow) due to mechanical compaction. (m) Baroque (saddle) dolomite with curved-face grew in silicified rock. (n) SEM photomicrograph showing the presence of detrital dolomite (broken and pitted) and Fe-dolomite overgrowth templating the detrital dolomite. (o) Fe-dolomite replacing some precursor rhombic dolomite crystals. (p) Fe-dolomite (blueish in color) replacement of preexisting mineral or grew as cement filling intragranular pores. (q) Fe-dolomite as cement and replacement of calcite cement. Noted that diagenetic microcrystalline quartz replacing diagenetic calcite and dolomite. (r) Albite grain under SEM indicating albitization process. Noted that the albite was replaced by calcite cement in the center. (s) SEM photomicrograph showing the presence of framboidal pyrite and titanium oxide minerals. (t) A photomicrograph of Energy Dispersive X-ray (EDX) map confirming the presence of calcite cement, quartz cement, titanium oxide, and pyrite. (u) Moldic pore resulted from dissolution of probably a sponge spicule. (v) Dissolution of calcite cement and peloid. Noted the presence of poikilotopic cement. (w) Dissolution of silica (microcrystalline quartz). Noted that in the pore area (indicated by blue epoxy) some quartz remains undissolved. (x) SEM photomicrograph showing dissolution of calcite cement and resulted in the formation of micropores.

formation. However, based on cross-cutting relationships, precipitation of some calcite fills must have taken place after the fracturing.

Quartz Cement

Quartz cement is also a dominant alteration product in the Mississippian rocks. Quartz cement is present as quartz-grain overgrowths. The cement growth is restricted by another quartz grains or other minerals. The presence of clay minerals occasionally inhibits the cement growth (Figure 2.9g). The quartz grains typically appear to be monocrystalline angular to sub-angular grains under cross-polarized light. This appearance makes the quartz overgrowth difficult to distinguish from the host detrital quartz grains when observed under an optical microscope. Cathodoluminescence (CL) technique permitted the differentiation of authigenic overgrowths from detrital quartz grains and revealed syntaxial overgrowths of quartz cement rimming host detrital quartz grains that are predominantly angular to sub-rounded and silt size (Figure 2.9h – 2.9k). Because quartz overgrowths alter the original shape of quartz grains, quartz grain size analysis becomes unreliable when it is performed using thin sections with an optical microscope. Quartz overgrowths also inhibit quartz grain surface texture analysis for interpreting transportation process and deposition environmental. The primary source of silica in this system was likely dissolved biogenic silica (e.g., sponge spicules), hydrothermal fluids, or volcanic ashes (Roger, 2001). The source of silica as well as calcium can also be derived during the smectite – illite conversion at relatively higher temperature, approximately 60 - 70⁰C (Curtis et al., 1985).

Diagenetic Silica

Diagenetic silica is mainly present in the chert and cherty breccia lithofacies and very rare in other lithofacies. Silica, in this case, partially or completely replaces rock matrix, skeletal grains, or calcite mineral into microcrystalline quartz or chalcedony (e.g., Figures 2.9g and 2.9h). This process becomes dominant toward the northern area, particularly in the Anadarko Shelf, as seen in the Humble

Oil & Refining Company 1 Van Horn Unit well. The limiting factor for silicification is silica availability (Butt, 2014). Rogers (2001) suggested the silica in the Mississippian strata may be sourced from either sponge spicules, volcanic ashes, or hydrothermal fluid expelled by tectonic compression and sedimentary loading. Study of fluid inclusions (Sahar, 2016) confirmed the presence of the hydrothermal fluid events representing short-lived thermal anomalies compared to burial thermal conditions. The hydrothermal fluid most likely originated from deeper Ordovician and/or basement strata and moved upward along faults to invade the Mississippian strata (Sahar, 2016).

Compaction

The effect of mechanical compaction is pronounced in the Mississippian rocks. It normally increases grains packing, breaks skeletal grains (Figure 2.9c), and flattens burrows (Figure 2.5g). Ptygmatic fractures might form as a result of mechanical compaction of clay-rich beds with high compressibility, whereas the origin of vertical fractures in this study is debatable. They are either related to brittleness of calcite-rich beds or hydrocarbon expulsion from the organic-rich beds. The appearance of several vertical fractures, bounded by argillaceous-rich beds (see Figure 2.7a), suggests a potential barrier for hydraulic fractures to grow during completion in the Mississippian strata.

In Petrolia Drilling Corporation 1 Payne well, glauconite in siltstone to sandstone show glauconite has a weak structure and deforms plastically due to compaction. Glauconite suture-grain contacts are common and their grain boundaries are visible due to trapped organic material. Some dolomite rhombic crystals are cracked and probably filled by oil (Figure 2.9I).

Dolomite Crystals and Fe-Dolomite Cement

Dolomite crystals are rarely to moderately encountered in the study area. Only the glauconitic siltstone-sandstone in the Petrolia Drilling Corporation 1 Payne well shows pervasive dolomite crystals.

Most dolomite is cloudy turbid silt-size euhedral rhombic crystals (Figure 2.9i). The presence of cracked dolomite crystals indicates that these particular dolomite crystals have gone through compaction; therefore, dolomitization probably occurred prior to or during burial compaction. Montalvo (2015) documented the occurrence of multiple stage dolomitization in Mississippian rocks of the Anadarko Basin. Primary dolomite that precipitate in the near-surface environment from seawater-derived water, and secondary dolomite occurs in burial realms. In the latter case, the process typically involves magnesium resulting from the transformation of clay minerals (e.g., montmorillonite or smectite-to-illite conversion) during compaction (Kahle, 1965; Flügel, 2004; Sarg et al., 2013). The authigenic dolomites can also occur as baroque (saddle) dolomite with curved faces and sweeping extinction (Figure 2.9m). The saddle dolomite commonly takes place in a deeper-burial diagenetic setting, under a thermochemical sulfate-reducing condition, or during hydrothermal fluid migration. Stable isotope and fluid-inclusion studies are needed to confirm the saddle dolomite formation mechanisms.

Besides authigenic dolomite, detrital dolomite crystals are probably present. This type of dolomite can be recognized using a combination of SEM and EDX analysis where it shows a broken rhombic crystal shape, a pitted surface, and calcium and magnesium compositions. Fe-dolomite commonly overgrew on the detrital dolomite nuclei (Figure 2.9n), partially replaced dolomite crystals (Figure 2.9o), filled pore spaces as cement (Figure 2.9p), or partially replaced calcite cement (Figure 2.9q). Fe-dolomite is often of late diagenetic origin and indicates deep burial reducing condition (Flügel, 2004).

Clay Minerals

X-Ray Diffraction (XRD) data for Mississippian rock samples show small amounts of clay minerals such as Kaolinite, Illite/Mica, Smectite/Illite, and Chlorite (see Table 2.2). Some clay minerals could be authigenic and some could be detrital. Further quantitative analysis and crystal morphology

Table 2.2. XRD data of the Mississippian strata from 5 cored wells.

Well Name	Sample Depth (ft)	Unit	Chlorite	Kaolinite	Illite/Mica	Mx I/S	Calcite	Dolomite	Siderite	Quartz	K-spar	Plag.	Pyrite	Apatite	Fe-Dolomite	Albite
14-1 Musselman	9965.5	%	1.00	0.00	5.00	4.00	60.00	3.00	0.00	19.00	2.00	4.00	1.00	1.00	0.00	0.00
14-1 Musselman	9967.7	%	0.00	0.00	0.00	0.00	63.00	3.00	0.00	21.00	2.00	4.00	1.00	0.00	0.00	0.00
14-1 Musselman	9968.6	%	0.00	0.00	0.00	0.00	78.00	1.00	0.00	13.00	2.00	3.00	0.00	0.00	0.00	0.00
14-1 Musselman	9972.2	%	0.00	0.00	0.00	0.00	77.00	1.00	0.00	14.00	2.00	3.00	0.00	0.00	0.00	0.00
14-1 Musselman	9975.6	%	1.00	0.00	9.00	8.00	17.00	2.00	0.00	48.00	6.00	7.00	2.00	0.00	0.00	0.00
14-1 Musselman	9977.3	%	0.00	0.00	0.00	0.00	60.00	4.00	0.00	23.00	3.00	5.00	1.00	0.00	0.00	0.00
14-1 Musselman	9979.4	%	0.00	0.00	0.00	0.00	72.00	2.00	0.00	18.00	2.00	5.00	0.00	0.00	0.00	0.00
14-1 Musselman	9983.5	%	0.00	0.00	0.00	0.00	83.00	1.00	0.00	12.00	1.00	2.00	0.00	0.00	0.00	0.00
14-1 Musselman	9987.3	%	0.00	0.00	0.00	0.00	76.00	1.00	0.00	16.00	2.00	3.00	0.00	0.00	0.00	0.00
14-1 Musselman	9994.6	%	0.00	0.00	0.00	0.00	47.00	2.00	0.00	39.00	4.00	6.00	0.00	0.00	0.00	0.00
14-1 Musselman	9999.0	%	0.00	0.00	0.00	0.00	62.00	1.00	0.00	28.00	2.00	5.00	0.00	0.00	0.00	0.00
14-1 Musselman	10001.1	%	0.00	0.00	0.00	0.00	70.00	1.00	0.00	18.00	2.00	5.00	1.00	0.00	0.00	0.00
14-1 Musselman	10002.4	%	1.00	0.00	14.00	8.00	11.00	5.00	0.00	42.00	7.00	10.00	2.00	0.00	0.00	0.00
14-1 Musselman	10009.6	%	0.00	0.00	0.00	0.00	48.00	5.00	0.00	32.00	3.00	3.00	1.00	0.00	0.00	0.00
14-1 Musselman	10010.8	%	0.00	0.00	0.00	0.00	35.00	10.00	0.00	36.00	4.00	5.00	1.00	0.00	0.00	0.00
14-1 Musselman	10014.5	%	1.00	0.00	12.00	3.00	12.00	4.00	0.00	51.00	8.00	7.00	2.00	0.00	0.00	0.00
14-1 Musselman	10016.5	%	1.00	0.00	11.00	7.00	9.00	3.00	0.00	53.00	8.00	6.00	2.00	0.00	0.00	0.00
14-1 Musselman	10016.7	%	1.00	0.00	8.00	1.00	43.00	6.00	0.00	30.00	4.00	6.00	1.00	0.00	0.00	0.00
14-1 Musselman	10018.3	%	1.00	0.00	9.00	2.00	7.00	0.00	0.00	27.00	3.00	6.00	1.00	44.00	0.00	0.00
14-1 Musselman	10020.7	%	0.00	0.00	0.00	0.00	48.00	2.00	0.00	41.00	3.00	3.00	1.00	0.00	0.00	0.00

14-1 Musselman	10025.4	%	0.00	0.00	0.00	0.00	58.00	2.00	0.00	31.00	2.00	3.00	1.00	0.00	0.00	0.00
14-1 Musselman	10031.5	%	0.00	0.00	0.00	0.00	57.00	4.00	0.00	28.00	3.00	3.00	1.00	0.00	0.00	0.00
14-1 Musselman	10034.3	%	0.00	0.00	0.00	0.00	52.00	2.00	0.00	34.00	4.00	4.00	1.00	0.00	0.00	0.00
14-1 Musselman	10035.2	%	0.00	0.00	7.00	4.00	37.00	5.00	0.00	35.00	4.00	7.00	1.00	0.00	0.00	0.00
14-1 Musselman	10038.5	%	0.00	0.00	0.00	0.00	67.00	3.00	0.00	18.00	3.00	4.00	1.00	0.00	0.00	0.00
14-1 Musselman	10040.6	%	0.00	0.00	2.00	0.00	63.00	3.00	0.00	25.00	3.00	3.00	1.00	0.00	0.00	0.00
14-1 Musselman	10042.7	%	0.00	0.00	0.00	0.00	68.00	2.00	0.00	23.00	2.00	3.00	1.00	0.00	0.00	0.00
14-1 Musselman	10045.6	%	0.00	0.00	0.00	0.00	24.00	0.00	0.00	64.00	5.00	3.00	1.00	0.00	0.00	0.00
14-1 Musselman	10045.8	%	1.00	0.00	15.00	9.00	9.00	3.00	0.00	45.00	8.00	8.00	2.00	0.00	0.00	0.00
14-1 Musselman	10052.4	%	1.00	0.00	8.00	4.00	20.00	4.00	0.00	46.00	6.00	10.00	1.00	0.00	0.00	0.00
1-23 Shaffer	9868.2	wt%	1.03	0.23	2.96	0.00	13.87	0.00	0.00	14.30	1.06	2.13	0.14	0.00	0.83	0.00
1-23 Shaffer	9863.3	wt%	1.07	0.50	6.70	0.00	2.77	0.00	0.00	17.66	1.29	3.16	0.38	0.00	0.41	0.00
1-23 Shaffer	9862.3	wt%	0.52	0.31	2.28	0.00	19.52	0.00	0.00	11.40	0.43	1.41	0.16	0.00	0.59	0.00
1-23 Shaffer	9832.7	wt%	0.55	0.35	0.82	0.00	23.06	0.00	0.00	8.94	0.55	2.28	0.08	0.00	0.45	0.00
1-23 Shaffer	9816.5	wt%	0.45	0.42	0.41	0.00	25.35	0.00	0.00	7.51	0.43	2.05	0.08	0.00	0.34	0.00
1-23 Shaffer	9807.9	wt%	1.28	0.50	3.63	0.00	4.87	0.00	0.00	19.36	1.64	3.61	0.22	0.00	1.28	0.00
1-23 Shaffer	9791.8	wt%	0.62	0.35	1.61	0.00	7.82	0.00	0.00	21.43	1.33	2.21	0.08	0.00	0.97	0.00
1-23 Shaffer	9777.5	wt%	0.38	0.31	1.27	0.00	19.63	0.00	0.00	12.34	0.35	2.02	0.06	0.00	0.41	0.00
1-23 Shaffer	9769.9	wt%	0.69	0.35	2.81	0.00	12.36	0.00	0.00	13.96	0.90	2.47	0.14	1.48	0.86	0.00
1-23 Shaffer	9743.5	wt%	0.62	0.31	2.32	0.00	14.28	0.00	0.00	14.23	0.39	2.55	0.08	0.00	1.83	0.00
1-23 Shaffer	9733.0	wt%	0.62	0.42	2.58	0.00	10.18	0.00	0.00	17.02	0.78	2.97	0.08	0.00	1.79	0.00
1-23 Shaffer	9725.7	wt%	0.62	0.35	3.22	0.00	6.35	0.00	0.00	20.57	0.86	2.85	0.12	0.19	1.24	0.00
1-23 Shaffer	9717.2	wt%	1.24	0.46	3.97	0.00	6.49	0.00	0.00	16.98	1.21	2.97	0.28	0.88	1.28	0.00

1-23 Shaffer	9705.3	wt%	0.69	0.46	1.24	0.00	20.30	0.00	0.00	10.72	0.31	2.59	0.06	0.00	0.76	0.00
1-23 Shaffer	9704.5	wt%	0.79	0.38	3.71	0.00	2.55	0.00	0.00	19.36	1.21	4.30	0.22	0.00	3.45	0.00
1-23 Shaffer	9696.3	wt%	0.00	0.00	0.97	0.00	29.08	0.00	0.00	4.91	0.00	1.10	0.06	0.57	0.21	0.00
1-23 Shaffer	9688.0	wt%	0.34	0.27	1.69	0.00	12.44	0.00	0.00	17.81	0.27	2.28	0.06	0.28	1.17	0.00
1-23 Shaffer	9686.7	wt%	0.38	0.27	0.79	0.00	18.97	0.00	0.00	13.13	0.00	2.21	0.12	0.60	0.55	0.00
1-23 Shaffer	9670.6	wt%	0.90	0.42	2.13	0.00	8.45	0.00	0.00	17.58	0.27	2.85	0.16	0.28	3.28	0.00
1-23 Shaffer	9677.9	wt%	1.17	0.31	1.95	0.00	12.69	0.00	0.00	14.08	0.39	2.36	0.18	0.25	3.14	0.00
1-23 Shaffer	9669.5	wt%	0.45	0.27	1.57	0.00	18.82	0.00	0.00	10.45	0.20	2.59	0.06	0.22	1.76	0.00
1-23 Shaffer	9665.0	wt%	1.14	0.58	4.31	0.00	3.25	0.00	0.00	19.36	0.78	3.73	0.26	0.00	0.34	0.00
1-23 Shaffer	9663.2	wt%	0.55	0.35	1.09	0.00	27.90	0.00	0.00	4.19	0.20	1.71	0.06	0.00	0.90	0.00
1-23 Shaffer*	9663.4	wt%	8.37	0.00	22.94	4.23	7.39	0.00	0.00	39.00	0.00	0.00	2.61	0.45	0.00	9.00
1-23 Shaffer*	9728.5	wt%	9.28	0.00	7.86	6.53	17.13	0.00	0.00	37.30	0.00	0.00	5.82	0.04	0.00	8.06
1-23 Shaffer*	9777.5	wt%	4.98	0.00	0.14	0.00	69.18	0.00	0.00	13.52	0.00	0.00	4.65	0.07	0.00	4.38
1-23 Shaffer*	9837.5	wt%	9.59	0.00	13.91	4.50	12.87	1.76	0.00	31.10	0.00	0.00	5.73	0.08	0.00	5.96
1-23 Shaffer*	9887.5	wt%	2.46	0.00	4.01	5.21	51.45	0.00	0.00	25.07	0.00	0.00	0.41	0.34	0.00	3.75
1 Payne	8948.0	wt%	1.00	1.00	7.00	9.00	31.00	0.00	0.00	43.00	0.00	8.00	2.00	0.00	0.00	0.00
1 Van Horn	7754.0	%	0.00	0.00	1.00	1.00	91.00	0.00	0.00	6.00	1.00	1.00	0.00	0.00	0.00	0.00
1 Van Horn	7833.0	%	0.00	0.00	1.00	1.00	80.00	0.00	0.00	14.00	1.00	2.00	1.00	0.00	0.00	0.00
1 Van Horn	7925.0	%	1.00	0.00	11.00	12.00	38.00	0.00	0.00	39.00	0.00	4.00	3.00	0.00	0.00	0.00
1 Van Horn	8104.0	%	0.00	0.00	0.00	0.00	59.00	0.00	0.00	39.00	0.00	0.00	1.00	0.00	0.00	0.00
1 L. L. Hawkins	7738.6	wt%	1.85	0.00	21.94	1.23	15.73	5.31	0.00	41.12	1.74	8.23	1.90	0.94	0.00	0.00
1 L. L. Hawkins	7741.2	wt%	2.58	0.00	19.58	0.51	10.25	4.69	0.00	47.70	2.43	10.34	1.91	0.00	0.00	0.00
1 L. L. Hawkins	7757.8	wt%	1.47	0.00	13.69	1.56	37.47	3.83	0.00	32.89	2.02	5.88	1.19	0.00	0.00	0.00

1 L. L. Hawkins	7771.2	wt%	0.33	0.00	5.12	0.00	50.48	0.79	0.00	34.52	2.27	6.08	0.41	0.00	0.00	0.00
1 L. L. Hawkins	7778.0	wt%	0.61	0.00	3.47	0.00	54.44	0.80	0.00	32.19	1.85	6.26	0.38	0.00	0.00	0.00
1 L. L. Hawkins	7780.4	wt%	0.50	0.00	5.32	0.00	19.38	4.68	0.00	56.92	2.49	10.29	0.42	0.00	0.00	0.00
1 L. L. Hawkins	7784.3	wt%	0.52	0.00	6.52	0.00	18.31	7.55	0.00	56.68	2.33	7.50	0.58	0.00	0.00	0.00
1 L. L. Hawkins	7797.7	wt%	0.48	0.00	4.60	1.22	19.30	5.75	0.00	56.74	3.03	7.91	0.24	0.72	0.00	0.00
1 L. L. Hawkins	7805.6	wt%	0.48	0.00	4.45	1.22	17.34	4.45	0.00	59.80	2.94	8.95	0.37	0.00	0.00	0.00
1 L. L. Hawkins	7811.1	wt%	0.58	0.00	4.90	0.56	19.27	7.47	0.00	56.05	2.47	7.67	0.32	0.71	0.00	0.00
1 L. L. Hawkins	7820.1	wt%	0.58	0.00	5.07	0.49	20.25	1.90	0.00	59.82	2.57	8.30	0.37	0.65	0.00	0.00
1 L. L. Hawkins	7822.8	wt%	0.87	0.00	7.38	0.00	18.53	1.48	0.00	59.99	2.31	8.38	0.37	0.70	0.00	0.00
1 L. L. Hawkins	7826.5	wt%	0.66	0.00	3.81	0.00	52.70	3.25	0.00	29.98	1.88	6.61	0.20	0.90	0.00	0.00
1 L. L. Hawkins	7835.0	wt%	0.85	0.00	6.18	2.44	18.78	2.29	0.00	58.73	2.51	7.91	0.30	0.00	0.00	0.00
1 L. L. Hawkins	7836.7	wt%	0.35	0.00	5.71	0.00	52.10	0.83	0.00	32.53	2.11	6.21	0.16	0.00	0.00	0.00
1 L. L. Hawkins	7844.2	wt%	1.68	0.00	21.50	6.03	9.20	1.86	0.00	46.45	2.22	9.10	1.40	0.57	0.00	0.00
1 L. L. Hawkins	7865.3	wt%	1.30	0.00	17.98	5.05	11.25	1.80	0.00	50.48	2.49	8.53	1.11	0.00	0.00	0.00
1 L. L. Hawkins	7873.9	wt%	0.96	0.00	11.34	1.47	28.32	17.42	0.00	32.73	1.05	5.75	0.95	0.00	0.00	0.00
1 L. L. Hawkins	7891.6	wt%	0.86	0.00	12.64	1.97	31.65	5.95	0.00	39.30	1.73	4.96	0.93	0.00	0.00	0.00
1 L. L. Hawkins	7898.9	wt%	0.69	0.00	8.95	0.00	45.25	2.69	0.00	35.00	1.62	4.46	0.86	0.49	0.00	0.00
1 L. L. Hawkins	7908.8	wt%	0.50	0.00	6.51	0.00	52.80	1.79	0.00	33.69	0.83	1.83	0.92	1.13	0.00	0.00
1 L. L. Hawkins	7916.1	wt%	0.00	0.00	2.13	0.00	77.34	0.60	0.00	17.88	0.00	1.53	0.00	0.52	0.00	0.00
1 L. L. Hawkins	7916.8	wt%	0.00	0.00	2.50	0.00	73.09	0.88	0.00	20.76	0.00	1.89	0.00	0.89	0.00	0.00
1 L. L. Hawkins	7918.8	wt%	0.00	0.00	5.04	0.00	42.43	2.74	0.00	42.22	1.25	4.54	0.42	1.37	0.00	0.00
1 L. L. Hawkins	7926.6	wt%	0.00	0.00	3.92	0.00	68.40	0.82	0.00	25.42	0.00	1.06	0.37	0.00	0.00	0.00
1 L. L. Hawkins	7936.6	wt%	0.00	0.00	3.65	0.00	70.71	1.31	0.00	23.08	0.00	1.11	0.14	0.00	0.00	0.00

1 L. L. Hawkins	7945.1	wt%	0.00	0.00	2.18	0.00	60.76	0.00	0.00	34.36	1.19	1.28	0.23	0.00	0.00	0.00
1 L. L. Hawkins	7948.6	wt%	0.02	0.00	3.27	0.00	67.60	1.03	0.00	22.96	1.47	2.66	0.27	0.72	0.00	0.00
1 L. L. Hawkins	7952.1	wt%	0.00	0.00	5.60	0.00	64.59	0.65	0.00	24.69	0.85	2.41	0.39	0.81	0.00	0.00
1 L. L. Hawkins	7954.3	wt%	1.06	0.00	15.37	3.96	28.24	3.14	0.00	39.79	1.79	3.95	1.31	1.40	0.00	0.00
1 L. L. Hawkins	7958.2	wt%	0.00	0.00	2.68	0.00	63.63	3.46	0.00	27.38	0.71	1.85	0.28	0.00	0.00	0.00
1 L. L. Hawkins	7959.3	wt%	0.00	0.00	3.08	0.00	48.83	3.84	0.00	41.09	0.00	1.92	0.33	0.92	0.00	0.00
1 L. L. Hawkins	7963.9	wt%	0.00	0.00	1.42	0.00	85.18	0.88	0.00	11.44	0.00	1.08	0.00	0.00	0.00	0.00
1 L. L. Hawkins	7967.9	wt%	0.00	0.00	1.30	0.00	81.57	1.06	0.00	15.21	0.00	0.86	0.00	0.00	0.00	0.00
1 L. L. Hawkins	7972.2	wt%	0.00	0.00	3.57	0.00	77.42	0.46	0.00	16.96	0.52	1.06	0.00	0.00	0.00	0.00
1 L. L. Hawkins	7979.7	wt%	0.00	0.00	4.38	0.00	28.82	3.24	0.00	61.09	0.30	1.97	0.21	0.00	0.00	0.00
1 L. L. Hawkins	7984.1	wt%	0.00	0.00	2.66	0.00	31.28	1.74	0.00	59.52	1.28	2.29	0.35	0.87	0.00	0.00
1 L. L. Hawkins	7986.7	wt%	0.00	0.00	2.69	0.00	83.99	0.62	0.00	10.76	0.19	1.76	0.00	0.00	0.00	0.00
1 L. L. Hawkins	7991.6	wt%	0.00	0.00	4.19	0.00	56.88	4.99	0.00	30.93	0.57	1.57	0.00	0.88	0.00	0.00
1 L. L. Hawkins	7998.5	wt%	0.59	0.00	9.56	1.70	14.64	29.92	0.00	36.82	1.03	4.65	1.09	0.00	0.00	0.00
1 L. L. Hawkins	8006.1	wt%	0.28	0.00	7.49	0.00	40.35	18.55	0.00	26.14	2.48	3.90	0.80	0.00	0.00	0.00

observations are needed to distinguish them. The EDX analysis on several points in the polished thin sections only indicate chlorite. The EDX spectrums of chlorite yields the major elements Si and Al, with a minor amount of Mg, K, and Fe (Figure 2.10). Based on these elements, the chlorite type is possibly corrensite $[(Ca, Na, K) (Mg, Fe, Al)_9 (Si, Al)_8 O_{20} (OH)_{10} n(H_2O)]$.

Most of the observed clay minerals are brown to yellowish brown under the optical microscope. Yet, their types are difficult to identify on the basis of crystal morphology with the SEM (e.g., Figure 2.9g). Clay minerals have potential to inhibit calcite and quartz cementation, occlude pores throat, and reduce reservoir permeability.

Other Minor Authigenic Minerals

Hardwick (2018) documented the presence of albite overgrowths that occlude intergranular pores in Mississippian strata of central Oklahoma. In the study, partial and complete albitization of K-feldspar or Ca-rich plagioclase grains were observed (Figure 2.9r). Albitization is a dissolution-precipitation process in which a single large grain of Ca-rich plagioclase or K-feldspar is commonly replaced by numerous, micron-size, elongate albite crystals (laths) that are oriented in roughly the same direction (Seyedolali and Boggs, 1996). Albitization is a temperature-dependent process and less likely to occur below 60⁰C (Boggs and Seyedolali, 1992; Seyedolali and Boggs 1996). It typically takes place during sediment burial and at relatively higher temperatures, typically ranging from 65 – 160⁰C (Aagaard et al., 1990; Boles, 1982; Boles and Ramseyer, 1988; Morad et al., 1990). Laboratory experiments by Baccar et al. (1993) showed that the albitization of K-feldspar is enhanced by increasing temperature and most likely occurs at 120-150⁰C whereas albitization of plagioclase may occur in a temperature range from 60⁰C to 100⁰C and decreases with increasing temperature. Besides temperature, albitization may also be affected by partial pressure of carbon dioxide (pCO₂), fluid flux, variations in the structural state, and chemical composition (Baccar et al., 1993).

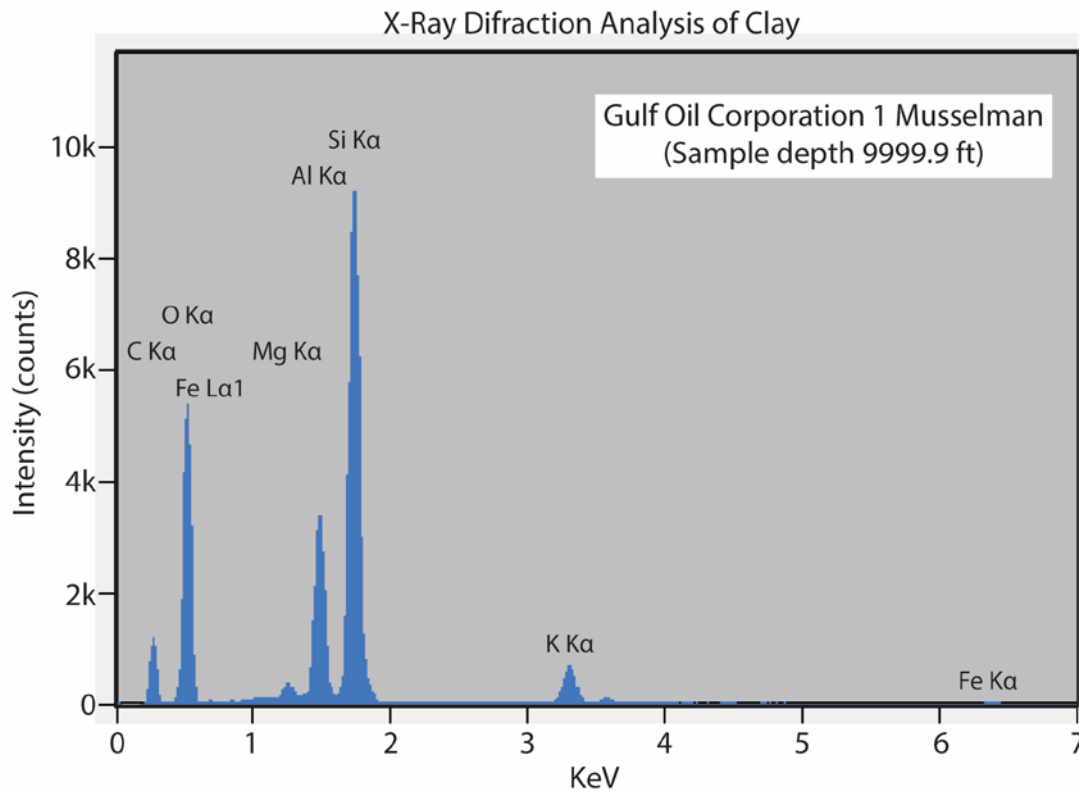


Figure 2.10. Energy Dispersive X-ray spectrum of a sample (9999.9 ft) from the Gulf Oil Corporation 1 Musselman suggests the presence of Chlorite mineral as indicated by the major elements Si and Al, with a minor amount of Mg, K, and Fe.

Other authigenic minerals including glauconite, pyrite, apatite, and titanium oxide are present. Pyrite appears to be either framboidal or a cubic metallic gold mineral under reflected light and black (opaque) under transmitted light. Similarly, titanium oxide also appears as an opaque mineral under transmitted light. However, it exhibits snowy white color under reflected light. SEM and EDX analysis confirms the present of these minerals (e.g., [Figure 2.9s and 2.9t](#))

Secondary Porosity

Intergranular and moldic secondary porosity has resulted from dissolution of skeletal grains, calcite cement, or quartz. Secondary porosity is mainly present in structureless sandstone, laminated siltstone, and chert/cherty breccia ([Figure 2.9u – 2.9x](#)). Considerable micropores were also observed under SEM analysis (e.g., [Figure 2.9x](#)). However, micropores do not appear connected as suggested by very low permeability (<0.1mD); and possibly due to cemented pore throats, the presence of isolated pores, or authigenic clays that line pore walls. Micropore characteristics are similar to the Mississippian Limestone reservoirs of the Anadarko Shelf, northern Oklahoma (e.g., [Vanden Berg and Grammer, 2016](#); [Suriamin and Pranter, 2018](#)).

Paragenesis

Deciphering major paragenetic sequence of Mississippian strata in the eastern Anadarko Basin is challenging. This is due to the lack of clear cross-cutting relationships as observed in thin sections. The interpreted paragenetic sequence inferred for the Mississippian strata is shown in [Figure 2.11](#).

[Montalvo \(2015\)](#) measured the salinity of fluid inclusions of quartz crystals from Mississippian strata in south-central Kansas and revealed that they have values consistent with seawater and evaporated seawater (early hypersalinity). Therefore, he suggests that the silicification began shortly after deposition of the sediments and before complete lithification. It appears that this process continued

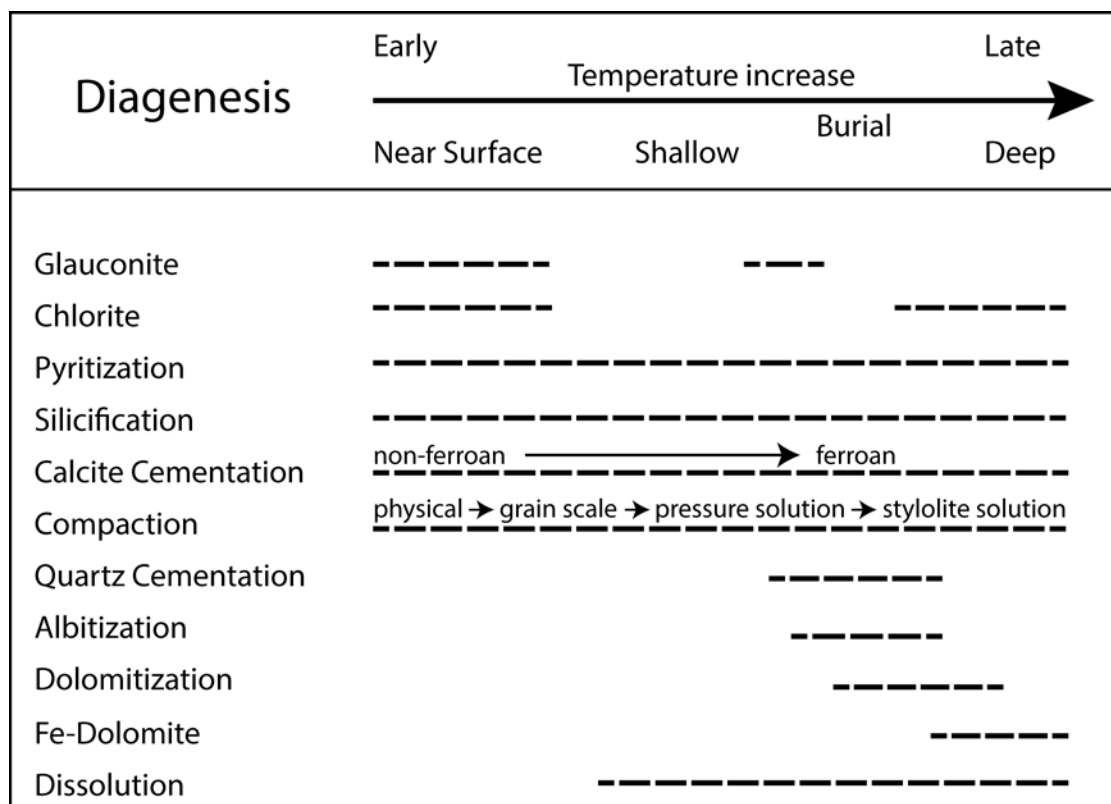


Figure 2.11. Paragenetic sequence inferred for the diagenesis of the Mississippian strata in the Anadarko Basin, central Oklahoma. This analysis is based on cross-cutting relationship and in the context of temperature dependency. Glaucanite and chlorite, and pyrite could be formed in the earlier stage of diagenesis at near surface under reduction condition. Quartz cementation, albitization, dolomitization, and Fe-dolomite cementation commonly associated with late diagenesis in the deep burial setting above 60°C. Pyrite formation, silicification, calcite cementation, and compaction appear to take place throughout early to late stage of diagenesis.

until the deep burial stage as suggested by silicification of dolomite which is interpreted to be formed at a late stage of diagenesis.

Precipitation of pyrite and alteration of fecal pellets to glauconite could have resulted from a reducing condition in marine pore fluids shortly after burial (Higley et al, 1997). The presence of disseminated pyrite within calcite-cement-filled fractures suggest that pyritization also takes place after calcite cementation and fracturing whereas calcite cementation can occur at any stage from deposition through deep burial.

Similarly, mechanical compaction is also a diagenetic event that can take place at any stage. The presence of quartz-skeletal concave-convex contact and broken skeletal suggest that mechanical compaction occurred at an earlier stage prior to calcite cementation whereas cracked dolomite rhombic crystals indicate compaction after dolomitization. The presence of quartz cementation, albitization, dolomitization, and Fe-dolomite cementation commonly correlate to hydrothermal alteration or burial diagenesis processes. Based on the temperature preferential formation, quartz cementation is attributed to earlier diagenesis at around 60 – 80⁰C (Ulmer-Scholle et al., 2014; Walderhaug, 2000). Albitization can form coeval with quartz overgrowths at 65 -160⁰C. Fe-dolomite cementation is the latest authigenic mineral formed. With an average thermal gradient of 15 – 20⁰C/km in the Anadarko Basin (Frone, 2014), quartz cementation and albitization could have initiated at depth as deep as 3 km below mean sea level.

The chlorite may be both detrital and formed diagenetically. The precipitation of chlorite might have resulted from a reducing condition in marine pore fluids shortly after burial (Higley et al, 1997). During burial diagenesis, ‘smectite-chlorite’ or ‘vermiculite-chlorite’ could evolve into pure chlorite. Kaolinite could also be replaced by chlorite at burial depth of 11500 – 14500 ft (3500 -4500 m), at a relatively higher temperature range of 165 – 200⁰C (Curtis, 1985).

As for dissolution, it appears to take place after calcite cementation as a result of the production of CO₂ by thermal decarboxylation of organic matter and carboxylic acid from maturation of kerogen. This chemical-driven dissolution typically occurs at a temperature window of 80 – 140⁰C (Taylor et al., 2010).

Reservoir Inferences

The patterns of diagenetic evolution recognized in this study allow discussion of the conditions for optimum porosity preservation in the Mississippian reservoirs. From cross-plots of mineralogy and porosity (Figure 2.12), it appears that porosity is affected by the presence of clay minerals. The presence of clay minerals, particularly chlorite and illite/smectite (e.g., Tang et al., 2018), could have coated detrital quartz grains and hindered syntaxial quartz overgrowth, leaving minor empty pore spaces. However, the clays might have decreased the reservoir quality as well when they dispersed and migrated inducing permeability damage. As shown in Figure 2.12a, porosity values tend to increase as the percentage of clays decrease.

Price et al. (2017) documented that the reservoir quality in the Mississippian strata of the eastern Anadarko Basin is controlled by the percentage of calcite cement; porosity values decreases with an increase in calcite cement. That relationship is not observed in the crossplot (Figure 2.12b). The cause of this lack of relationship is unknown. Similarly, cross-plot between quartz percentage and porosity also

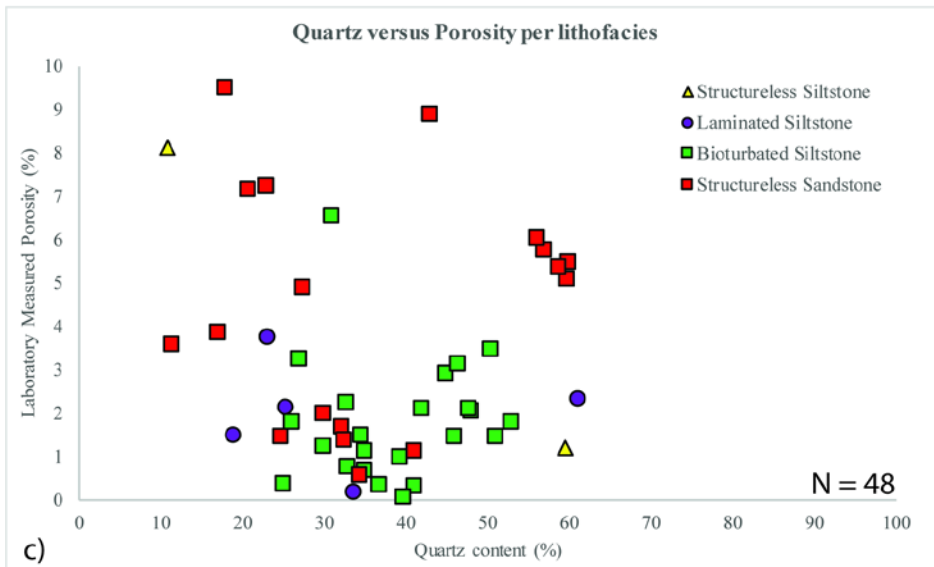
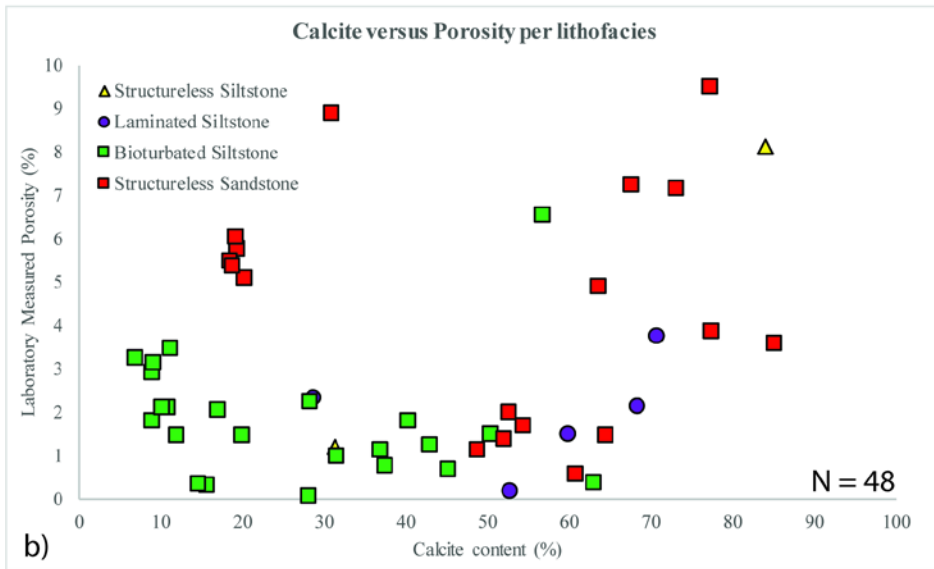
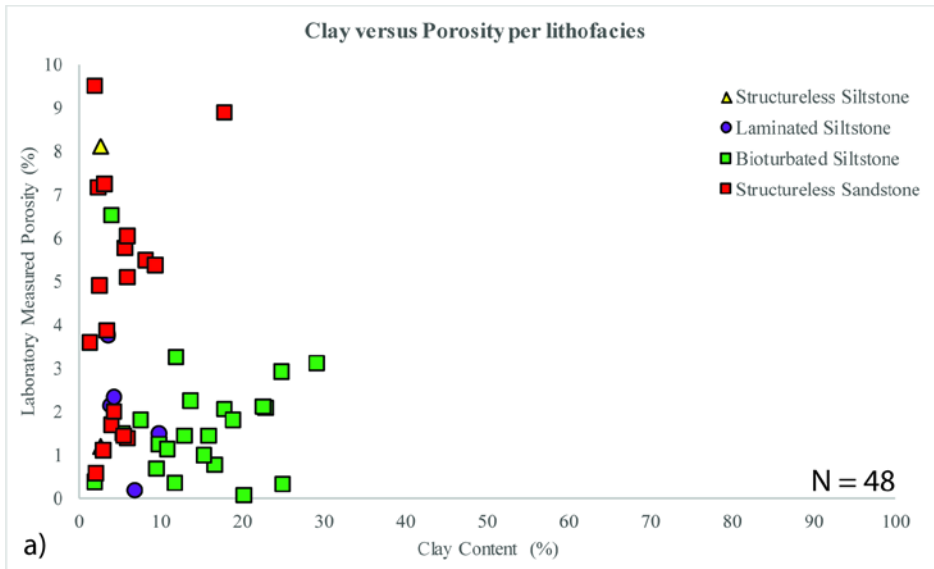


Figure 2.12. Cross-plot of main composition XRD data ($n = 48$) such as clay, calcite, and quartz against laboratory measured porosity. (a) cross-plot of clay versus porosity. Noted that the porosity decreases as the clay content increases. (b) cross-plot shows scattered data point and lack of relationships between calcite and porosity. (c) cross-plot shows scattered quartz versus porosity data points and no simple linear relationship.

showed no simple linear relationship (Figure 2.12c). Based on thin section observation, well cemented lithofacies (either by calcite or quartz cements) typically has poor reservoir quality.

The data of five wells in this study show that Mississippian strata porosity ranges from 0.1 – 8.8 % with permeability values between 0.001 - 0.1mD (Figure 2.13). However, these data represent 5 out of 8 observed lithofacies with 1 lithofacies having only 1 data point; therefore, a detailed assessment of facies control on reservoir quality was not possible.

Figures 2.13a to 2.13p show lithofacies variations and diagenetic alterations; and how they relate to reservoir quality. In general, all lithofacies were effected by mechanical compaction which reduced overall porosity. As shown in Figure 2.13, the structureless sandstone lithofacies has a relatively wide range of porosity (0.6 – 8.8 %) with permeability values consistently higher than that of other lithofacies. Half of the structureless sandstone lithofacies data set show relatively higher porosity values above 5%. Relatively higher porosity and permeability values indicate that this lithofacies, which is a channel or lobe deposit, has the best reservoir quality. It commonly has relatively coarse-grained, moderate to well grain sorting, relatively low abundance of clay minerals (<8.25 wt.%). The structureless sandstone also have prominent secondary porosity, which was created by dissolution of cements and grains (skeletal and feldspar) during deep burial diagenesis. The dissolution of calcite minerals possibly occurred when organic acids related to the influx of oil dissolved the existing calcite cement.

On the contrary, the structureless siltstone, laminated siltstone, and bioturbated siltstone lithofacies, which were deposited in upper shoreface to upper offshore environments and a restricted marine setting, have lower to moderate reservoir quality. They consistently show porosity below 4% with permeability less than 0.001mD. Many thin sections of these lithofacies show a substantial amount of clay minerals (>10 wt.%), calcite cement, quartz cement, and Fe-dolomite cement (see Table 2.2).

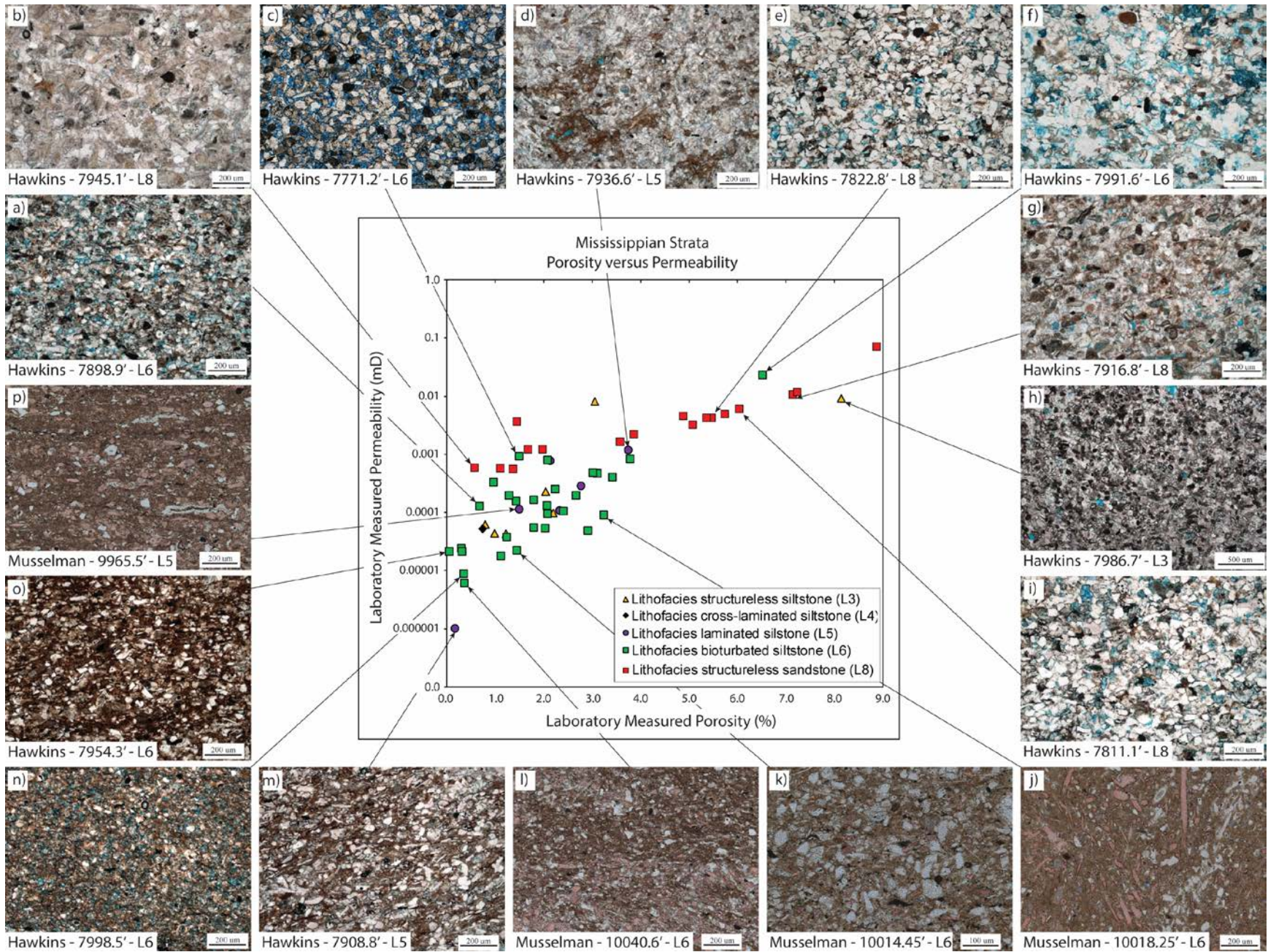


Figure 2.13. Porosity and permeability cross-plot and its relationship with lithofacies and diagenesis. Good reservoir quality rocks, which have relatively higher porosity and permeability values mainly associated with structureless sandstone with minor amount of calcite cement and clay content, and have considerable dissolution (labelled as red square). Noted the presence of Fe-dolomite and quartz cements decreasing reservoir quality. Relatively poor and moderate reservoir quality rocks, which have relatively low to moderate porosity but relatively low permeability, typically associated with structureless siltstone, laminated siltstone, and bioturbated siltstone (labelled as yellow triangle, purple circle, and green square respectively) with considerable amount of clay, calcite composition, and minor to no dissolution.

These cements might occlude the pore spaces between detrital grains or block pore throats and therefore decrease the reservoir quality. The other dominant diagenetic process that controlled porosity is compaction. Mechanical compaction due to burial apparently resulted in deformation of clays, grains breakage, and rotations that led to tighter grain packing and thus lower overall porosity.

The findings in this study reveal that the differences in reservoir quality appear to be strongly correlated to depositional environment and percentage of clay, quartz cement, and calcite cements. The presence of secondary porosity associated with deep burial dissolution tend to increase reservoir quality while compaction tend to decrease overall porosity.

CONCLUSIONS

In the eastern Anadarko Basin, Mississippian strata consist of skeletal wackestone-packstone, chert to cherty breccia, structureless siltstones, cross-laminated siltstones, laminated siltstones, bioturbated siltstones, glauconitic siltstones-sandstones, and structureless sandstones. A few lithofacies contain abundant indicators of wave influences including planar parallel laminations and ripple stratification. Storm influences may culminate as abundant hummocky cross-stratification. The aforementioned sedimentary features indicate that many of the studied strata were deposited above storm-weather wave base. Therefore, the Mississippian strata of the eastern Anadarko Basin are interpreted to represent deposition in a wave-influence near-shore setting. This setting has a semi enclosed embayment or restricted area (lagoon) located behind a shoal as indicated by the presence of wispy lamination, oncoids, aggregate grains, and sponge spicules. The successions illustrate decreasing wave-energy toward the offshore, suggesting a low gradient and dissipative system. Channels or lobes were likely present in this setting as indicated by relatively thick structureless sandstones with moderate to well sorting.

Petrographic analysis under optical microscope, scanning electron microscope, and cathodoluminescence microscope, as well as energy dispersive x-ray spectroscopy reveal several diagenetic alterations occurred including calcite cementation, mechanical compaction, albitization, quartz cementation, silicification, dolomitization, Fe-dolomite formation, pyritization, and dissolution.

Considerable variations in reservoir quality exist in the Mississippian strata. The variations are primarily controlled by depositional environment and percentage of clay, quartz, and calcite cements. The structureless sandstone associated with channel or lobe tend to have better reservoir quality due to better sorting, less clay minerals, and the occurrence of secondary porosity related to dissolution. On the contrary, the structureless siltstone, laminated siltstone, and bioturbated siltstone have lower to moderate reservoir quality depending on grain sorting and the amount of clay, quartz, and calcite minerals. Bioturbation that altered the original rock fabric and introduced more fine-material to the rocks may also play a role in deteriorating reservoir quality. However, as documented previously, *Phycosiphon*, which is the pervasive burrow type in the Mississippian strata, has the potential to enhance burrow-associated permeability. Further analysis using CT-Scan and steady-state permeability analysis needs to be done to prove this hypothesis. Other important diagenetic features and processes are the syntaxial quartz overgrowths on detrital quartz grains as well as the albitization of K-feldspar or plagioclase.

Fractures tend to occur vertically within calcite-rich beds and are restricted by argillaceous-rich beds or folded (ptygmatic fractures) within argillaceous-rich beds. Therefore, the presence of argillaceous-rich beds has potential to create hydraulic-fracture barriers.

REFERENCES

- Aagaard, P., P. K. Egeberg, G. C. Saigal, S. Morad, and K. Bjorlykke, 1990, Diagenetic albitization of detrital K-Feldspar in Jurassic, Lower Cretaceous and Tertiary clastic reservoir rocks from offshore Norway, II. Formation water chemistry and kinetics considerations: *Journal of Sedimentary Petrology*, **60**, 575 – 581.
- Baccar, M. B., B. Fritz, and B. Made, 1993, Diagenetic albitization of K-Feldspar and Plagioclase in sandstone reservoir: Thermodynamic and kinetic modeling: *Journal of Sedimentary Petrology*, **63**, 1100 - 1109
- Birch, C. B., 2015, Reservoir-scale stratigraphy, sedimentology, and porosity characteristics of Mississippian reservoirs, northeastern Anadarko Shelf, Oklahoma: Master's thesis, University of Oklahoma, Norman, Oklahoma, 81.
- Boggs, S. Jr., and A. Seyedolali, 1992, Diagenetic albitization, zeolitization, and replacement in Miocene sandstones, sites 796,797, and 799, Japan Sea: *Proceeding of the Ocean Drilling Program, Scientific Results*, 127/128, 131 – 151.
- Boggs, S., Jr and D. Krinsley, 2006, *Applications of Cathodoluminescence imaging to the study of sedimentary rocks*: Cambridge, New York, Melbourne, Cambridge University Press, 16, doi:10.1017/S0016756808004779.
- Boles, J. R., 1982, Active albitization of Plagioclase, Gulf Coast Tertiary: *American Journal of Science*, **282**, 165 – 180.
- Boles, J. R., and K. Ramseyer, 1988, Albitization of Plagioclase and vitrinite reflectance as paleothermal indicator, San Joaquin Basin, *in* Graham, S. A., ed., *Studies of the Geology of the San Joaquin Basin*: Society of Economic Paleontologists and Mineralogists, 129 – 139.
- Boyd, D. T., 2008, *Stratigraphic guide to Oklahoma oil and gas reservoir*: Oklahoma Geological Survey, Special Publication 2008-1.
- Butt, S.H., 2014, Silicification: *Paleontological Society Paper*, **20**, 15-33.
- Campbell, J. A., C. J. Mankin, A. B. Schwarzkopf, and J. J. Raymer, 1988, Habitat of petroleum in Permian rocks of the Midcontinent region, *in* Morgan, W. A., and Babcock, J. A., eds., *Permian Rocks of the Midcontinent*: Midcontinent Society of Economic Paleontologists and Mineralogists (SEPM) Special Publication **1**, 13-35.
- Childress, M., and G. M. Grammer, 2015, High resolution sequence stratigraphic architecture of a Midcontinent Mississippian outcrop in southwest Missouri: *Shale Shaker*, **66**, 206–234.
- Clair, J. H., 1949, Lithologic criteria of Mississippian rocks in western Kansas: *World Oil*, **122**, 61- 66.

- Cullen, A., 2017, Devonian-Mississippian petroleum systems of southern Laurasia: What makes the STACK-Merge-SCOOP Play in Oklahoma so special: AAPG Search and Discovery Article# 10998, 29.
- Curtis C. D., D. G. Murchison, R. A. Berner, H. Shaw, M. Sarnthein, B. Durand, D. Eglinton, A. S. Mackenzie, and R. C. Surdam, 1985, Clay mineral precipitation and transformation during burial diagenesis: *Philosophical Transactions of the Royal Society of London*, **315**, 91 – 105.
- Curtis, D.M., and S. C. Champlin, 1959, Depositional environments of Mississippian limestones of Oklahoma: *Tulsa Geological Society Digest*, **27**, 90 - 103
- Dehcheshmehi, S. M., 2016, Regional diagenesis of Mississippian strata of the southern Midcontinent, USA; Ph.D.'s dissertation, Oklahoma State University, Stillwater, Oklahoma, 134.
- Drummond, K., 2018, Regional stratigraphy and proximal to distal variation of lithology and porosity within a mixed carbonate-siliciclastic system, Meramec and Osage series (Mississippian), central Oklahoma: Master's thesis, University of Oklahoma, Norman, Oklahoma, 155.
- Dutton, S. P., 1984, Fan-delta Granite Wash of the Texas Panhandle: *Oklahoma City Geological Society Short Course*, 1-144.
- Flügel, E., 2004, *Microfacies of carbonate rocks: Analysis, interpretation, and application*: New York, Springer, 976.
- Frone, Z., 2014, Heat flow and thermal history of the Anadarko Basin, Oklahoma: AAPG Search and discovery Article# 10657, 28.
- Hardwick, J., 2018, Reservoir quality evaluation of the Meramec and Upper Osage units in the Anadarko Basin: Master's thesis, University of Oklahoma, Norman, Oklahoma, 63.
- Harris, 1975, Hydrocarbon accumulation in "Meramec-Osage" (Mississippian) rocks, Sooner trend, northwest-central Oklahoma: *AAPG Bulletin*, **59**, 633 – 664.
- Hickman, G. J., 2018, Parasequence-scale stratigraphy variability of lithology and porosity of Mississippian Meramec reservoirs and the relationship to production characteristics, STACK trend, Oklahoma: Master's thesis, University of Oklahoma, Norman, Oklahoma, 94.
- Higley, D. K., M. P. Pantea, and R. M. Slatt, 1997, 3-D reservoir characterization of the House Creek Oil field, Powder River Basin, Wyoming, accessed April 20, 2019, https://pubs.usgs.gov/dds/dds-033/USGS_3D/ssx_txt/homepage.htm
- Johnson, K. S., and K. V. Luza, 2008, Earth sciences and mineral resources of Oklahoma: Educational Publication 9, Oklahoma Geological Survey, 22.
- Kahle, C. F., 1965, Possible roles of clay minerals in the formation of dolomite: *Journal of sedimentary petrology*, **35**, 448 – 453.

- Leavitt, A., 2018, Depositional systems of the STACK and SCOOP Mississippian units: regional understanding from logs and core: Oklahoma Geological Survey – The STACK Play Workshop, Abstract.
- LeBlanc, S., 2014, High resolution sequence stratigraphy and reservoir characterization of the “Mississippian Limestone” in North-Central Oklahoma: Master’s thesis, Oklahoma State University, Stillwater, Oklahoma, 444.
- Lemiski R. T., S. G. Pemberton, J. Hovikoski, and M. Gingras, 2011, Sedimentological, ichnological and reservoir characteristics of the low-permeability, gas-charged Alderson Member (Hatton gas field, southwest Saskatchewan): Implication for resource development: Bulletin of Canadian Petroleum Geology, **59**, 27 – 53.
- LoCricchio, E., 2012, Granite Wash play overview, Anadarko Basin: Stratigraphic framework and controls on Pennsylvanian Granite Wash production, Anadarko Basin, Texas and Oklahoma: AAPG Annual Convention and Exhibition, 1-17.
- Mazzullo, S. J., 2011, Mississippian oil reservoirs in the Southern Midcontinent: New exploration concepts for a mature reservoir objective: AAPG Search and Discovery #10373, 34.
- Mazzullo, S. J., B. W. Wilhite, and D. R. Boardman, 2011, Lithostratigraphic architecture of the Mississippian Reeds Spring Formation (Middle Osagean) in S. W. Missouri, N. W. Arkansas, and N. E. Oklahoma, Outcrop analog of subsurface petroleum reservoirs: Shale Shaker, **61**, 254–269.
- Mazzullo, S. J., B. W. Wilhite, D. R. Boardman, B. T. Morris, and C. J. Godwin, 2016, Stratigraphic architecture and petroleum reservoirs in lower to middle Mississippian strata (Kinderhookian to basal Meramecian in subsurface central to southern Kansas and northern Oklahoma: Shale Shaker, **67**, 20-49.
- McConnell, D. A., M. J. Goydas, G. N. Smith, and J. P. Chitwood, 1989, Morphology of the frontal fault zone, southwest Oklahoma: Implications for deformation and deposition in the Wichita uplift and Anadarko basin: Geology, **18**, 634-637.
- McDuffie, R. H., 1959, Lithologic basis for correlation of Mississippian rocks in the subsurface between Kansas and north central Oklahoma: Oklahoma Academy of Science, **39**, 133 – 135.
- Miller, J. C., 2018, Regional stratigraphy and organic richness of the Mississippian Meramec and associated strata, Anadarko Basin, central Oklahoma: Master’s thesis, University of Oklahoma, Norman, Oklahoma, 143.
- Montalvo-Llitas, L.G., 2015, Petrography and paragenesis of diagenetic mineral phases in cherty and dolomitic spiculite strata, Mississippian, south-central Kansas; Master’s thesis, University of Kansas, Lawrence, Kansas, 174.

- Morad, S., M. Bergan, R. Knarud, and J. P. Nystuen, 1990, Albitization of detrital plagioclase in Triassic reservoir sandstones from the Snorre field, Norwegian North Sea: *Journal of Sedimentary Petrology*, **60**, 411- 425.
- Morsilli, M., and L. Pomar, 2012, Internal waves vs. surface storm waves: a review on the origin of hummocky cross-stratification: *Terra Nova*, **24**, 273 – 282.
- Northcutt, R. A., and J. A. Campbell, 1995, Geologic provinces of Oklahoma: Oklahoma Geological Survey Open-File Report 5-95, 1 sheet, scale 1 : 750,000, 6.
- Price, B., K. Haustveit, and A. Lamb, 2017, Influence of stratigraphy on barriers to fracture growth and completion optimization in the Meramec STACK play, Anadarko Basin, Oklahoma: Unconventional Resources Technology Conference# 2697585, 8.
- Rogers, S. M., 2001, Deposition and diagenesis of Mississippian chat reservoirs, north central Oklahoma: *AAPG Bulletin*, **85**, 115–129.
- Rottmann, K., 2018, Well-log characterization of the Devonian and Mississippian Groups in central and northern Oklahoma with emphasis on correlation and depositional environment: Oklahoma Geological Survey – STACK Workshop, 73.
- Rowland, T.L., 1961, Mississippian rocks in the subsurface of the Kingfisher-Guthrie area, Oklahoma: *Shale Shaker Digest IV*, **12 – 14**, 145 – 162.
- Sarg, J. F., Suriamin, K. Tanavsuu-Milkeviciene, and J. D. Humphrey, 2013, Lithofacies, stable isotope composition, and stratigraphic evolution of microbial and associated carbonates, Green River Formation (Eocene), Piceance Basin, Colorado: *AAPG Bulletin*, **97**, 1937 – 1966.
- Seyedolali, A., and S. Boggs, Jr., 1996, Albitization of Miocene deep-sea sandstone from the Japan Sea Backarc Basin: *Journal of the Sedimentological Society of Japan*, **43**, 1 -18.
- Shelley, S., G. M. Grammer, and M. J. Pranter, 2017, Reservoir characterization and modeling of a subsurface Meramec analog from a quarry in northeastern Oklahoma: *Shale Shaker*, **68**, 224-243.
- Strasser, A., 1986, Ooids in Purbeck limestones (lowermost Cretaceous) of the Swiss and French Jura: *Sedimentology*, **33**, 711 – 727.
- Stukey, B., C. J. Godwin, and J. O. Puckette, 2018, Biostratigraphically constrained ages of Mississippian mixed carbonate-siliciclastic sequences, STACK Play, Anadarko Basin, Oklahoma: Oklahoma Geological Survey – STACK Workshop, **29**.
- Suriamin, F., and M. J. Pranter, 2018, Stratigraphic and lithofacies control on pore characteristics of Mississippian limestone and chert reservoirs of north-central Oklahoma: *Interpretation*, **6**, T1001 – T1022.

- Tang, L., J. Gluyas, S. Jones, L. Bowen, and B. Besly, 2018, The grain-coating Illite/Smectite (I/S): A new discovery on its positive effect on porosity preservation: AAPG Search and Discovery #51451, 9.
- Taylor T. R., M. R. Giles, L. A. Hathon, T. N. Diggs, N. R. Braunsdorf, G. V. Birbiglia, M. G. Kittridge, C. I. Macaulay, and I. S. Espejo, 2010, Sandstone diagenesis and reservoir quality prediction: models, myths, and reality: AAPG Bulletin, **94**, 1093 – 1132.
- Ulmer-Scholle, D. S., P. A. Scholle, J. Schieber, and R. J. Raine, 2014, A color guide to the petrography of sandstone, siltstone, shale, and associated rocks: AAPG Memoir **109**, 526.
- Ulrich, E. O., 1904, Preliminary notes on classification and nomenclature of certain Paleozoic rock unit in eastern Missouri: in Buckley E.R., and Buehler, H. A., The quarry industry in Missouri: Missouri Bureau of Geology and Mines, **2**, 109 – 111.
- Vanden Berg, B., and G. M. Grammer, 2016, 2-D pore architecture characterization of a carbonate mudrock reservoir: Insight from the Midcontinent “Mississippi Lime”, in Olson, T., ed., Imaging unconventional reservoir pore systems: AAPG Memoir **112**, 185–232.
- Walderhaug, O., and P. A. Bjorkum, 1998, Calcite cement in shallow marine sandstone: growth mechanism and geometry, in S. Morad, ed., Carbonate cementation in sandstones: distribution patterns and geochemical evolution: The International Association of Sedimentologists, Special Publication **26**, 179 – 192.
- Walderhaug, O., 2000, Modeling quartz cementation and porosity in Middle Jurassic Brent Group sandstones of the Kvitebjorn field, northern North Sea: AAPG Bulletin, **84**, 1325 – 1339.
- Watney, W. L., W. J. Guy, A. P. Byrnes, 2001, Characterization of the Mississippian chert in south-central Kansas: AAPG Bulletin, **85**, 85 – 113.
- Welker, C., S. Feiner, R. Lishansky, W. Phiukhao, J. Chao, R. Moore, and D. Hall, 2016, Trapped Fluid Analysis of 58 wells from SCOOP and STACK Plays: Unconventional Resources Technology Conference# 2461587, 12.

3. PETROPHYSICAL ANALYSIS OF MISSISSIPPIAN ROCK TYPES AND RESERVOIR PROPERTIES WITHIN A SEQUENCE-STRATIGRAPHIC FRAMEWORK, EASTERN ANADARKO BASIN, OKLAHOMA, USA

ABSTRACT

Knowledge of mineral volumes are crucial in the Mississippian strata as they are primary control on porosity and permeability. A matrix algebra inversion method used to calculate the mineral volume has relatively good predictive accuracy for carbonate ($R^2 = 0.73$), quartz ($R^2 = 0.66$), and clay ($R^2 = 0.76$) minerals. Based on the calculated mineral volumes and effective porosity, the Mississippian strata are classified into 3 rock types. Rock type 1 is characterized by relatively moderate clay (22% - 39%), quartz (26% - 43%), and carbonate (25% - 47%) contents and lower effective porosity (<2%). Rock type 2 has relatively higher quartz (43% - 48%), moderate carbonate (20% - 45%) and clay (6% - 18%) contents and higher effective porosity (4% - 7%). Rock type 3 has relatively higher percentage of carbonates (61% - 85%), lower clay (<11%) and quartz (8% - 30%) contents and moderate effective porosity (2% - 4%). In terms of reservoir quality, rock type 1 is the worst reservoir rock and rock type 2 is the best reservoir rocks with high storage capacity and brittleness.

Mississippian strata of the Anadarko Basin in Kingfisher and Canadian counties consist of 1 low-order stratigraphic unit with overall upward-deepening profile. The intermediate order correlates to multiple depositional episodes consisting of lowstand-, transgressive-, and highstand systems tract. Clay-rich rock type 1 typically increases during late highstand systems tract and lowstand system tract and quartz-rich rock type 2 typically increases during transgressive systems tract and early highstand systems tract. Higher order cycle exhibits an ideal upward-shallowing succession within parasequences that consists of bioturbated siltstone, laminated-siltstone, structureless siltstone, and cross-laminated siltstone. Proximally, individual cycles are often capped by skeletal wackestone-packstone. A sequence

boundary is characterized by a subaerial exposure with brecciated chert or an erosional surface; and glauconitic siltstone-sandstone is typically present atop of this boundary. The threefold (low, intermediate, and high) stratigraphic orders combined with a dip-oriented 3D model indicate that the reservoir sweet spots containing higher percentage of quartz-rich rock type 2 occur during deepening in the transgressive and highstand systems tract (parasequence Miss 9 to Miss 12). These stratigraphic orders provide a predictive framework that aids in reservoir characterization for optimal development of the Mississippian reservoirs.

INTRODUCTION

The Anadarko Basin is one of the earliest basins in Oklahoma to start being explored in the early 1900s. The basin is approximately 70,000 mi² (~180,000 km²) in size (Figure 3.1) and has production comes from Cambro-Ordovician through Permian-aged strata. One of the important hydrocarbon reservoirs in this basin is the Mississippian strata. The Mississippian strata contains unconventional reservoirs. Unconventional reservoirs, collectively known as the Mississippian Limestones or “Chat”, are primarily porous weathered limestone and chert associated with the Mississippian-Pennsylvanian unconformity (Rogers, 2001). These reservoirs are located mainly across the Anadarko shelf. Other unconventional reservoirs within the Mississippian strata of the Anadarko Basin produce hydrocarbon from a fine-grained mixed siliciclastic-carbonate system composed of quartz siltstone and sandstone with varying amount of carbonate grains and clay. These mixed system reservoirs are known as the core of the Sooner Trend in the Anadarko [Basin] in Canadian and Kingfisher counties (STACK) play (Figure 3.1). In the play area, reservoir distribution and quality are poorly understood. Several recent studies of the Mississippian strata in the Anadarko Basin have focused on regional stratigraphy and organic richness (Miller, 2018) control of depositional environment and sequence stratigraphy on

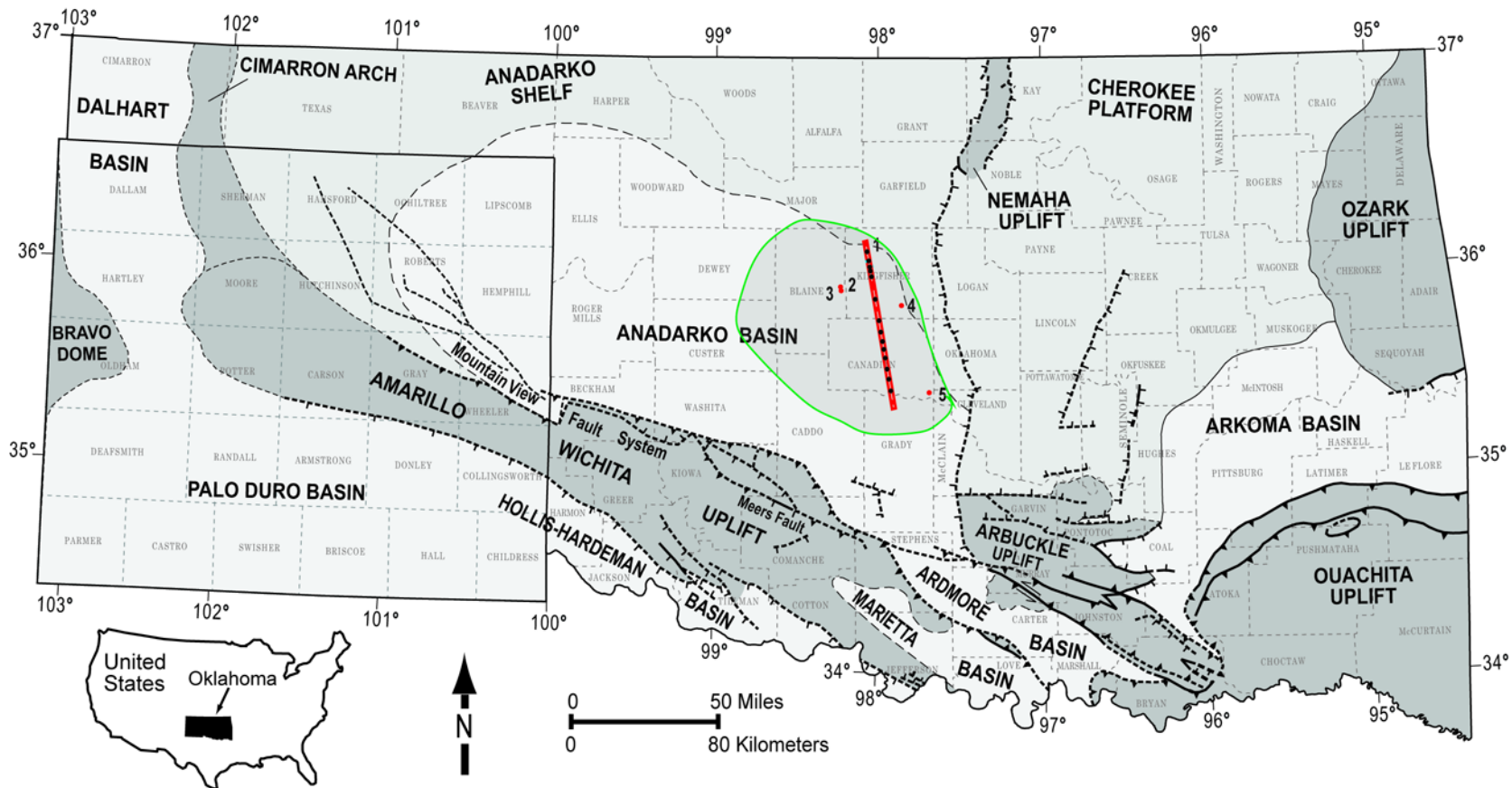


Figure 3.1. Regional base map showing the major tectonic and basinal features of Oklahoma and Texas Panhandle (modified after Dutton, 1984; Campbell et al., 1988; McConnell et al., 1989; Northcutt and Campbell, 1995; Johnson and Luza, 2008; LoCricchio, 2012). Cored well were located on the Anadarko Basin: Humble Oil & Refining Company 1 Van Horn Unit (1), Gulf Oil Corporation 1 Musselman (2), Gulf Oil Corporation 1-23 Shaffer (3), Humble Oil & Refining Company 1 Lloyd L Hawkins (4), and Petrolia Drilling Corporation 1 Payne (5) (labelled as red dots). STACK Play area is annotated as green polygon. The modeling study area is annotated as red polygon.

reservoir quality and reservoir distribution (Price et al., 2020); control of stratigraphy on fracture growth and completion optimization (Price et al., 2017); diagenesis of Mississippian strata of the southern Mid-Continent (Dehcheshmehi, 2016; Hardwick, 2018); lithology variation and vertical reservoir segregation (Drummond, 2018; Hickman, 2018; Miller 2019); understanding of the regional distribution of fluid composition and properties (Welker et al., 2016); characterizing and modeling the reservoirs (Shelley et al., 2017; Hickman, 2018; Miller, 2019), and reservoir quality of the Mississippian strata in the Anadarko Basin (Hardwick, 2018; Drummond, 2018; Hickman, 2018; Miller 2019).

Petrophysical properties, mineral-based rock-typing, and their distribution within a sequence-stratigraphic framework are addressed in this study. The study is based on X-Ray Diffraction (XRD), laboratory-measured core porosity data, well-log data for 19 wells, log-derived effective porosity, log-derived water saturation, and log-derived mineralogy.

In conventional reservoirs, rock typing typically can be achieved through the use of cross-plots of core-derived porosity-permeability or well-log derived porosity-permeability values. In unconventional reservoirs (e.g. tight sandstone reservoirs), this rock-typing method is generally insufficient (e.g., Rushing, 2008). Therefore, other petrophysical properties such as Total Organic Content (TOC), Mercury Injection Capillary Pressure (MICP), and mineralogy are integrated for rock-typing in unconventional reservoirs such as the Barnett, Eagle Ford, Wolfcamp, and Woodford shales (e.g., Kale et al., 2010; Gupta, 2017).

In this study, log-derived effective porosity and mineral volumes (carbonate, quartz, and clay) were trained as inputs for rock typing. Rock-typing was performed using K-Means clustering method. Then, Random Forests was used to predict rock types for wells with no mineral volume data. These rock types and their petrophysical properties were mapped into a dip-oriented cross-sectional model using Sequential Indicator Simulation (SIS) and Sequential Gaussian Simulation (SGS), respectively. Their

distributions within a sequence-stratigraphic framework illustrate the spatial variability of “sweet-spots” in the Mississippian mixed siliciclastic-carbonate system of the eastern Anadarko Basin.

GEOLOGICAL SETTING

The Anadarko Basin was a relatively stable basin until the deposition of the Hunton dolomite in early Devonian. At the end of early Devonian, the Hunton dolomite was eroded into canyons wherein the Late Devonian Woodford Shale was deposited (Harris, 1975; Rottmann, 2018). The Devonian Woodford Shale was overlain by the Mississippian Kinderhook Shale either conformably (Harris, 1975) or unconformably (Curtis and Champlin, 1959; Rowland, 1961) depending on the location. Due to compaction, these shales formed drape folds that controlled the deposition of younger Mississippian strata such as Osagean, Meramecian, and Chesterian rocks (ascending order). These younger Mississippian strata were deposits in a failed rift known as the Oklahoma aulacogen (Keller, 2014). The generalized stratigraphic column of the Anadarko Basin is shown in Figure 3.2.

The Osagean rocks are mainly carbonate (Curtis and Champlin, 1959; Harris, 1975; Boyd, 2008). These carbonate rocks are typically brown, dolomitic, fine crystalline limestone to off white limestone and interbedded brownish gray, finely crystalline, cherty limestone; however, some facies variations occur as chert, shale, siltstone, and sandstone.

The contact between Osagean-Meramecian deposits is unconformable (Rowland, 1961); yet it is challenging to determine using cores due to similarity in their lithology.

The Meramecian deposits comprise light to dark, coarse to fine-crystalline limestone with the presence of oolite, dolomite, and chert (Ulrich, 1904; Clair, 1949; McDuffie, 1959). Even though the Meramecian deposits have long been attributed as carbonate rocks (Ulrich, 1904; Clair, 1948; McDuffie, 1959; Curtis and Champlin, 1959; Harris, 1975; Boyd, 2008), recent investigations suggested Meramecian deposits of

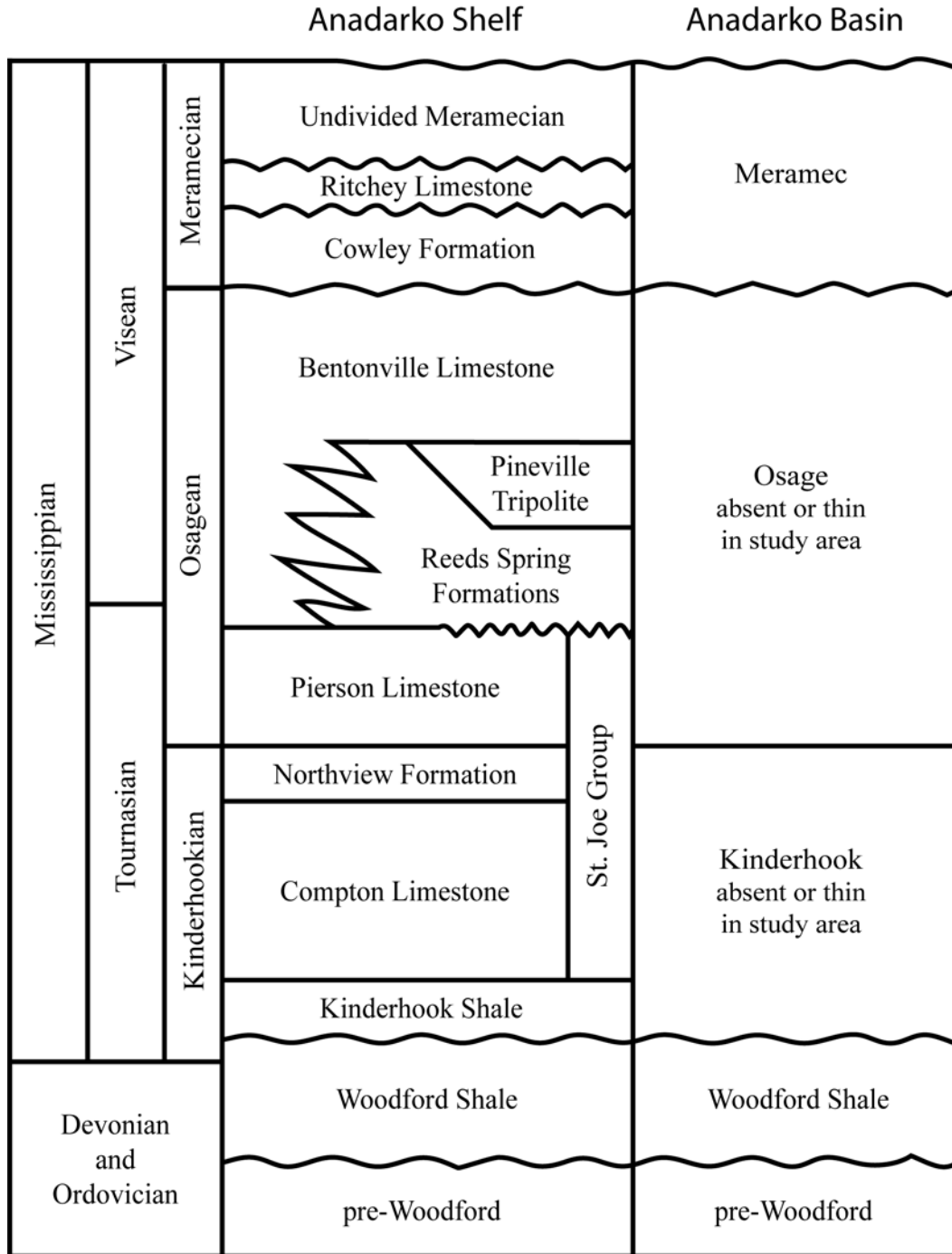


Figure 3.2. Generalized stratigraphic summary of Mississippian strata in the Anadarko Shelf and Anadarko Basin at the north and central Oklahoma (Modified after [Mazzullo, 2011](#); [Mazzullo et al., 2011](#); [Mazzullo et al., 2016](#); [Stukey et al., 2018](#)).

the Anadarko Basin in central Oklahoma primarily represent a siliciclastic system consisting of argillaceous to calcareous siltstones or very fine sandstones or a mixed siliciclastic-carbonate system (e.g., [Price et al., 2017](#); [Miller, 2018](#)). The Meramecian deposits are overlain by Chesterian rocks unconformably that comprise oolitic to fossiliferous limestone in northern Oklahoma to interbedded sandstone, shale, and fossiliferous fragmental limestones in southern Oklahoma ([Curtis and Champlin, 1959](#)).

Due to unsolved age and boundary among Kinderhookian, Osagean, Meramecian, and Chesterian series in subsurface, this study does not subdivide the Mississippian strata into the different series.

The Mississippian strata in the Anadarko Basin contain an unconventional play that has thickness range from 0 – 190 m (0 – 630 ft.) and reservoir depth range from 1,700 m – 4,500 m (~5,500 ft. – 15,000 ft.). Several studies (e.g. [Drummond, 2018](#); [Hickman, 2018](#), [Miller, 2019](#) and [Price et al., 2020](#)) documented prograding parasequences striking along northeast-southwest and prograding to the southeast. Their work also showed a shallowing-upward sequence from argillaceous and quartz siltstone into calcareous siltstone and sandstone.

The depositional environment of Mississippian strata in the Anadarko Basin remains a geological mystery. Studies on potential age-equivalent Mississippian strata to the north in the “Anadarko Shelf” area indicate deposition on a carbonate ramp with a very low gradient ([Rogers, 2001](#); [Watney et al., 2001](#); [Mazzullo et al., 2011](#); [Leblanc, 2014](#); [Birch, 2015](#); [Childress and Grammer, 2015](#); [Vanden Berg and Grammer, 2016](#); [Suriamin and Pranter, 2018](#)). The depositional environment has been interpreted to change to the south to a subaqueous delta complex fed by fine-grained fluvial input ([Price et al., 2017](#); [Price et al., 2020](#)). [Suriamin et al. \(in prep\)](#) showed that the Mississippian strata represent wave-dominated nearshore, restricted embayment (lagoon), and channel or lobe deposits. Other work suggests

the Mississippian strata were deposited via storm or turbidite flows transporting eolian-sourced silt and detrital carbonates (Leavitt, 2018).

DATA AND METHODOLOGY

This study integrates X-Ray Diffraction (XRD), laboratory-measured core porosity, and well-log data for solving mineral composition and calculating porosity and water saturation. The data for each well is shown in Table 3.1.

Mineral Volume Calculation

Mineral volume, particularly the amount of calcite cement, in the Mississippian strata of the Anadarko Basin plays an important role in controlling reservoir quality (Price et al., 2020). In general, the volume of calcite exhibits a strong negative correlation with porosity. Therefore, it is useful to estimate volume of minerals in the Mississippian strata. As XRD mineral volume data are limited, well logs were used to estimate the volume of carbonate, quartz, and clay minerals. The volume of minerals was calculated using a matrix algebra inversion method (Doveton, 1994). The method involves a linear equations system that relates log parameters of known minerals, unknown volume of minerals, and well-log measurements. Furthermore, it can be expressed as (Doveton, 1994):

$$C V = L$$

where C is a matrix of log parameters of known minerals, V is a vector of the unknown minerals volume, and L is a vector of well-log measurements. Defined in this manner, the solution for the unknown minerals volume vector, V, is rewritten as:

$$V = C^{-1} L$$

where C^{-1} is the inverse of the C matrix. For example, in an extended way, integrating the litho-density logging suite and log response parameter for known minerals, the equation can be written as:

Table 3.1. Summary of available well data.

Well Name	Core	XRD	GR	RES	RHOB	NPHI	PE
Humble Oil And Refining Company 1 Lloyd L Hawkins	X	X	X	X	X		
Gulf Oil Exploration And Production Company 1-14 Musselman	X	X	X	X	X	X	
Petrolia Drilling Corporation 1 Payne	X	X	X	X	X	X	
Gulf Oil Exploration And Production Company 1-23 Shaffer	X	X	X	X	X	X	X
Humble Oil And Refining Company 1 Van Horn Unit	X	X	X				
Andover Oil Company 7-3 Adams Park			X	X	X	X	
Brg Petroleum Llc 1-3 Benson			X	X	X	X	X
Pan American 1 Effie B York			X	X		X	
Kaiser Francis Oil Company 1 Estes			X	X	X	X	X
L G Williams Oil Company 29-1 Girard			X	X	X	X	
Western Oil And Gas Corp. 2-14 Guth			X	X	X	X	X
Magic Circle Energy Corporation 2 Kunneman			X	X	X	X	X
Texas Oil And Gas Corporation 1 Matthies C			X	X	X	X	
The Rodman Corporation 1 Maxwell 4			X	X	X		
Mack Oil Company 3 Merveldt			X	X	X	X	
Ofs-Tulsa Corp 4-31 Moshe			X	X	X	X	
Bristol Resources Corporation 9-1A Siegrist			X	X	X	X	
Kaiser Francis Oil Company 1 State Of Oklahoma			X	X	X	X	
Range Production Company 1-5 Unity			X	X	X	X	

$$\begin{bmatrix} Vol_{carb} \\ Vol_{qtz} \\ Vol_{clay} \\ \phi_{tot} \end{bmatrix} = \begin{bmatrix} \alpha_{1,1} & \alpha_{1,2} & \alpha_{1,3} & \alpha_{1,4} \\ \alpha_{2,1} & \alpha_{2,2} & \alpha_{2,3} & \alpha_{2,4} \\ \alpha_{3,1} & \alpha_{3,2} & \alpha_{3,3} & \alpha_{3,4} \\ \alpha_{4,1} & \alpha_{4,2} & \alpha_{4,3} & \alpha_{4,4} \end{bmatrix}^{-1} \begin{bmatrix} \rho_{log} \\ \phi_{Neu,log} \\ Pe_{log} \\ 1 \end{bmatrix}$$

where $\alpha_{i,j}$ is log response parameter for known minerals.

A litho-density logging suite consisting of bulk density, neutron porosity, and photoelectric effect (PE) logs was sufficient to solve 4 unknown components of quartz, carbonate, clays, and total porosity. The photoelectric effect log is an important log as it has very definitive matrix values for determining minerals.

The challenge of the procedure is determining an accurate log-response parameter for known minerals. Standard log-response parameters (e.g., photoelectric effect of quartz is 1.8 barns/electron, neutron porosity for quartz is -2 p.u., bulk density of quartz is 2.64 g/cm³) might be inaccurate to use because the reservoirs contain other impurity minerals such as opal, Fe-calcite, Fe-dolomite, siderite, and several types of clay which affect the standard log-response values. Therefore, an optimization tool (solver in Excel), was used to find optimum values for the log-response parameters. The optimum values are typically achieved when the total least square difference of log-derived mineral volume and XRD mineral volumes is set to minimum.

Result of the matrix algebra inversion method provided equations to calculate mineral volumes (in v/v) as follow:

$$Vol_{carb} = (-1.27 * \rho_{bulk}) + (-1.20 * \phi_{Neu}) + (0.62 * P_e) + (1.85)$$

$$Vol_{qtz} = (0.23 * \rho_{bulk}) + (-1.29 * \phi_{Neu}) + (-0.52 * P_e) + (1.58)$$

$$Vol_{clay} = (1.89 * \rho_{bulk}) + (2.76 * \phi_{Neu}) + (-0.15 * P_e) + (-4.50)$$

Petrophysical Properties Calculation.

In these unconventional reservoirs, the total porosity was solved simultaneously using the matrix algebra inversion method. The equation for calculating total porosity was:

$$\phi_{tot} = (-0.84 * \rho_{bulk}) + (-0.27 * \phi_{Neu}) + (0.06 * P_e) + (2.05)$$

In wells that have no photoelectric effect log, the total porosity was calculated as the root mean square (RMS) of the neutron porosity and density porosity logs:

$$\phi_{tot} = \sqrt{\frac{DPHI^2 + NPFI^2}{2}}$$

The density porosity (DPHI) was calculated using bulk density and associated matrix density value as:

$$DPHI = \frac{\rho_{ma} - \rho_{bulk}}{\rho_{ma} - 1}$$

The effective porosity was calculated by excluding pore volumes occupied by water adsorbed in clay. The equation is expressed as:

$$\phi_{eff} = \phi_{tot} - (Vol_{clay} * \phi_{wet\ clay})$$

where Vol_{clay} is volume of clay derived from matrix algebra inversion method and $\phi_{wet\ clay}$ is porosity of wet clay determined using a bulk density and neutron porosity crossplot. In wells where mineral volumes were not available, volume of clay was calculated as 0.6 * volume of shale (Bhuyan and Passey, 1994), which was derived based on gamma-ray log response as:

$$Vol_{shale} = \frac{GR - GR_{min}}{GR_{max} - GR_{min}}$$

Water saturation (S_w) was calculated using the Archie equation as:

$$S_w^n = \frac{a R_w}{\phi^m R_t}$$

where the saturation exponent (n) = 2, true resistivity (R_t) is deep resistivity log, m is the cementation exponent (m), and R_w is resistivity of formation water. In Oklahoma, Puzin (1951) suggested 1.8 as the cementation exponent (m) and resistivity of formation water (R_w) in the Mississippian strata is 0.05 ohm-m.

Sequence Stratigraphy

The stratigraphy of the Mississippian was developed using well logs including gamma-ray, resistivity, bulk density, and neutron porosity (when available) and core-based lithofacies. Tops, represent flooding surfaces of parasequence, were interpreted in 19 wells to correlate the Mississippian strata. In this setting, the parasequences are commonly recognized as coarsening-upward motifs on the gamma-ray logs; and the flooding surfaces are recognized as abrupt increases in shale content that correlates to high gamma-ray values.

Rock Typing

Rock typing involves several steps: 1) calculating mineral volumes of 5 wells that have litho-density logs using matrix algebra inversion method; 2) clustering the mineral volumes using K-Means algorithm to form different rock types; 3) correlating the rock types with commonly available well logs (gamma-ray, neutron porosity, and bulk density, but no photoelectric effect log) using a machine learning technique called Random Forests; 4) predicting rock types for wells with the commonly available well logs using Random Forests. The rock-typing procedure was executed in R, an open-source data science software.

K-means Clustering Method

K-Means ([Macqueen, 1967](#)) is one of the simplest unsupervised learning methods to solve clustering problems. The method typically comprises four steps. 1) determine number of clusters (K). The optimum number of clusters was defined based on the elbow method that illustrates crossplot of inter-cluster variance (Sum of Square Between (SSB)) and intra-cluster variance (Sum of Square Within) with number of clusters. The optimum number of clusters is commonly associated to a point when the SSB and SSW start to flatten or the SSB line intersects with the SSW line. 2) assign data points to the nearest centroid. 3) re-calculate the mean of each cluster and assign the result as a new centroid. 4) repeat second and third steps until the centroids no longer move.

A dataset consisting mineral volumes and effective porosity from 5 wells that have photoelectric effect logs was used as input in the K-means clustering method. The wells are Gulf Oil Exploration and Production Company 1-23 Shaffer, BRG Petroleum LLC 1-3 Benson, Kaiser Francis Oil Company 1 Estes, Western Oil and Gas Corporation 1 Guth, and Magic Circle Energy Corporation 1 Matthies C. The clustering result, representing rock types, was investigated for its properties. The clustering result was also utilized for Random Forests classification.

Random Forests Classification

Random Forests are a combination of tree predictor such that each tree depends on the values of a random vector sampled independently and with the same distribution for all trees in the forests ([Breiman, 2001](#)). This supervised classification algorithm creates a set of rules based on a training dataset with features and targets as trees in a forest. These rules are used to predict a target based on test dataset features. The Random Forests classification schematic is shown in [Figure 3.3](#).

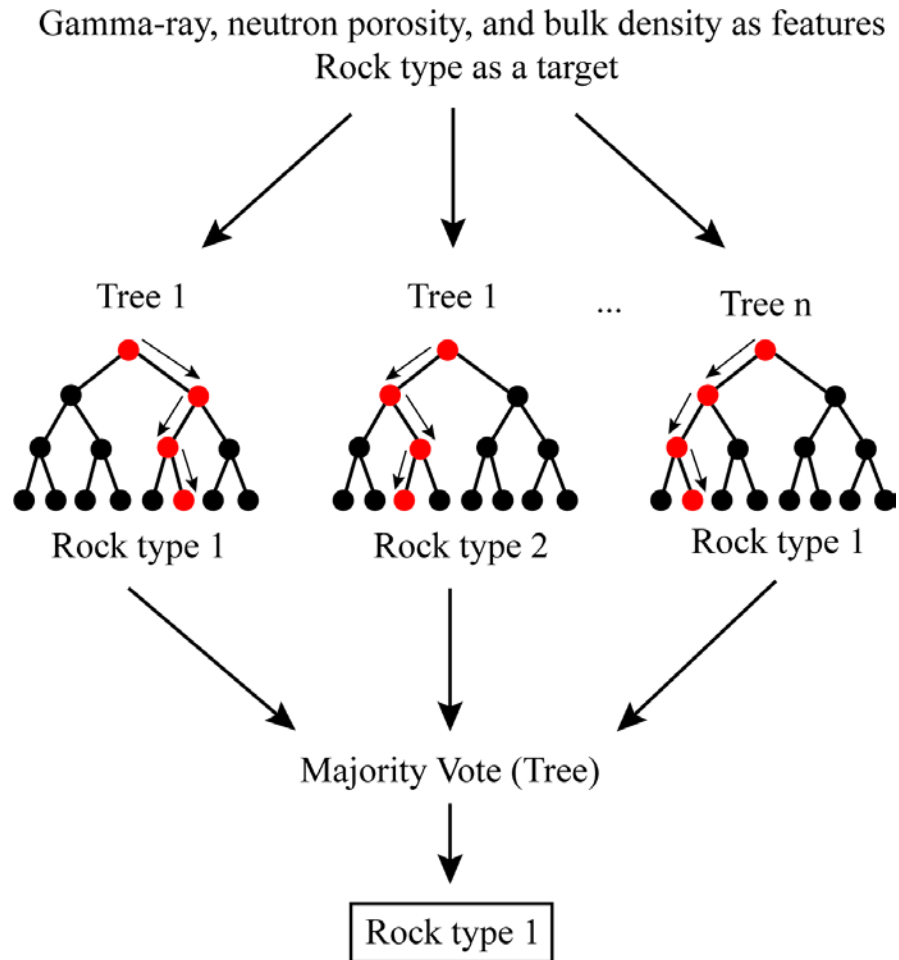
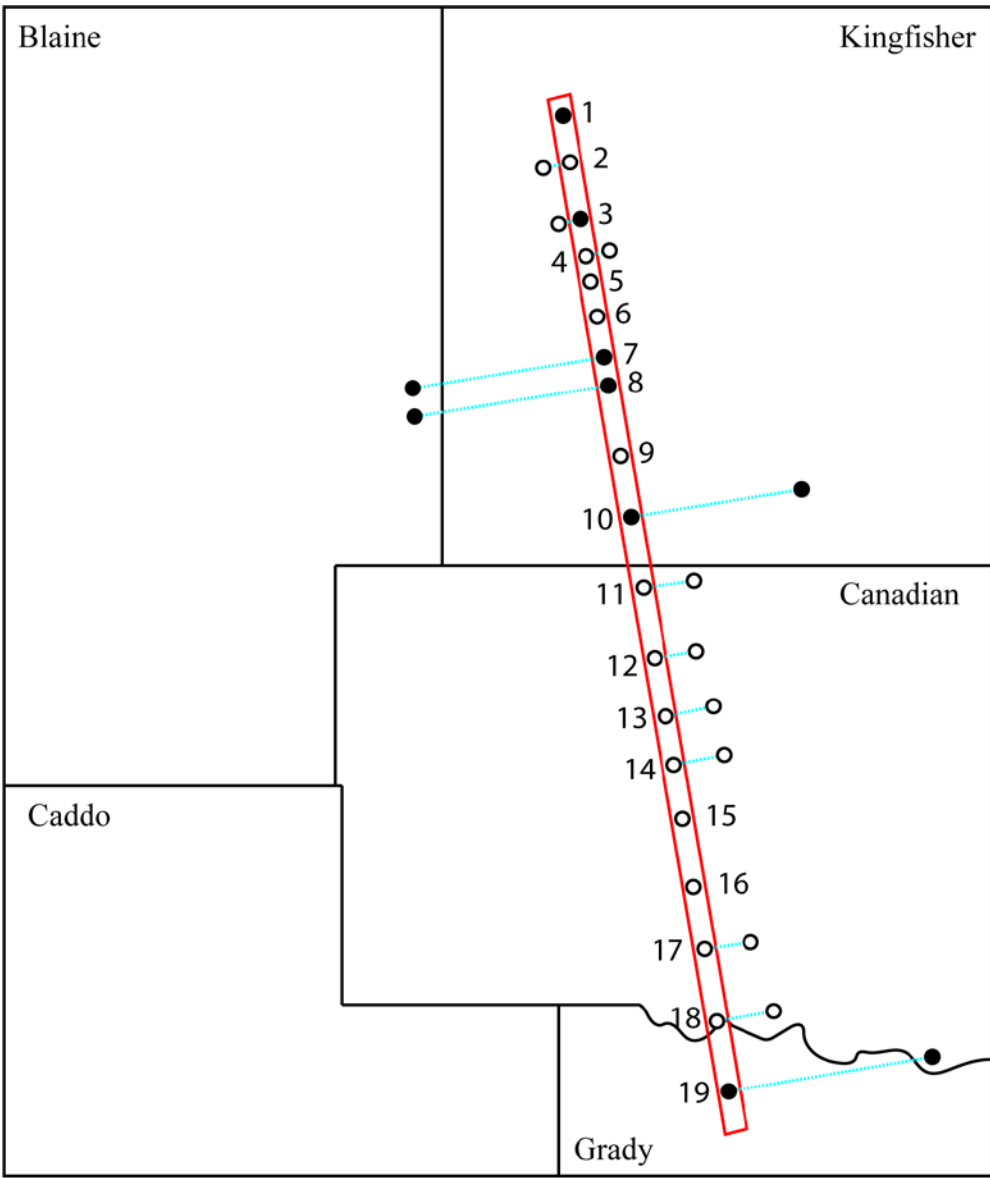


Figure 3.3. Random Forests classification schematic. This supervised classification algorithm creates a model based on a training dataset with features (gamma-ray, neutron porosity, and bulk density) and targets (rock types). The model is applied to another dataset where Random Forests will create an n number of decision trees that evaluate the data and predict a rock type based on the input data. The rock type outcomes from all of the decision trees are then counted to determine majority votes. The majority vote is used as the final rock type for that data point.

For this purpose, a dataset consisting of prevalent well logs such as gamma-ray, neutron porosity, and bulk density (as features) and K-means-based clusters (as targets) was used to build a Random Forests model. The dataset was divided into two data sets, a training set and a testing set. The training comprised of 70% of the dataset (N = 3209) and the testing set comprised of 30% (N = 1363) of the dataset. Once the model was built based on the training set, it was applied to the testing set. Performance and accuracy of a model was measured based on a confusion matrix which compares the actual rock type of testing set and its predicted rock type. The final Random Forests model was then applied to predict rock type (cluster) in wells that have no mineral volumes data (i.e. wells without photoelectric effect logs).

Reservoir Modeling

The sequence stratigraphy, mineral-based rock types, and calculated petrophysical properties were integrated to build a dip-oriented, proximal to distal cross-sectional reservoir model from northwestern Kingfisher County to southeastern Canadian County to evaluate the spatial variability of these properties. The model was constrained to 5 cored and 14 non-cored wells. Cored wells including the Humble Oil & Refining Company 1 Van Horn Unit, Gulf Oil Corporation 1 Musselman, Gulf Oil Corporation 1-23 Shaffer, Humble Oil & Refining Company 1 Lloyd L Hawkins, and Petrolia Drilling Corporation 1 Payne wells (Figure 3.1). The 19 wells were projected into the model cross section (Figure 3.4). The model cross section was flattened to eliminate the effect of structural displacement, so that the well positions represent the proximal to the distal area. Surfaces and isochore maps for Woodford Shale and Mississippian parasequences were created to represent horizons and model zones. Each zone is further subdivided with proportional layering or an onlapping scheme to achieve an average layer thickness of 2 ft (0.61 m).



- Wells with LAS files
- Cored wells with LAS files
- Study Area
- County Lines
- Projection Lines

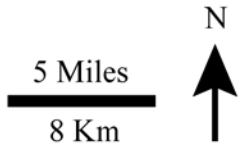


Figure 3.4. A basemap showing the location of 19 wells used in a 3D modeling area (red polygon). Note all of the wells outside the red polygon were perpendicularly projected into the center of modeling area. The wells are 1). Humble Oil and Refining Company 1 Van Horn Unit. 2). Pan American 1 Effie B York. 3). OFS-Tulsa Corp 4-31 Moshe. 4). The Rodman Corporation 1 Maxwell 4. 5). Kaiser Francis Oil Company 1 State of Oklahoma. 6). Magic Circle Energy Corporation 2 Kunneman. 7). Gulf Oil Exploration and Production Company 1-14 Musselman. 8). Gulf Oil Exploration and Production Company 1-23 Shaffer. 9). BRG Petroleum LLC 1-3 Benson. 10). Humble Oil and Refining Company 1 Lloyd L Hawkins. 11). Range Production Company 1-5 Unity. 12). L G Williams Oil Company 29-1 Girard. 13). Bristol Resources Corporation 9-1A Siegrist. 14). Mack Oil Company 3 Merveldt. 15). Andover Oil Company 7-3 Adams Park. 16). Texas Oil and Gas Corporation 1 Matthies C. 17). Western Oil and Gas Corp. 2-14 Guth. 18). Kaiser Francis Oil Company 1 Estes. 19). Petrolia Drilling Corporation 1 Payne.

Rock-type logs were upscaled to the model cells in which the most abundant rock types within each cell were assigned to that cell. Sequential-indicator simulation (SIS) was used to model the rock types. Effective porosity and effective water saturation logs were upscaled to the model cell using an arithmetic average method. The logs were also biased to the upscaled rock-type logs. The upscaled effective porosity and effective water saturation logs were modeled using Sequential-Gaussian Simulation (SGS).

RESULTS

Mineral Volumes

When coded and executed as a simple computer program in the Excel, transforming well-logs to mineral volumes was straightforward. A coefficient matrix of the log response parameter for quartz, carbonate, and clay minerals was compiled and inverted. The mineral volumes of any sampling depth were calculated by multiplying the log readings at a depth with the inverse matrix. The result of the matrix algebra inversion processing of the Mississippian strata in the Gulf Oil Corporation 1-23 Shaffer well is shown in [Figure 3.5](#). The mineral volumes result was calibrated using XRD mineral data (shown in tracks 7 through 9 of [Figures 3.5 and 3.6](#)). The comparison of log-based calculated mineral volumes with XRD mineral data has R-squared values range from 0.66 to 0.76 suggesting the model has relatively good predictive accuracy ([Figure 3.6](#)). After more representative mineral volumes were achieved, the coefficient matrix was used to calculate mineral volumes in other wells that have a litho-density logging suite.

GULF OIL CORPORATION 1-23 SHAFFER API 35011215220000

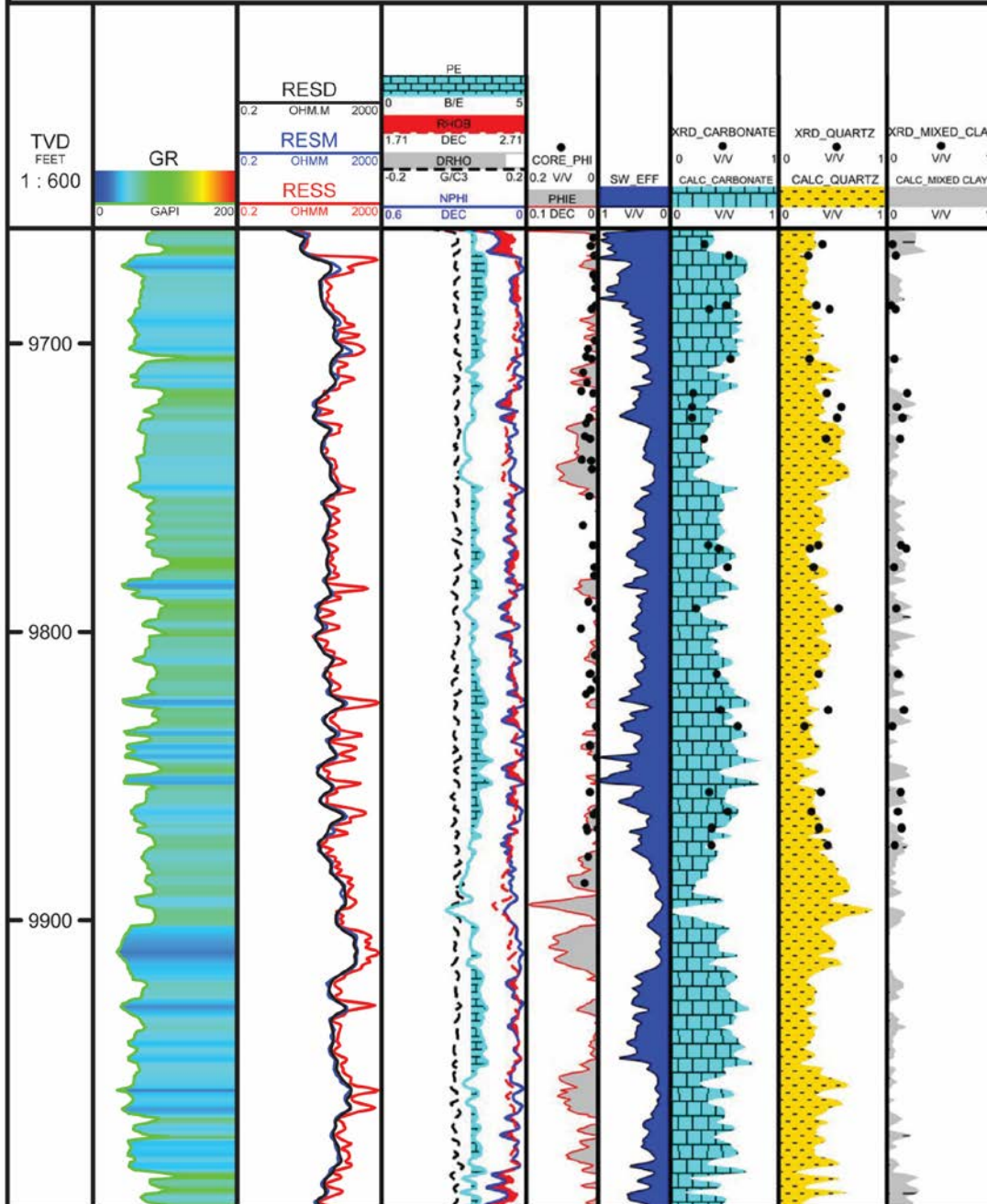


Figure 3.5. Well-log data of Gulf Oil Exploration and Production Company 1-23 Shaffer. Track 7 – 9 show the result of dominant mineral volumes using a matrix algebra inversion method. Track 7 is the calculated volume of carbonate minerals compared with volume of carbonate measured using X-Ray Diffraction method (black dot). Track 8 is the calculated volume of quartz mineral compared with volume of quartz measured using X-Ray Diffraction method (black dot). Track 9 is the calculated volume of clay minerals compared with volume of clay minerals measured using X-Ray Diffraction method (black dot). (TVD= True Vertical Depth, GR = Gamma-Ray, RESS = shallow depth resistivity, RESM= intermediate depth resistivity, RESD = true deep resistivity, PE = photoelectric effect, RHOB = bulk density, DRHO = bulk density correction, NPHI = neutron porosity, PHIE = log-based effective porosity, Core PHIE = effective porosity measured from core plugs, SW EFF = log-based effective water saturation, CALC CARBONATE = calculated volume of carbonate minerals, XRD CARBONATE = volume of carbonate minerals measured using XRD, CALC QUARTZ = calculated volume of quartz minerals, XRD QUARTZ = volume of quartz mineral measured using XRD, CALC CLAY = calculated volume of clay minerals, XRD CLAYS = volume of clay minerals measured using XRD).

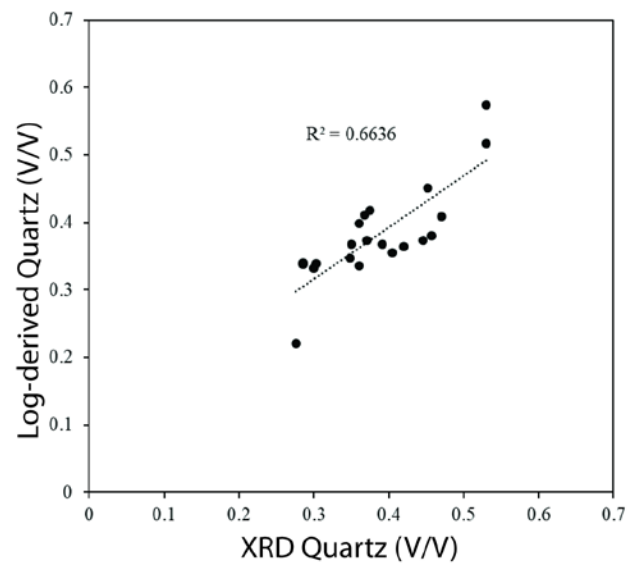
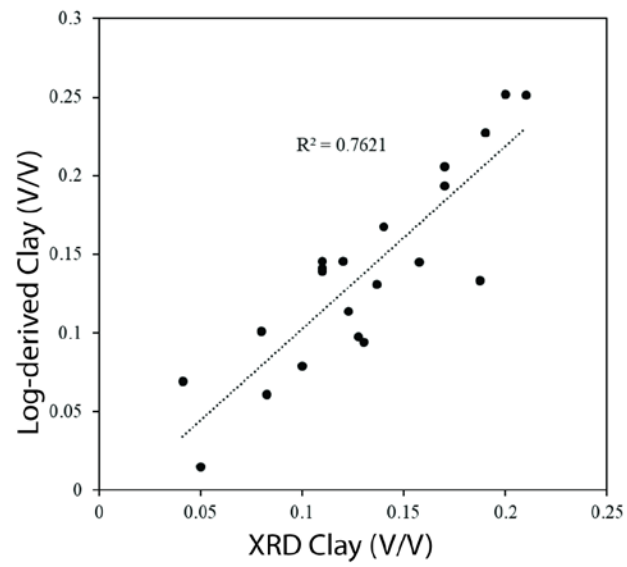
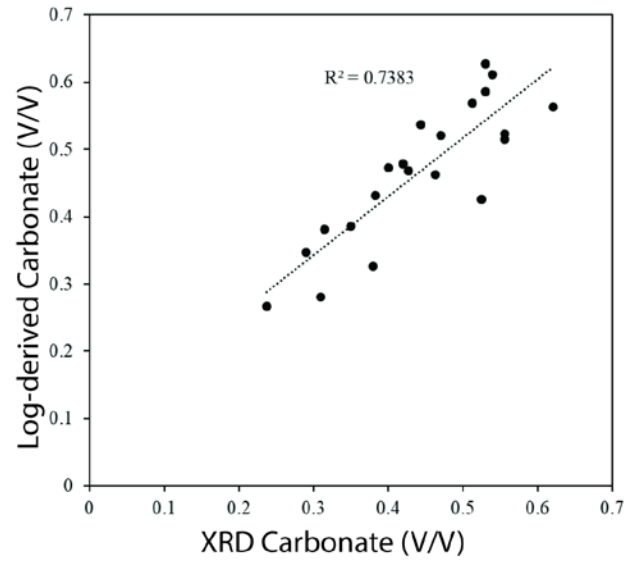


Figure 3.6. Comparison of mineral volumes obtained from XRD measurement and log-derived using matrix algebra inversion method in the Gulf Oil Exploration and Production Company 1-23 Shaffer well. a). Comparison of carbonate mineral volume obtained from XRD measurement and log-derived. b). Comparison of clay mineral volume obtained by XRD measurement and log-derived. c) Comparison of quartz mineral volume obtained from XRD measurement and log-derived. Note all three comparisons showing R^2 values of ~ 0.7 suggesting a relatively good predictive accuracy.

Mineral-based Rock Types.

The Mississippian strata consists of three rock types with varying mineral volumes that were defined using K-means clustering for the Gulf Oil Exploration and Production Company 1-23 Shaffer, BRG Petroleum LLC 1-3 Benson, Kaiser Francis Oil Company 1 Estes, Western Oil and Gas Corporation 1 Guth, and Magic Circle Energy Corporation 1 Matthies C. The optimum number of rock types was defined to be three based on the elbow method (Figure 3.7). The elbow method shows that the Sum of Square Between beyond 3 clusters has relatively lower variance between clusters and could result in difficulty to differentiate one cluster from another. However, when the data are classified into 3 clusters, each cluster represents an independent rock type that has unique mineral volumes and effective porosity (Figure 3.8).

Cluster 1, assigned as rock type 1, has a relatively moderate amount of clay (22% - 39%), quartz (26% - 43%), and carbonate (25% - 47%) with relatively lower effective porosity values (<2%). Cluster 2, assigned as rock type 2, is composed of relatively higher quartz (43% - 58%), and moderate carbonate (20% - 45%) and clay (6% - 18%) content with relatively higher effective porosity values (4% - 7%). Cluster 3, assigned as rock type 3, contains relatively higher carbonate content (61% - 85%), lower quartz (8% - 30%) and clay (<11%) content with relatively moderate effective porosity values (2% - 4%).

Extending Mineral-based Rock Types to Well Logs.

In the study area, gamma-ray, neutron porosity, and bulk density are the most common logs in most wells. Thus, these 3 logs were used for predicting rock types in 10 wells that lack the photoelectric effect log (or no mineral volumes data). The prediction utilized the supervised Random Forests classification method. The method resulted in up to ~80% overall accuracy. Based on the important

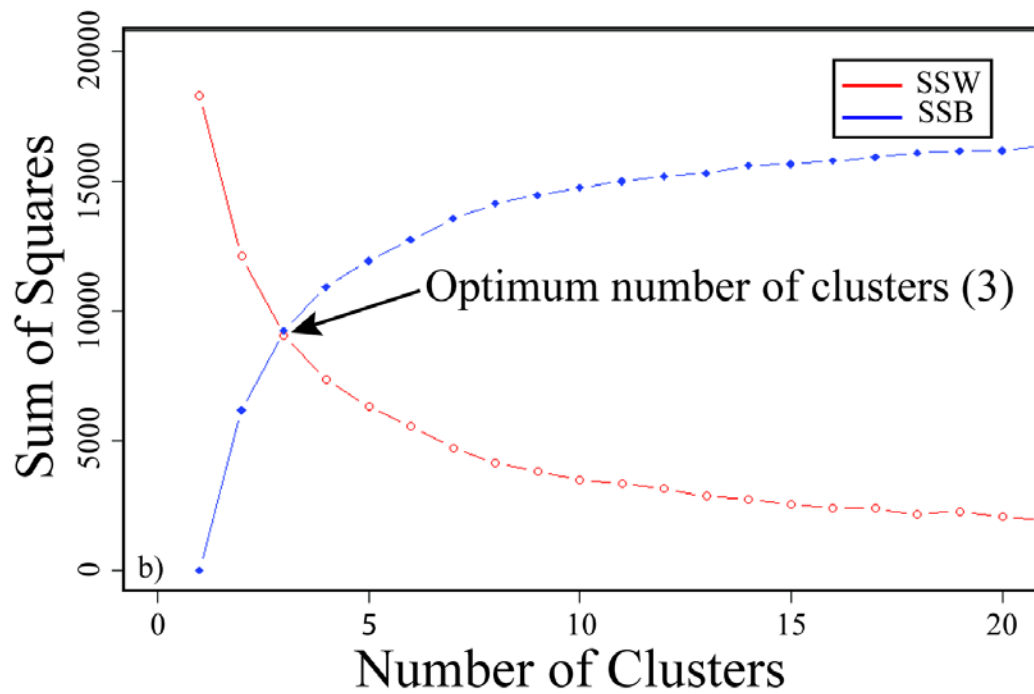


Figure 3.7. An elbow method showing the optimum clusters of 3 at a point where the sum of square between (SSB - blue line) intersect with the sum of square within (SSW - red line). SSW refers to the variance between data points in the same cluster and SSB line refers to the variance between data points of different clusters.

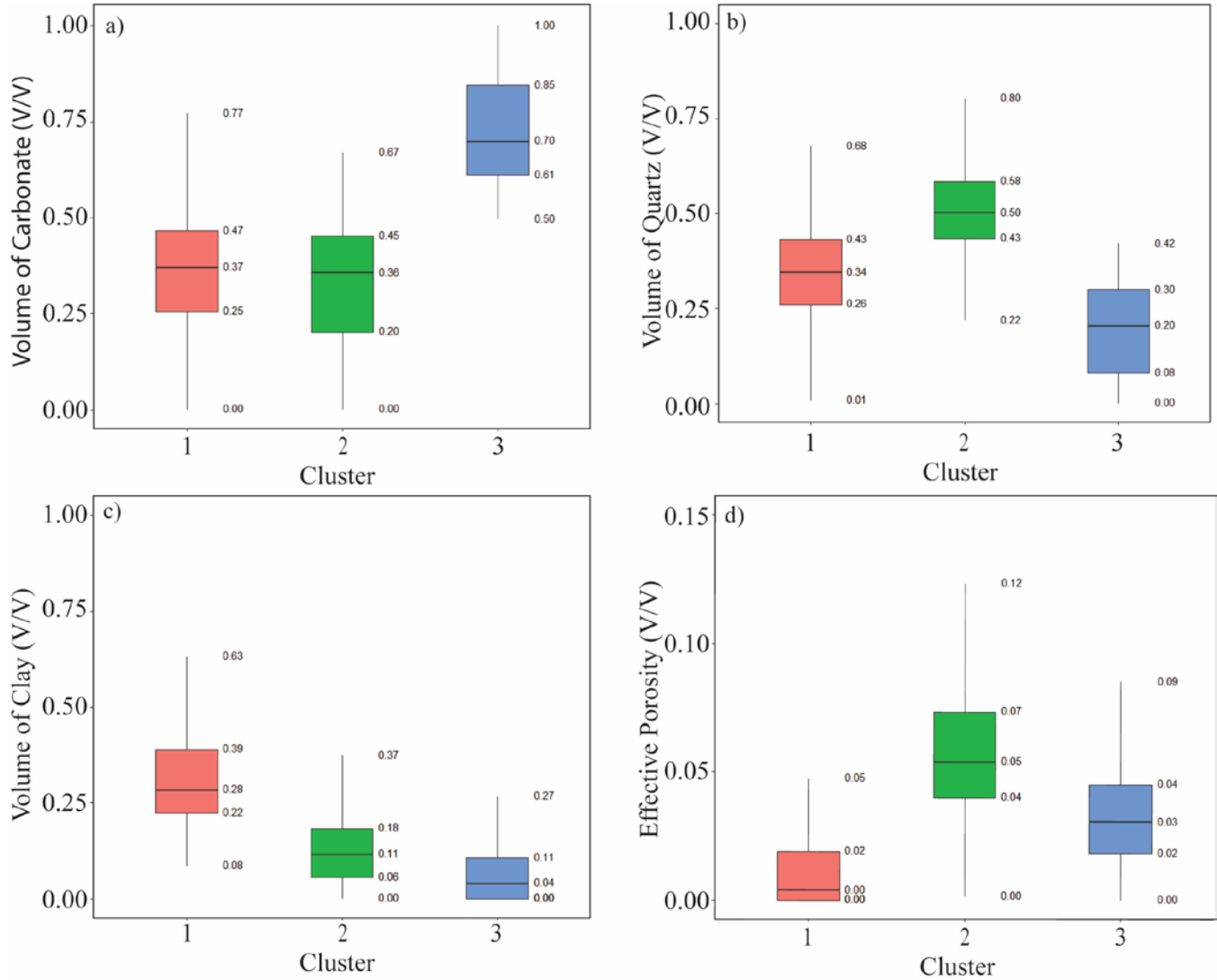


Figure 3.8. Boxplots showing the result summary of K-means clustering based on mineral volumes and effective porosity as the input. a). A boxplot showing statistical measures of volume carbonate minerals for 3 clusters. b). A boxplot showing statistical measures of volume of quartz mineral for 3 clusters. c). A boxplot showing statistical measures of volume of clays minerals for 3 clusters. d). A boxplot showing statistical measures of effective porosity for 3 clusters. Each cluster represent 1 rock type. Noted that rock type 1 has relatively moderate clays, quartz, carbonates contents, and lower effective porosity (<2 %). Rock type 2 has relatively higher quartz, moderate carbonates and clays contents, and higher effective porosity (4% – 7%). Rock type 3 has relatively higher percentage of carbonates, lower clays and quartz contents, and moderate effective porosity (2% – 4%). In terms of reservoir quality, rock type 1 is the worst reservoir rocks and rock type 2 is the best reservoir rocks with high storage capacity and brittleness.

variable analysis, the bulk density is the most important input to predict the rock type using a Random Forests classification. The second important variable is neutron porosity and then followed by gamma-ray log. The confusion matrices of the cross validation from the Random Forests is shown in [Table 3.2](#).

The resulting rock type logs for 15 wells are shown in [Figure 3.9](#). The parasequences Miss 1 to Miss 7 were dominated by carbonate-rich rock type 3. The parasequence Miss 8 to Miss 12 were relatively dominated by clay-rich rock type 1 and quartz-rich rock type 2. The parasequence Miss 13 has predominantly clay-rich rock type 1.

Mississippian Sequence Stratigraphy.

Mississippian strata were deposited as a shallowing-upward 2nd-order supersequence ([Sloss, 1963](#)). More recent works (e.g. [LeBlanc, 2014](#); [Drummond, 2018](#); [Hickman, 2018](#); [Miller 2019](#); [Price et al., 2020](#)) subdivide the Mississippian interval into numerous higher order sequences based on vertical succession of core-based lithofacies and gamma-ray-log response.

In this study, the Mississippian strata have 13 upward-shallowing cycles that are bounded by marine-flooding surfaces (in ascending order named parasequence Miss 1 through Miss 13) ([Figure 3.9](#)). The age of the strata was determined based on a study of conodont biozones ([Stukey et al., 2018](#)) in Pan American 2 Barnes Unit D well ([Figure 3.10](#)). A well-log correlation integrating conodont biozones and gamma-ray log from Pan American 2 Barnes Unit D to the Pan American 1 Effie B York shows that the Mississippian strata in Kingfisher and Canadian Counties is Meramecian to Chesterian in age ([Figure 3.10](#)). Therefore, the interval of interest of this study is interpreted to be Meramecian in age. The strata are relatively thin to the south and east toward the Nemaha ridge and basin margin. In the modeling area, the Mississippian strata total thickness ranges from 120 – 630 ft (~35 – 190 m).

Table 3.2. The confusion matrices of Random Forests classification for testing dataset.

		Predicted Rock Type			Class Error (%)
		1	2	3	
Actual Rock Type	1	926	17	141	0.1457565
	2	18	718	145	0.185017
	3	174	147	923	0.2580386

Northwest (A)

STRATIGRAPHIC CROSS-SECTION A-A'

Southeast (A')

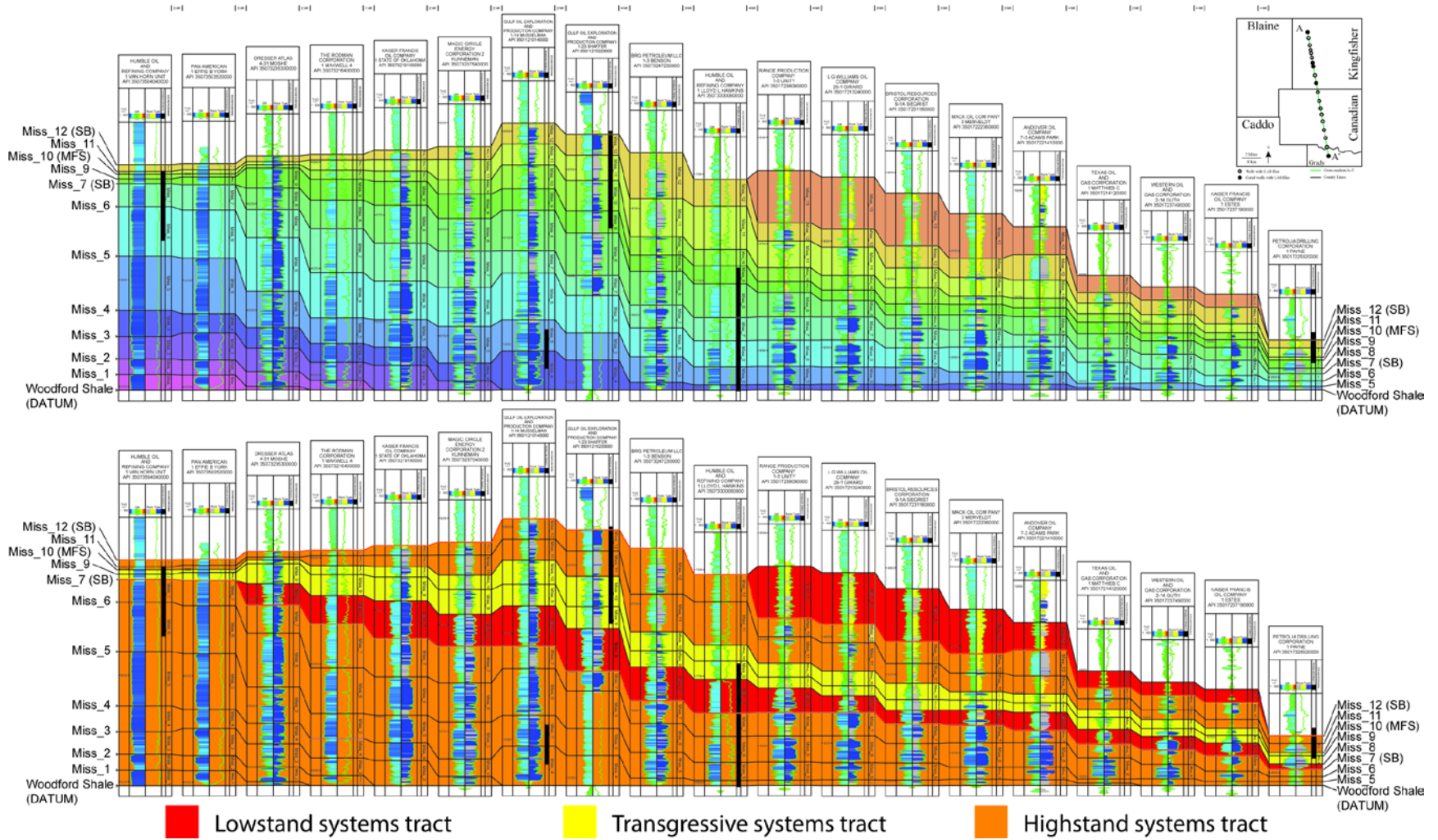


Figure 3.9. a) A stratigraphic cross-section of Mississippian strata from northwest (A) to southeast (A') with proportionally spaced gamma-ray log (2nd track). The cross-section was flattened at Woodford Shale (datum) and displayed with 1:600 ft scale. The cross section shows that the Mississippian strata in the study area of Anadarko Basin has at least 13 parasequences (represented by colors) that were bounded by flooding surfaces picked based on gamma-ray log responses. The cross-section shows that the Mississippian strata thins to the southeast. Noted the rock types of each wells are plotted in track 3. Four wells (Humble Oil and Refining Company 1 Van Horn Unit, Pan American 1 Effie B York, and Humble Oil and Refining Company 1 Lloyd L Hawkins) have incomplete dataset to predict rock type. Track 1 is depth, track 2 is gamma-ray log, track 3 is rock type, track 4 is core interval (black bar), and track 5 is parasequences. b). A stratigraphic cross section of Mississippian strata from northwest (A) to south east (A') showing the interpreted systems tract that correlate to intermediate sea-level changes. The parasequence Miss 1 to Miss 7 represent highstand systems tract. Parasequence Miss 8 represent a lowstand systems tract deposit, parasequence Miss 9 to Miss 10 are interpreted to be transgressive systems tract, parasequence Miss 11 and Miss 12 correlate to highstand systems tract, and finally parasequence Miss 13 is a lowstand systems tract.

PAN AMERICAN
2 BARNES D UNIT
API 35093358760000

(Well used in this study)

PAN AMERICAN
1 EFFIE B YORK
API 35073503520000

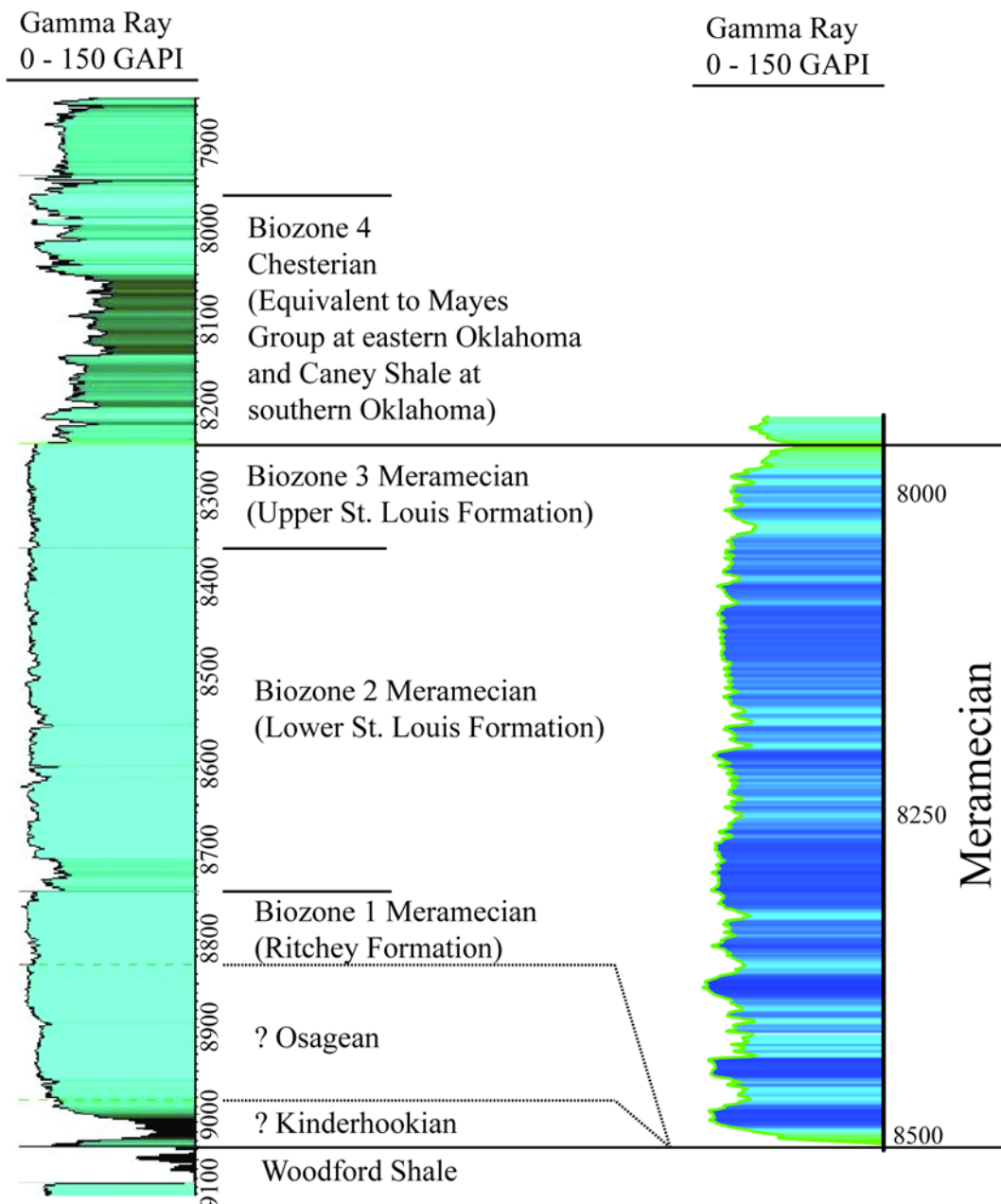


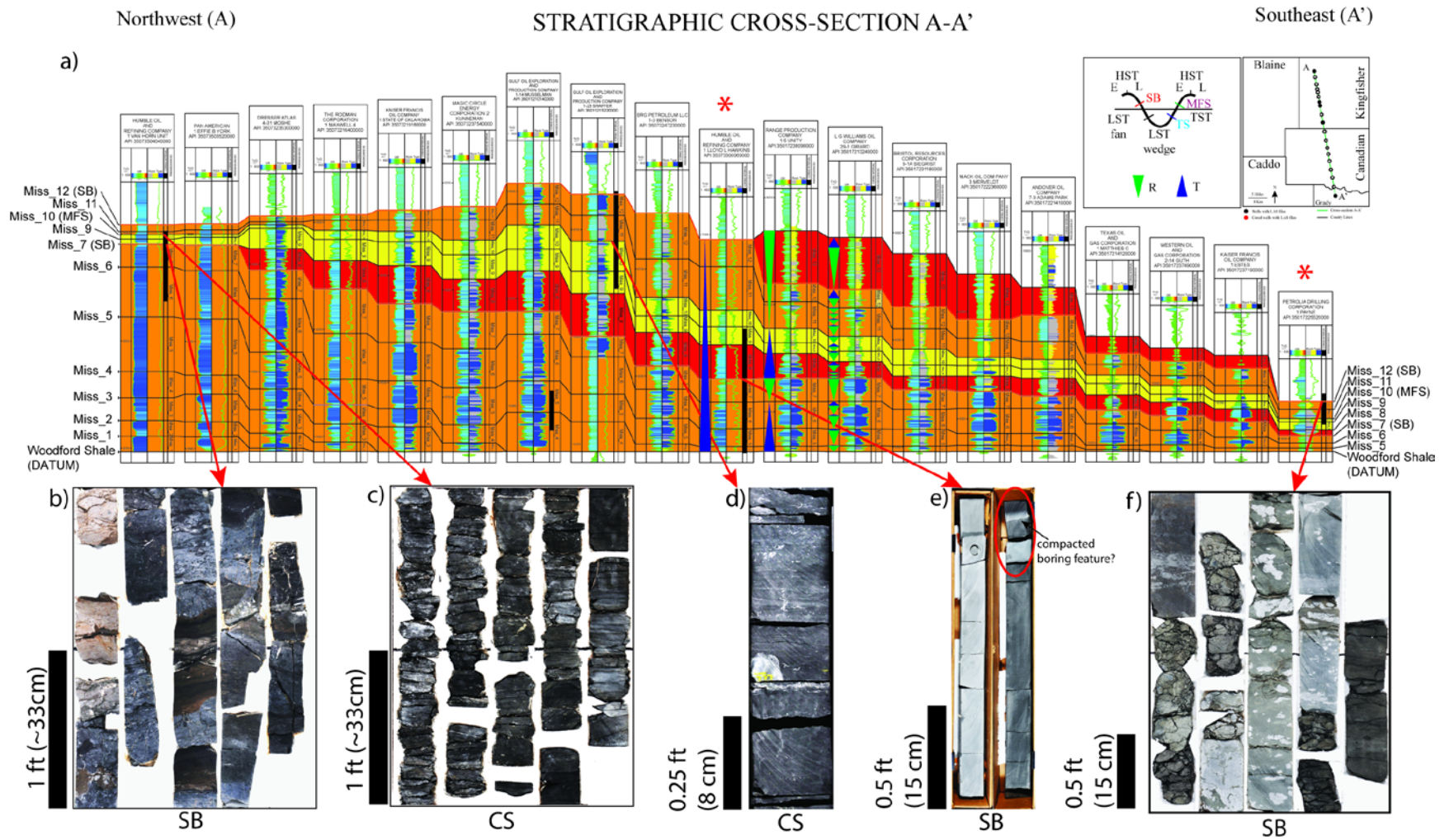
Figure 3.10. Biozones based on study of conodonts from Pan American D-2 Barnes Unit well that is located at Major County. The Biozones were associated to the well's gamma-ray log and correlated to Pan American 1 Effie B York well that is used in this study. The correlation shows the Mississippian strata in the study area is Meramecian in age. (Modified from [Stukey et al., 2018](#)).

The top of interval of interest (Miss 13) corresponds to a regionally correlative increase in resistivity and decrease in neutron porosity and bulk density; and the base, which corresponds to the top of Woodford Shale, is defined as a regionally correlative increase in gamma-ray (above 150 API) and neutron porosity as a result of the shale effect along with a decrease of bulk density (see [Figure 3.9](#)). The boundary between Woodford Shale and Meramec rocks was characterized by the presence of glauconitic siltstone-sandstone (e.g. at. Humble Oil & Refining Company 1 Lloyd L Hawkins core).

Following the deposition of Woodford Shale, Mississippian parasequences prograde into the basin ([Figures 3.9 and 3.11](#)). Parasequences Miss 1 to Miss 7 exhibit a progradational geometry in the northwest to southeast cross-section. Their topsets characteristic is not observable in the study area. However, [Price et al. \(2020\)](#) documented that topsets were truncated to the northwest. [Price et al. \(2020\)](#) also recorded a parasequence that is equivalent to parasequence Miss 7 (below the sequence boundary) was developed during a late highstand systems tract.

The parasequence Miss 8 reflects a relative sea-level fall, forming a lowstand systems tract. The sequence boundaries were observed in basin margin wells (e.g. Humble Oil and Refining Company 1 Van Horn Unit and Humble Oil & Refining Company 1 Lloyd L Hawkins) as brecciated chert or an erosional surface (see [Figure 3.11](#)).

Parasequences Miss 9 through Miss 10 represented a transgressive systems tract with retrogradational trend in response to a relative sea-level rise. The top of parasequence Miss 10 show a maximum flooding surface capping the transgressive systems tract. The maximum flooding surfaces occur as a platy black shale interval in the Humble Oil and Refining Company 1 Van Horn Unit core and as an interval with moderate skeletal grains in the Gulf Oil Corporation 1-23 Shaffer core (see [Figure 3.11](#)). Parasequences Miss 11 and Miss 12 prograde to the southeast as the highstand systems tract deposits. Immediately after that, parasequence Miss 13 shows a seaward



*well that is located at basin margin at the east but projected into cross section

Figure 3.11. a). Interpreted systems tract of the Mississippian strata. Parasequence Miss 1 through Miss 7 were interpreted as highstand systems tract. Parasequence Miss 8 represented a lowstand systems tract deposits. Parasequences Miss 9 and 10 were part of transgressive systems tract. The subsequent Miss 11 and 12 were interpreted as highstand systems tract, and the uppermost parasequence Miss 13 represented another lowstand systems tract. b). Core photo showing a brecciated chert lithofacies associated with subaerial exposure (sequence boundary) in the updip well. c). Core photo showing a platy black shale interval associated with a condensed section (maximum flooding surface) in the updip well. d). Core photo showing a blocky black shale associated with a condensed section in a deeper water well. Noted the moderate amount of skeletal grains, probably reworked from shallow water deposits. E). Core photo showing an erosional surface associated with abrupt landward lithofacies shift (a channel eroded into deeper water bioturbated siltstone lithofacies) at the basin margin well (east of the Anadarko Basin). Noted the presence of possible boring features at the erosional surface. F). Core photo showing glauconitic siltstone to sandstone that associated with sequence boundary between parasequence Miss 12 and Miss 13 that occurs at a basin margin well (southeast of the Anadarko Basin). LST = Lowstand Systems Tract, TST = Transgressive Systems Tract, and HST = Highstand Systems Tract, SB = Sequence Boundary, TS = Transgressive Surface, MFS = Maximum Flooding Surface. Noted the threefold order cycles are shown at L G Williams Oil Company 29-1 Girard well (high order), Range Production Company 1-5 Unity well (intermediate order), and Humble Oil and Refining Company 2 Lloyd L Hawkins (low order). Blue triangle represents transgression and green triangle represents regression).

shoreline shift as a result of relative sea-level fall, indicating another lowstand systems tract. The sequence boundary between Miss 12 and Miss 13 occurs as an interval of glauconitic siltstone-sandstone in the Petrolia Drilling Corporation 1 Payne wells (see [Figure 3.11](#)).

An idealized upward-shallowing cycle was observed as (from base to top) bioturbated siltstone, laminated-siltstone, structureless siltstone, and cross-laminated siltstone. In the up-dip area, the vertical succession is commonly capped by carbonate lithofacies or subaerial exposure surface associated with brecciated chert (e.g. Humble Oil & Refining Company 1 Van Horn Unit). The glauconitic siltstone-sandstone is occasionally present and typically associated with a sequence boundary or correlative conformity (e.g. at Petrolia Drilling Corporation 1 Payne wells and Humble Oil & Refining Company 1 Lloyd L Hawkins). These upward-shallowing cycles are often incomplete or irregular and typically consist of only three or four of the eight lithofacies. Occasionally, the cycles are truncated by structureless sandstone channel-fills or lobe deposits.

Reservoir Modeling

The dip-oriented model was built based on surfaces and isochore maps for Woodford Shale and 13 Mississippian parasequences were created to represent horizons and model zones. The width of the cross-sectional model was arbitrarily set to 200 ft (61 m). The model grid cells have aerial dimensions of 50 x 50 ft. They were rotated by 9.5° to orientate the cells along the depositional trend from northwest to southeast. These configurations resulted in 4 x 6048 x 574 cells in I, J, and K direction and 13,886,028 cells in total.

Due to lack of outcrop analogous and limited data, the challenge within this study has been to build a model from a range of realistic parameters (major direction, minor direction, and vertical ranges) to capture the essence of progradational shallow-marine, mixed carbonate-siliciclastic system reservoirs.

Therefore, the spatial correlation of rock types, effective porosity, and effective water saturation in the study was determined using published variogram data. Based on study of 56 modern and ancient shallow-marine depositional systems, Howell et al. (2008) recorded facies thickness for shallow marine facies (in upper shoreface – lower shoreface) varies from 5 – 10 ft (~1.5 - 3.3 m); and architectural element distance range from 2300 – 16000 ft (700 – 5000 m). Based on this data, the horizontal rock-type variogram for the major and minor direction were set to 10000 ft (~3000 m) and 10000 ft (~3000 m), respectively, for each rock type throughout 13 zones. The vertical range for rock type was set as 5 ft (~1.5 m). The azimuth for the major direction horizontal rock-type variogram was set to 80° N, approximately parallel the depositional strike from northeast to southwest. The Sill and Nugget for each variogram was set to one and zero, respectively, to honor all the upscaled rock-type logs.

Similarly, the spatial correlation of the petrophysical parameters was also quantified based on published variogram data. The major and minor ranges were determined to be less than that of the rock types and were set to 8000 ft (~2500 m) and 8000 ft (~2500 m), respectively. The vertical range for these parameters was set as 4 ft (~1.2 m). The azimuth of major direction was set to 80° N, along the depositional strike.

The dip-oriented cross-sectional reservoir model, constrained by the sequence-stratigraphic framework and populated with rock-types, total porosity, effective porosity, and total water saturation, is shown in [Figures 3.12 and 3.13](#). The rock type percentage for each parasequences is shown in [Table 3.3](#). In general, the percentage of carbonate-rich rock type 3 decreases from parasequence Miss 1 to Miss 13

NW

SE

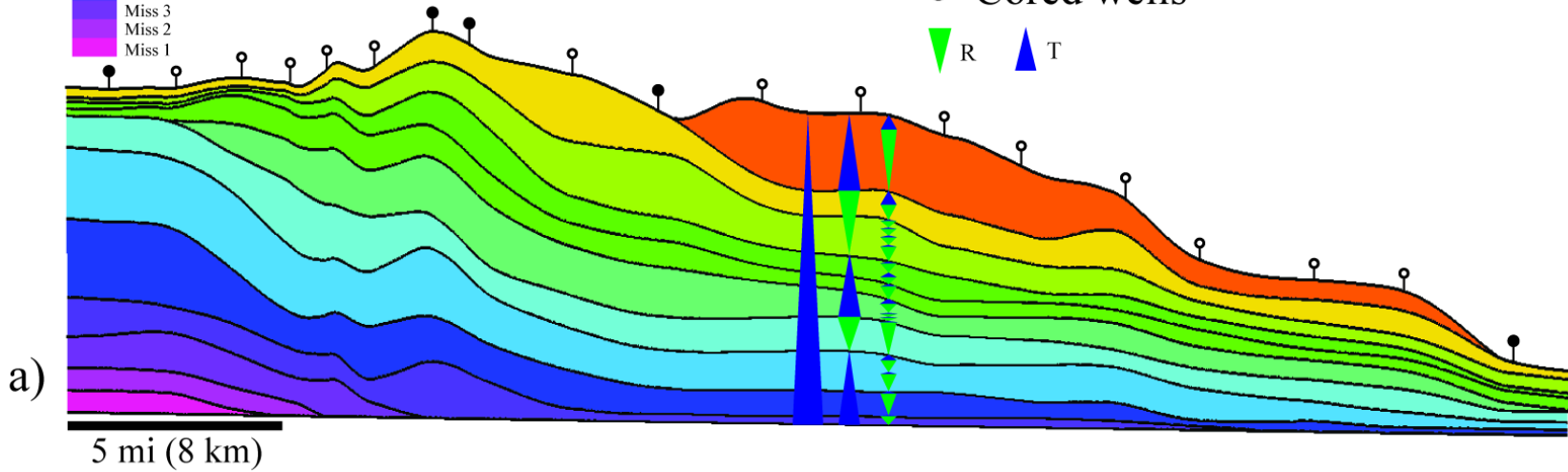
- Miss 13
- Miss 12
- Miss 11
- Miss 10
- Miss 9
- Miss 8
- Miss 7
- Miss 6
- Miss 5
- Miss 4
- Miss 3
- Miss 2
- Miss 1

V.E 125X

Flattened on the Woodford Shale

- Uncored wells
- Cored wells

▼ R ▲ T



- Rock Type 1 (Clay rich siltstone)
- Rock Type 2 (Quartz rich siltstone)
- Rock Type 3 (Carbonate rich siltstone)

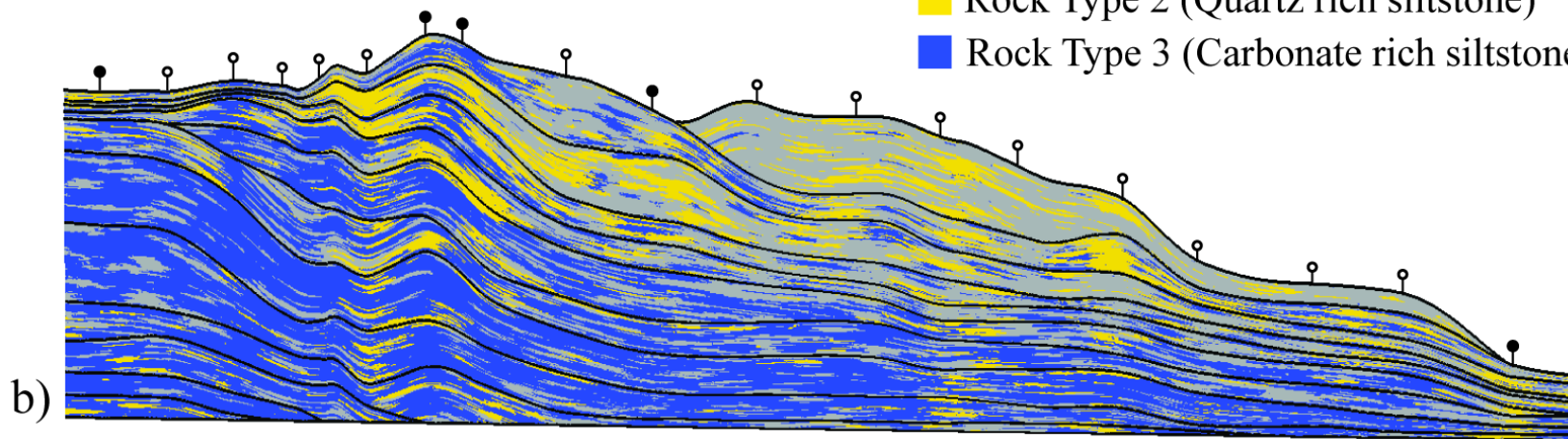


Figure 3.12. A dip-oriented models flattened on top of Woodford Shale. The models were displayed with 125X vertical exaggeration. Both cored and un-cored wells were displayed along the cross-section of the model. a). Zones index model showing the stratigraphic zones through which rock types, effective porosity, and effective water saturations were modeled within. The zones were defined by the parasequences of Miss 1 through Miss 13 that were picked using gamma-ray log. The threefold stratigraphy order (low, intermediate, and high orders) as indicated by transgression and regression arrow b). A zone model populated with rock types showing Miss 1 - 8 has predominantly carbonate-rich rock type 3 ranging from 55% - 91%, Miss 9 – 12 are richer in clay-rich rock type 1 ranging from 43% – 52%, and Miss 13 has 77% of clay-rich rock type 1. Noted that the interval suggests an overall deepening-upward with the increase of clay-rich rock type 1 and decrease of carbonate rich-rock type 3.

NW

SE

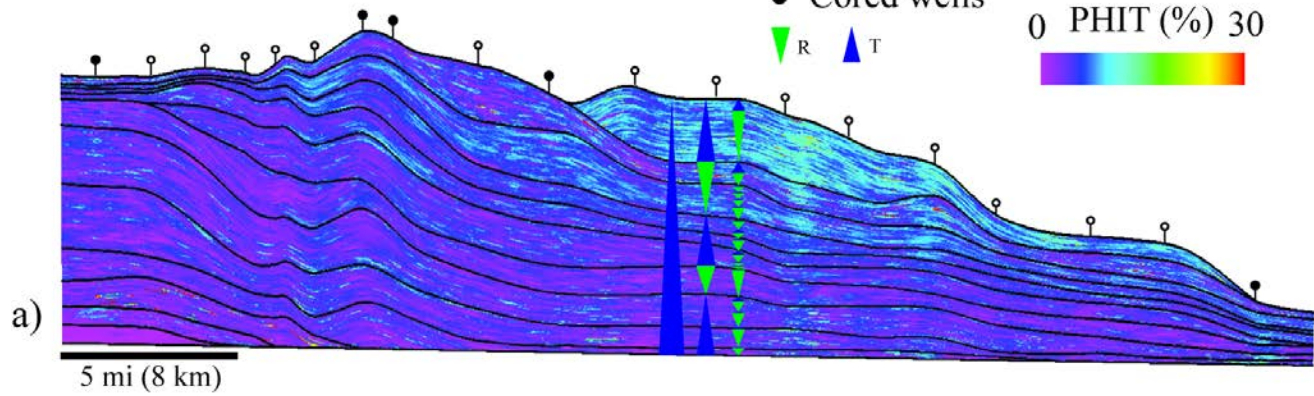
V.E 125X

Flattened on the Woodford Shale

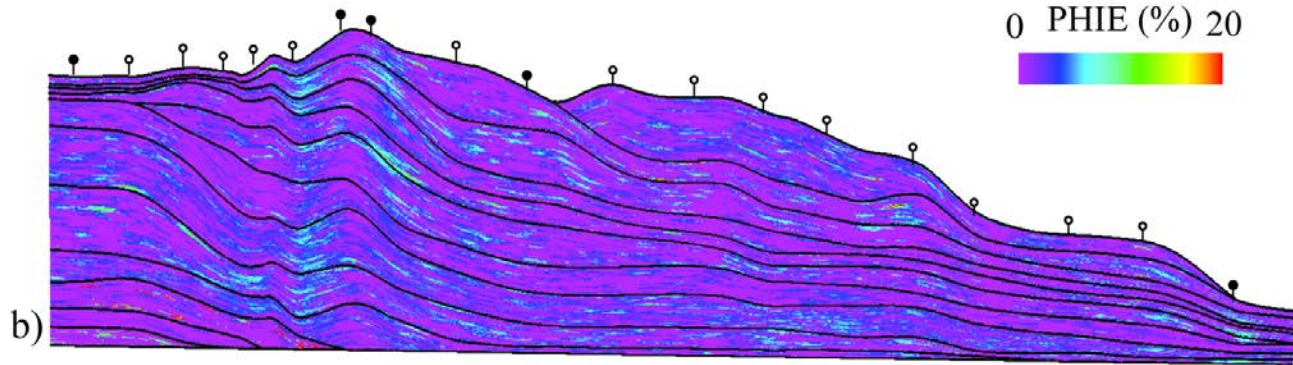
- Uncored wells
- Cored wells

▼_R ▲_T

0 PHIT (%) 30



0 PHIE (%) 20



Sw total (%)



0 100

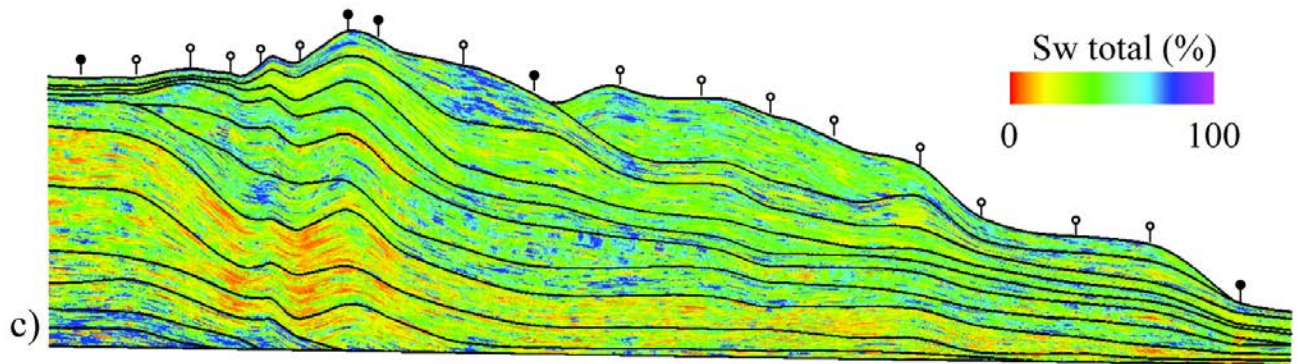


Figure 3.13. A dip-oriented models flattened on top of Woodford Shale. The models were displayed with 125X vertical exaggeration. Both cored and un-cored wells were displayed along the cross-section of the model. a). A total porosity model shows the increase of total porosity upward following the increase of clay-rich rock type 1. b). An effective porosity model shows indeterminate relationship between effective porosity distribution within parasequences. c) A total water saturation model show that total water saturation decreases along with the carbonate-rich rock type 3 from parasequence Miss 1 to Miss 6. total water saturation is relatively high in the parasequence Miss 7 to Miss 8 during the late highstand systems tract and lowstand systems tract following the increase of clay-rich rock type 1, moderate in parasequence Miss 10 and Miss 11, and relatively high in the parasequence Miss 12 and Miss 13 following the increase of clay-rich rock type 1 (early highstand systems tract and lowstand system tract). Noted that the total porosity and total water saturation typically increase with the increase of clay-rich rock type 1. This is most likely associated with the clay-bound-water (CBW)

Table 3.3. Rock type percentage per stratigraphic zones.

Zone	Rock Type 1 (%)	Rock Type 2 (%)	Rock Type 3 (%)
Miss 12 - Miss 13	76.97	22.18	0.85
Miss 11 - Miss 12	43.21	27.69	29.1
Miss 10 - Miss 11	52.11	30.76	17.13
Miss 9 - Miss 10	47.78	23.61	28.61
Miss 8 - Miss 9	49.07	15.61	35.32
Miss 7 - Miss 8	34.44	9.6	55.95
Miss 6 - Miss 7	36.34	10.02	53.64
Miss 5 - Miss 6	18.91	6.61	74.47
Miss 4 - Miss 5	22.88	9.45	66.67
Miss 3 - Miss 4	25.53	10.85	65.62
Miss 2 - Miss 3	20.76	8.99	70.26
Miss 1 - Miss 2	7.2	1.23	91.57
Woodford Shale - Miss 1	5.93	20.4	76.67

along with the increase of clay-rich rock type 1 percentage. The percentage of quartz-rich rock type 2 also increases gradually from parasequence Miss 1 to Miss 13.

The total porosity model (Figure 3.13a) shows a trend in which total porosity increase following the increase of clay-rich rock type 1, particularly during the late highstand systems tract and lowstand systems tract (parasequence Miss 7, 8, 12, and 13). On the other hand, the effective porosity model shows an unclear trend. This could be due to diagenesis imprint in the rock types.

The total water saturation varies throughout the study area (from 30 % - 70%). The total water saturation model (Figure 3.13c) shows decrease total water saturation moving up section from parasequence Miss 1 to Miss 7 (70% to 33%). The total water saturation typically increases during late highstand systems tract (parasequences Miss 7 and Miss 12) and lowstand systems tract (parasequence Miss 8 and Miss 13). For example, in the parasequence 6 (middle of highstand systems tract) to parasequence 7 (late highstand systems tract) the total water saturation increases from 33% to 57% following the increase of clay-rich rock type 1 from 19% to 36%.

DISCUSSION

Spatial Distribution of Rock Types within Sequence Stratigraphy Framework.

Low Order

The interval of interest is Meramec in age that represents a low stratigraphic order. Although the Meramec deposits show progradational successions, the overall sea-level change within the third order sequence resulted in an overall upward-deepening profile. Price et al. (2020) also observed this low-order deepening-upward cycle and suggested that tightly cemented lithofacies typically occurs at the base of the interval. Based on the rock type model, the vertical succession exhibits an overall increase of clay-rich rock type 1 (from 5% to 76%) and decrease of carbonate-rich rock type 2 (from 76% – 1%) from top of the Woodford Shale to the top of parasequence Miss 13. The total porosity generally

increases upward with the increase of clay-rich rock type 1. This increase might be associated with clay bound water (CBW) of the clay-rich rock type 1. Permeability within the deepest water setting at the top of the interval might be extremely low due to compaction or high-clay contents blocks pore throat.

Intermediate Order

In intermediate stratigraphic order, the distribution of rock types within systems tract can also be identified. Parasequence Miss 1- Miss 7 are dominated by carbonate-rich rock types 3 (50 – 90%). These underlying carbonate-rich parasequences were interpreted to be deposited in a shallow water, high energy condition; and probably represented an early and late highstand systems tract (HST). As relative sea level started to fall, it formed parasequence 7 as a late highstand systems tract deposit. The parasequence 7 correlates with a significant increase of clay-rich rock type 1 (from ~18% to ~36%) and decrease of carbonate-rich rock type 3 (from ~75% to ~50%).

Parasequence Miss 8, deposited directly above a sequence boundary, is interpreted to be a lowstand system tract (LST) formed in response to normal regression. In core, the parasequence was characterized by increase in high energy lithofacies. In the model, the parasequence 8 was dominated by carbonate-rich rock type 3 (~50 %). However, the percentage of carbonate-rich rock type 3 decrease compare to those of highstand systems tract; and the percentage of clay-rich rock type 1 is similar to that of late highstand systems tract (~34 %). It suggested that during relative sea level fall (late HST and LST) clay-rich rock type 1 tend to increase while carbonate-rich rock type 3 tend to decrease.

Parasequences Miss 9 and Miss 10 represent a transgressive systems tract in response to relative sea-level rise. Retrogradational stacking pattern was indicated by increase of clay-rich rock type 1 (47% - 49%) that corresponds to relatively lower energy, deeper water depositions. Previous studies ([Miller, 2018](#); [Price et al., 2020](#)) also observed this retrogradational stacking pattern. [Miller \(2018\)](#) documented retrogradational stacking pattern within his Meramec parasequence 1 to parasequence 3; and other four

younger parasequences (Meramec Parasequence 4 to parasequence 7) showing progradational stacking pattern. Similarly, progradational stacking pattern was observed in parasequences Miss 11 and Miss 12 that continue to prograde to the southeast after the deposition of a condensed section. These parasequences were interpreted to be highstand systems tract, deposited during slowing rate of relative sea-level rise. The model shows a continued upward-deepening profile with increases in clay-rich rock type 1 (43% - 52%) and decreases of carbonate-rich rock types 3. After deposition of highstand systems tract, the model of parasequence Miss 13 showed a significant increase of clay-rich rock type 1 and decrease of carbonate-rich rock type 3. In each well, quartz-rich rock types 2 dominates the interval (see [Figure 3.9](#)) and probably correlates to higher energy deposition. The overall quartz-rich rock type 2 gradually increases from parasequence Miss 1 to parasequence Miss 13. This quartz-rich rock types 2 exceeds 15 % in the upper parasequence Miss 9 through Miss 13 with a maximum percentage of 30% within parasequence Miss 11.

High Order

In cores, the high order cycle occurs as the idealized vertical succession which consists of (from base to top) bioturbated siltstone, laminated-siltstone, structureless siltstone, and cross-laminated siltstone, and occasionally skeletal wackestone-packstone lithofacies. This succession suggests an upward-shallowing cycle. It is also manifested as an upward-decreasing gamma-ray values punctuated by a sharp increase in gamma-ray response at the top of each cycles.

Core analysis tied to gamma-ray illustrate a series of continuous mappable high order cycles within parasequence. Bases of each parasequence associated with bioturbated siltstone that was deposited in deeper-water and lower energy setting typically has higher clay content; and the cross-laminated siltstone that was deposited in proximal area (at top of each cycles) is typically well

cemented. Therefore, rocks with relatively good reservoir quality typically occurs in the middle of the higher order cycle with a balance of volume of clay and carbonate cements.

Sequence-Stratigraphic Control of Porosity Distribution.

A simplified threefold hierarchy sequence stratigraphy evidently provides a powerful predictive framework of rock type distribution. Different order sequences distinctly controlled rock types and lithofacies distribution, which, in turn, affected the distribution of their porosity.

The low third-order cycle resulted in an overall upward-deepening profile. The profile exhibits an overall increase of clay-rich rock type 1 (from 6% to 76%) and decrease of carbonate-rich rock type 3 (from 76% – 1%). Therefore, tightly cemented rocks with effective porosity varies from 2% - 4% were concentrated at the lower section. The porosity generally increases upward along with the gradual increase of quartz-rich rock type 2.

[Price et al. \(2020\)](#) showed superimposed sea-level rise-fall-rise has resulted in shallow water and deeper water depositions within intermediate order cycle. Based on this sea-level cycle, carbonate-rich rock types 3 within parasequence Miss 1 to Miss 8 was likely deposited under shallow water condition. Then relatively deeper water, lower energy condition occurred during sedimentation of parasequence Miss 9 –Miss 12, and followed by shallow water condition during deposition of parasequence Miss 13. Shallow water parasequences contain more carbonate-rich rock type 3 with moderate overall porosity. Deepening in the parasequence Miss 9 – Miss 12 yielded an increase of clay-rich rock type 1 with effective porosity less than 2%. These deepening parasequences also exhibits gradual increase of quartz-rich rock type 2 with high effective porosity (4% - 7%). The shallow water condition during the deposition of parasequence 13 contain abundant clay-rich rock type 1 (~76%). This abundance might have resulted from extensive erosion of preceding parasequence deposits. The abundance of clay-rich

rock type 1 contributed to relatively low porosity in this parasequence as high volume of clay blocks pore throats and creates permeability barrier.

The higher order cycle that correlates to high frequency relative sea-level changes occurs as upward-shallowing cycle within each parasequence. Lithofacies with a balance between clay and carbonate cement typically occurs in the middle of the high order cycle. The lithofacies in the proximal area tend to be eroded or cemented while lithofacies in the distal area tend to have high clay content that might reduce its quality.

Sweet Spot Identification

Reservoir intervals in the Meramec unconventional play typically has porosity of 4% to 6%. Based on this threshold integrated with rock types, reservoir sweet spots were identified within the dip-oriented 3D model. Quartz-rich rock type 2 has effective porosity ranges from 4% to 7 % and effective water saturation varies from 8% to 35%. The effective porosity is a direct indicator of storage potential while the mineral volumes are an indicator of brittleness. Rock type 2 with relatively high quartz content is the most brittle of the three rock types. Coupled with high effective porosity indicating high storage potential, this rock type is expected to have a significant impact on production. The parasequence Miss 9 to Miss 12 has relatively high percentage of quartz-rich rock type 2 (from 15% – 30%) compare to other parasequences. Therefore, these parasequences are potential sweet spots in the Meramec unconventional play.

CONCLUSIONS

The application of least square inverse method was a robust solution for estimating mineral volumes in the Mississippian strata because they provide results that can be fine-tuned by adjusting the

input parameters to get a good match between the result and XRD mineral data. The method was proven successful in using neutron porosity, bulk density, and photoelectric effect logs to predict volume of quartz, clay, and carbonate minerals. Different results may arise due to the differences in the mineral model definition (mineral endpoint) and assumptions regarding the tool physics of the logs used.

The Random Forests classification technique, using the predicted mineral volumes and calculated effective porosity as its input, has 80% accuracy in predicting 3 rock types in the Mississippian strata. Rock type 1 is characterized by relatively moderate clays, quartz, carbonates contents and lower effective porosity (<2%). In terms of reservoir quality, rock type 1 is the worst rock type. Rock type 2 has relatively higher quartz, moderate carbonates and clays contents and higher effective porosity (4% - 7%). It is the most brittle and the best reservoir rock with high storage capacity potential. Rock type 3 has relatively higher percentage of carbonates, lower clays and quartz contents and moderate effective porosity (2% - 4%).

Sequence stratigraphy control on rock types and their properties distribution at multiple scales is observed within a dip-oriented 3D geological model. The low stratigraphic order with an upward-deepening trend resulted in overall increase of clay-rich rock type 1 (6% to 76%) and decrease of carbonate rich rock type 3 (76% to 1%). The intermediate stratigraphic order that correlated to sea-level changes controls depositional sequences, which, in turn, drove the rock types and their porosity distribution. The relative sea-level fluctuation generated 13 parasequences within multiple systems tract. Sea level rise produced a highstand systems tract with predominant carbonate-rich rock type 2 during the early to middle parasequences (Miss 1 – Miss 7). A lowstand systems tract of parasequence 8 with predominantly shallow water, high energy lithofacies was formed during relative sea-level fall. Sea-level rise formed a transgressive to highstand systems tract with predominant clay-rich rock type 1 and quartz-rich rock type 2 during the parasequence Miss 9 – Miss 12. Finally, a sea-level fall immediately

after the highstand systems tract produced a lowstand systems tract with abundance clay-rich rock type 1. In higher frequency, a relative sea level change forms an ideal upward-shallowing cycle within a parasequence that consists of (from base to top) bioturbated siltstone, laminated-siltstone, structureless siltstone, and cross-laminated siltstone. The lithofacies in the distal area is often rich in clay and prone to compaction. The presence of clay commonly hinder cementation and block pore throat. The lithofacies in the proximal area tend to be cemented. Therefore, lithofacies with good porosity typically has a balance volume of clay and carbonate cements. Based on integration of 3D modeling and sequence stratigraphy analysis, the model shows optimum sweet spots occur during the deposition of parasequences Miss 9 to Miss 12 with 15% - 30% of quartz-rich rock type 2. The threefold stratigraphic cyclicity provides a predictive model for reservoir rocks and petrophysical property distribution.

REFERENCES

- Birch, C. B., 2015, Reservoir-scale stratigraphy, sedimentology, and porosity characteristics of Mississippian reservoirs, northeastern Anadarko Shelf, Oklahoma, Master's thesis, University of Oklahoma, Norman, Oklahoma, 81.
- Bhuyan, K., and Q. R. Passey, 1994, Clay estimation from Gr and Neutron-Density porosity logs: Society of Petrophysicist and Well-Log Analysts, Tulsa, Oklahoma, 15.
- Boyd, D. T., 2008, Stratigraphic guide to Oklahoma oil and gas reservoir: Oklahoma Geological Survey, Special Publication 2008-1.
- Breiman, L., 2001, Random Forests: Machine Learning, **45-1**, 5 - 32.
- Campbell, J. A., Mankin, C. J., Schwarzkopf, A. B., and Raymer, J. J., 1988, Habitat of petroleum in Permian rocks of the Midcontinent region, in Morgan, W. A., and Babcock, J. A., eds., Permian Rocks of the Midcontinent: Midcontinent Society of Economic Paleontologists and Mineralogists (SEPM) Special Publication 1, 13-35.
- Childress, M., and G. M. Grammer, 2015, High resolution sequence stratigraphic architecture of a Mid-Continent Mississippian outcrop in southwest Missouri: The Shale Shaker, **66-4**, 206-234.
- Clair, J. H., 1949, Lithologic criteria of Mississippian rocks in western Kansas: World Oil, **122**, 61- 66.
- Curtis, D. M., and S. C. Champlin, 1959, Depositional environments of Mississippian limestones of Oklahoma: Tulsa Geological Society Digest, **27**, 90 – 103.
- Dehcheshmehi, S. M., 2016, Regional diagenesis of Mississippian strata of the southern Midcontinent, USA: Ph.D.'s dissertation, Oklahoma State University, Stillwater, Oklahoma, 134.
- Doveton, J. H., 1994, Compositional analysis of lithologies from wireline logs, in J. H. Doveton, ed., Geologic log analysis using computer methods: AAPG Computer Applications in Geology 2, Tulsa, 169.
- Drummond, K., 2018, Regional stratigraphy and proximal to distal variation of lithology and porosity within a mixed carbonate-siliciclastic system, Meramec and Osage series (Mississippian), central Oklahoma: Master's thesis, University of Oklahoma, Norman, Oklahoma, 155.
- Dutton, S. P., 1984, Fan-delta Granite Wash of the Texas Panhandle: Oklahoma City Geological Society Short Course, 1-144.
- Gupta, I., 2017, Rock typing in organic shales: Eagle Ford, Woodford, Barnett, and Wolfcamp Formations: Master's thesis, University of Oklahoma, Norman, Oklahoma, 173.

- Hardwick, J., 2018, Reservoir quality evaluation of the Meramec and Upper Osage units in the Anadarko Basin: Master's thesis, University of Oklahoma, Norman, Oklahoma, 63.
- Harris, S. A., 1975, Hydrocarbon accumulation in "Meramec-Osage" (Mississippian) rocks, Sooner Trend, northwest-central Oklahoma: AAPG Bulletin, **59**, 633-664.
- Hickman, G. J., 2018, Parasequence-scale stratigraphy variability of lithology and porosity of Mississippian Meramec reservoirs and the relationship to production characteristics, STACK trend, Oklahoma: Master's thesis, University of Oklahoma, Norman, Oklahoma, 94.
- Howell, J. A., A. Skorstad, A. MacDonald, A. Fordham, S. Flint, B. Fjellvoll, T. Manzocchi, 2008, Sedimentological parameterization of shallow-marine reservoirs; Petroleum Geoscience, **14**, 17 - 34
- Johnson, K. S., and K. V. Luza, 2008, Earth sciences and mineral resources of Oklahoma: Educational Publication 9, Oklahoma Geological Survey, 22.
- Kale, S., C. Rai, C. Sondergeld, 2010, Rock Typing in Gas Shales: Society of Petroleum Engineer, Florence, Italy, SPE#134539, 20.
- Keller, R., 2014, The southern Oklahoma Aulacogen: It's a classic, in N. H. Suneson, ed. Igneous and tectonic history of the southern Oklahoma aulacogen, Oklahoma Geological Survey Guidebook 38, Norman, Oklahoma, 406.
- Leavitt, A., 2018, Depositional systems of the STACK and SCOOP Mississippian units: regional understanding from logs and core: Oklahoma Geological Survey – The STACK Play Workshop, Abstract.
- LeBlanc, S., 2014, High resolution sequence stratigraphy and reservoir characterization of the "Mississippian Limestone" in North-Central Oklahoma, Master's thesis, Oklahoma State University, Stillwater, Oklahoma, 443.
- LoCricchio, E., 2012, Granite Wash play overview, Anadarko Basin: Stratigraphic framework and controls on Pennsylvanian Granite Wash production, Anadarko Basin, Texas and Oklahoma: AAPG Annual Convention and Exhibition, 1-17.
- MacQueen, J. B. 1967. Some Methods for classification and Analysis of Multivariate Observations: Proceedings of 5th Berkeley Symposium on Mathematical Statistics and Probability, University of California Press, 281–297.
- Mazzullo, S. J., 2011, Mississippian oil reservoirs in the Southern Midcontinent: New exploration concepts for a mature reservoir objective: AAPG Search and Discovery #10373, 34 .
- Mazzullo, S. J., B. W. Wilhite, and D. R. Boardman, March 2011, Lithostratigraphic architecture of the Mississippian Reeds Spring Formation (Middle Osagean) in S. W. Missouri, N. W. Arkansas,

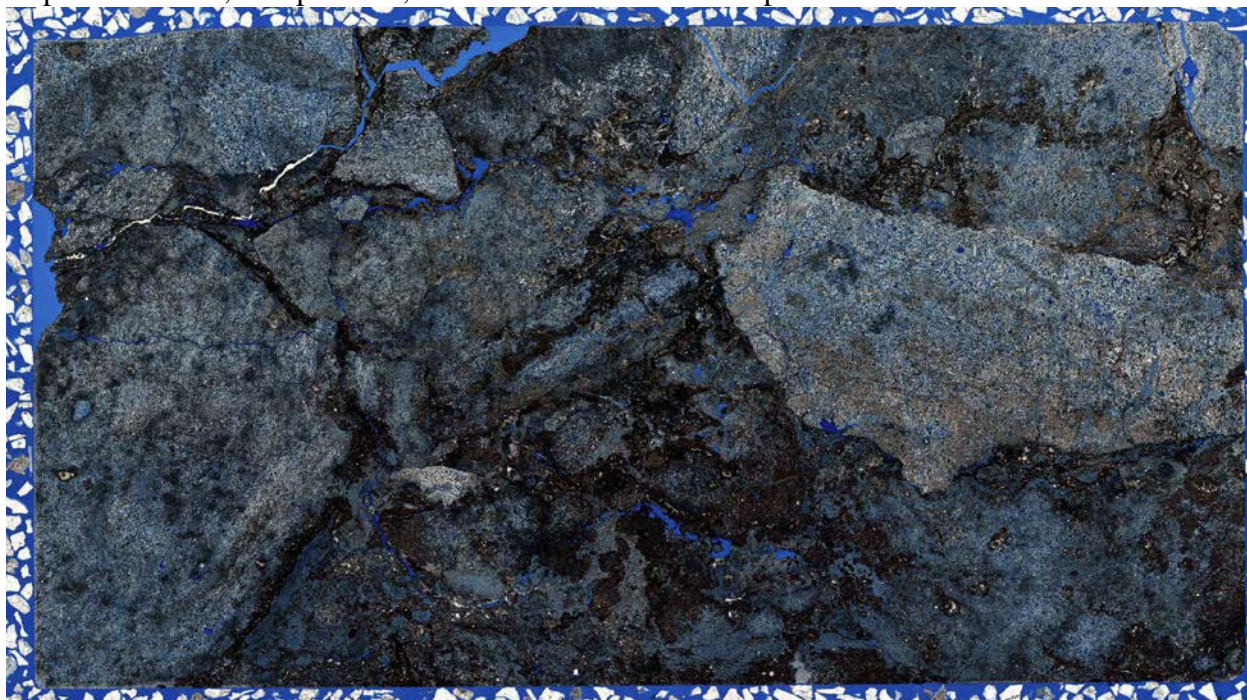
- and N. E. Oklahoma: Outcrop analog of subsurface petroleum reservoirs: *Shale Shaker*, **61**, 254–269.
- Mazzullo, S. J., B. W. Wilhite, D. R. Boardman, B. T. Morris, and C. J. Godwin, 2016, Stratigraphic architecture and petroleum reservoirs in lower to middle Mississippian strata (Kinderhookian to basal Meramecian in subsurface central to southern Kansas and northern Oklahoma: *Shale Shaker*, **67**, 20-49.
- McConnell, D. A., Goydas, M. J., Smith, G. N., and Chitwood, J. P., 1989, Morphology of the frontal fault zone, southwest Oklahoma: Implications for deformation and deposition in the Wichita uplift and Anadarko basin: *Geology*, **18**, 634-637.
- McDuffie, R. H., 1959, Lithologic basis for correlation of Mississippian rocks in the subsurface between Kansas and north central Oklahoma: *Oklahoma Academy of Science*, **39**, 133 – 135.
- Miller, J. C., 2018, Regional stratigraphy and organic richness of the Mississippian Meramec and associated strata, Anadarko Basin, central Oklahoma: Master's thesis, University of Oklahoma, Norman, Oklahoma, 143.
- Miller, M., 2019, Mississippian Meramec lithologies and petrophysical properties variability, STACK Trend, Anadarko Basin, Oklahoma; Master's Thesis, University of Oklahoma, Norman, Oklahoma, 106.
- Northcutt, R. A., and Campbell, J. A., 1995, Geologic provinces of Oklahoma: Oklahoma Geological Survey Open-File Report 5-95, 1 sheet, scale 1 : 750,000, 6.
- Puzin, L. A., 1951, A chart of connate water resistivity in Oklahoma and its application to electric log interpretation: *Petroleum Engineering*, **24-9**, B67-B78.
- Price, B., K. Haustveit, and A. Lamb, 2017, Influence of stratigraphy on barriers to fracture growth and completion optimization in the Meramec STACK play, Anadarko Basin, Oklahoma: Unconventional Resources Technology Conference, Article#2697585, 8.
- Price, B. J. A. C. Pollack, A. P. Lamb, T. C. Peryam, J. R. Anderson, 2020, Depositional interpretation and sequence stratigraphy control on reservoir quality and distribution in the Meramecian Sooner trend Anadarko Basin, Canadian, and Kingfisher Counties (STACK) play, Anadarko Basin, Oklahoma, United States: *AAPG Bulletin*, **104-2**, 357 – 386.
- Rogers, S. M., 2001, Deposition and diagenesis of Mississippian chat reservoirs, north central Oklahoma: *AAPG Bulletin*, **85**, 115-129.
- Rottmann, K., 2018, Well-log characterization of the Devonian and Mississippian Groups in central and northern Oklahoma with emphasis on correlation and depositional environment: Oklahoma Geological Survey – STACK Workshop, 73.

- Rowland, T.L., 1961, Mississippian rocks in the subsurface of the Kingfisher-Guthrie area, Oklahoma: Shale Shaker Digest IV, **12 – 14**, 145 – 162.
- Rushing, J. A., K. E. Newsham, T. A. Blasingame, 2008, Rock Typing: Keys to Understanding Productivity in Tight Gas Sands: SPE Unconventional Reservoirs Conference, Keystone, Colorado, SPE#114164-MS, 31.
- Shelley, S., G. M. Grammer, M. J. Pranter, 2017, Reservoir characterization and modeling of a subsurface Meramec analog from a quarry in northeastern Oklahoma: Shale Shaker, **68**, 224-243.
- Sloss, L. L., 1963, Sequences in the cratonic interior of North America: Geological Society of America Bulletin, **74**, 93-114.
- Stukey, B., C. J. Godwin, J. O. Puckette, 2018, Biostratigraphically constrained ages of Mississippian mixed carbonate-siliciclastic sequences, STACK Play, Anadarko Basin, Oklahoma: Oklahoma Geological Survey – STACK Workshop, 29.
- Suriamin, F., and M. J. Pranter, 2018, Stratigraphic and lithofacies control on pore characteristics of Mississippian limestone and chert reservoirs of north-central Oklahoma: Interpretation, **6**, T1001 – T1022.
- Suriamin, F., M. J. Pranter, A. Seyedolali, *in prep*, Variability of Mississippian lithofacies, depositional environments, diagenetic processes, and reservoir quality within a mixed siliciclastic-carbonate system, eastern Anadarko Basin, Oklahoma, USA.
- Ulrich, E. O., 1904, Preliminary notes on classification and nomenclature of certain Paleozoic rock unit in eastern Missouri: in Buckley E.R., and Buehler, H. A., The quarry industry in Missouri: Missouri Bureau of Geology and Mines, **2**, 109 – 111.
- Vanden Berg, B., and G. M. Grammer, 2016, 2-D pore architecture characterization of a carbonate mudrock reservoir: Insight from the Midcontinent “Mississippi Lime”, in Olson, T., ed., Imaging unconventional reservoir pore systems: AAPG Memoir **112**, 185–232.
- Watney, W. L., W. J. Guy, A. P. Byrnes, 2001, Characterization of the Mississippian chert in south-central Kansas: AAPG Bulletin, **85**, 85 – 113.
- Welker, C., S. Feiner, R. Lishansky, W. Phiukhao, J. Chao, R. Moore, and D. Hall, 2016, Trapped Fluid Analysis of 58 wells from SCOOP and STACK Plays, Oklahoma: Unconventional Resources Technology Conference# 2461587, 12.

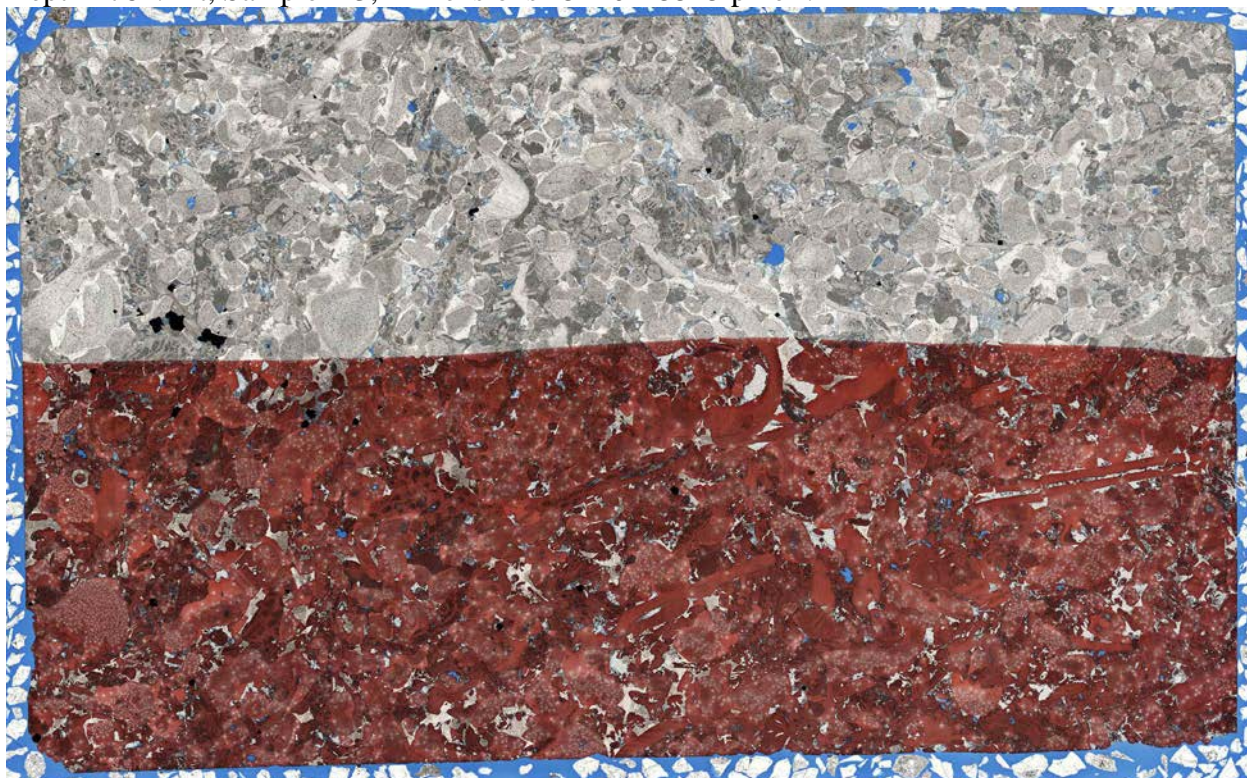
APPENDIX A: THIN SECTION AND SEM PHOTOMICROGRAPHS

APPENDIX A1: Whole Thin Section Photo (Devon Energy 1–7 SWD Frieouf)

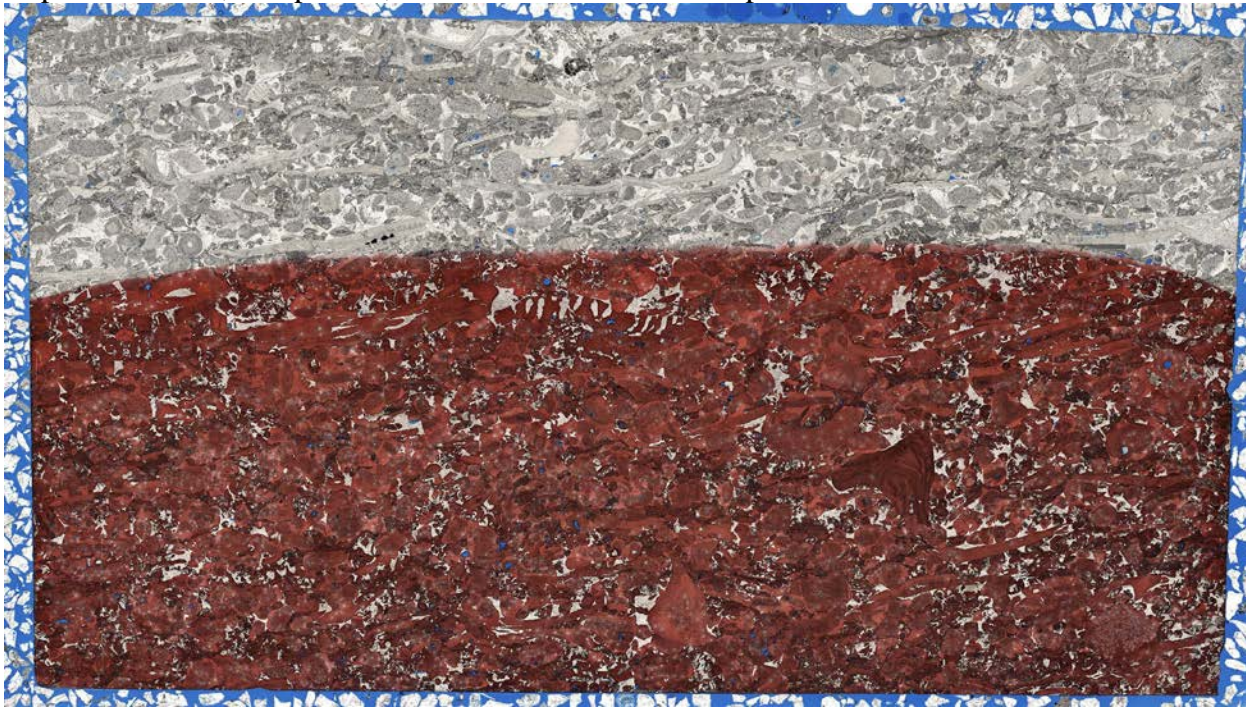
All these section photos use scale 1.4814222246 $\mu\text{m}/\text{pixel}$
Depth 4776.75 ft, Sample 1-61, Dimensions 26838x14985 pixel².



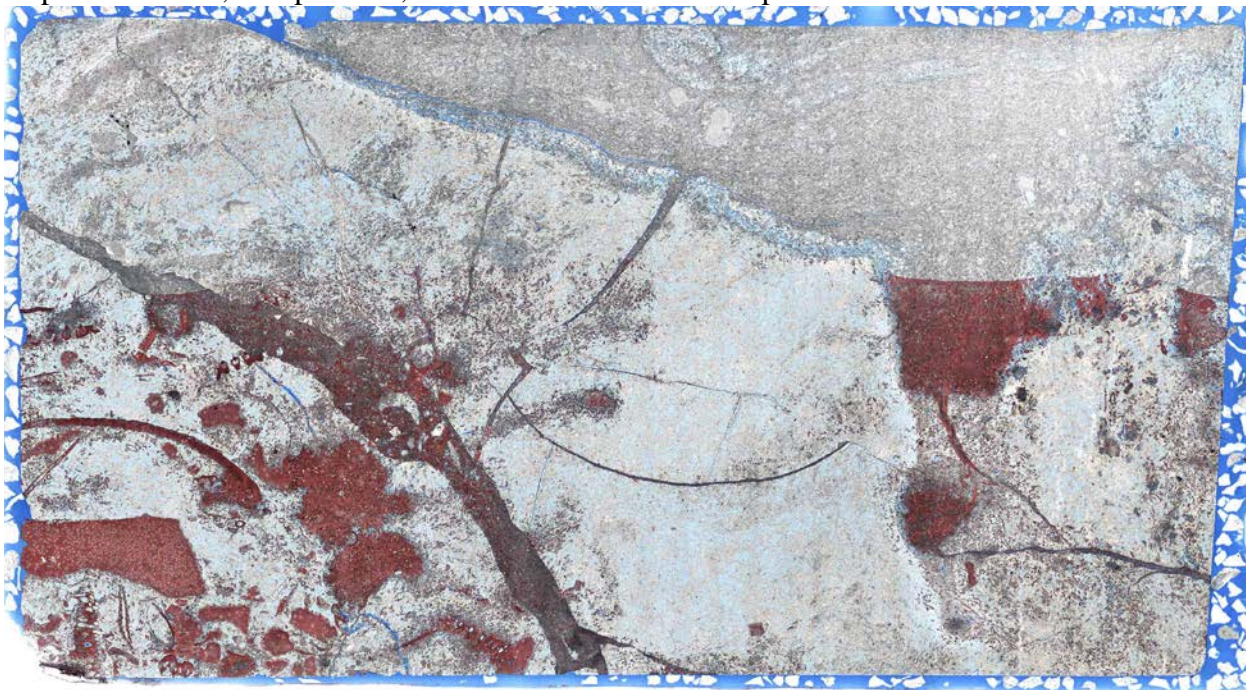
Depth 4782.4 ft, Sample 2-3, Dimensions 25120x15545 pixel².



Depth 4784.95 ft, Sample 2-5, Dimensions 27117x15303 pixel².



Depth 4794.95 ft, Sample 2-15, Dimensions 28045x15490 pixel².



Depth 4797.1 ft, Sample 2-18, Dimensions 28076x15296 pixel².



Depth 4804.75 ft, Sample 2-25, Dimensions 26650x15715 pixel².



Depth 4810.4 ft, Sample 2-31, Dimensions 27596x15702 pixel².



Depth 4813.1 ft, Sample 2-34, Dimensions 27317x15367 pixel².



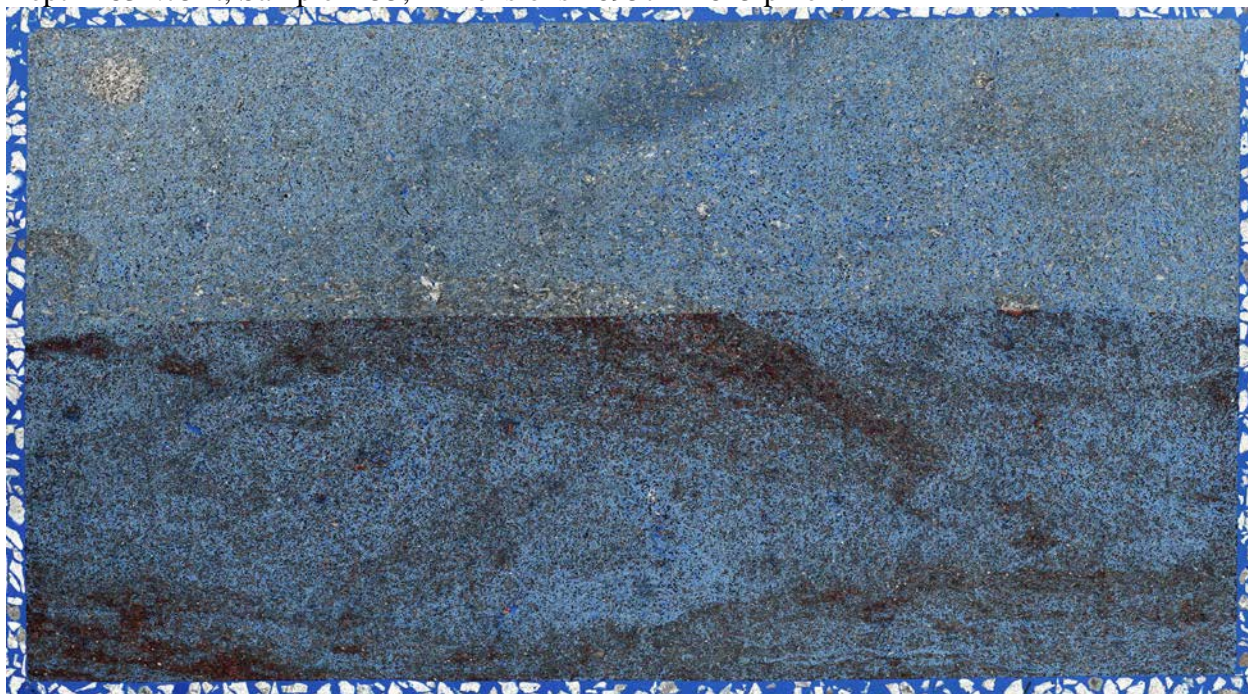
Depth 4814.85 ft, Sample 2-35, Dimensions 28195x15024 pixel².



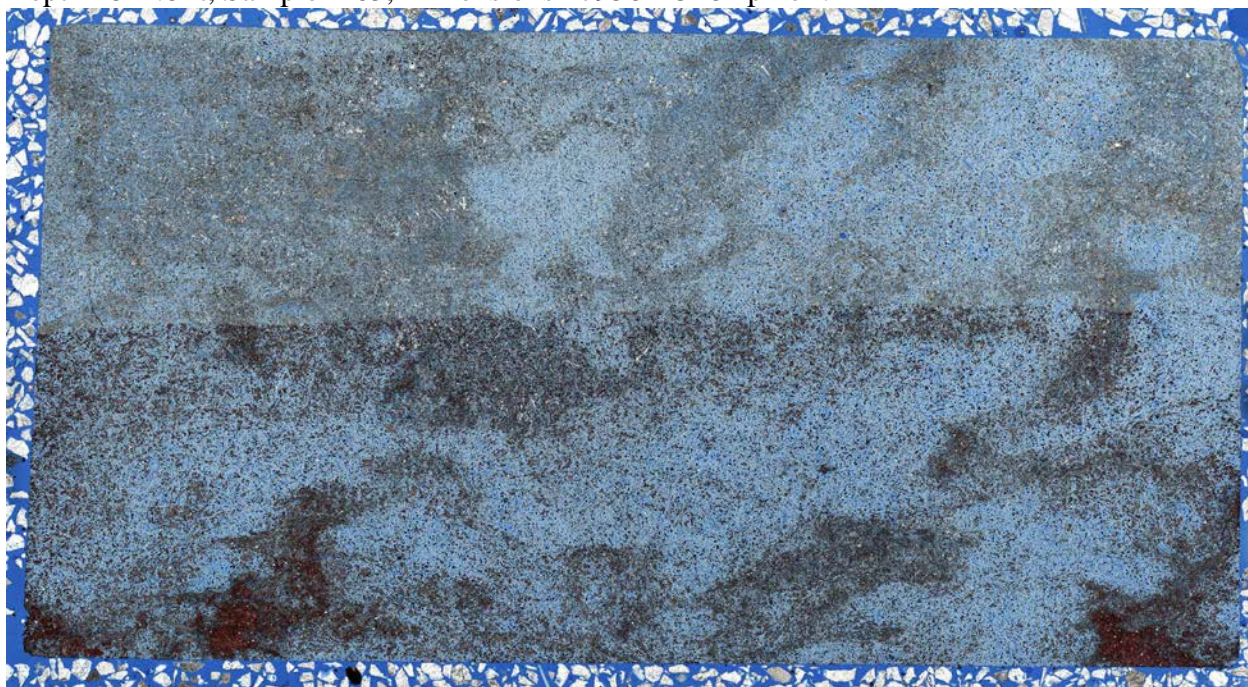
Depth 4824.8 ft, Sample 2-45, 27636x14785 pixel².



Depth 4834.75 ft, Sample 2-55, Dimensions 26957x14825 pixel².



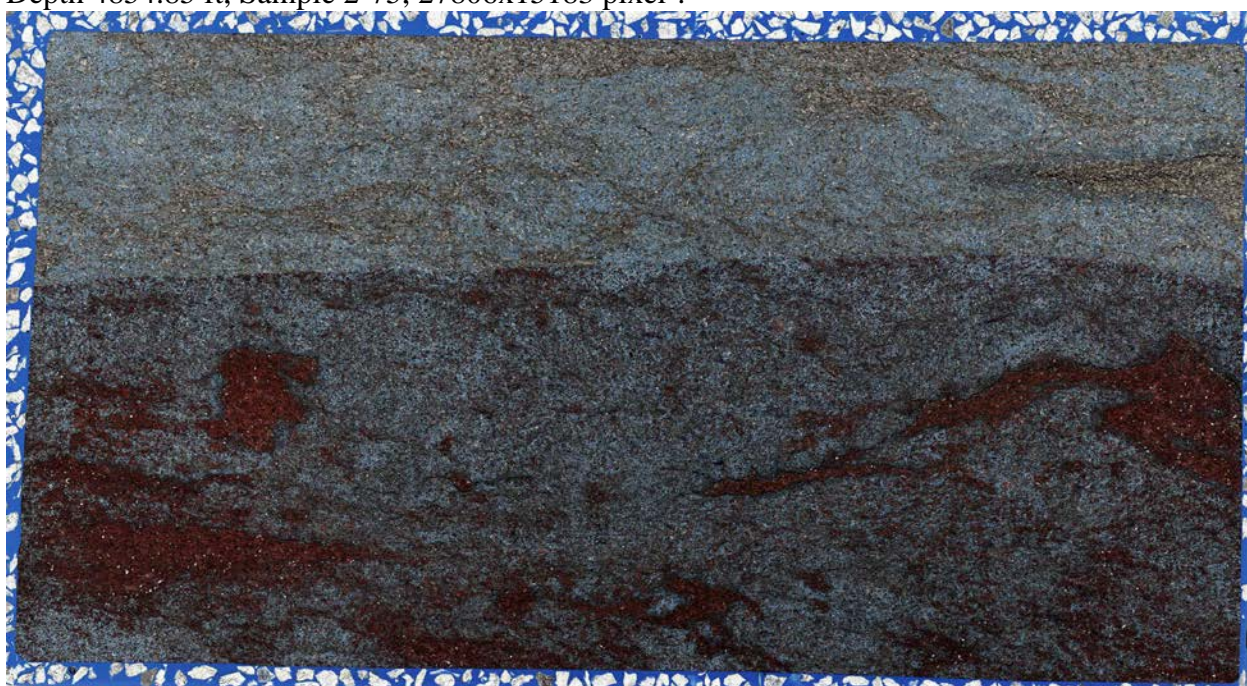
Depth 4844.8 ft, Sample 2-65, Dimensions 27956x15264 pixel².



Depth 4848.9 ft, Sample 2-69, Dimensions 27077x15383 pixel².



Depth 4854.85 ft, Sample 2-75, 27806x15183 pixel².



Depth 4864.8 ft, Sample 2-85, Dimensions 27696x14849 pixel².



Depth 4867.15 ft, Sample 2-88, Dimensions 27739x15288 pixel².



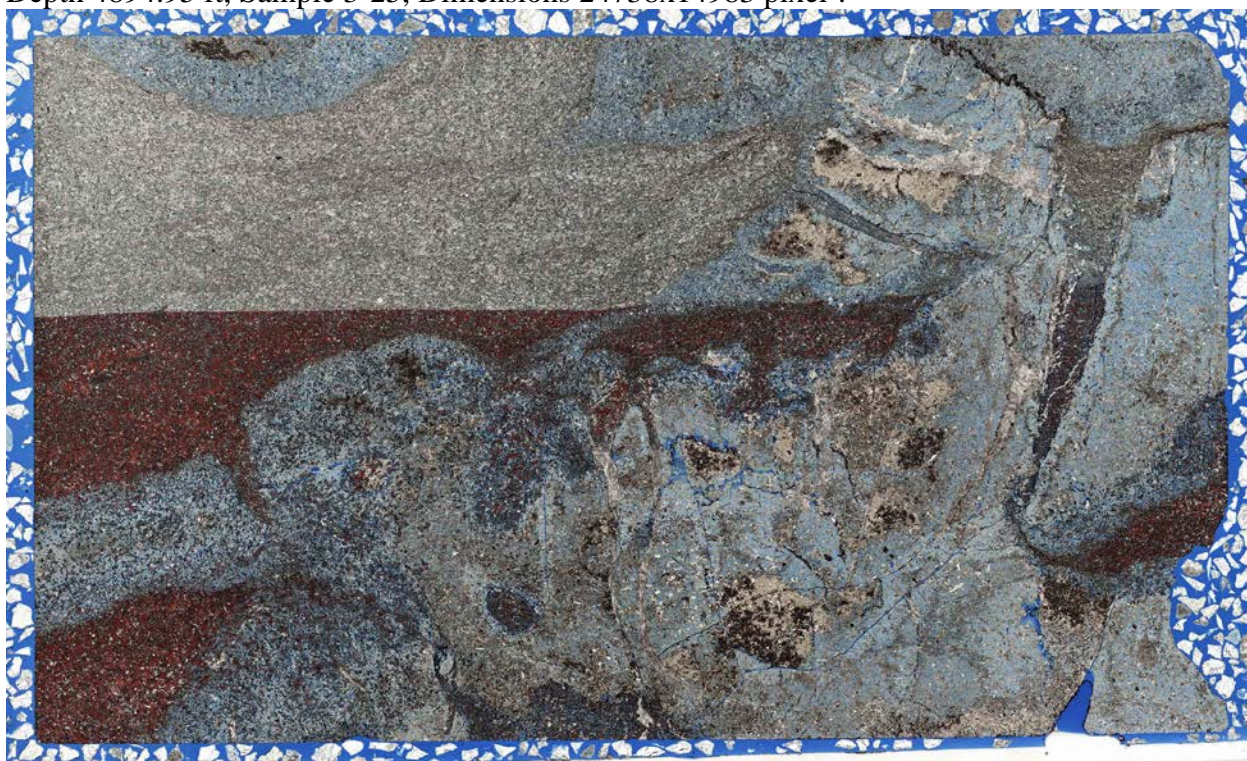
Depth 4875.15 ft, Sample 3-6, Dimensions 27897x15048 pixel².



Depth 4884.95 ft, Sample 3-15, Dimensions 27821x14815 pixel².



Depth 4894.95 ft, Sample 3-25, Dimensions 24738x14983 pixel².



Depth 4904.85 ft, Sample 3-35, Dimensions 25822x15340 pixel².



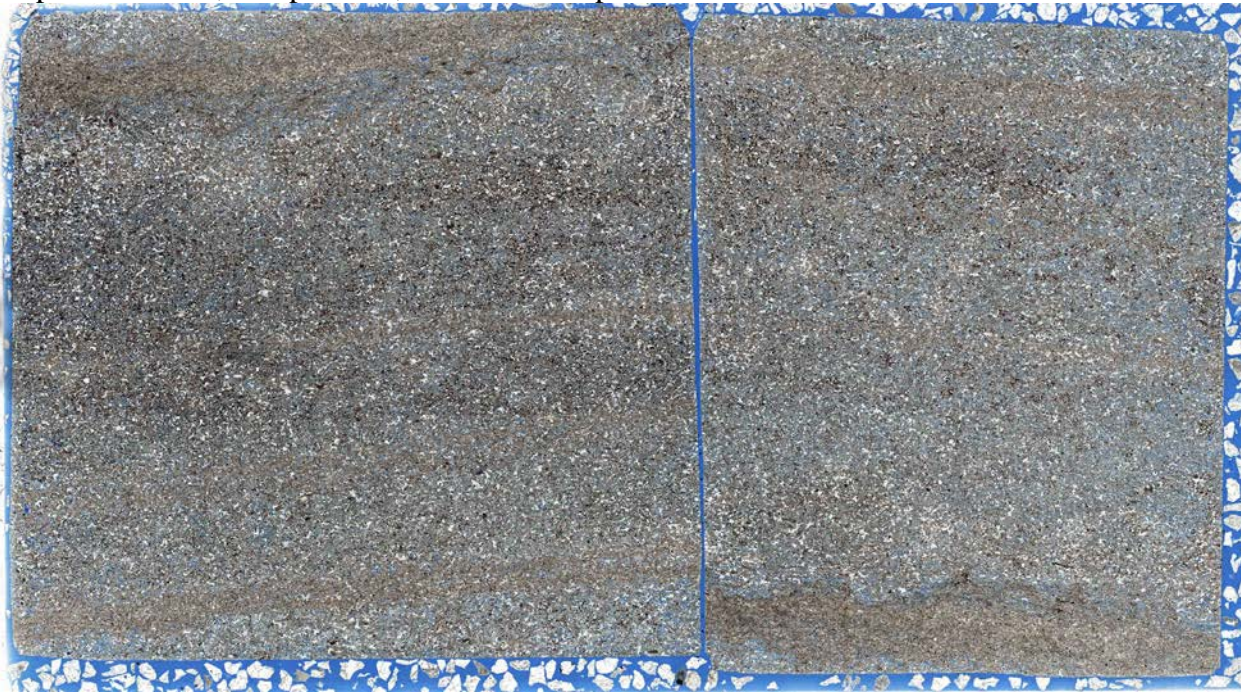
Depth 4907.7 ft, Sample 3-38, Dimensions 27906x15455 pixel².



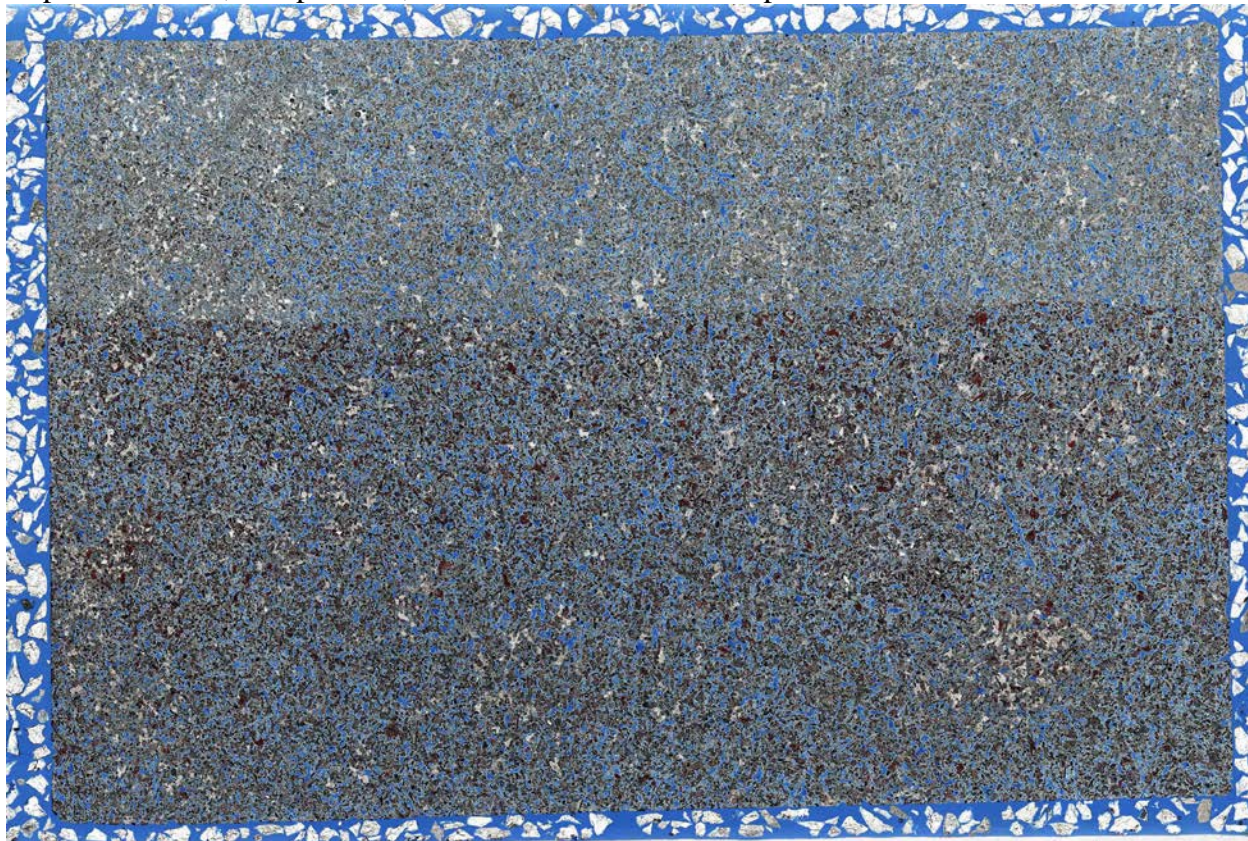
Depth 4914.65 ft, Sample 3-45, Dimensions 25772x14862 pixel².



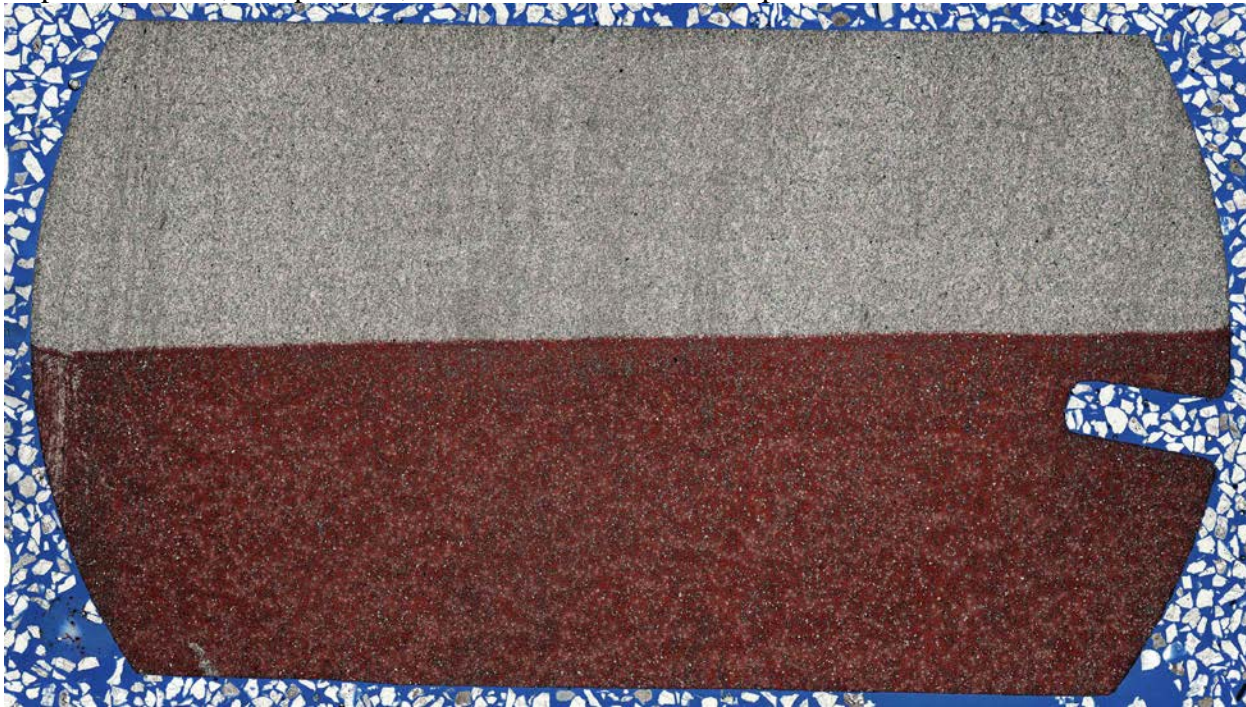
Depth 4921.35 ft, Sample 3-52, 27623x15176 pixel².



Depth 4925.25 ft, Sample 3-56, Dimensions 22858x15428 pixel².



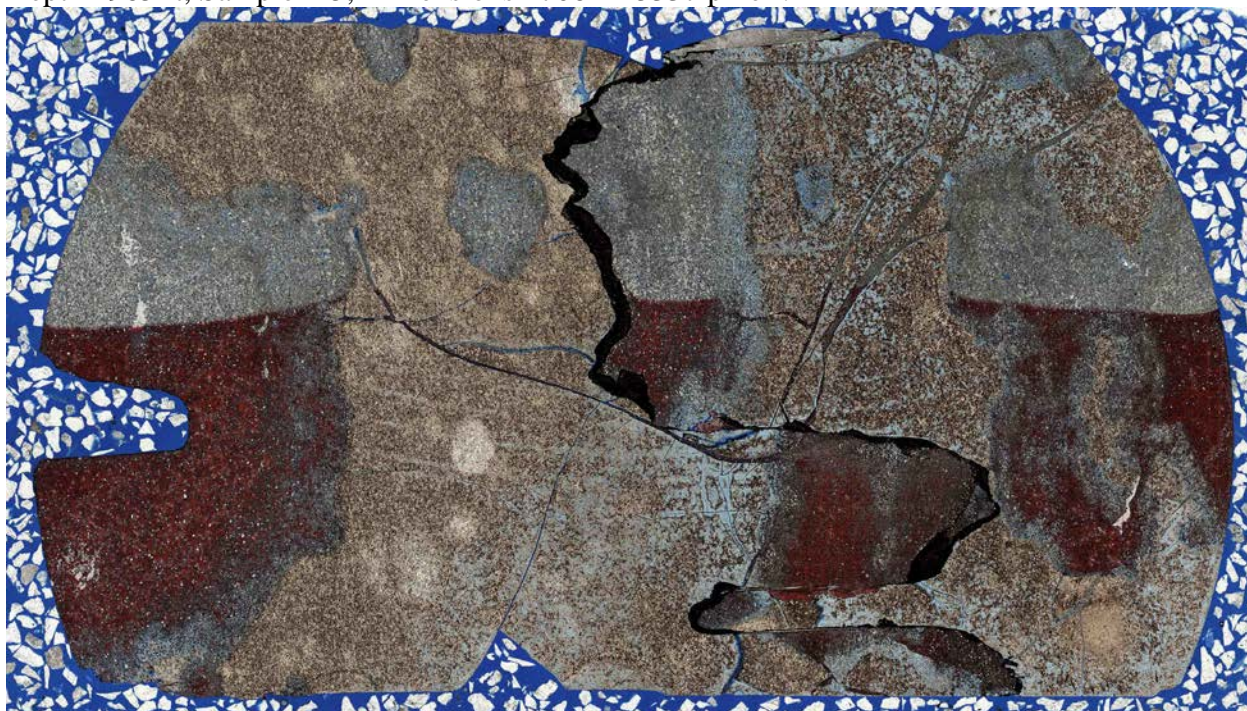
Depth 4933.95 ft, Sample 3-64, Dimensions 26902x15178 pixel².



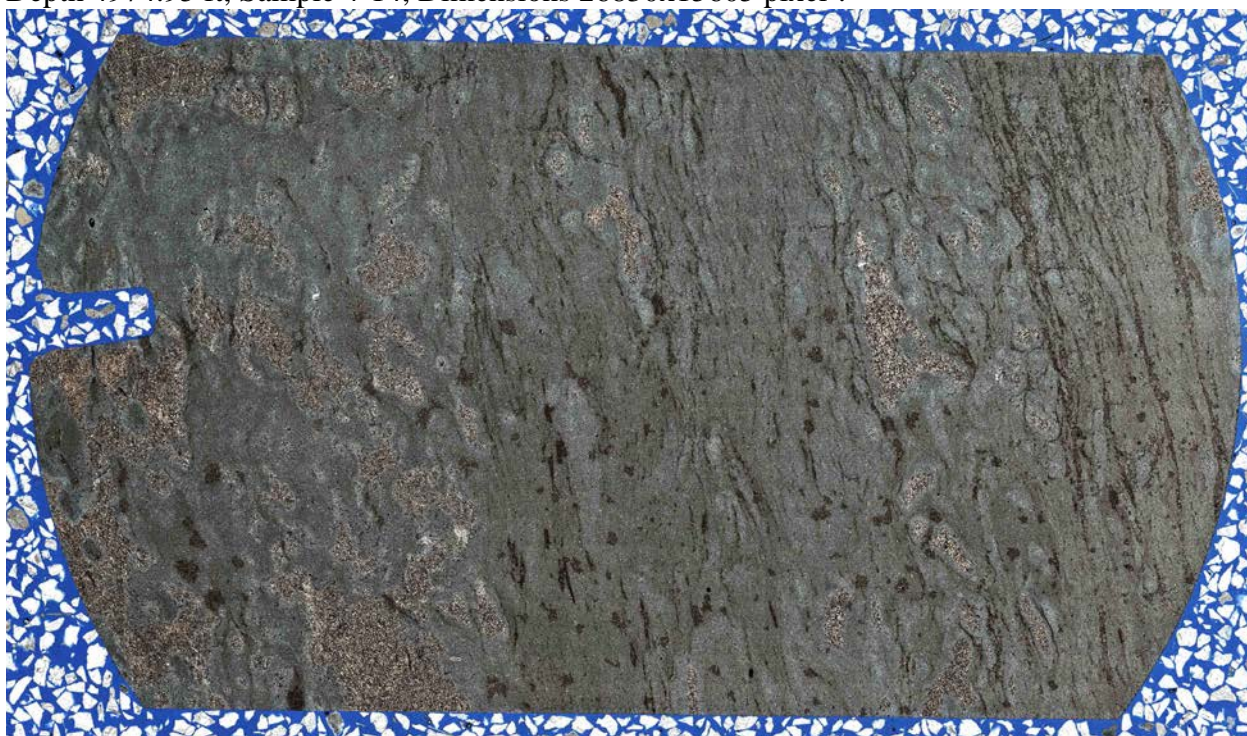
Depth 4943.55 ft, Sample 3-74, Dimensions 26398x14825 pixel².



Depth 4965 ft, Sample 4-5, Dimensions 27061x15337 pixel².



Depth 4974.95 ft, Sample 4-14, Dimensions 26830x15605 pixel².



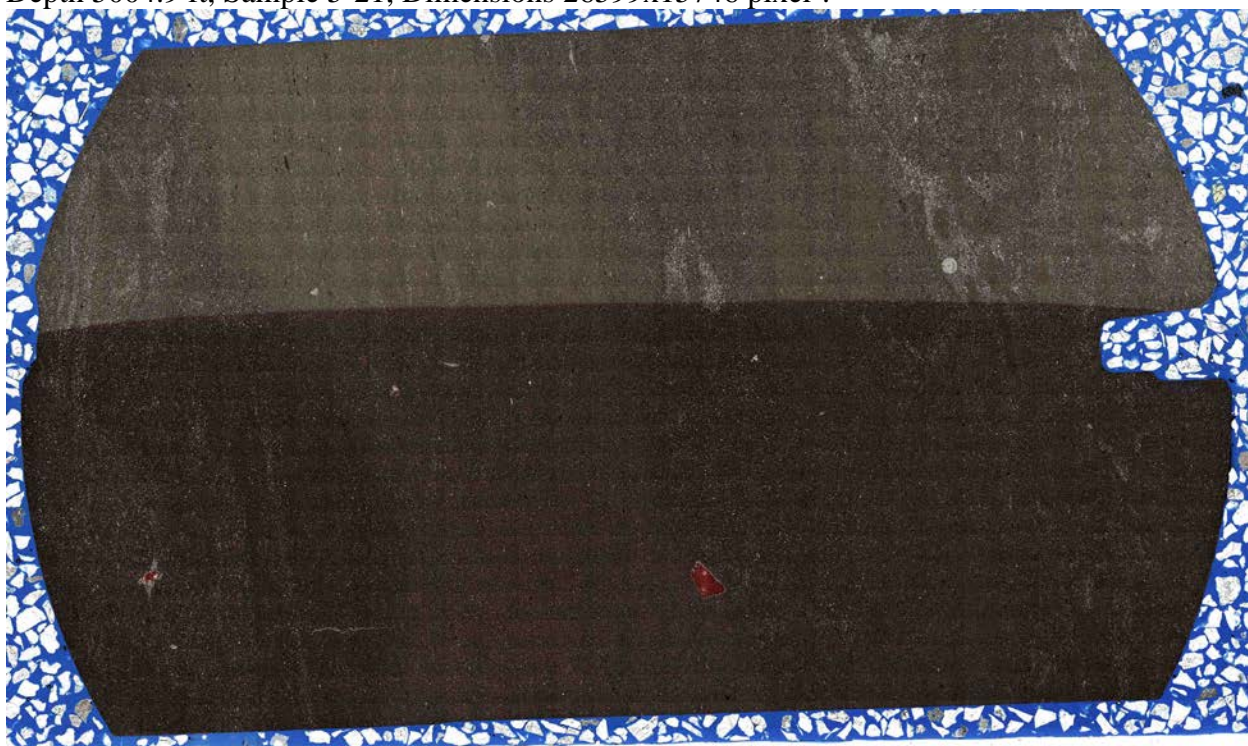
Depth 4986.4 ft, Sample 5-3, Dimensions 26760x15240 pixel².



Depth 4995.3 ft, Sample 5-12, 26880x15160 pixel².



Depth 5004.9 ft, Sample 5-21, Dimensions 26599x15746 pixel².



Depth 5015.35 ft, Sample 6-9, 26378x15298 pixel².



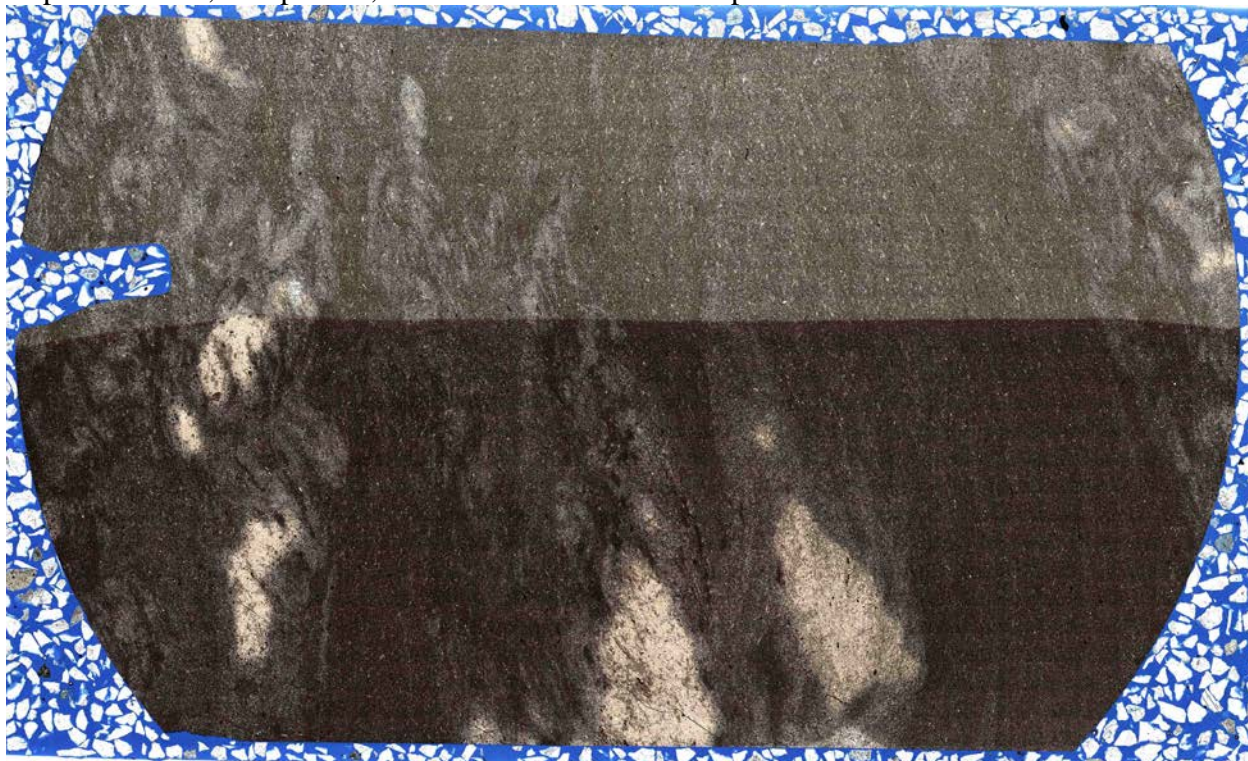
Depth 5024.45 ft, Sample 6-18, Dimensions 24267x15765 pixel².



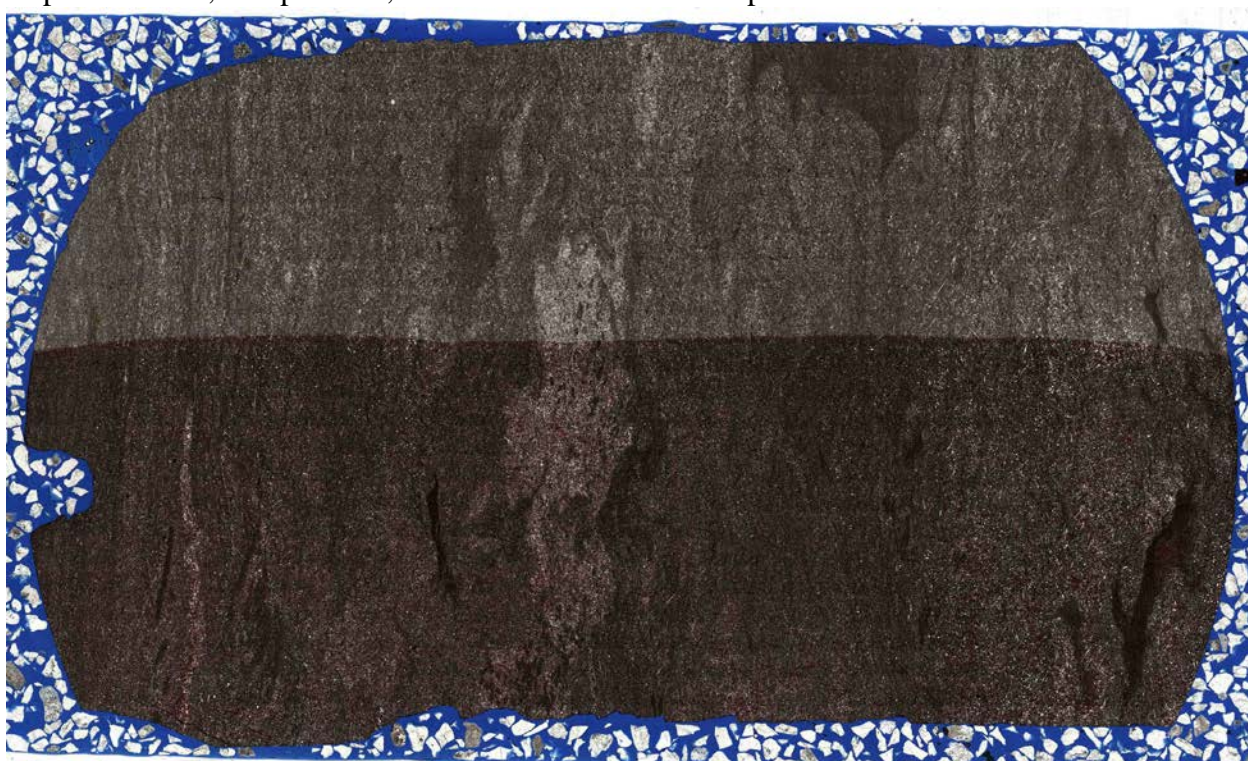
Depth 5035.5 ft, Sample 7-8, Dimensions 26672x15116 pixel².



Depth 5043.9 ft, Sample 8-3, Dimensions 26279x16002 pixel².



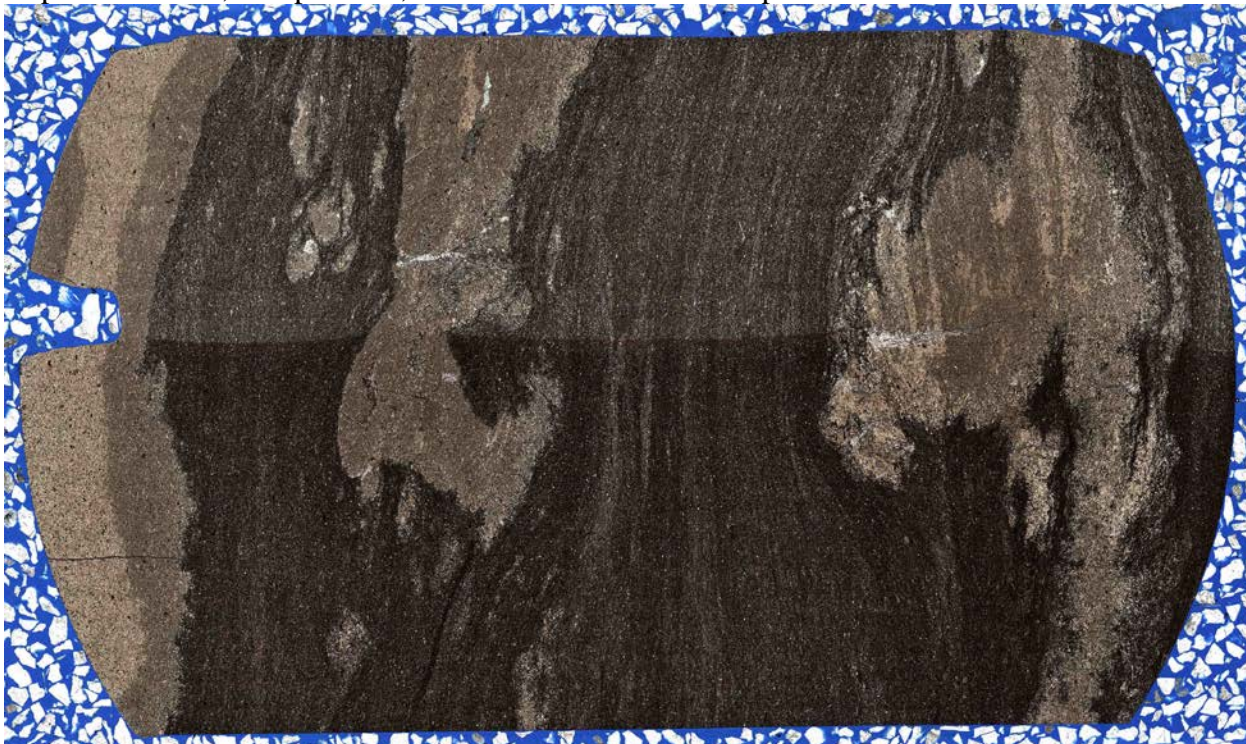
Depth 5053.8 ft, Sample 8-13, Dimensions 26512x16117 pixel².



Depth 5064.9 ft, Sample 9-3, Dimensions 26132x15521 pixel².



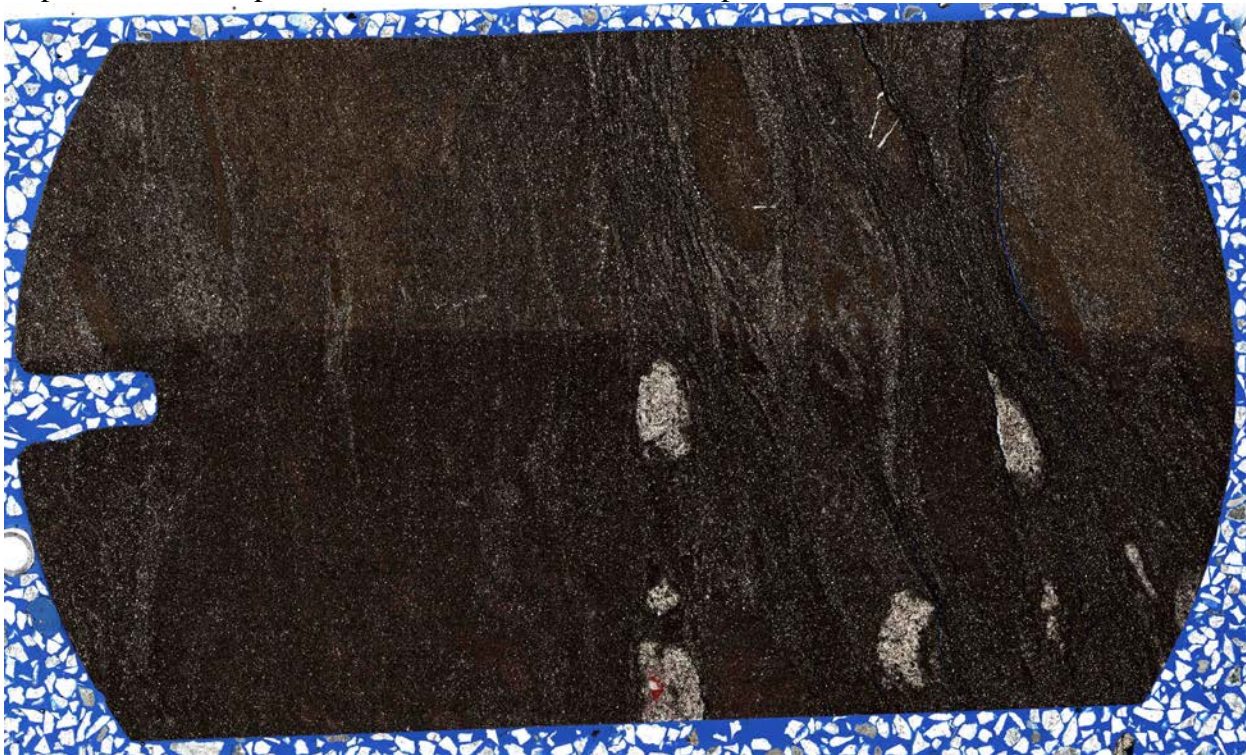
Depth 5074.95 ft, Sample 9-13, Dimensions 26440x15722 pixel².



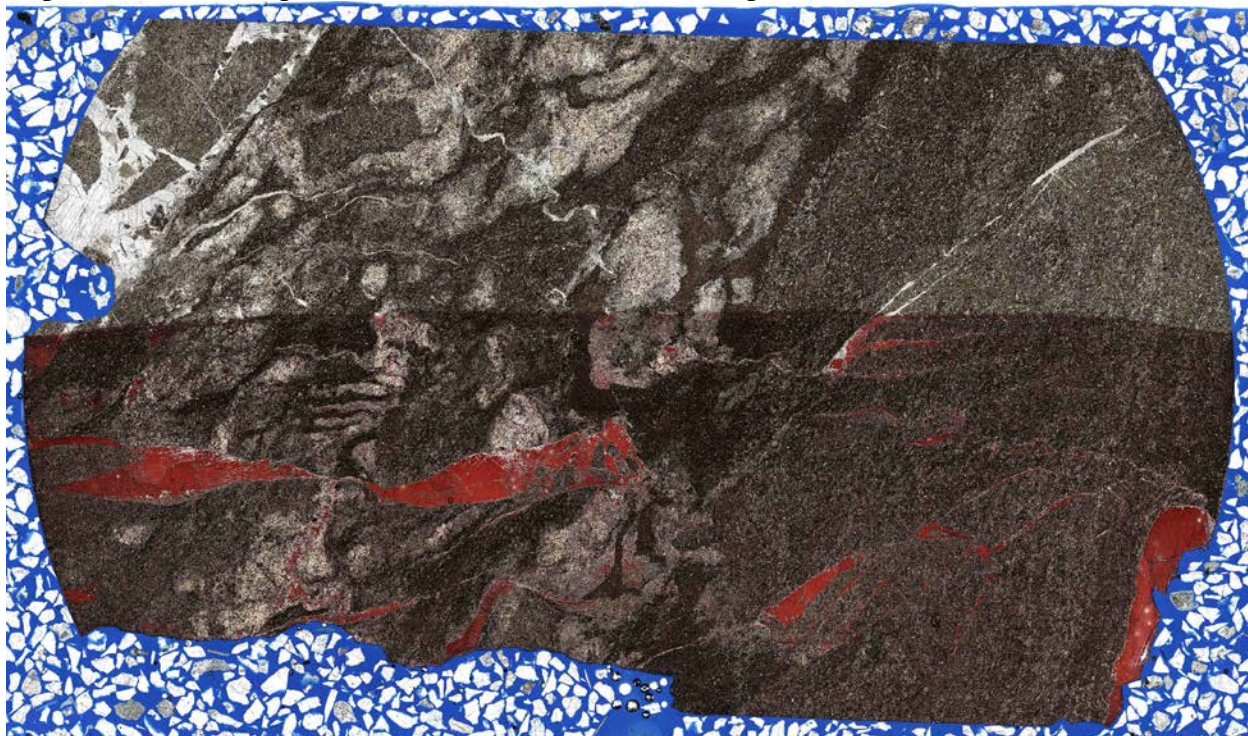
Depth 5085 ft, Sample 9-24, Dimensions 26360x16043 pixel².



Depth 5095 ft, Sample 9-34, Dimensions 26360x15882 pixel².



Depth 5105.2 ft, Sample 9-44, Dimensions 26600x15682 pixel².



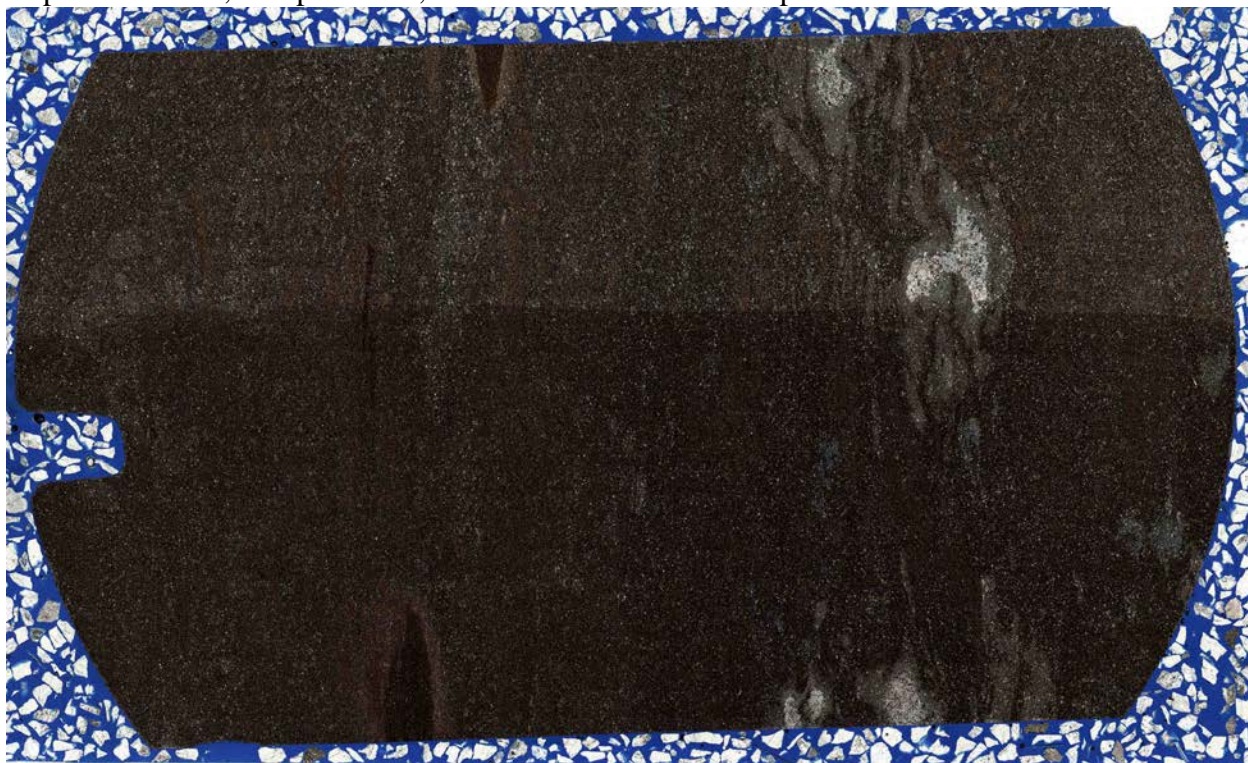
Depth 5115 ft, Sample 9-54, Dimensions 26560x15922 pixel².



Depth 5134.85 ft, Sample 10-12, Dimensions 26200x15882 pixel².



Depth 5144.75 ft, Sample 10-22, Dimensions 26311x16036 pixel².



Depth 5155.15 ft, Sample 11-1, 26680x16043 pixel².



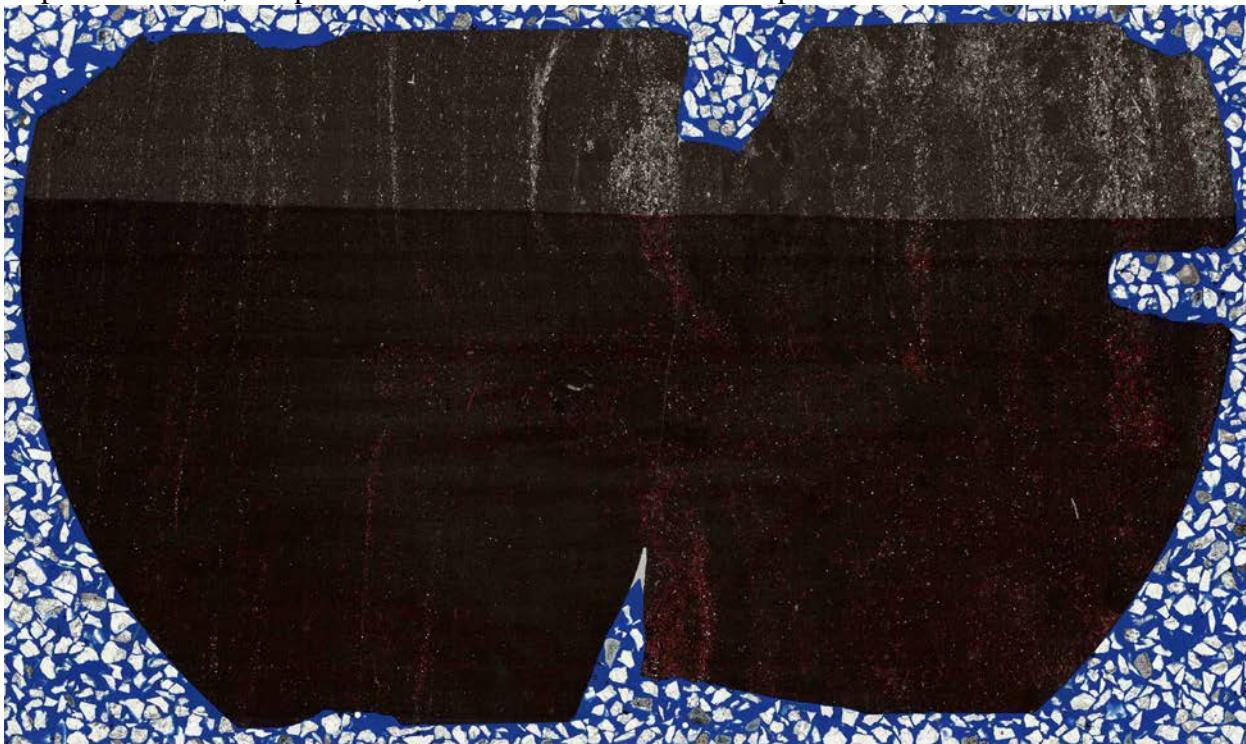
Depth 5165.1 ft, Sample 11-11, Dimensions 26426x14759 pixel².



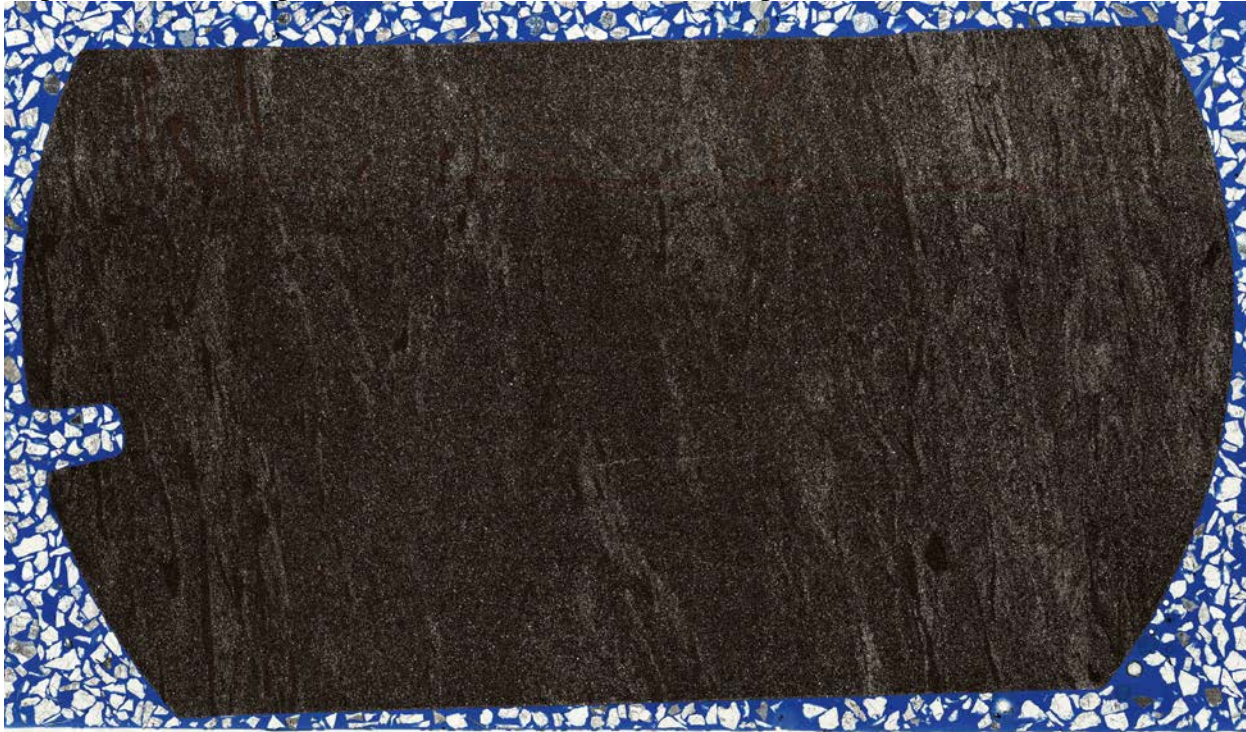
Depth 5215.15 ft, Sample 13-18, Dimensions 24389x15909 pixel².



Depth 5224.75 ft, Sample 13-27, Dimensions 26391x15716 pixel².



Depth 5245.2 ft, Sample 13-48, Dimensions 26552x15596 pixel².



Depth 5255.15 ft, Sample 13-58, Dimensions 26672x15637 pixel².

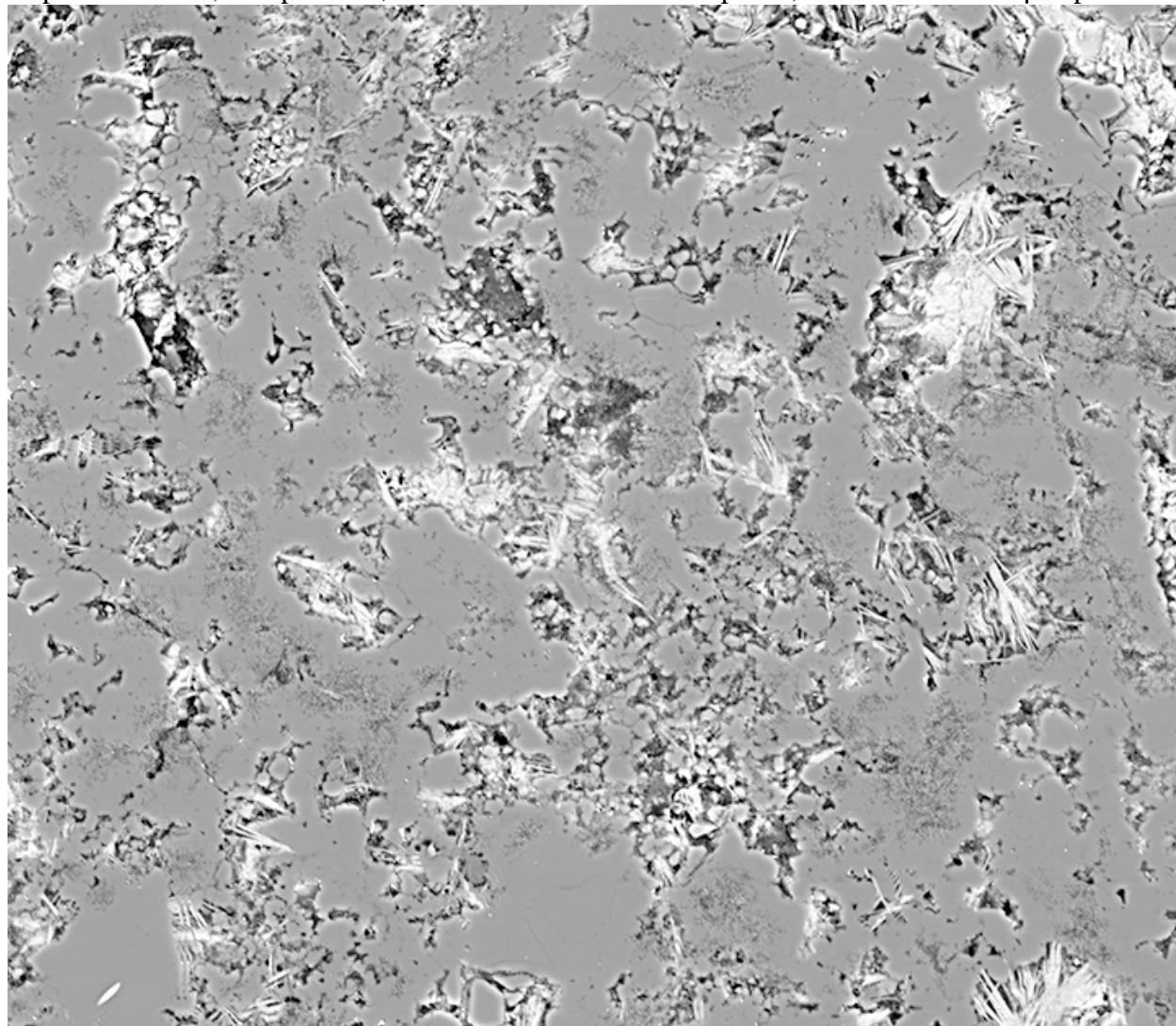


Depth 5265.15 ft, Sample 13-68, Dimensions 26299x14819 pixel².

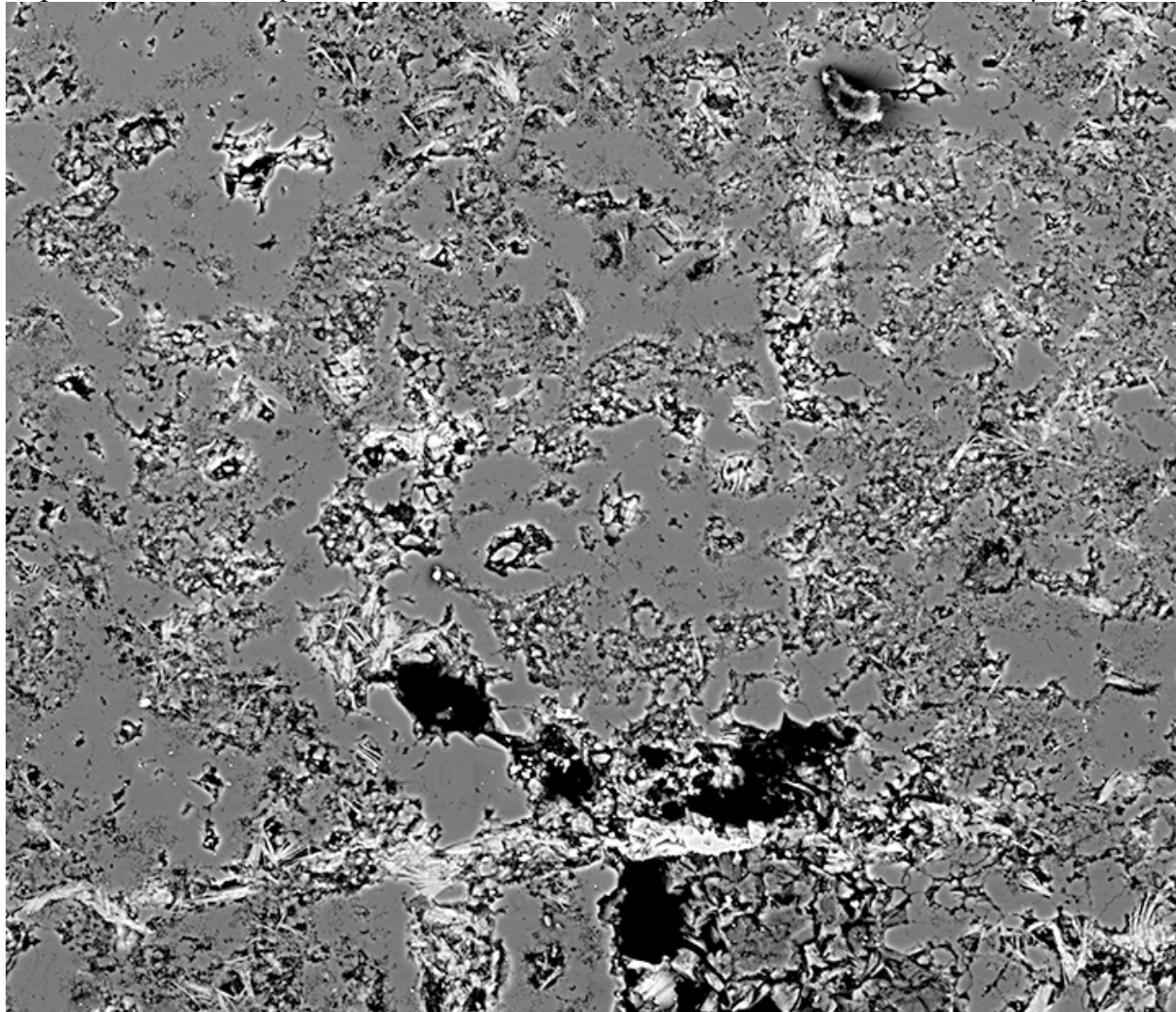


APPENDIX A2: SCANNING ELECTRON MICROSCOPE PHOTOMICROGRAPHS

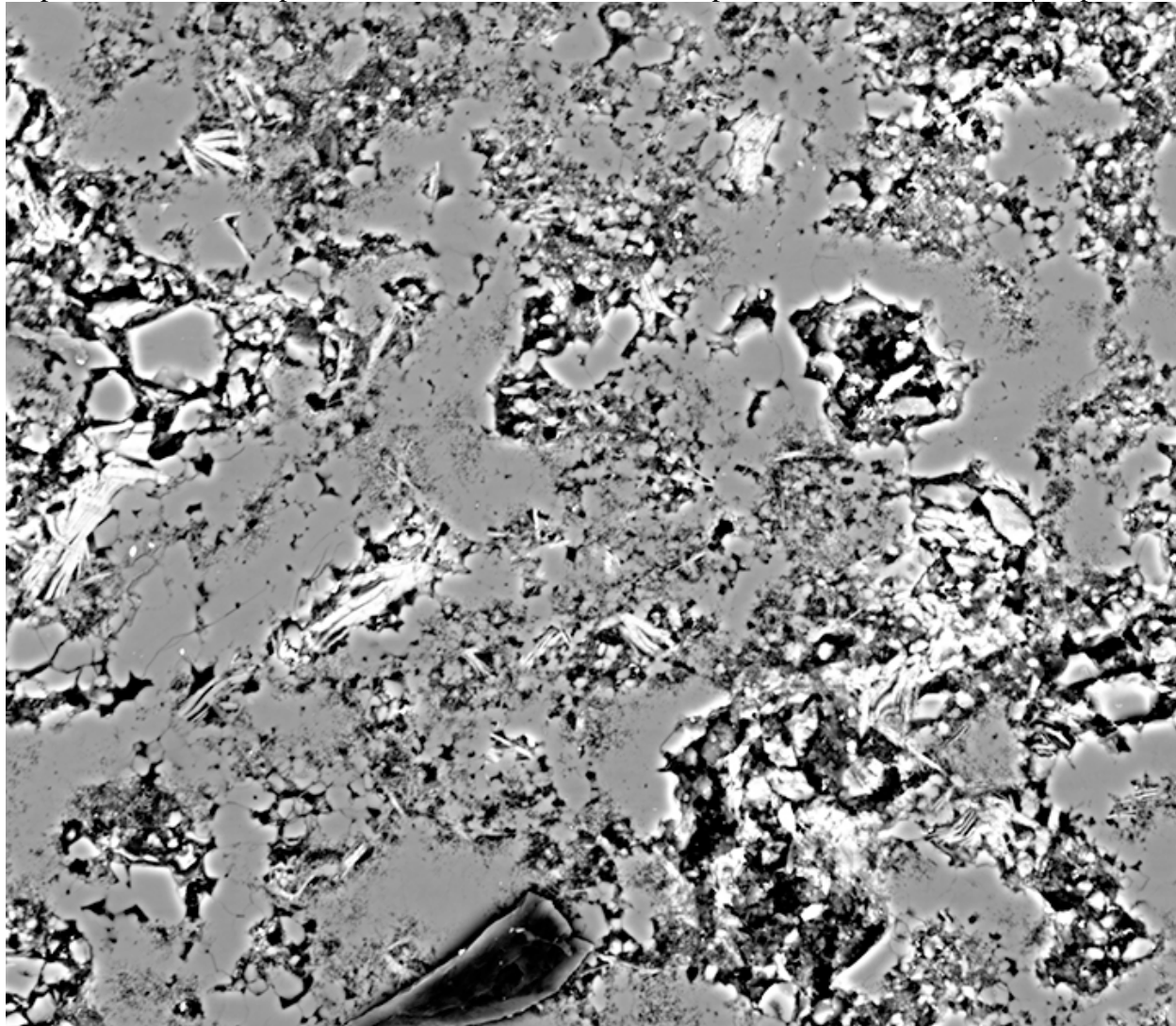
Depth 4776.75 ft, Sample 1-61, Dimensions 25950x22590 pixel², scale 0.00835066 $\mu\text{m}/\text{pixel}$



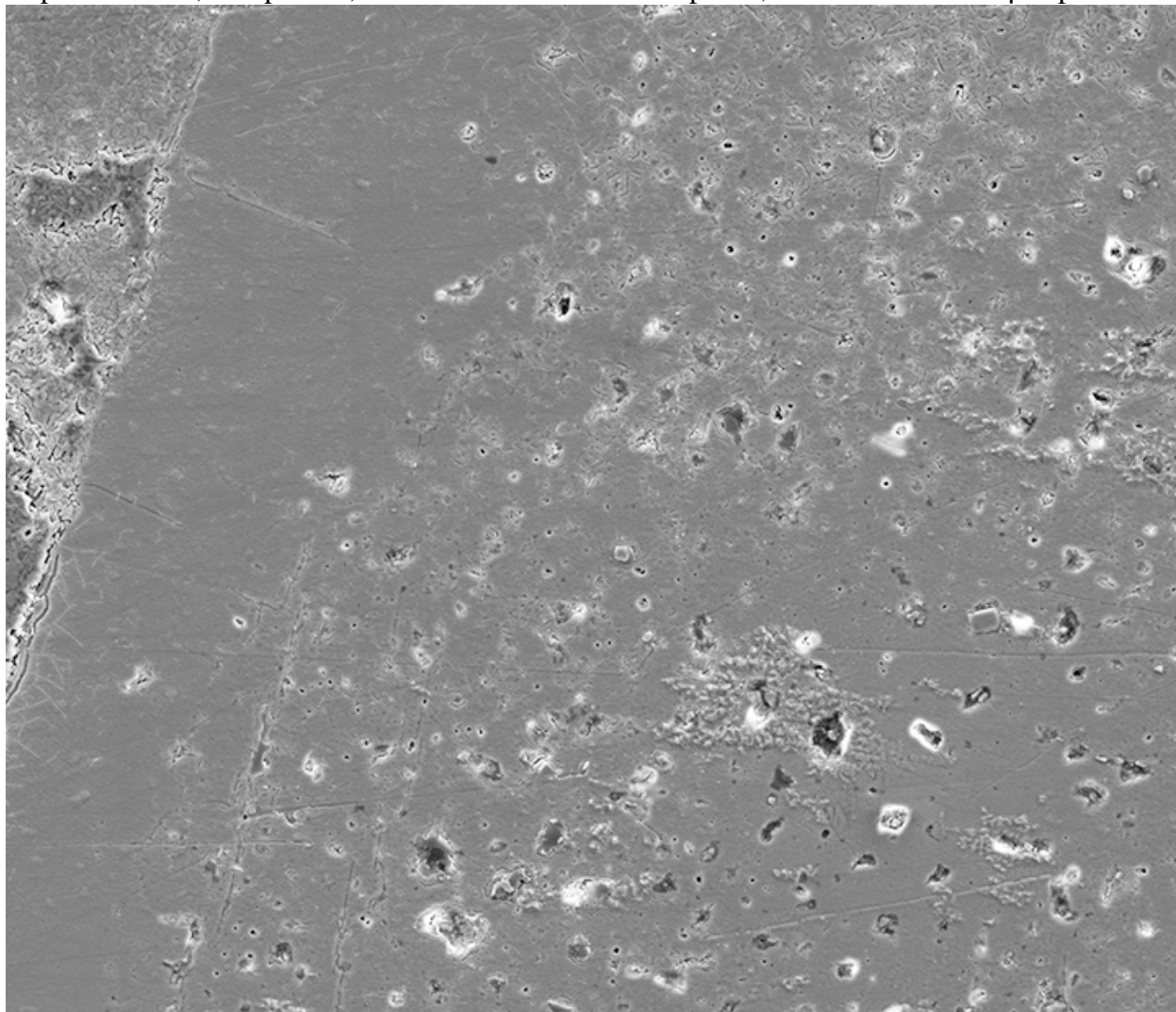
Depth 4776.75 ft, Sample 1-61, Dimensions 18603x16048pixel², scale 0.015315137 μm/pixel



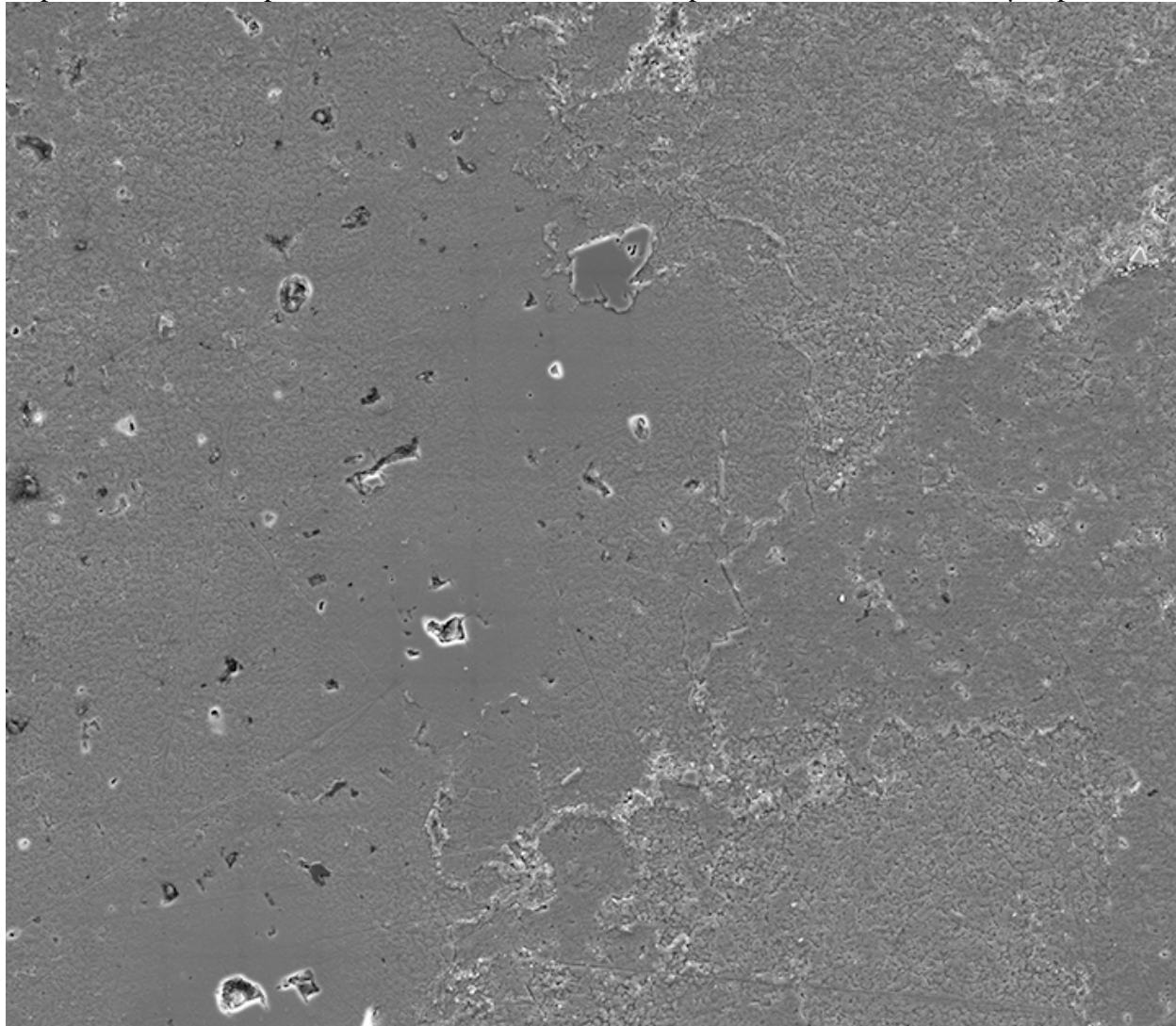
Depth 4776.75 ft, Sample 1-61, Dimensions 18779x16297pixel², scale 0.007657568 μm/pixel



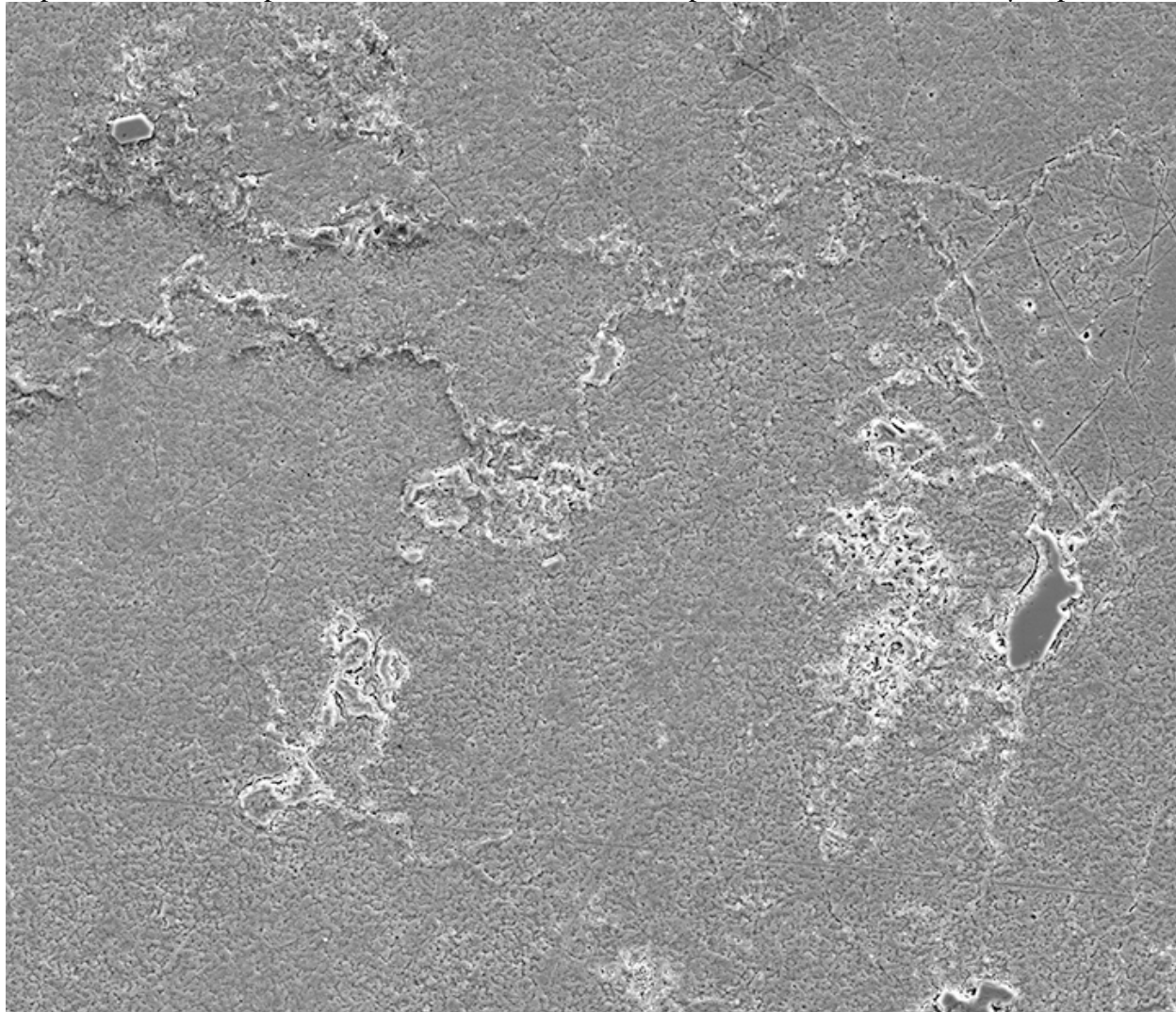
Depth 4782.4 ft, Sample 2-3, Dimensions 18671x16062 pixel², scale 0.016992188 μm/pixel



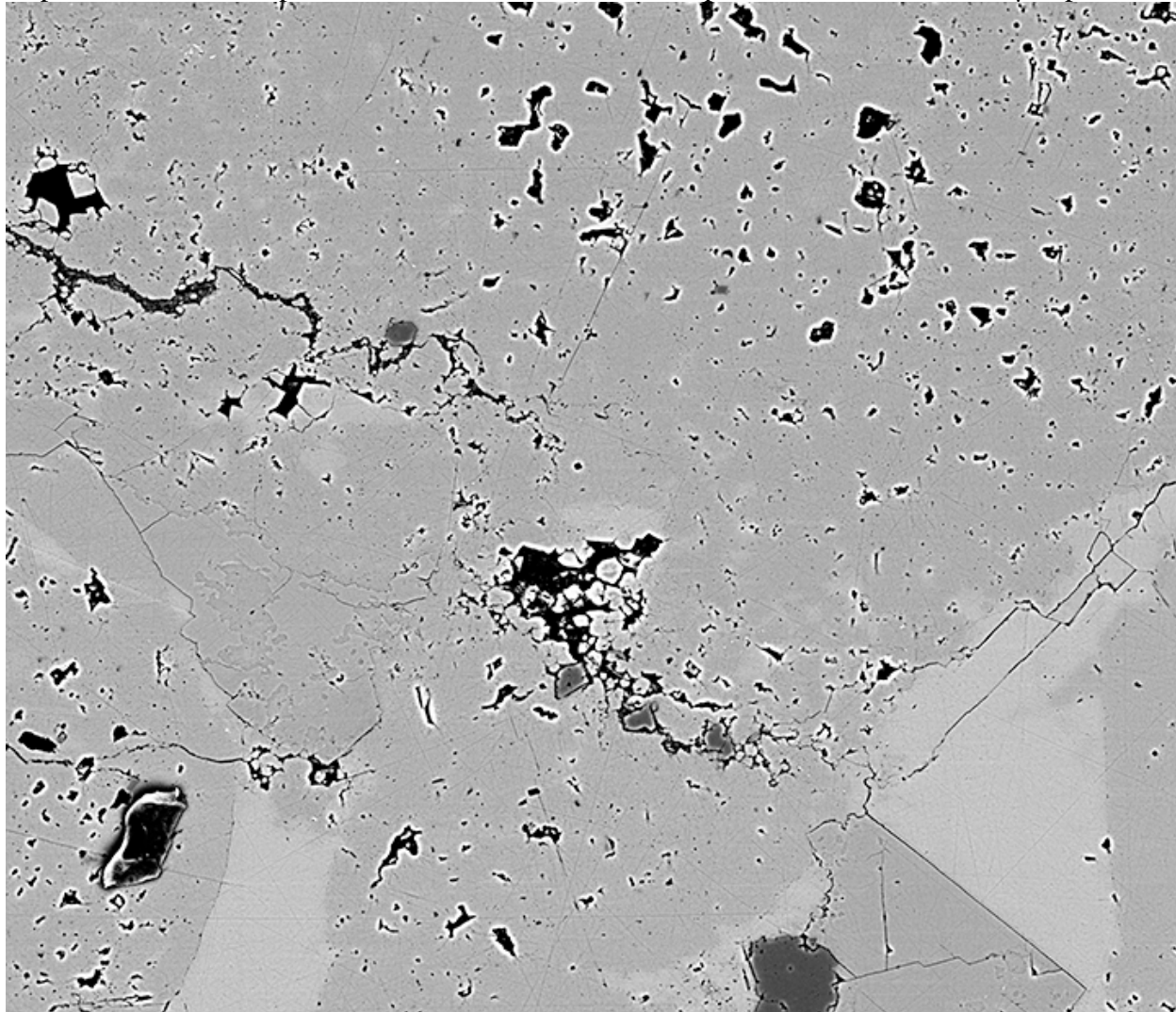
Depth 4782.4 ft, Sample 2-3, Dimensions 27820x24095 pixel², scale 0.012890625 μm/pixel



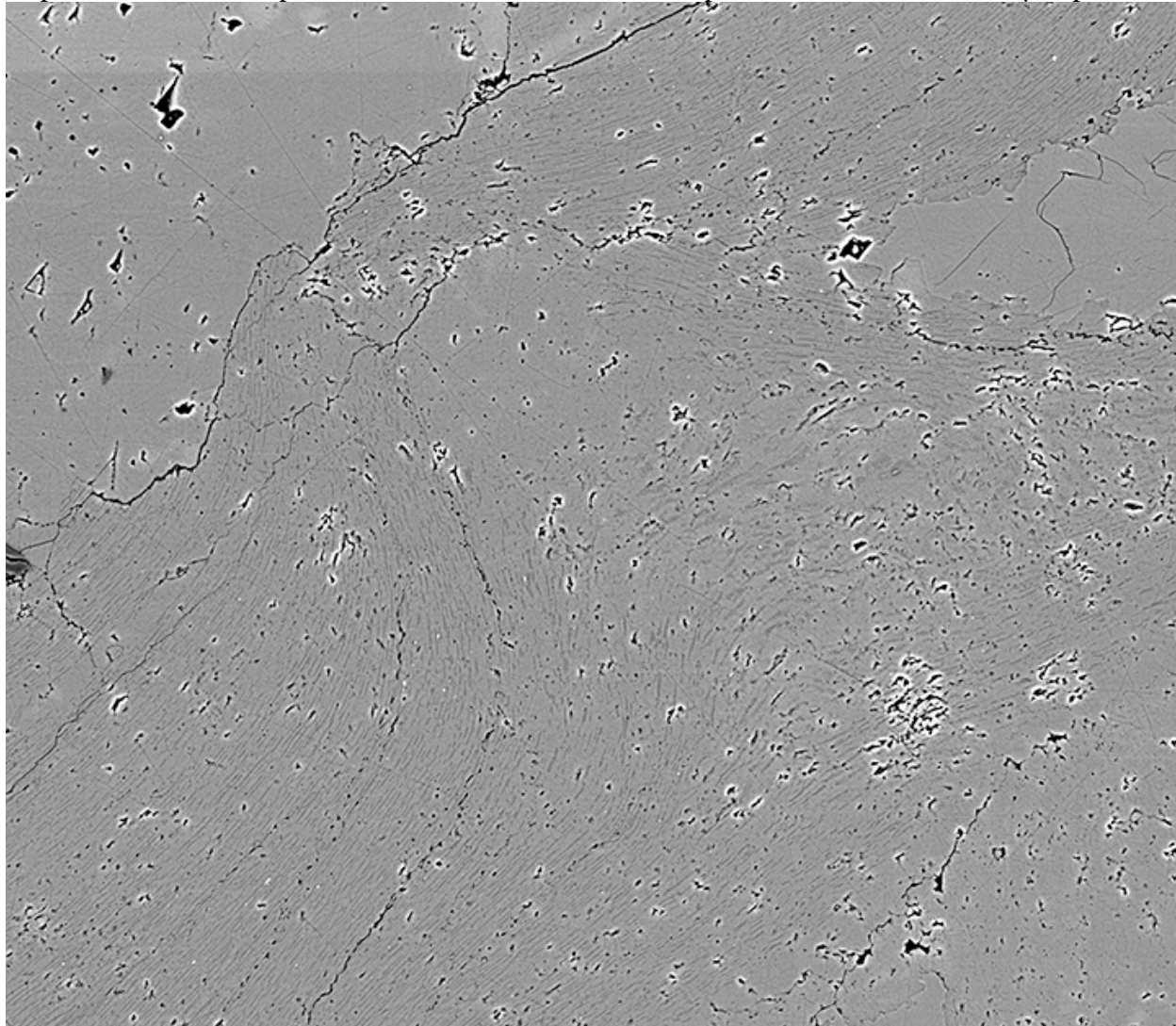
Depth 4782.4 ft, Sample 2-3, Dimensions 27926x24132 pixel², scale 0.012890625 μm/pixel



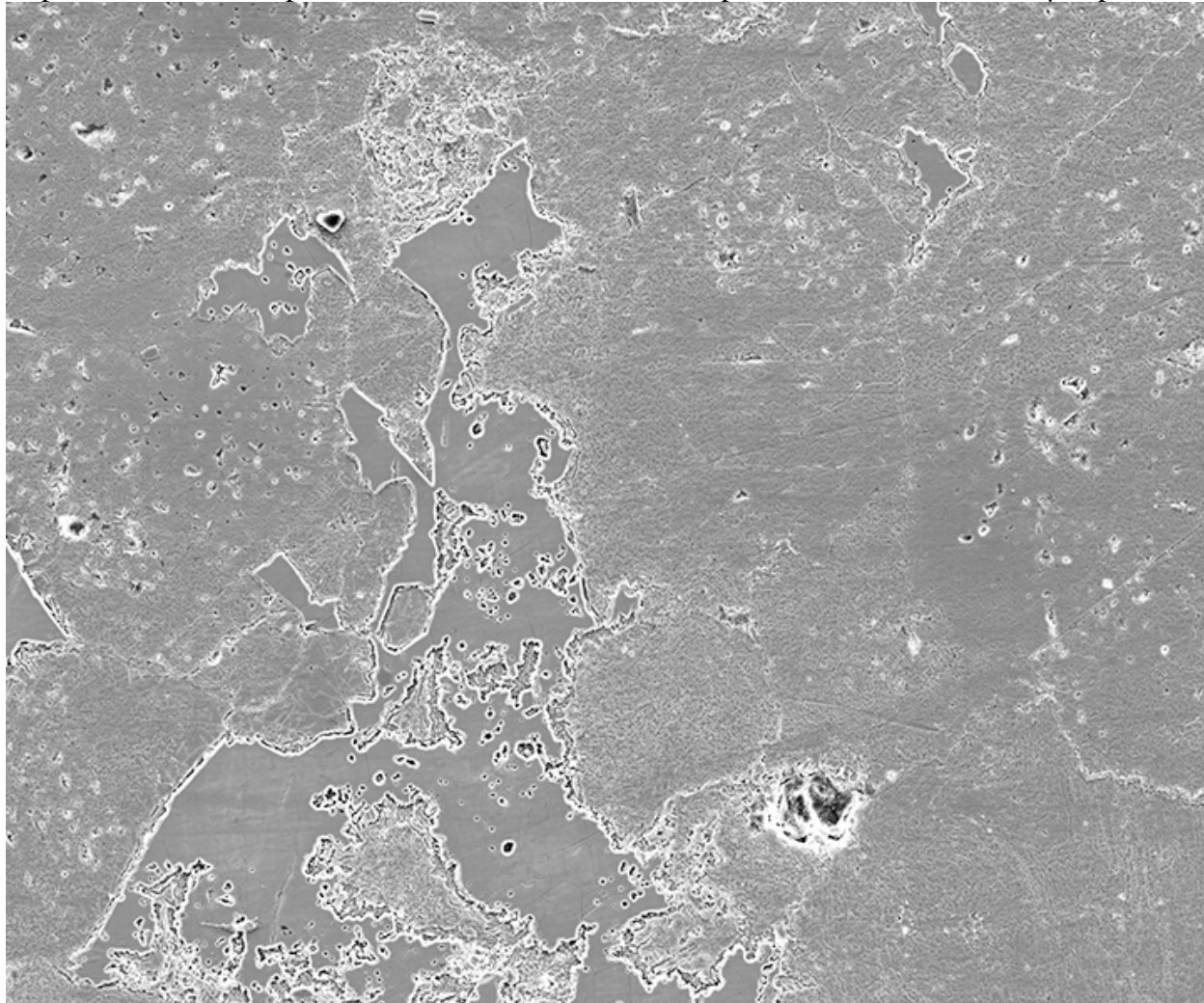
Depth 4784.95 ft, Sample 2-5, Dimensions 27902x24088 pixel², scale 0.012890625μm/pixel



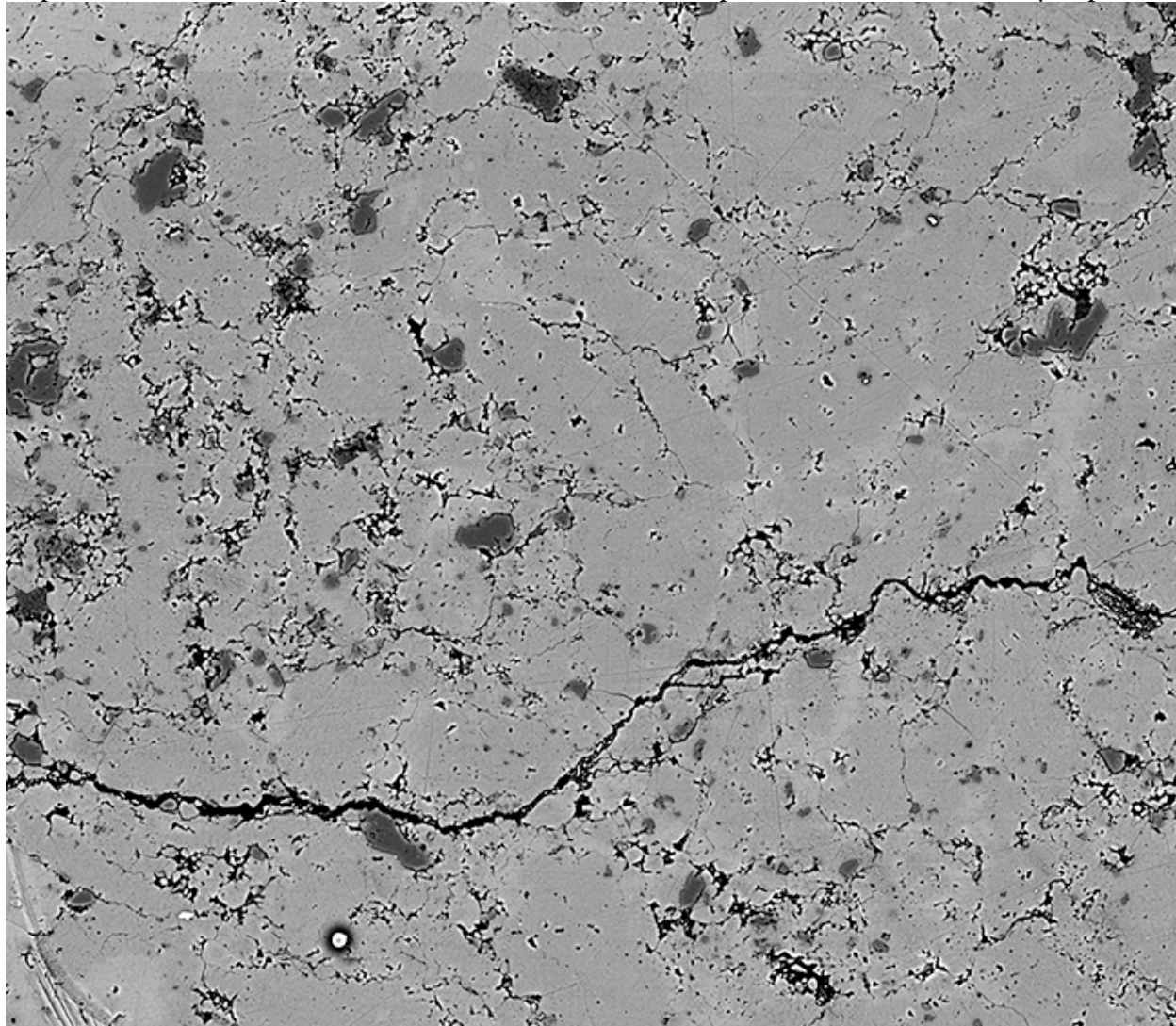
Depth 4784.95 ft, Sample 2-5, Dimensions 27847x24183 pixel², scale 0.012890625 $\mu\text{m}/\text{pixel}$



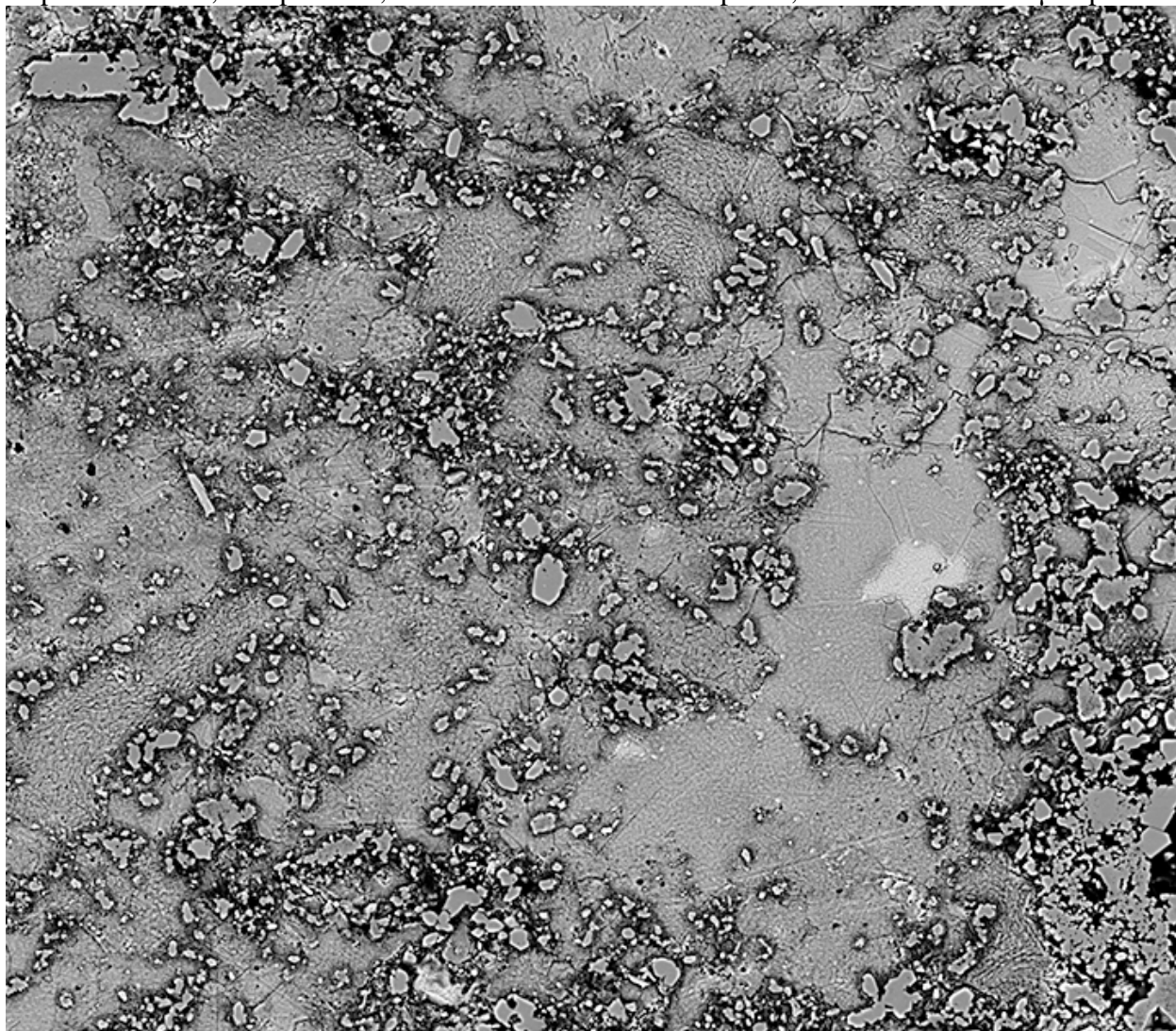
Depth 4784.95 ft, Sample 2-5, Dimensions 46382x38799 pixel², scale 0.012890625 μm/pixel



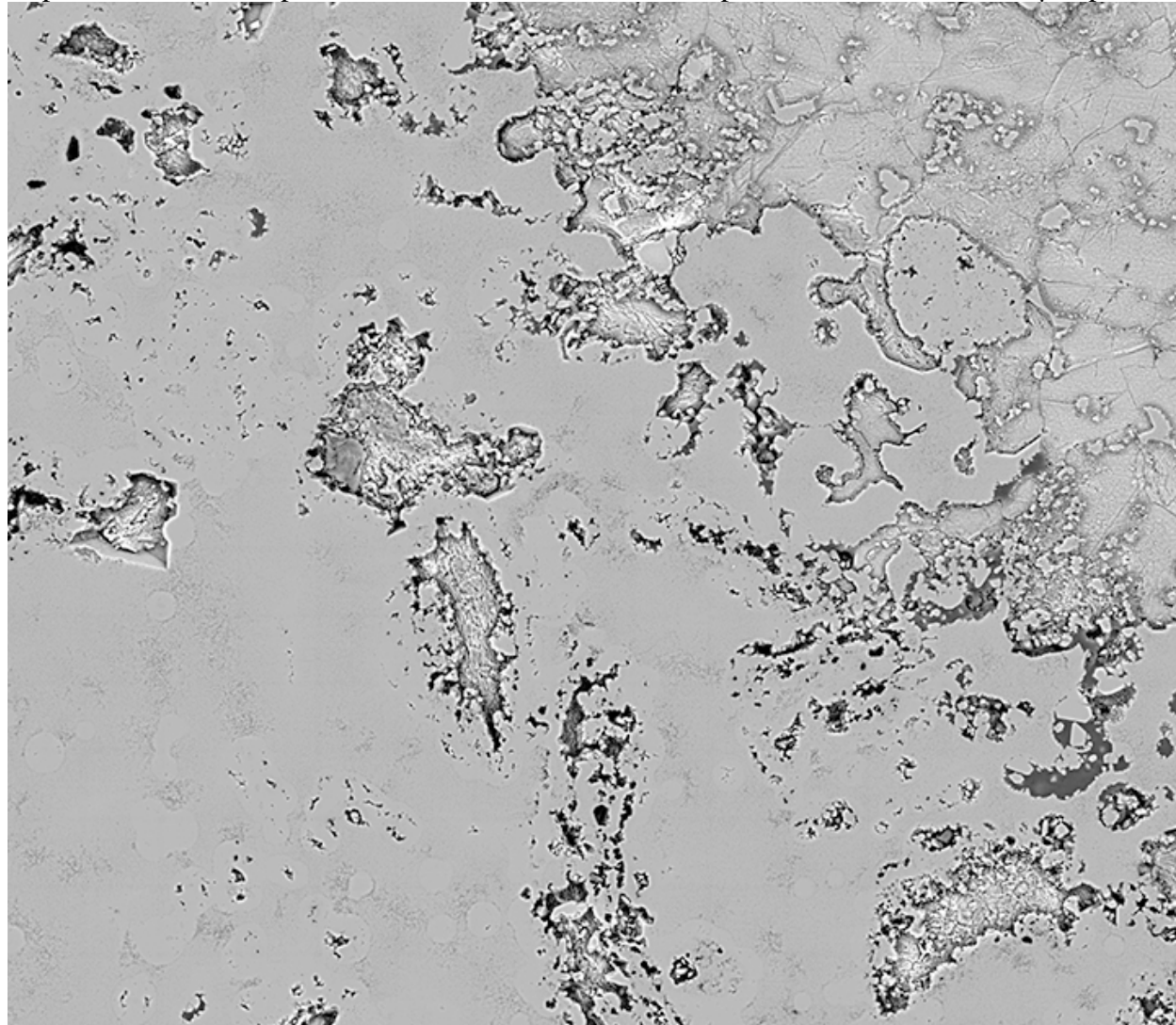
Depth 4794.95 ft, Sample 2-15, Dimensions 27339x23726 pixel², scale 0.014193555 μm/pixel



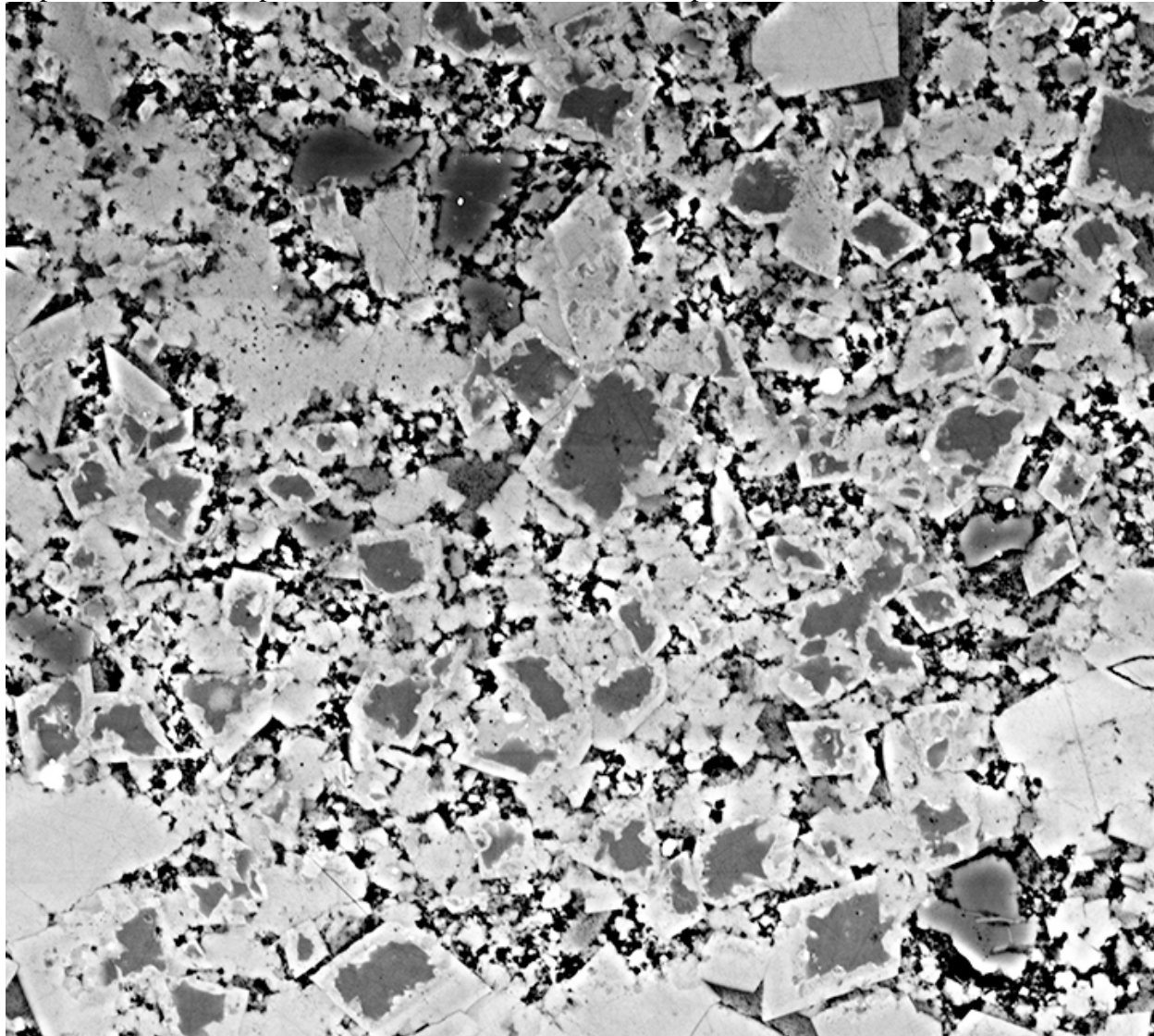
Depth 4794.95 ft, Sample 2-15, Dimensions 27705x24035 pixel², scale 0.014193555 μm/pixel



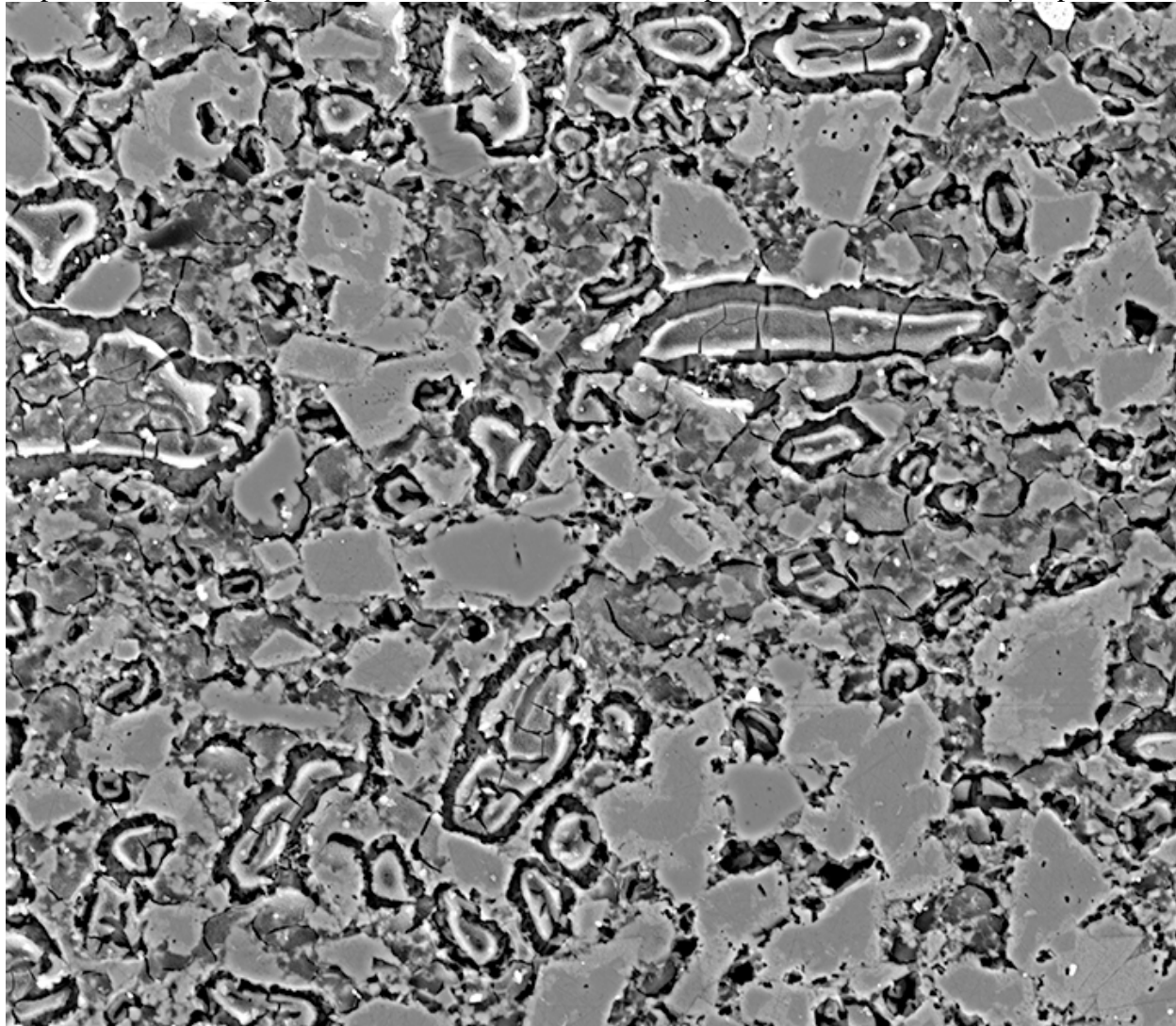
Depth 4794.95 ft, Sample 2-15, Dimensions 27652x23956 pixel², scale 0.016879053 μm/pixel



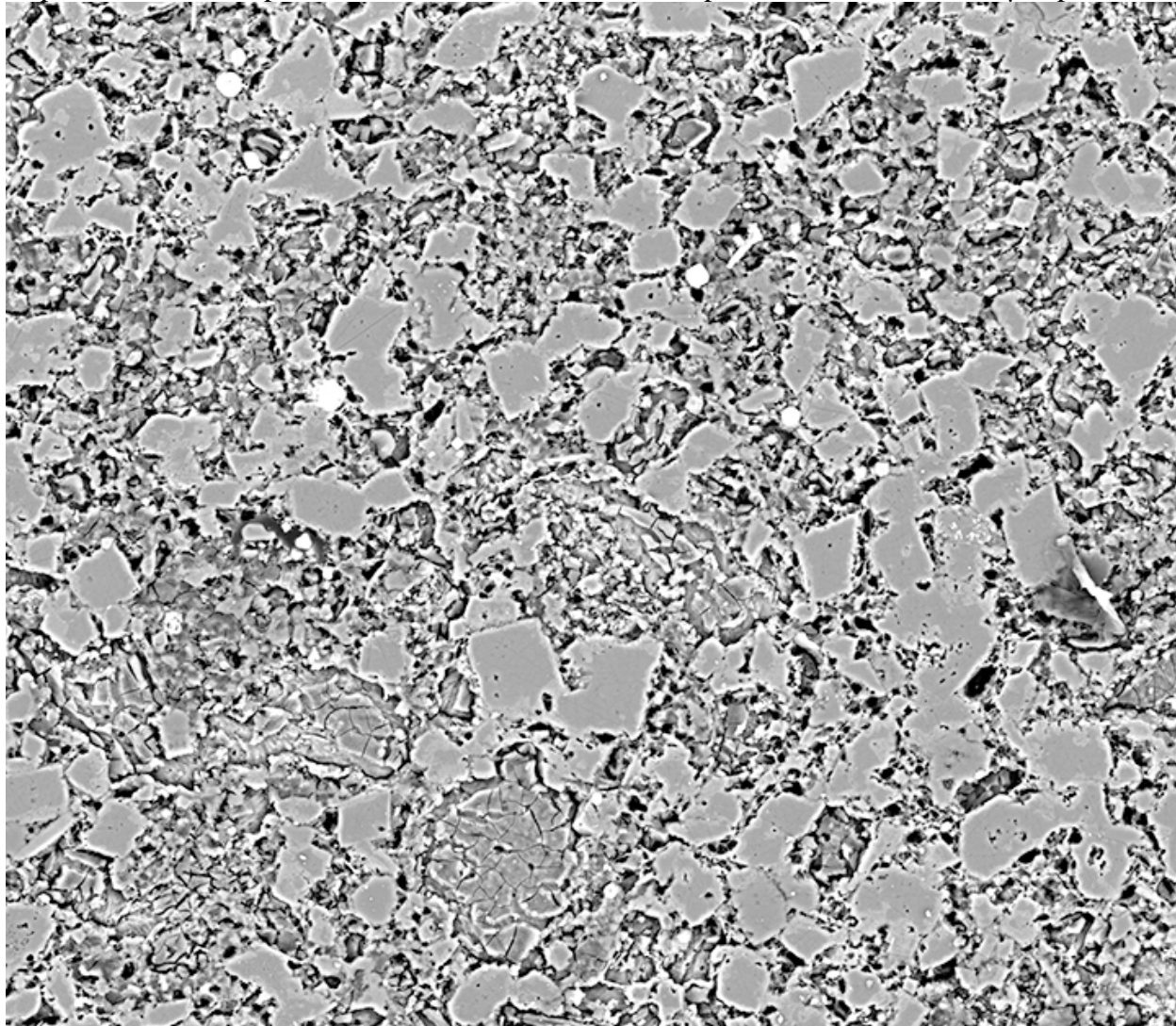
Depth 4797.1 ft, Sample 2-18, Dimensions 12631x11257 pixel², scale 0.12872467 μm/pixel



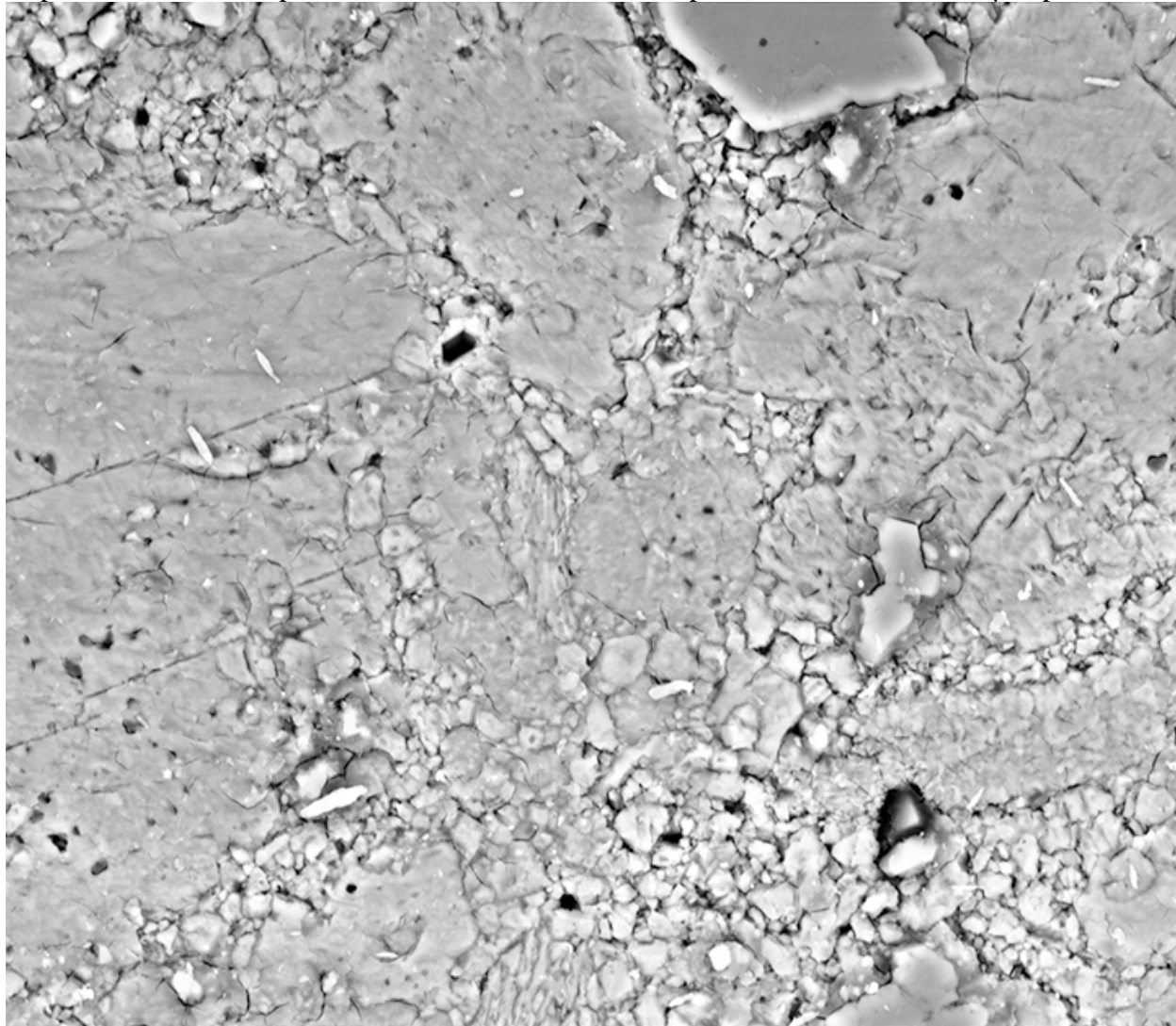
Depth 4797.1 ft, Sample 2-18, Dimensions 13038x11443 pixel², scale 0.12872467 μm/pixel



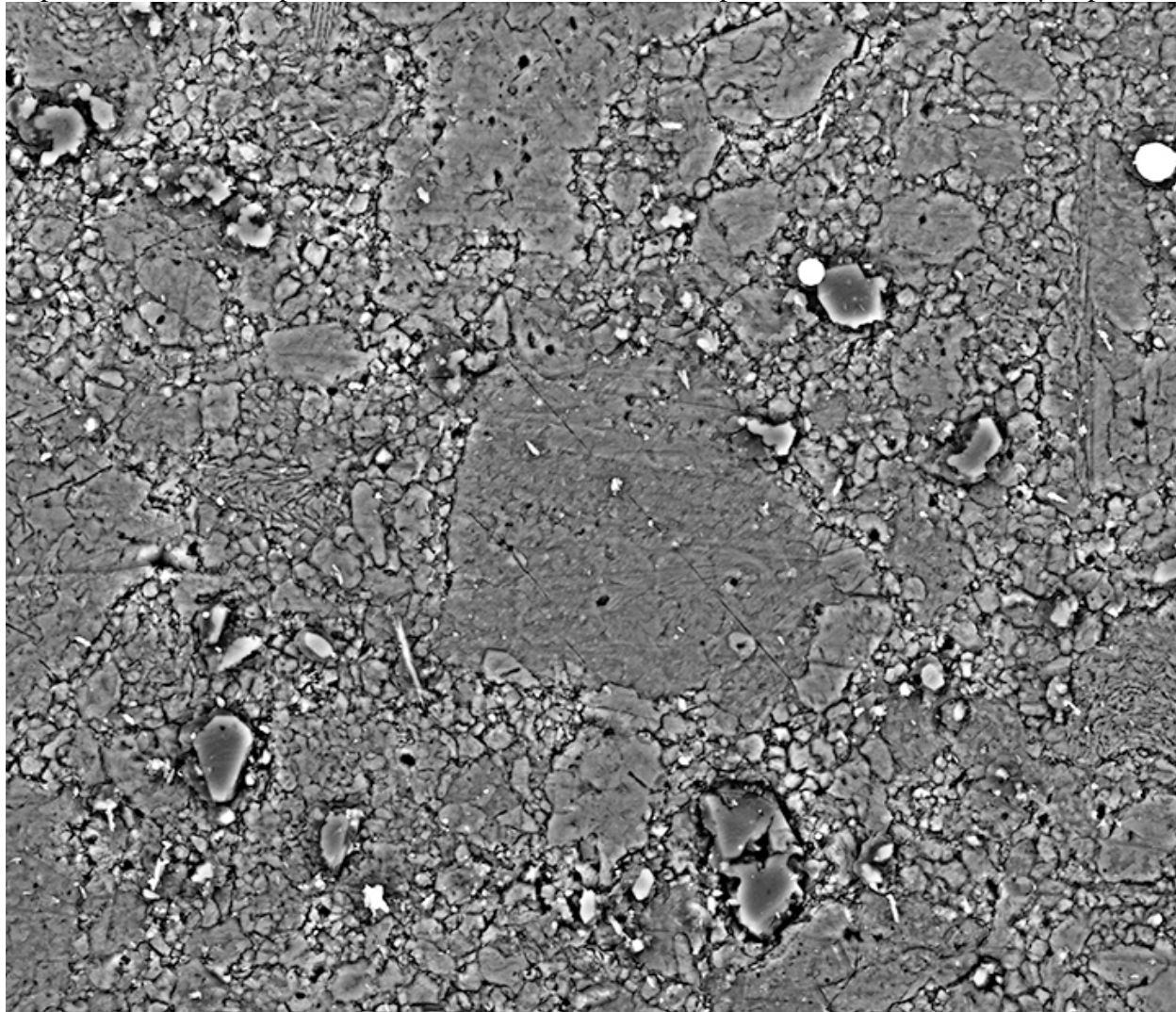
Depth 4797.1 ft, Sample 2-18, Dimensions 18654x16255 pixel², scale 0.12872467 μm/pixel



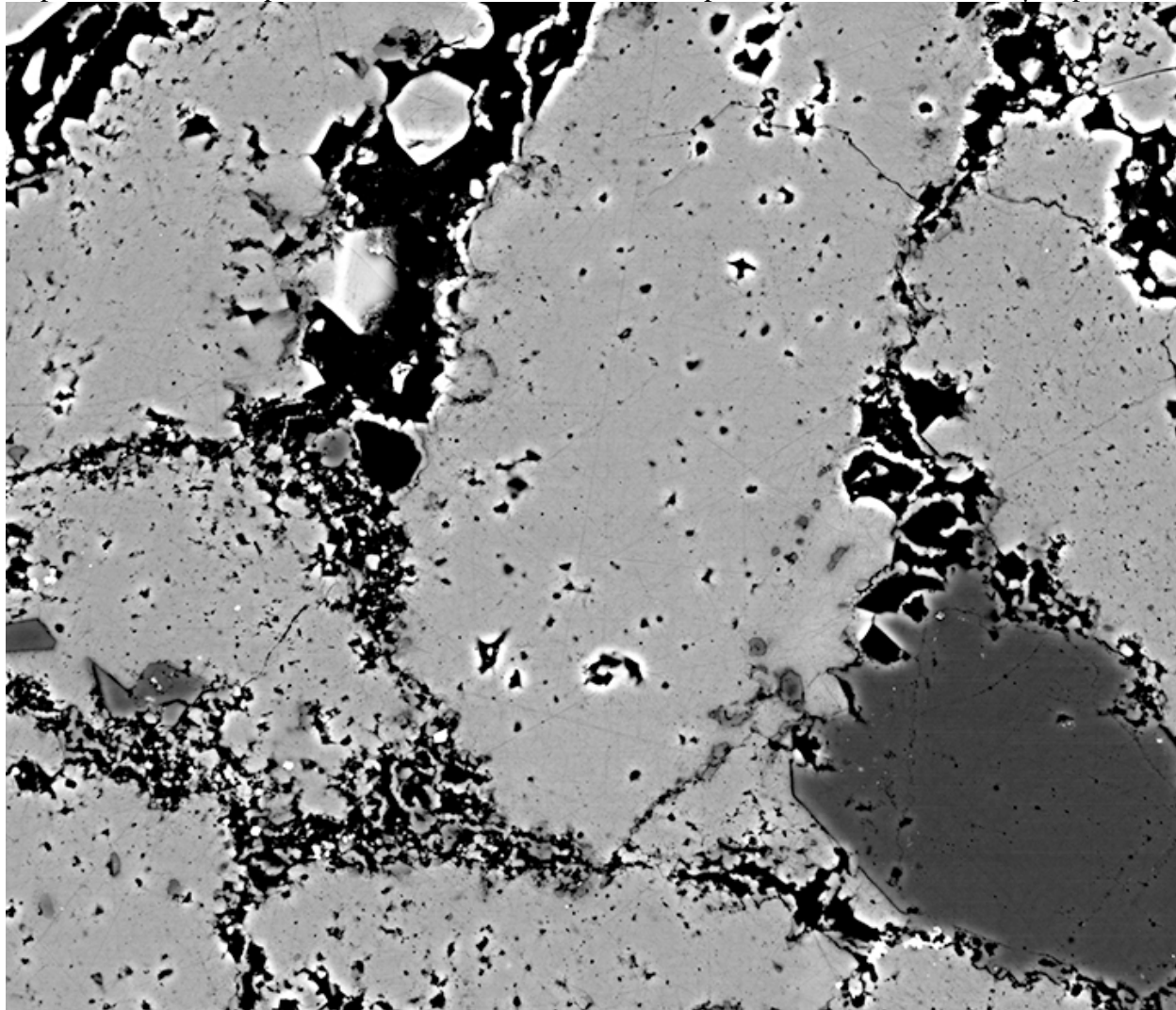
Depth 4804.75 ft, Sample 2-25, Dimensions 9309x8146 pixel², scale 0.11809619 μm/pixel



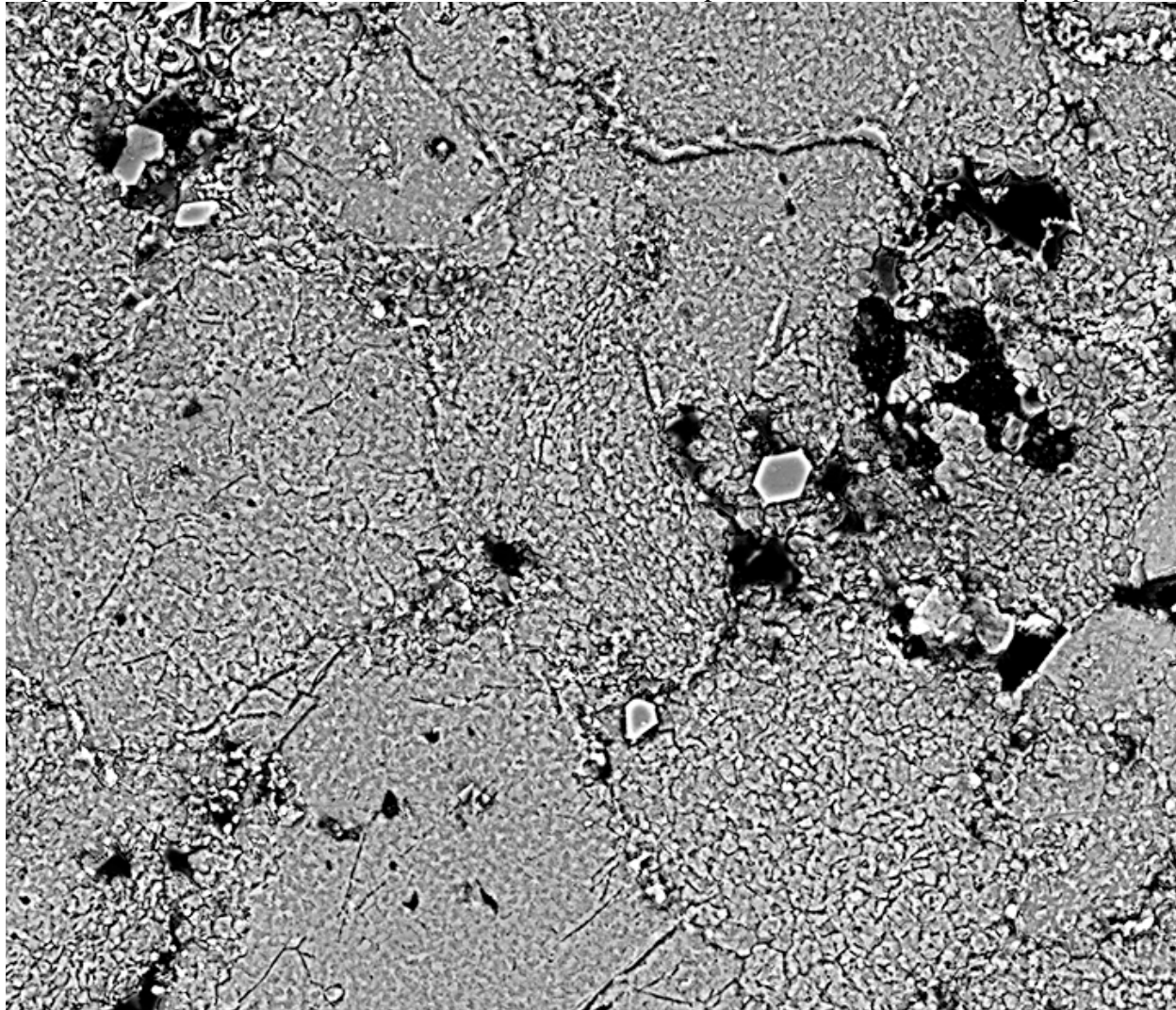
Depth 4804.75 ft, Sample 2-25, Dimensions 13004x11254 pixel², scale 0.014351563 μm/pixel



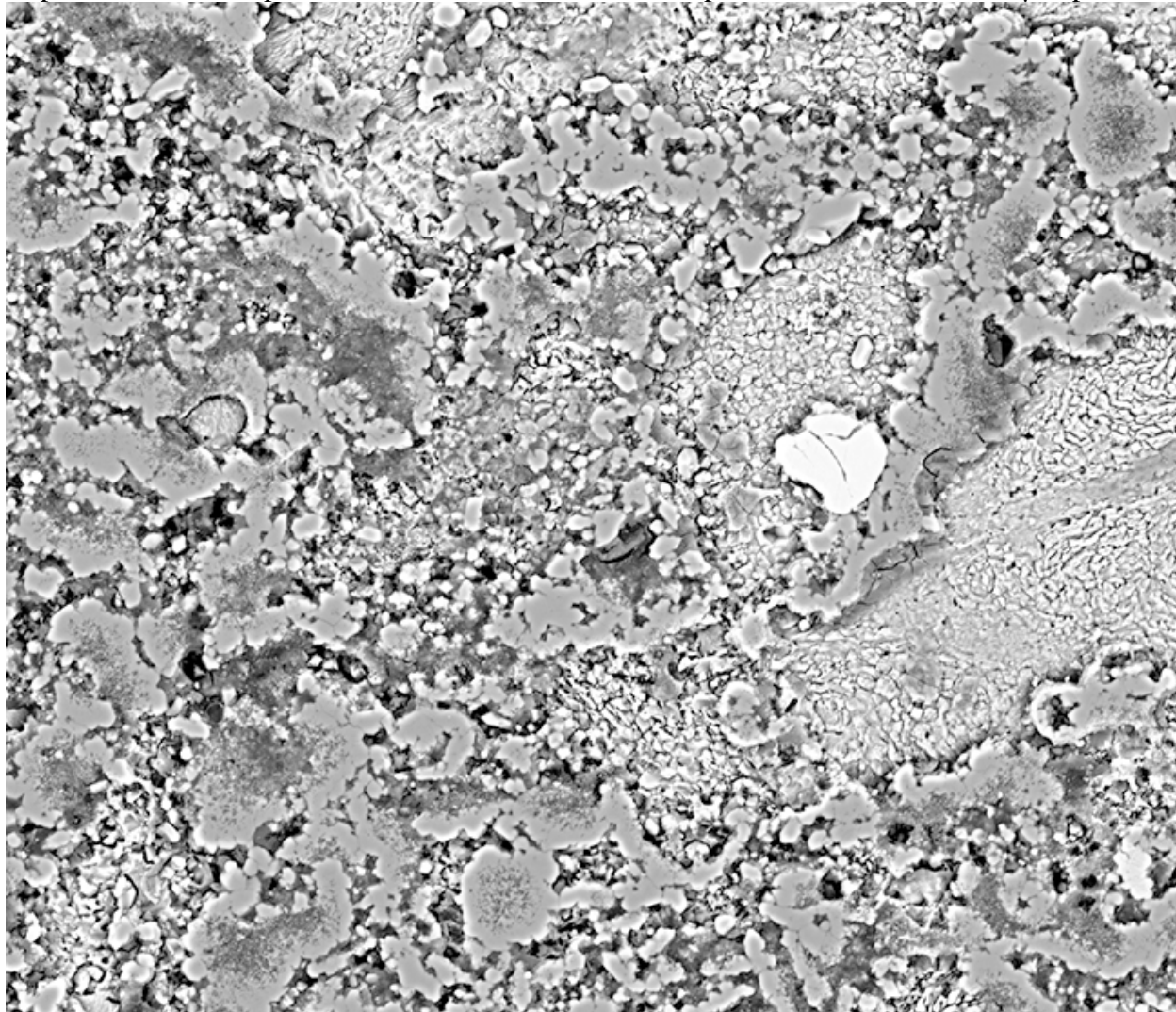
Depth 4810.4 ft, Sample 2-31, Dimensions 25991x22441 pixel², scale 0.007657568 μm/pixel



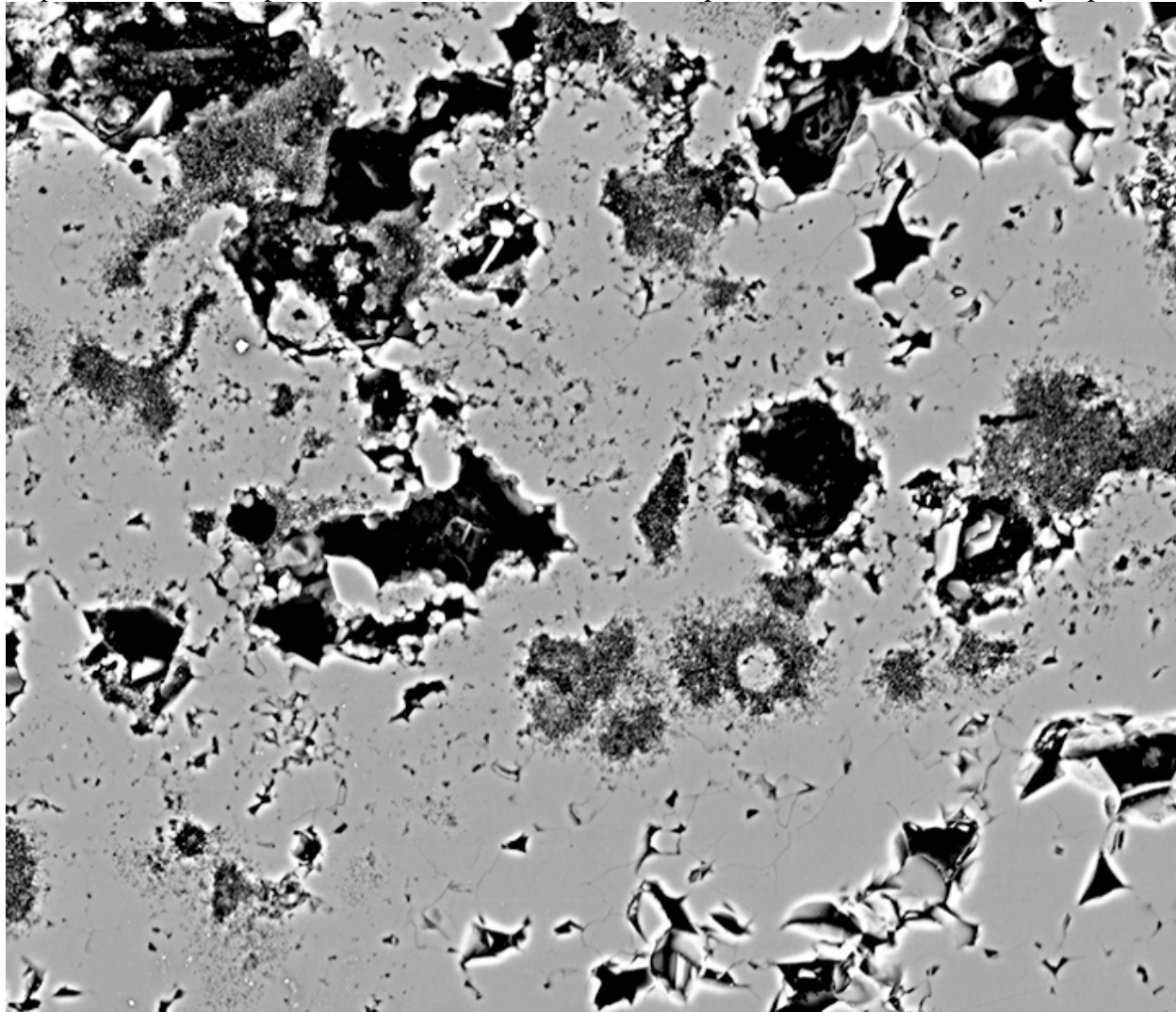
Depth 4810.4 ft, Sample 2-31, Dimensions 26215x22685 pixel², scale 0.007657568 $\mu\text{m}/\text{pixel}$



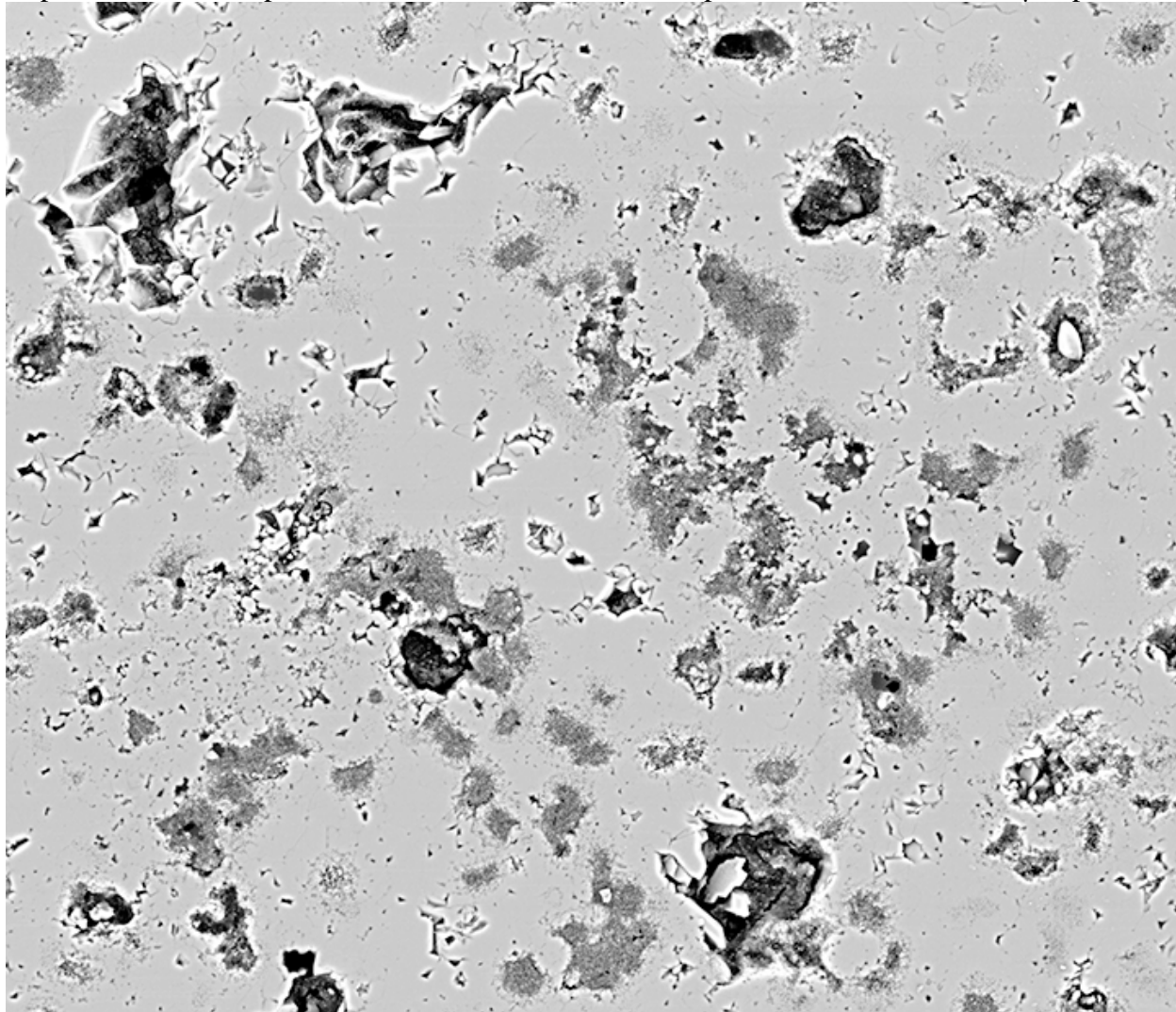
Depth 4810.4 ft, Sample 2-31, Dimensions 26074x22401 pixel², scale 0.007657568 μm/pixel



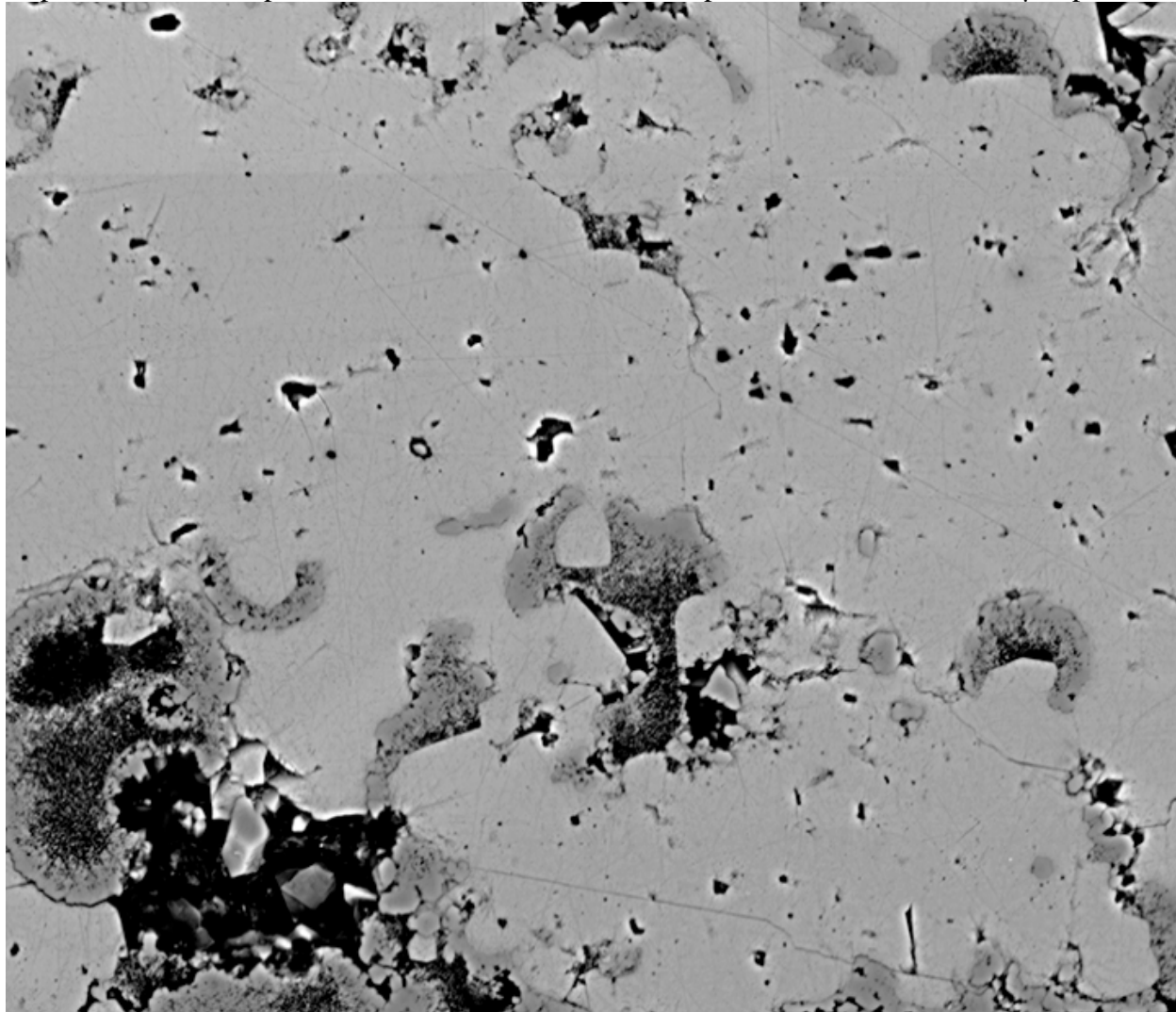
Depth 4813.1 ft, Sample 2-34, Dimensions 22507x19481 pixel², scale 0.0076575686 μm/pixel



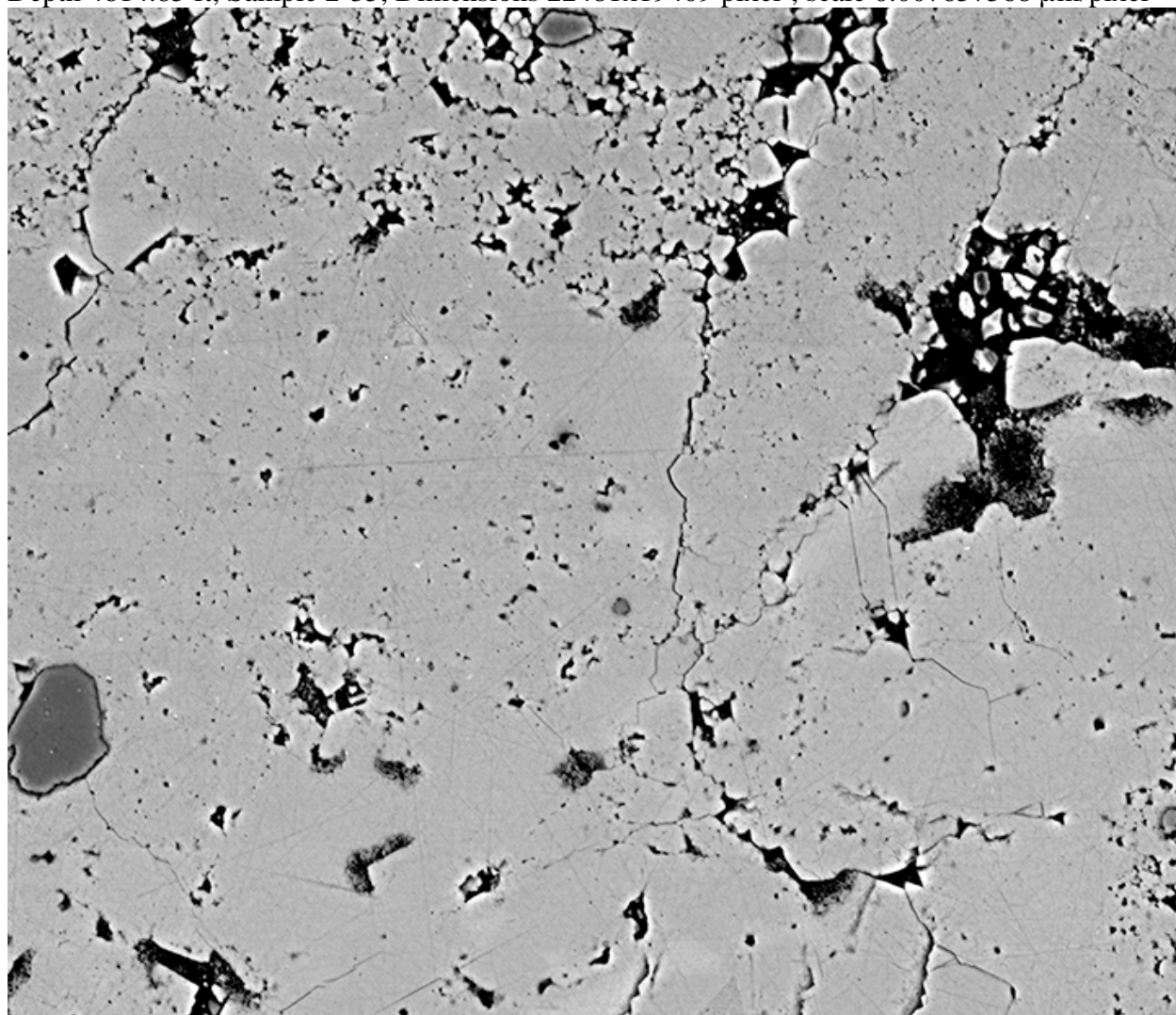
Depth 4813.1 ft, Sample 2-34, Dimensions 18641x16087 pixel², scale 0.007657568 μm/pixel



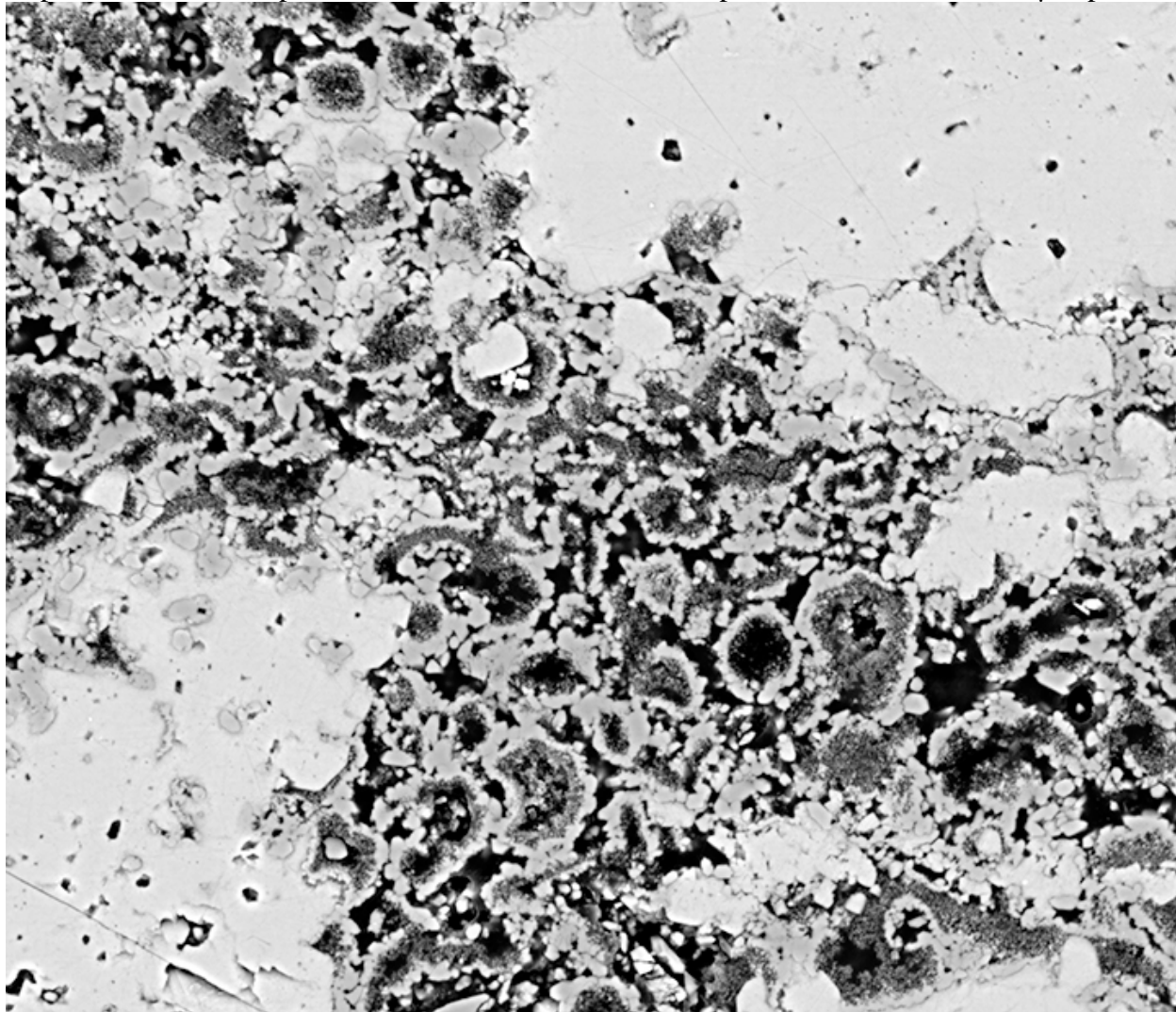
Depth 4813.1 ft, Sample 2-34, Dimensions 22640x19442 pixel², scale 0.007022021 μm/pixel



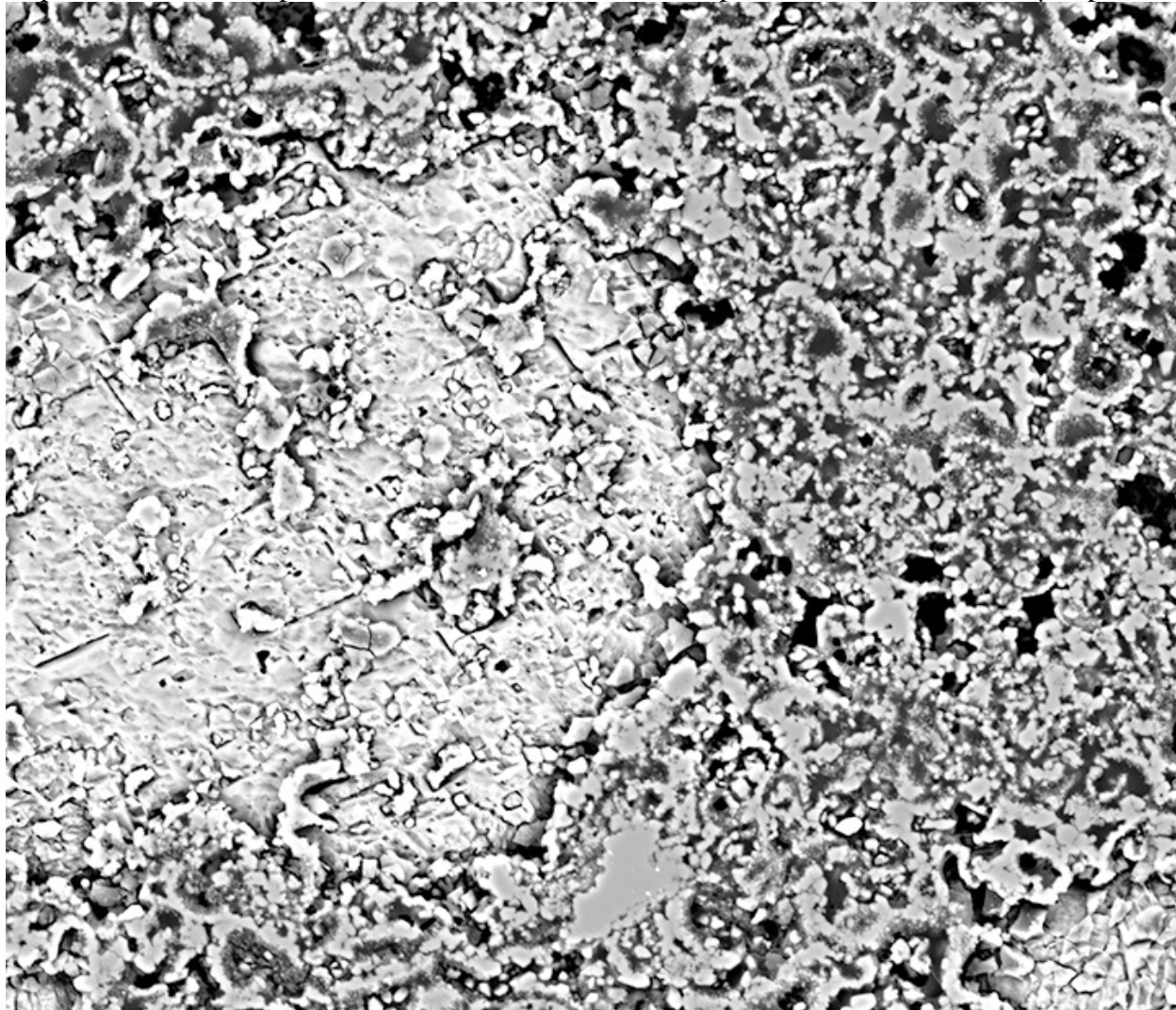
Depth 4814.85 ft, Sample 2-35, Dimensions 22481x19409 pixel², scale 0.007657568 μm/pixel



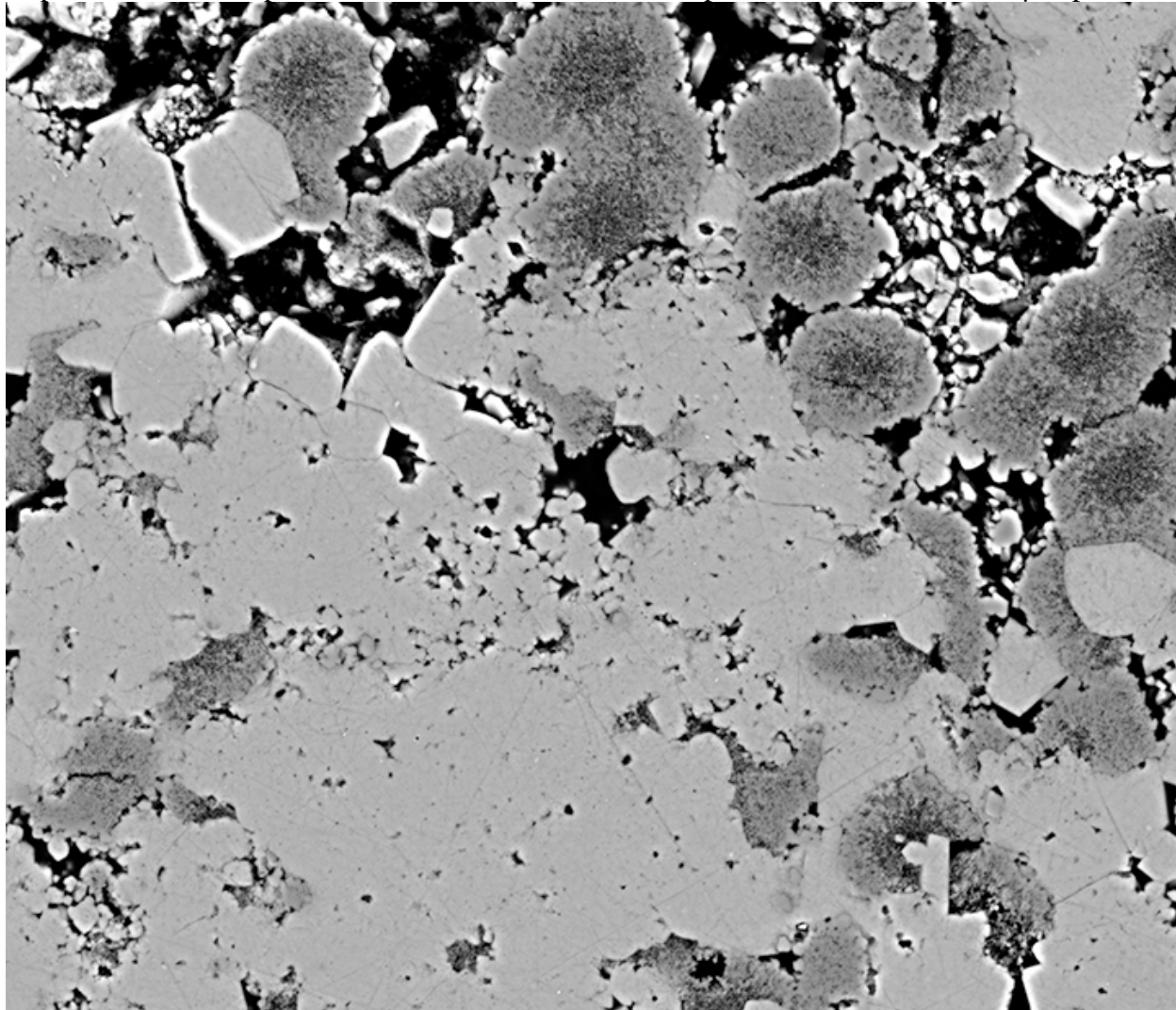
Depth 4814.85 ft, Sample 2-35, Dimensions 22422x19409 pixel², scale 0.007657568 $\mu\text{m}/\text{pixel}$



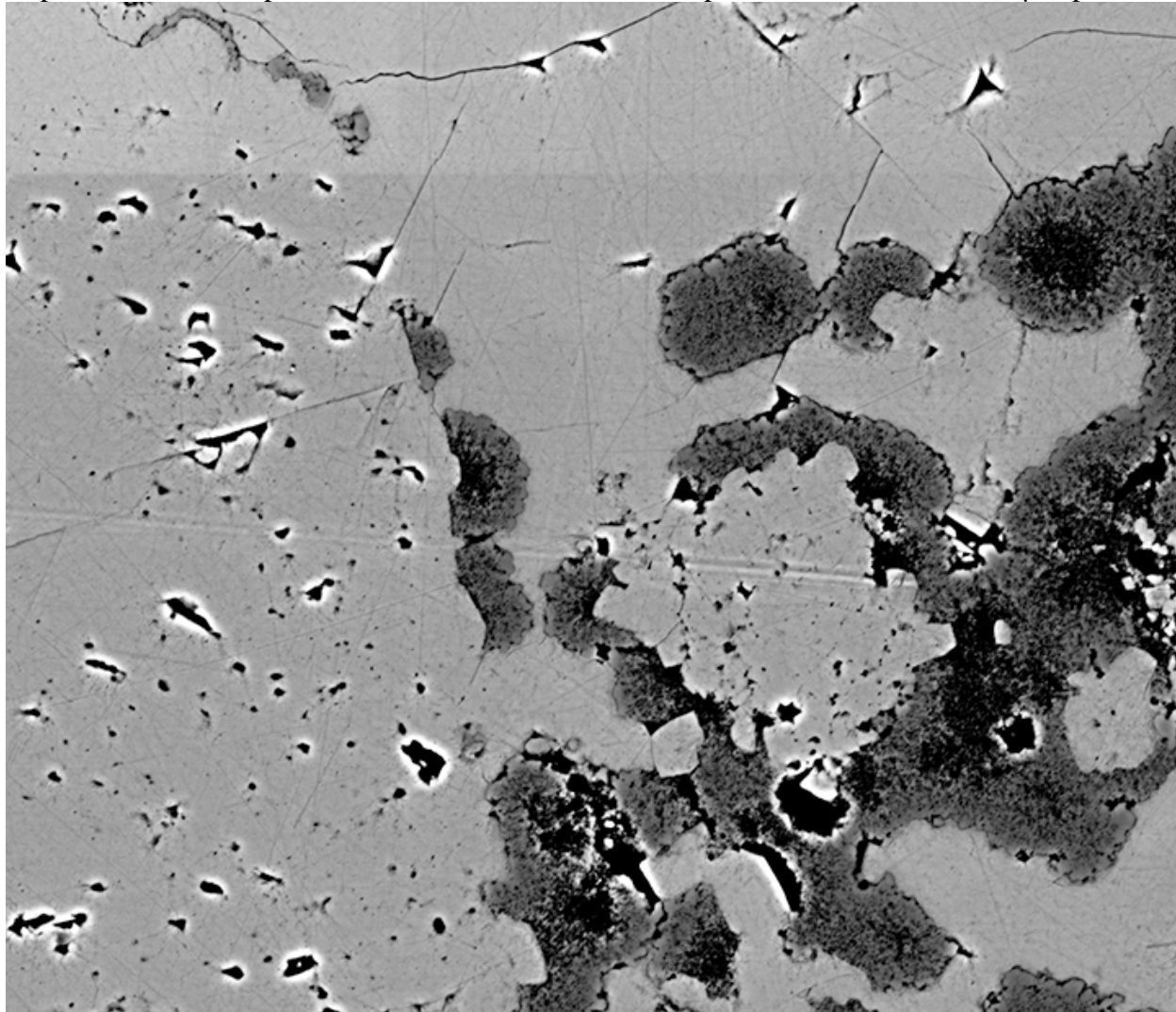
Depth 4814.85 ft, Sample 2-35, Dimensions 22431x19314 pixel², scale 0.007657568 μm/pixel



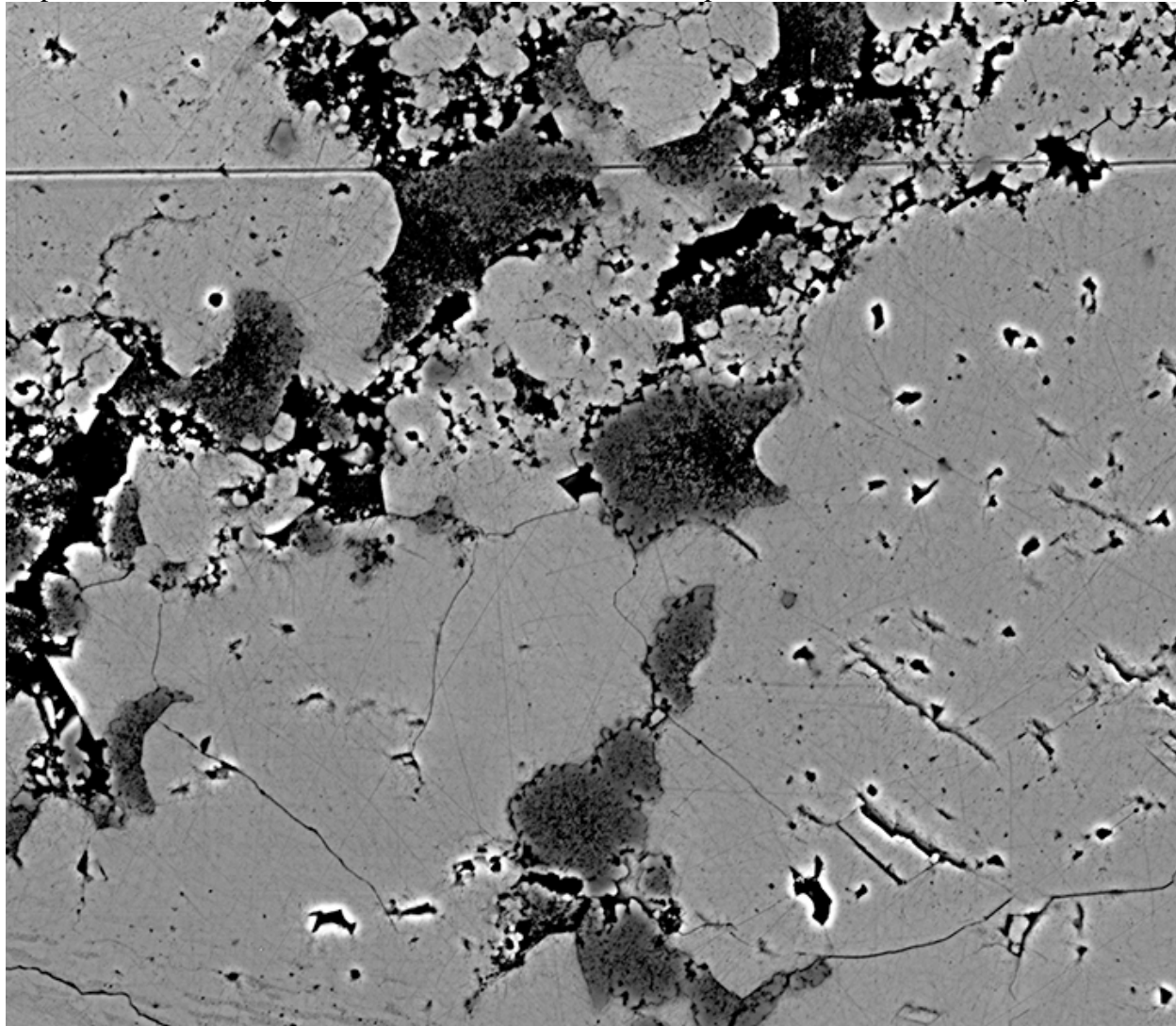
Depth 4824.8 ft, Sample 2-45, Dimensions 22495x19385 pixel², scale 0.007022021 $\mu\text{m}/\text{pixel}$



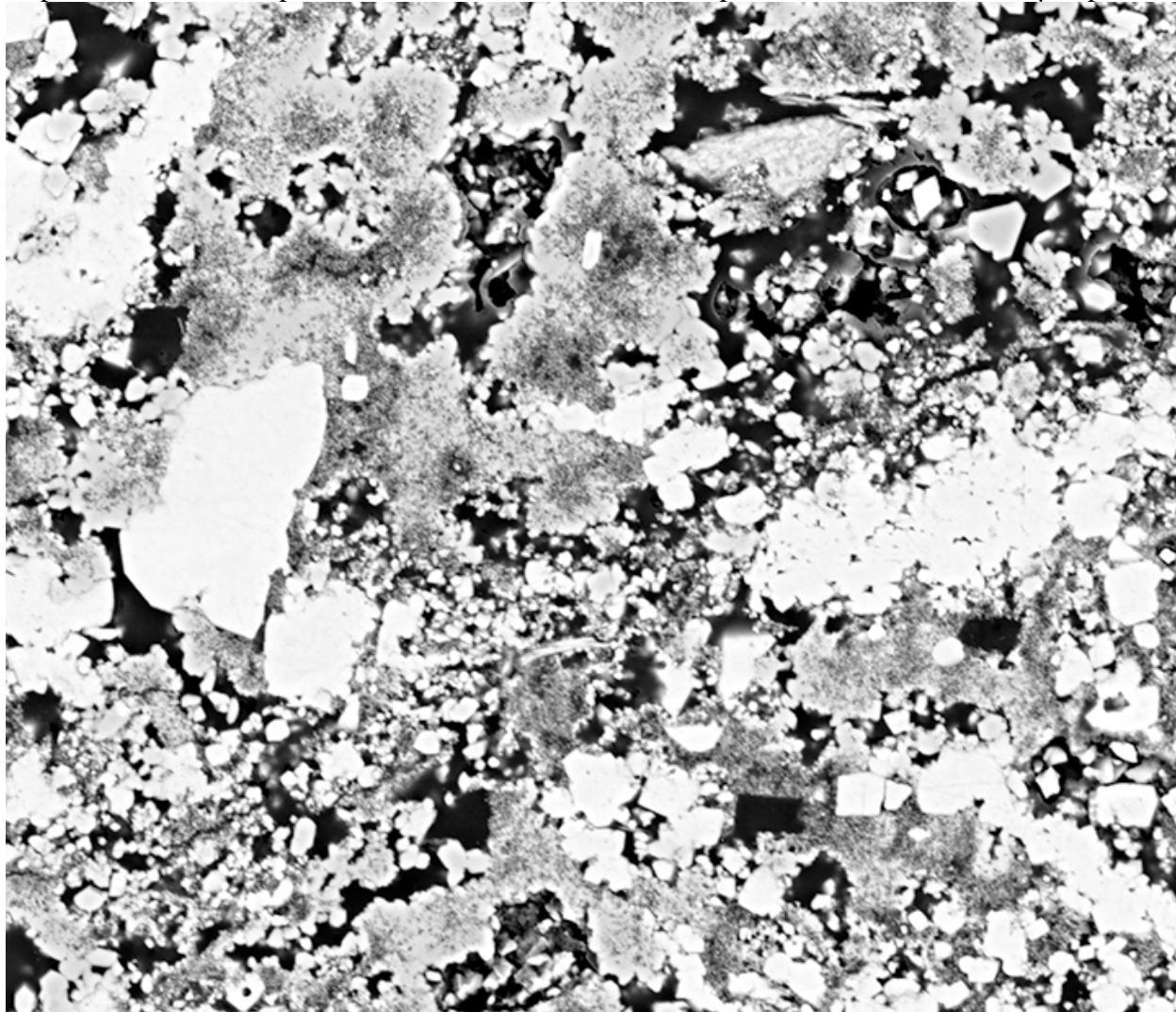
Depth 4824.8 ft, Sample 2-45, Dimensions 22493x19427 pixel², scale 0.007022021 μm/pixel



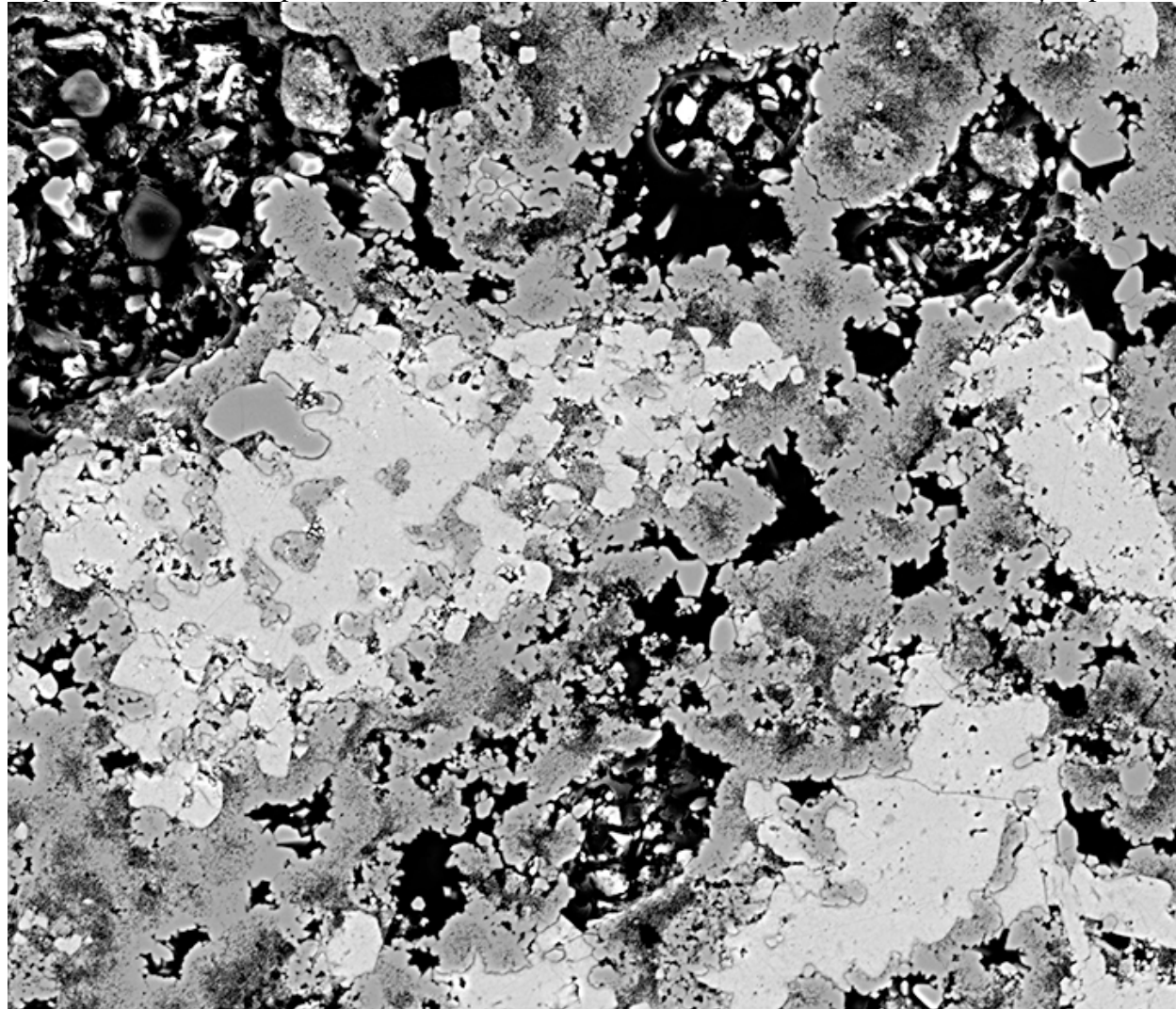
Depth 4824.8 ft, Sample 2-45, Dimensions 22418x19431 pixel², scale 0.007022021 μm/pixel



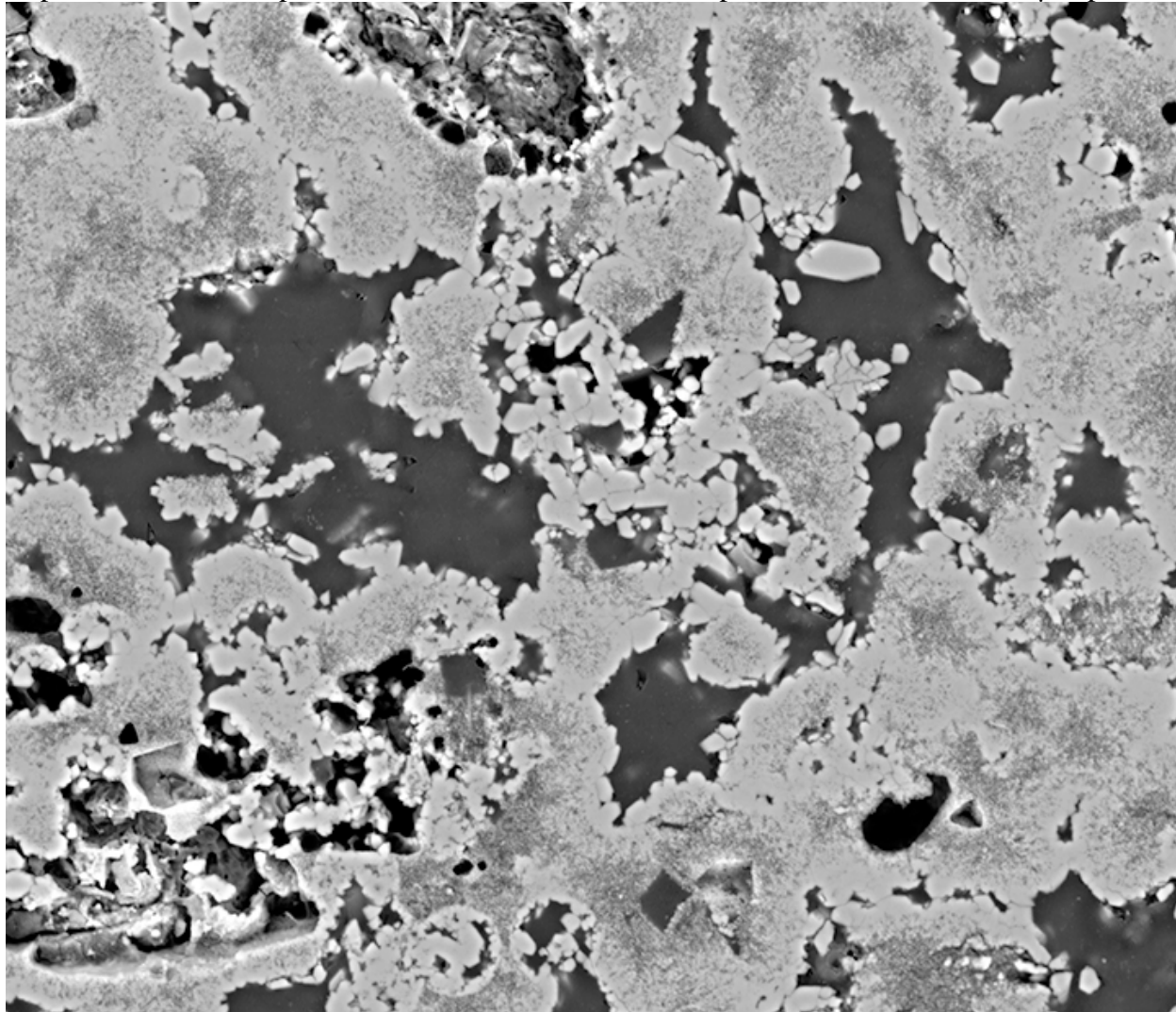
Depth 4834.75 ft, Sample 2-55, Dimensions 22474x19322 pixel², scale 0.006342554 μm/pixel



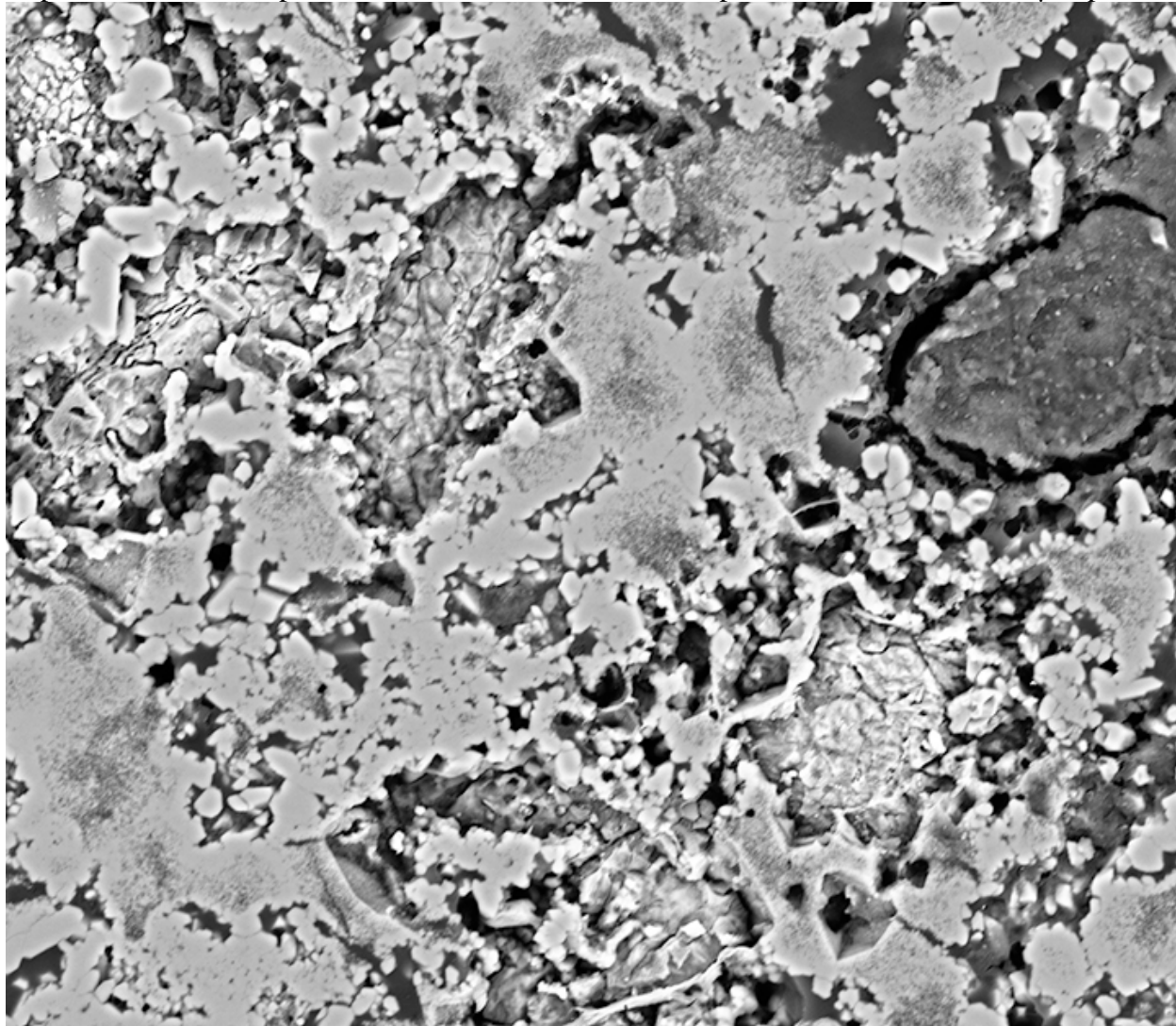
Depth 4834.75 ft, Sample 2-55, Dimensions 37093x31946 pixel², scale 0.006342554 μm/pixel



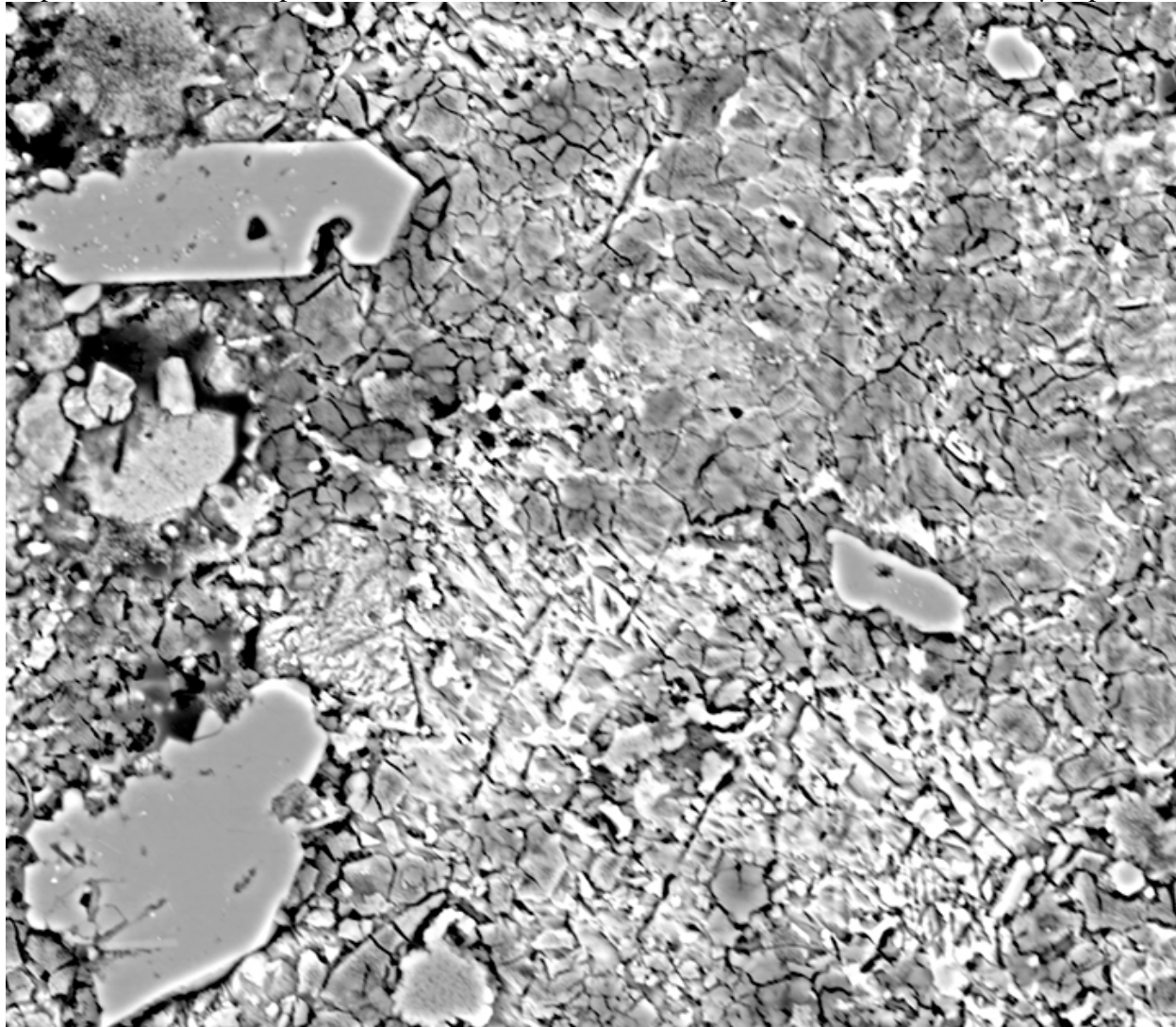
Depth 4834.75 ft, Sample 2-55, Dimensions 22504x19242 pixel², scale 0.007068066 μm/pixel



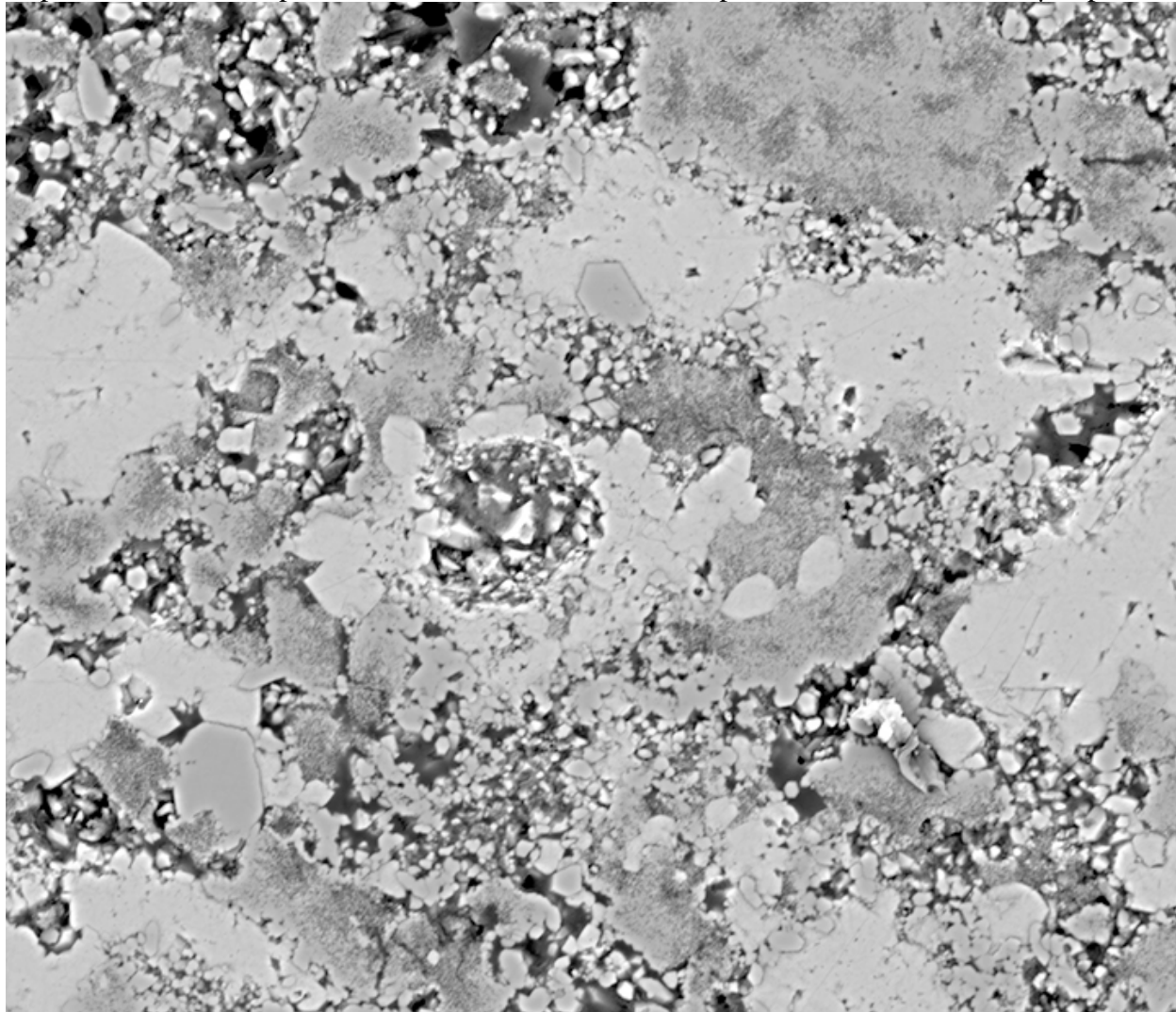
Depth 4834.75 ft, Sample 2-65, Dimensions 18713x16228 pixel², scale 0.008225293 $\mu\text{m}/\text{pixel}$



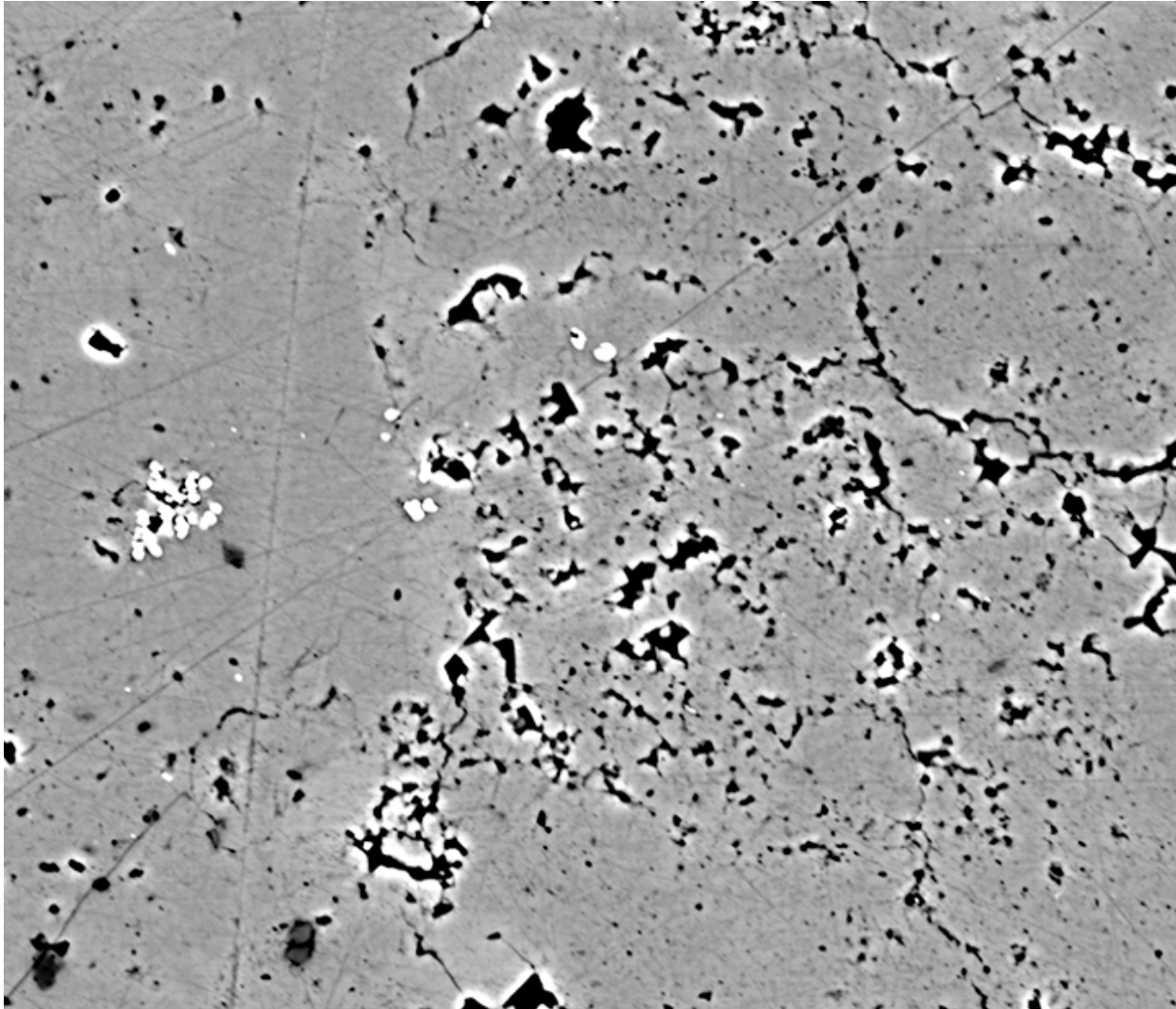
Depth 4834.75 ft, Sample 2-65, Dimensions 18635x16337 pixel², scale 0.006342554 $\mu\text{m}/\text{pixel}$



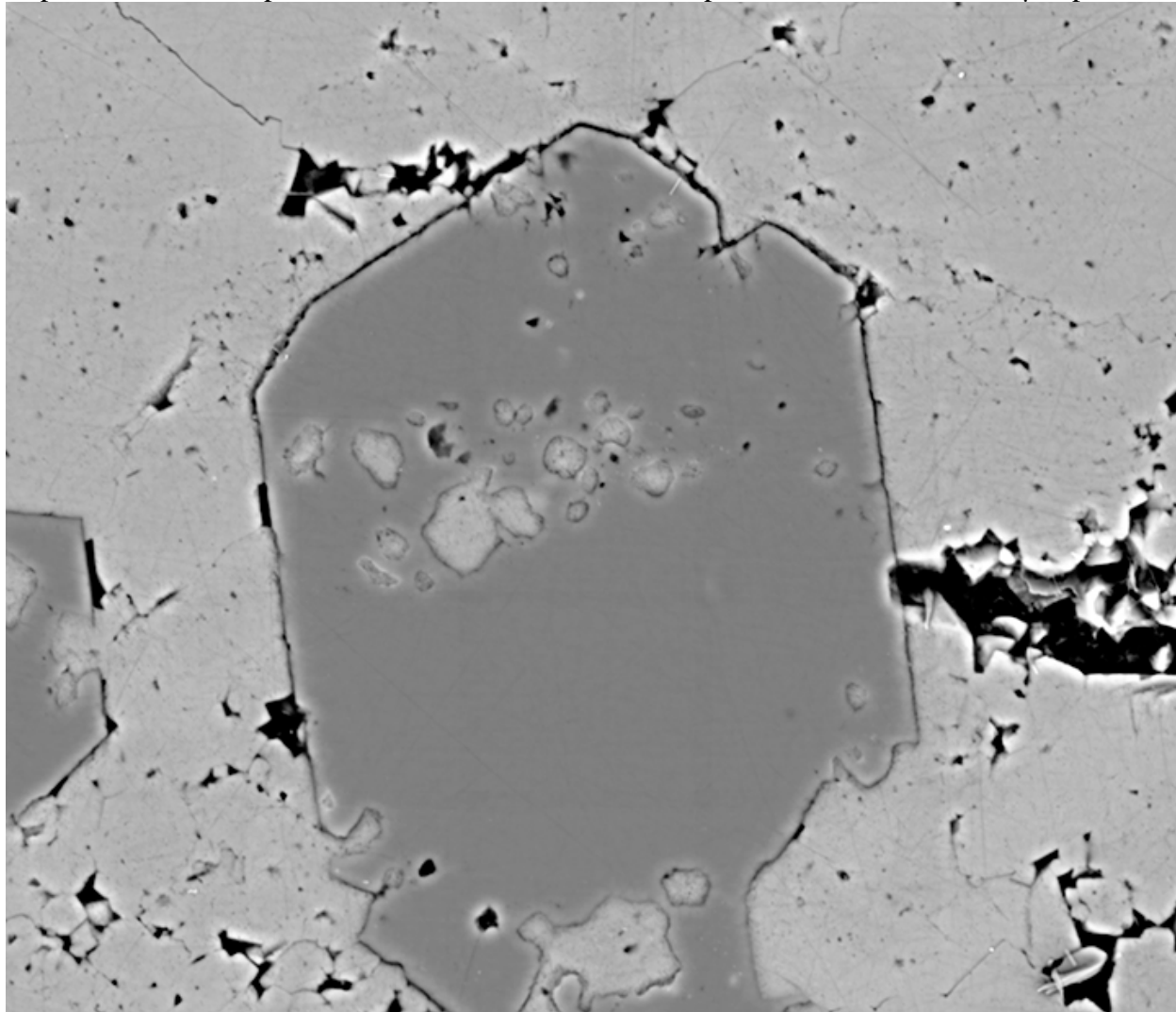
Depth 4834.75 ft, Sample 2-65, Dimensions 26184x22623 pixel², scale 0.006342554 μm/pixel



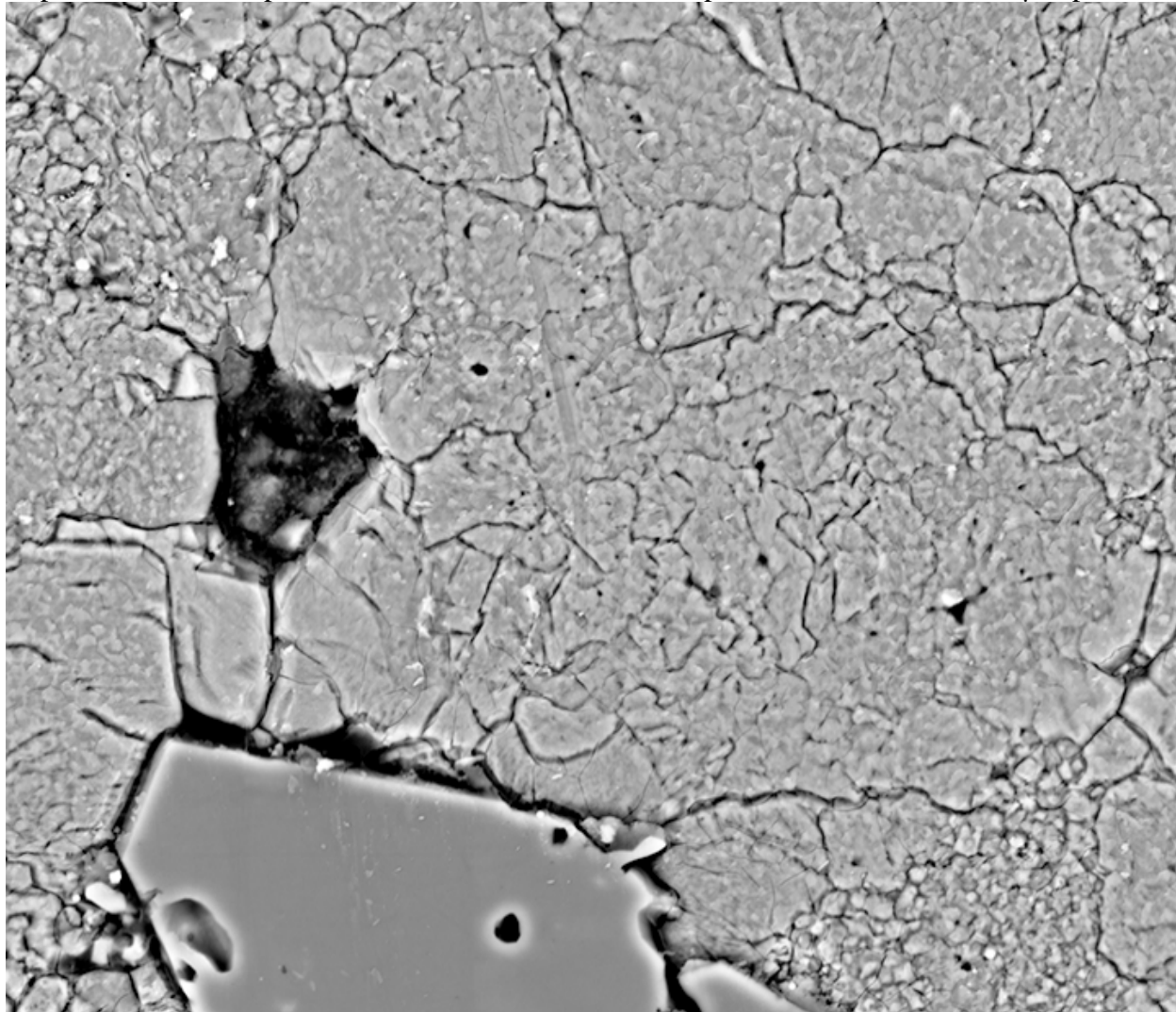
Depth 4848.9 ft, Sample 2-69, Dimensions 9268x8024 pixel², scale 0.012978955 μm/pixel



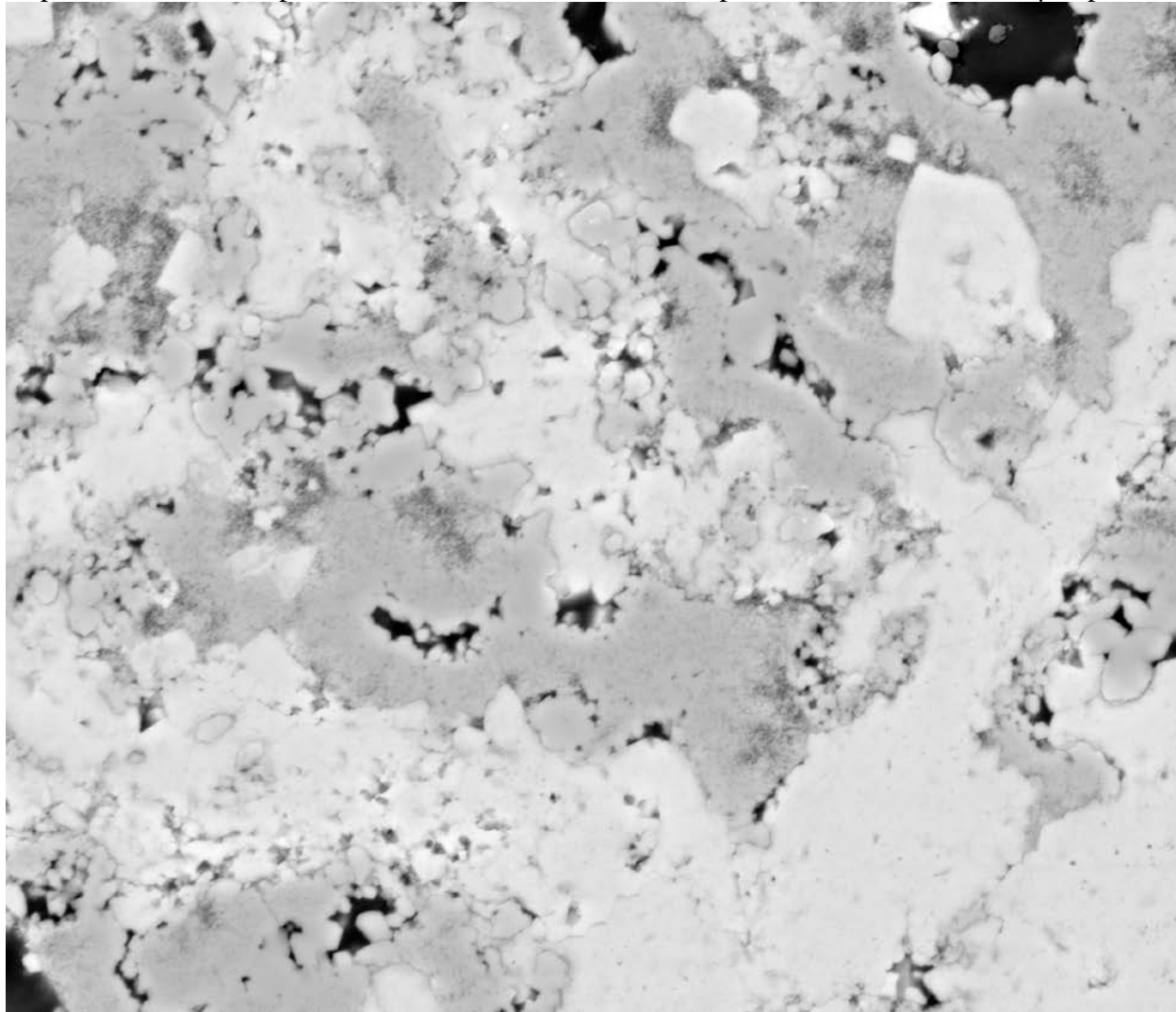
Depth 4848.9 ft, Sample 2-69, Dimensions 18684x16153 pixel², scale 0.006489478 μm/pixel



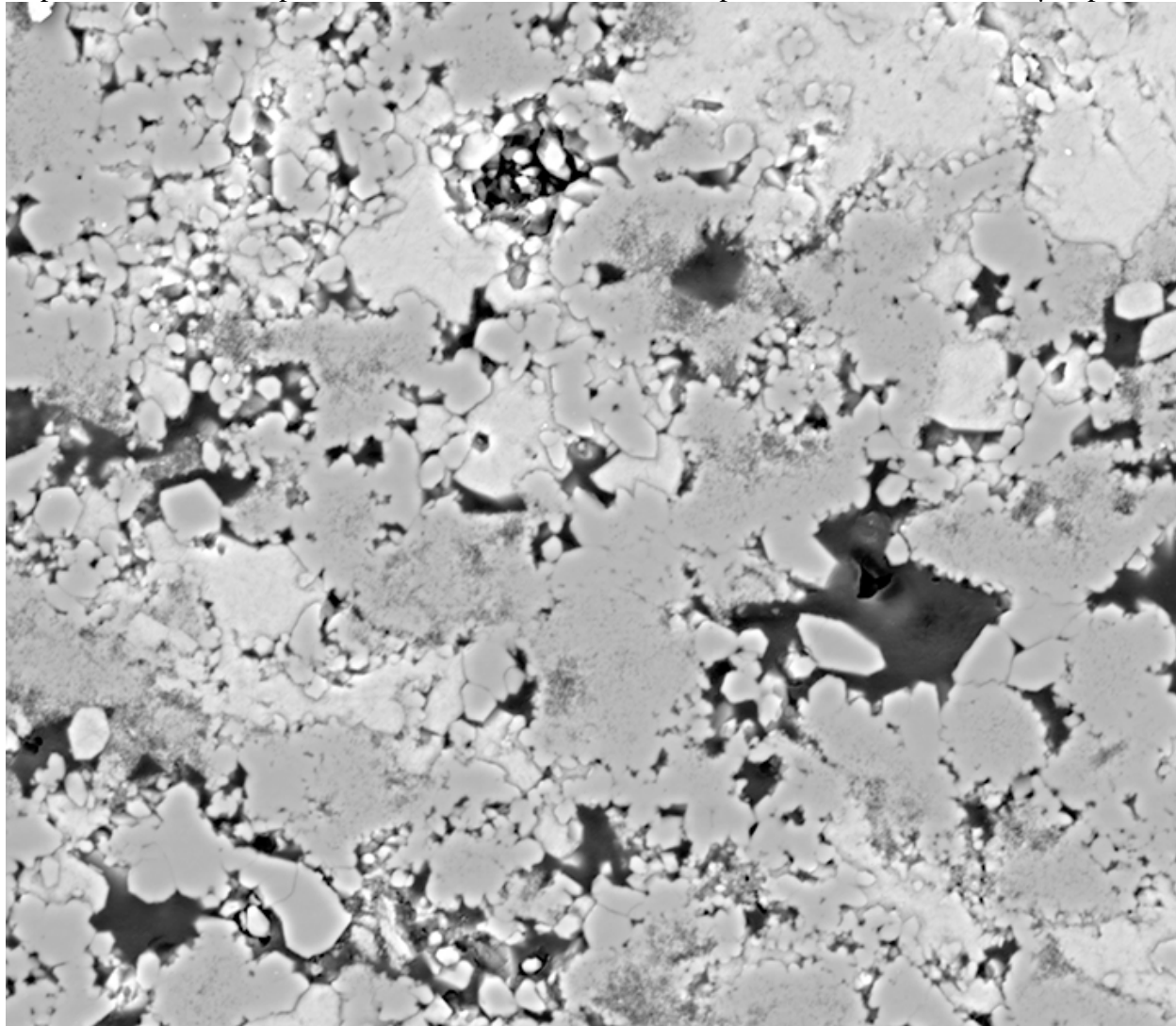
Depth 4848.9 ft, Sample 2-69, Dimensions 18608x16089 pixel², scale 0.007717334 μm/pixel



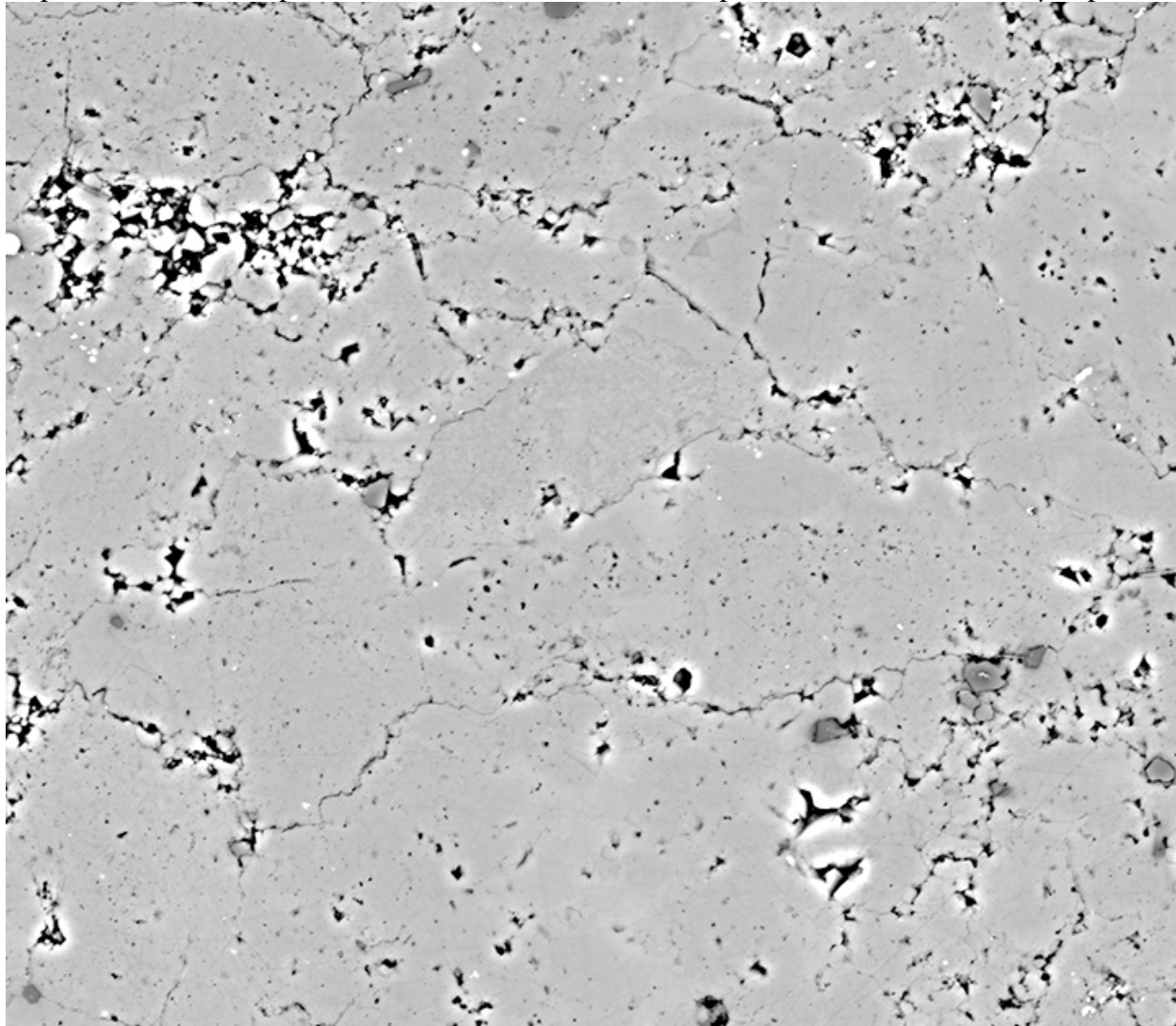
Depth 4854.85 ft, Sample 2-75, Dimensions 18602x16167 pixel², scale 0.006489478 μm/pixel



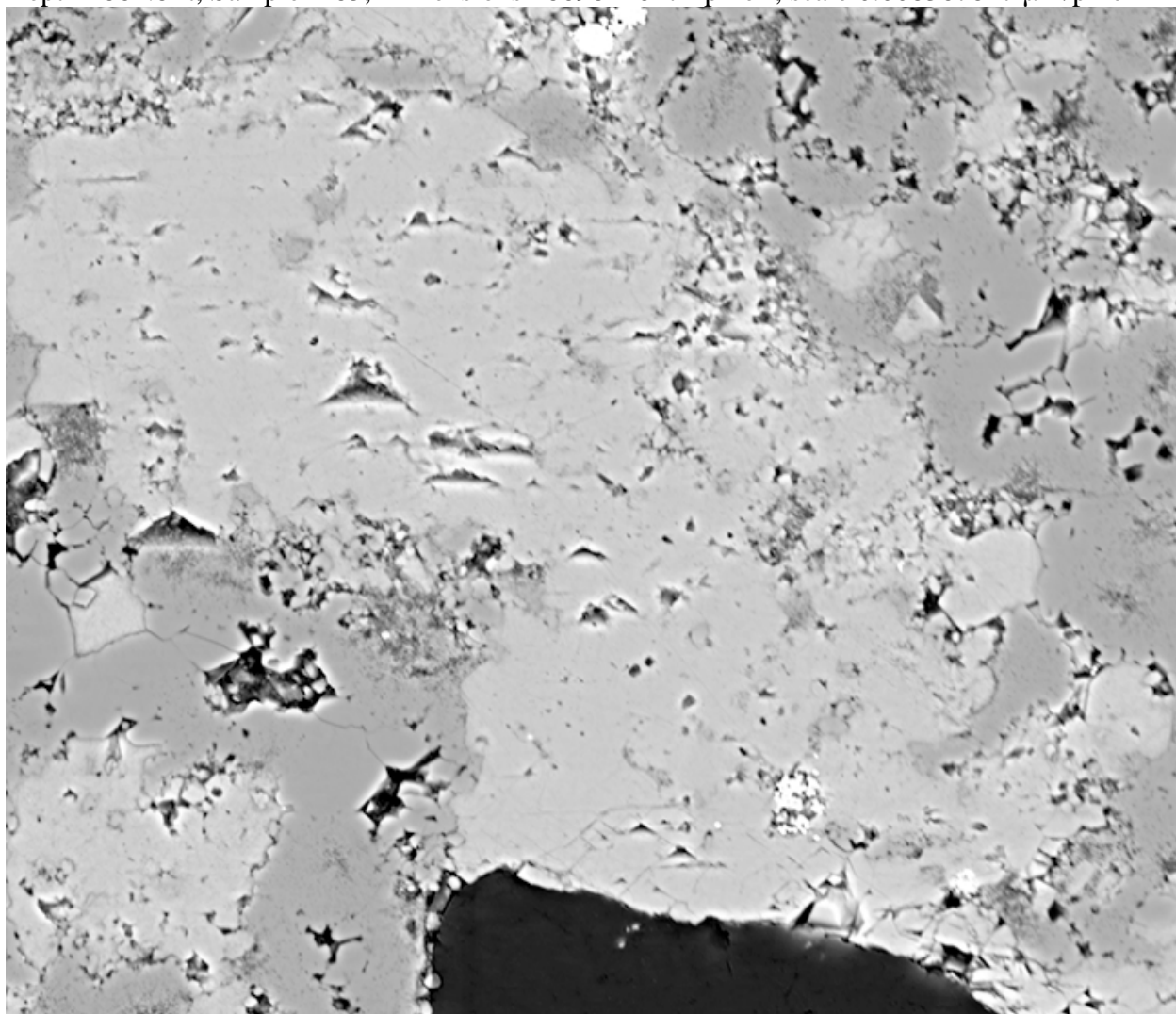
Depth 4854.85 ft, Sample 2-75, Dimensions 18740x16259 pixel², scale 0.006489478 μm/pixel



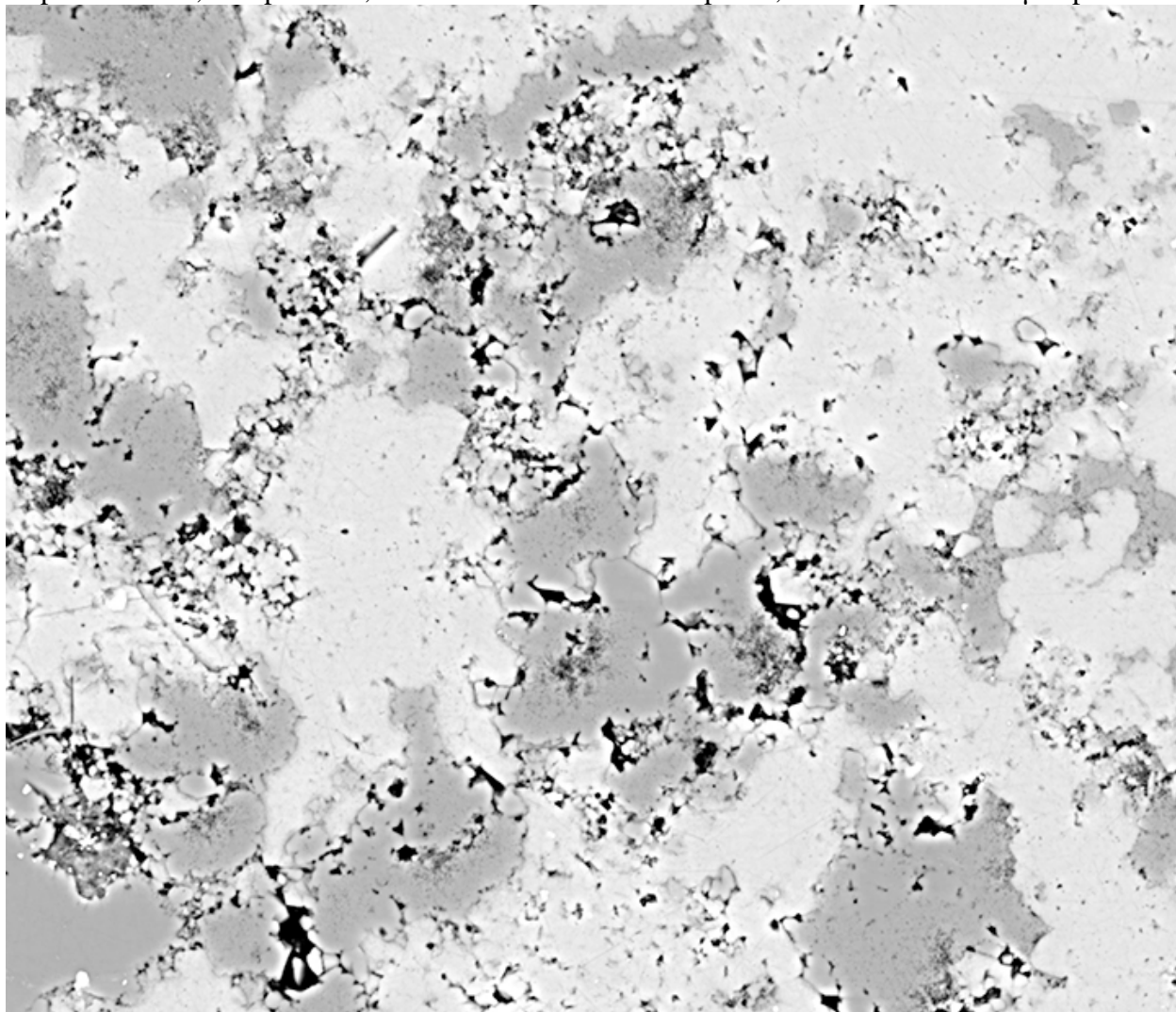
Depth 4854.85 ft, Sample 2-75, Dimensions 29472x25710 pixel², scale 0.006489478 μm/pixel



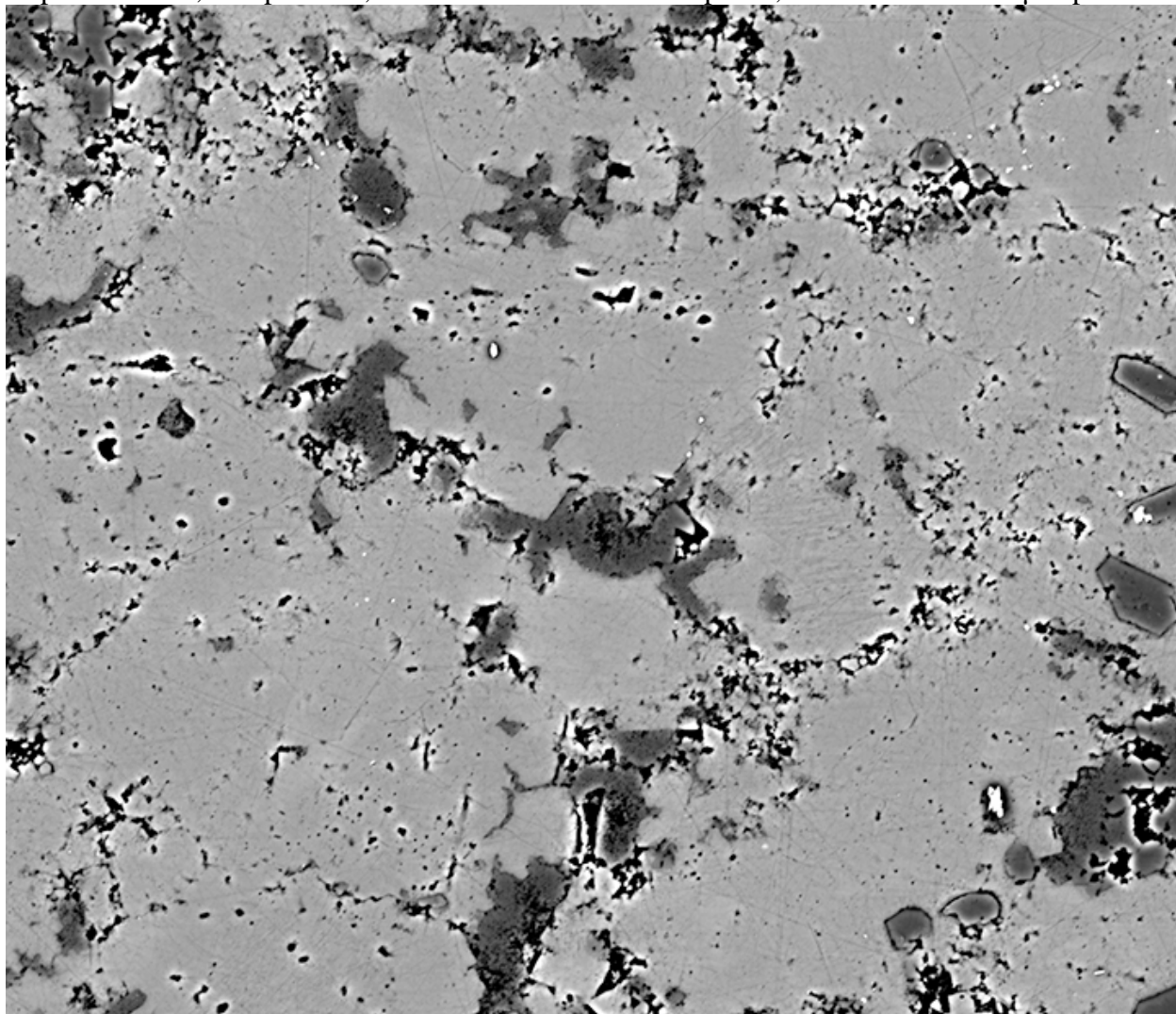
Depth 4864.8 ft, Sample 2-85, Dimensions 18698x16171 pixel², scale 0.008367847 μm/pixel



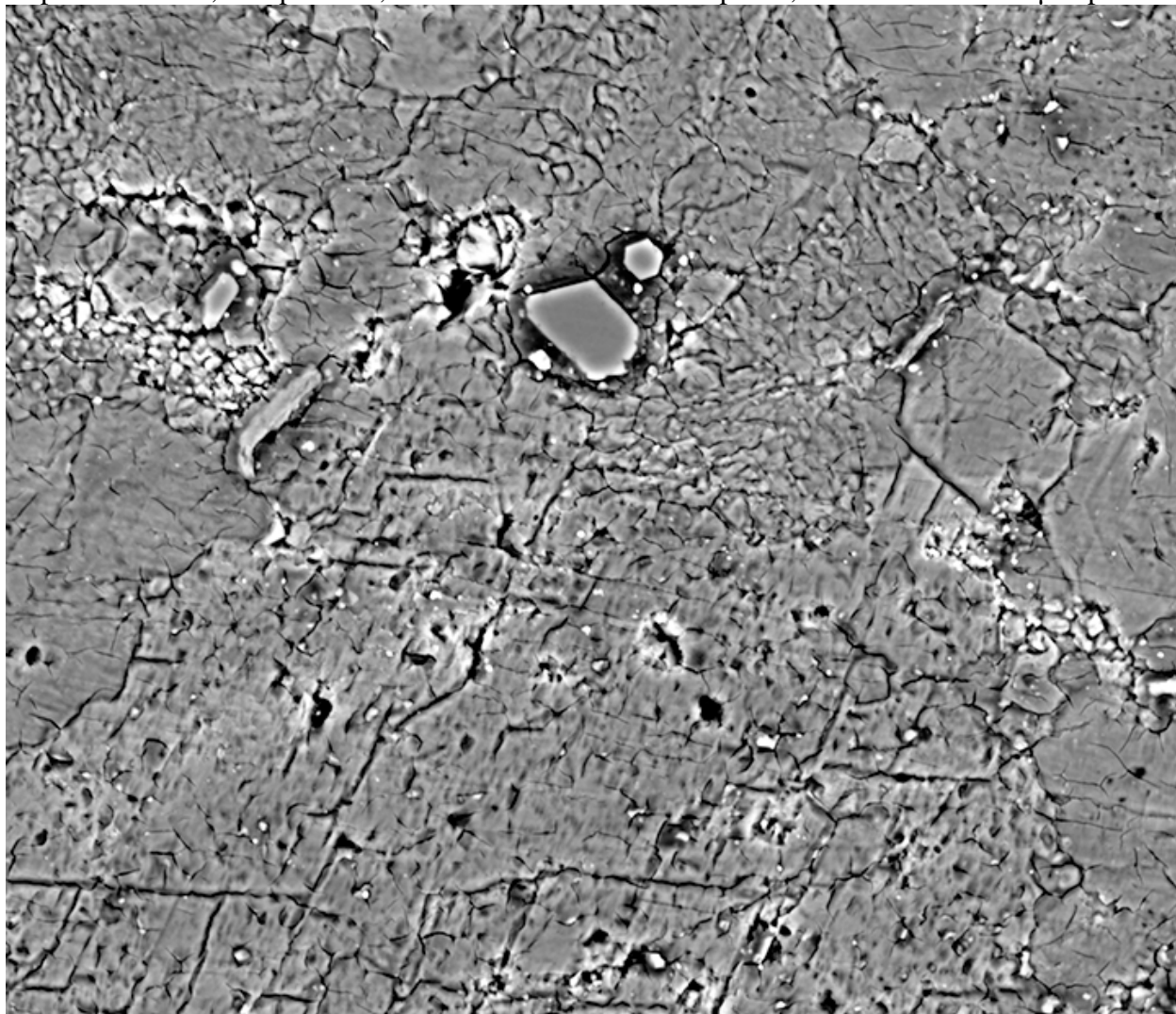
Depth 4864.8 ft, Sample 2-85, Dimensions 18782x16180 pixel², scale 0.008367847 μm/pixel



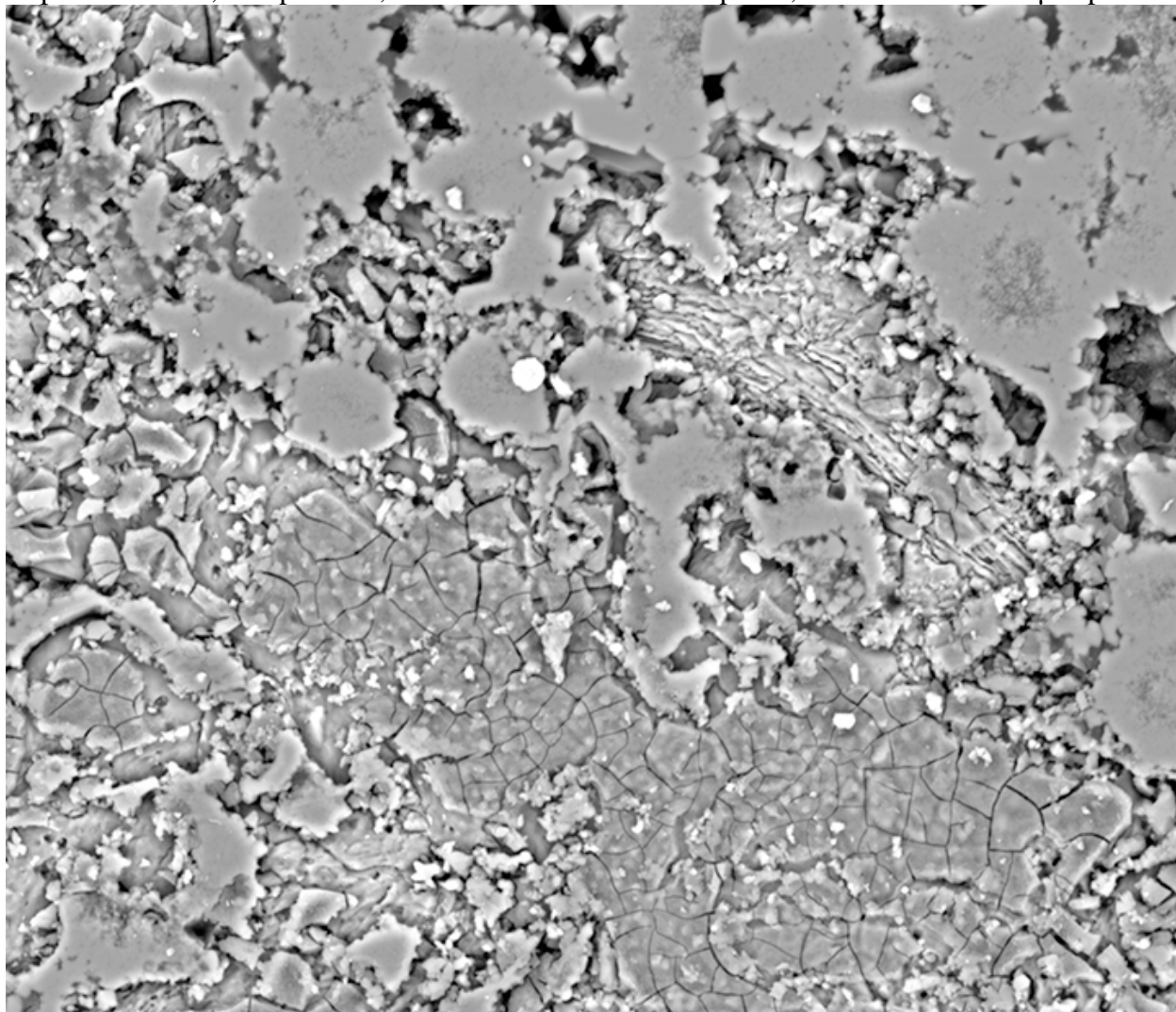
Depth 4864.8 ft, Sample 2-85, Dimensions 22429x19265 pixel², scale 0.008367847 μm/pixel



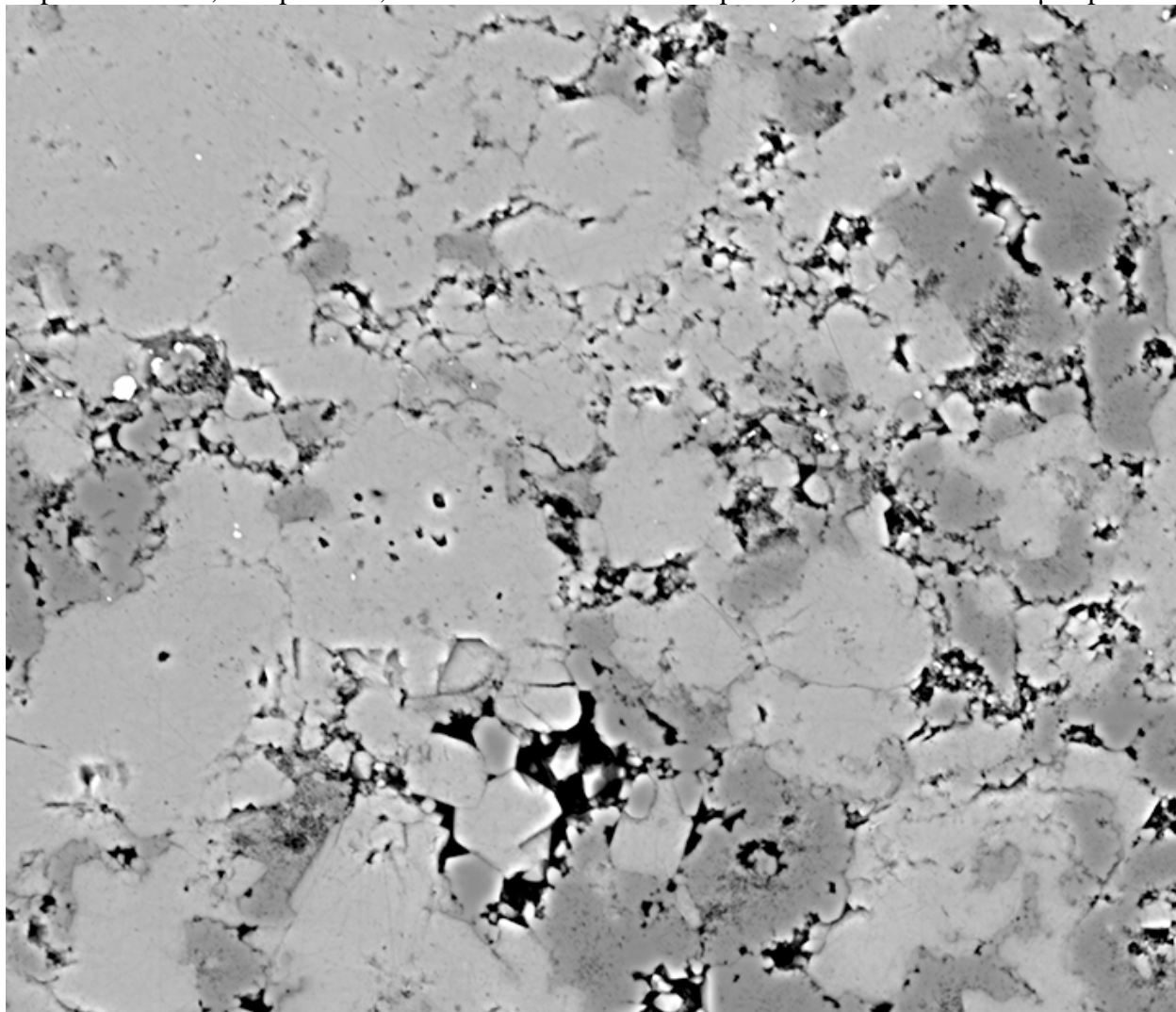
Depth 4867.15 ft, Sample 2-88, Dimensions 18708x16161 pixel², scale 0.007036499 $\mu\text{m}/\text{pixel}$



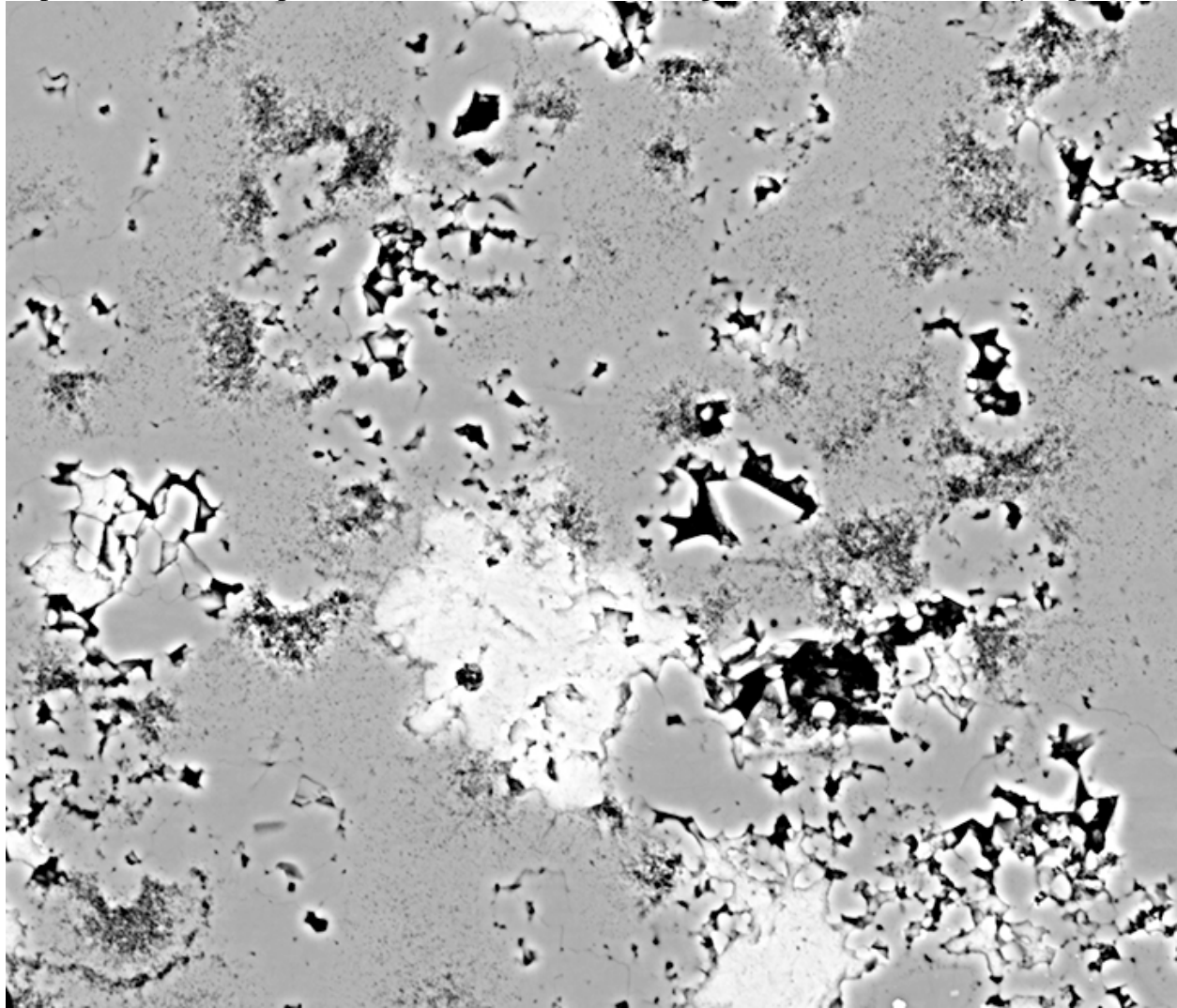
Depth 4867.15 ft, Sample 2-88, Dimensions 18776x16141 pixel², scale 0.007036499 μm/pixel



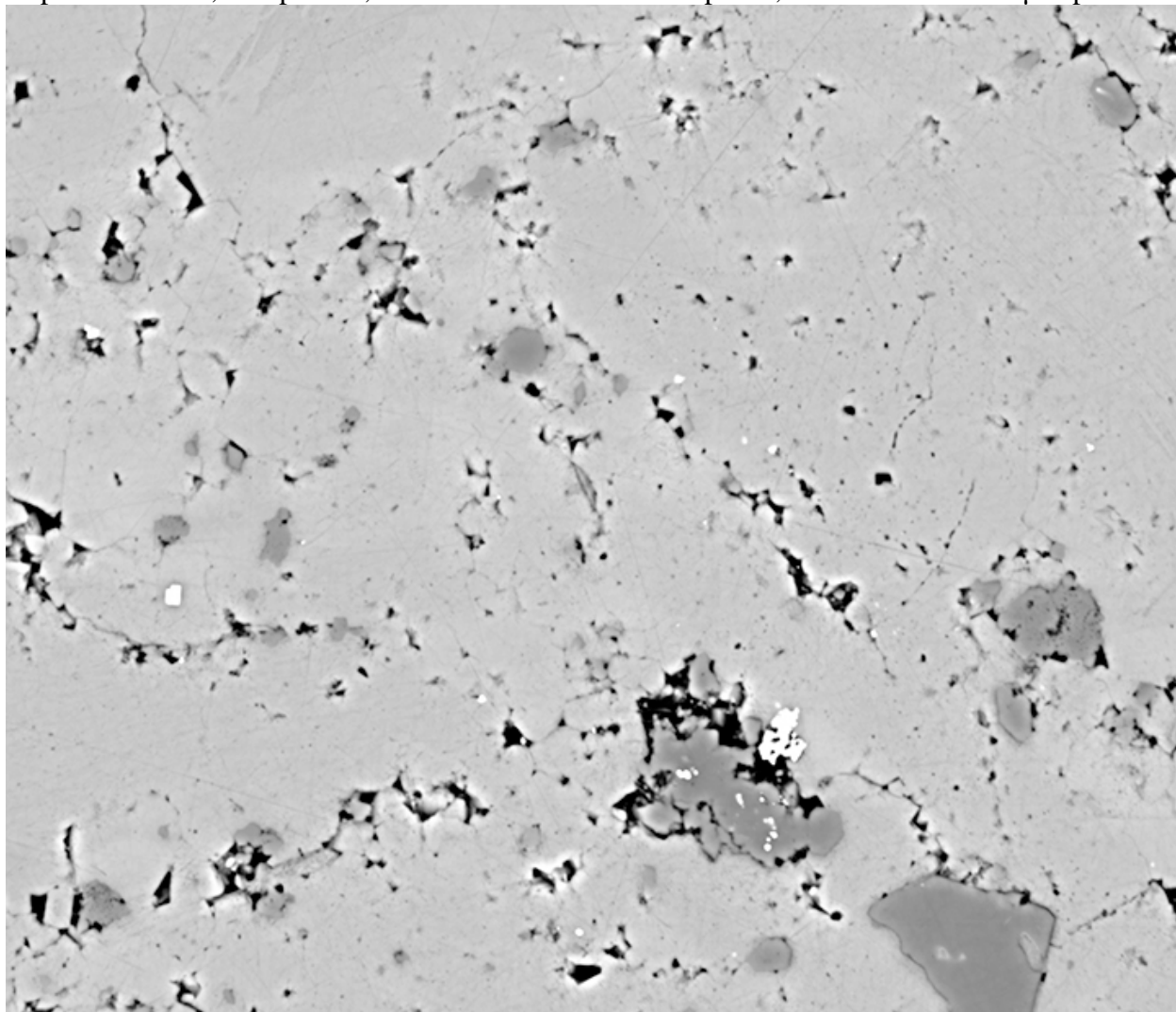
Depth 4867.15 ft, Sample 2-88, Dimensions 18680x16137 pixel², scale 0.007036499 μm/pixel



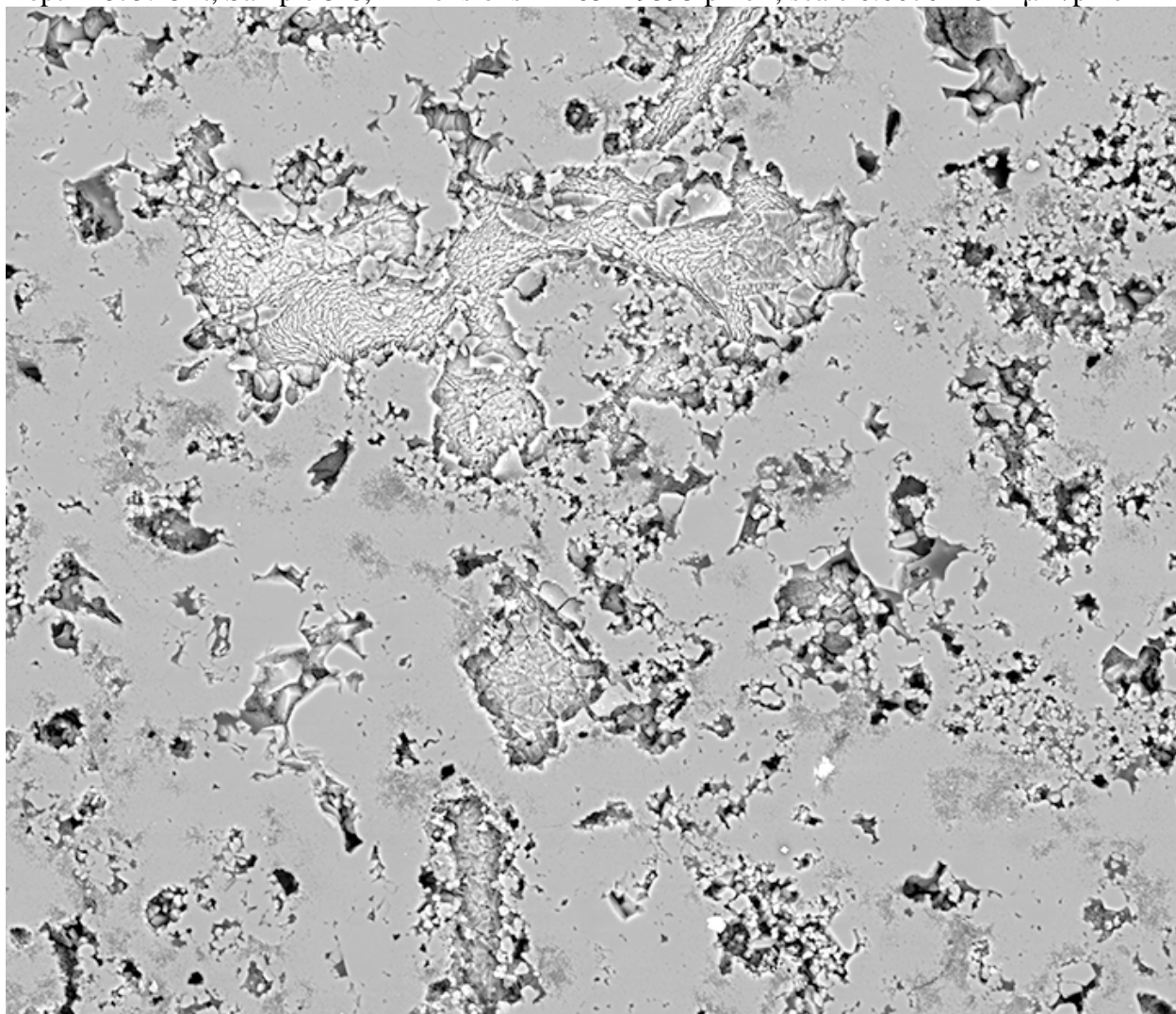
Depth 4875.15 ft, Sample 3-6, Dimensions 18765x16133 pixel², scale 0.007022021 $\mu\text{m}/\text{pixel}$



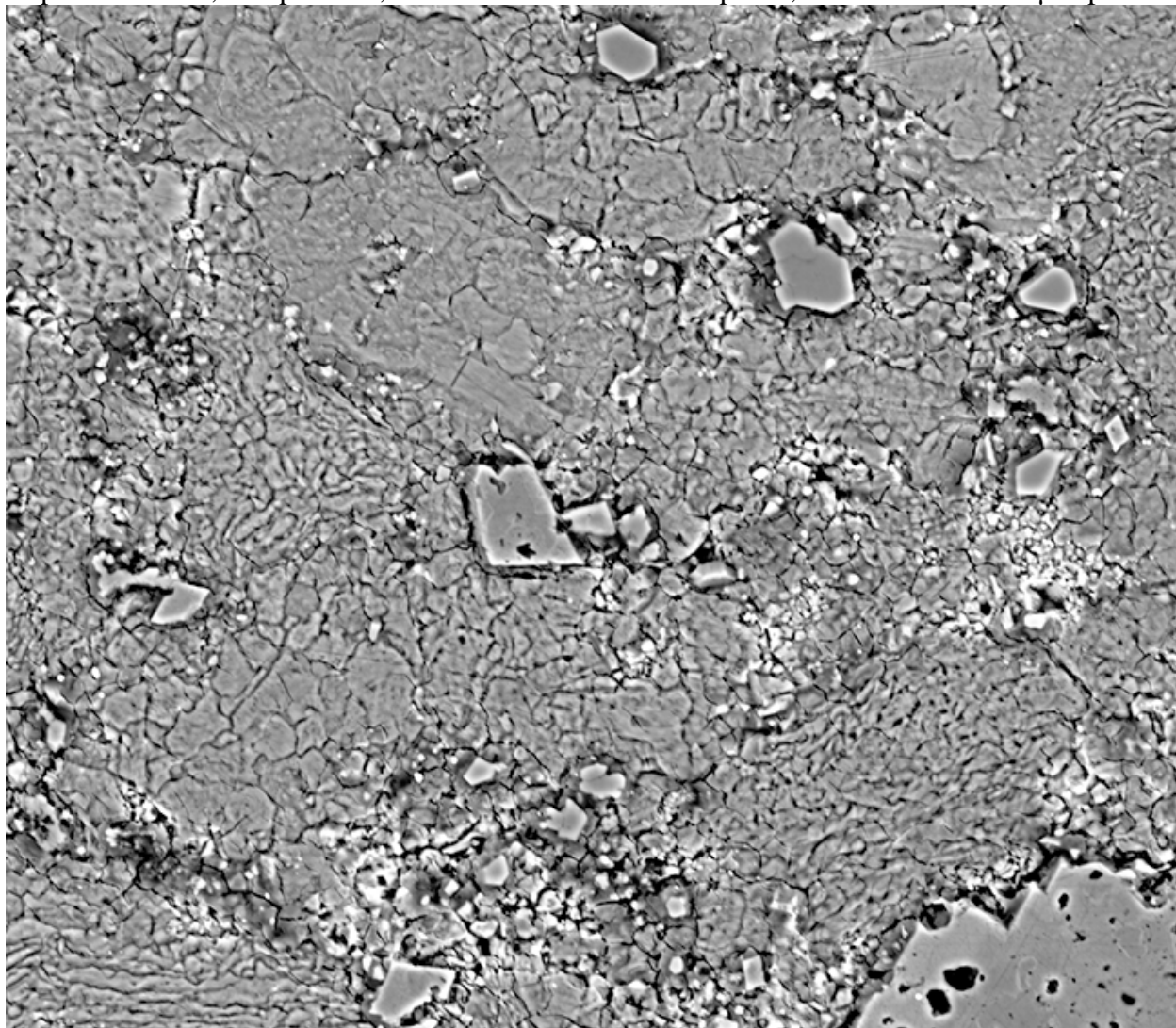
Depth 4875.15 ft, Sample 3-6, Dimensions 18718x16123 pixel², scale 0.007022021 μm/pixel



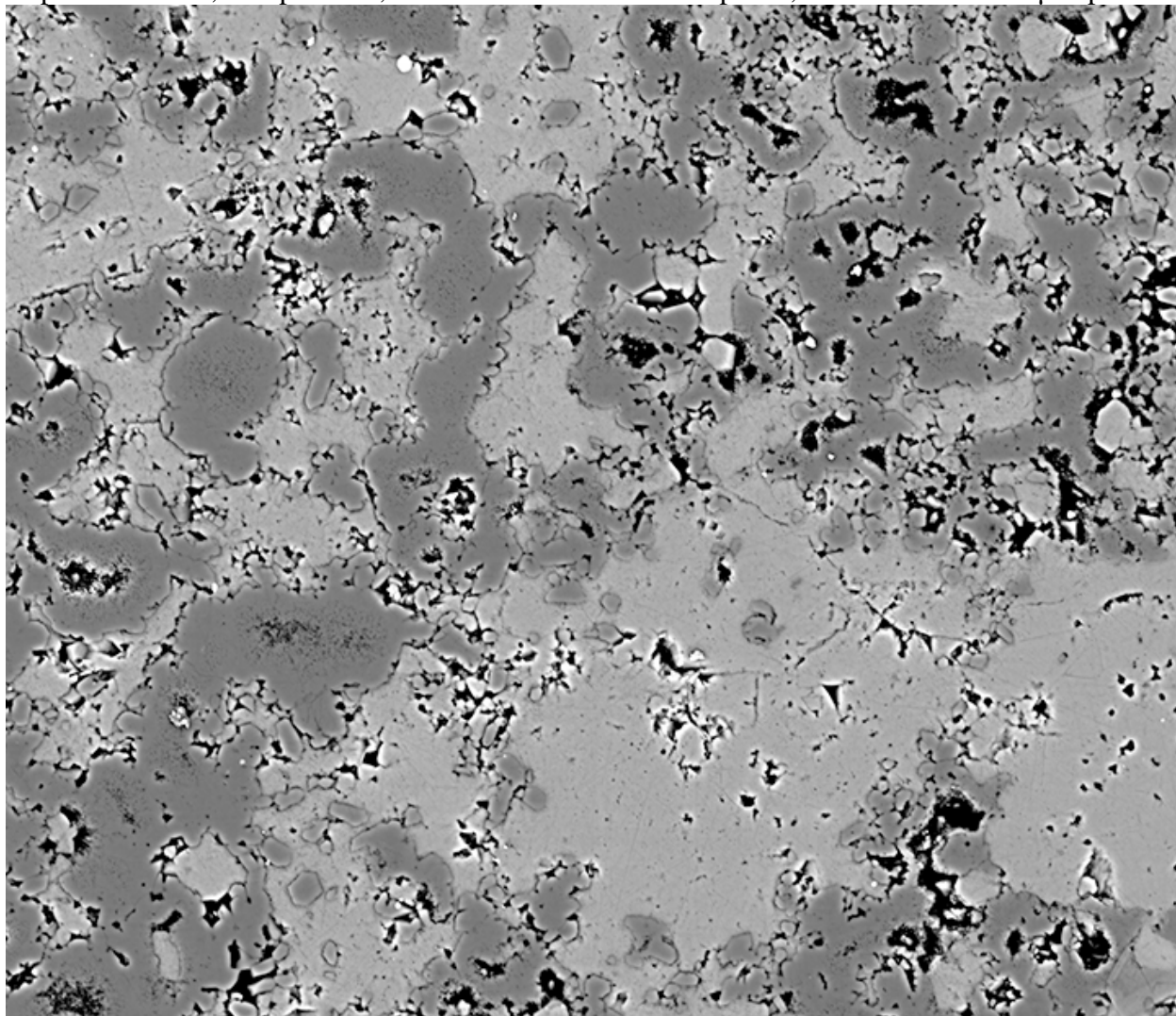
Depth 4875.15 ft, Sample 3-6, Dimensions 22483x19393 pixel², scale 0.007022021 $\mu\text{m}/\text{pixel}$



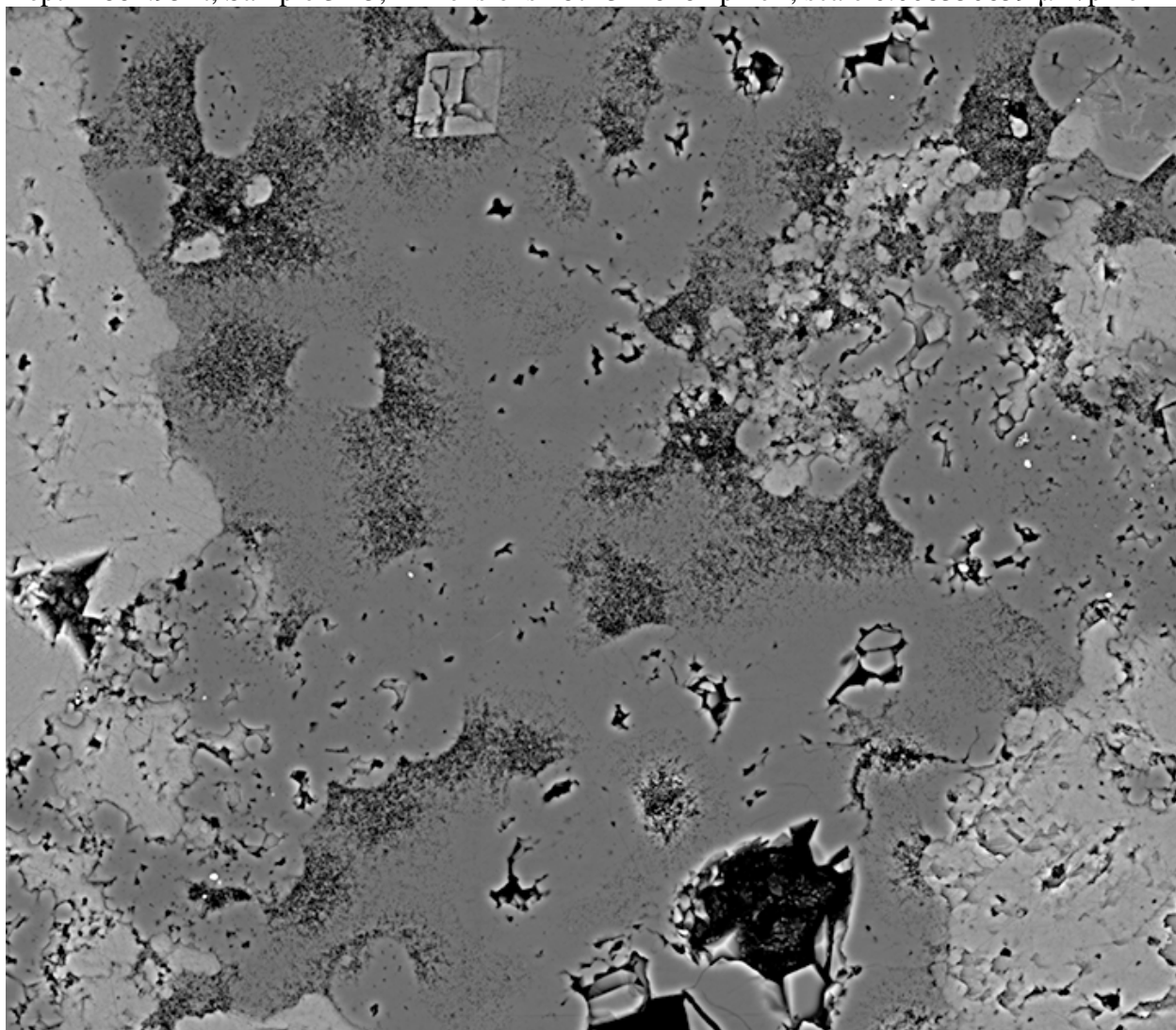
Depth 4884.95 ft, Sample 3-15, Dimensions 18718x16276 pixel², scale 0.008350659 μm/pixel



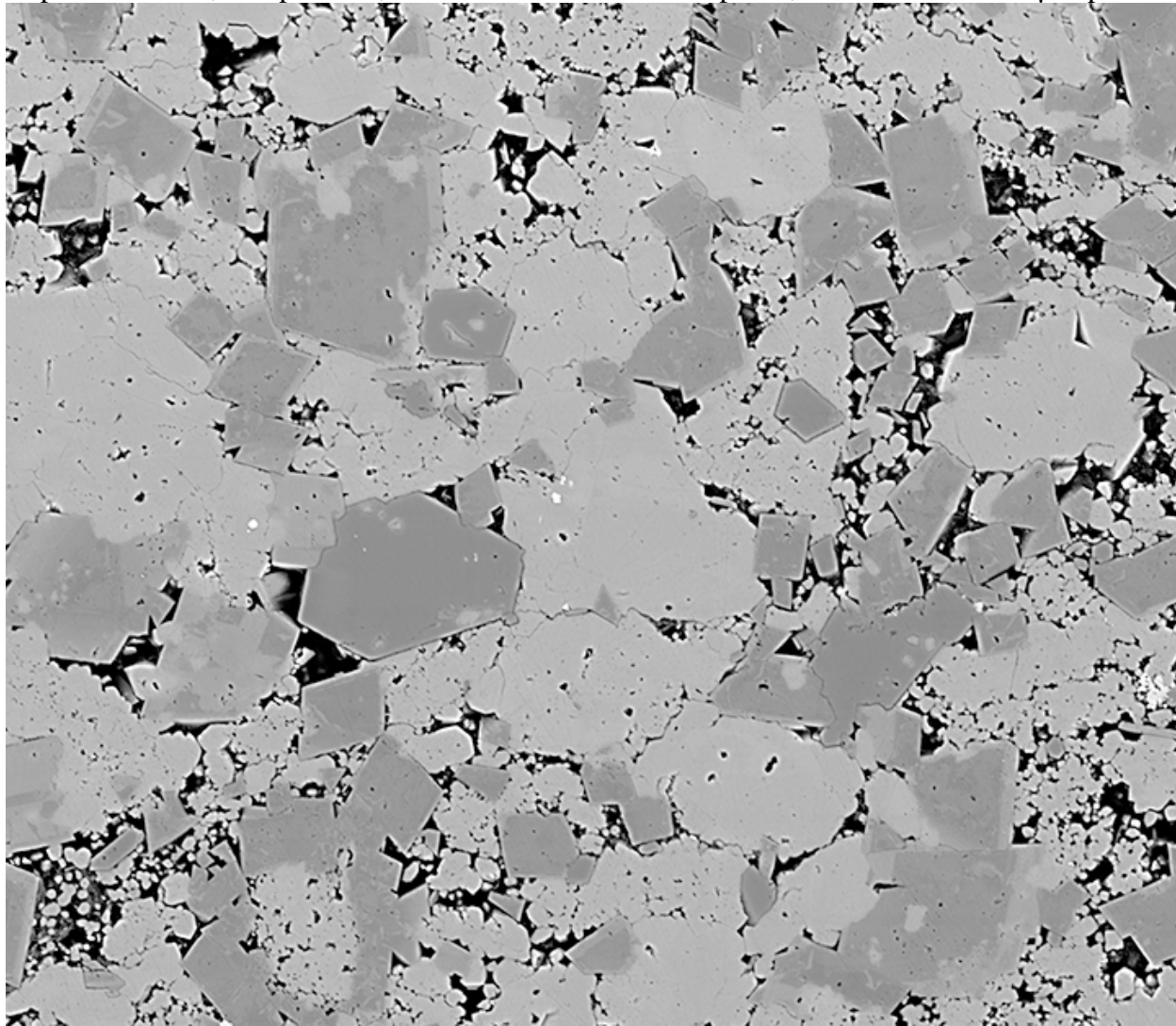
Depth 4884.95 ft, Sample 3-15, Dimensions 22515x19413 pixel², scale 0.008350659 μm/pixel



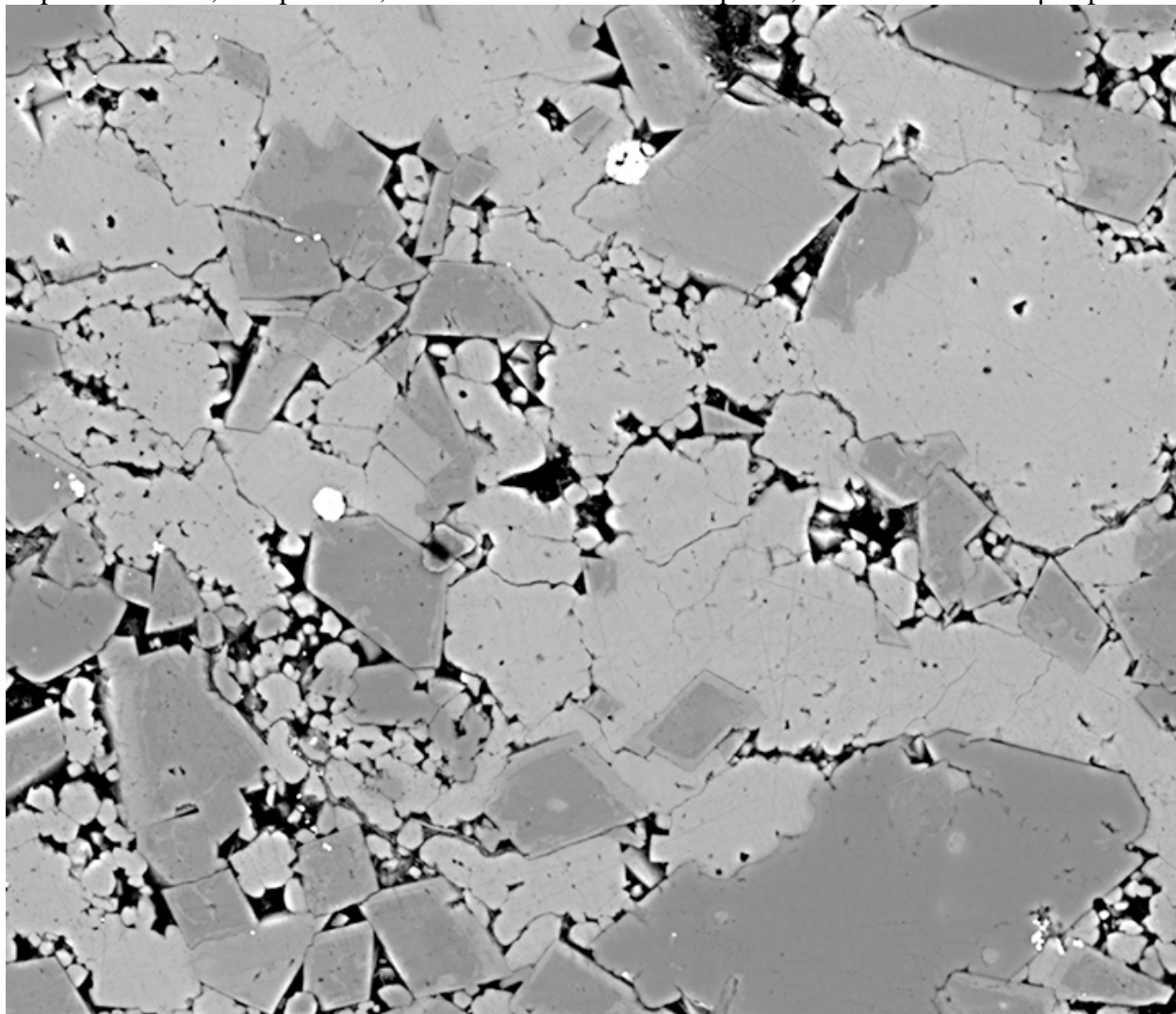
Depth 4884.95 ft, Sample 3-15, Dimensions 18723x16264 pixel², scale 0.008350659 μm/pixel



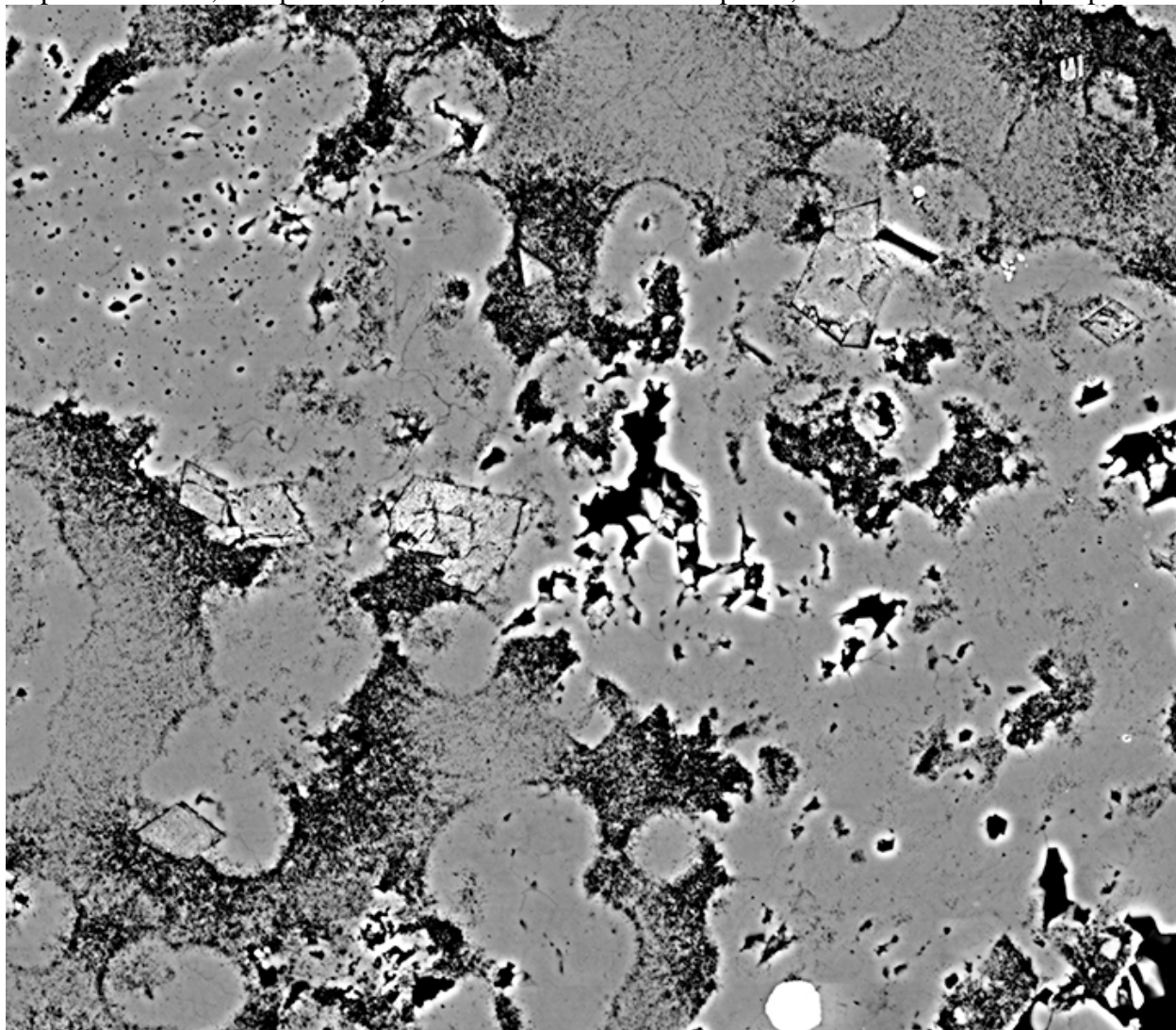
Depth 4894.95 ft, Sample 3-25, Dimensions 36282x31555 pixel², scale 0.009300513 μm/pixel



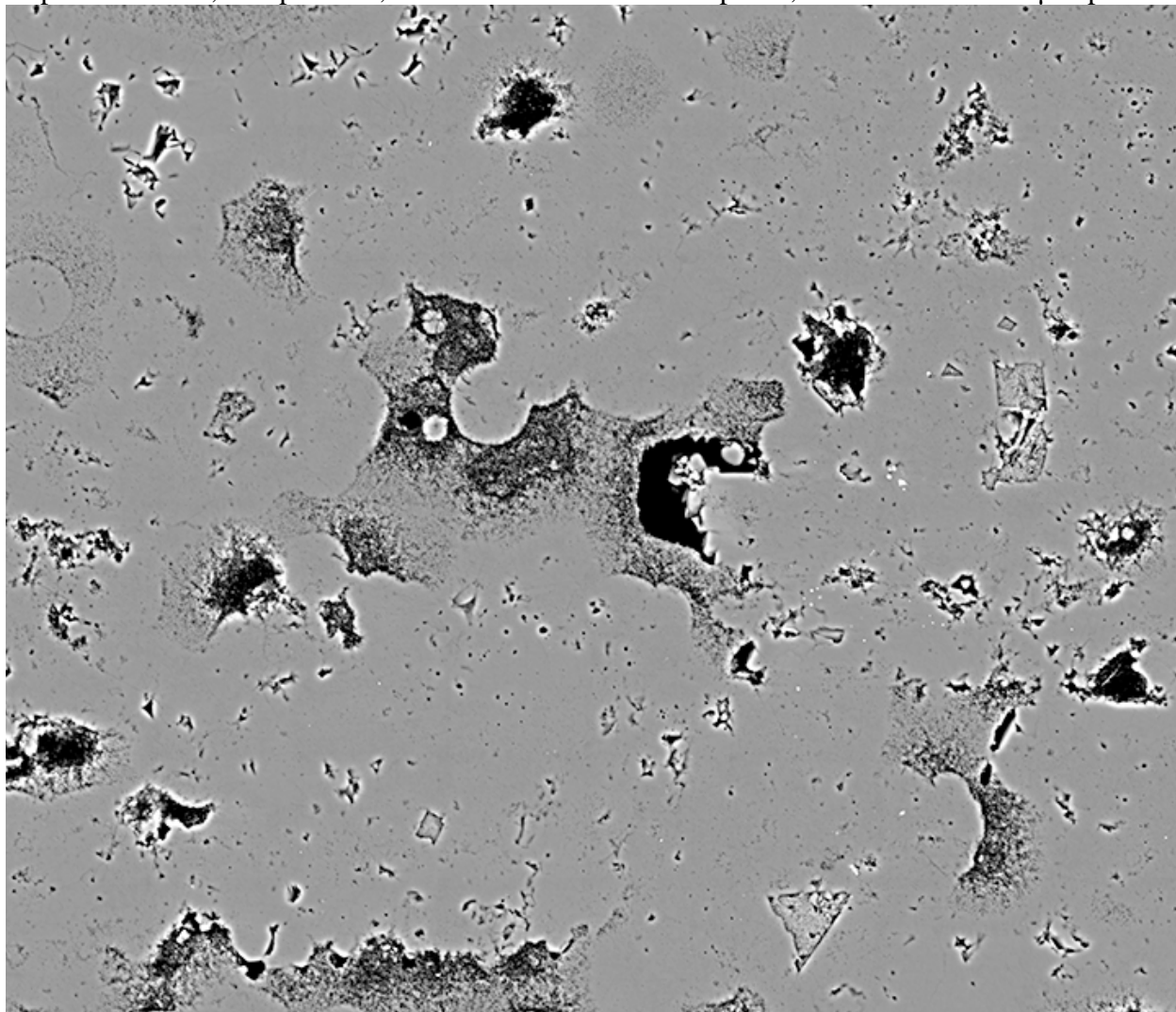
Depth 4894.95 ft, Sample 3-25, Dimensions 18803x16193 pixel², scale 0.009300513 μm/pixel



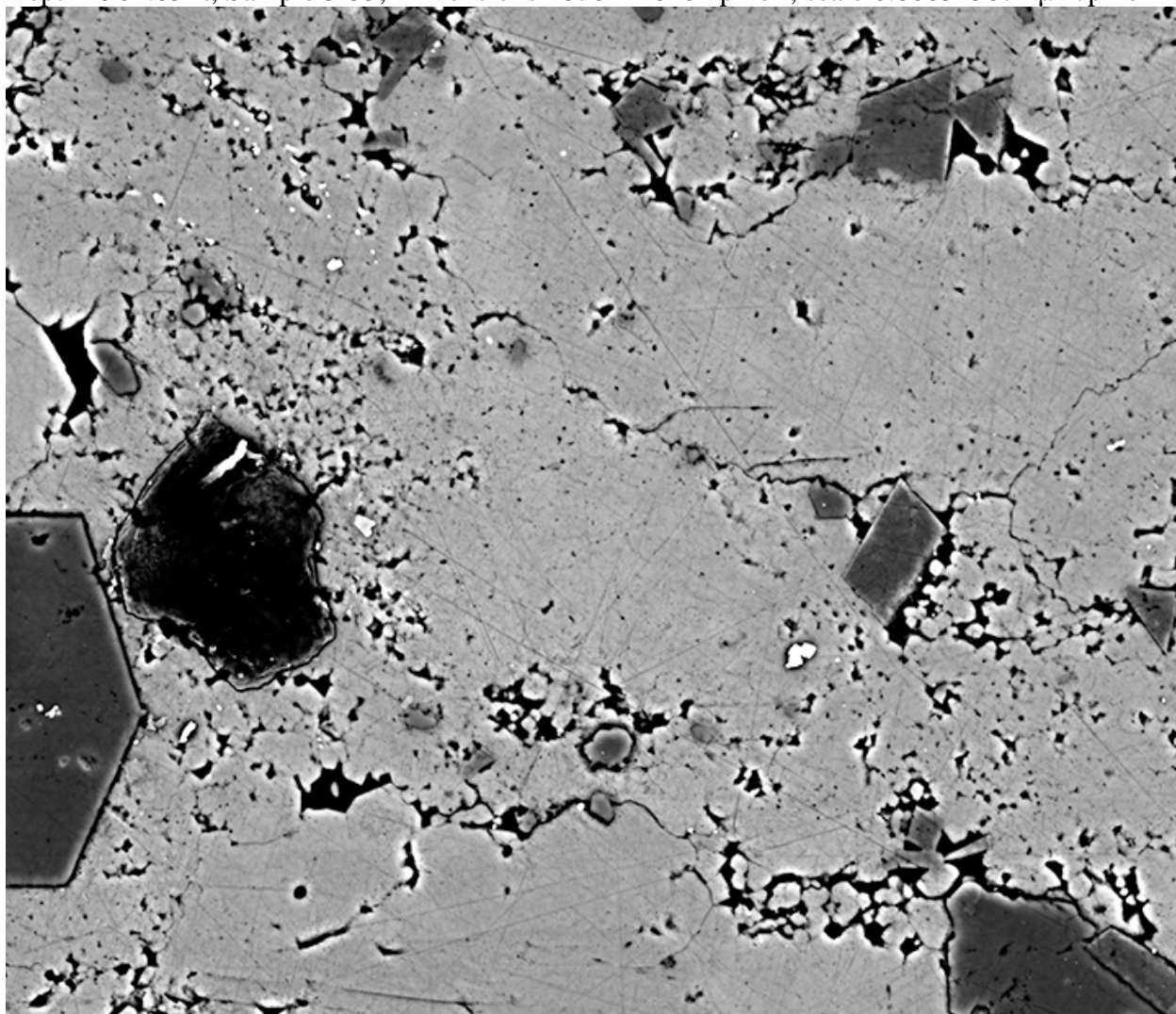
Depth 4894.95 ft, Sample 3-25, Dimensions 18778x16349 pixel², scale 0.009300513 μm/pixel



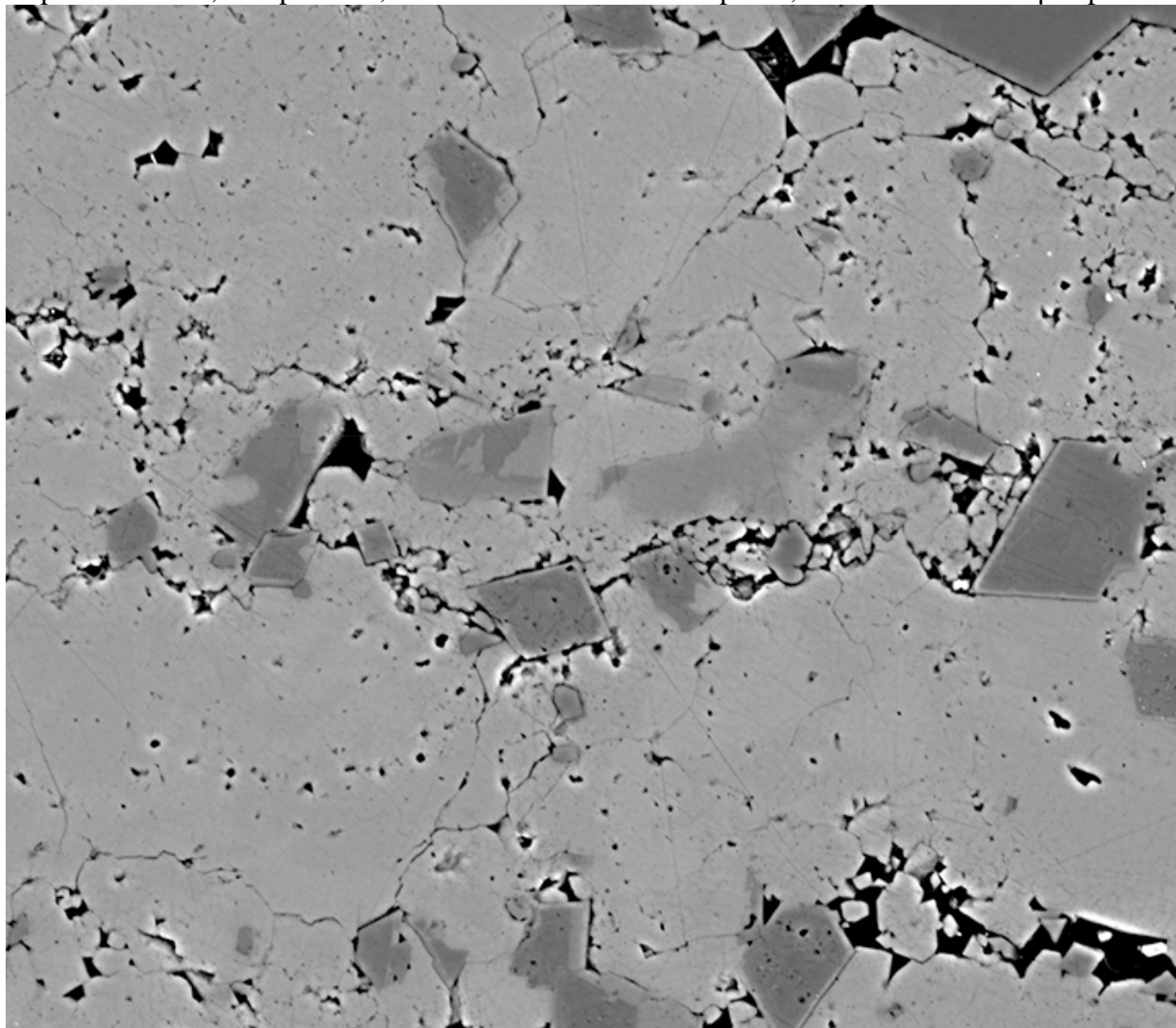
Depth 4904.85 ft, Sample 3-35, Dimensions 29840x25828 pixel², scale 0.008345874 μm/pixel



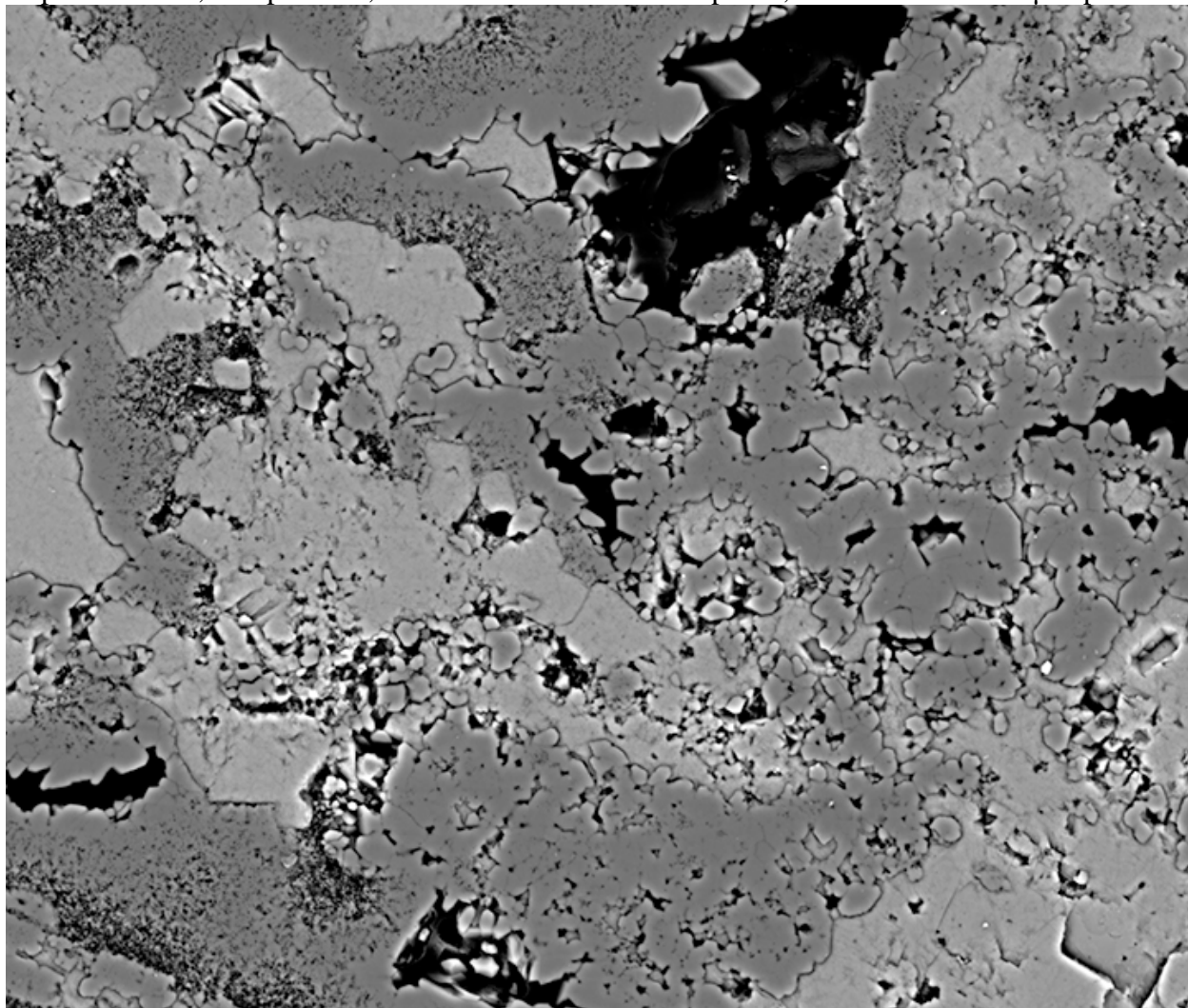
Depth 4904.85 ft, Sample 3-35, Dimensions 18762x16201 pixel², scale 0.008345874 μm/pixel



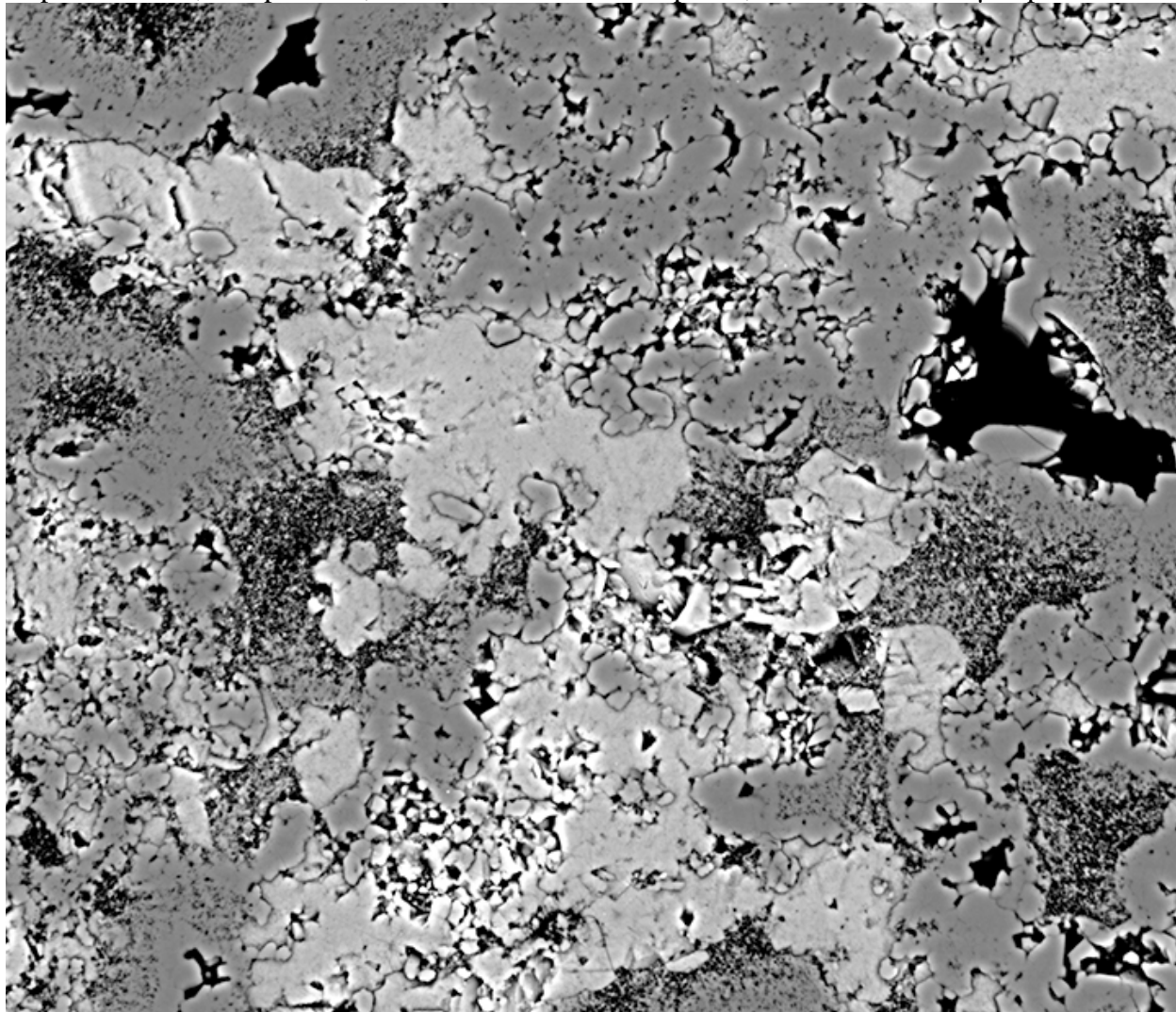
Depth 4904.85 ft, Sample 3-35, Dimensions 18733x16313 pixel², scale 0.008345874 μm/pixel



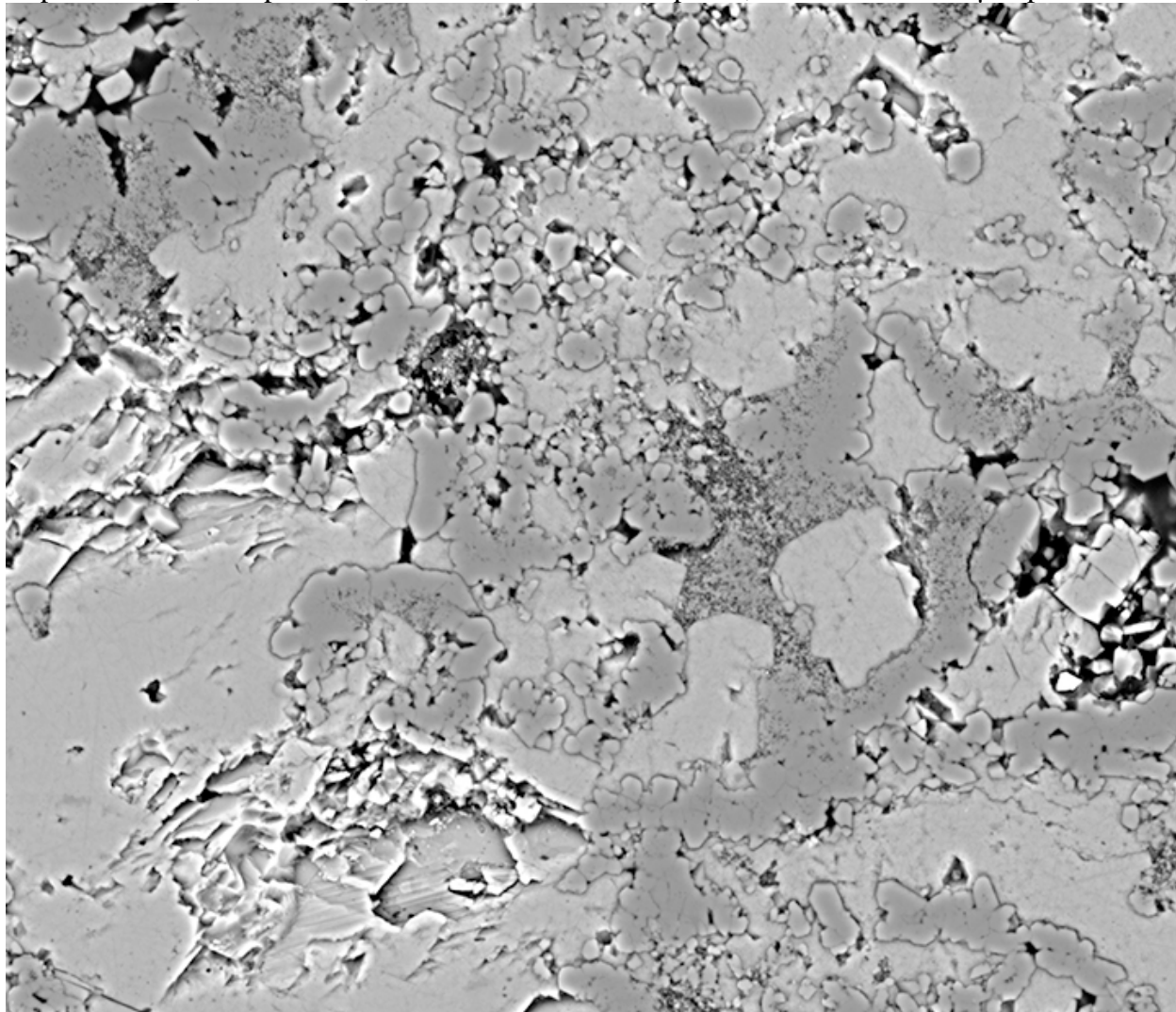
Depth 4907.7 ft, Sample 3-38, Dimensions 18724x15947 pixel², scale 0.009074487 μm/pixel



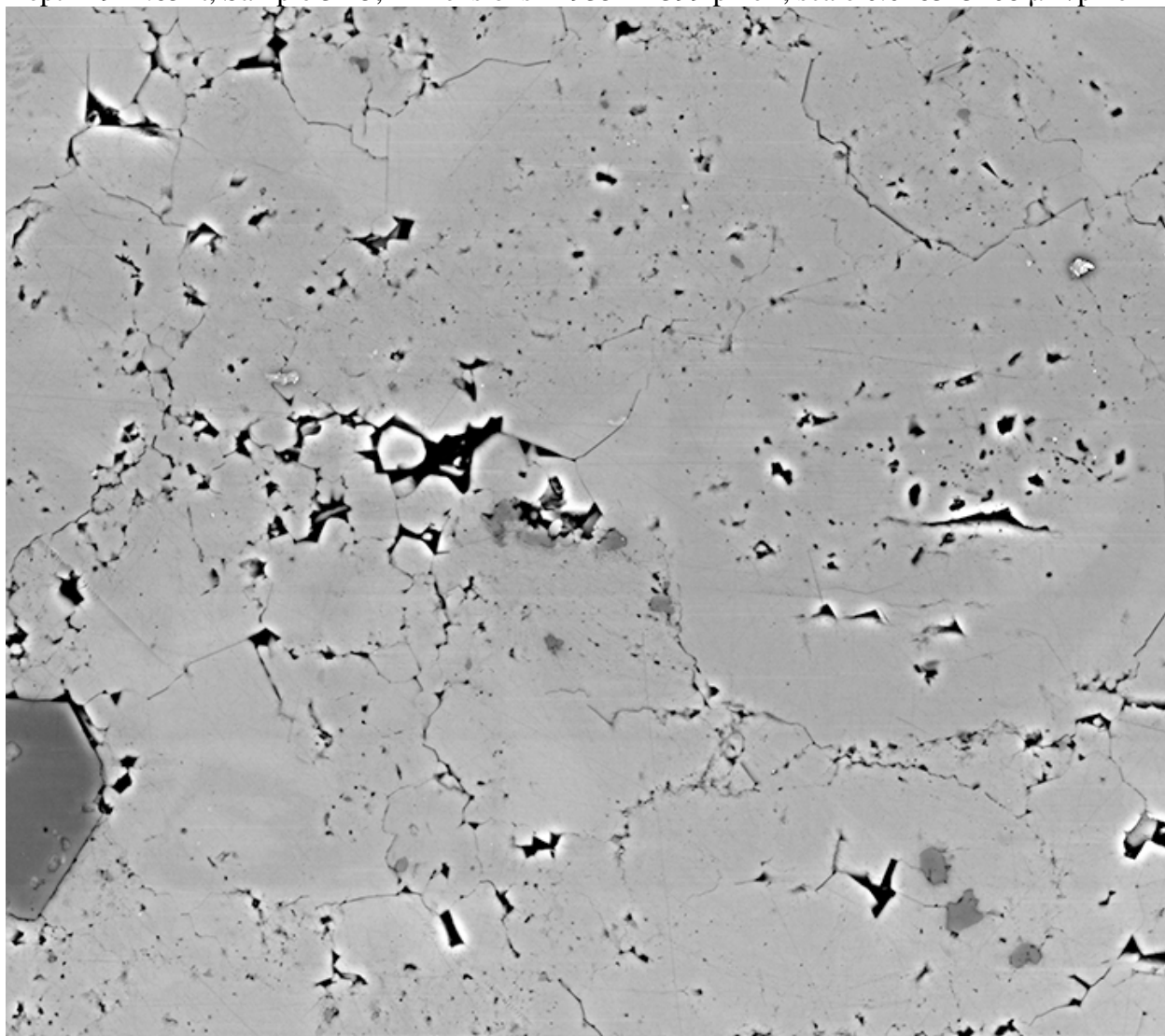
Depth 4907.7 ft, Sample 3-38, Dimensions 9387x8119 pixel², scale 0.01700708 μm/pixel



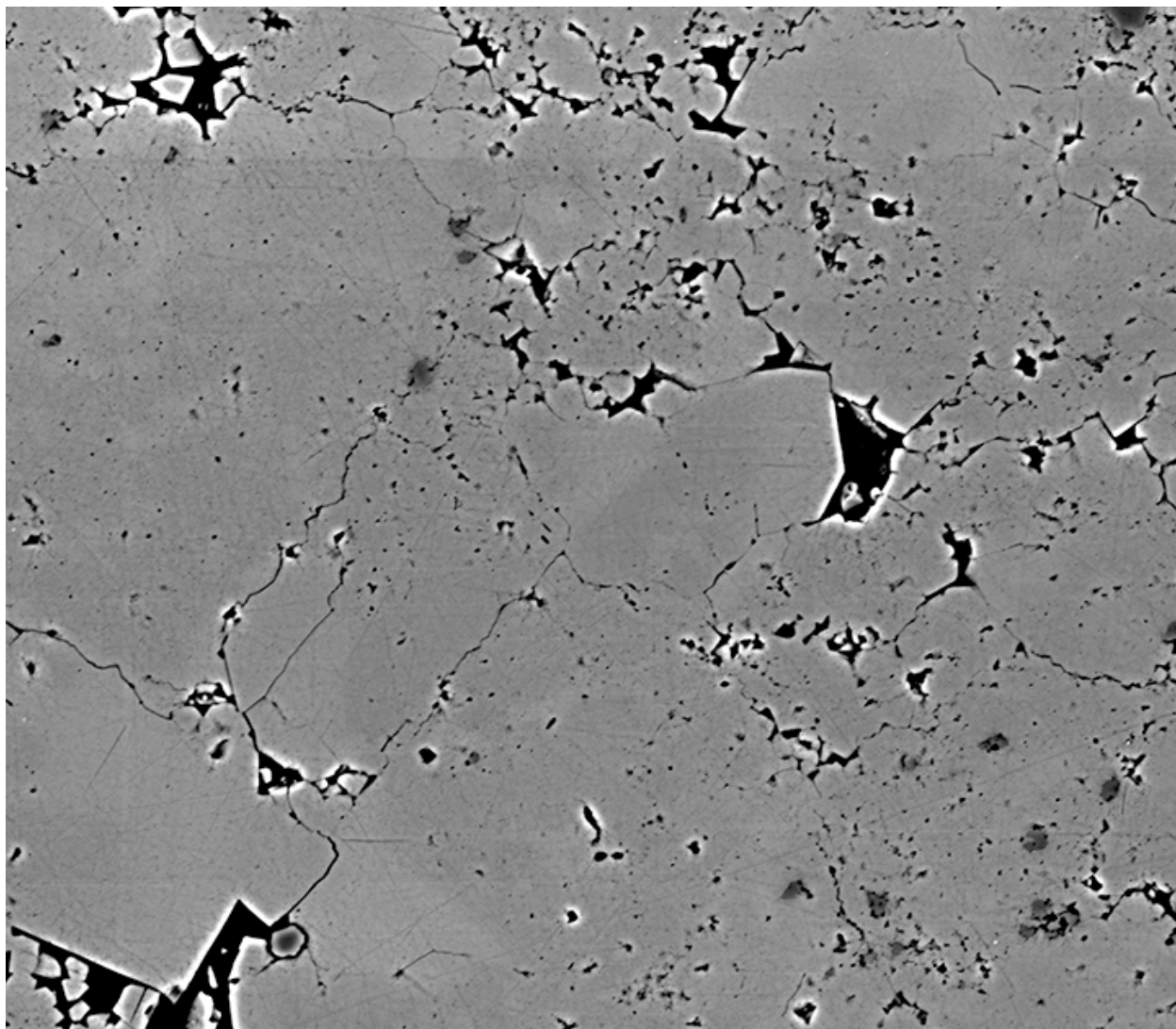
Depth 4907.7 ft, Sample 3-38, Dimensions 9416x8120 pixel², scale 0.01700708 μm/pixel



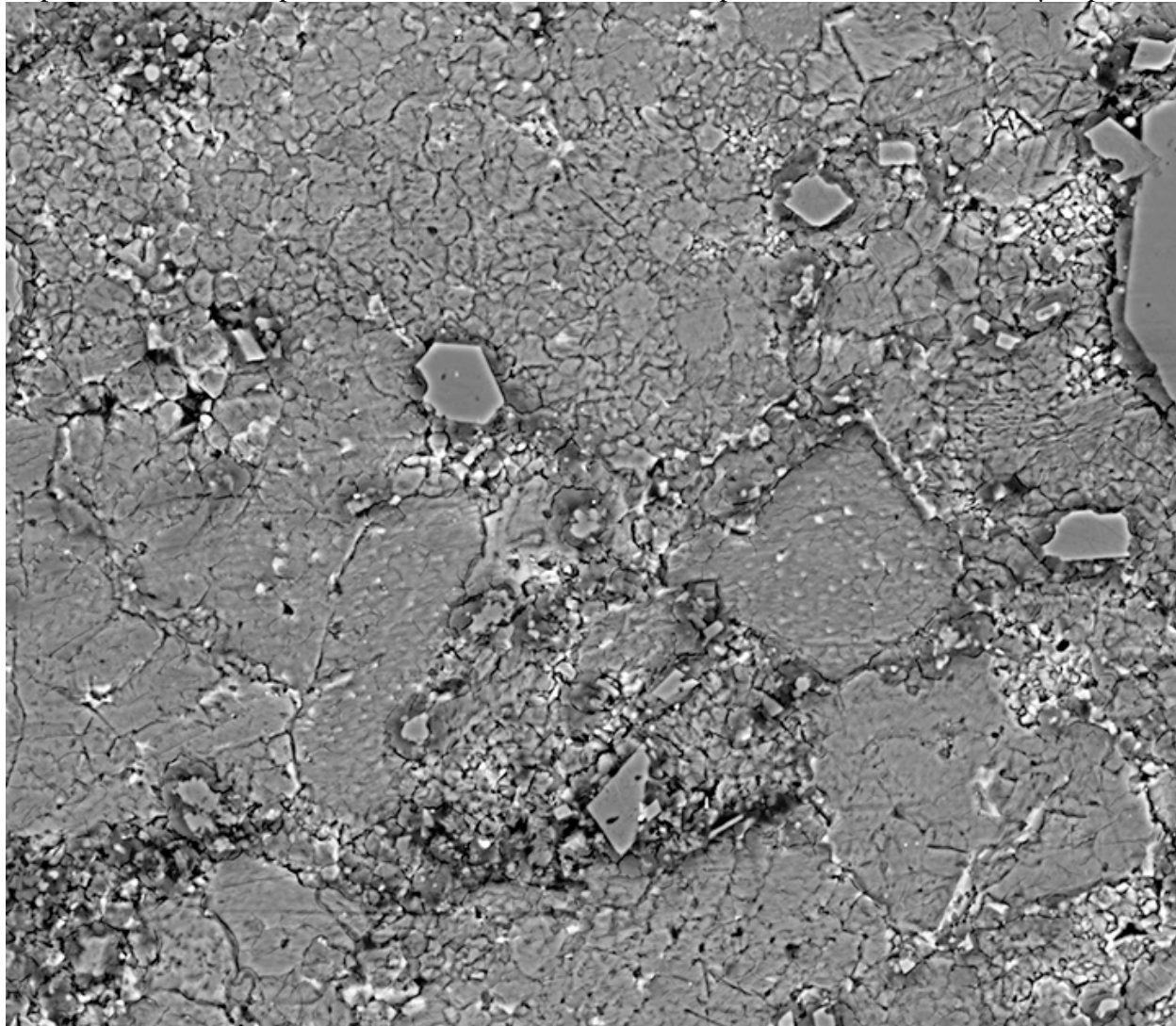
Depth 4914.65 ft, Sample 3-45, Dimensions 12935x11399 pixel², scale 0.016343408 μm/pixel



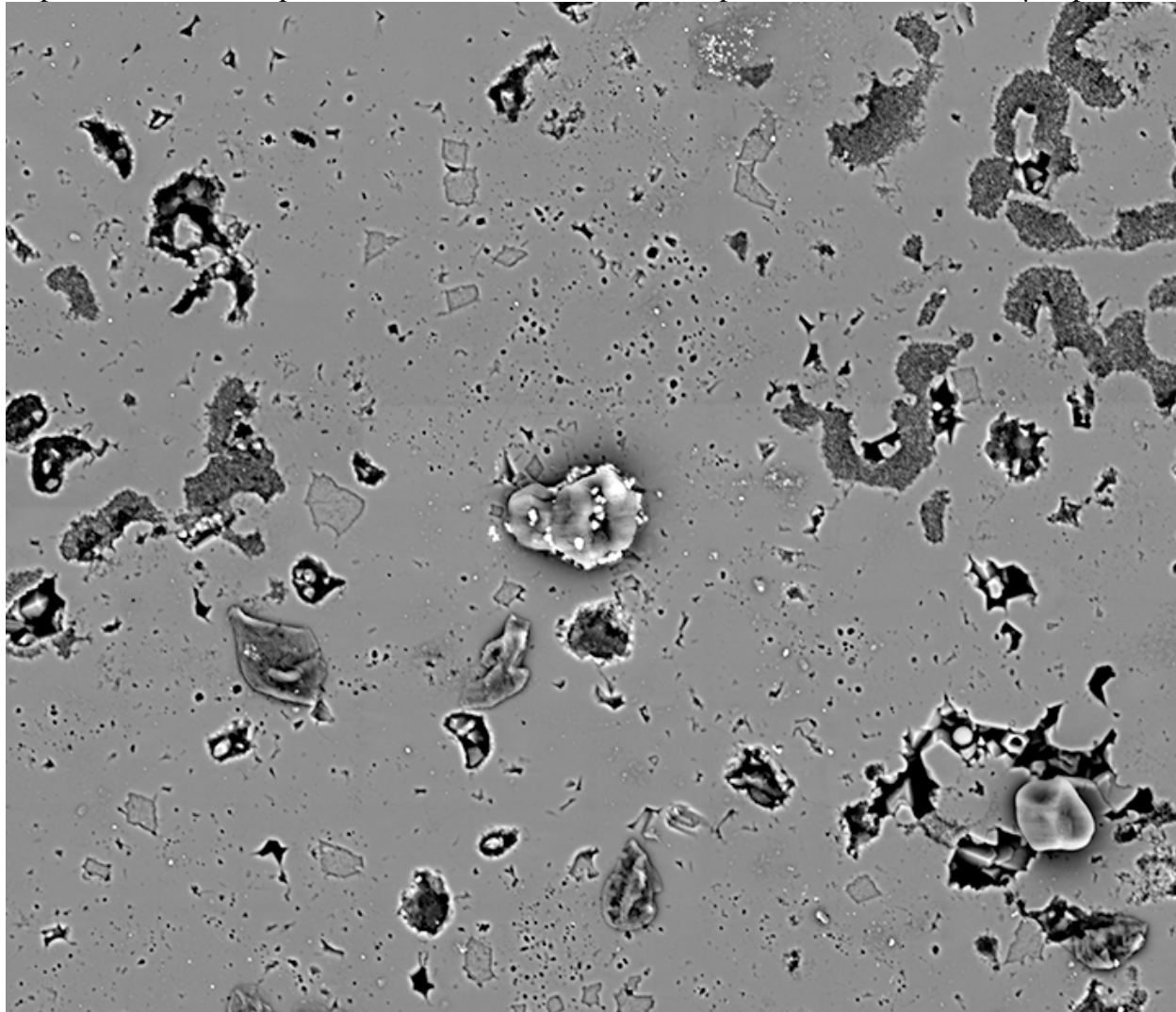
Depth 4914.65 ft, Sample 3-45, Dimensions 13028x11315 pixel², scale 0.013743115 μm/pixel



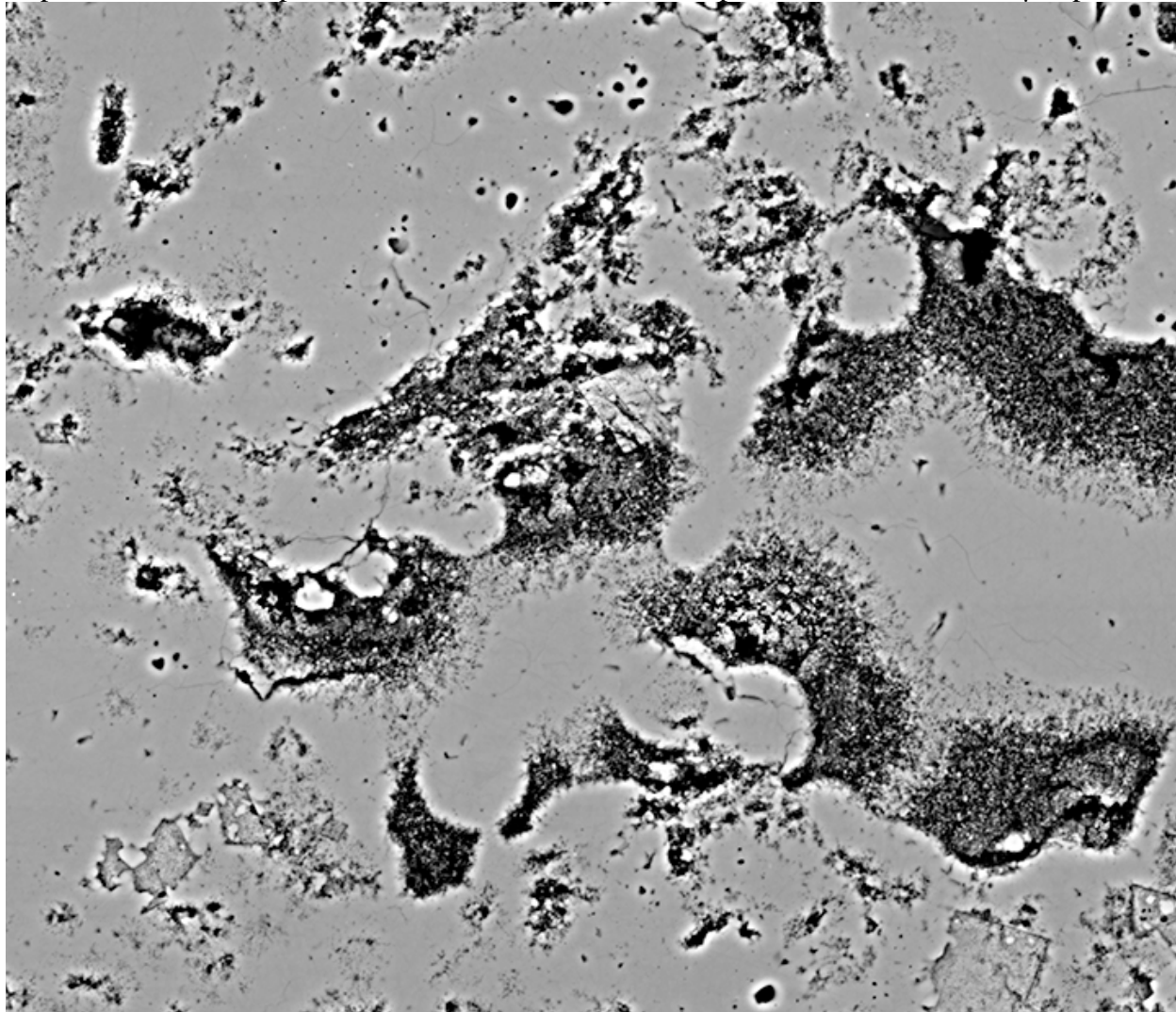
Depth 4914.65 ft, Sample 3-45, Dimensions 13073x11360 pixel², scale 0.013743115 μm/pixel



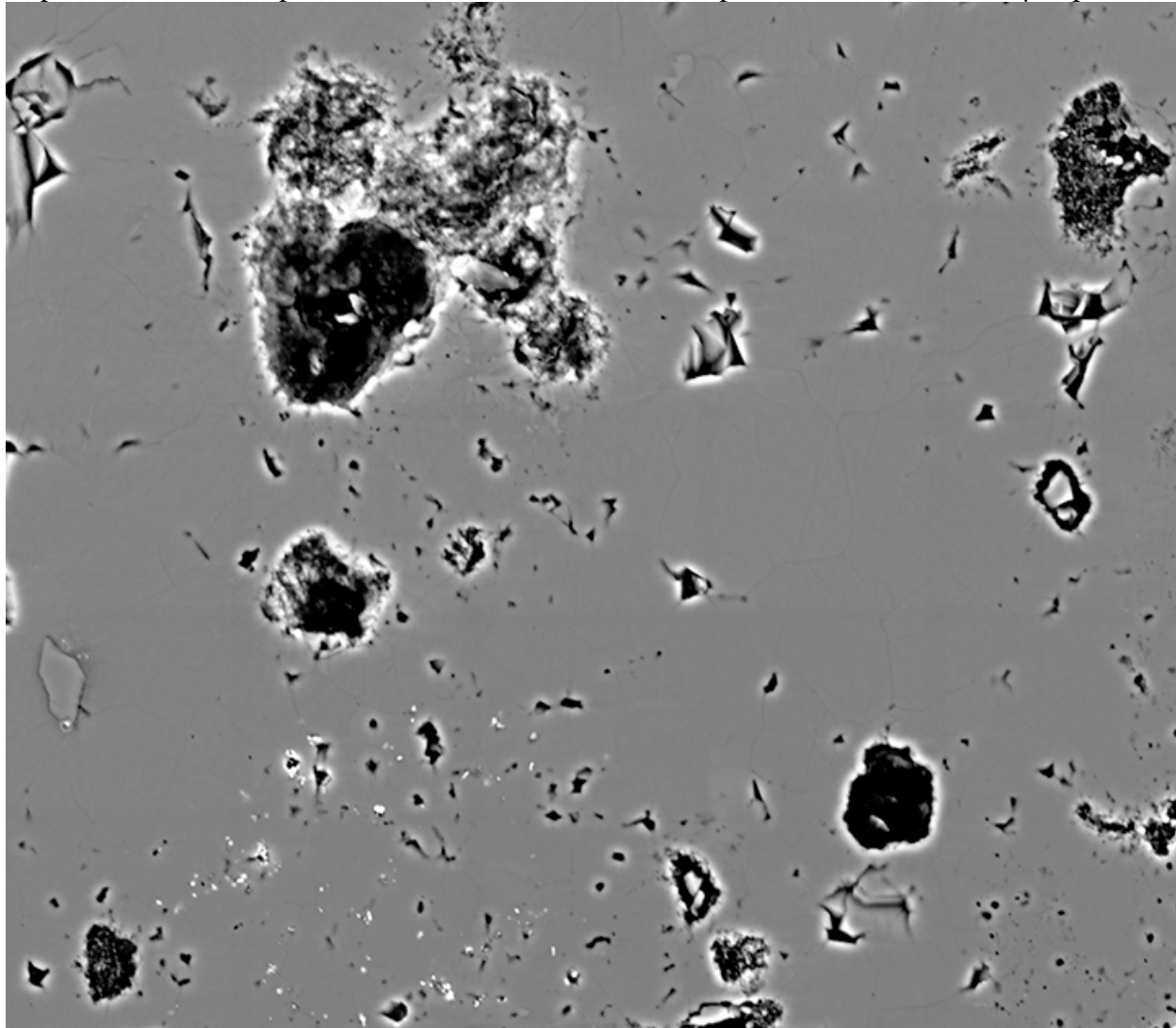
Depth 4921.35 ft, Sample 3-52, Dimensions 37094x31809 pixel², scale 0.00800144 μm/pixel



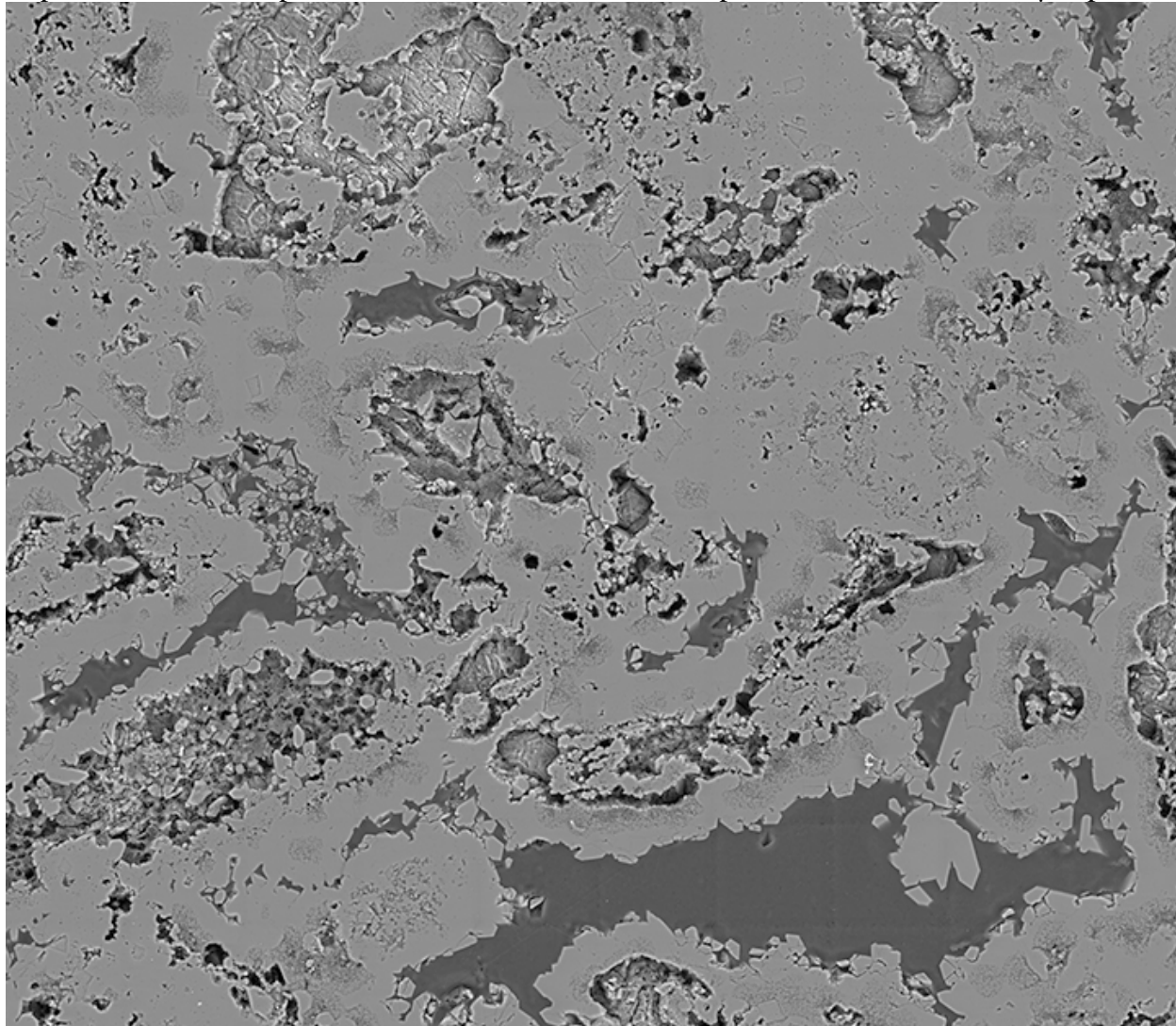
Depth 4921.35 ft, Sample 3-52, Dimensions 18764x16243 pixel², scale 0.00800144 μm/pixel



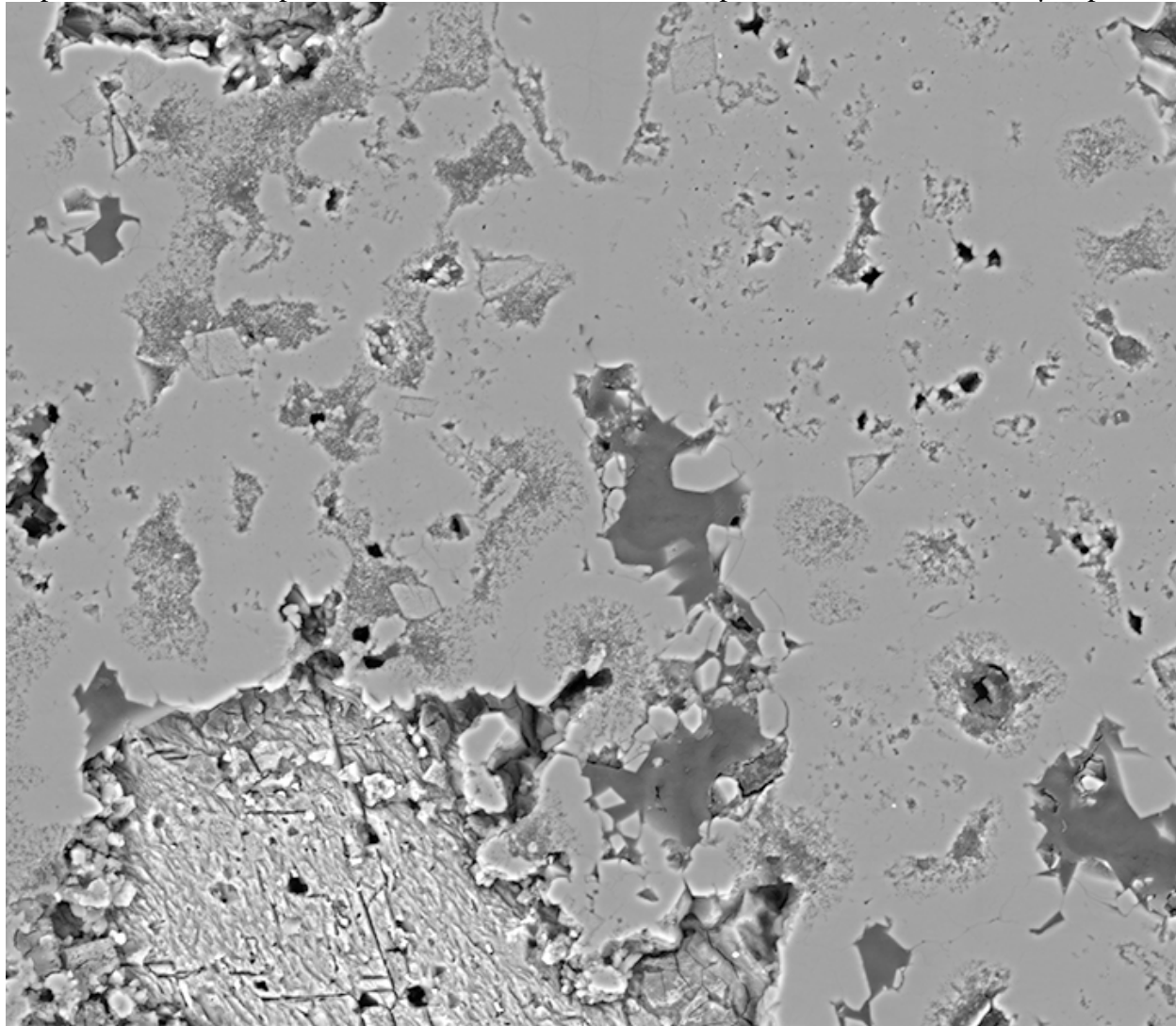
Depth 4921.35 ft, Sample 3-52, Dimensions 18736x16325 pixel², scale 0.00800144 μm/pixel



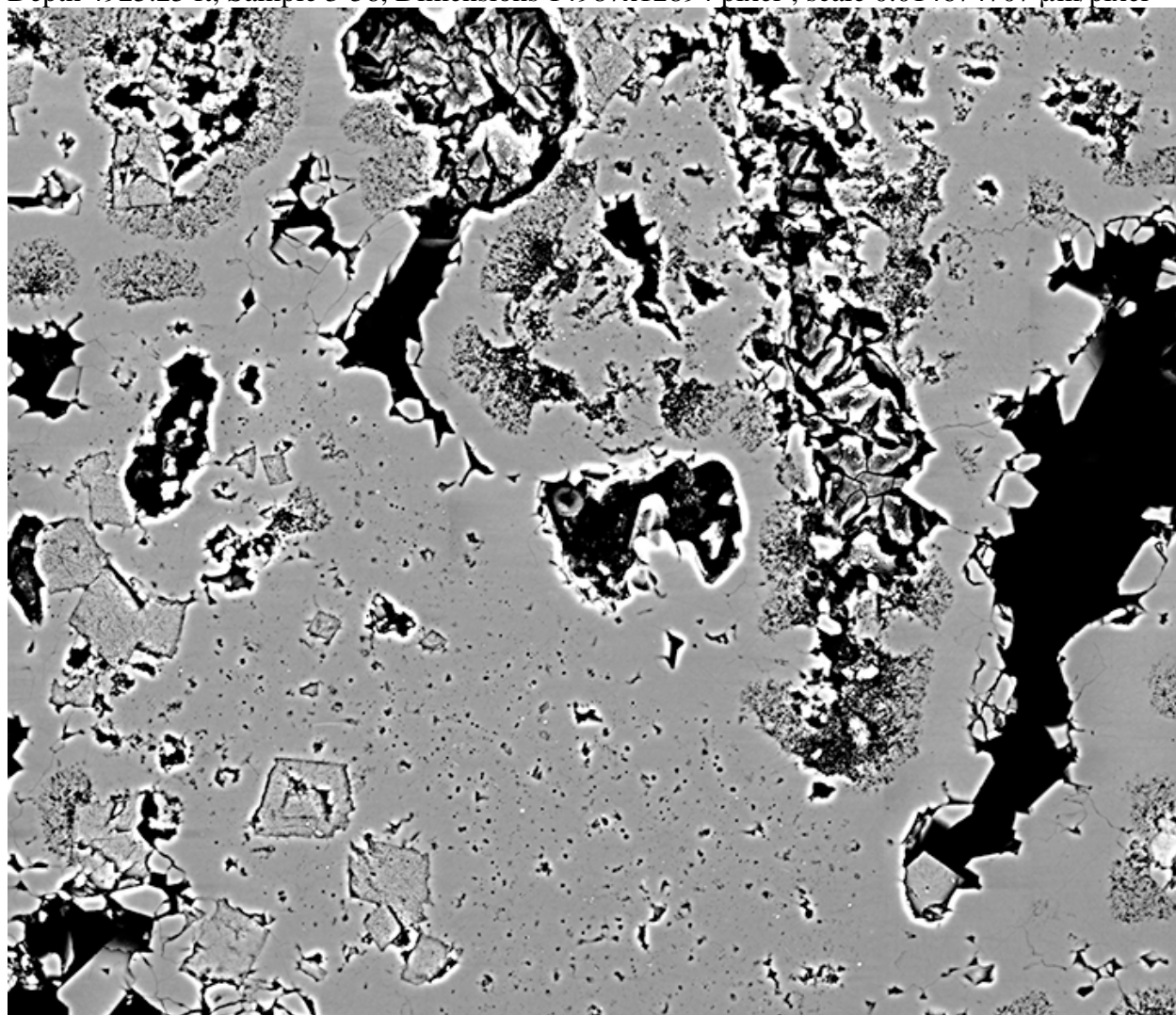
Depth 4925.25 ft, Sample 3-56, Dimensions 14987x12894 pixel², scale 0.013456787 μm/pixel



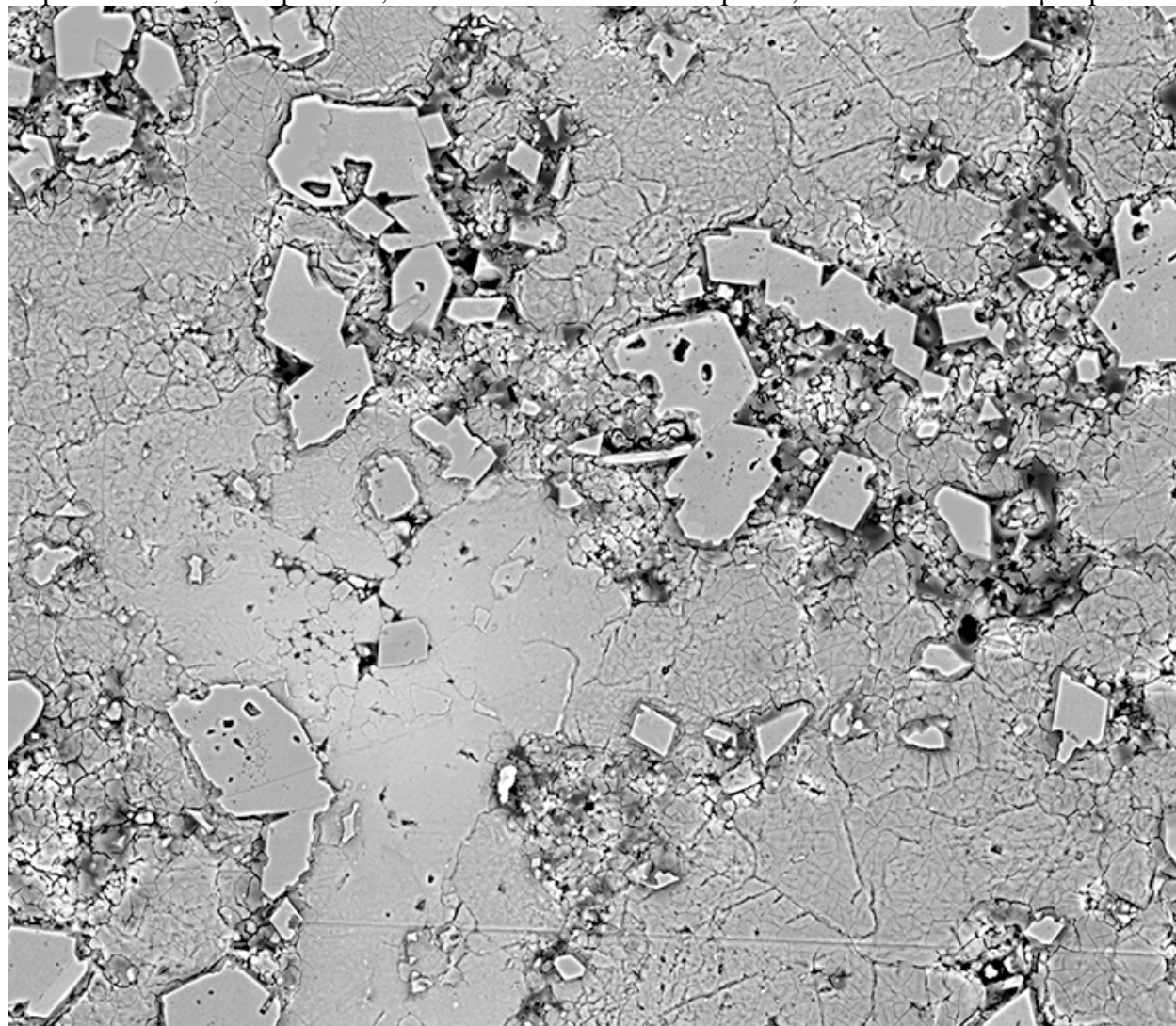
Depth 4925.25 ft, Sample 3-56, Dimensions 22407x19577 pixel², scale 0.008725635 μm/pixel



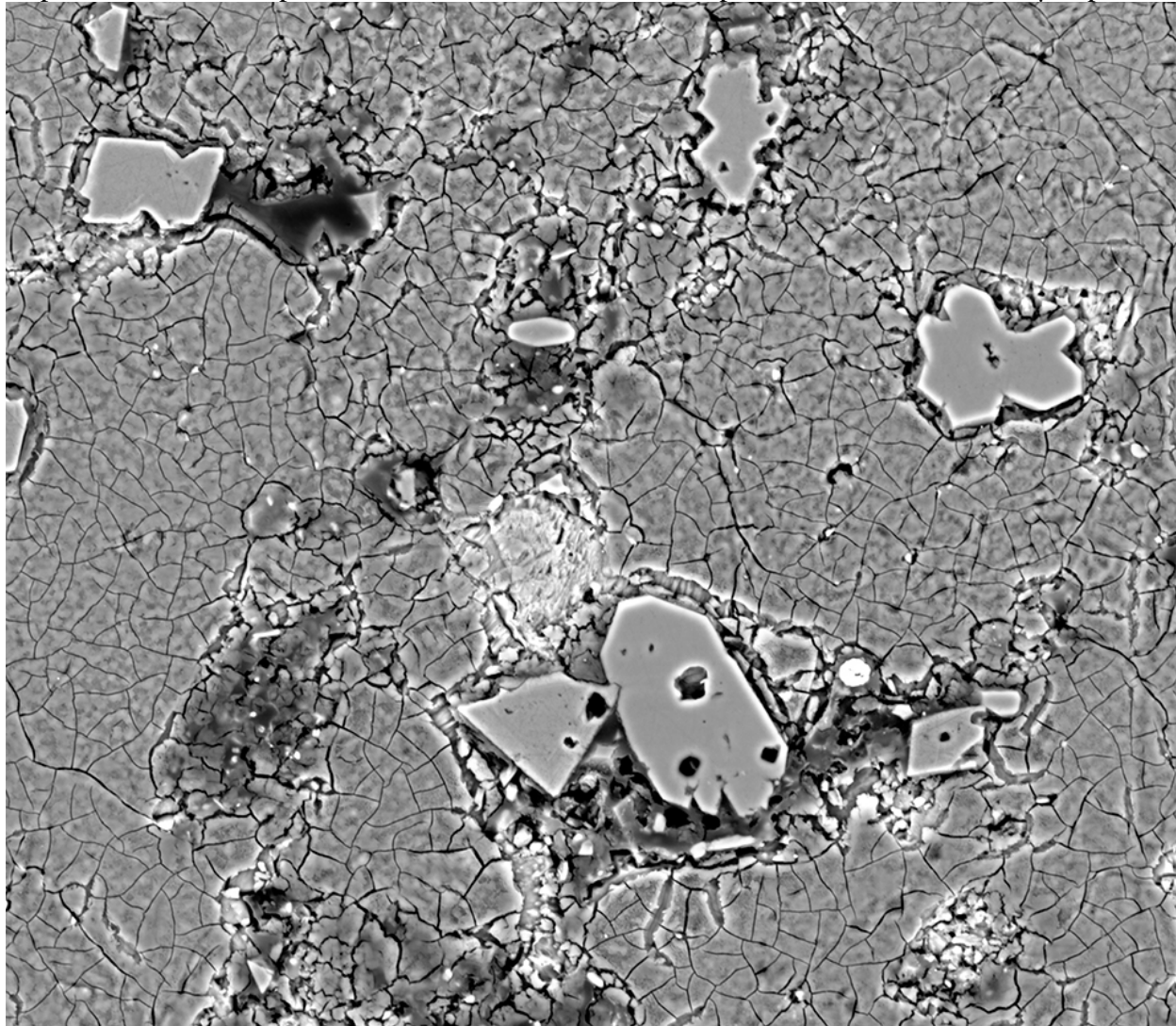
Depth 4925.25 ft, Sample 3-56, Dimensions 14987x12894 pixel², scale 0.014674707 μm/pixel



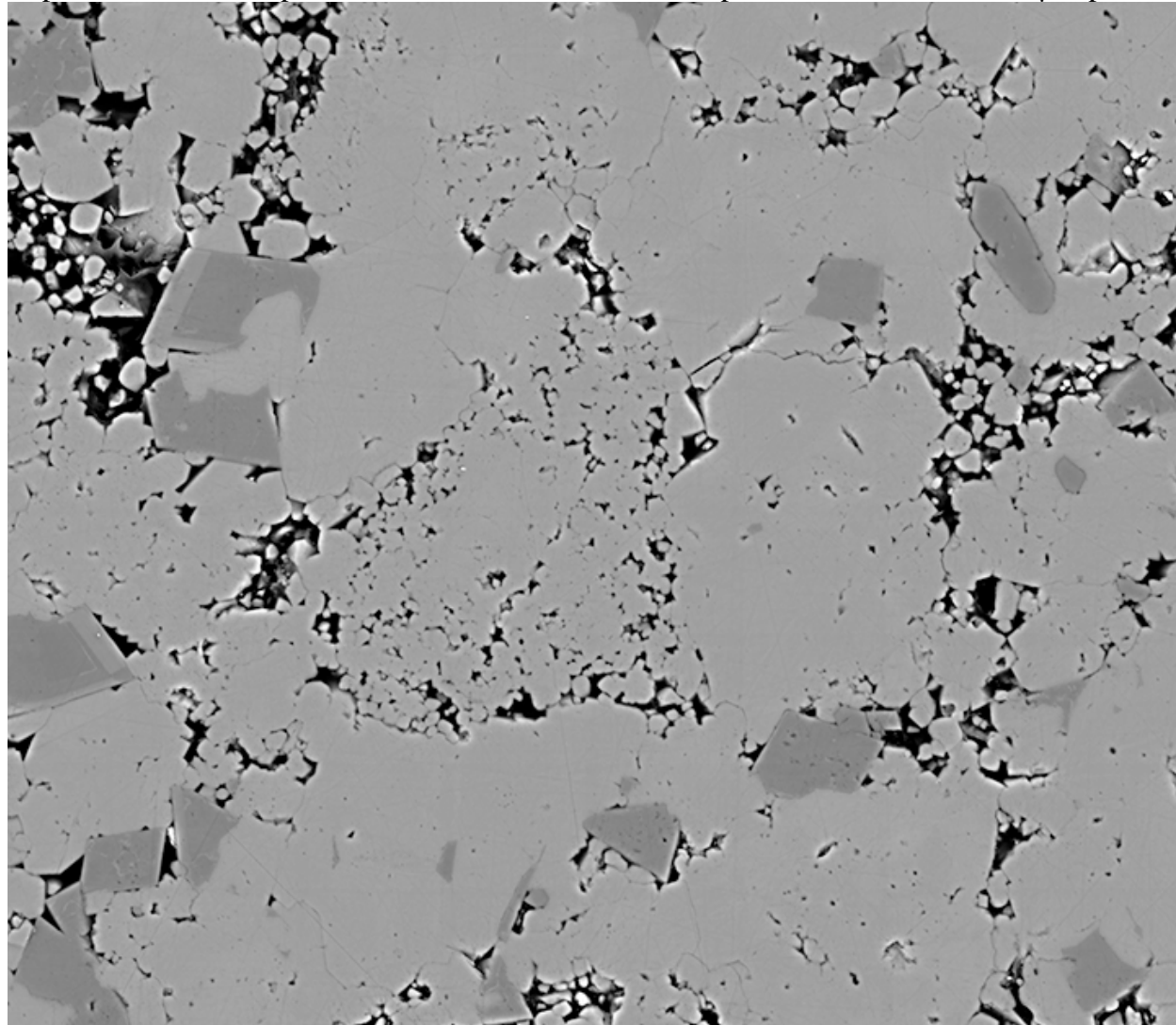
Depth 4933.95 ft, Sample 3-64, Dimensions 18622x16247 pixel², scale 0.015261377 μm/pixel



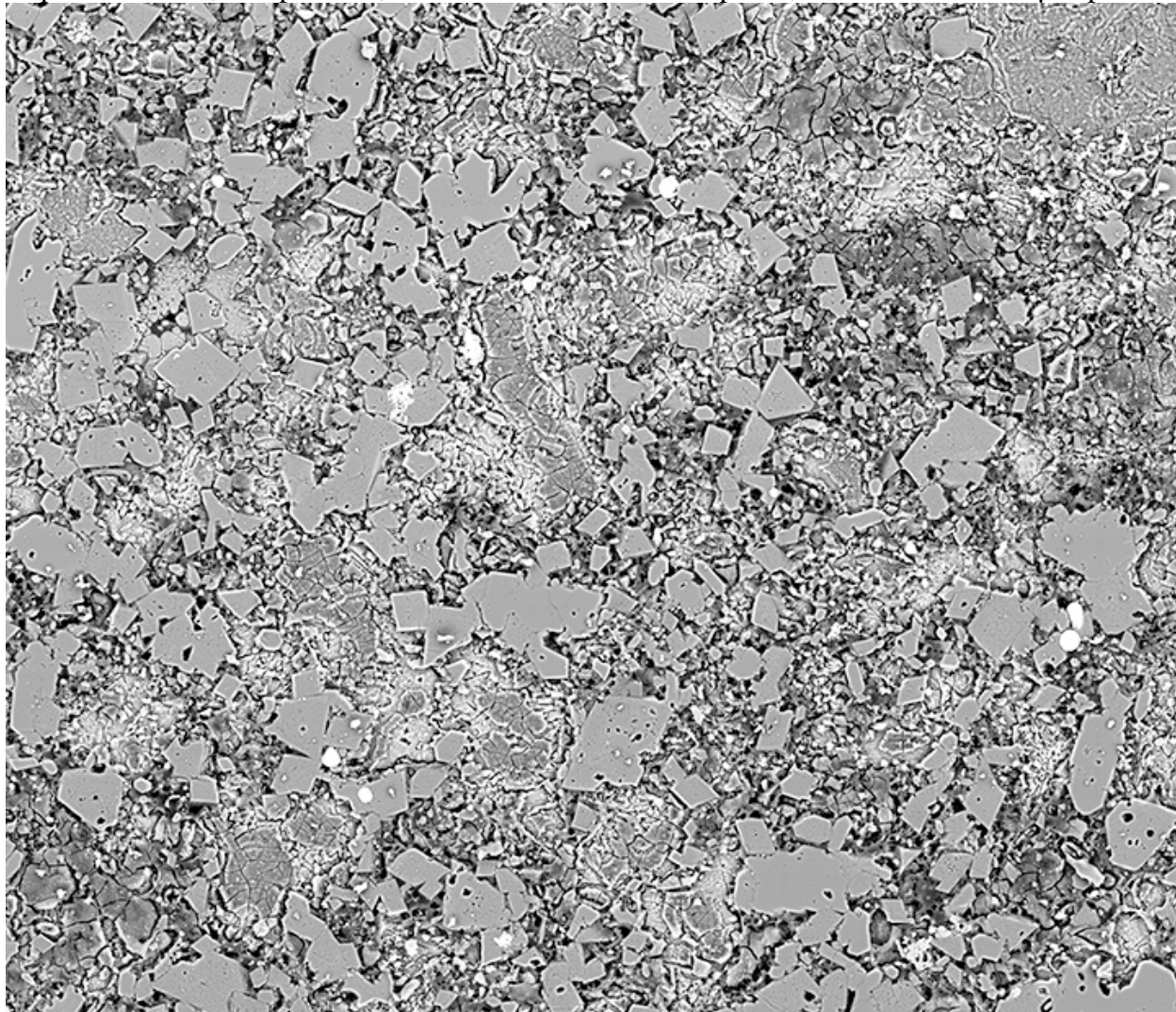
Depth 4933.95 ft, Sample 3-64, Dimensions 18628x16246 pixel², scale 0.018148975 μm/pixel



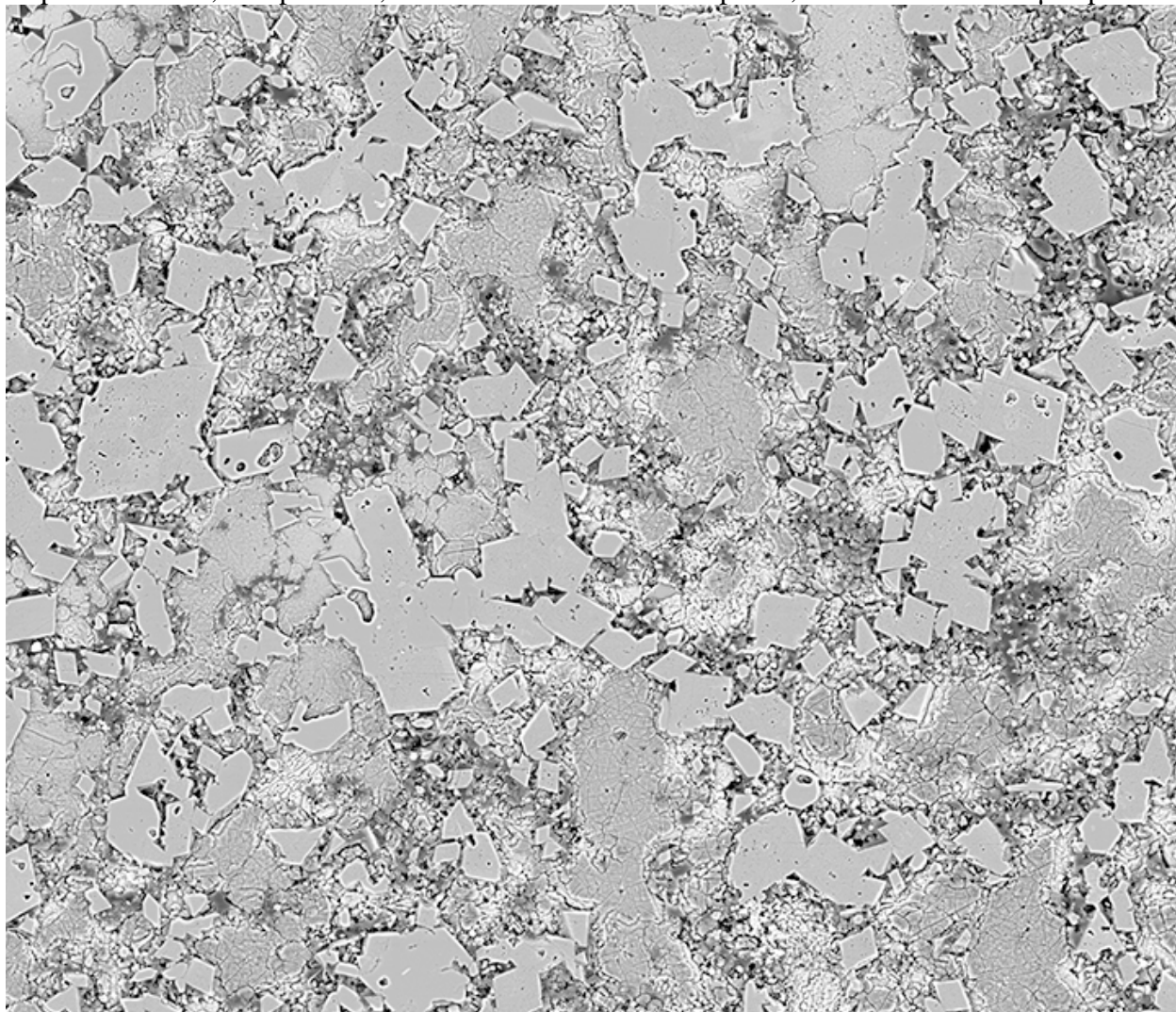
Depth 4933.95 ft, Sample 3-64, Dimensions 29804x25968 pixel², scale 0.006997388 μm/pixel



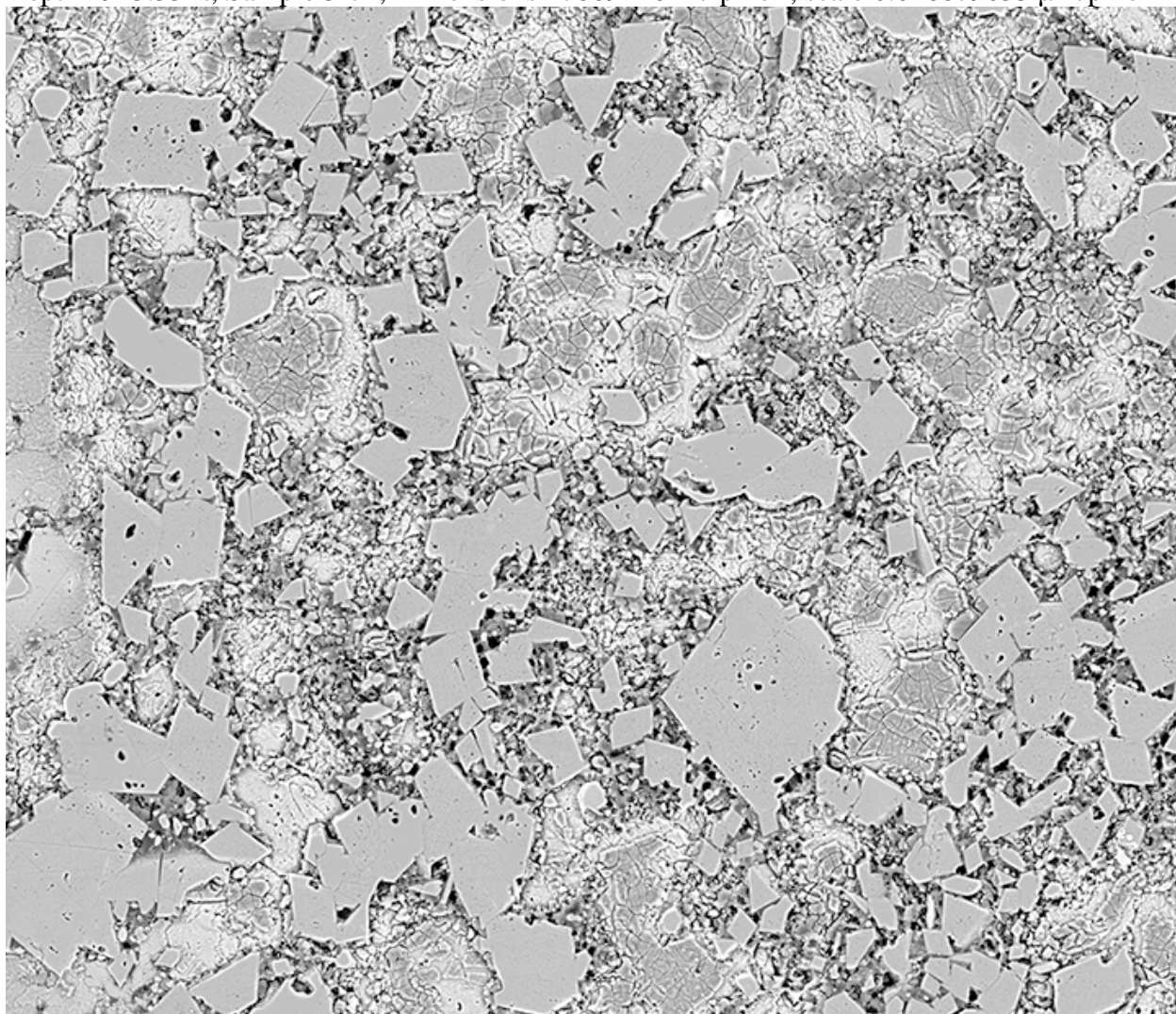
Depth 4943.55 ft, Sample 3-74, Dimensions 27628x23872 pixel², scale 0.017248682 μm/pixel



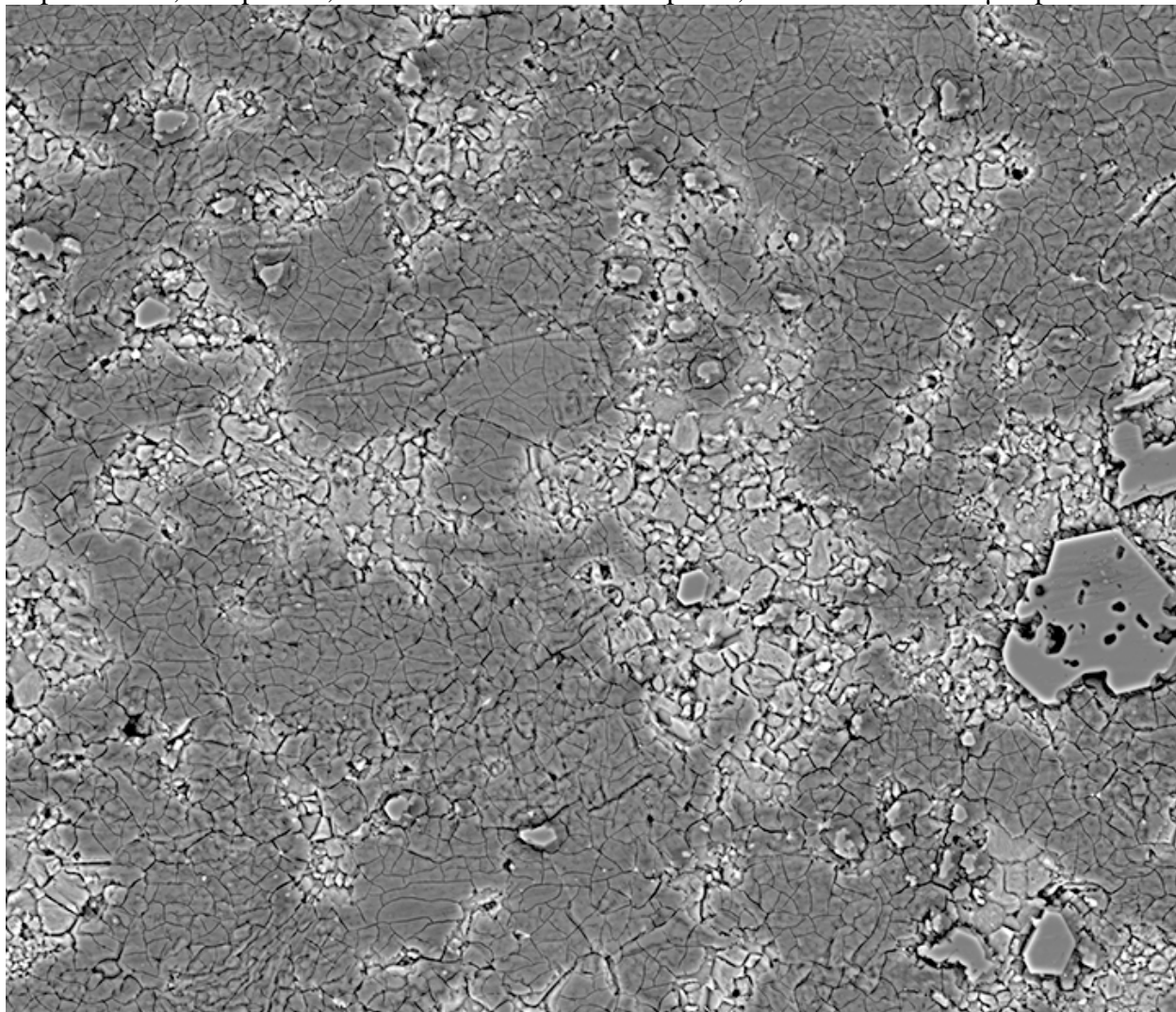
Depth 4943.55 ft, Sample 3-74, Dimensions 27901x24091 pixel², scale 0.017248682 μm/pixel



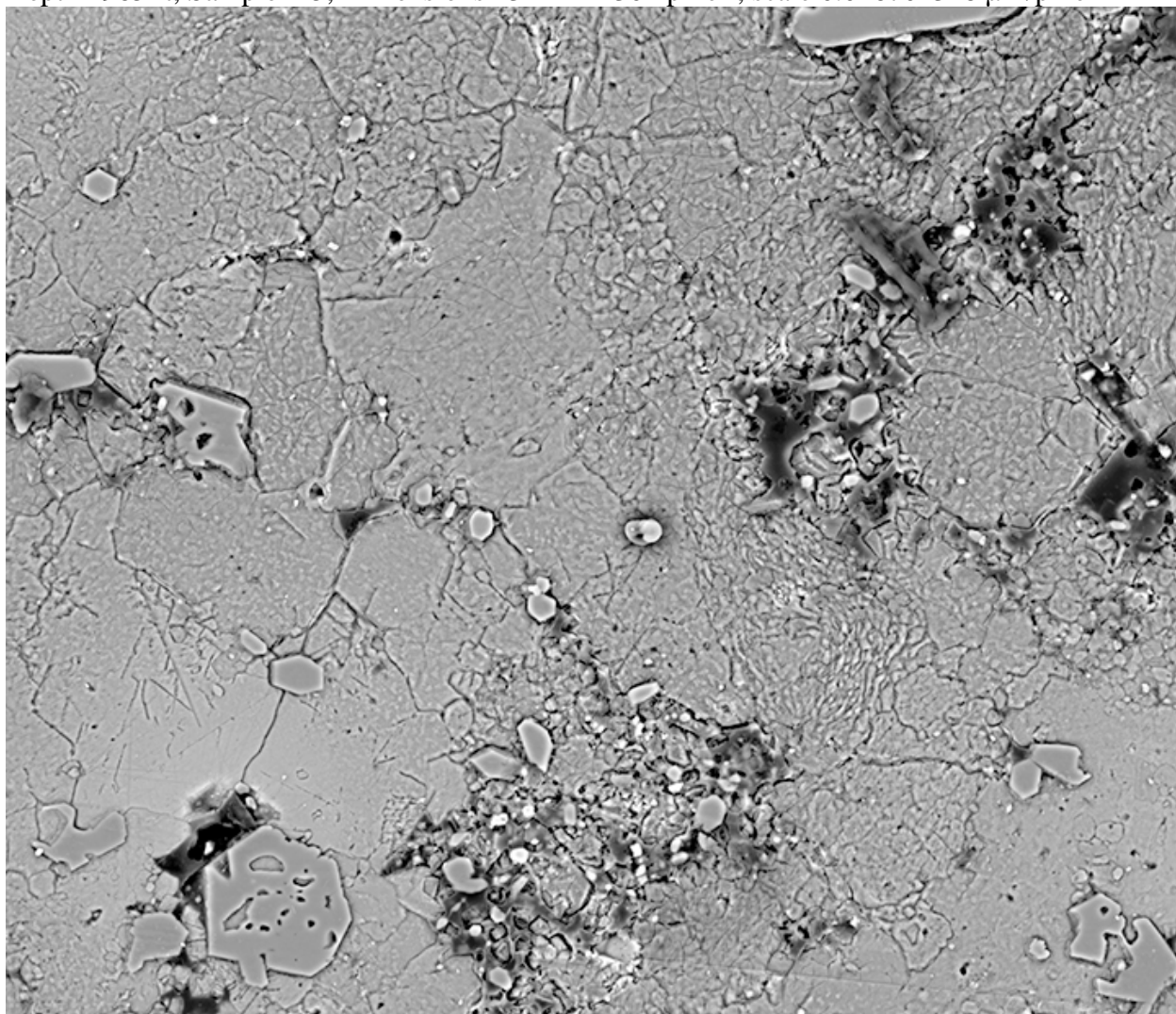
Depth 4943.55 ft, Sample 3-74, Dimensions 27869x16247 pixel², scale 0.016879053 μm/pixel



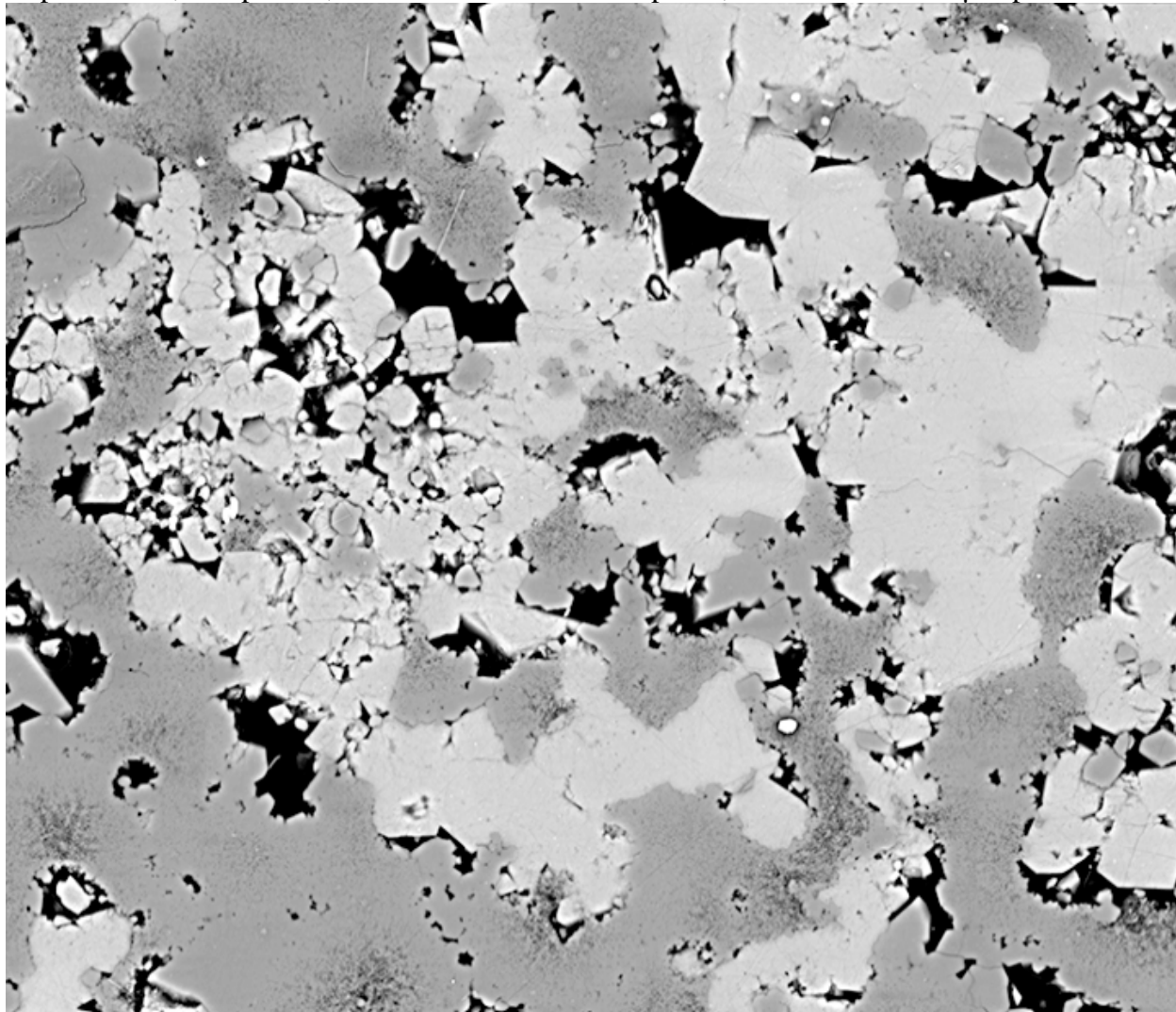
Depth 4965 ft, Sample 4-5, Dimensions 13136x11318 pixel², scale 0.018212891 $\mu\text{m}/\text{pixel}$



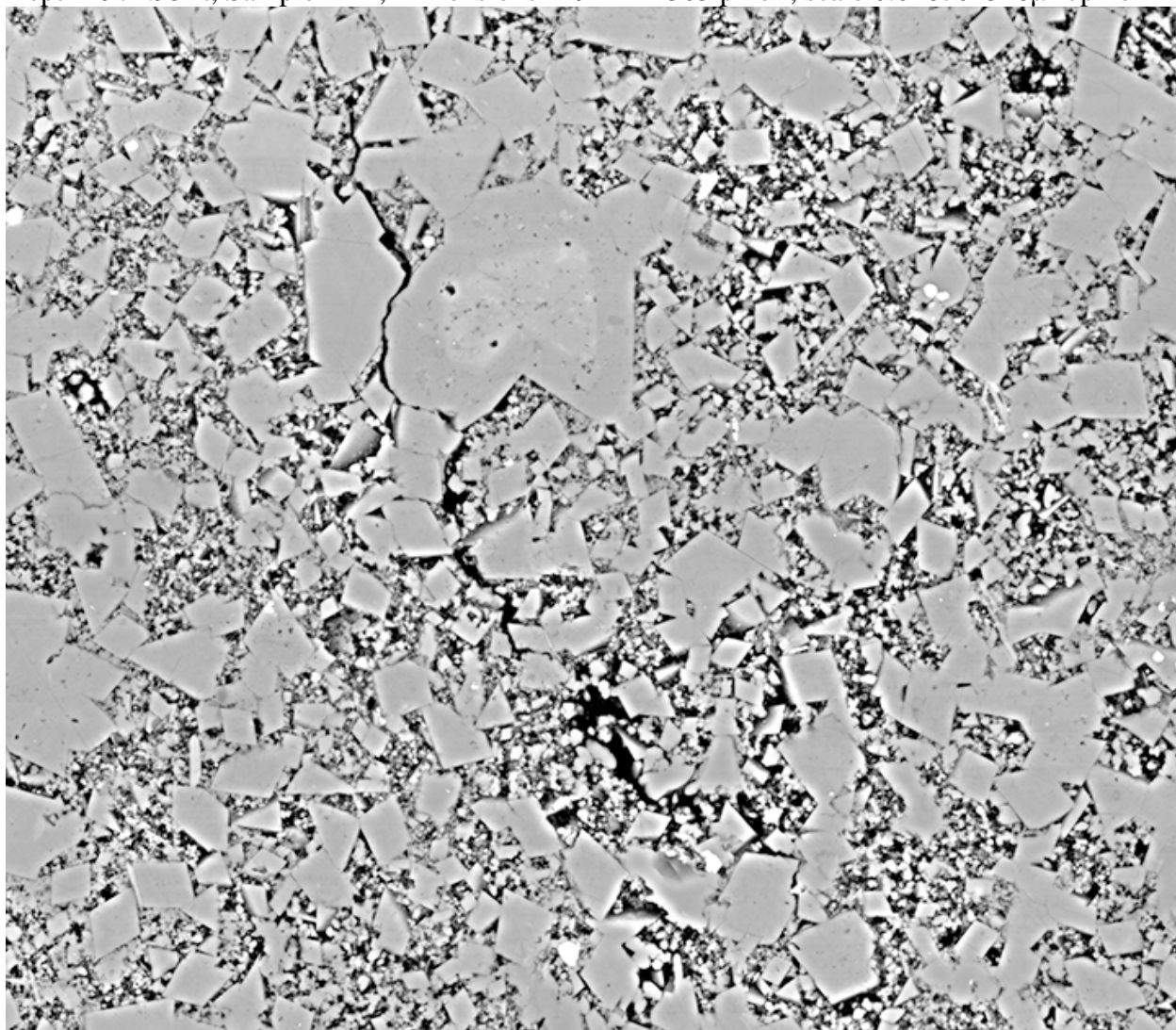
Depth 4965 ft, Sample 4-5, Dimensions 13111x11304 pixel², scale 0.016701318 μm/pixel



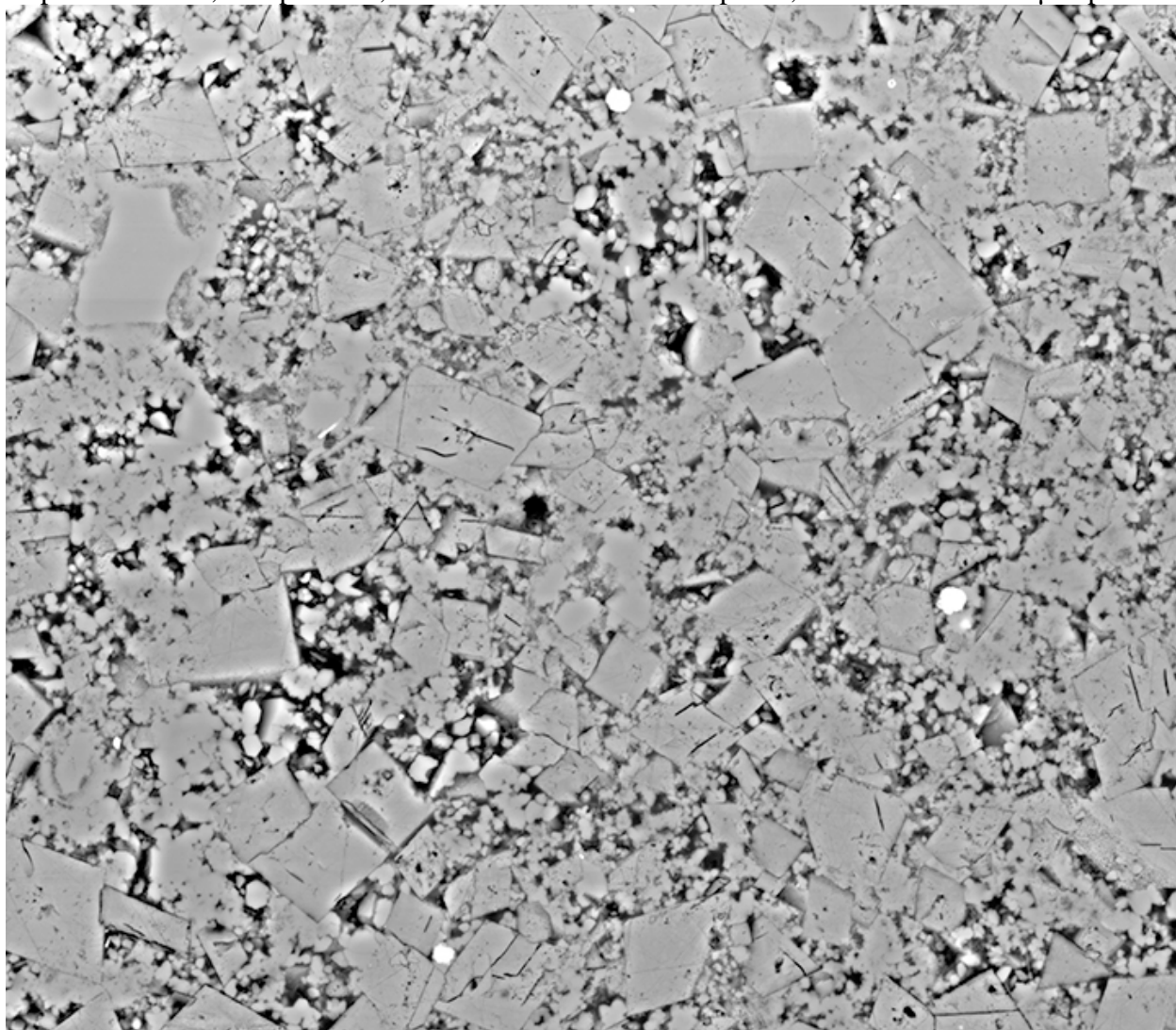
Depth 4965 ft, Sample 4-5, Dimensions 11262x9748 pixel², scale 0.016701318μm/pixel



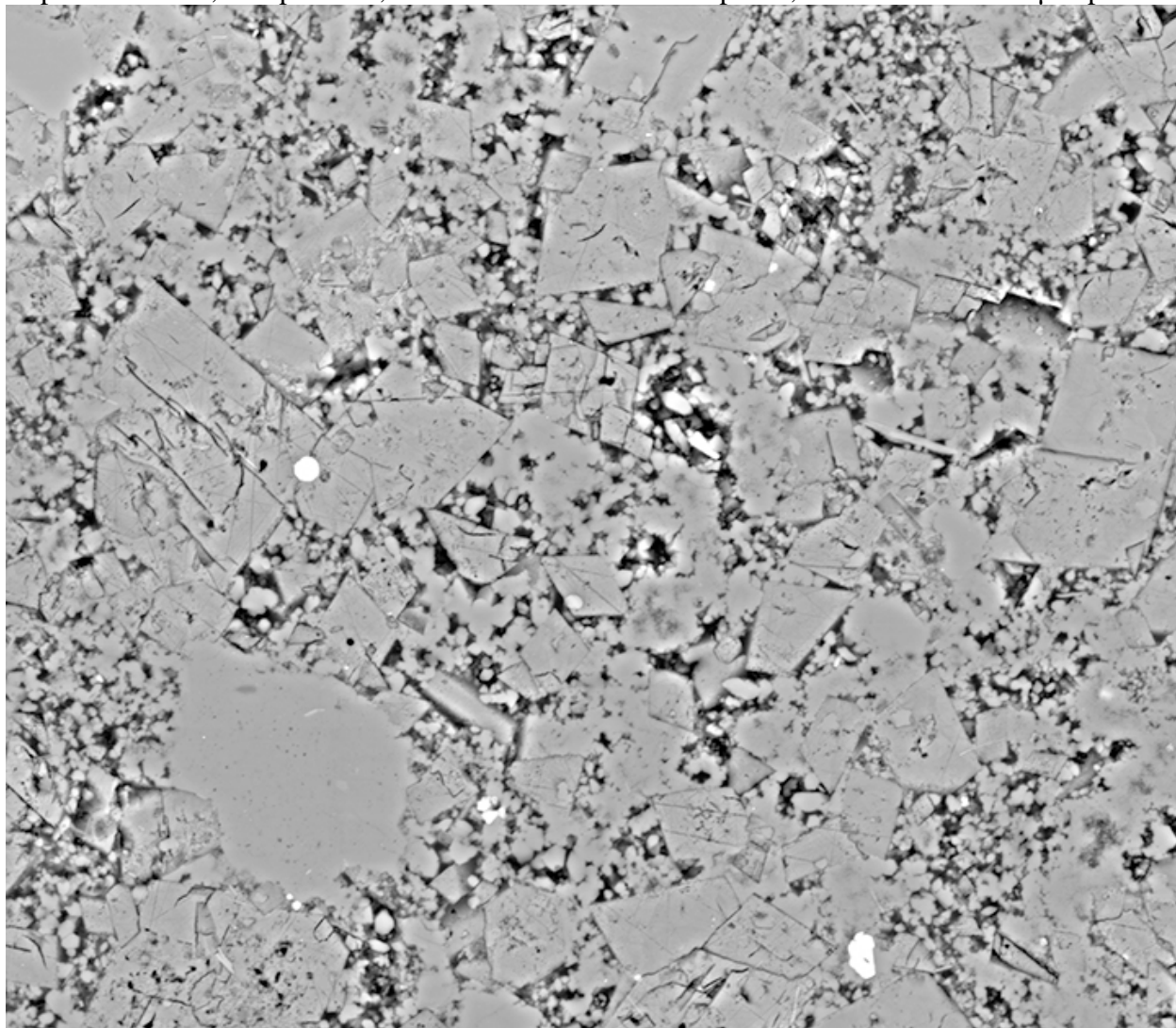
Depth 4974.95 ft, Sample 4-14, Dimensions 12944x11303 pixel², scale 0.016701318μm/pixel



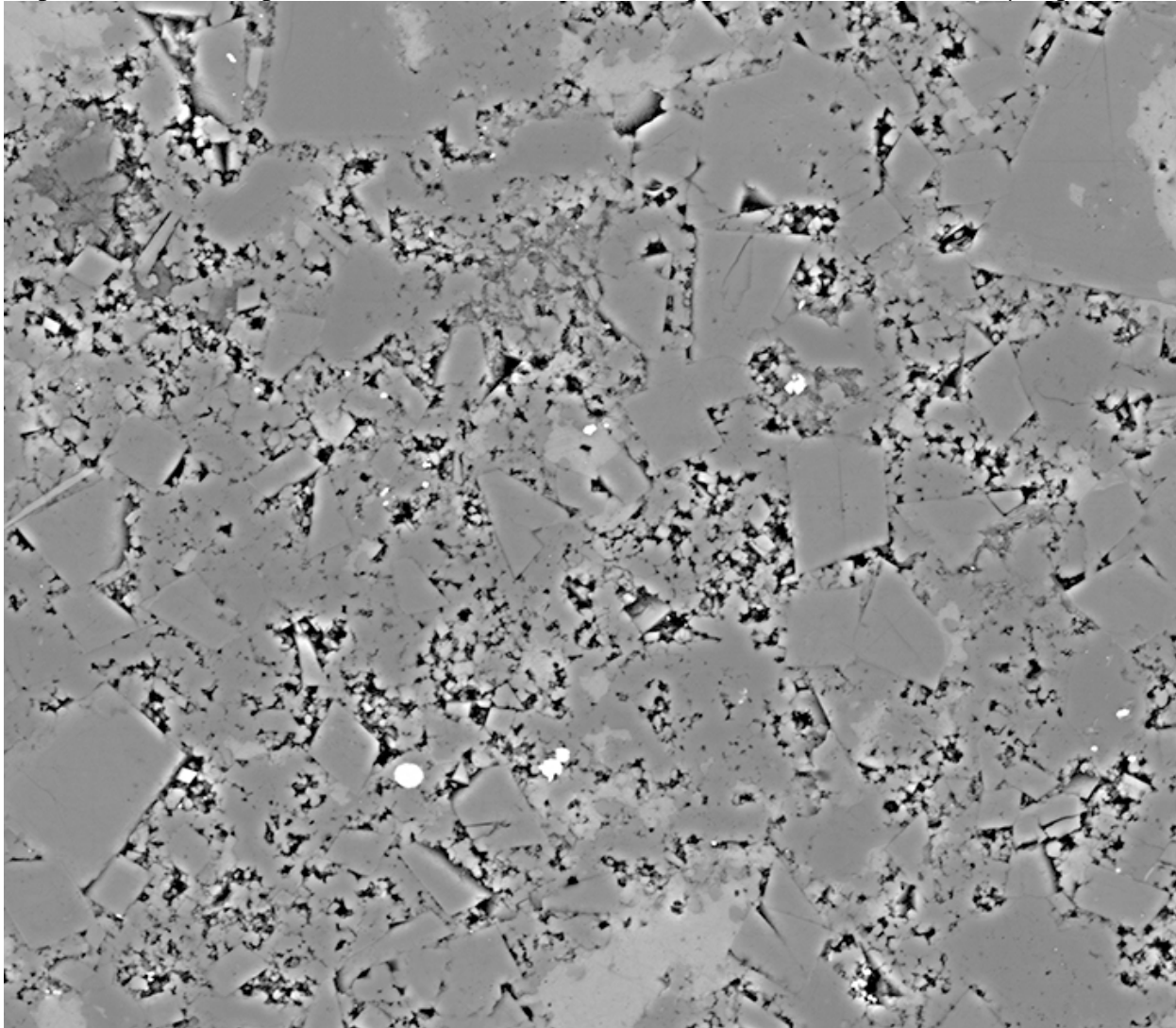
Depth 4974.95 ft, Sample 4-14, Dimensions 13012x11313 pixel², scale 0.016701318 μm/pixel



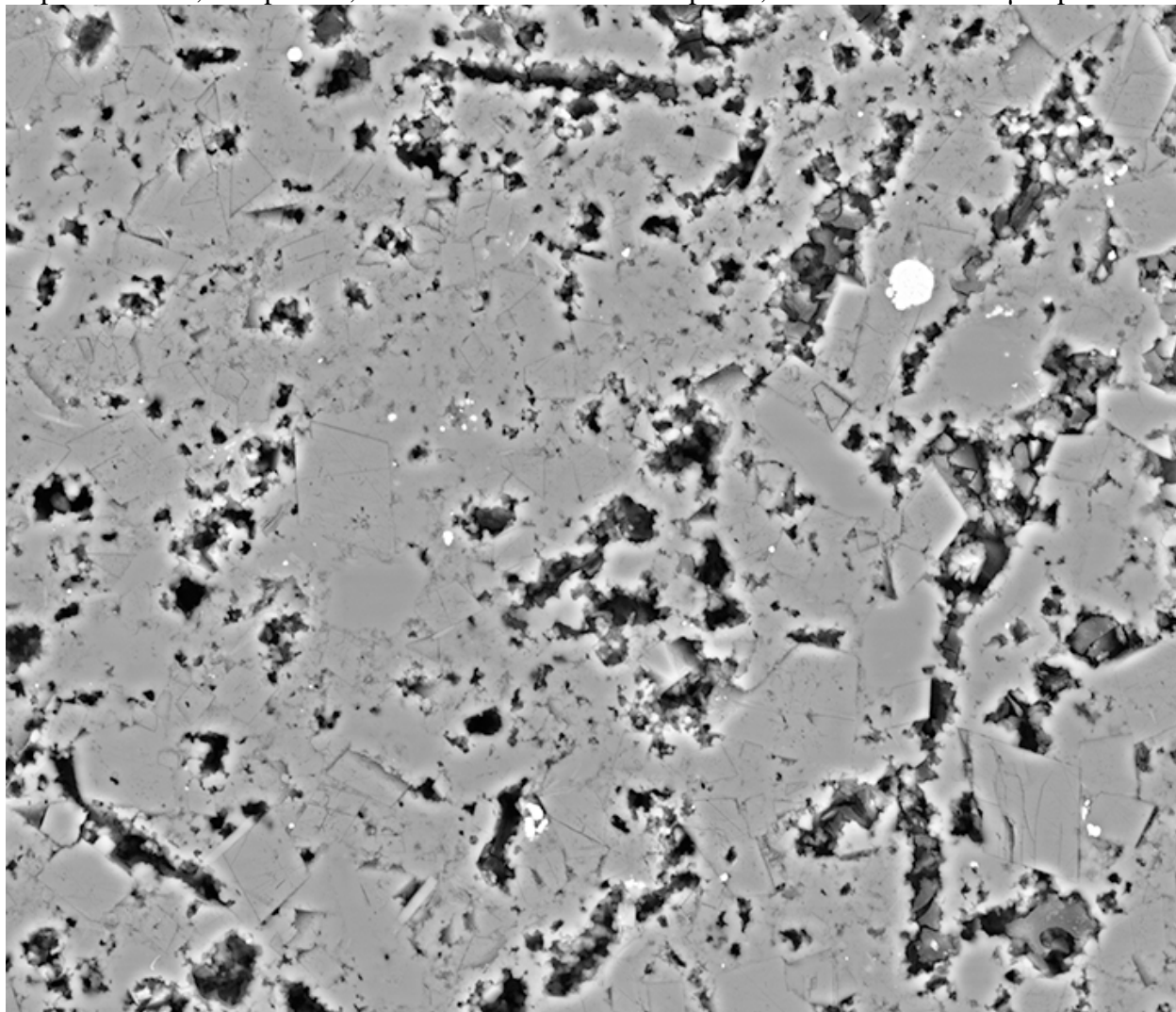
Depth 4974.95 ft, Sample 4-14, Dimensions 12959x11363 pixel², scale 0.016701318 μm/pixel



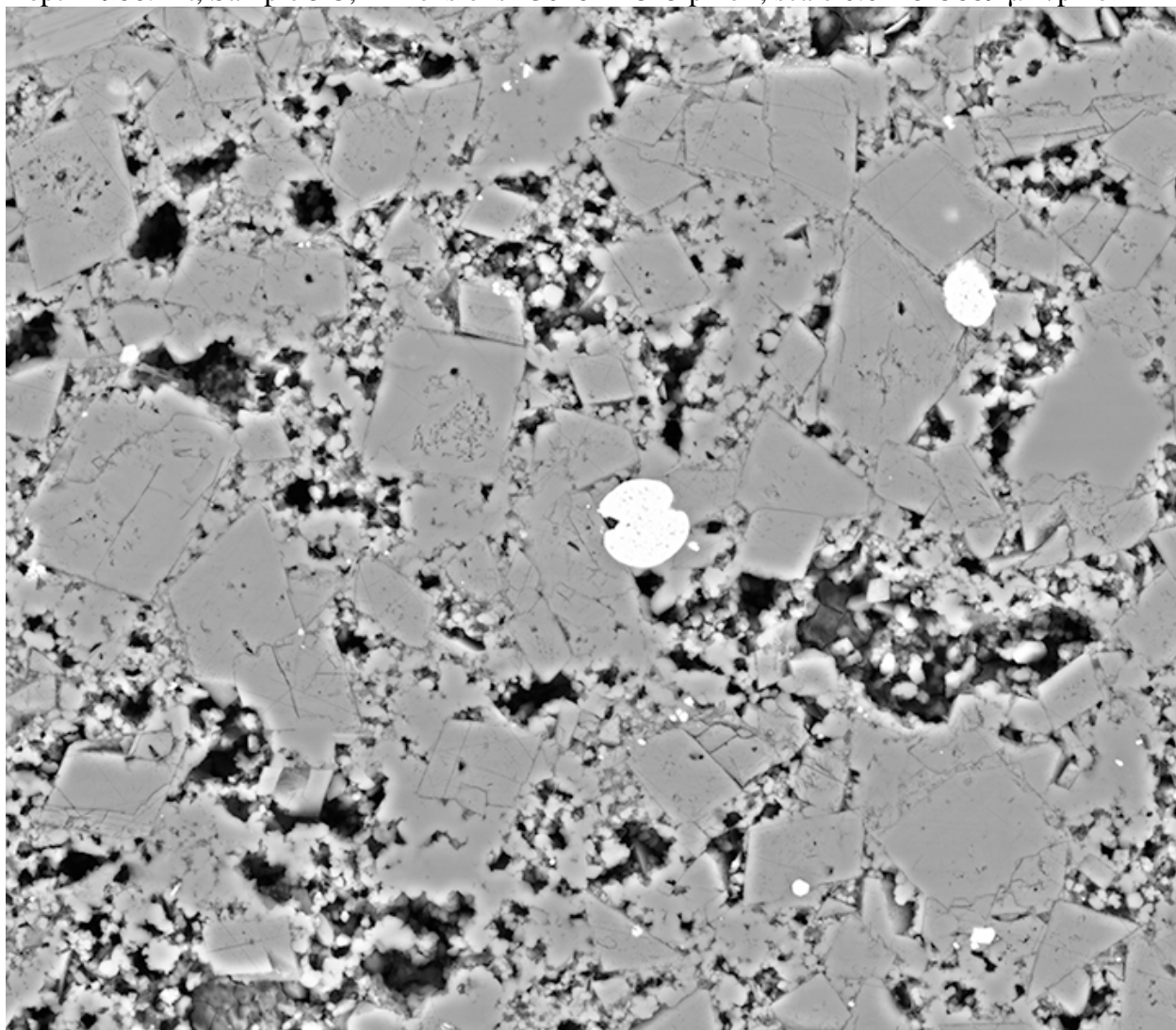
Depth 4986.4 ft, Sample 5-3, Dimensions 13051x11358 pixel², scale 0.015315137 μm/pixel



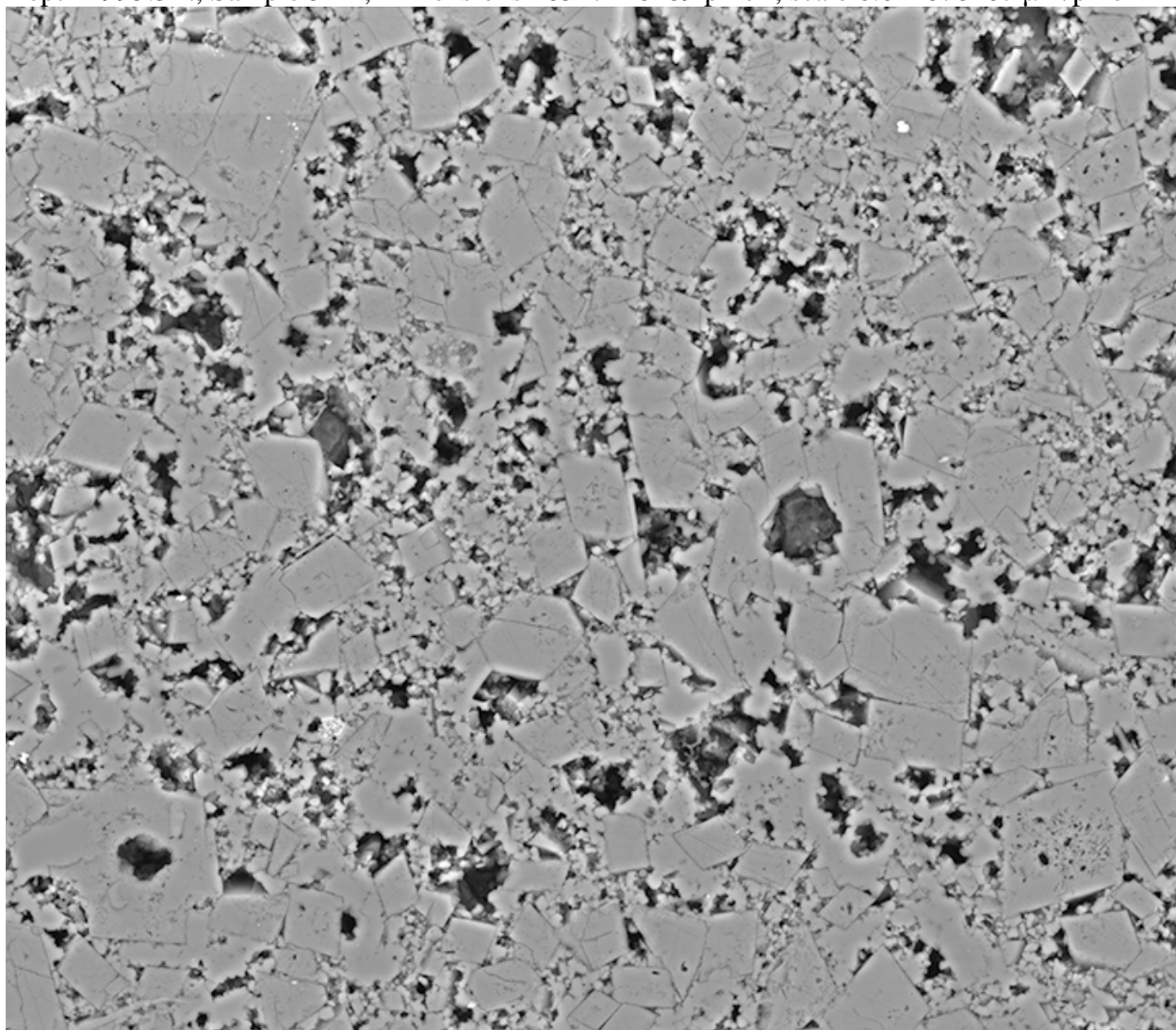
Depth 4986.4 ft, Sample 5-3, Dimensions 13035x11254 pixel², scale 0.012815889 μm/pixel



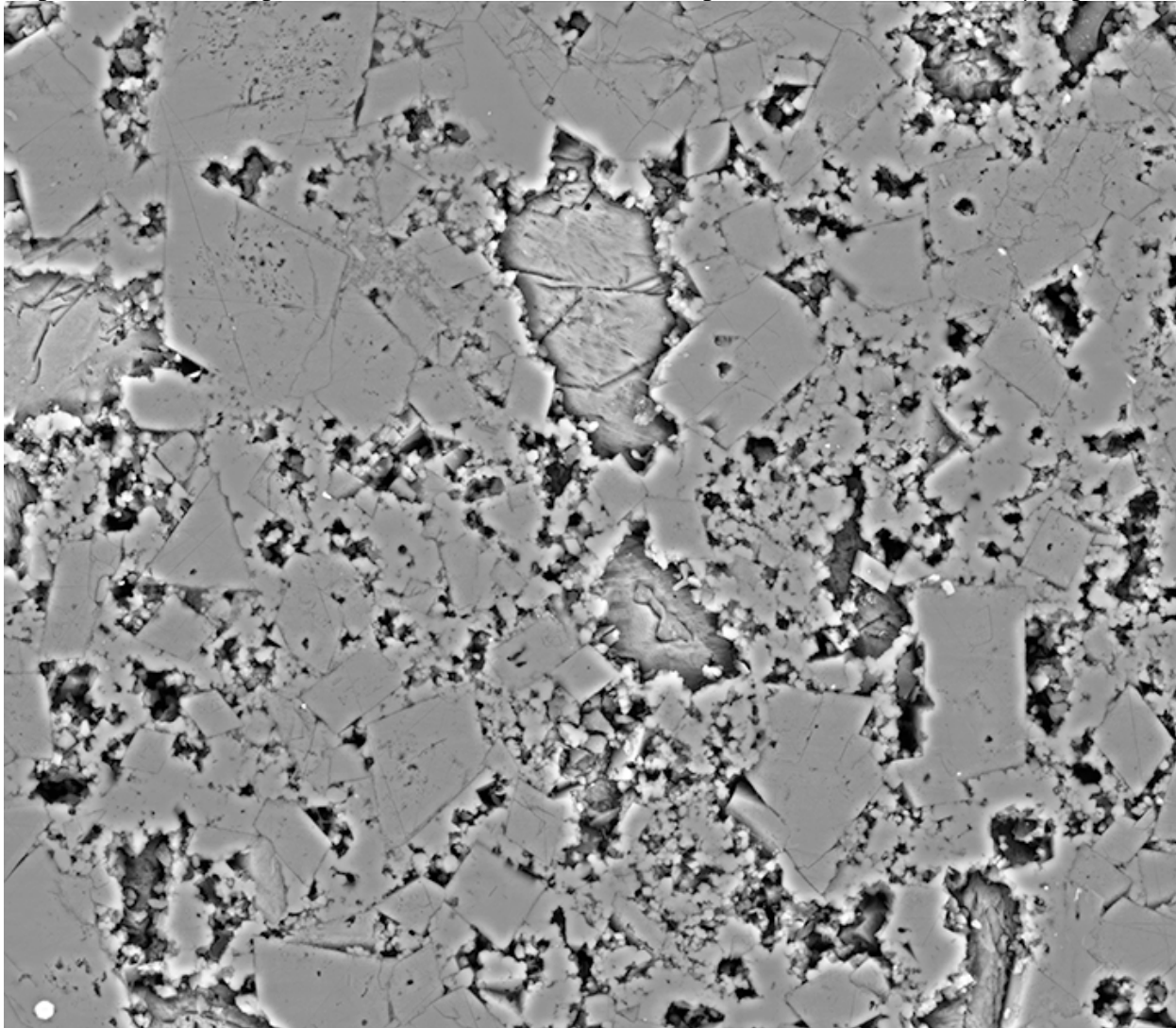
Depth 4986.4 ft, Sample 5-3, Dimensions 13028x11325 pixel², scale 0.012815889 μm/pixel



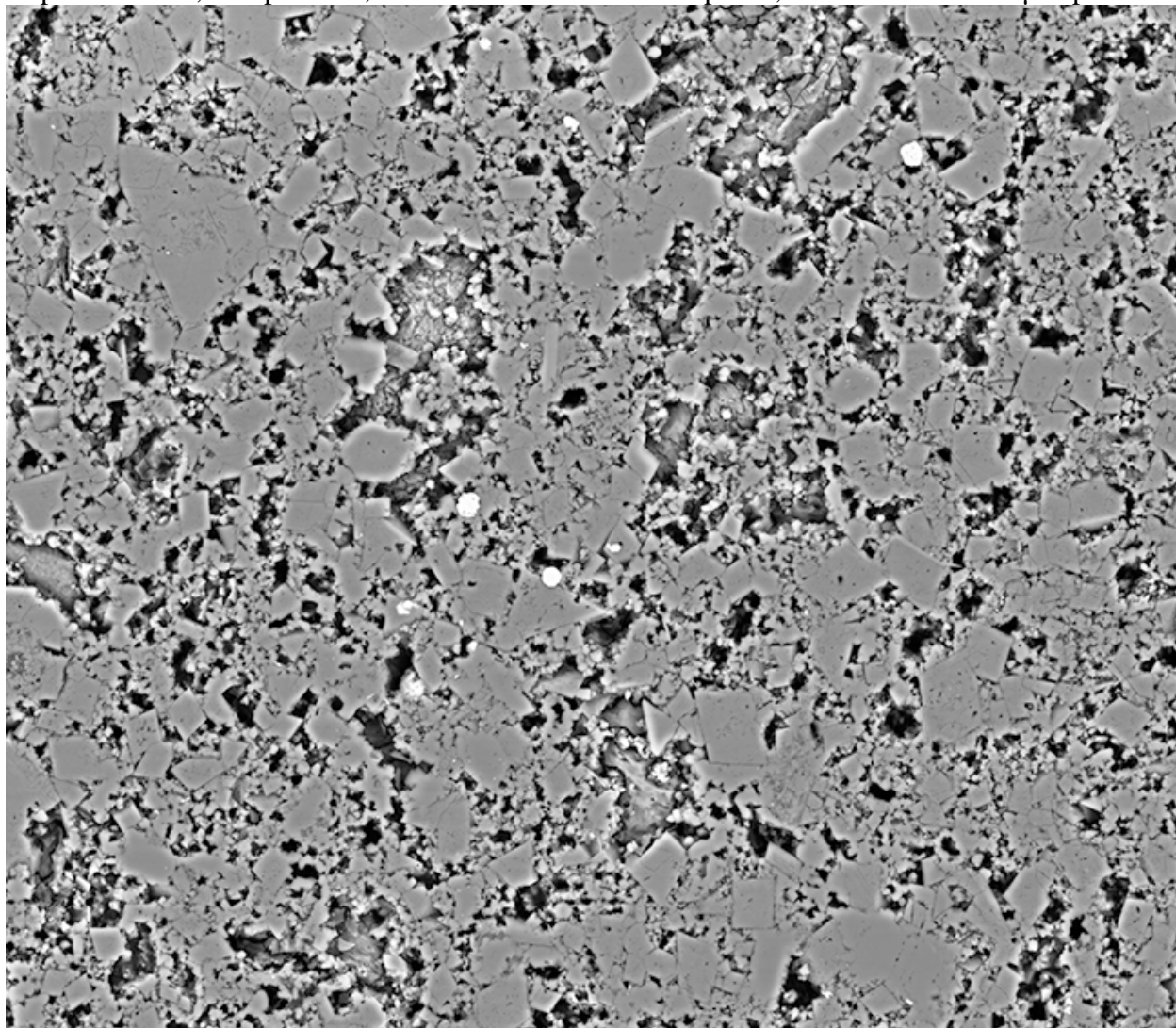
Depth 4995.3 ft, Sample 5-12, Dimensions 18547x16189 pixel², scale 0.012878467 μm/pixel



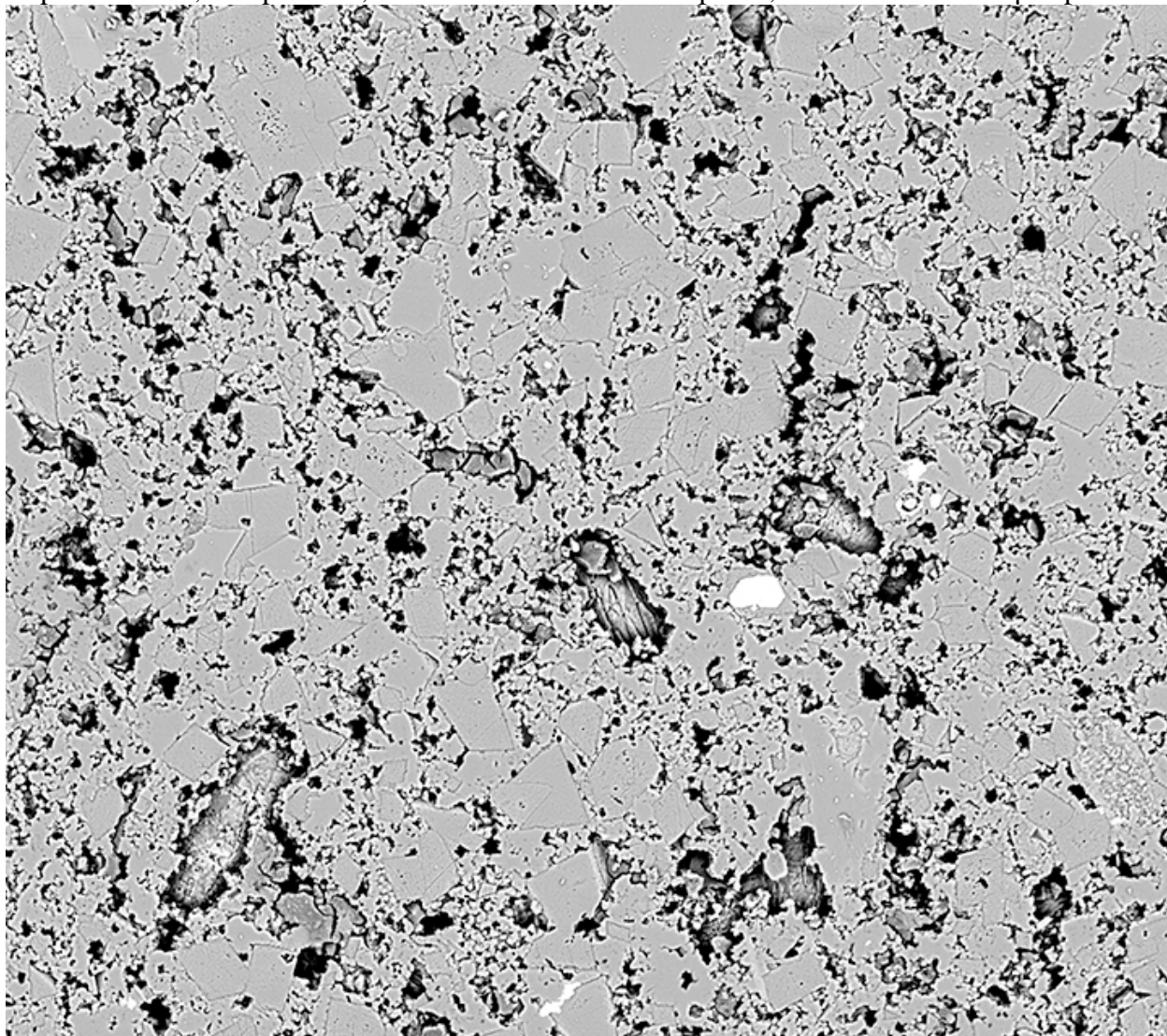
Depth 4995.3 ft, Sample 5-12, Dimensions 13047x11344 pixel², scale 0.015650488 μm/pixel



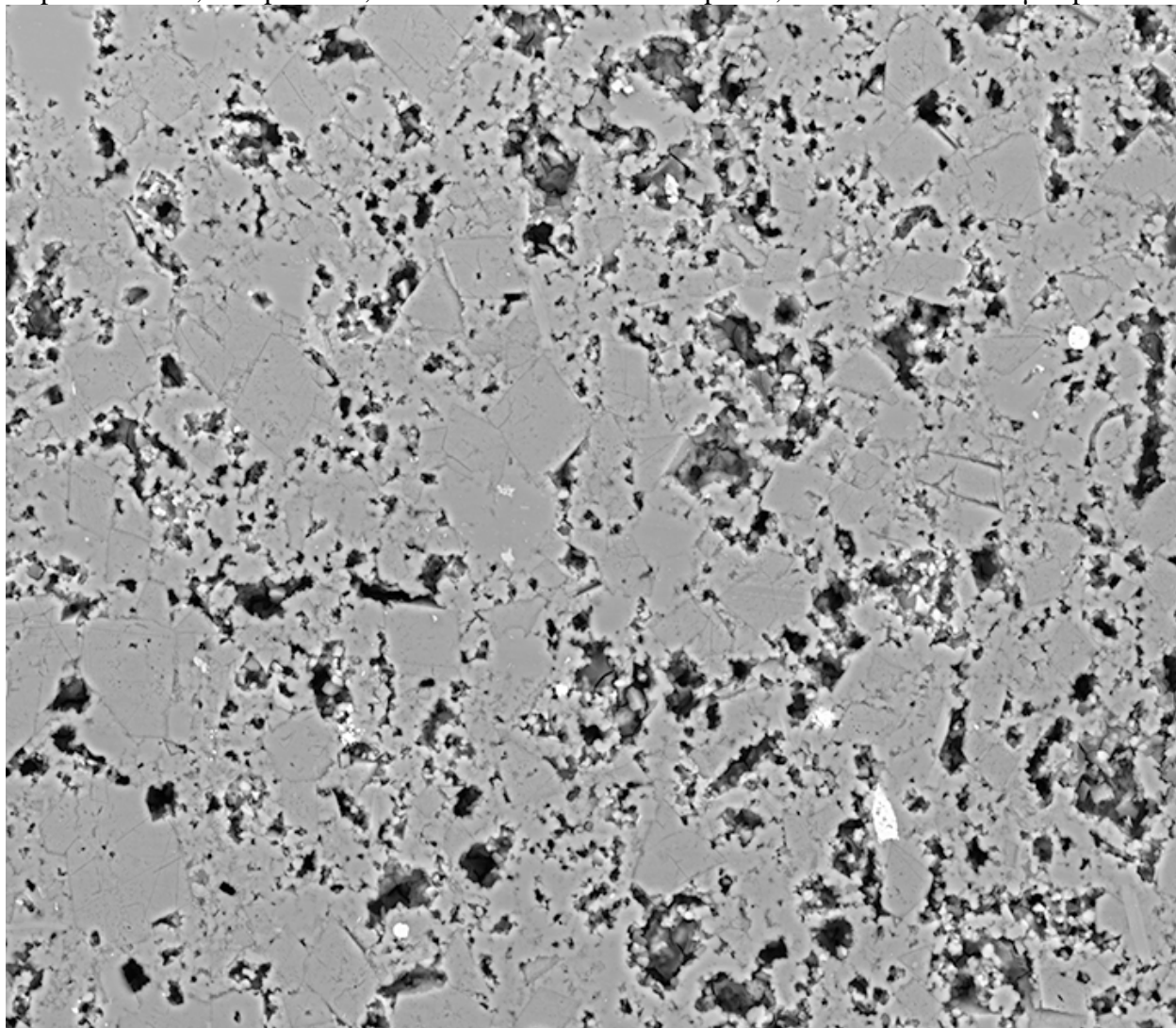
Depth 4995.3 ft, Sample 5-12, Dimensions 18568x16116 pixel², scale 0.015650488 μm/pixel



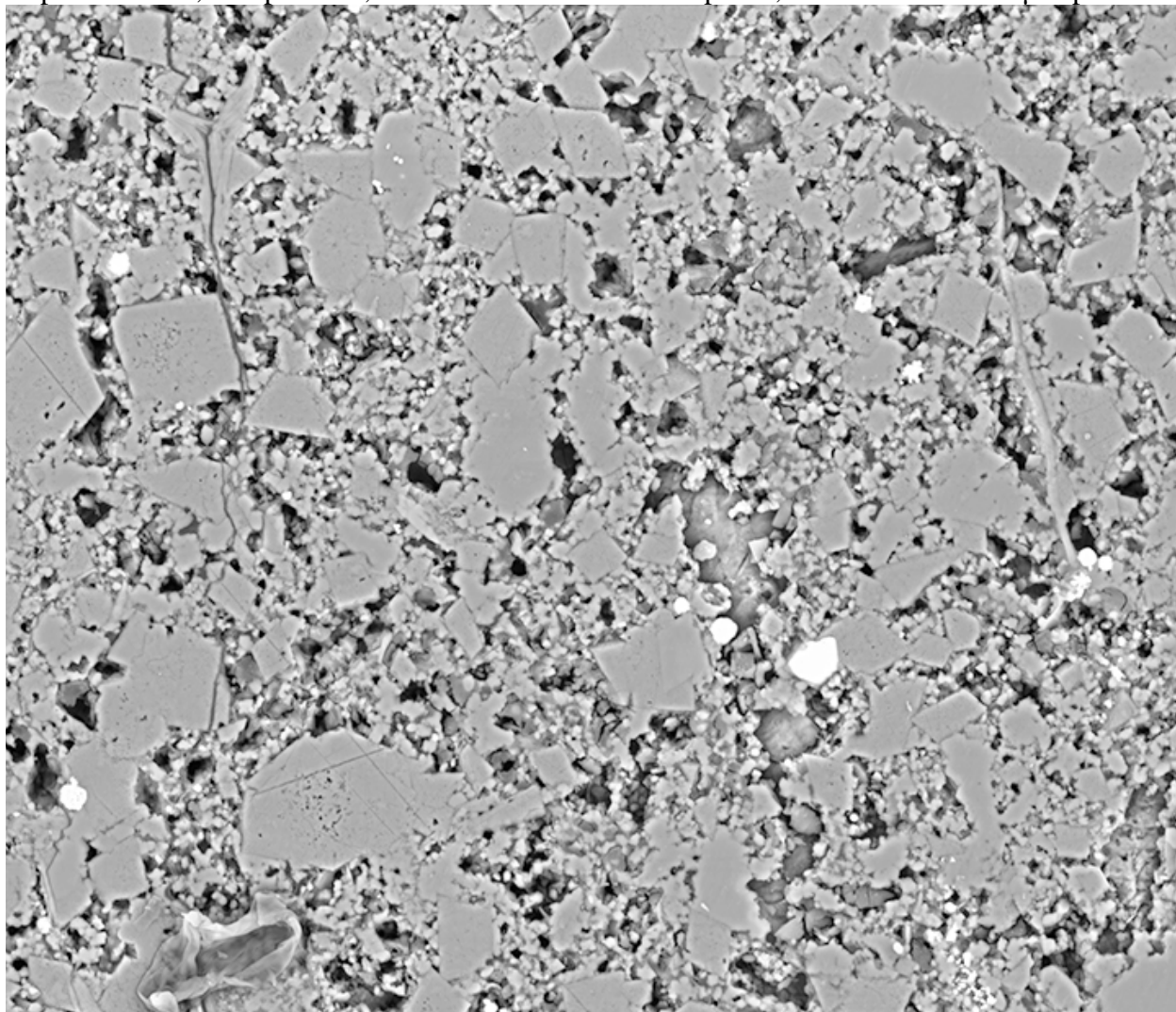
Depth 5004.9 ft, Sample 5-21, Dimensions 18622x16490 pixel², scale 0.014351563 $\mu\text{m}/\text{pixel}$



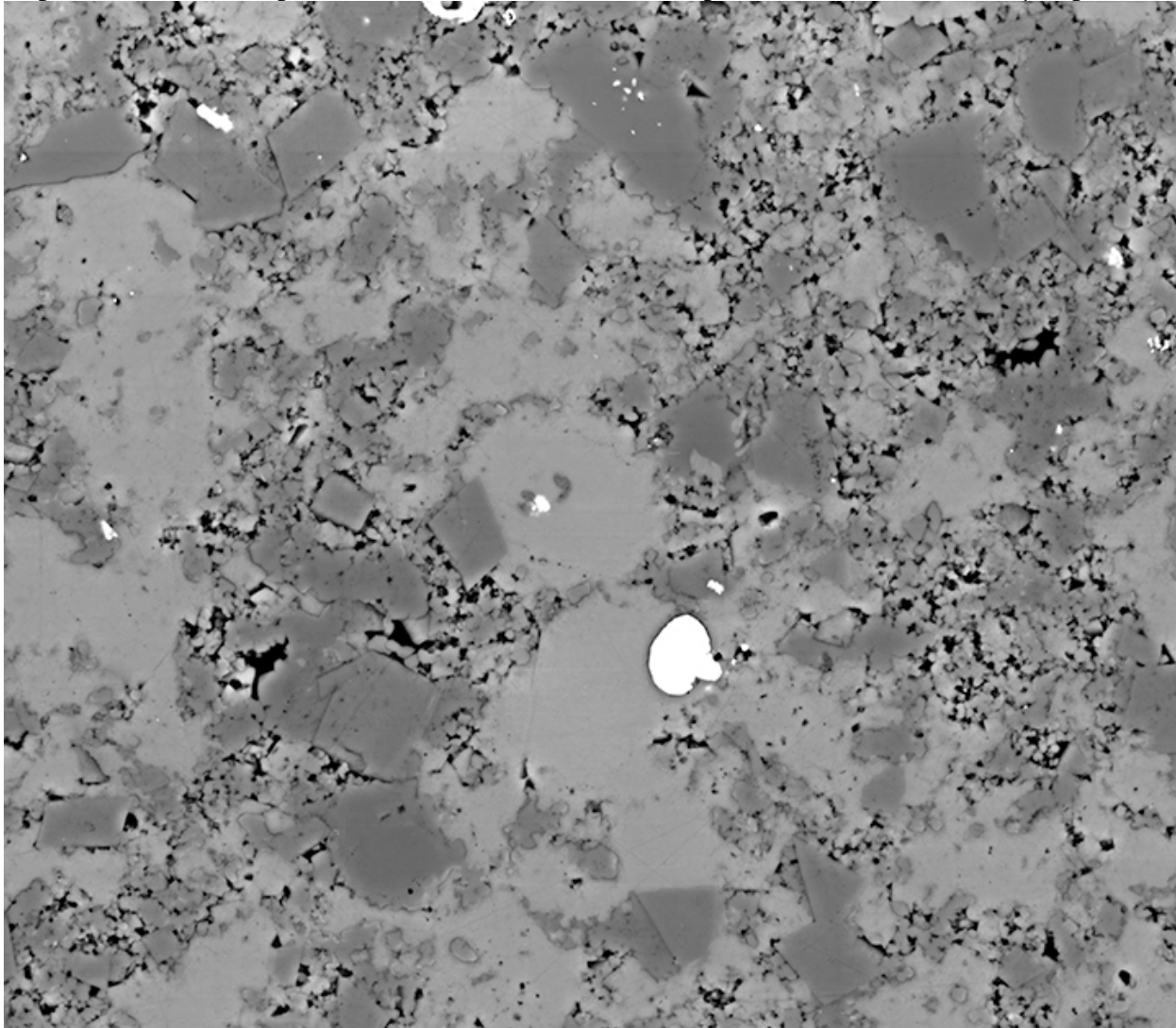
Depth 5004.9 ft, Sample 5-21, Dimensions 13063x11386 pixel², scale 0.014351563 μm/pixel



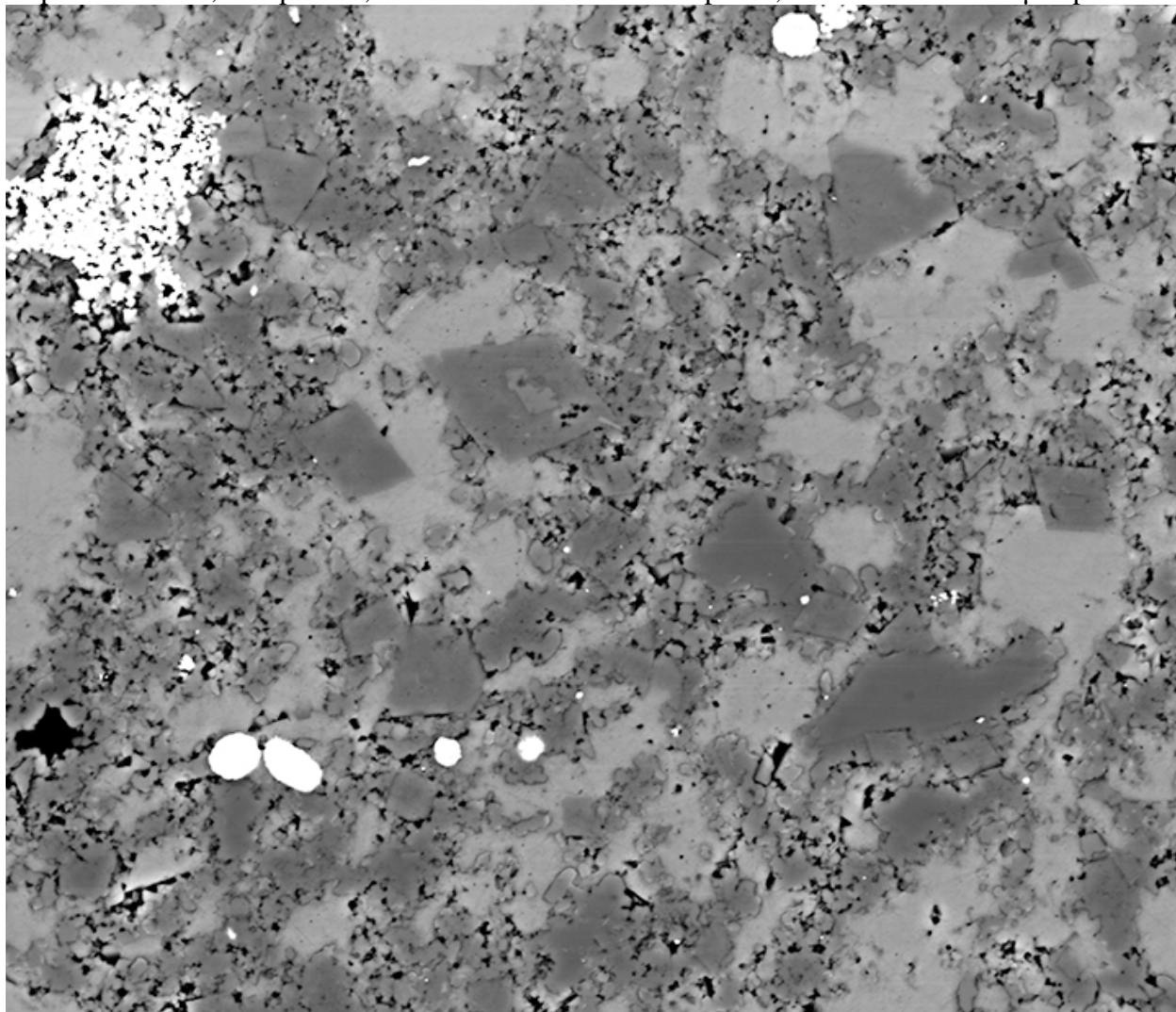
Depth 5004.9 ft, Sample 5-21, Dimensions 13090x11330 pixel², scale 0.014351563 μm/pixel



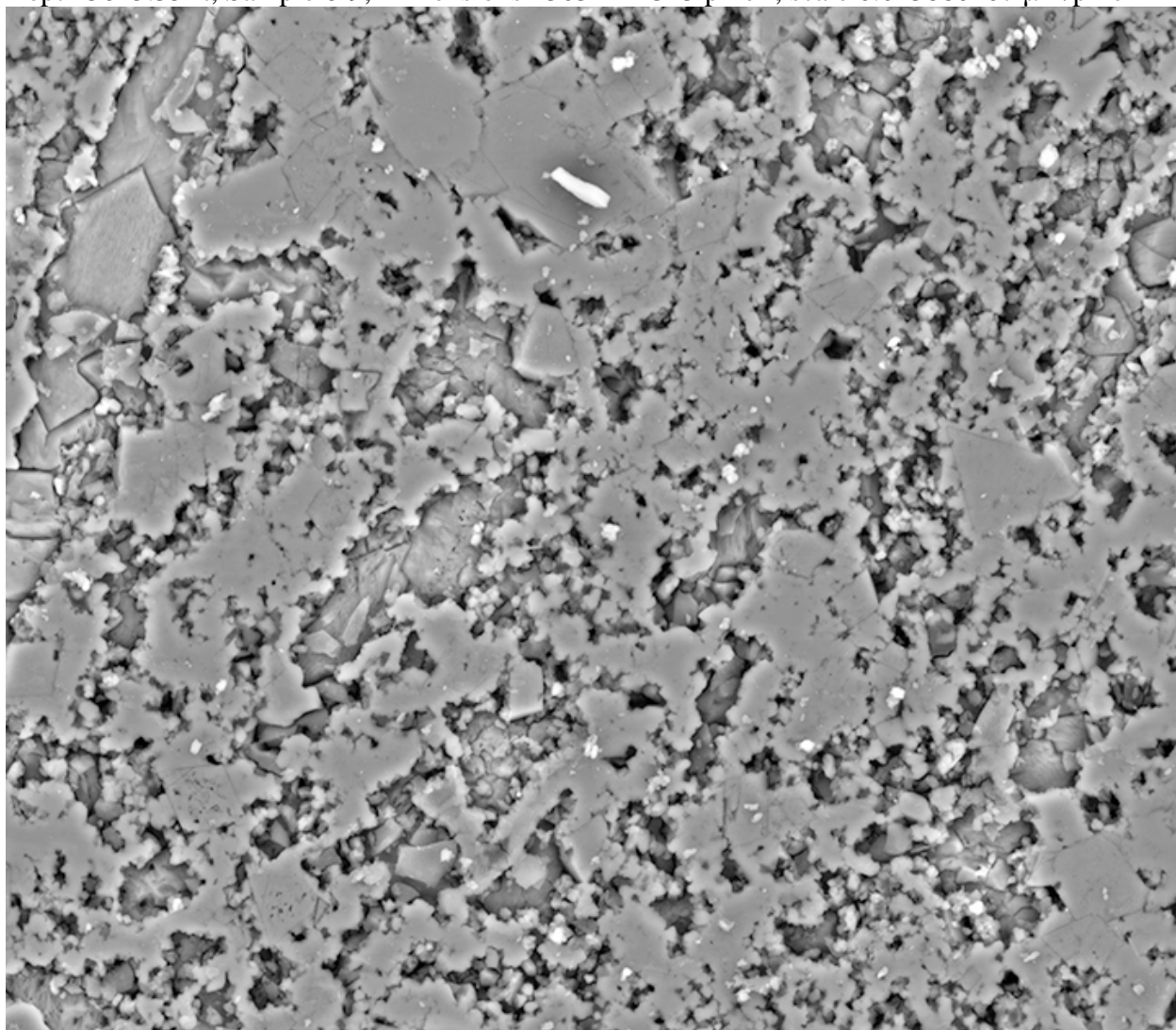
Depth 5015.35 ft, Sample 6-9, Dimensions 12986x11288 pixel², scale 0.013743115 μm/pixel



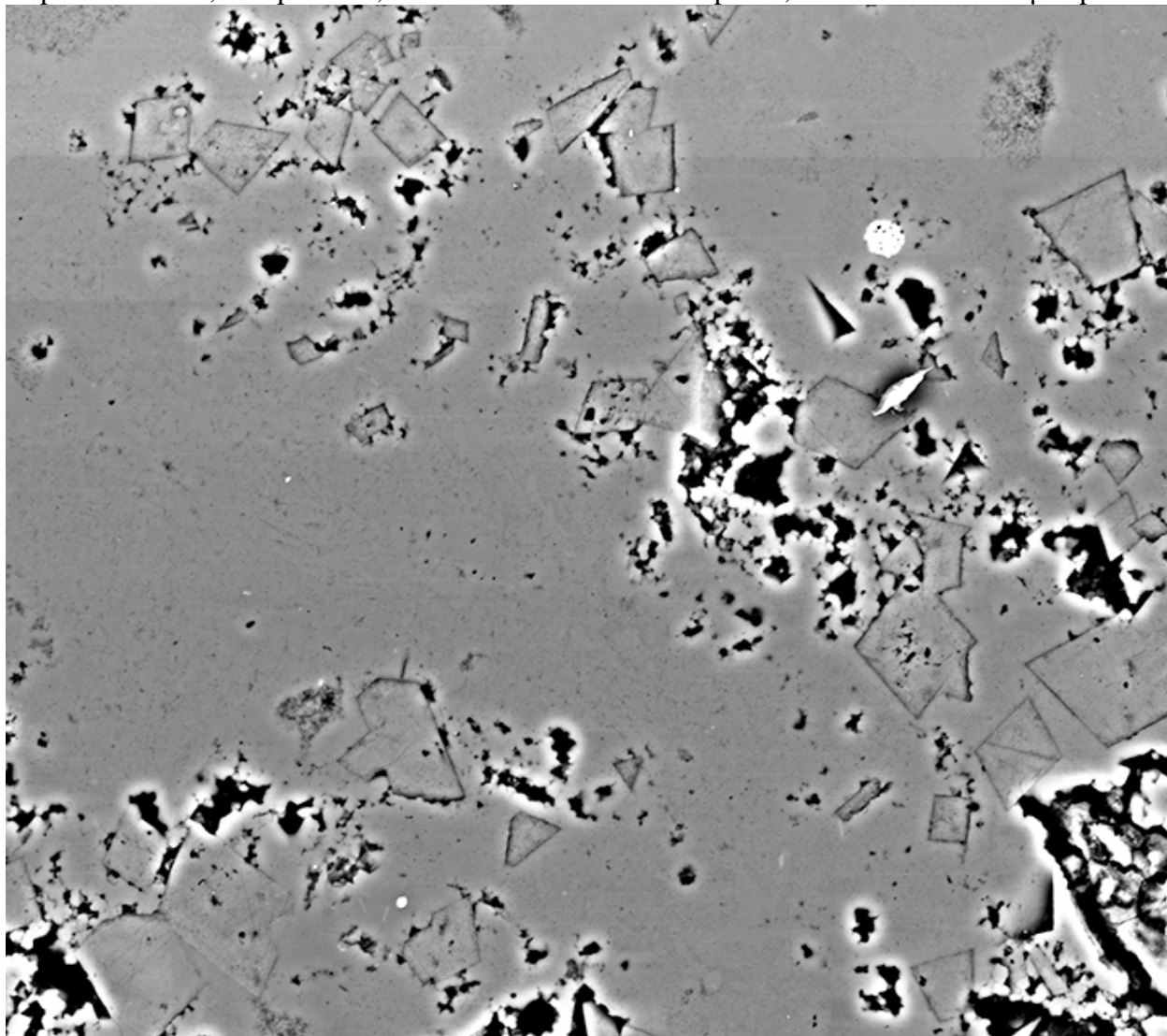
Depth 5015.35 ft, Sample 6-9, Dimensions 13045x11284 pixel², scale 0.013860107 μm/pixel



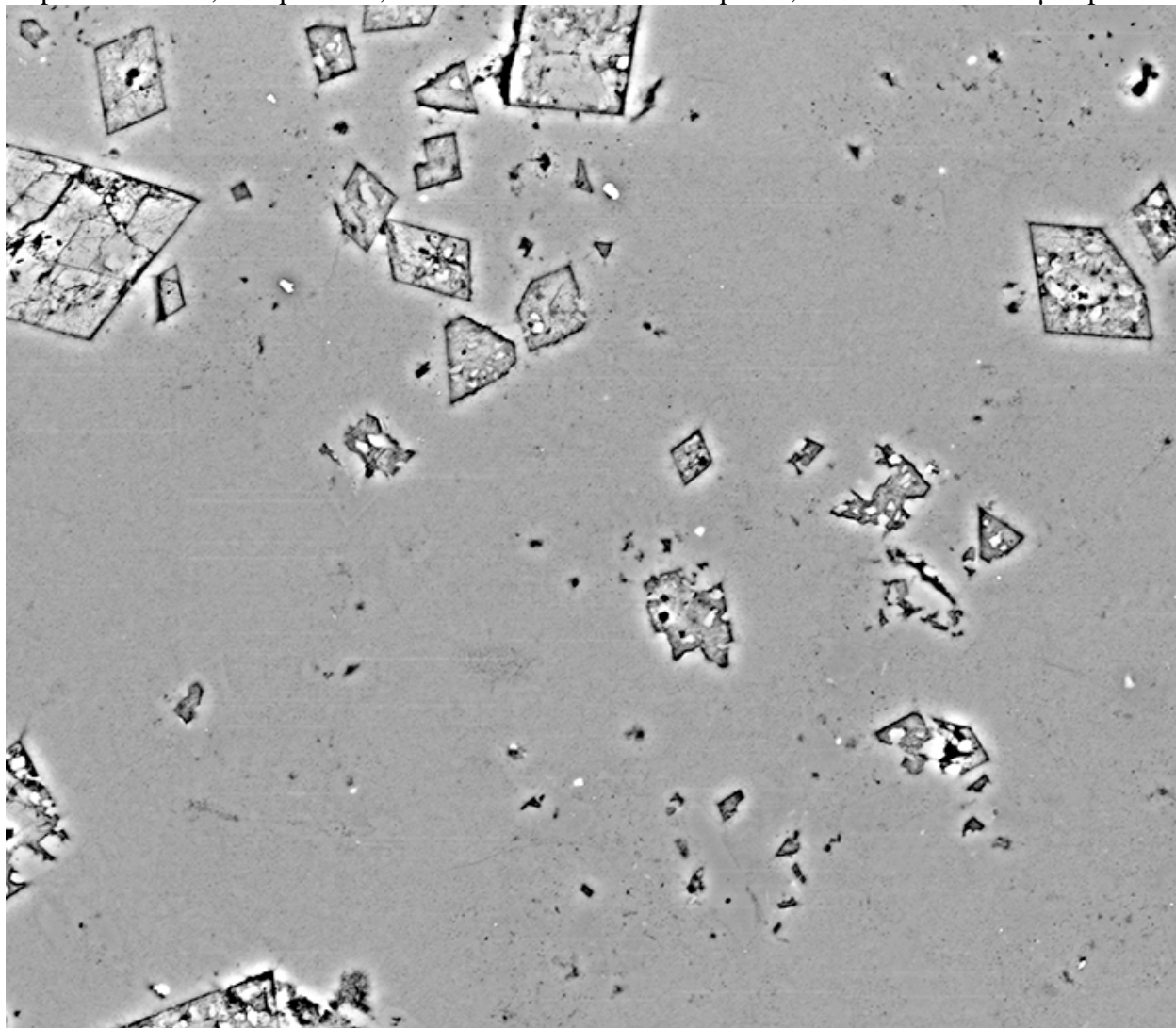
Depth 5015.35 ft, Sample 6-9, Dimensions 13032x11313 pixel², scale 0.013860107 μm/pixel



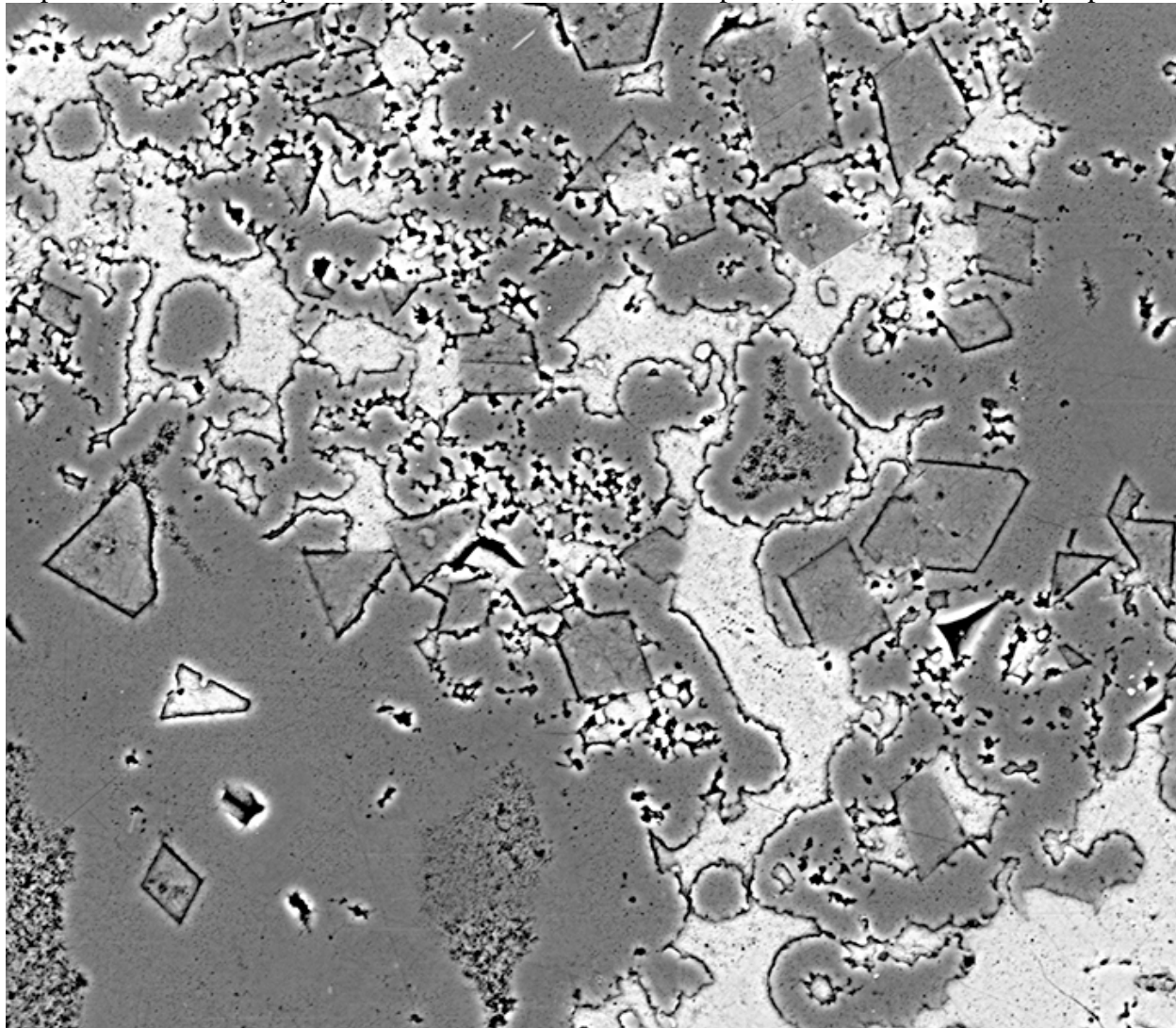
Depth 5024.45 ft, Sample 6-18, Dimensions 12915x11397 pixel², scale 0.012878467 μm/pixel



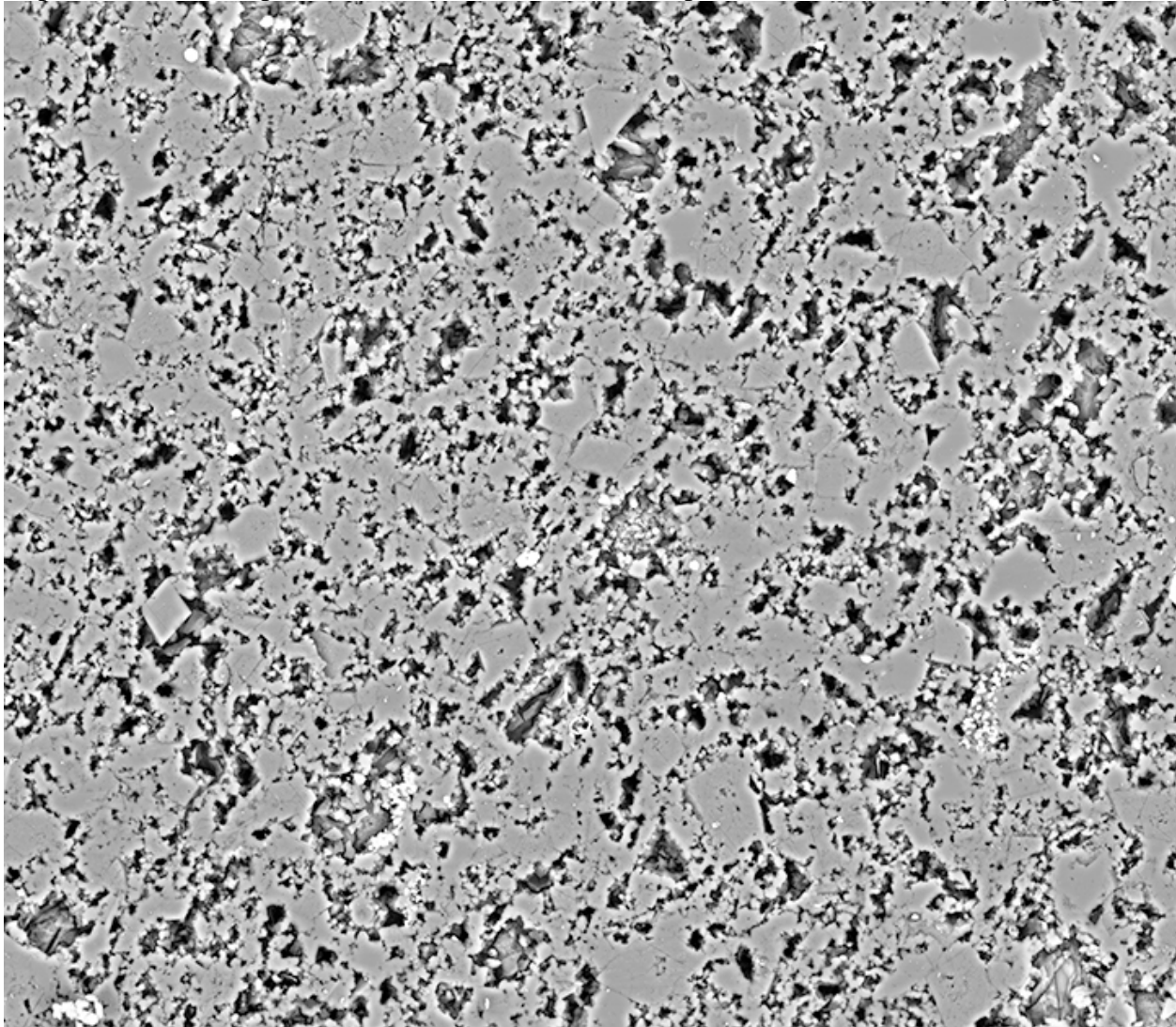
Depth 5024.45 ft, Sample 6-18, Dimensions 13009x11333 pixel², scale 0.012878467 $\mu\text{m}/\text{pixel}$



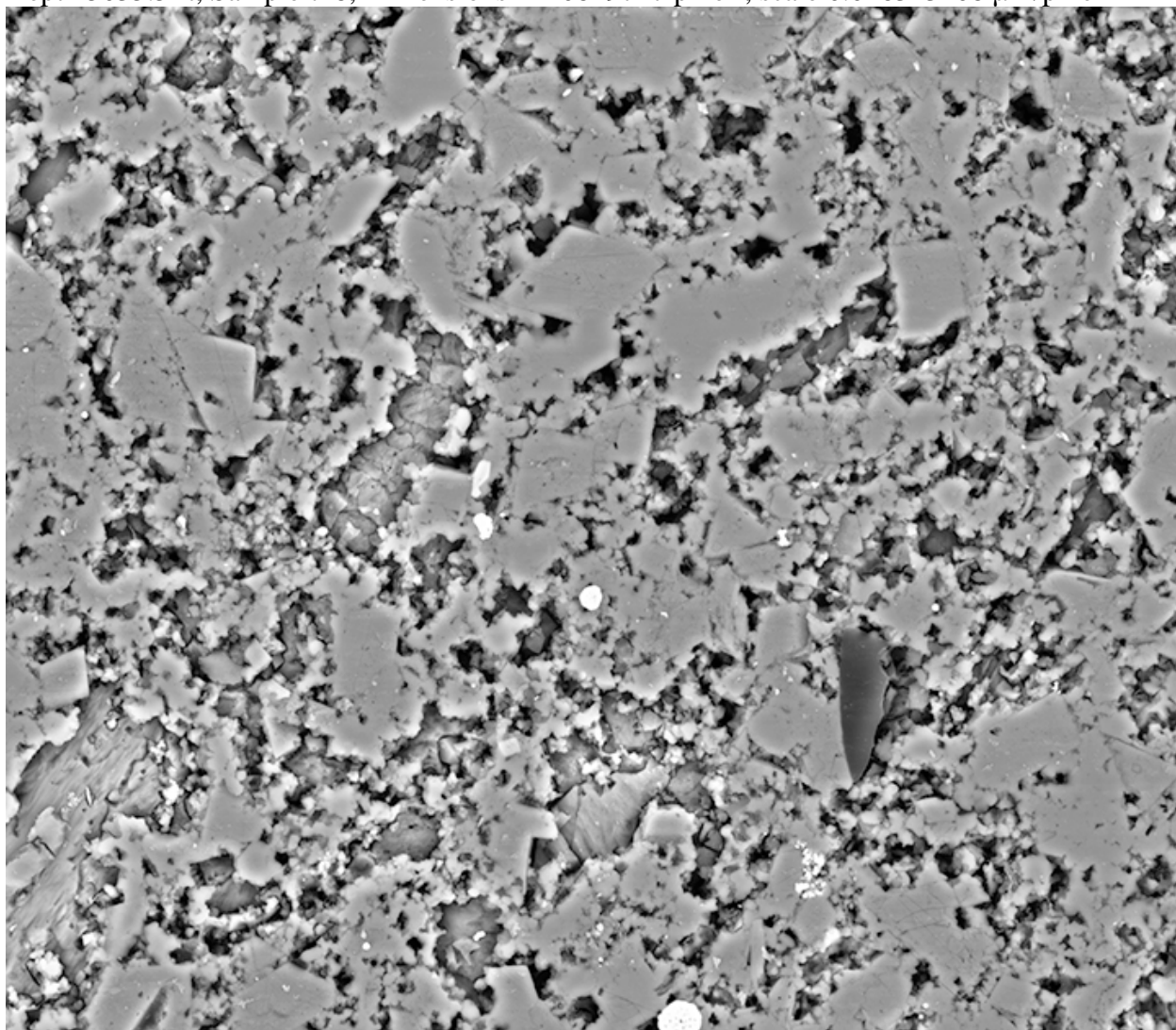
Depth 5024.45 ft, Sample 6-18, Dimensions 13111x11425 pixel², scale 0.012878467 μm/pixel



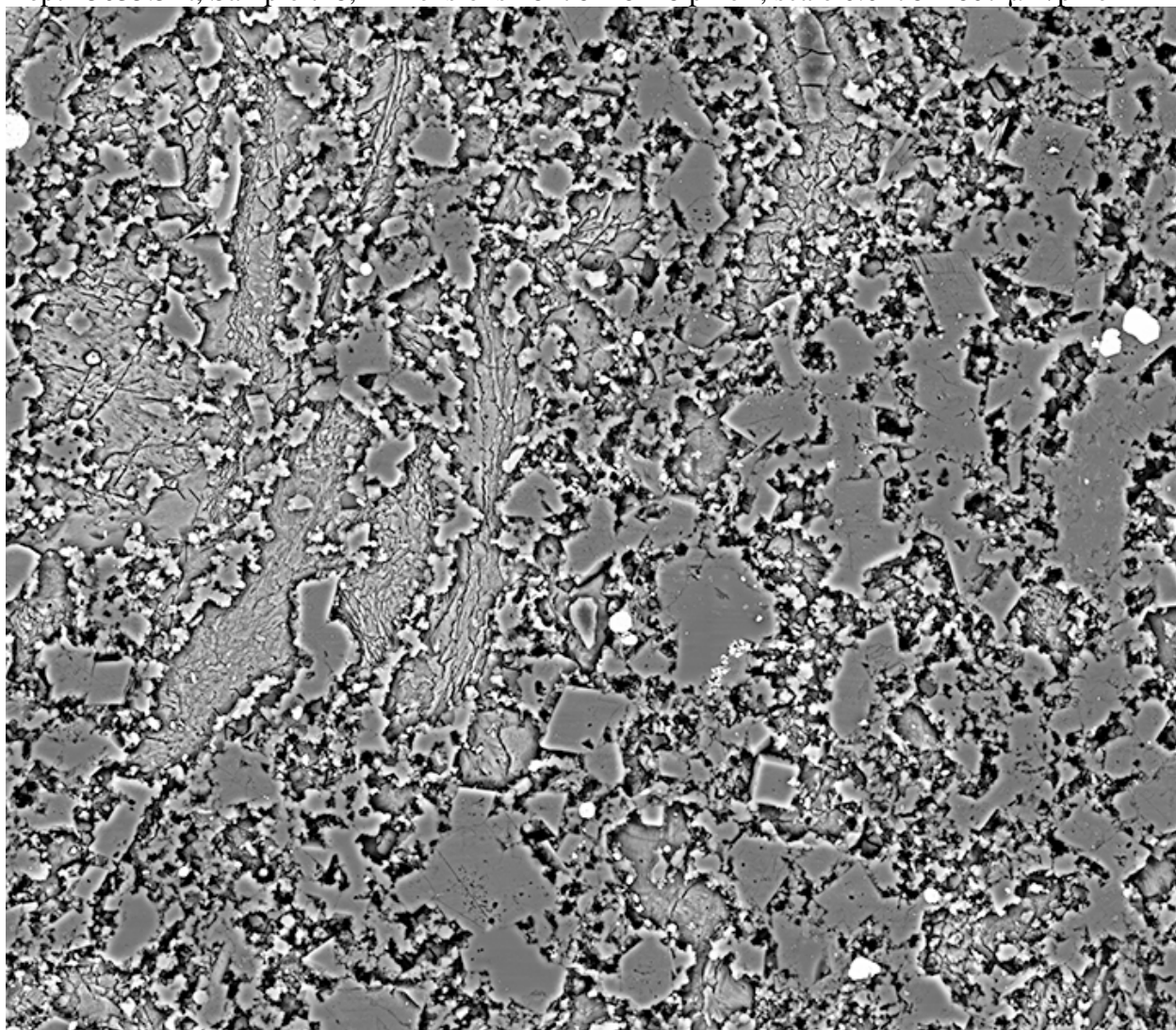
Depth 5035.5 ft, Sample 7-8, Dimensions 18457x16145 pixel², scale 0.016343408 μm/pixel



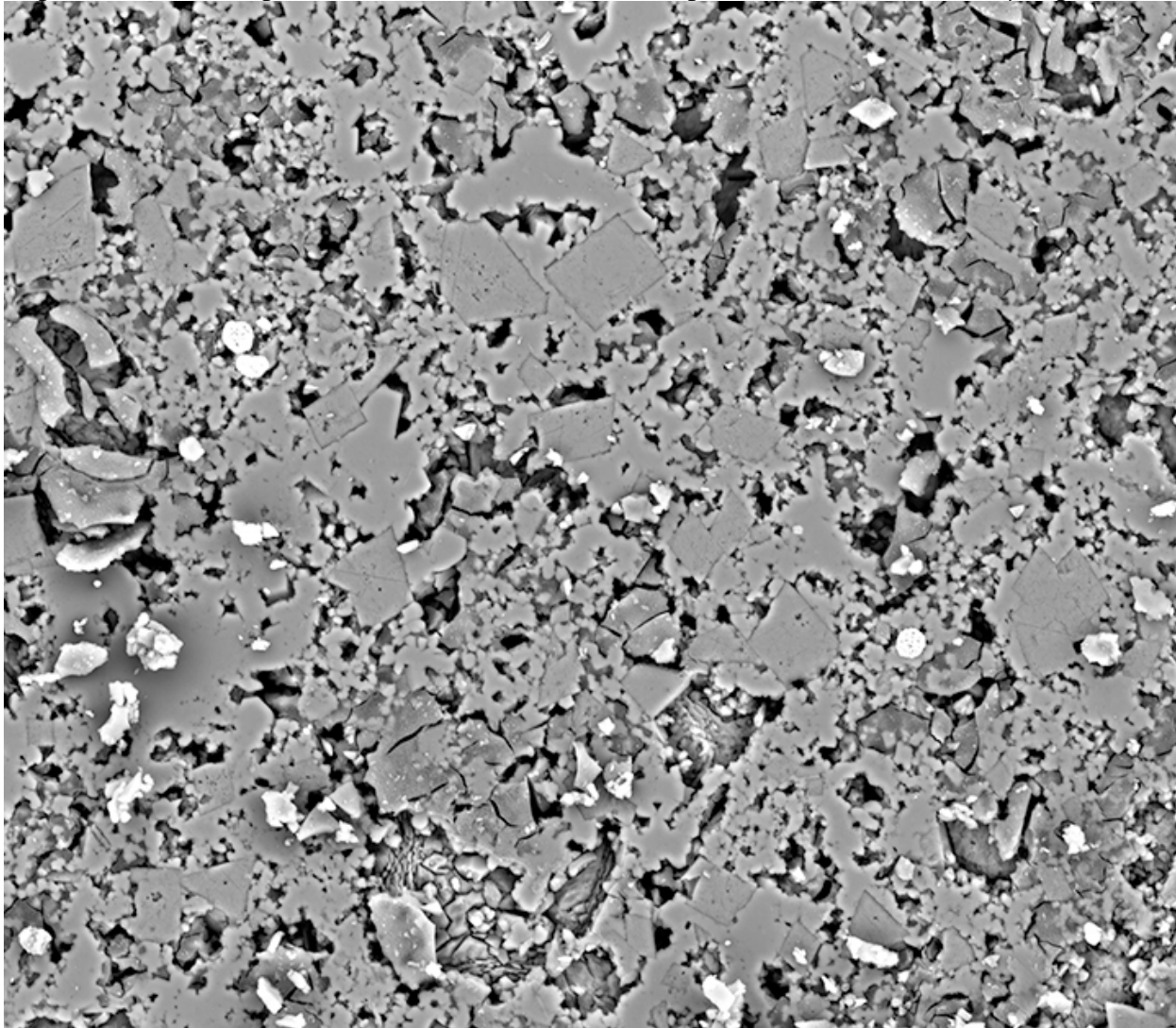
Depth 5035.5 ft, Sample 7-8, Dimensions 11208x9717 pixel², scale 0.016343408 μm/pixel



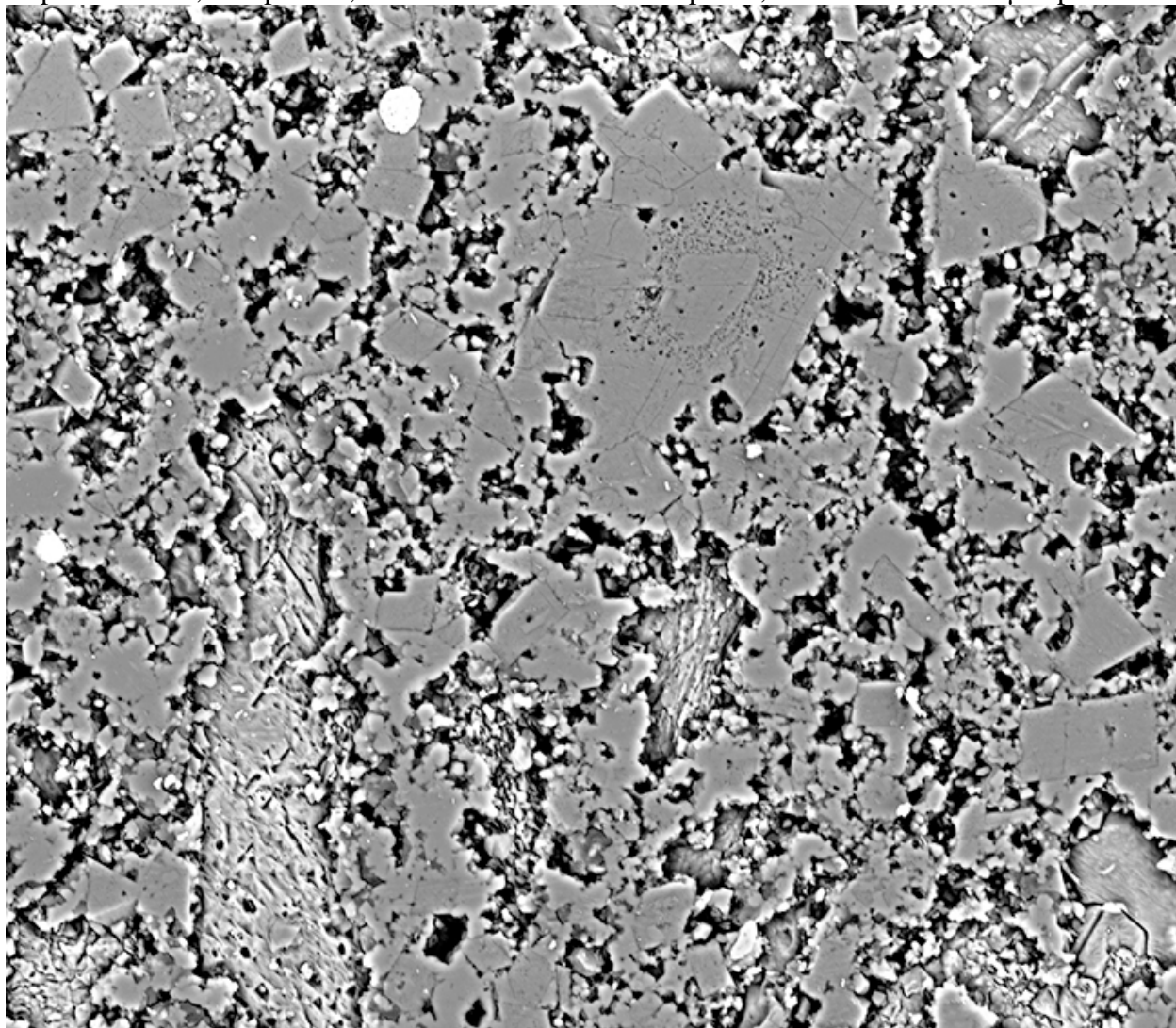
Depth 5035.5 ft, Sample 7-8, Dimensions 18476x16148 pixel², scale 0.017822607 μm/pixel



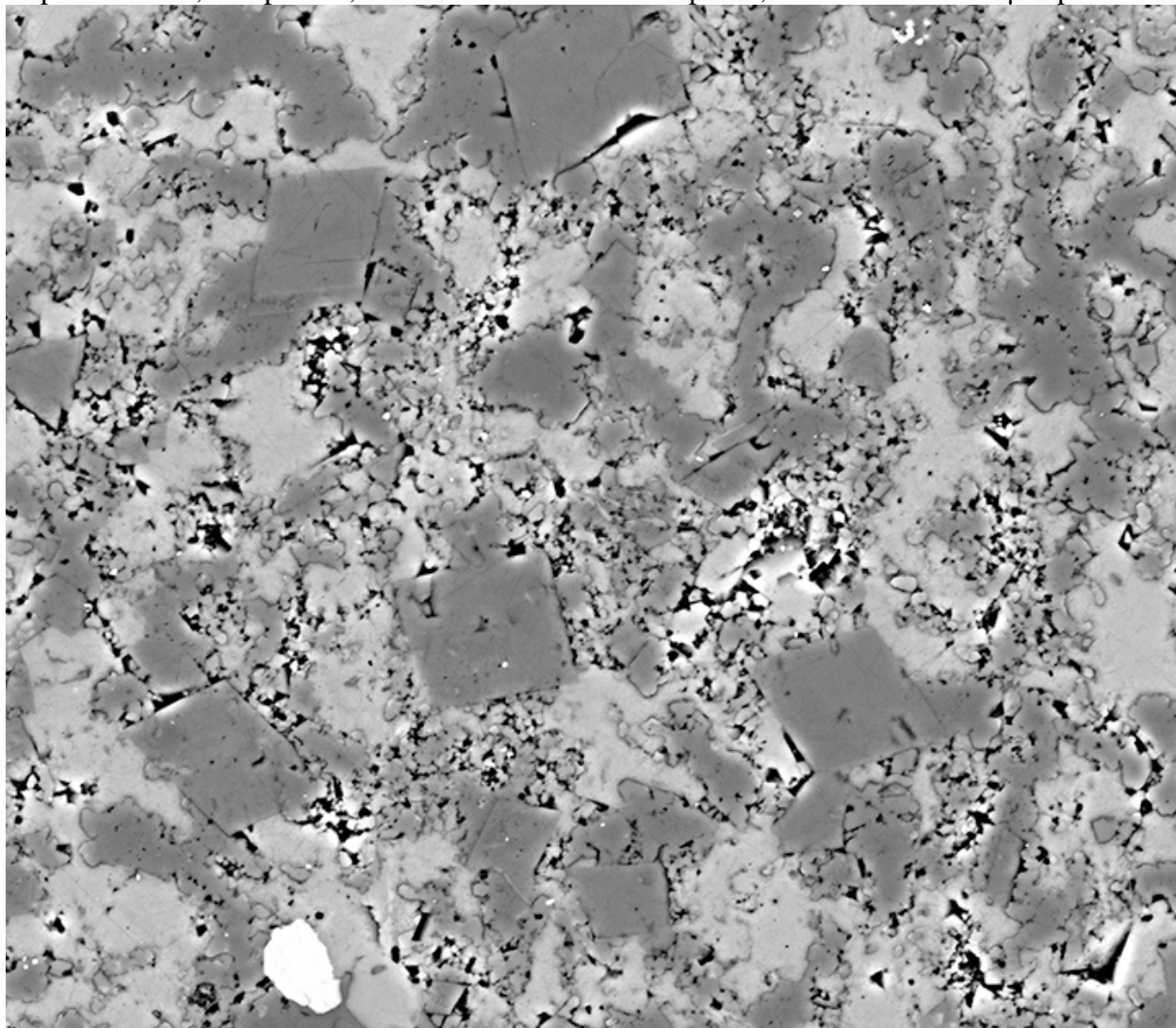
Depth 5043.9 ft, Sample 8-3, Dimensions 13058x11402 pixel², scale 0.014044043 μm/pixel



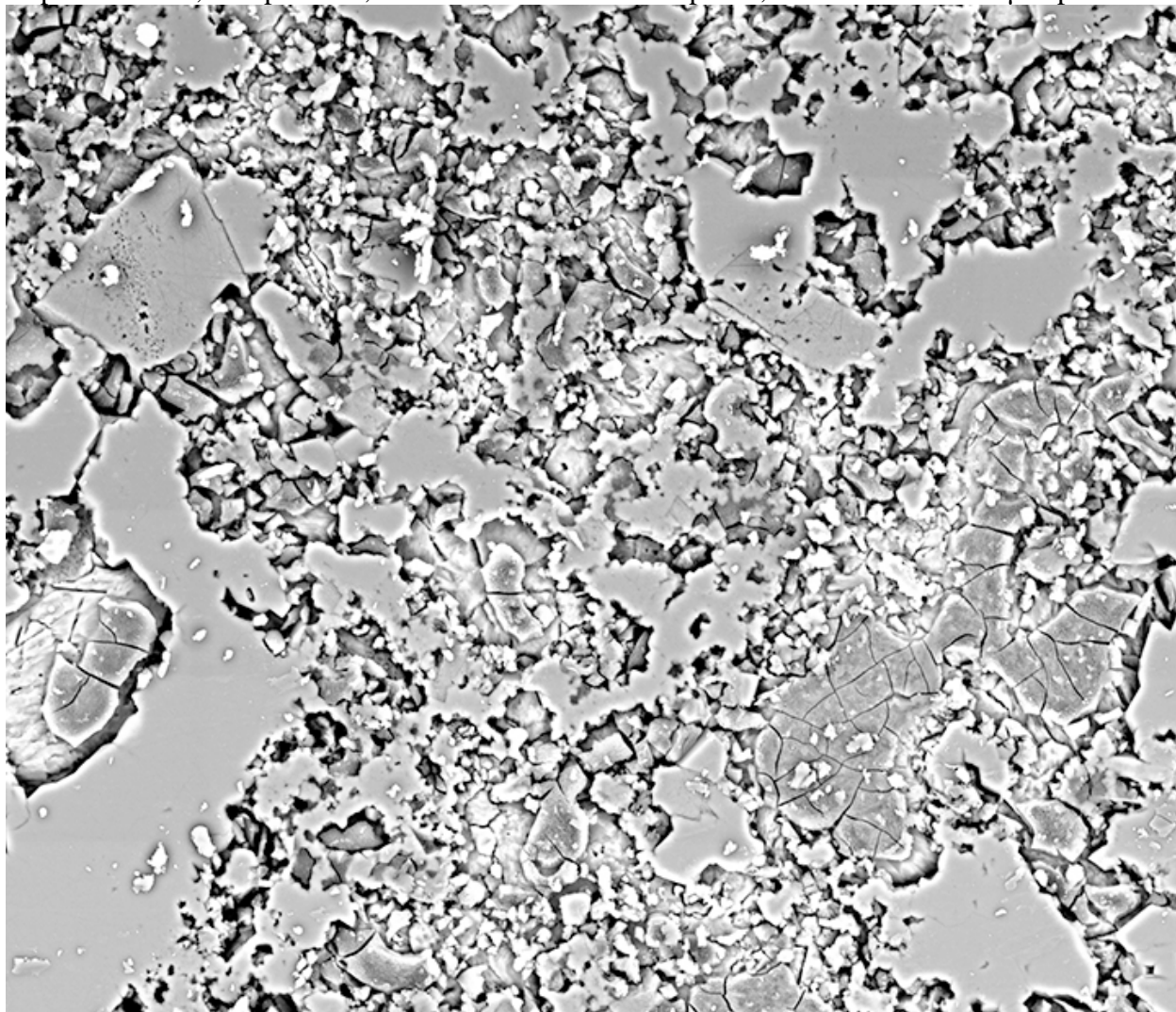
Depth 5043.9 ft, Sample 8-3, Dimensions 13034x11369 pixel², scale 0.014044043 μm/pixel



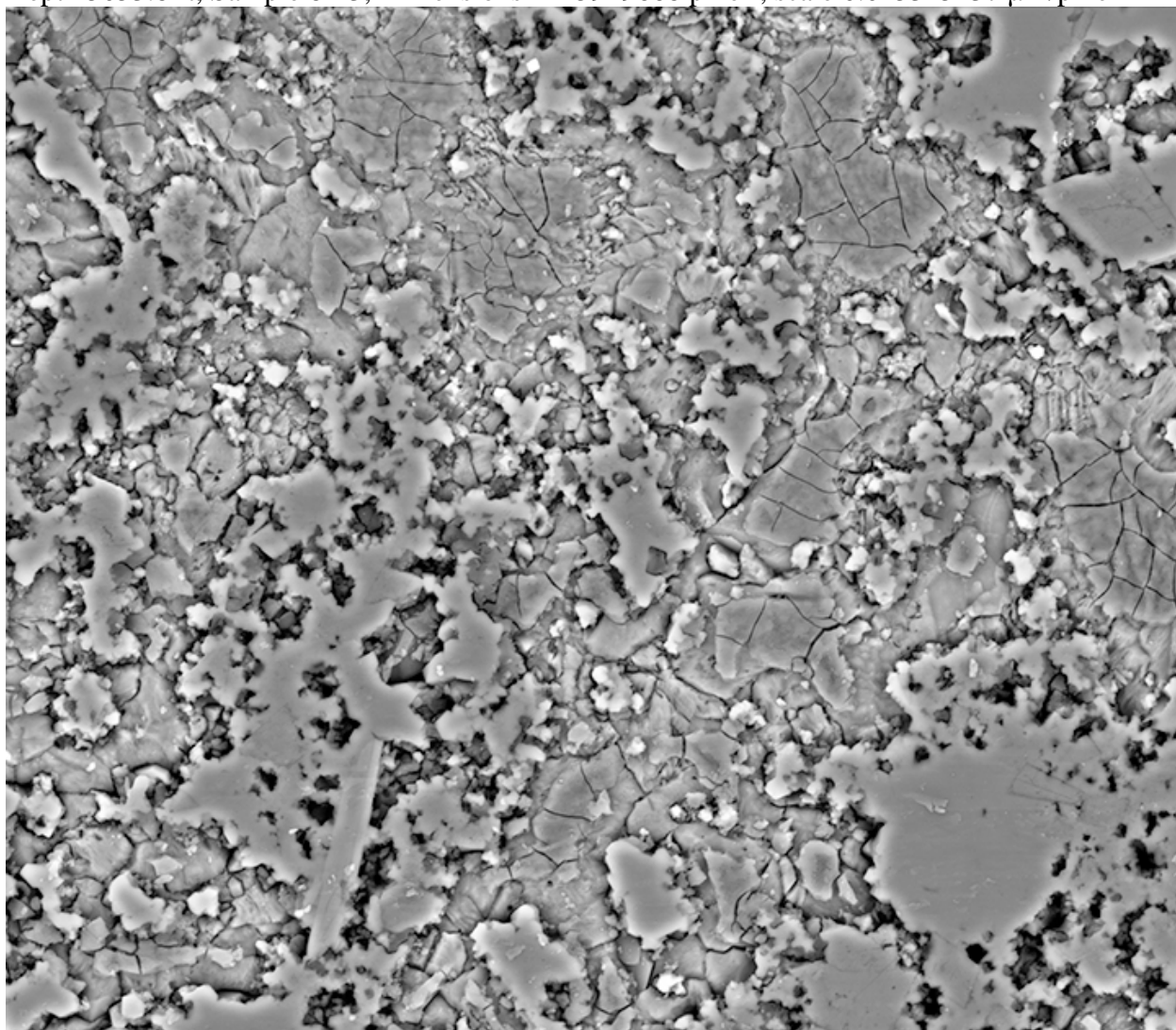
Depth 5043.9 ft, Sample 8-3, Dimensions 13078x11326 pixel², scale 0.014044043 μm/pixel



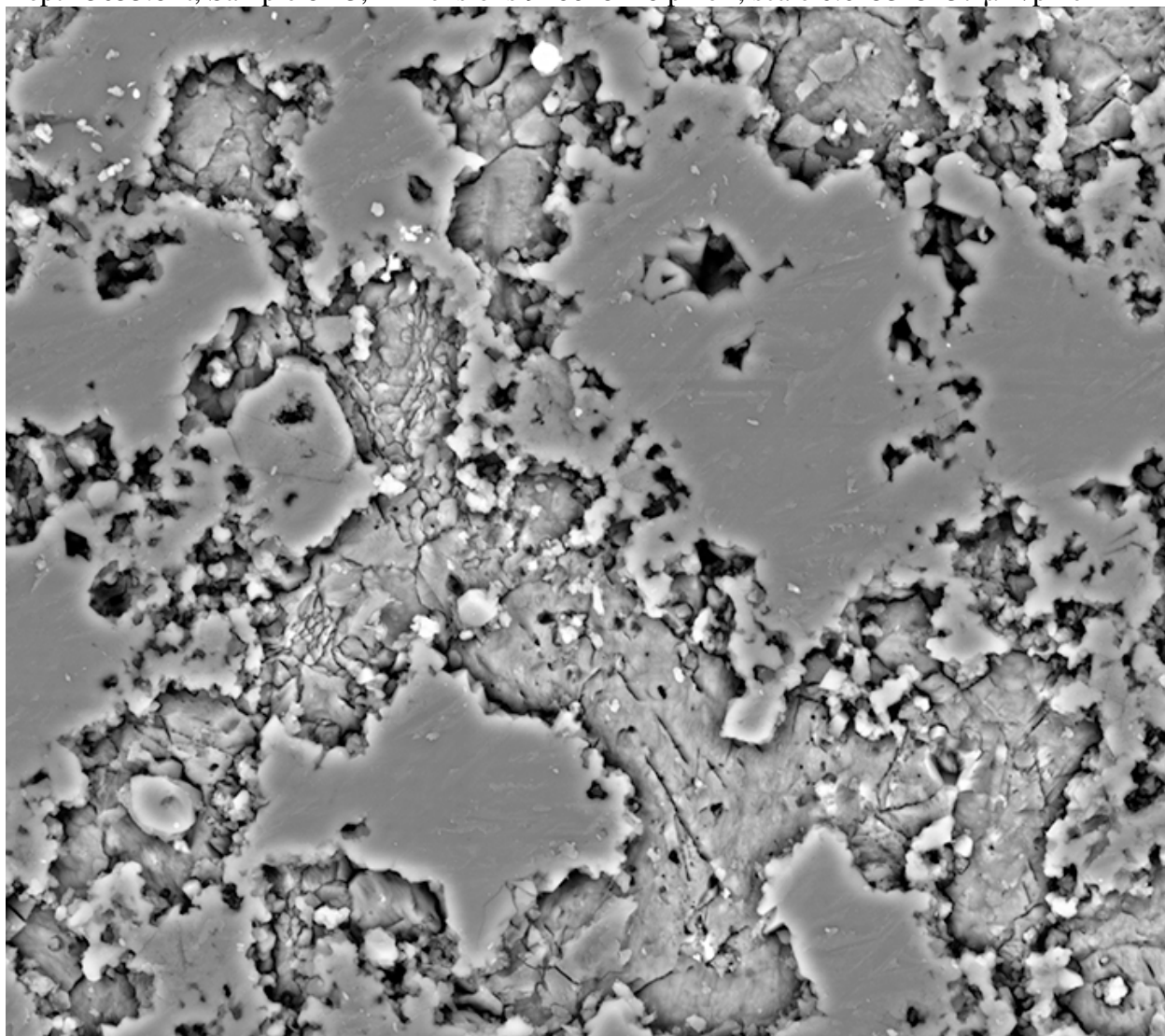
Depth 5053.8 ft, Sample 8-13, Dimensions 11202x9681 pixel², scale 0.016701318 μm/pixel



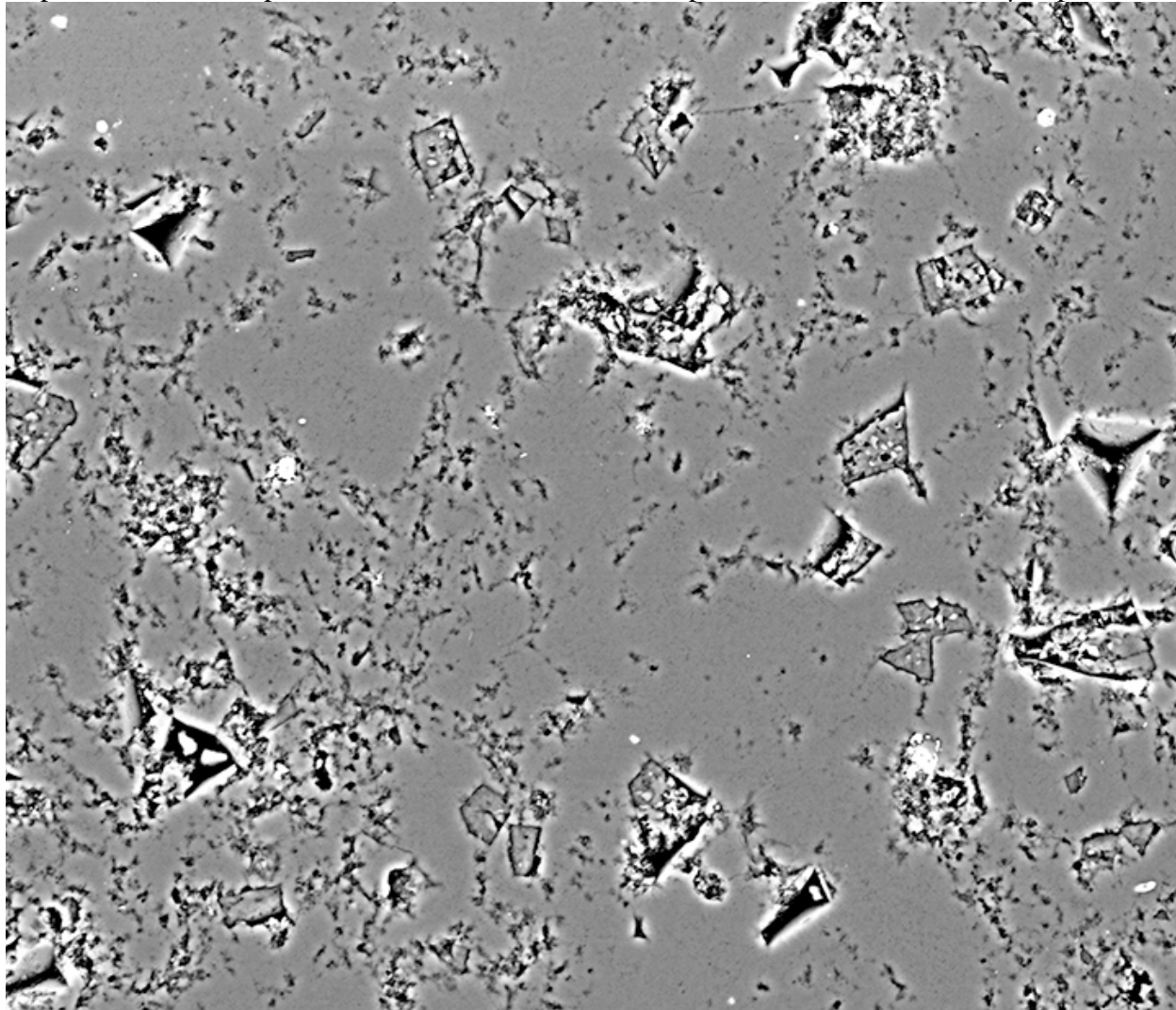
Depth 5053.8 ft, Sample 8-13, Dimensions 11159x9668 pixel², scale 0.015315137 μm/pixel



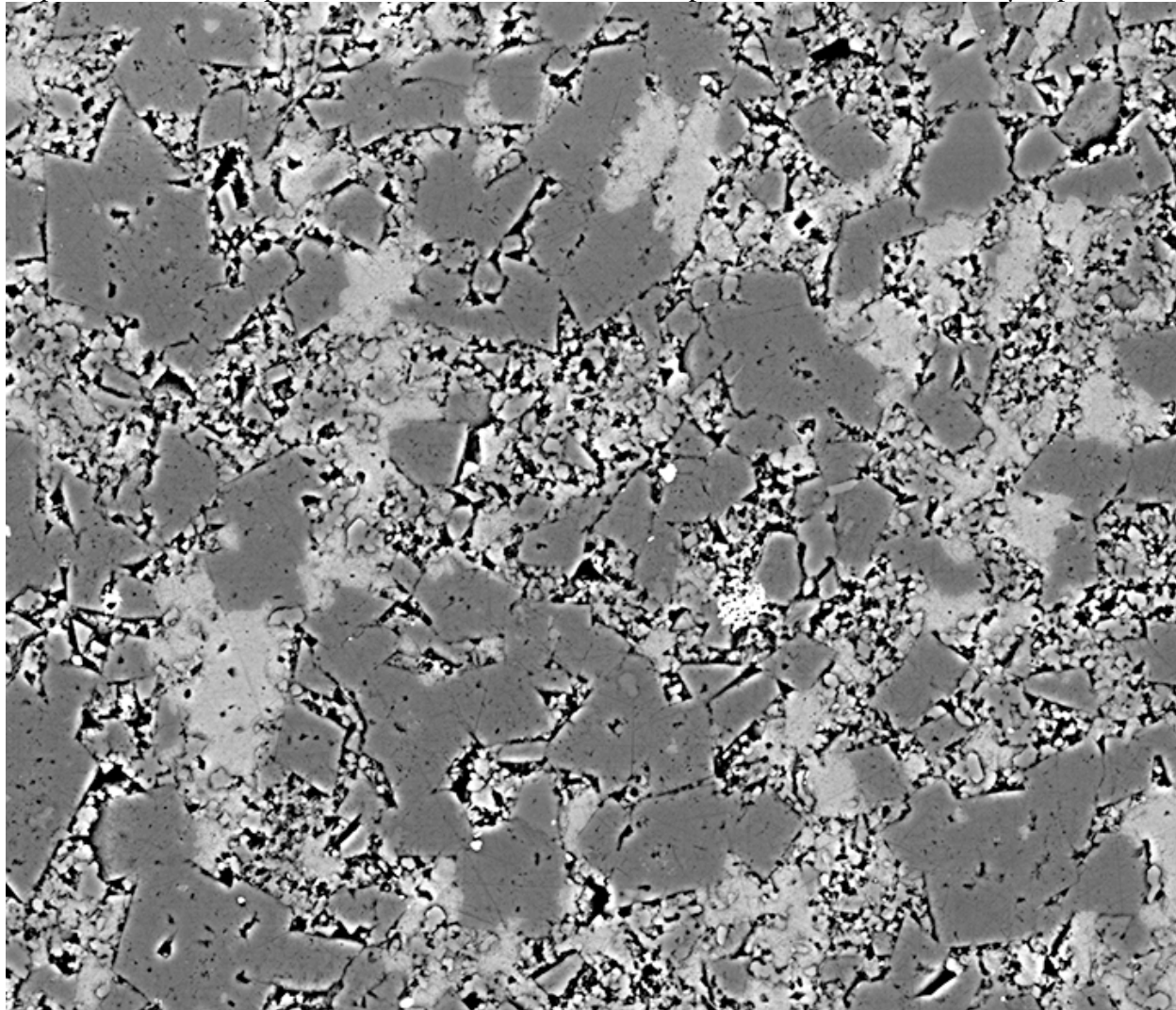
Depth 5053.8 ft, Sample 8-13, Dimensions 9266x8146 pixel², scale 0.015315137 μm/pixel



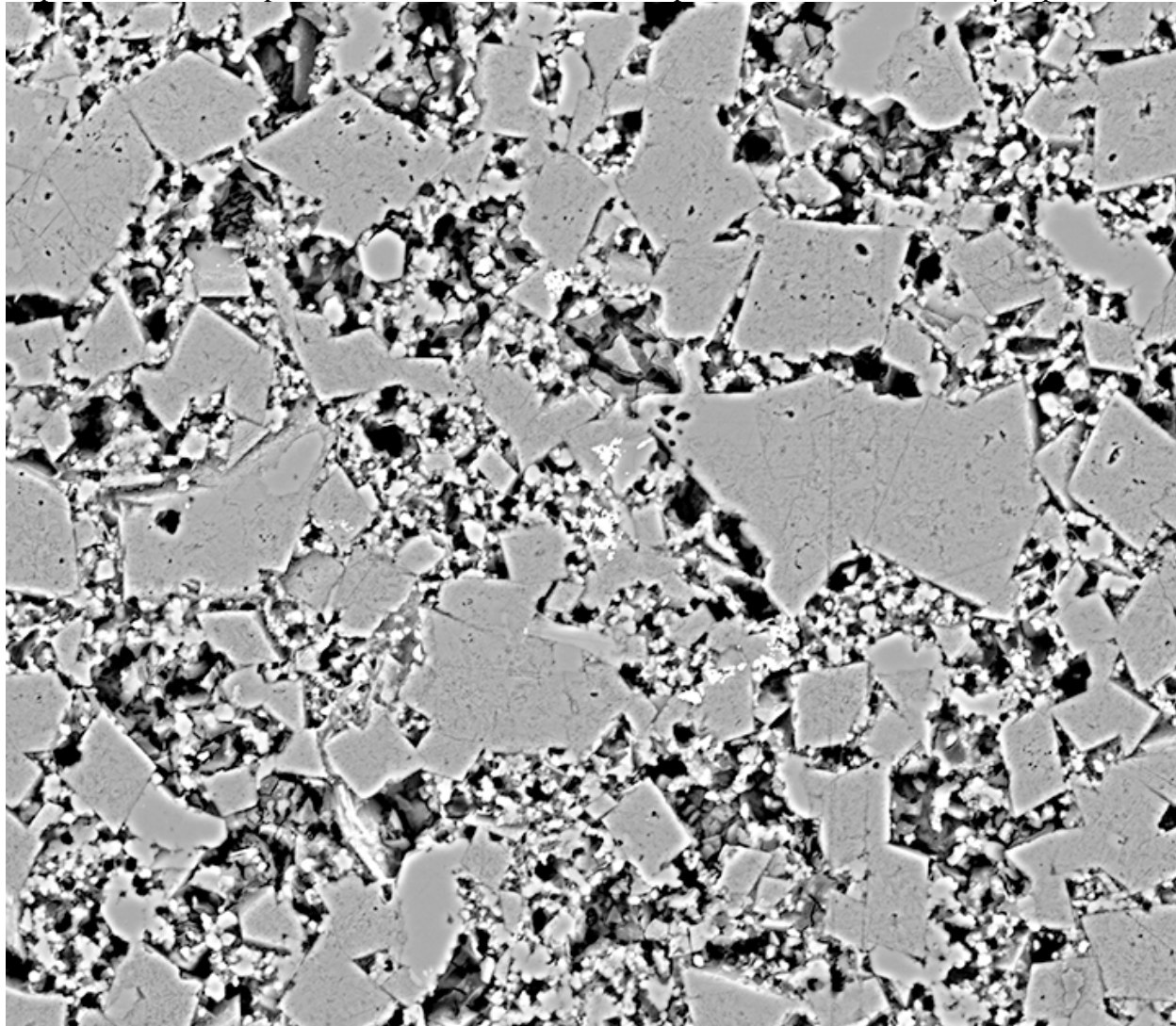
Depth 5064.9 ft, Sample 9-3, Dimensions 13124x11364 pixel², scale 0.012878467 $\mu\text{m}/\text{pixel}$



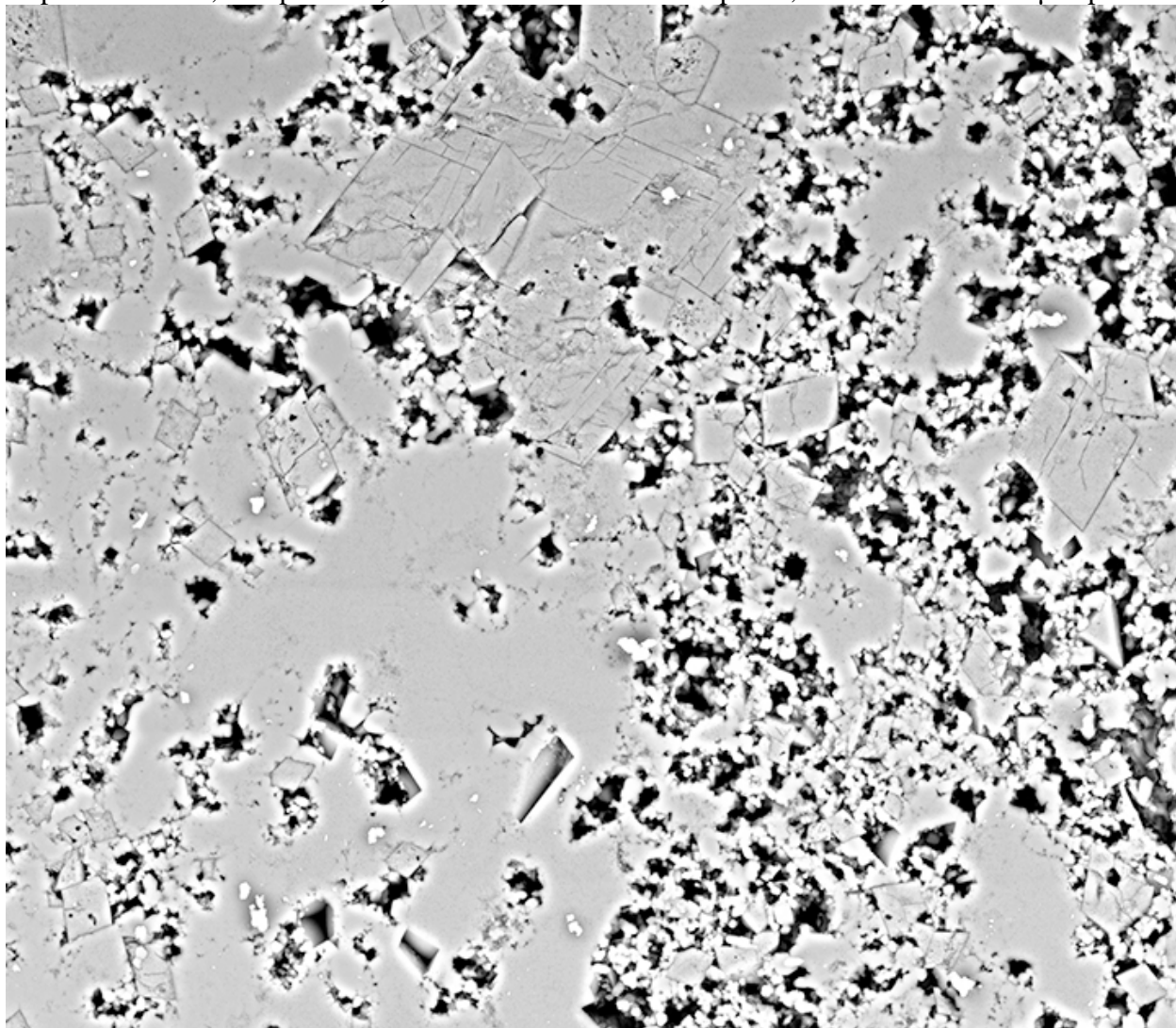
Depth 5064.9 ft, Sample 9-3, Dimensions 13108x11275 pixel², scale 0.012878467 μm/pixel



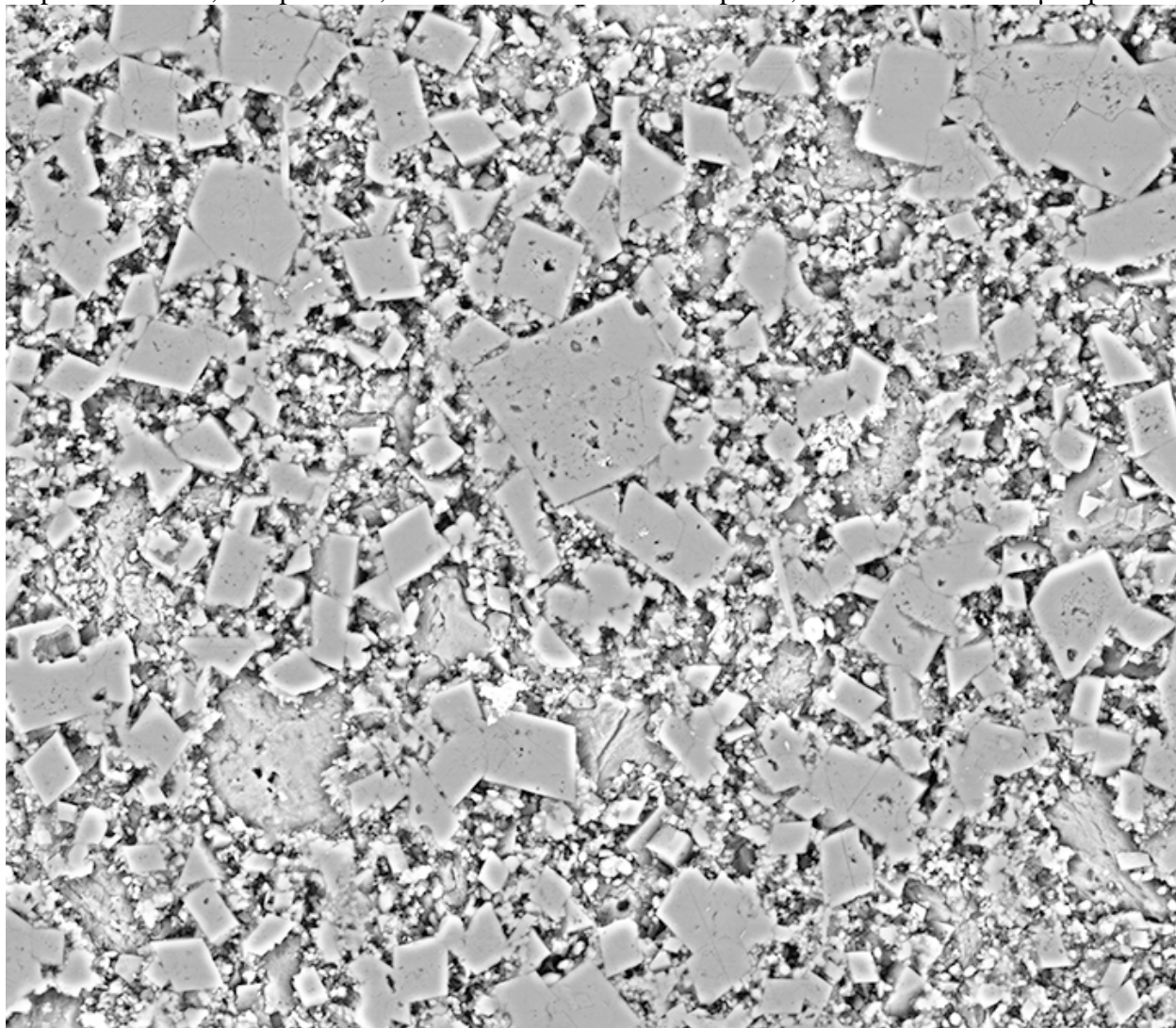
Depth 5064.9 ft, Sample 9-3, Dimensions 13089x9681 pixel², scale 0.012878467 μm/pixel



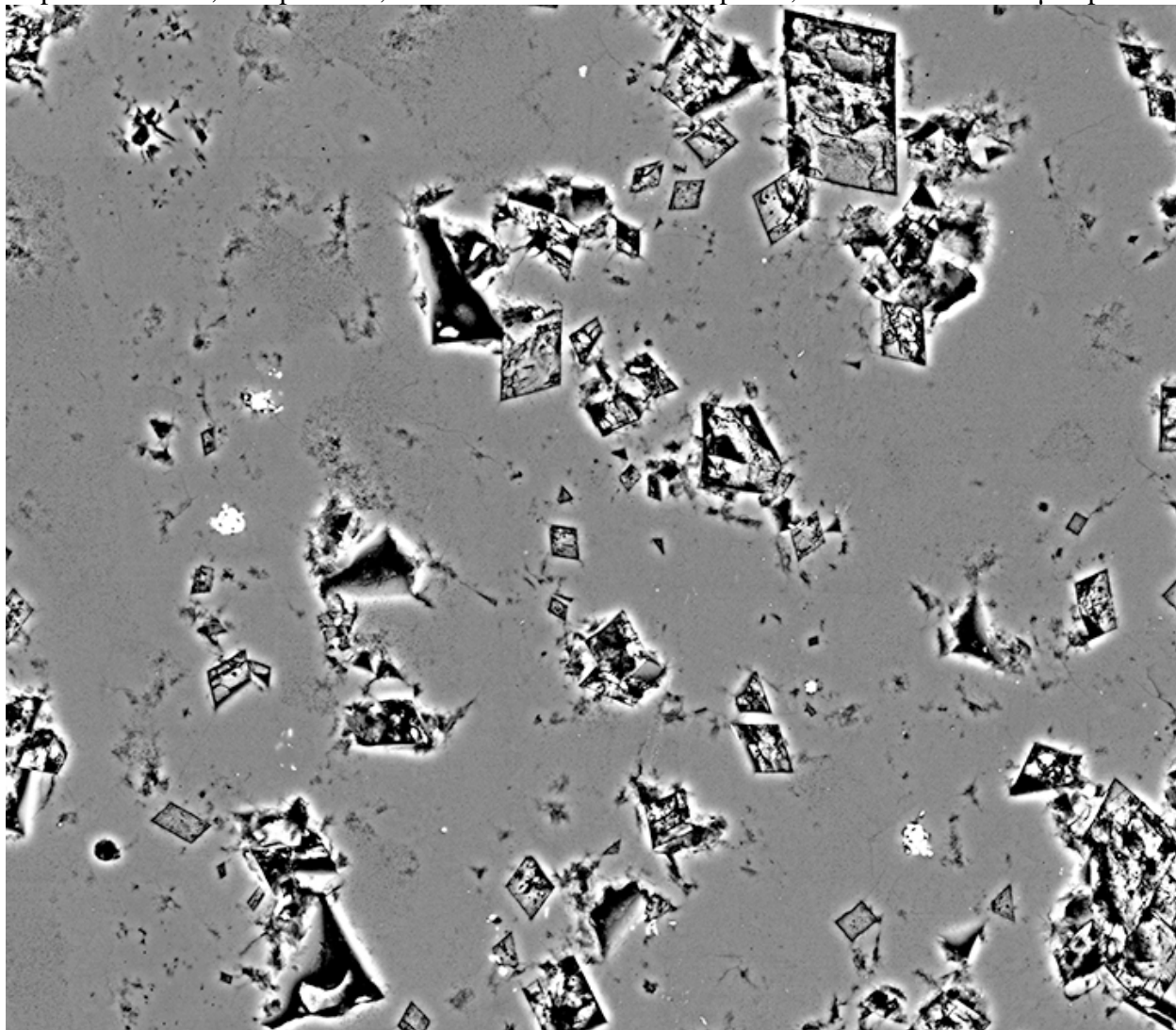
Depth 5074.95 ft, Sample 9-13, Dimensions 12816x11147 pixel², scale 0.018212891 μm/pixel



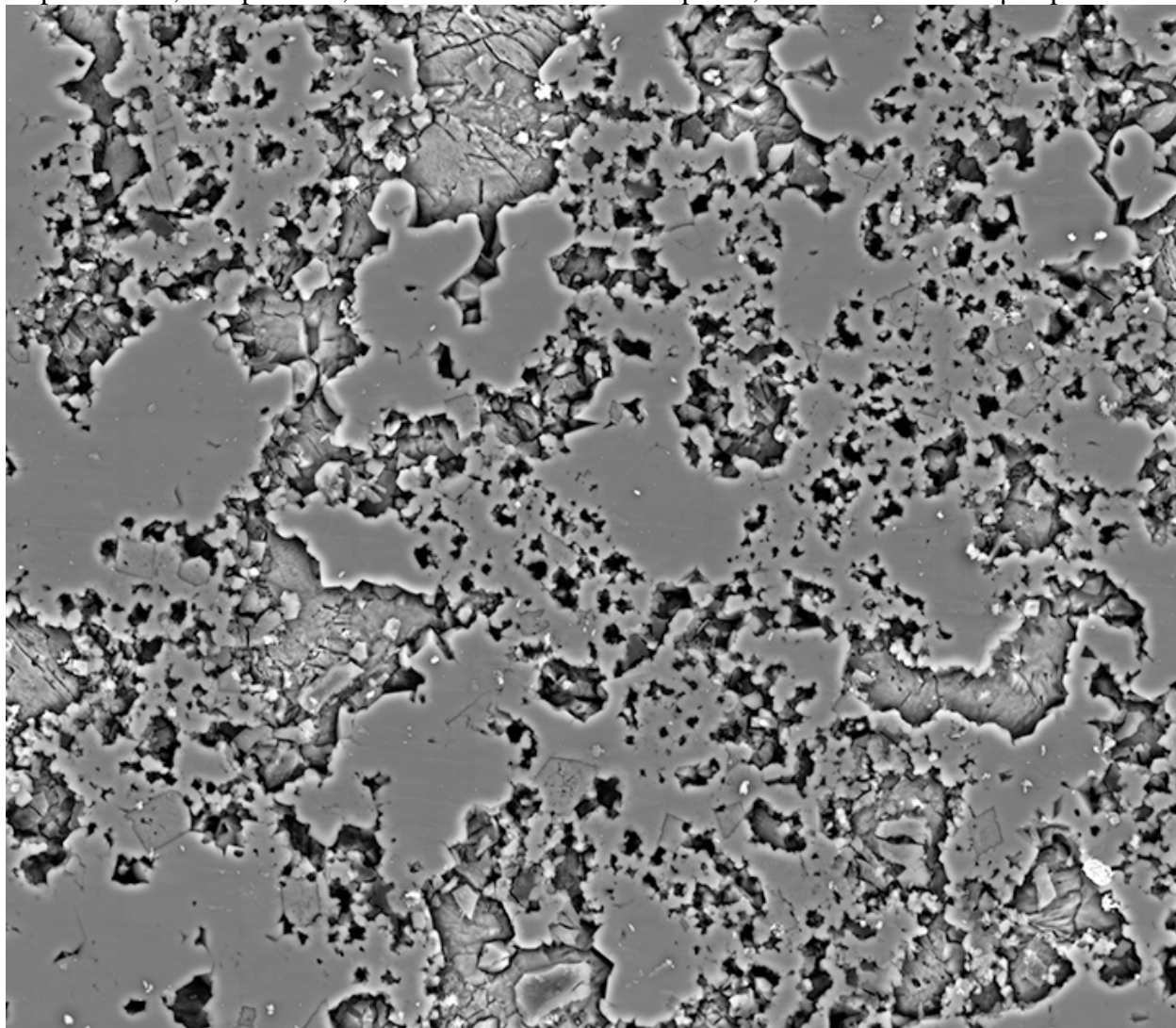
Depth 5074.95 ft, Sample 9-13, Dimensions 12938x11272 pixel², scale 0.018212891 $\mu\text{m}/\text{pixel}$



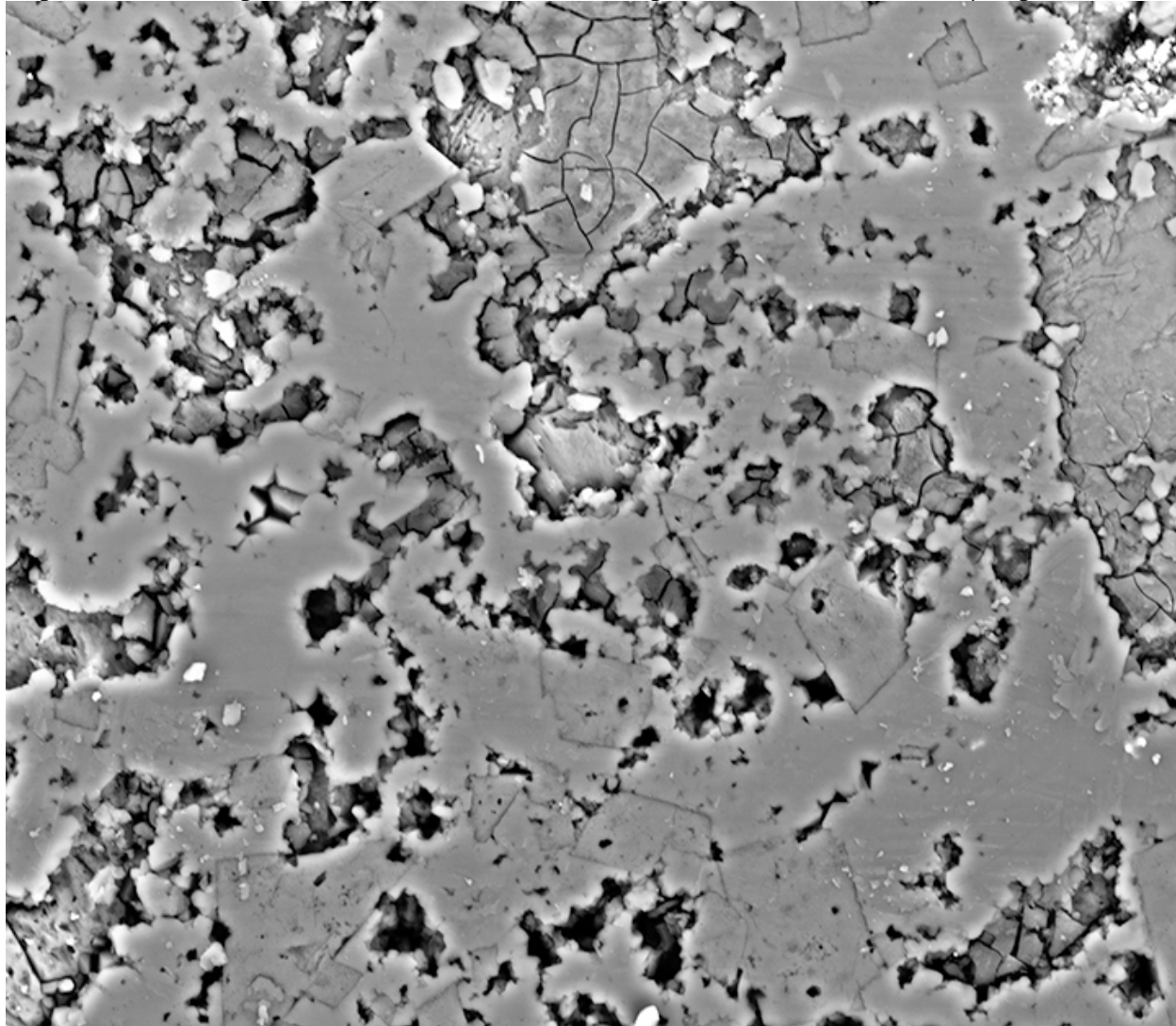
Depth 5074.95 ft, Sample 9-13, Dimensions 13032x11359 pixel², scale 0.018212891 $\mu\text{m}/\text{pixel}$



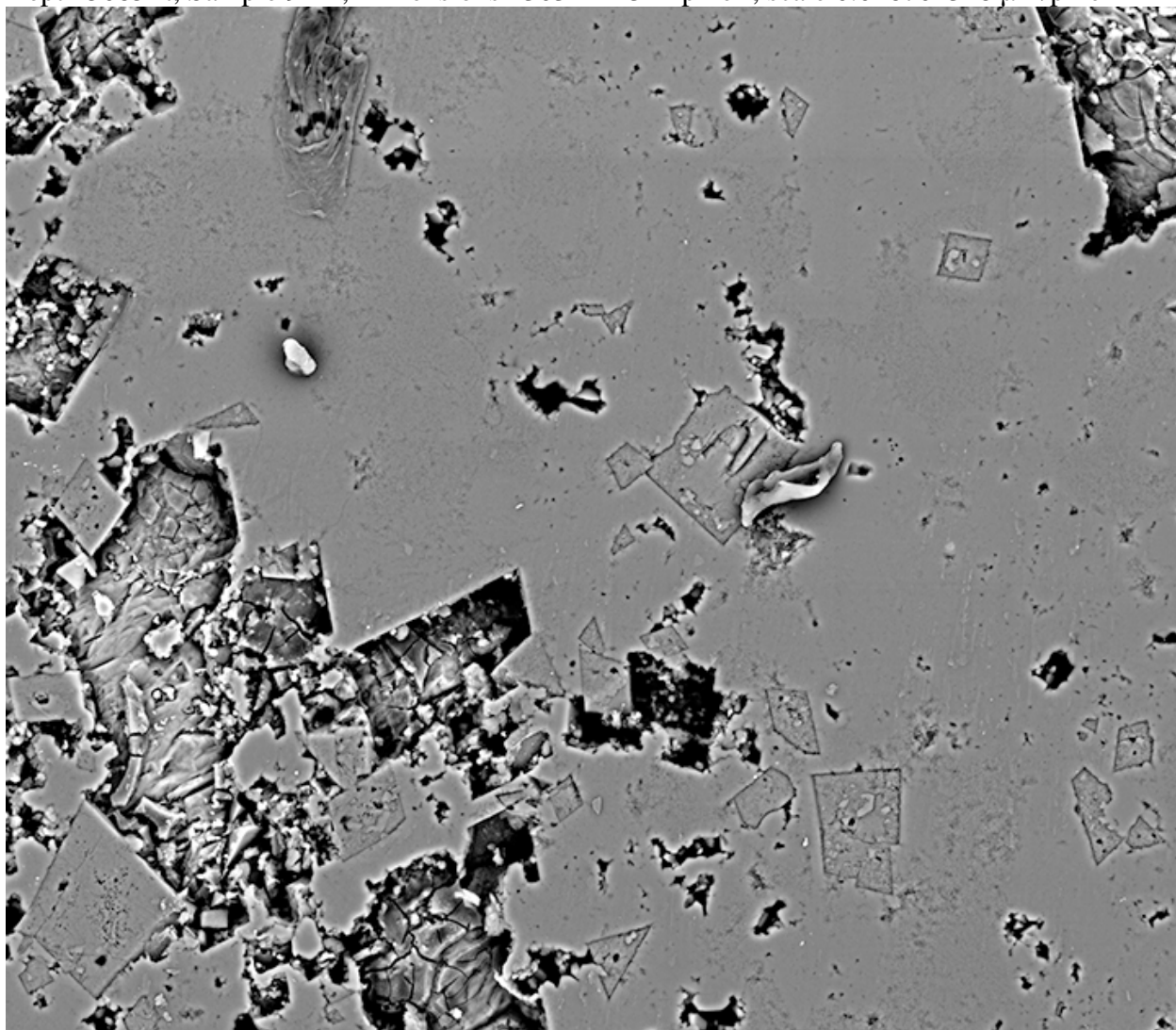
Depth 5085 ft, Sample 9-24, Dimensions 36988x32176 pixel², scale 0.007022021 μm/pixel



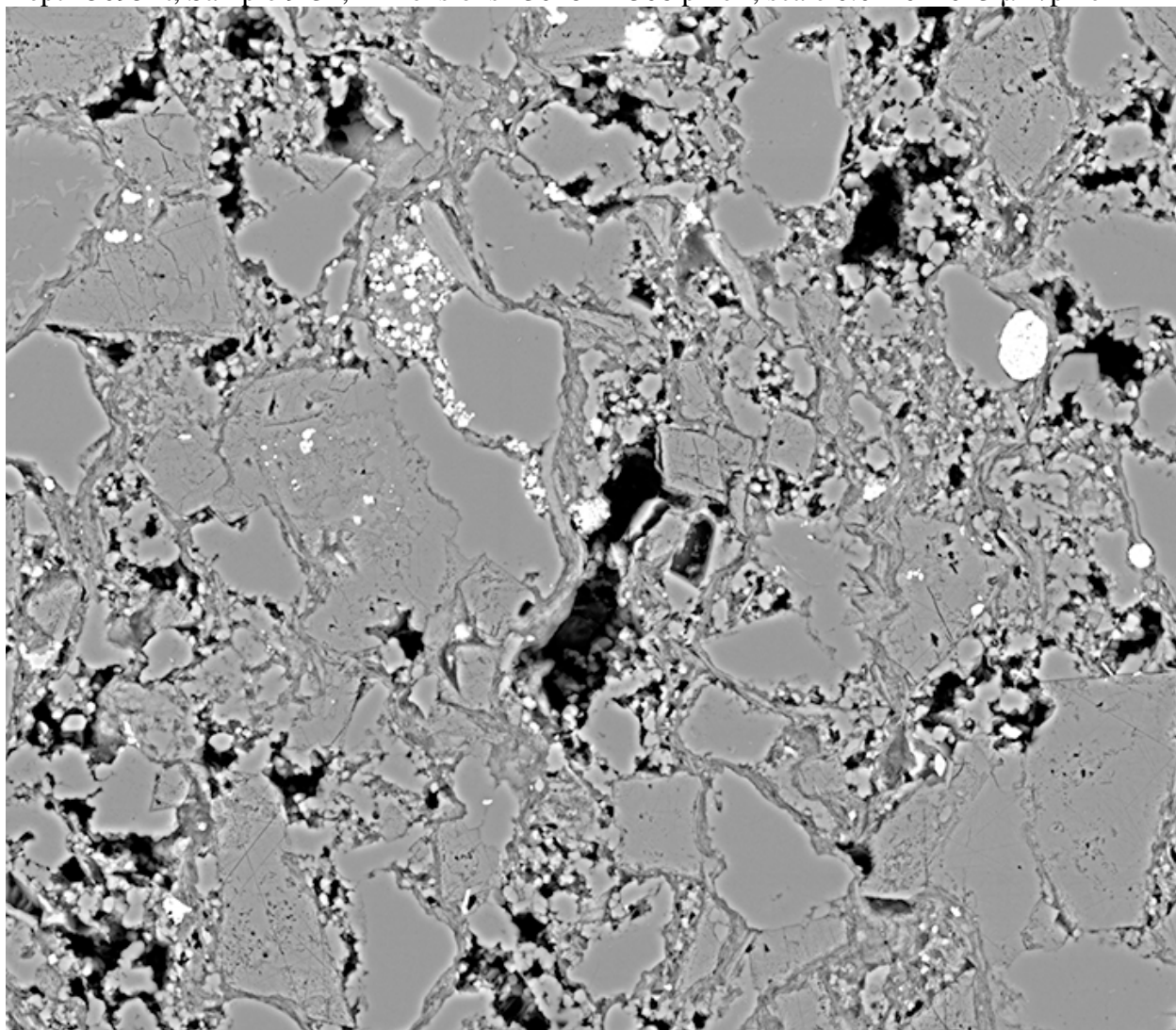
Depth 5085 ft, Sample 9-24, Dimensions 9305x8075 pixel², scale 0.016701318 μm/pixel



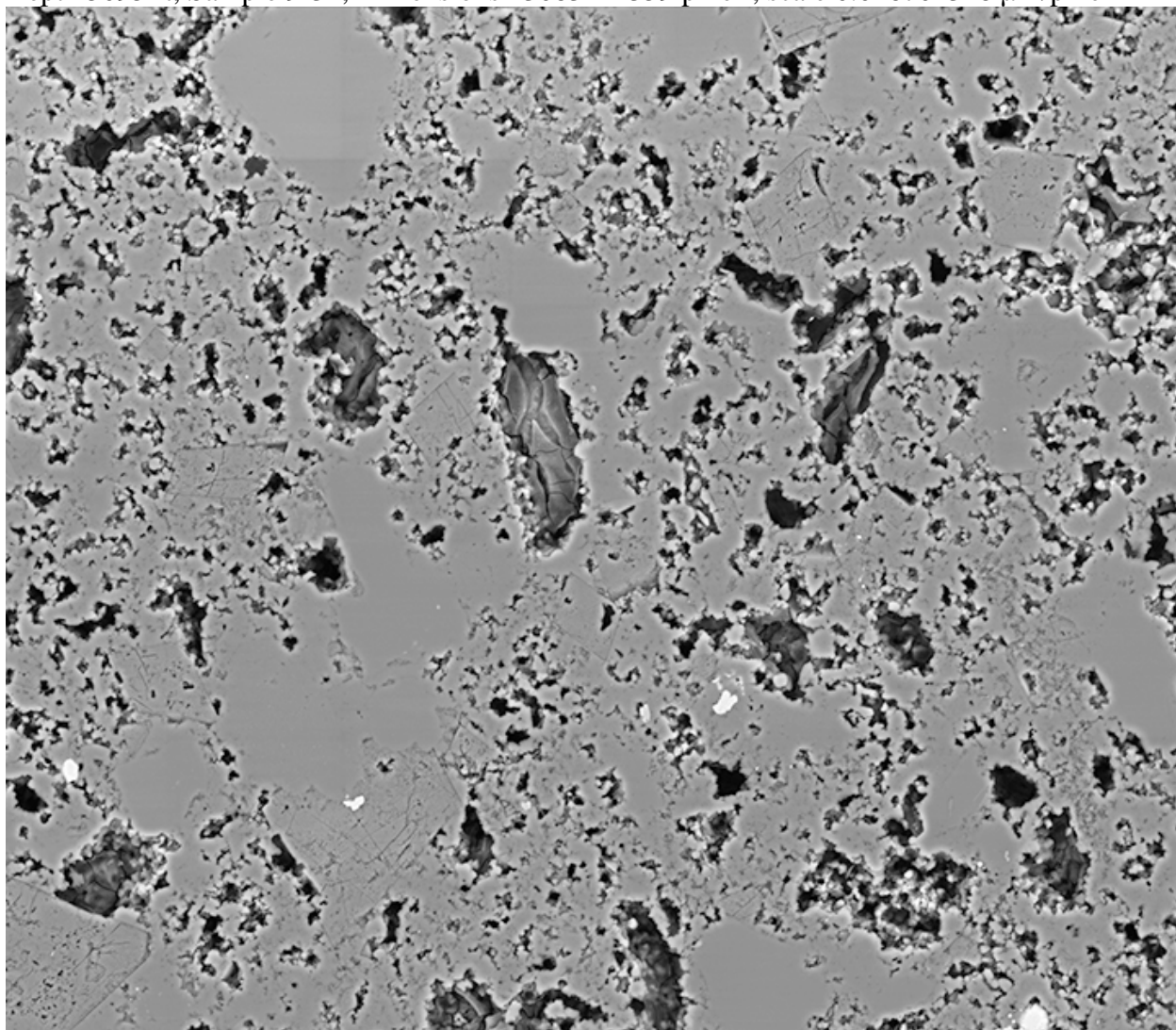
Depth 5085 ft, Sample 9-24, Dimensions 13032x11322 pixel², scale 0.016701318 μm/pixel



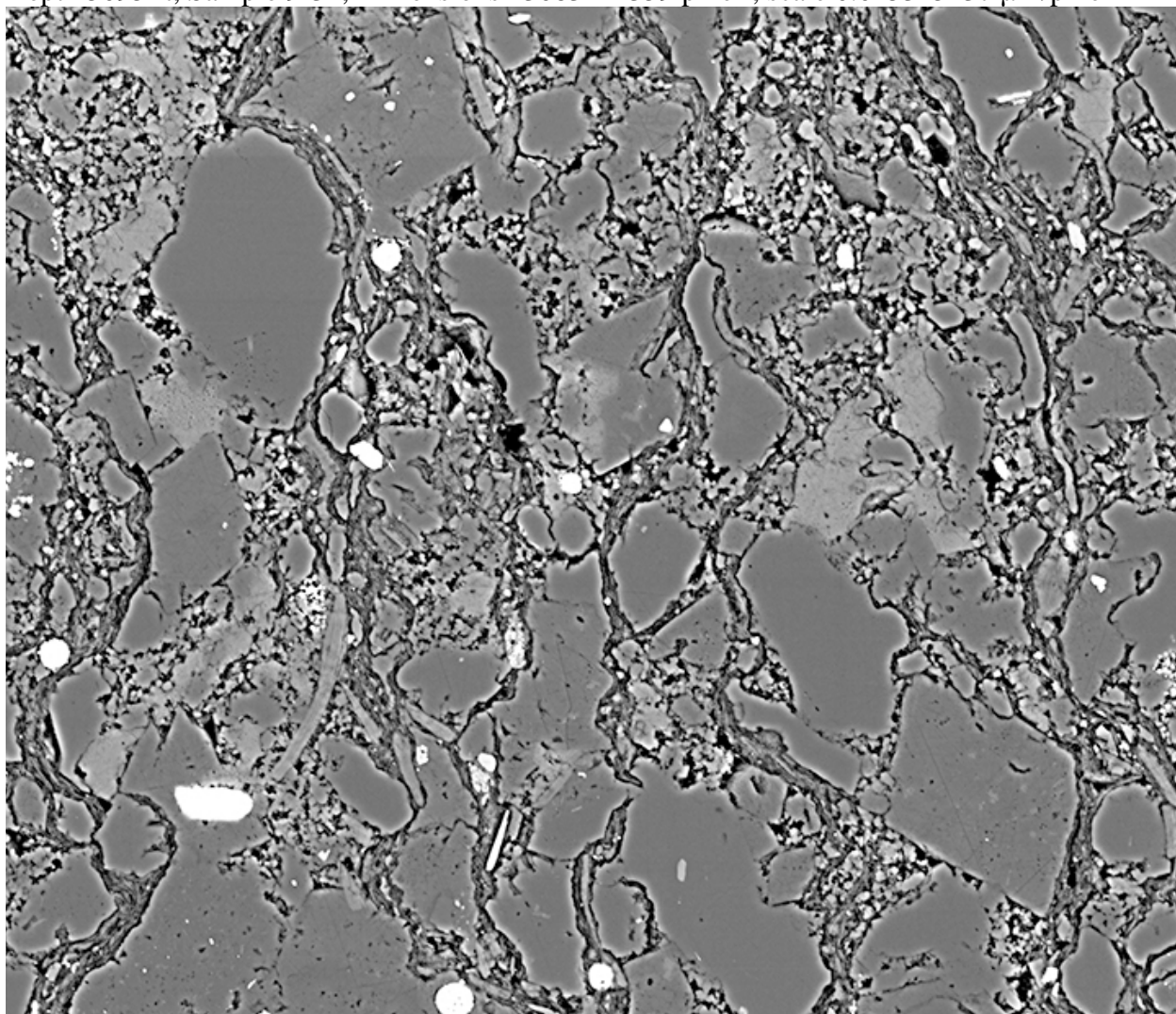
Depth 5095 ft, Sample 9-34, Dimensions 13028x11306 pixel², scale 0.014044043 μm/pixel



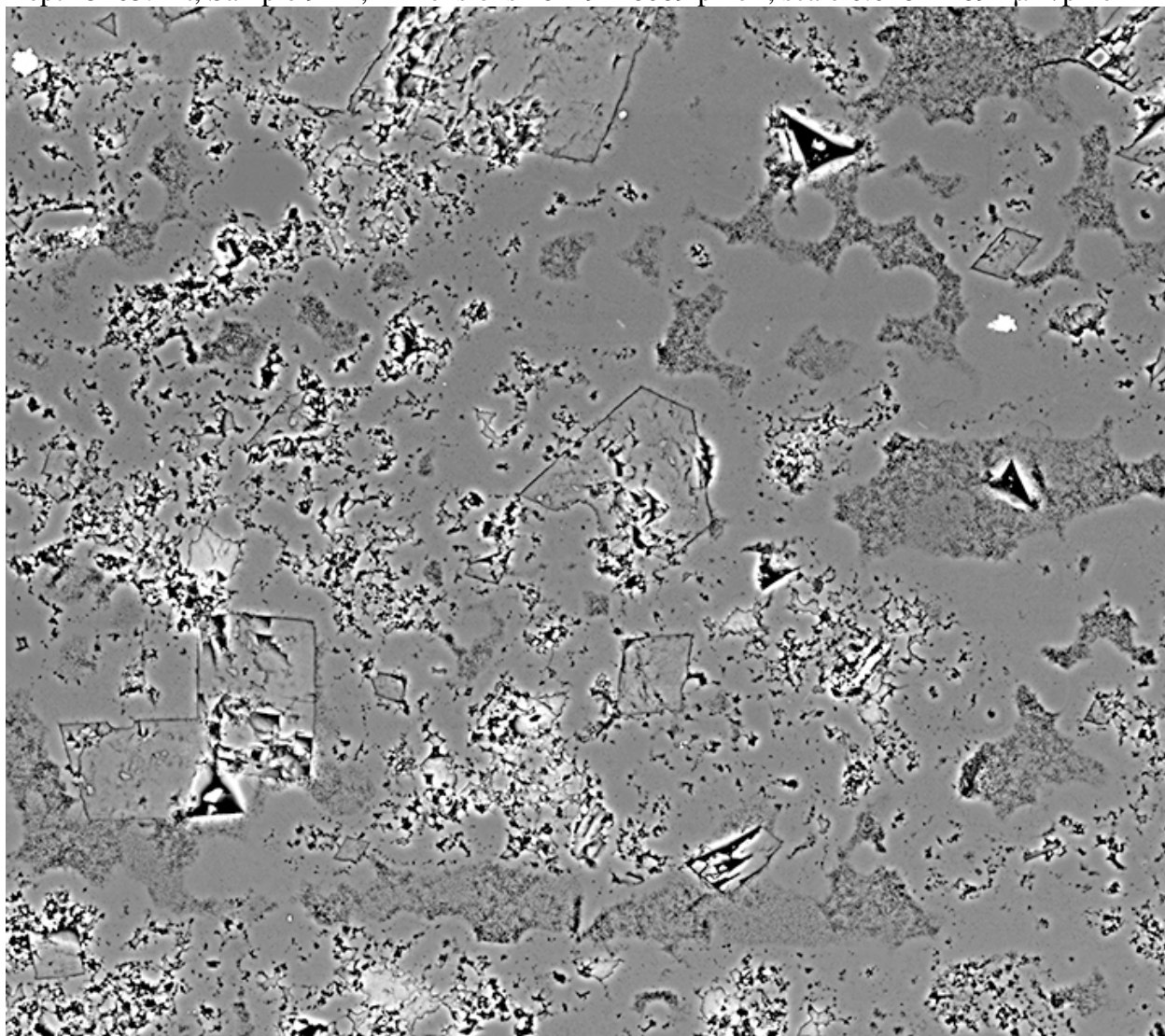
Depth 5095 ft, Sample 9-34, Dimensions 13083x11359 pixel², scale 0.016701318 μm/pixel



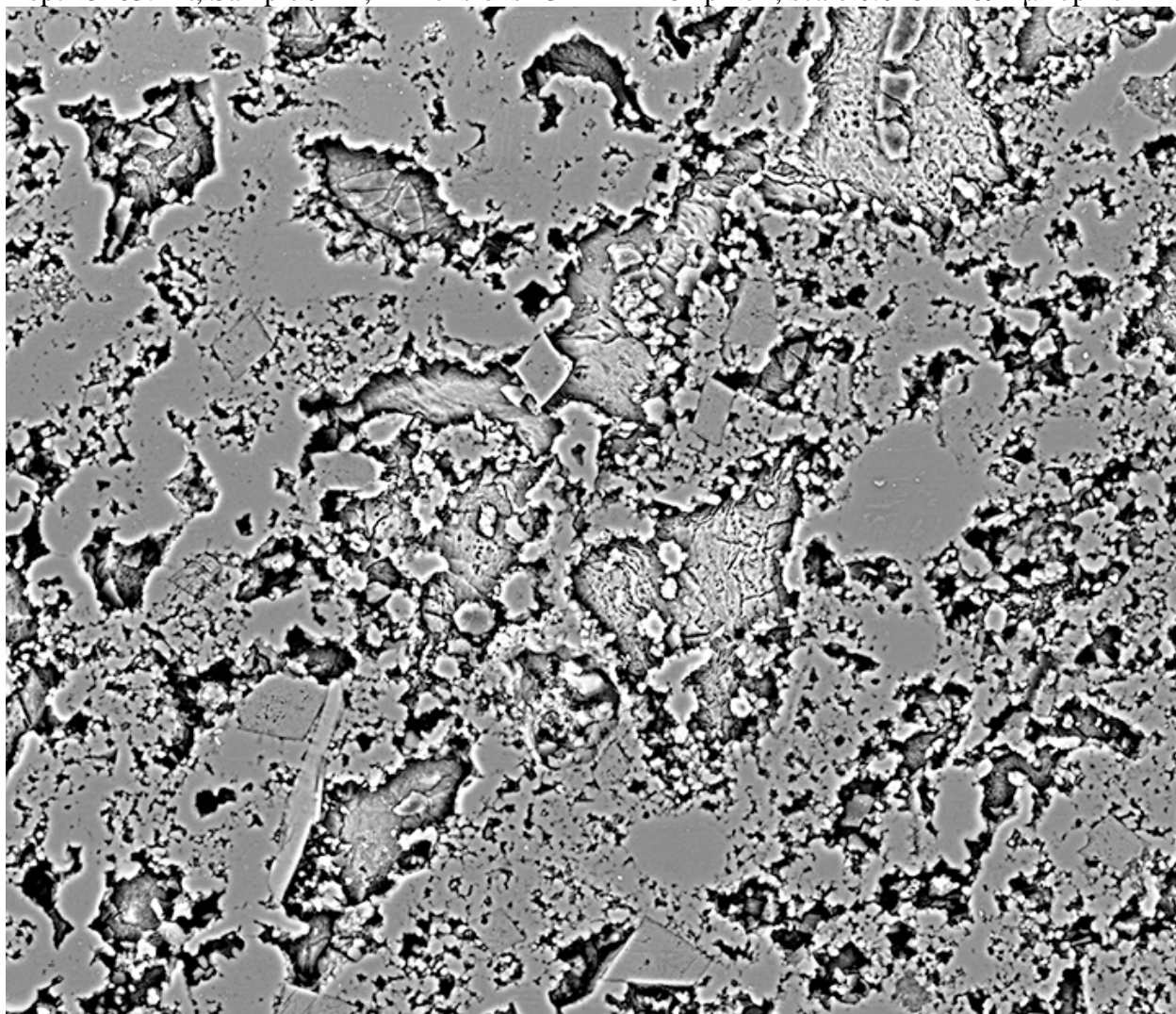
Depth 5095 ft, Sample 9-34, Dimensions 13083x11359 pixel², scale 0.015315137 μm/pixel



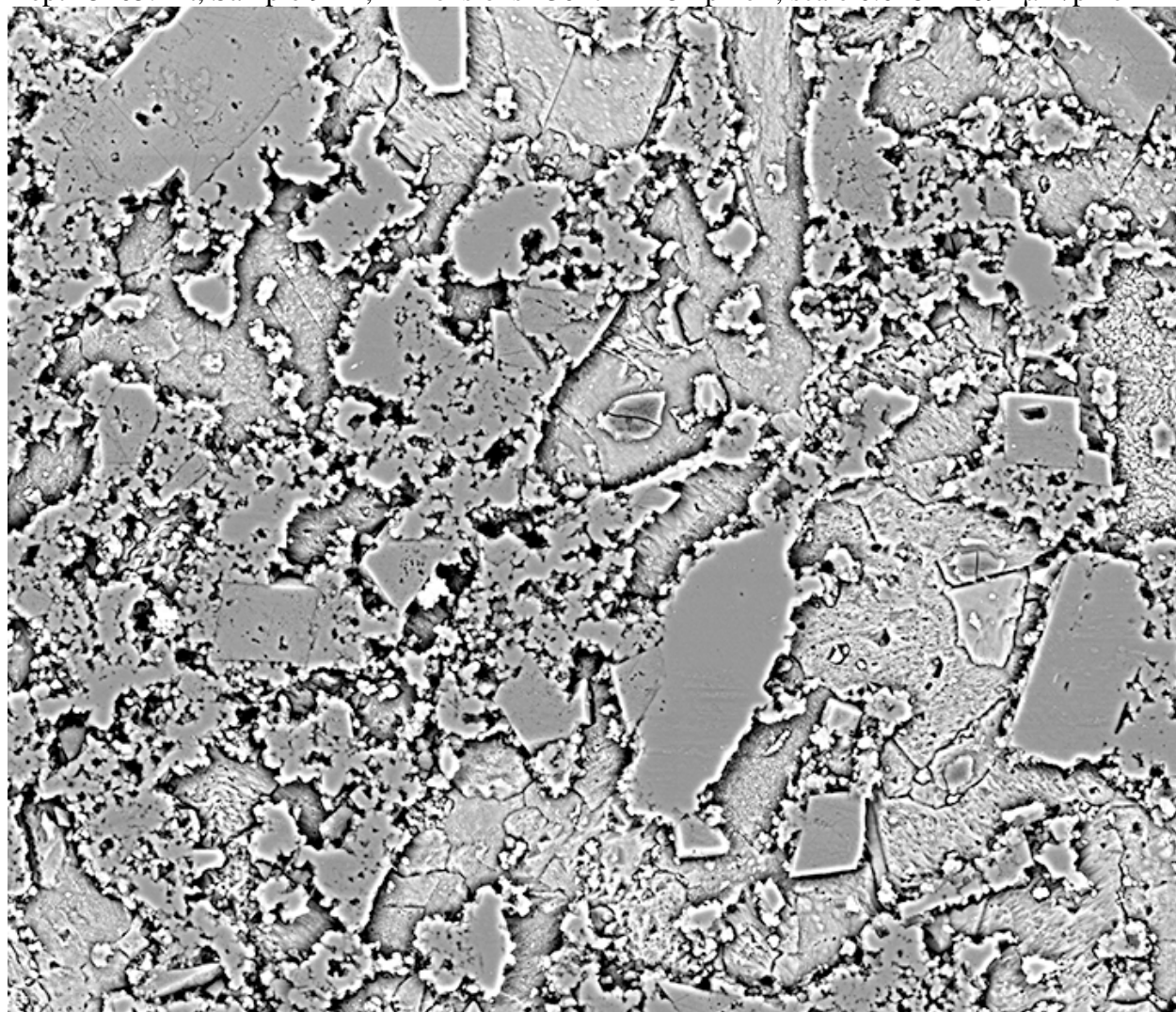
Depth 5105.2 ft, Sample 9-44, Dimensions 18129x16089 pixel², scale 0.018212891 μm/pixel



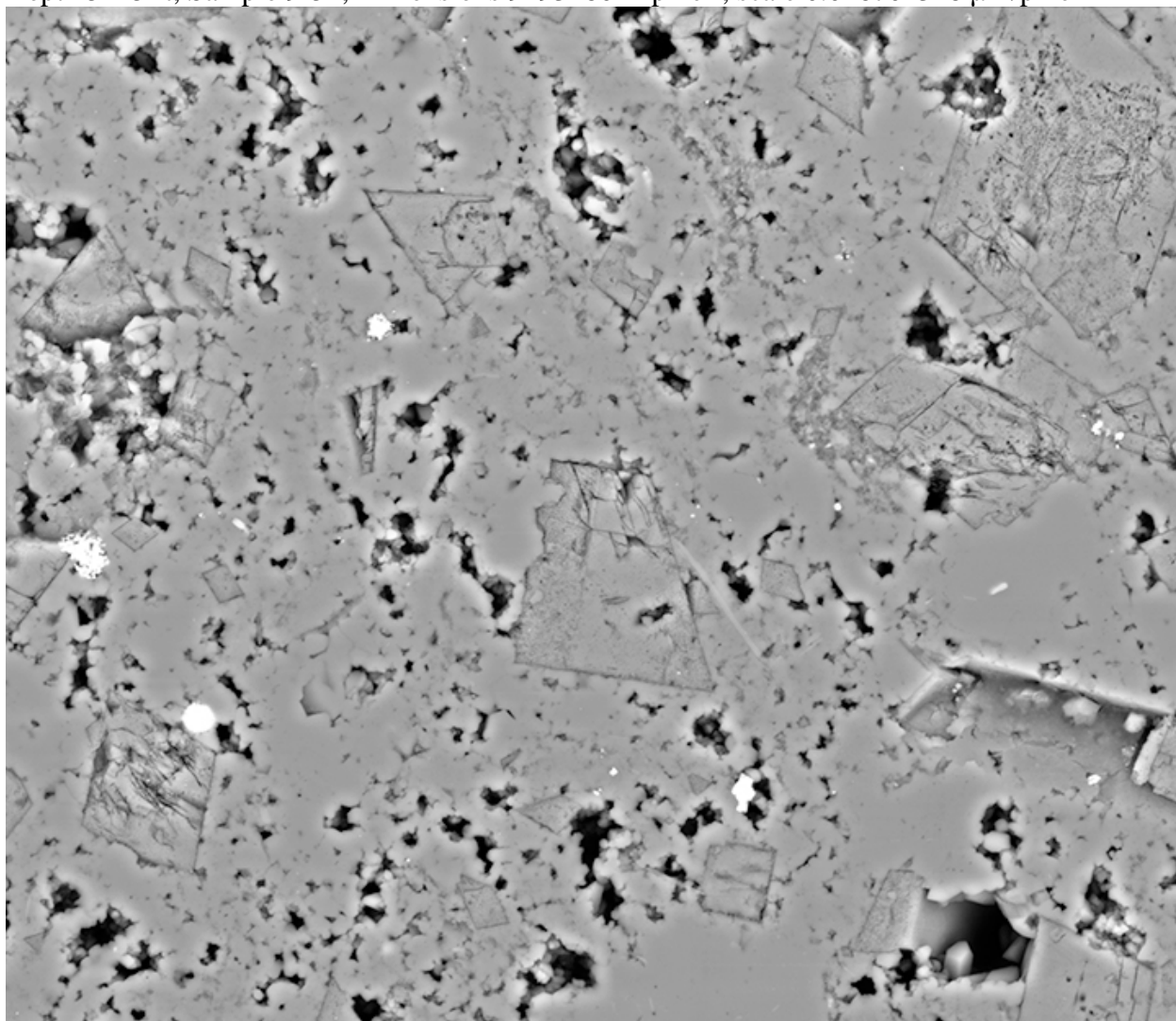
Depth 5105.2 ft, Sample 9-44, Dimensions 13112x11264 pixel², scale 0.018212891 $\mu\text{m}/\text{pixel}$



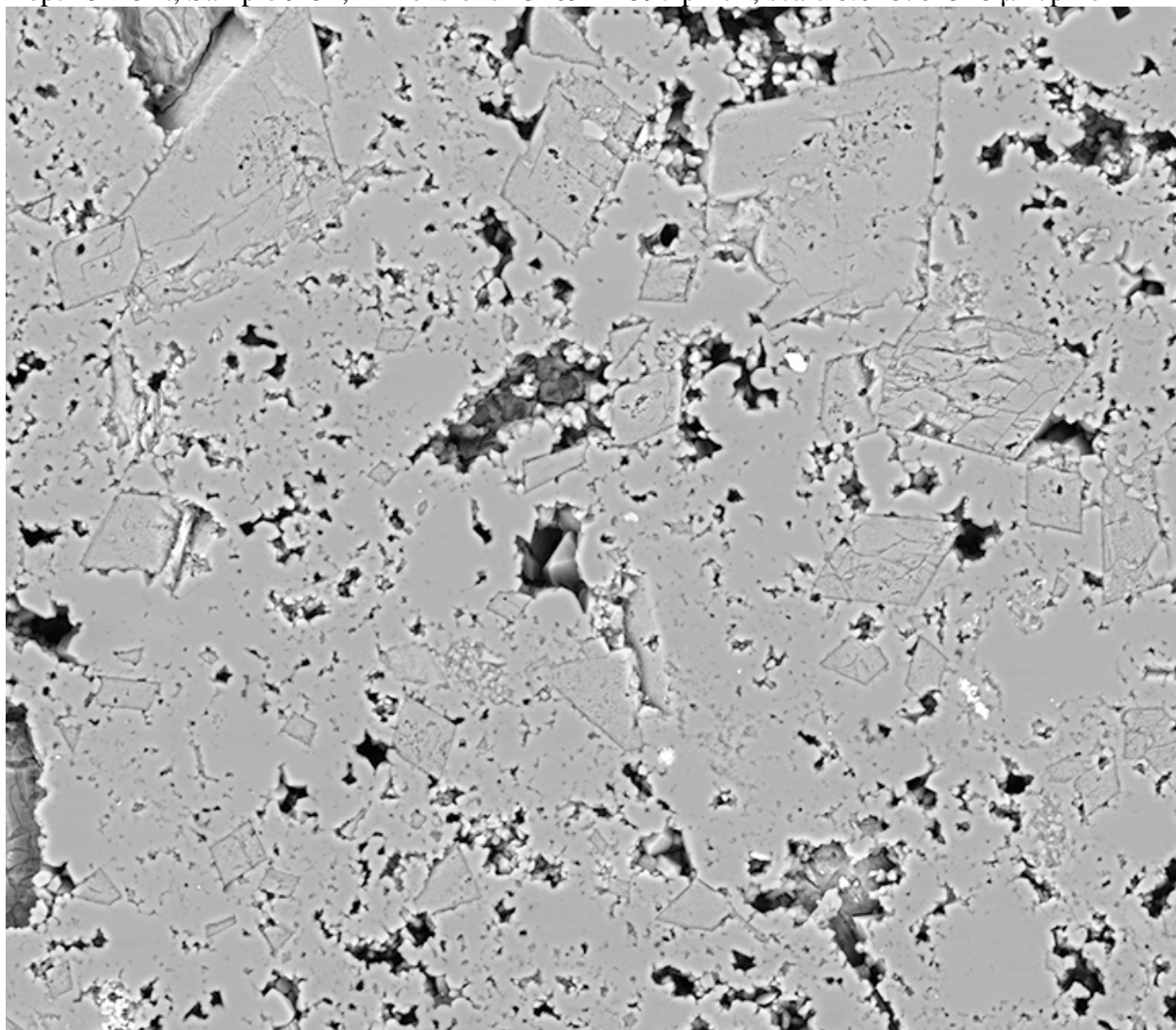
Depth 5105.2 ft, Sample 9-44, Dimensions 13047x11254 pixel², scale 0.018212891 μm/pixel



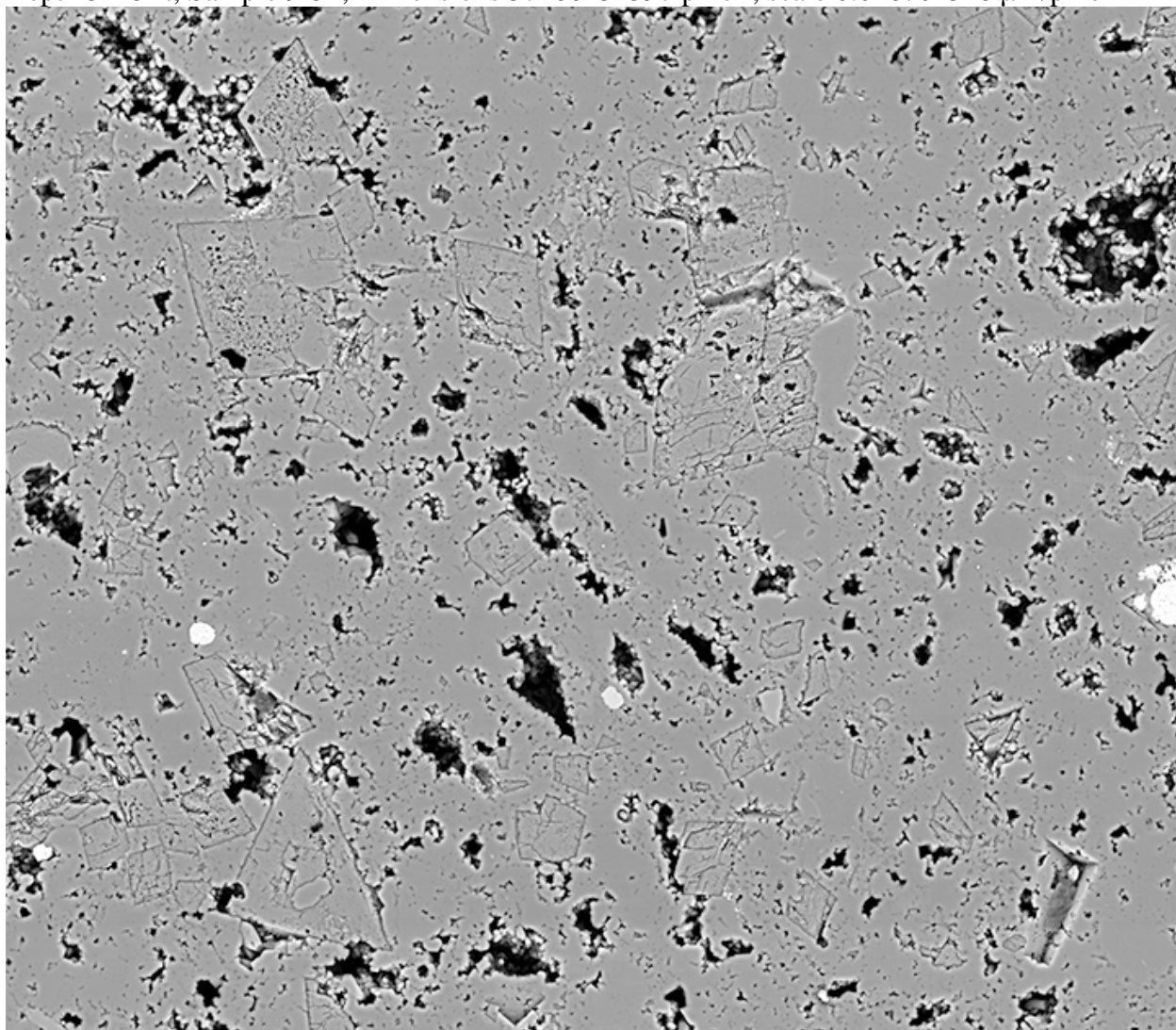
Depth 5115 ft, Sample 9-54, Dimensions 9293x8042 pixel², scale 0.016701318 μm/pixel



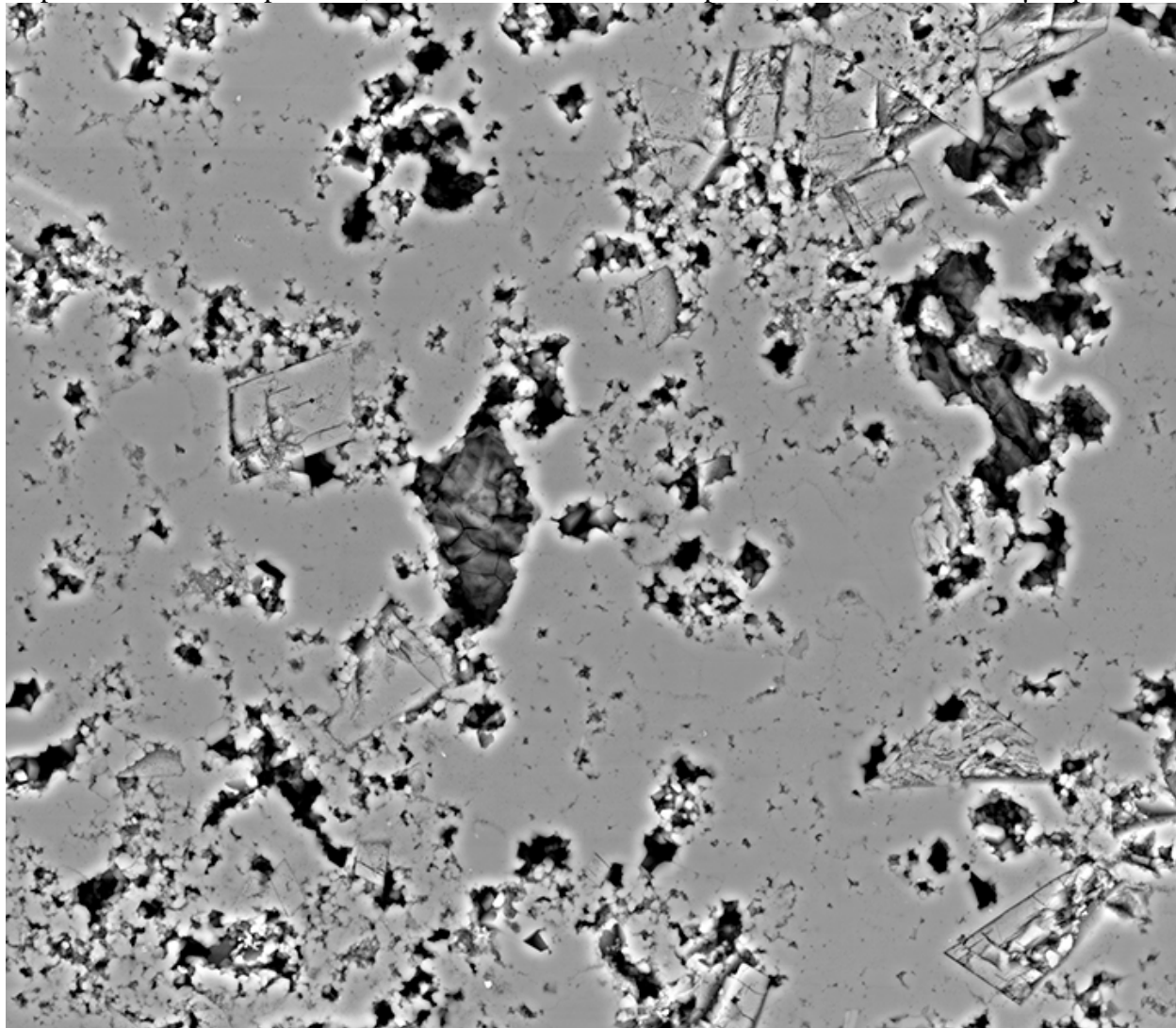
Depth 5115 ft, Sample 9-54, Dimensions 13109x11397 pixel², scale 0.016701318 μm/pixel



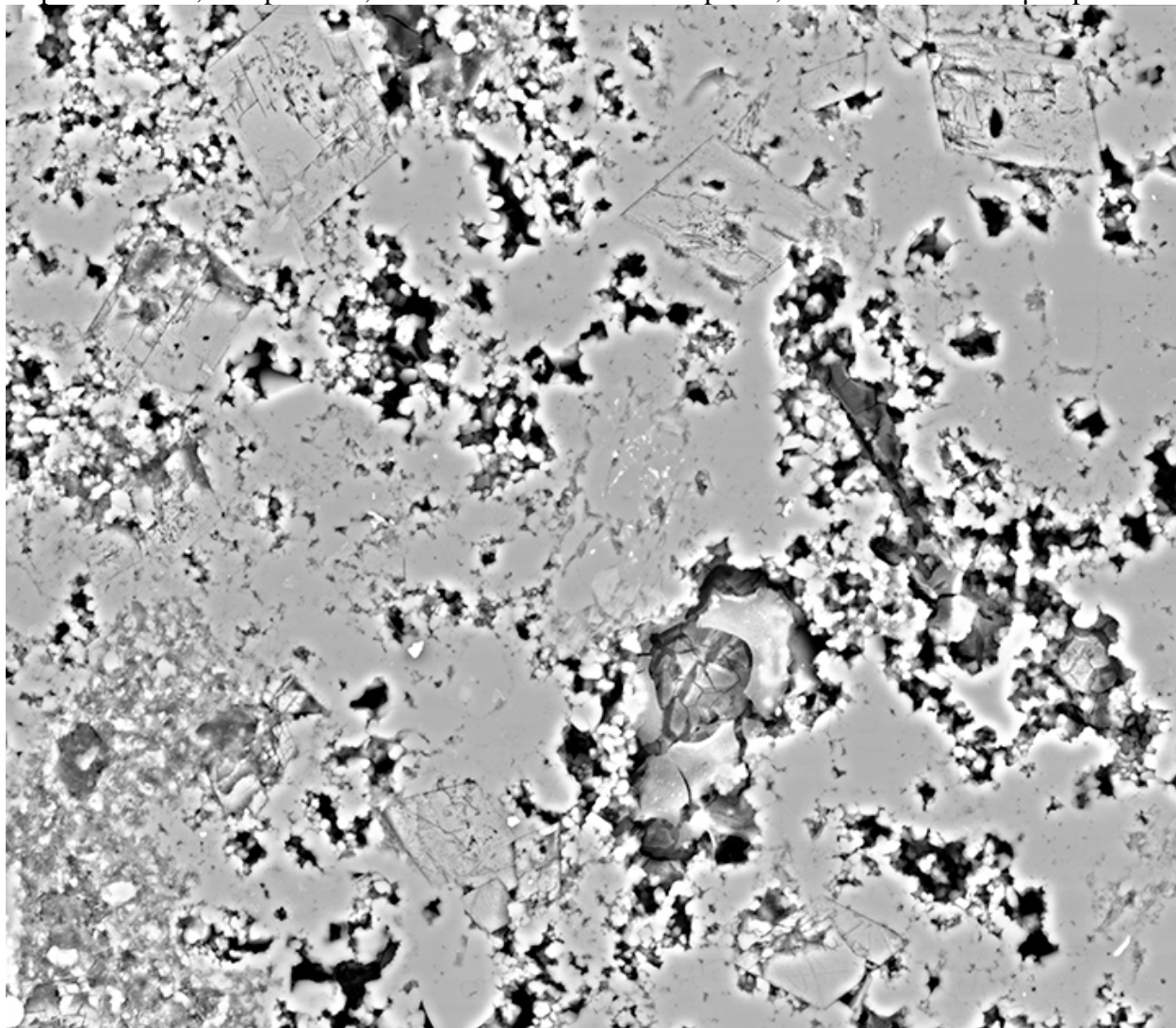
Depth 5115 ft, Sample 9-54, Dimensions 37288x32397 pixel², scale 0.016701318 μm/pixel



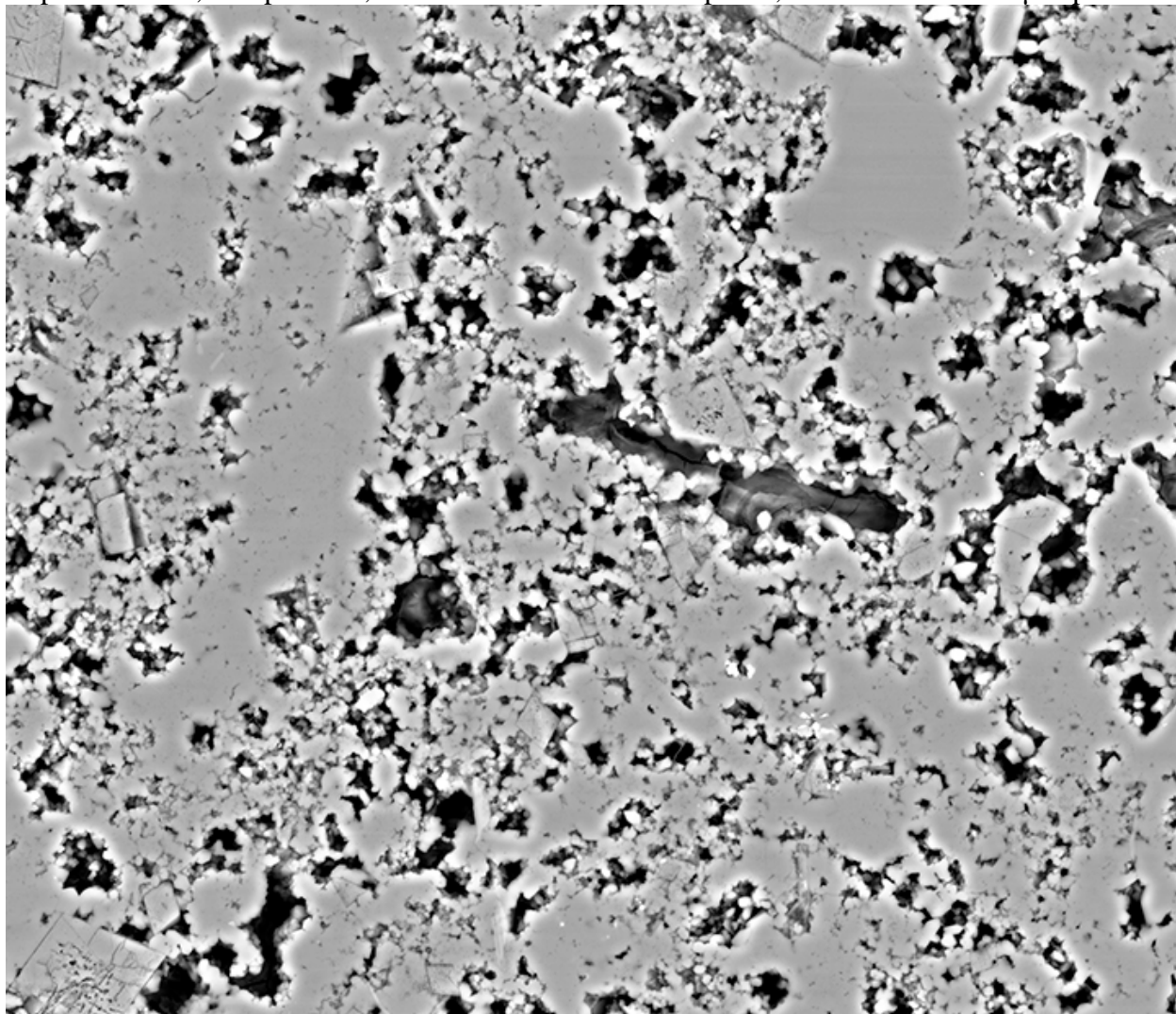
Depth 5125.2 ft, Sample 10-3, Dimensions 12731x11101 pixel², scale 0.014044043 μm/pixel



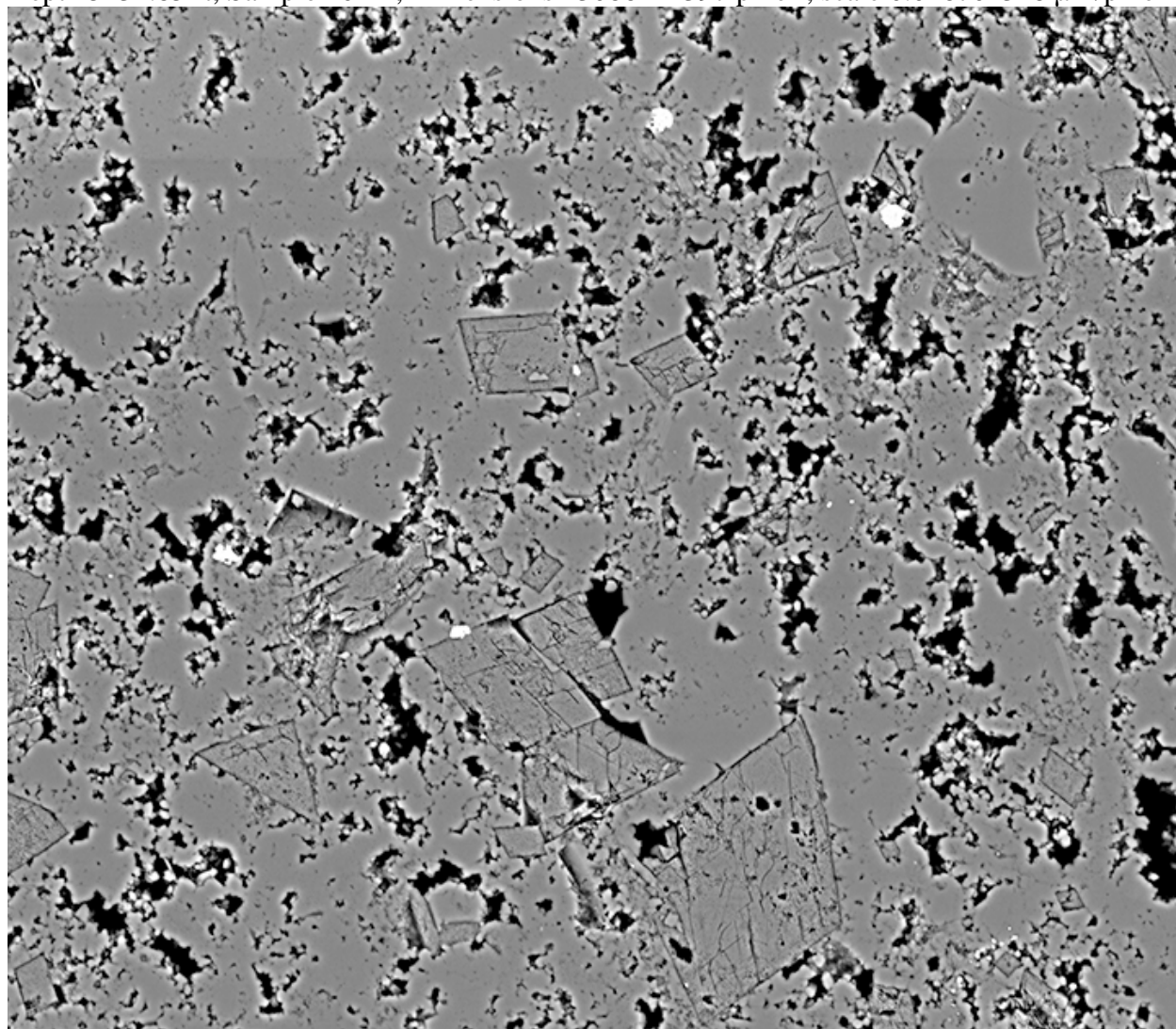
Depth 5125.2 ft, Sample 10-3, Dimensions 12972x11259 pixel², scale 0.014044043 μm/pixel



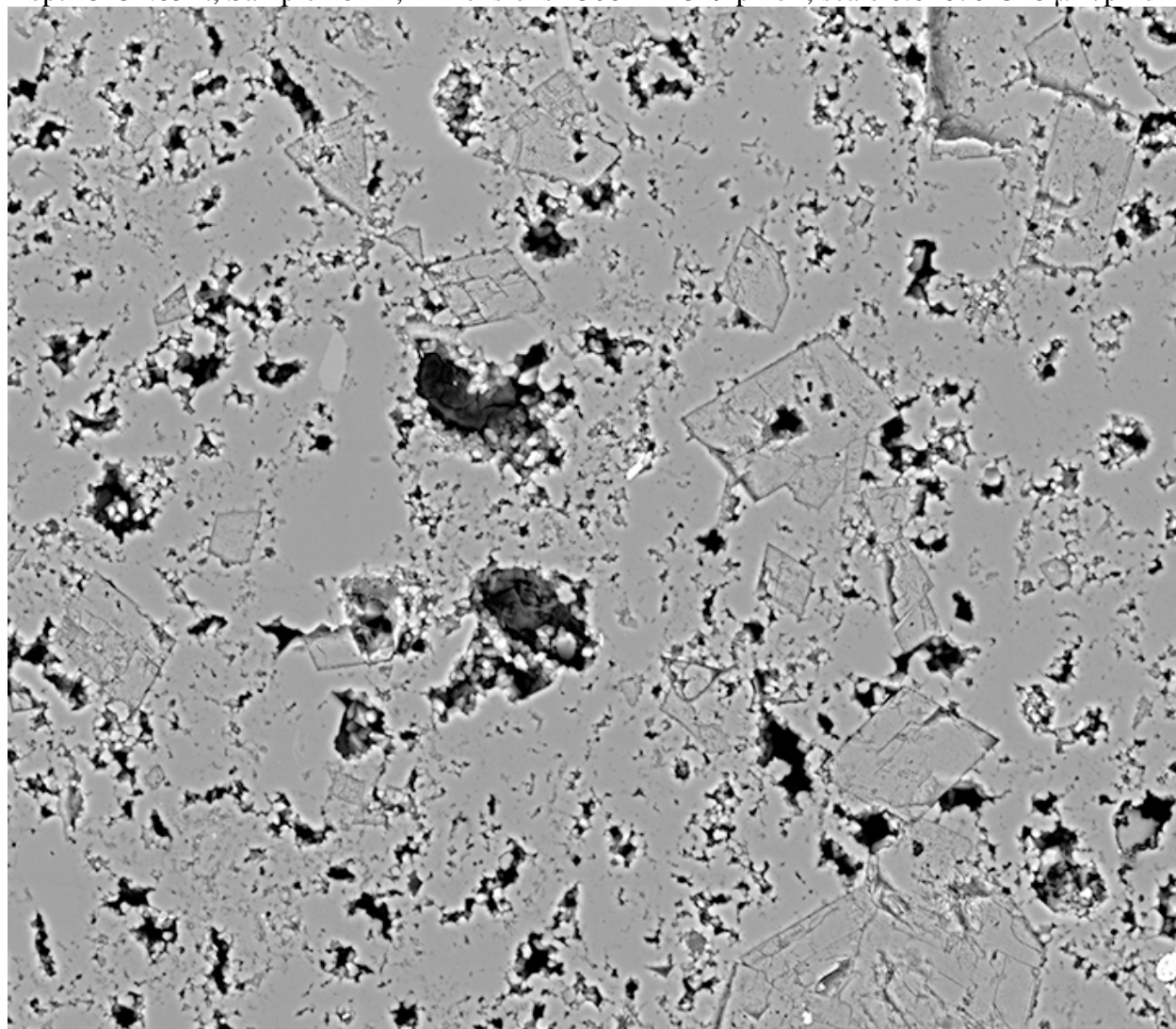
Depth 5125.2 ft, Sample 10-3, Dimensions 13007x11189 pixel², scale 0.014044043 μm/pixel



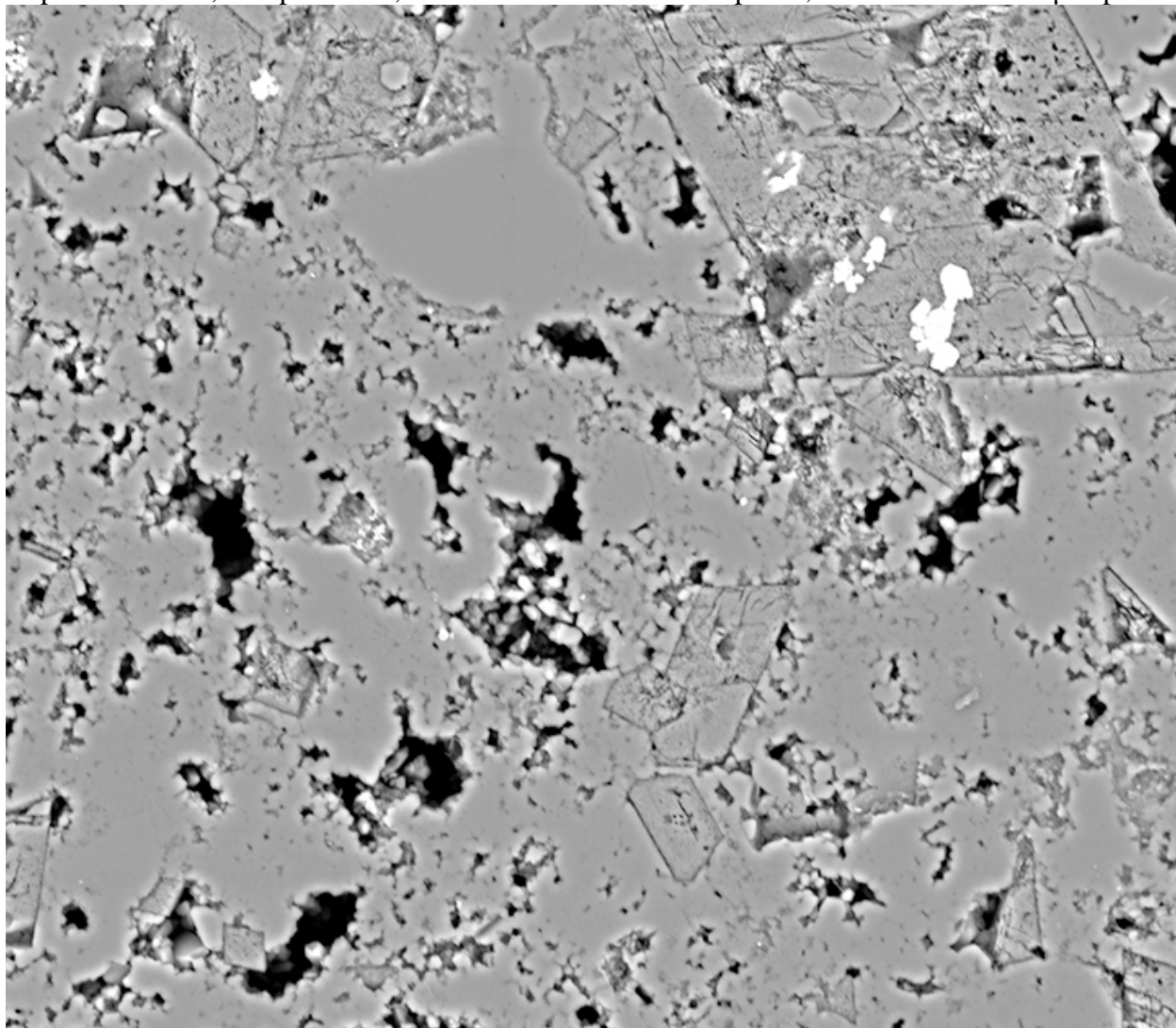
Depth 5134.85 ft, Sample 10-12, Dimensions 13086x11397 pixel², scale 0.016701318 $\mu\text{m}/\text{pixel}$



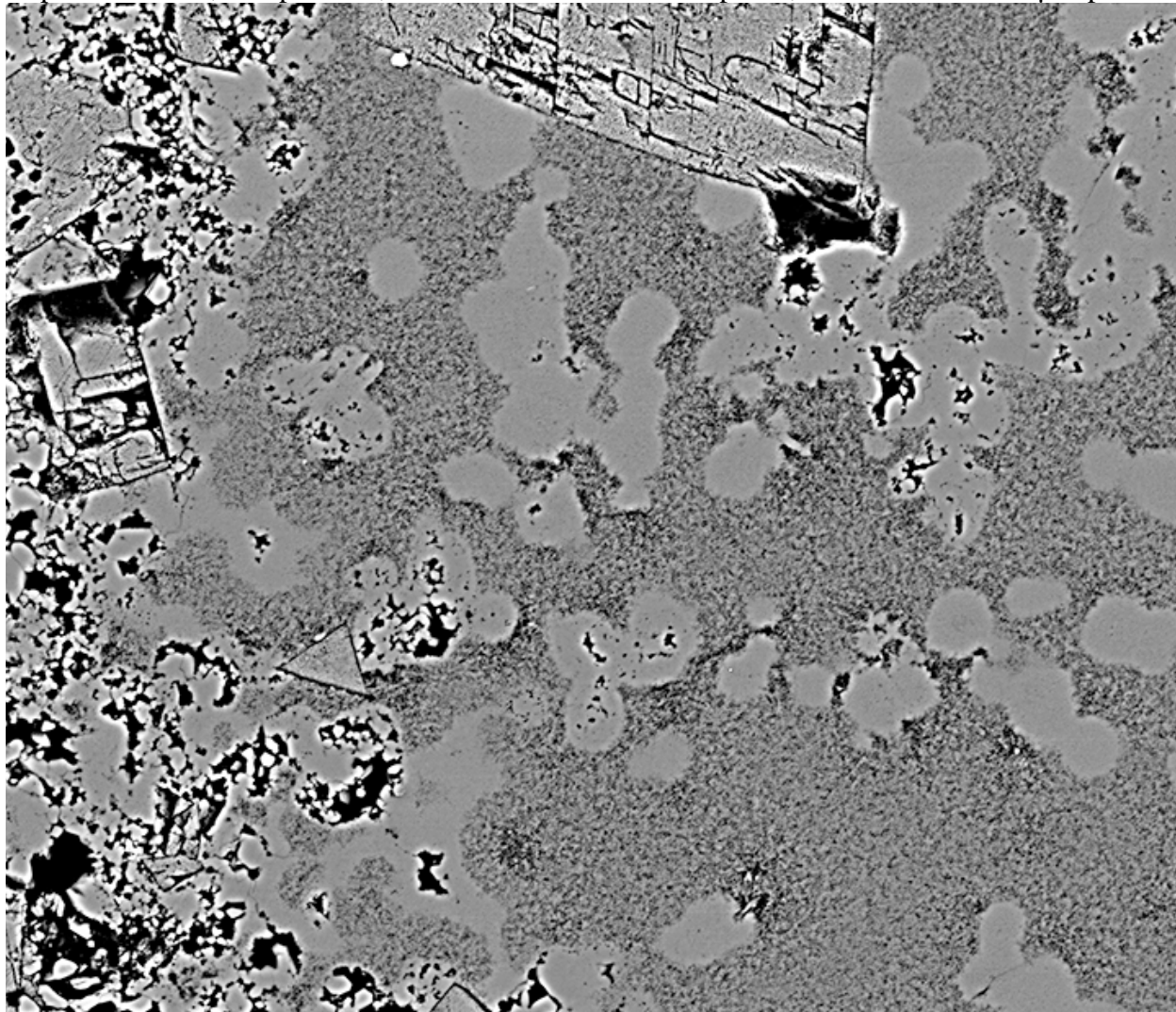
Depth 5134.85 ft, Sample 10-12, Dimensions 13082x11349 pixel², scale 0.016701318 μm/pixel



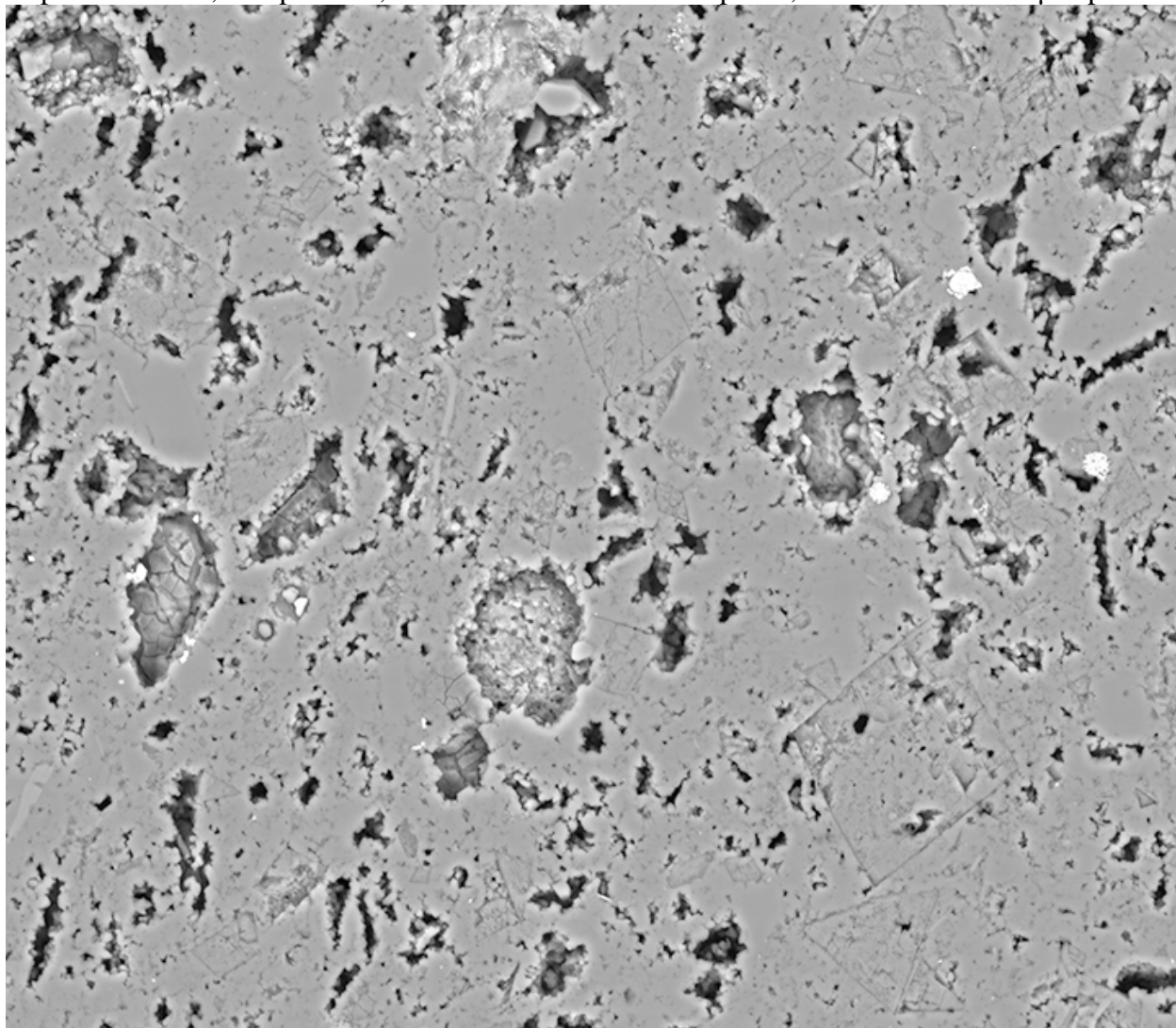
Depth 5134.85 ft, Sample 10-12, Dimensions 13012x11297 pixel², scale 0.010829443 μm/pixel



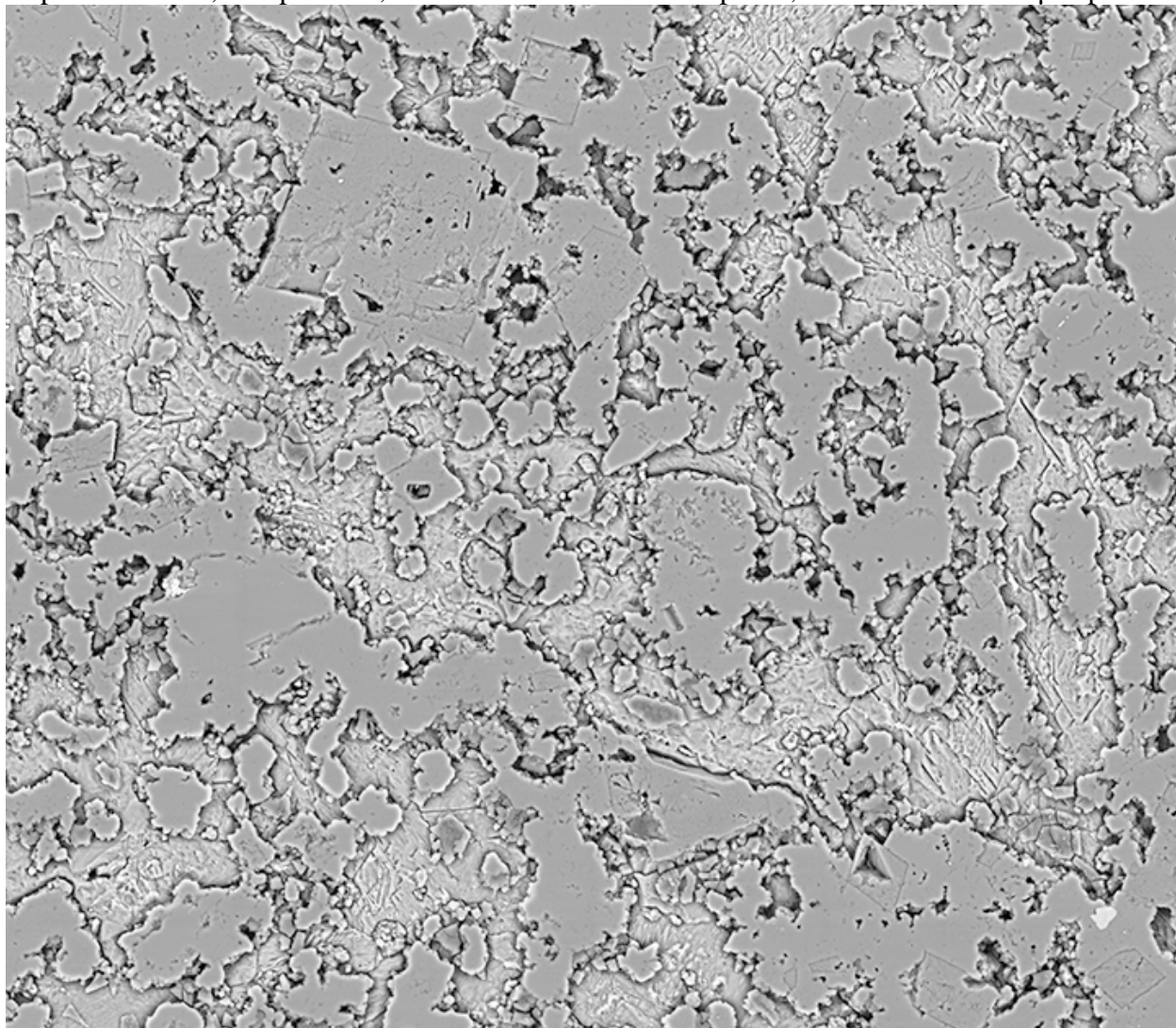
Depth 5155.15 ft, Sample 11-1, Dimensions 13103x11344 pixel², scale 0.016701318 μm/pixel



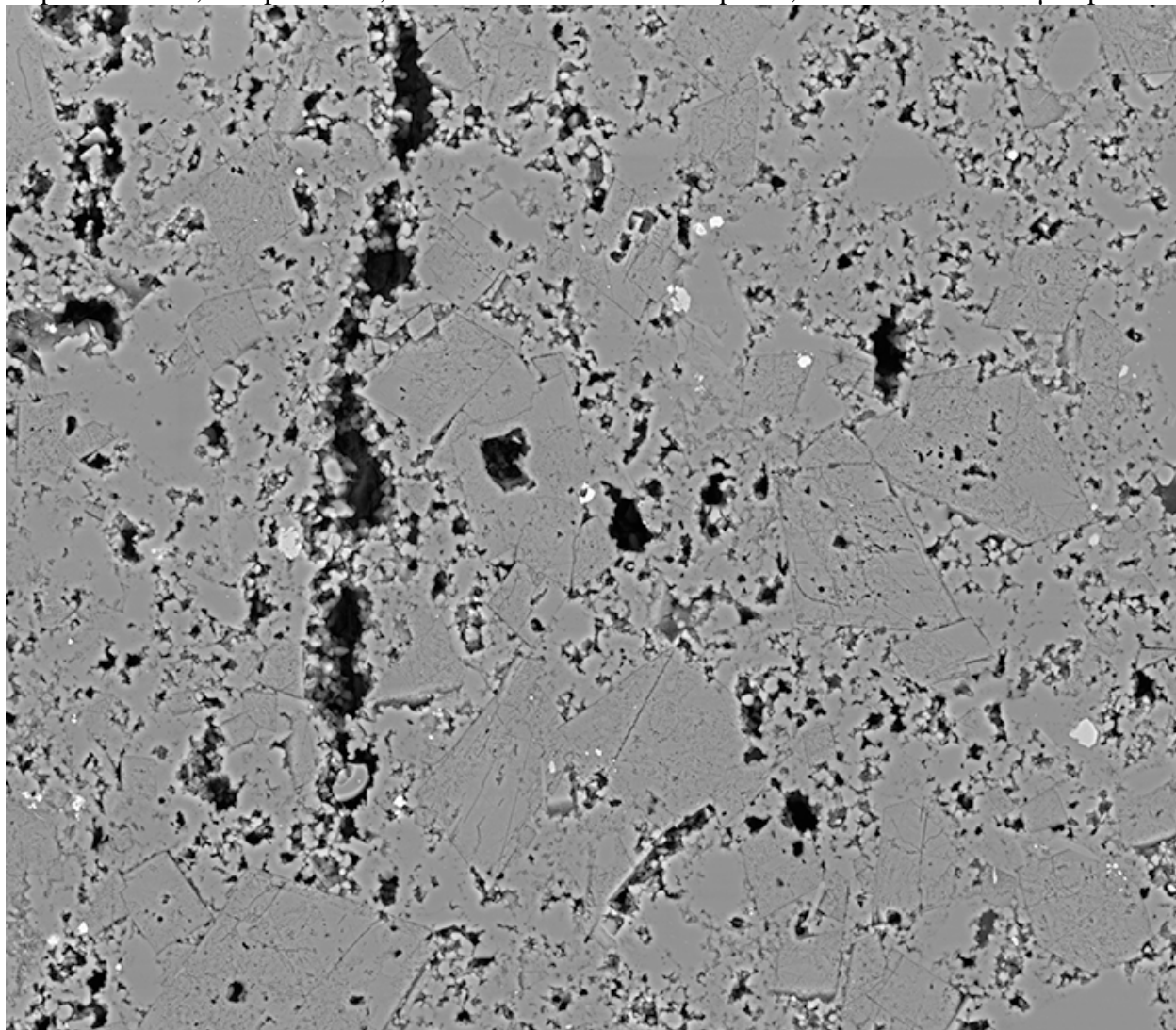
Depth 5155.15 ft, Sample 11-1, Dimensions 13011x11364 pixel², scale 0.019861279 μm/pixel



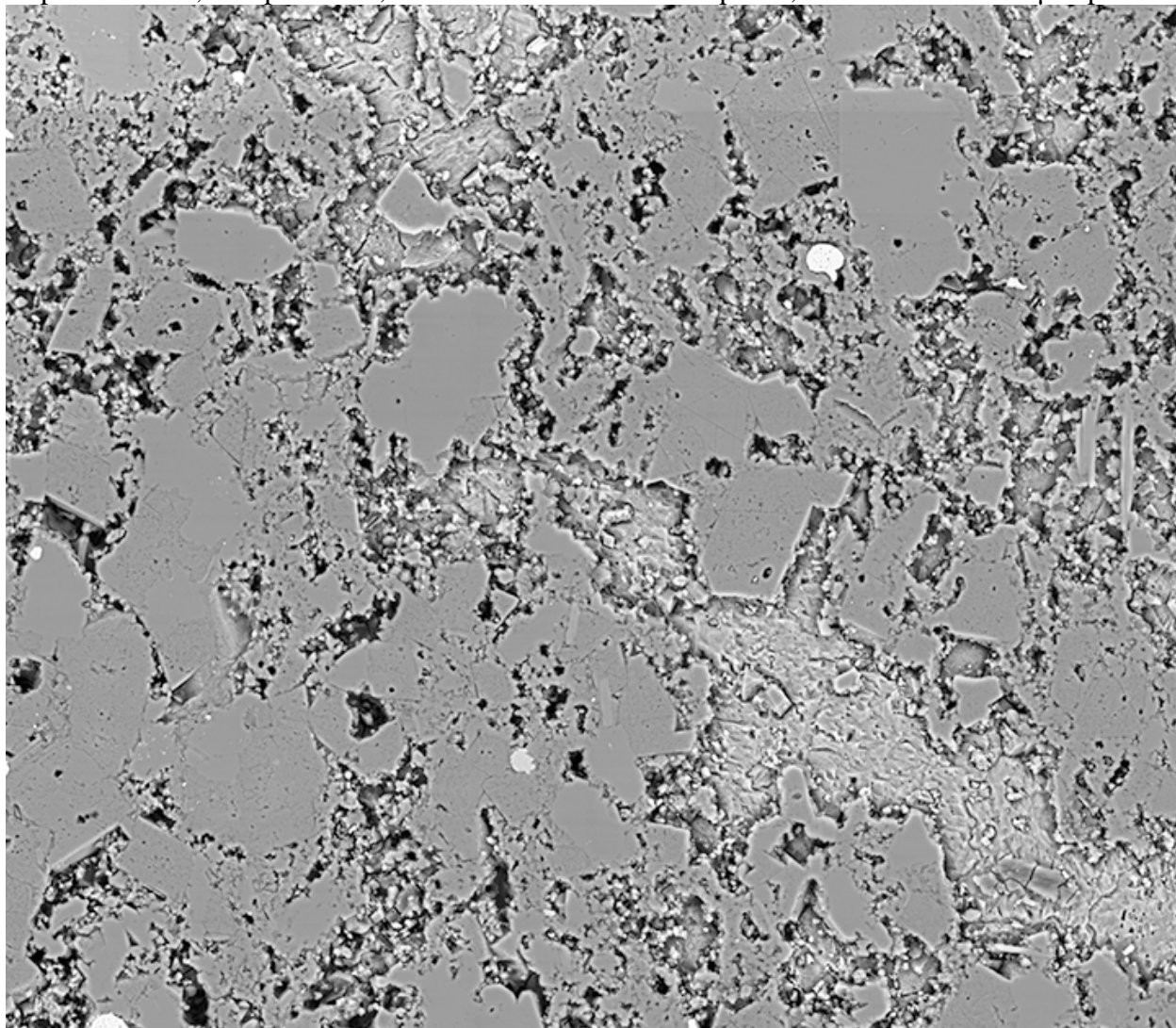
Depth 5155.15 ft, Sample 11-1, Dimensions 18641x16165 pixel², scale 0.018212891 μm/pixel



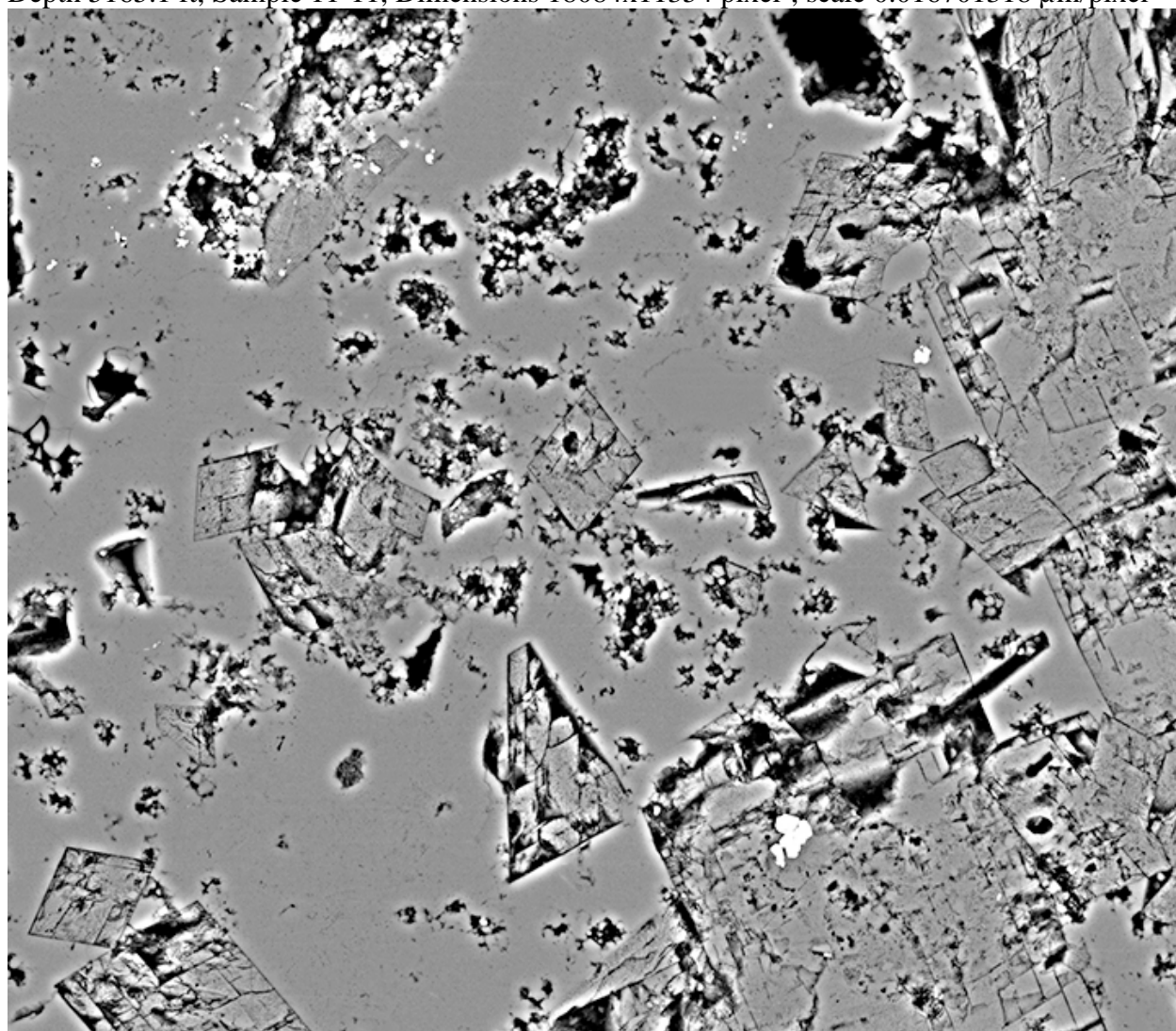
Depth 5165.1 ft, Sample 11-11, Dimensions 13087x11380 pixel², scale 0.016701318 μm/pixel



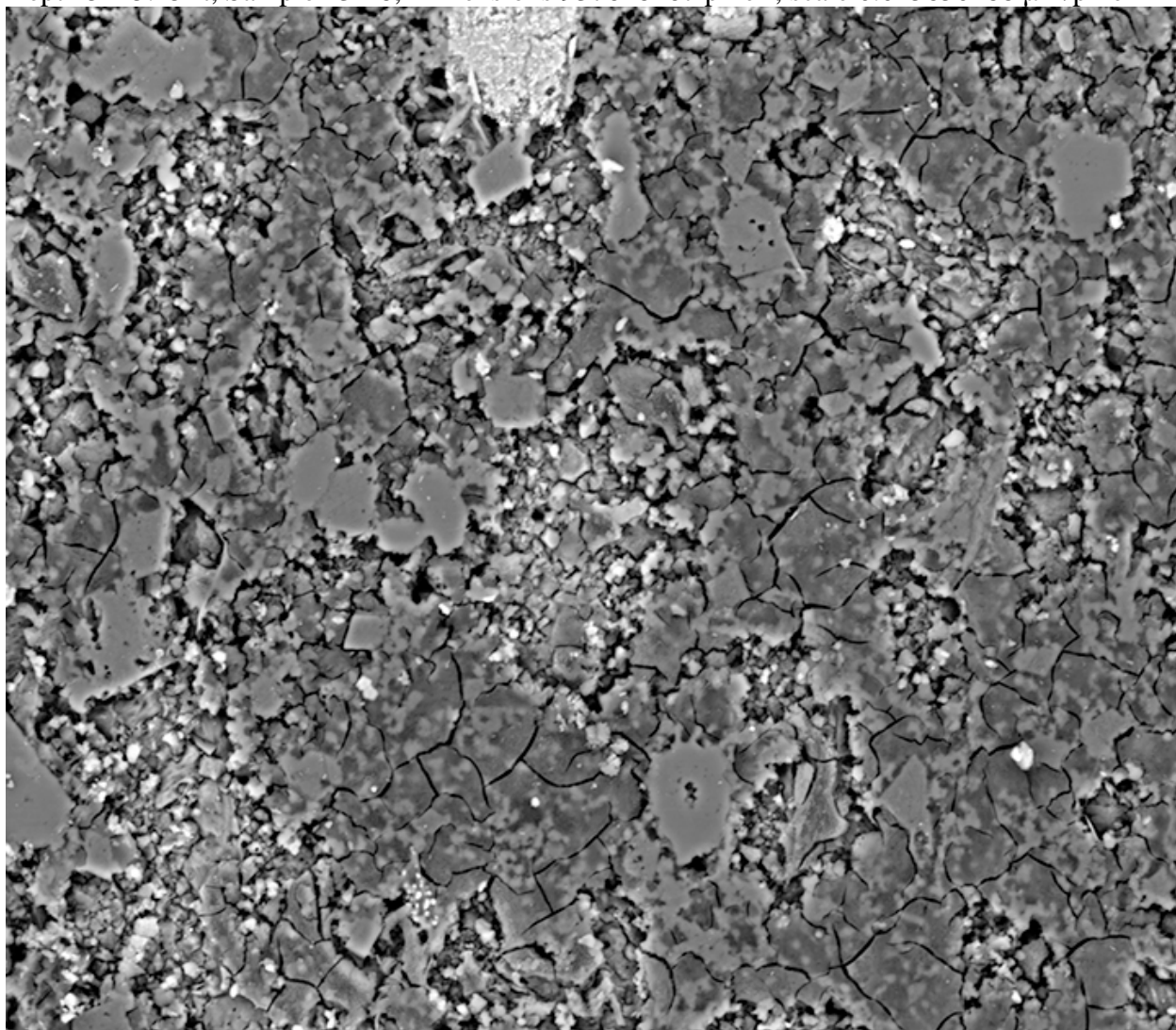
Depth 5165.1 ft, Sample 11-11, Dimensions 18596x16123 pixel², scale 0.016701318 μm/pixel



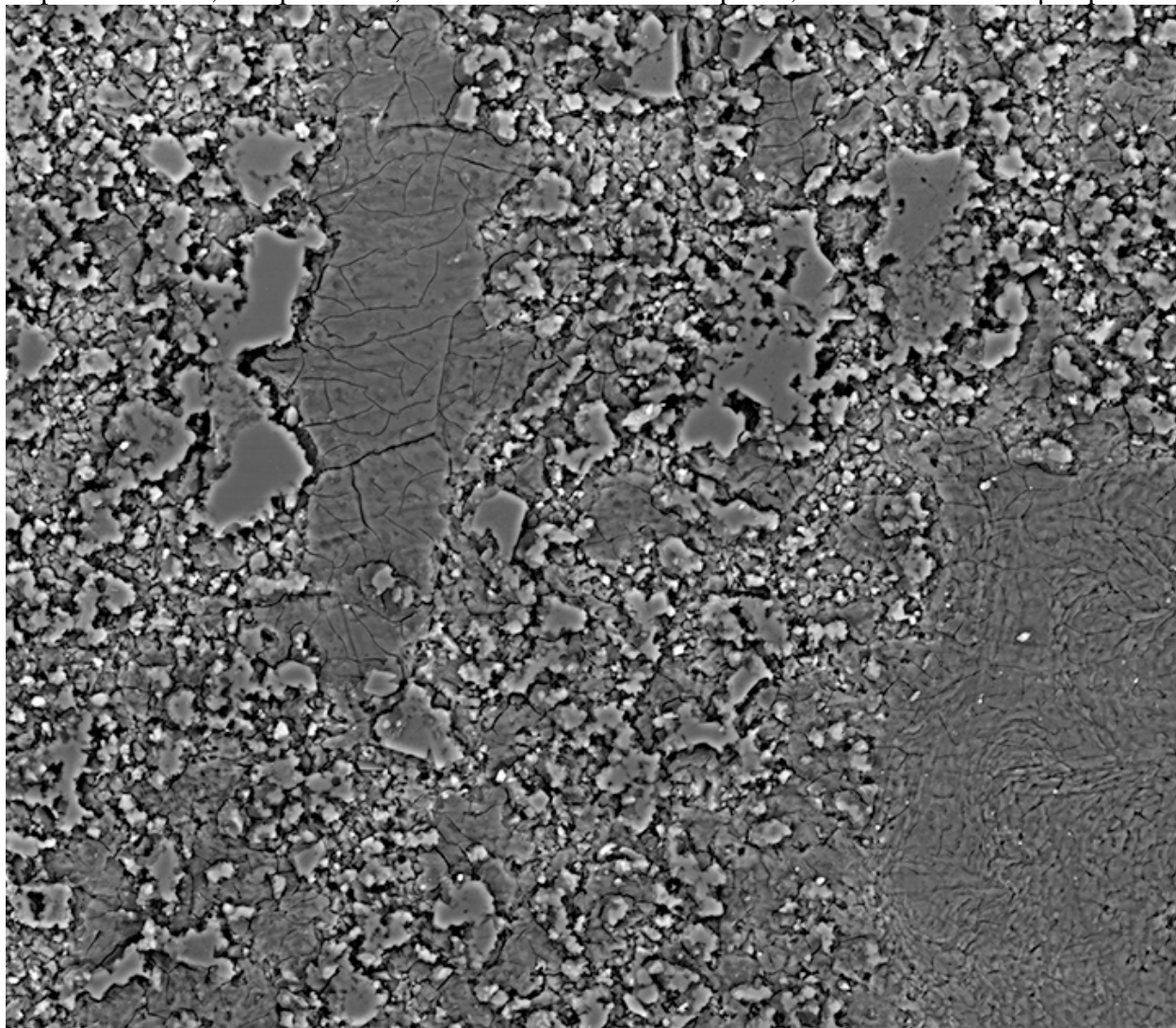
Depth 5165.1 ft, Sample 11-11, Dimensions 18084x11354 pixel², scale 0.016701318 μm/pixel



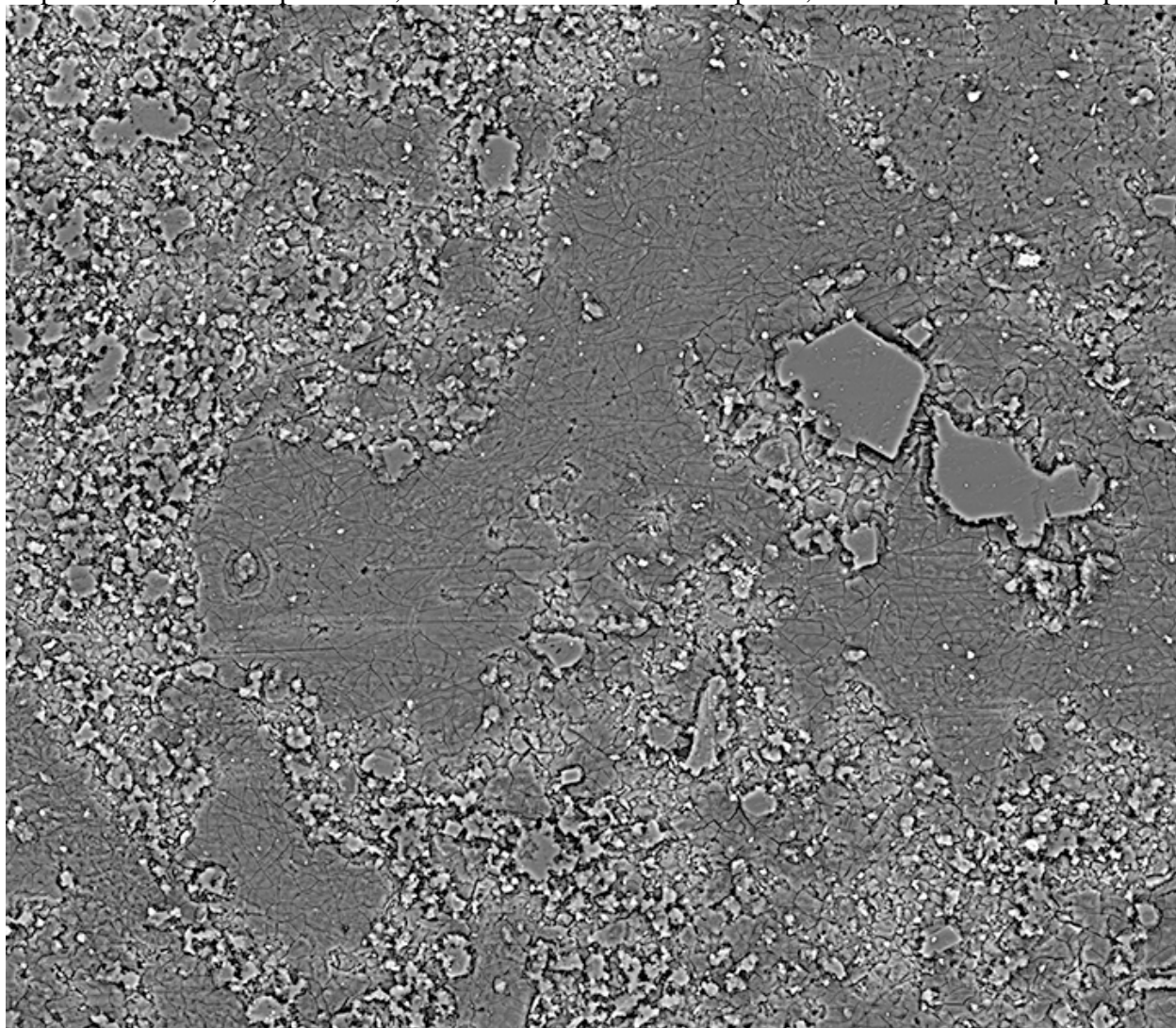
Depth 5215.15 ft, Sample 13-18, Dimensions 9376x8167 pixel², scale 0.015650488 μm/pixel



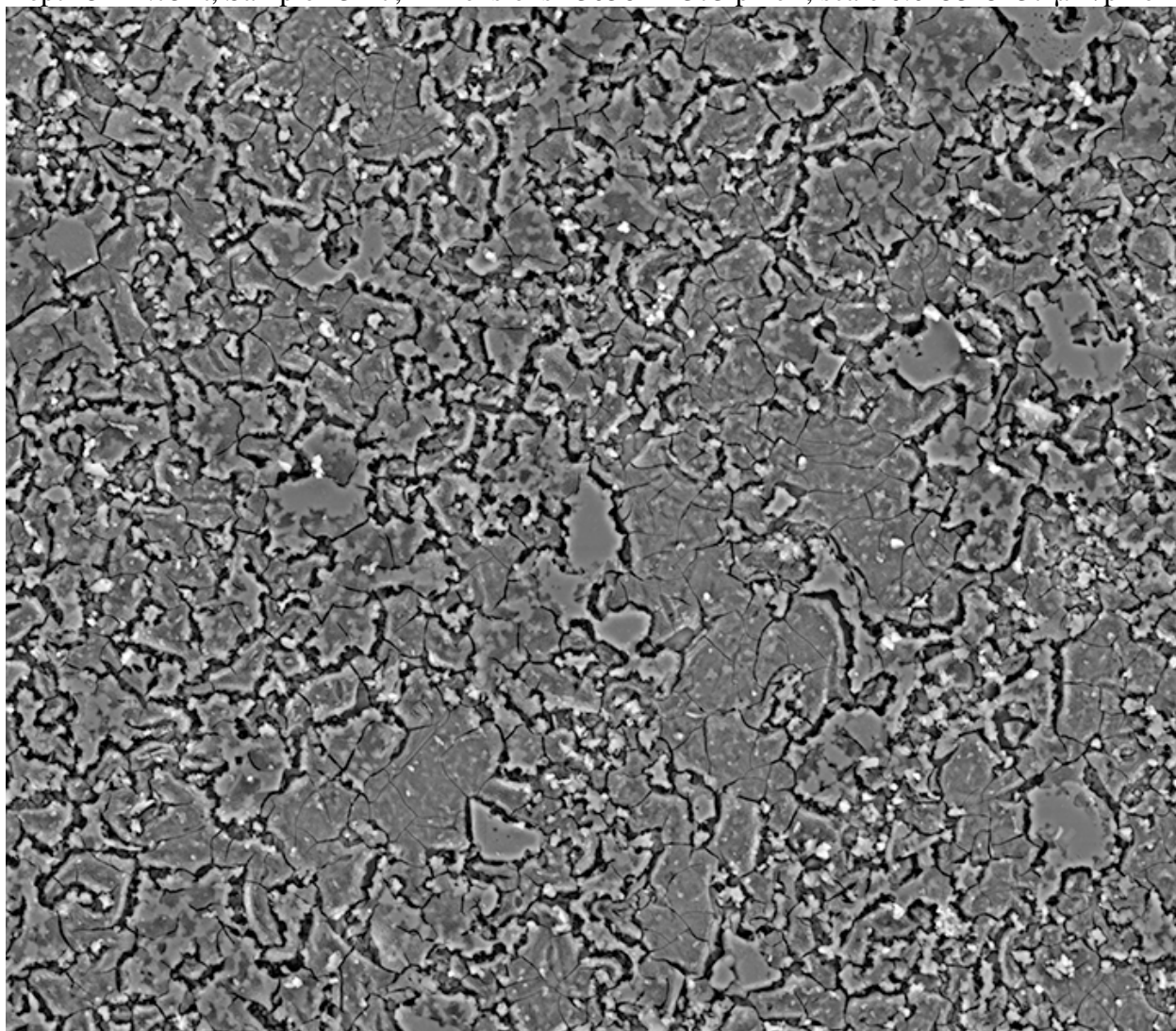
Depth 5215.15 ft, Sample 13-18, Dimensions 11244x9807 pixel², scale 0.015650488 μm/pixel



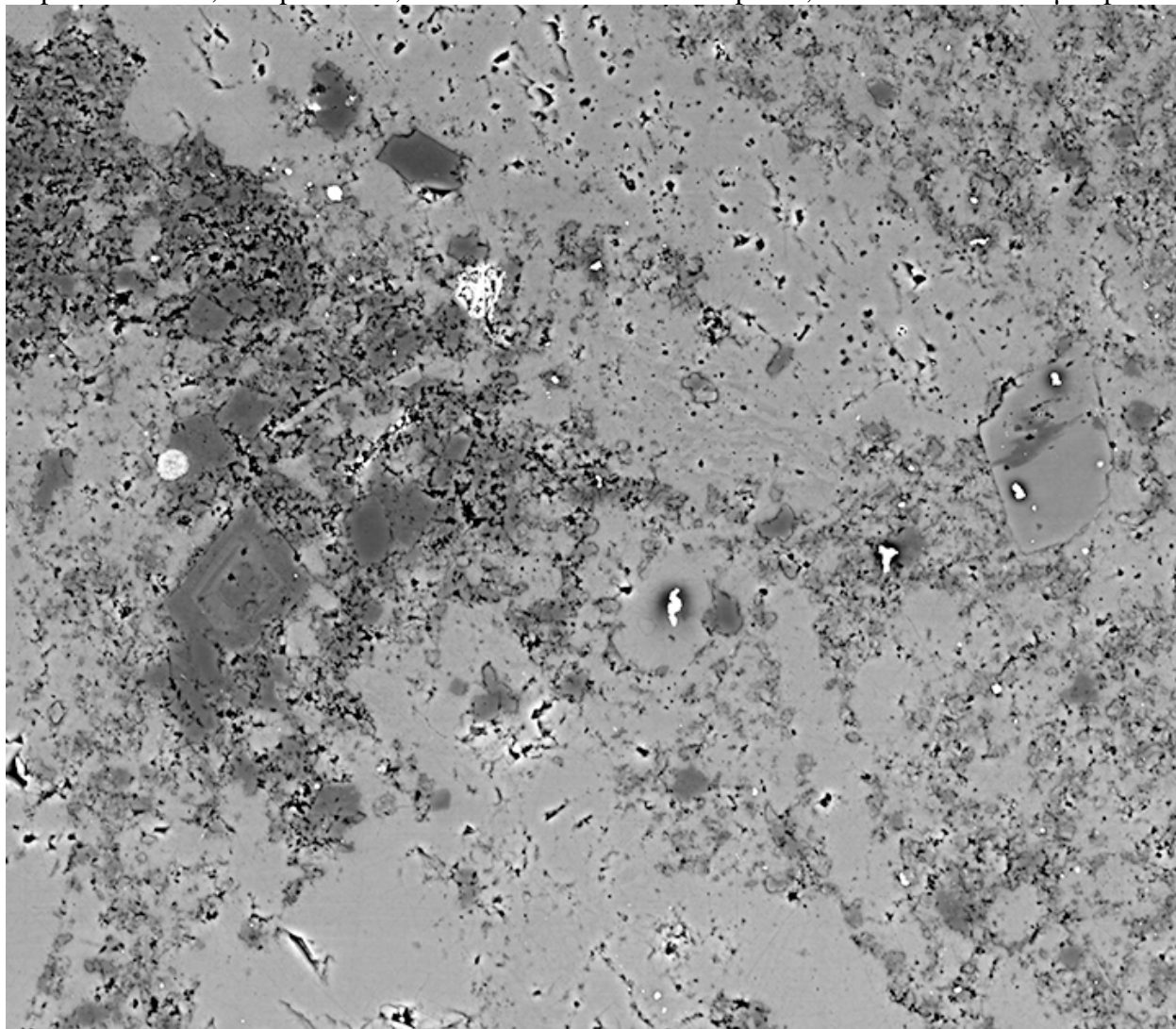
Depth 5215.15 ft, Sample 13-18, Dimensions 18530x16095 pixel², scale 0.015650488 μm/pixel



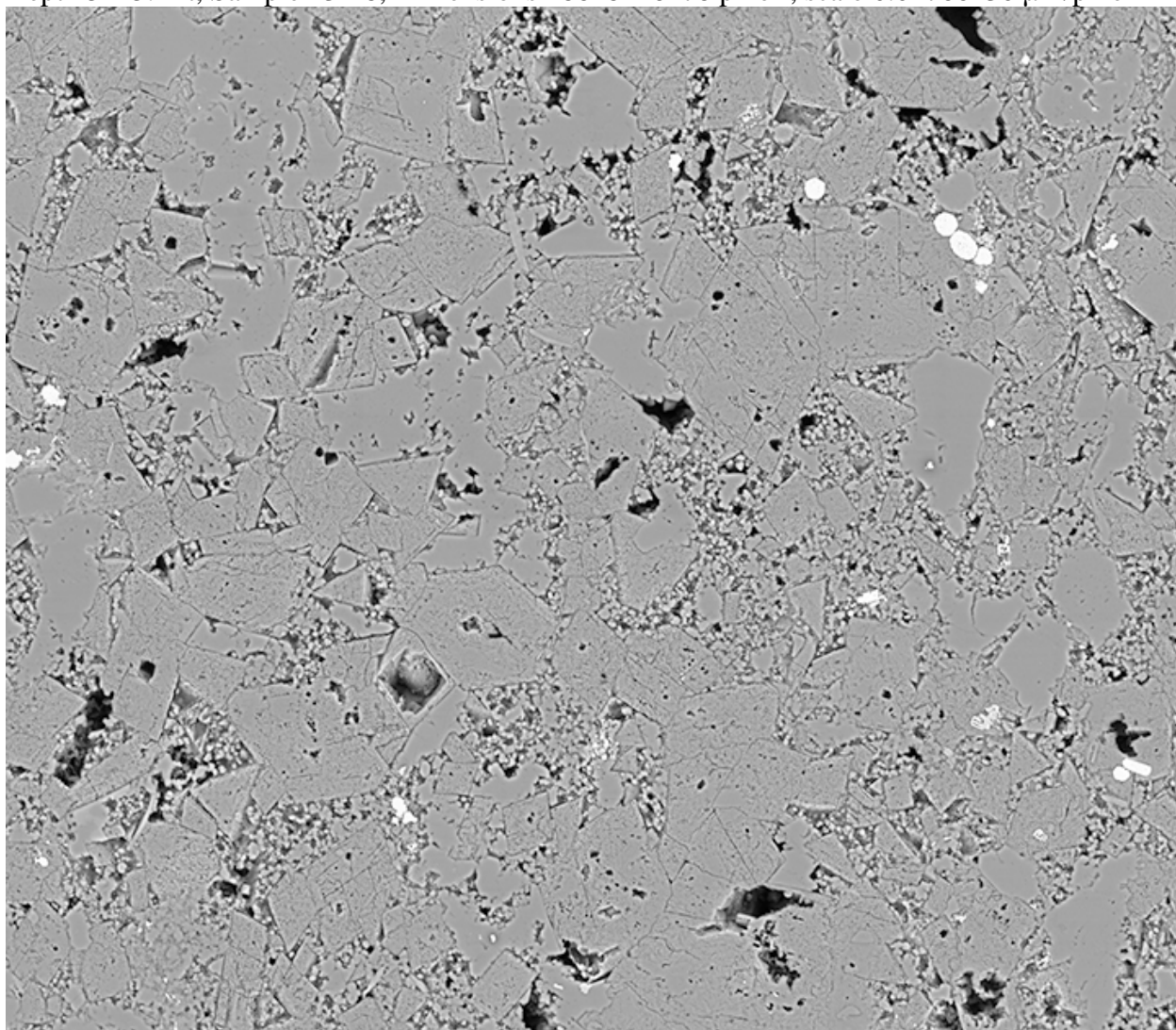
Depth 5224.75 ft, Sample 13-27, Dimensions 13056x11373 pixel², scale 0.015315137 μm/pixel



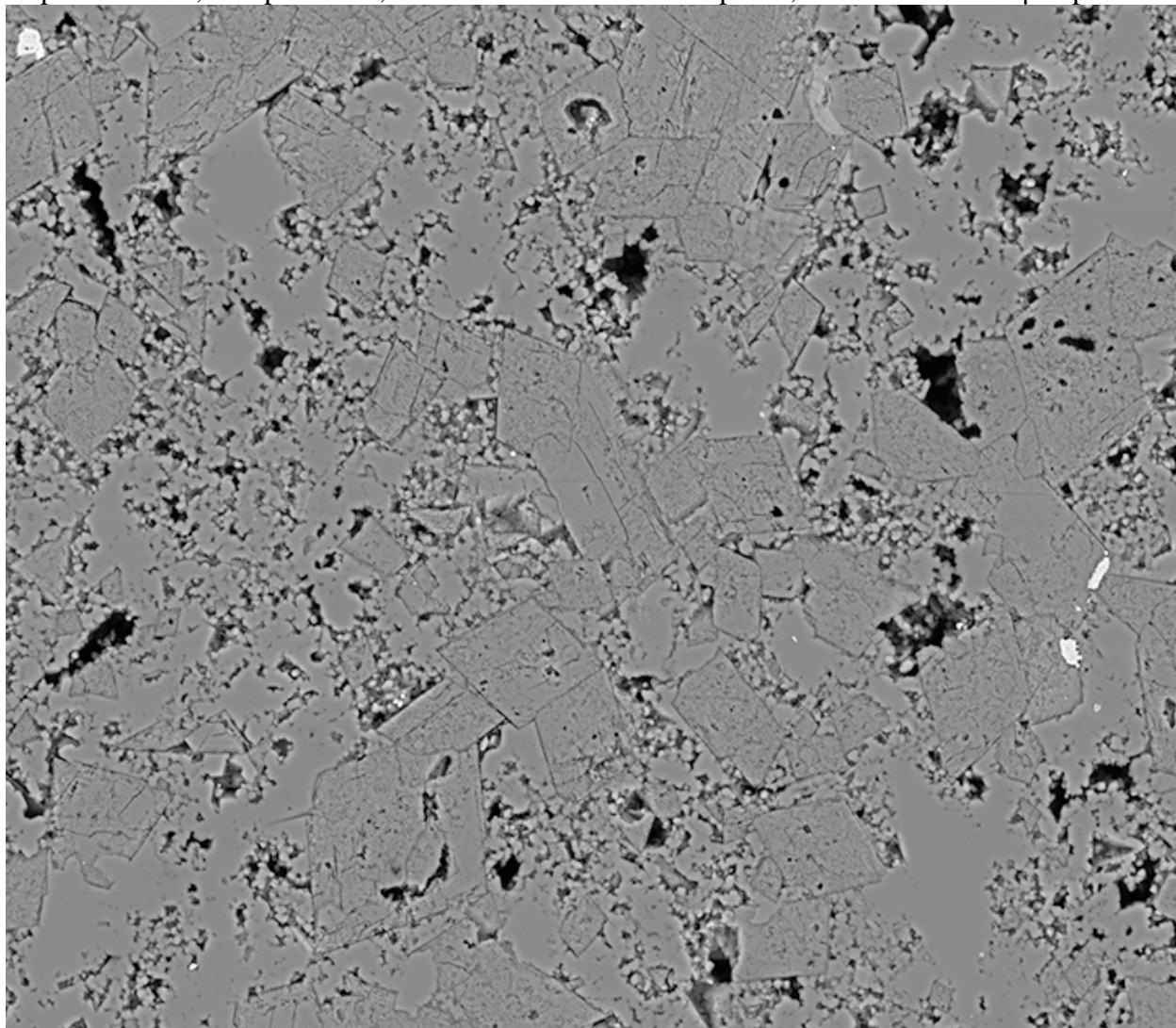
Depth 5224.75 ft, Sample 13-27, Dimensions 37083x32216 pixel², scale 0.007825244 μm/pixel



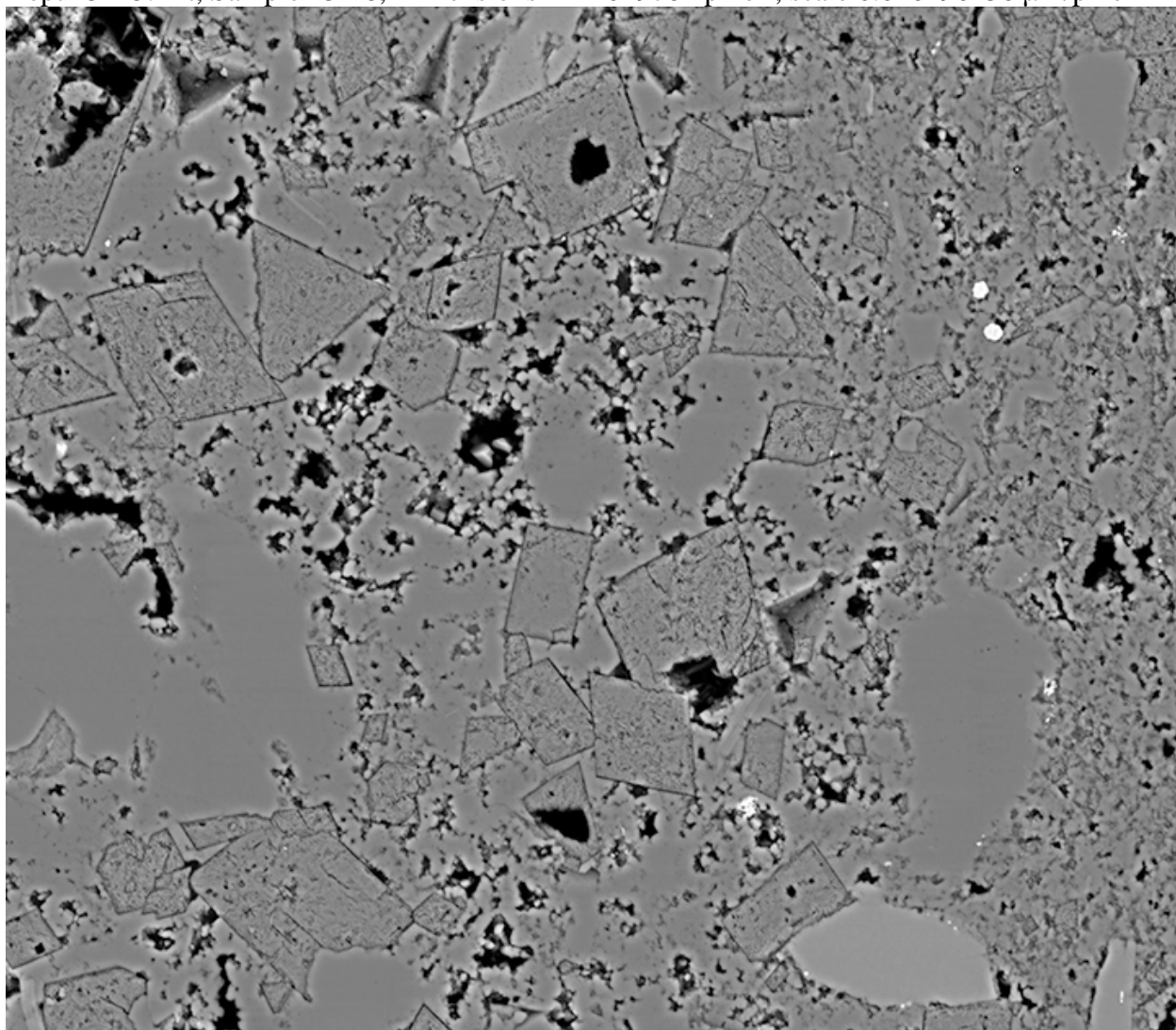
Depth 5245.2 ft, Sample 13-48, Dimensions 18648x16178 pixel², scale 0.01766230 μm/pixel



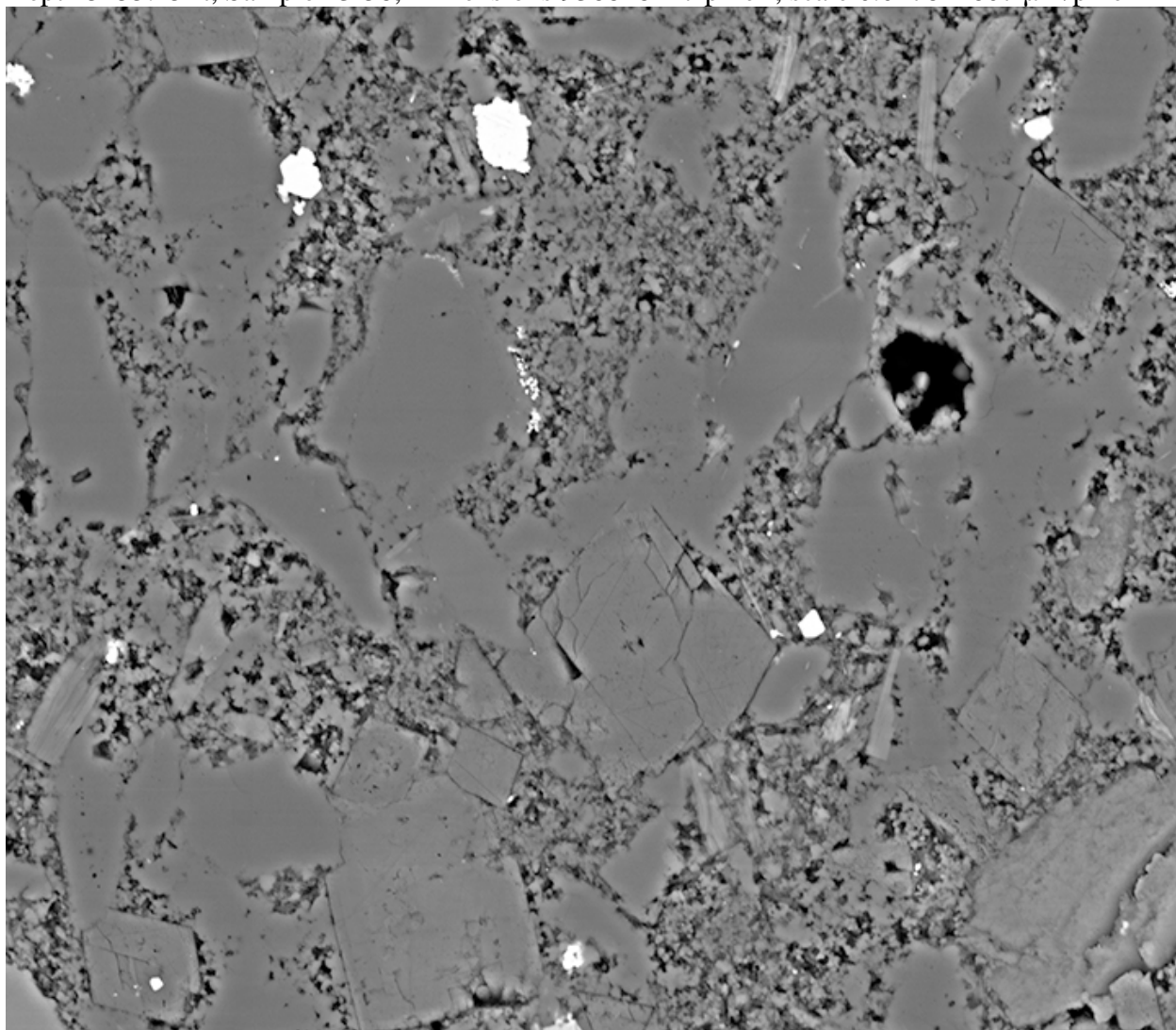
Depth 5245.2 ft, Sample 13-48, Dimensions 13038x11297 pixel², scale 0.01766230 μm/pixel



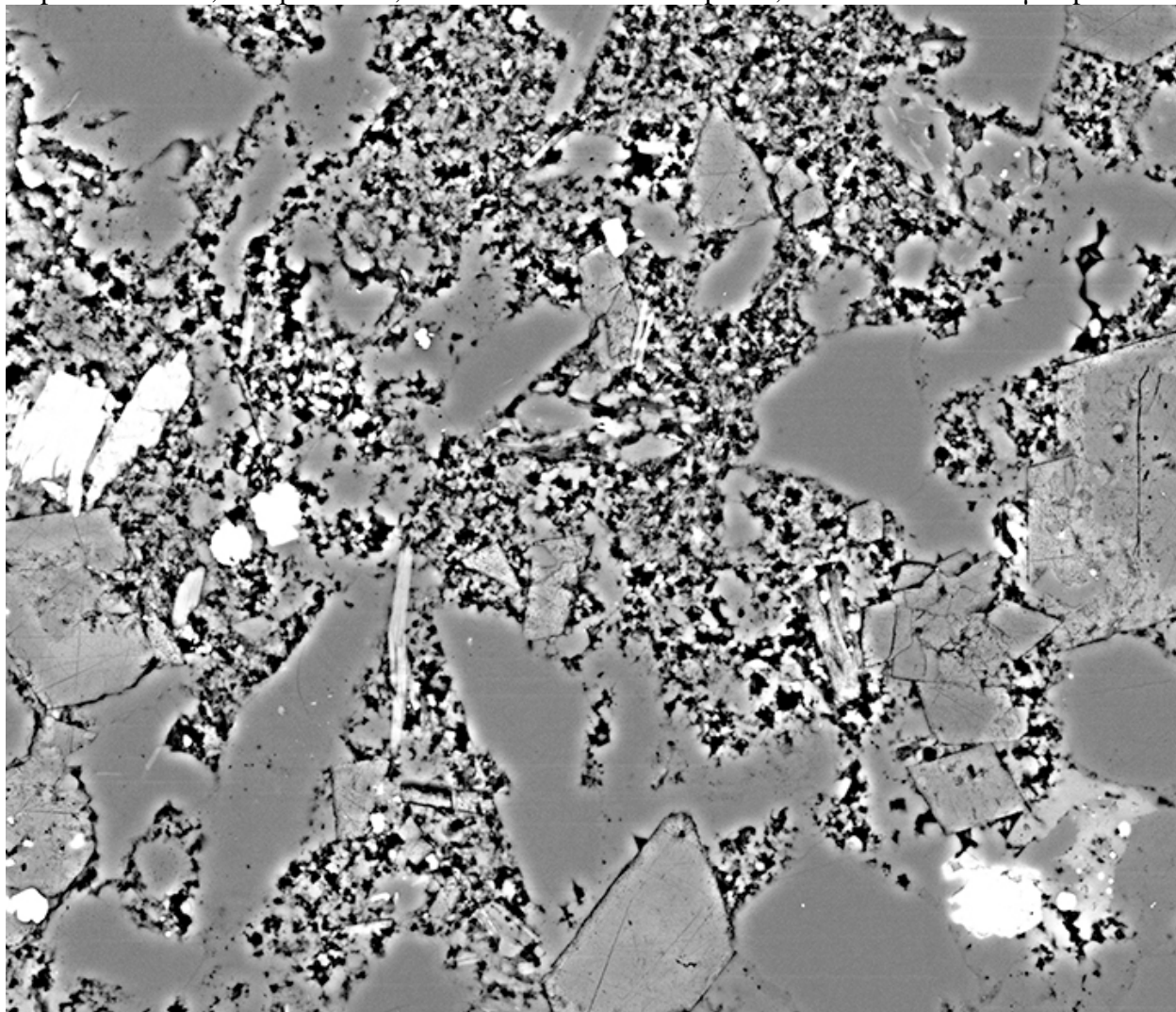
Depth 5245.2 ft, Sample 13-48, Dimensions 11210x9782 pixel², scale 0.016196436 μm/pixel



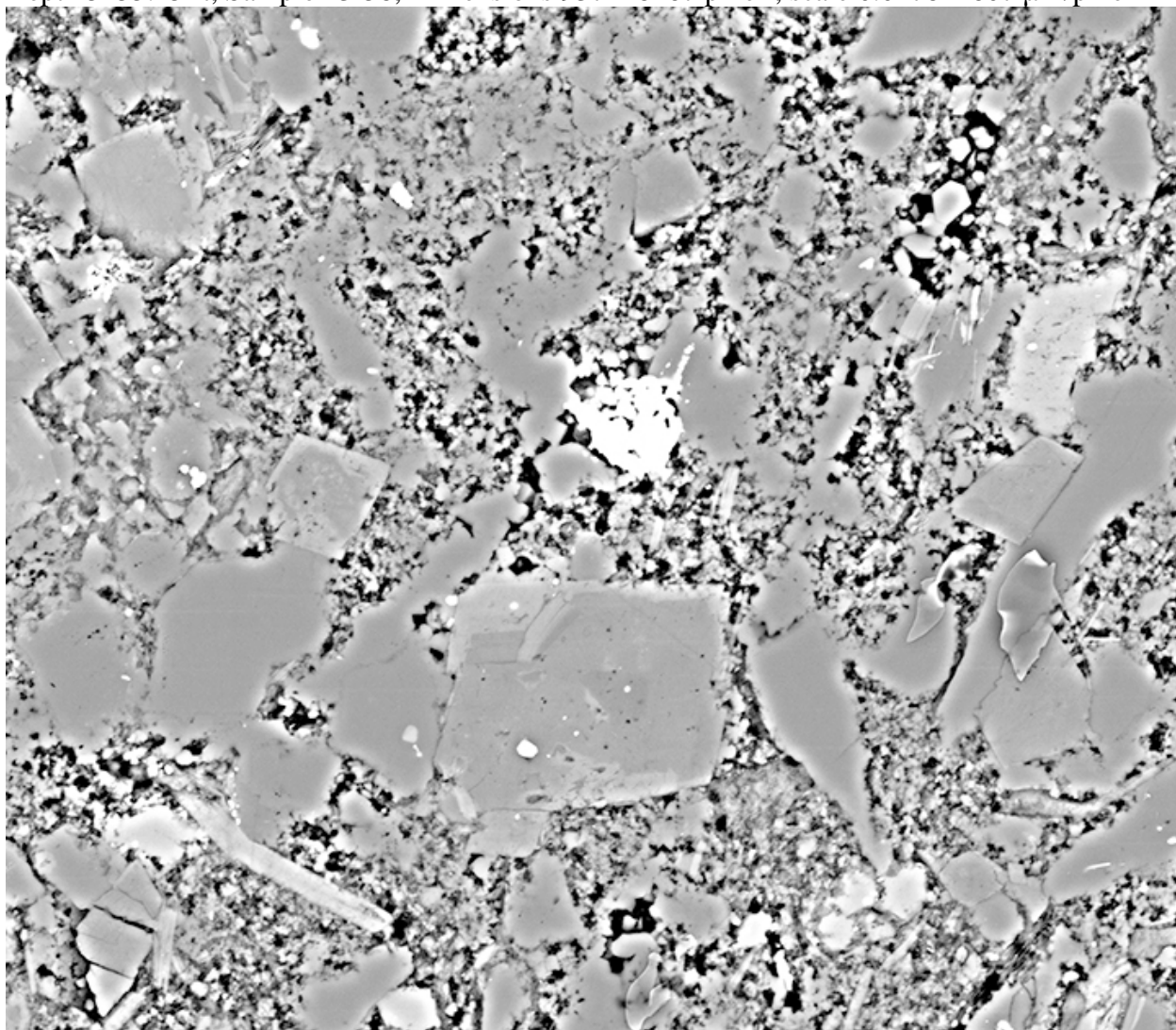
Depth 5255.15 ft, Sample 13-58, Dimensions 9368x8117 pixel², scale 0.017822607 μm/pixel



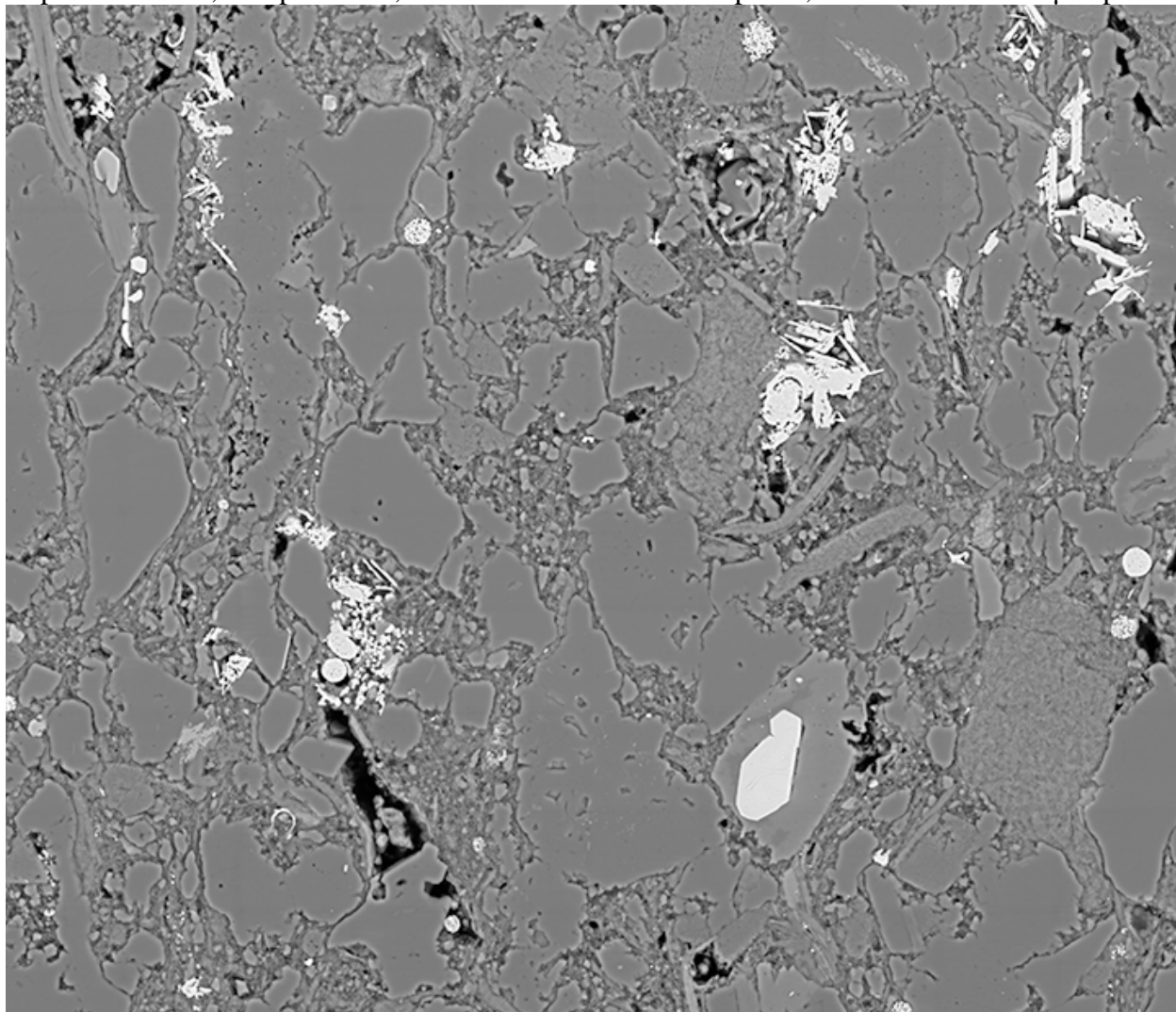
Depth 5255.15 ft, Sample 13-58, Dimensions 9363x8094 pixel², scale 0.017736006 μm/pixel



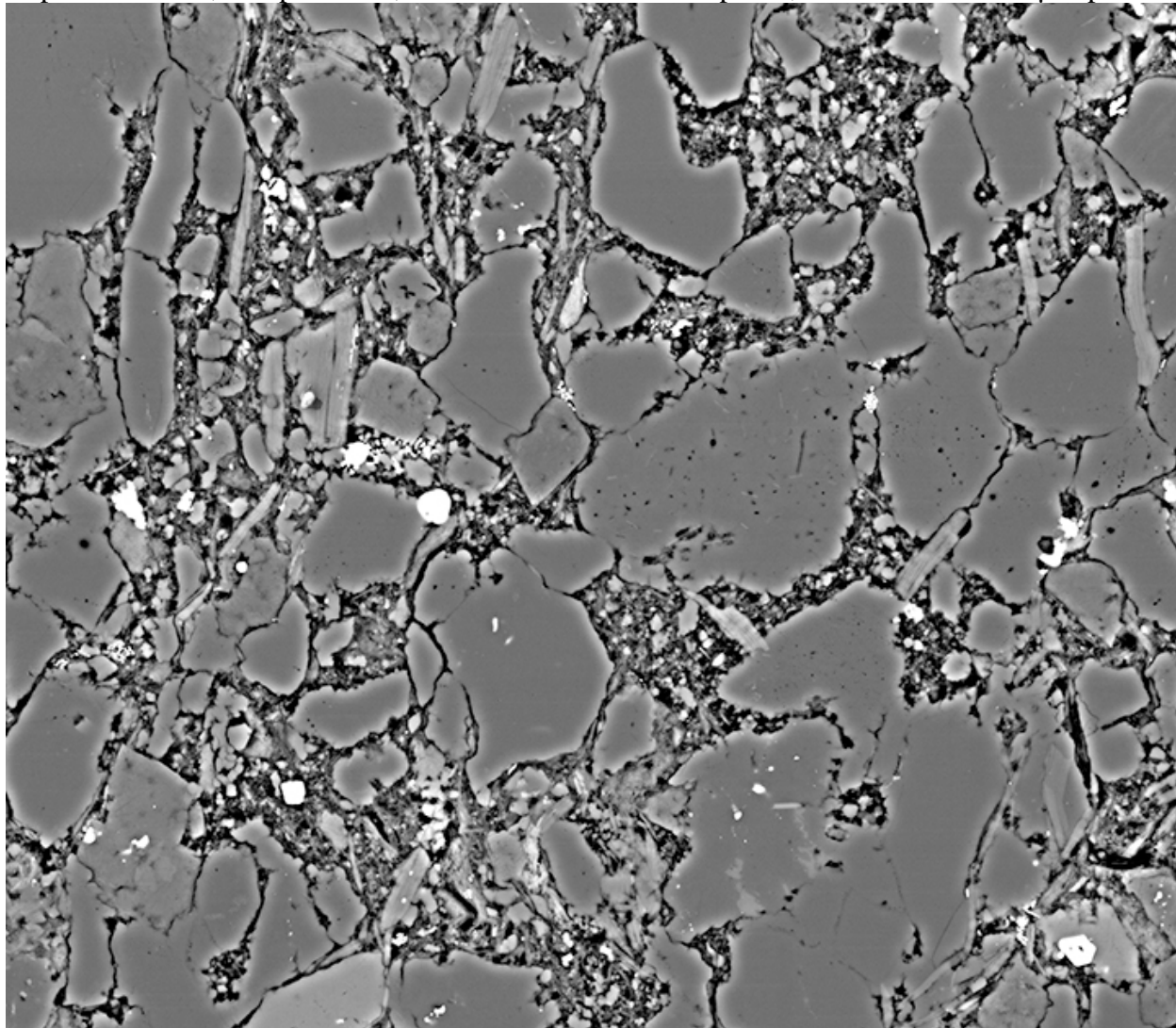
Depth 5255.15 ft, Sample 13-58, Dimensions 9372x8167 pixel², scale 0.017822607 μm/pixel



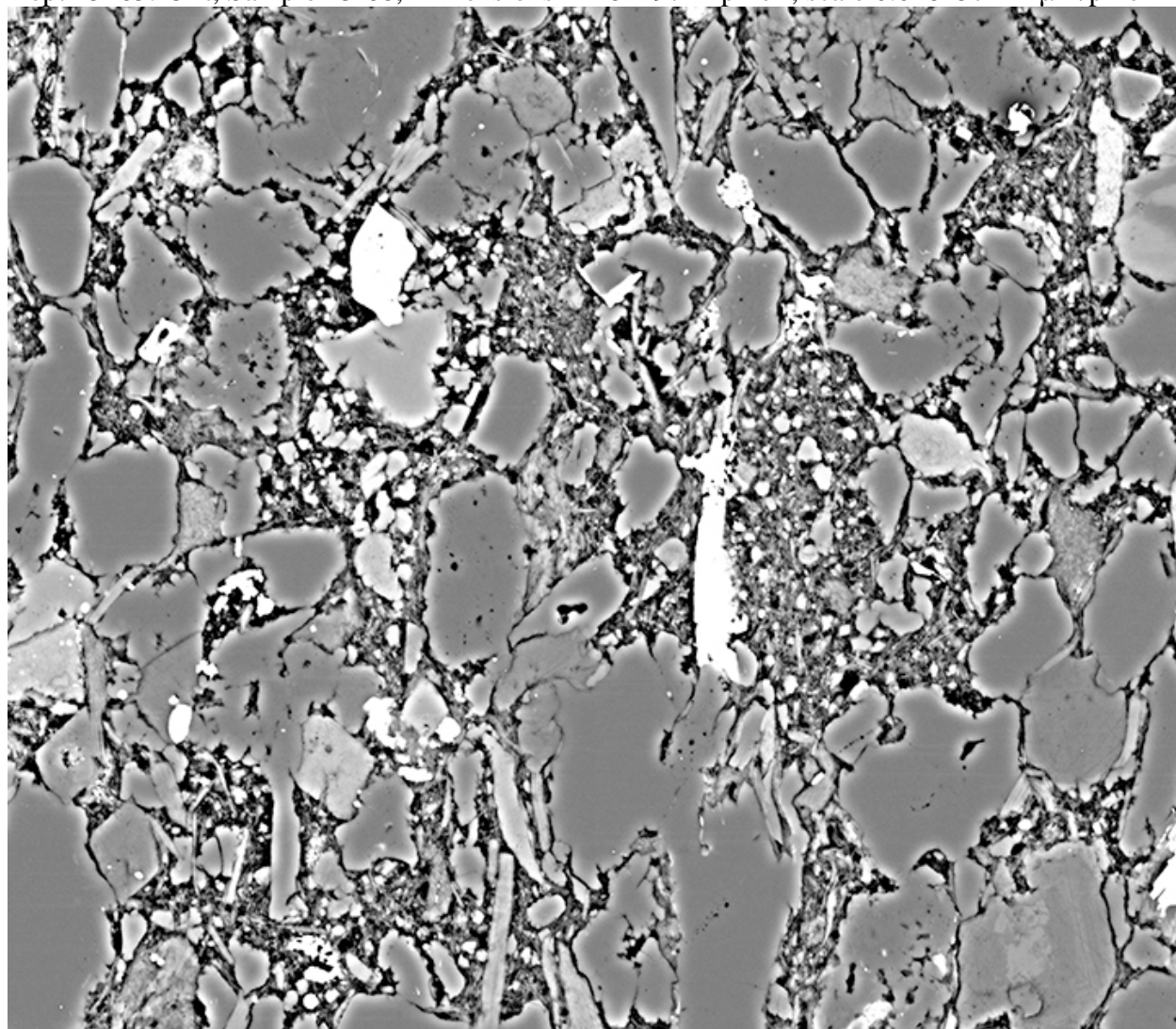
Depth 5265.15 ft, Sample 13-68, Dimensions 37218x32217 pixel², scale 0.006888354 μm/pixel



Depth 5265.15 ft, Sample 13-68, Dimensions 11156x9762 pixel², scale 0.017866162 μm/pixel



Depth 5265.15 ft, Sample 13-68, Dimensions 11182x9744 pixel², scale 0.018257422 μm/pixel



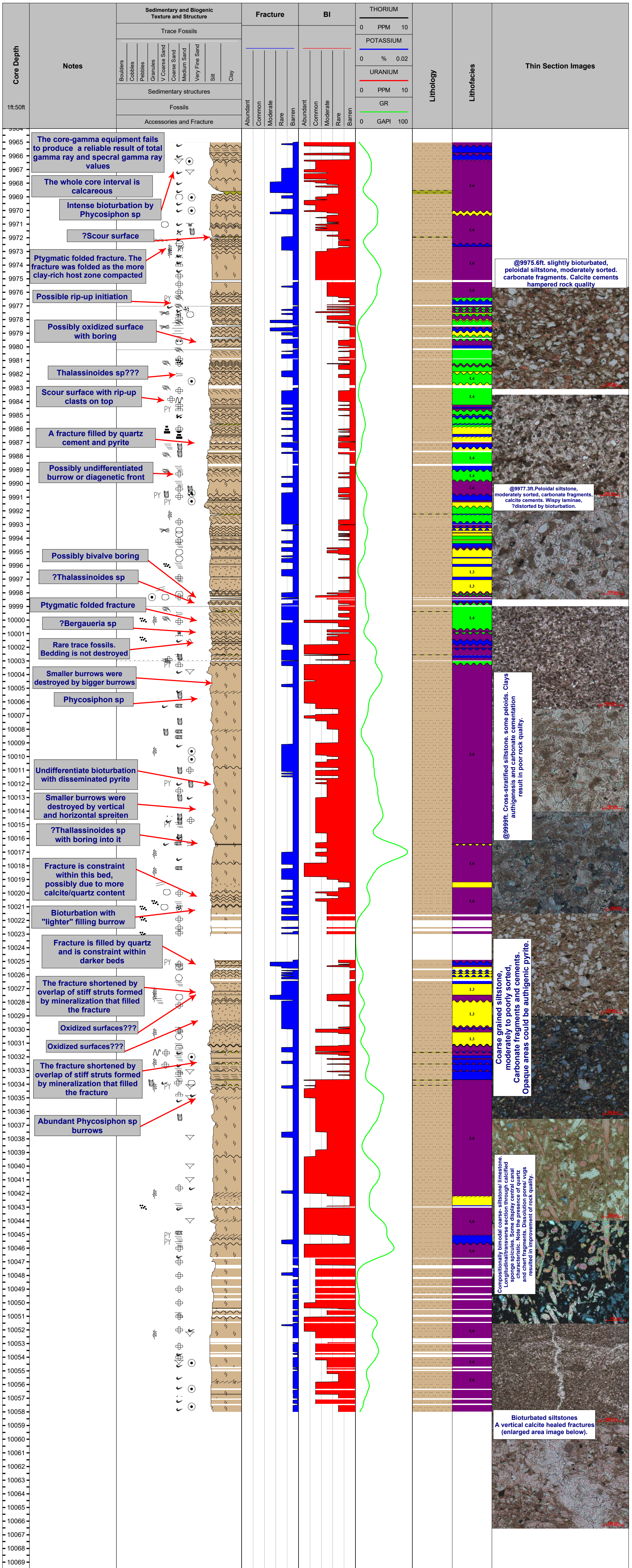
APPENDIX B: CORE DESCRIPTION

WELL: GULF OIL & E&P COMPANY 1-14 MUSSELMAN
 DESCRIBED BY: FNU SURIAMIN
 COUNTRY: UNITED STATES OF AMERICA

COUNTY: BLAINE
 STATE: OKLAHOMA
 KB: 1232 FT

Legend

LITHOLOGY Siltstone Mudstone Missing Core		FOSSILS Brachiopods Crinoids Radiolarians																																													
CONTACTS sharp scoured bioturbated uncertain gradational undulating faulted inclined Suture firmground hardground no contact		TRACE FOSSILS Vertical Spreiten Horizontal Spreiten Bioturbation undiff Planolites Phycosiphon Thalassinoides Chondrites Bored Surface Bergaueria Bivalve burrow Asterosoma																																													
LITHOFACIES L3 - Structureless Siltstone L4 - Cross-laminated Siltstone L5 - Laminated Siltstone L6 - Bioturbated Siltstone																																															
SEDIMENTARY STRUCTURES <table border="0"> <tr> <td> High angle tabular cross bedding</td> <td> Wisp lamination</td> <td> Soft sediment faulting</td> <td> Churned or chaotic bedding</td> </tr> <tr> <td> High angle trough cross bedding</td> <td> Dish and pillar</td> <td> Symmetrical ripples</td> <td> Conglomerate - sand matrix supported</td> </tr> <tr> <td> Low angle cross bedding</td> <td> Soft sedimentary deformation</td> <td> Climbing ripples</td> <td> Minor scour</td> </tr> <tr> <td> Faint continuous horizontal lamination</td> <td> Rip up</td> <td> Horizontal planar lamination</td> <td> Graded, fining</td> </tr> <tr> <td> Discontinuous horizontal lamination</td> <td> Load cast</td> <td> High angle planar lamination</td> <td> Graded coarsening upwards</td> </tr> <tr> <td> Horizontal non-parallel undulose lamination</td> <td> Ripple lamination</td> <td> Low angle planar lamination</td> <td> Desiccation cracks</td> </tr> <tr> <td> Horizontal parallel undulose lamination</td> <td> Aeolian ripple lamination</td> <td> Flaser bedding</td> <td> Syneresis cracks</td> </tr> <tr> <td> Bioturbated</td> <td> Current ripple lamination</td> <td> Parallel wavy bedding</td> <td> Mud drapes</td> </tr> <tr> <td> Structureless</td> <td> Climbing current ripple lamination</td> <td> Lenticular</td> <td> Stylolites</td> </tr> <tr> <td> Convolute lamination</td> <td> Wave ripple lamination</td> <td> Herringbone cross-bedding</td> <td></td> </tr> <tr> <td> Brecciated strata</td> <td> Geopetal</td> <td> Hummocky cross-stratification</td> <td></td> </tr> </table>				High angle tabular cross bedding	Wisp lamination	Soft sediment faulting	Churned or chaotic bedding	High angle trough cross bedding	Dish and pillar	Symmetrical ripples	Conglomerate - sand matrix supported	Low angle cross bedding	Soft sedimentary deformation	Climbing ripples	Minor scour	Faint continuous horizontal lamination	Rip up	Horizontal planar lamination	Graded, fining	Discontinuous horizontal lamination	Load cast	High angle planar lamination	Graded coarsening upwards	Horizontal non-parallel undulose lamination	Ripple lamination	Low angle planar lamination	Desiccation cracks	Horizontal parallel undulose lamination	Aeolian ripple lamination	Flaser bedding	Syneresis cracks	Bioturbated	Current ripple lamination	Parallel wavy bedding	Mud drapes	Structureless	Climbing current ripple lamination	Lenticular	Stylolites	Convolute lamination	Wave ripple lamination	Herringbone cross-bedding		Brecciated strata	Geopetal	Hummocky cross-stratification	
High angle tabular cross bedding	Wisp lamination	Soft sediment faulting	Churned or chaotic bedding																																												
High angle trough cross bedding	Dish and pillar	Symmetrical ripples	Conglomerate - sand matrix supported																																												
Low angle cross bedding	Soft sedimentary deformation	Climbing ripples	Minor scour																																												
Faint continuous horizontal lamination	Rip up	Horizontal planar lamination	Graded, fining																																												
Discontinuous horizontal lamination	Load cast	High angle planar lamination	Graded coarsening upwards																																												
Horizontal non-parallel undulose lamination	Ripple lamination	Low angle planar lamination	Desiccation cracks																																												
Horizontal parallel undulose lamination	Aeolian ripple lamination	Flaser bedding	Syneresis cracks																																												
Bioturbated	Current ripple lamination	Parallel wavy bedding	Mud drapes																																												
Structureless	Climbing current ripple lamination	Lenticular	Stylolites																																												
Convolute lamination	Wave ripple lamination	Herringbone cross-bedding																																													
Brecciated strata	Geopetal	Hummocky cross-stratification																																													
ACCESSORIES AND FRACTURE Disseminated Pyrite Rip-up clasts Organic fragments Pygmatically Folded Fractures																																															



WELL: GULF OIL CORPORATION 1-23 SHAFFER

COUNTY: BLAINE

DESCRIBED BY: FNU SURIAMIN

STATE: OKLAHOMA

COUNTRY: UNITED STATES OF AMERICA


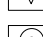

KB : 1250 FT

Legend


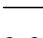

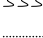

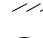
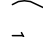
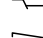

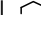
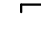

LITHOLOGY

-  Siltstone
-  Mudstone


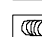
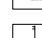

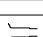
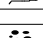

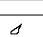
FOSSILS

-  Brachiopods
-  Crinoids
-  Skeletal, undiff

CONTACTS

-  sharp
-  scoured
-  bioturbated
-  uncertain
-  gradational
-  undulating
-  faulted
-  inclined
-  Suture
-  firmground
-  hardground
-  no contact


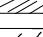



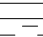
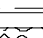

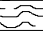
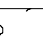
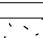
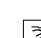
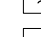
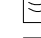

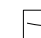



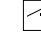
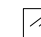
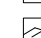

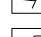






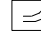


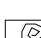






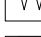

TRACE FOSSILS

-  Vertical Spreiten
-  Horizontal Spreiten
-  Skolithos
-  Phycosiphon
-  Thalassinoides
-  Chondrites
-  Teichichnus
-  Cosmorhaphe

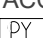
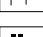

LITHOFACIES

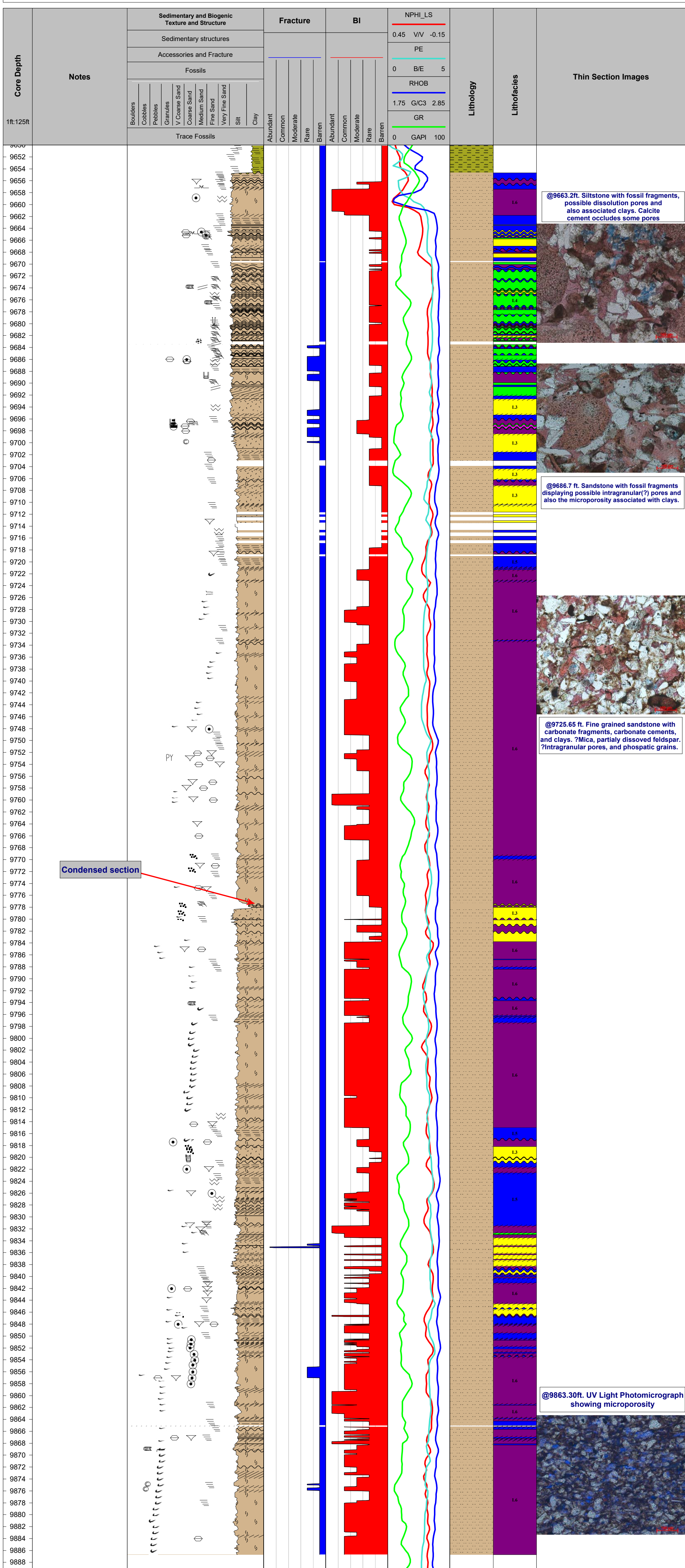
-  L3 - Structureless Siltstone
-  L4 - Cross-laminated Siltstone
-  L5 - Laminated Siltstone
-  L6 - Bioturbated Siltstone
-  L8 - Structureless Sandstone

SEDIMENTARY STRUCTURES

-  High angle tabular cross bedding
-  High angle trough cross bedding
-  Low angle cross bedding
-  Faint continuous horizontal lamination
-  Discontinuous horizontal lamination
-  Horizontal non-parallel undulose lamination
-  Horizontal parallel undulose lamination
-  Bioturbated
-  Structureless
-  Convolute lamination
-  Brecciated strata
-  Wisp lamination
-  Dish and pillar
-  Soft sedimentary deformation
-  Rip up
-  Load cast
-  Ripple lamination
-  Aeolian ripple lamination
-  Current ripple lamination
-  Climbing current ripple lamination
-  Wave ripple lamination
-  Geopetal
-  Soft sediment faulting
-  Symmetrical ripples
-  Climbing ripples
-  Horizontal planar lamination
-  High angle planar lamination
-  Low angle planar lamination
-  Flaser bedding
-  Parallel wavy bedding
-  Lenticular
-  Herringbone cross-bedding
-  Hummocky cross-stratification
-  Churned or chaotic bedding
-  Conglomerate - sand matrix supported
-  Minor scour
-  Graded, fining
-  Graded coarsening upwards
-  Desiccation cracks
-  Syneresis cracks
-  Mud drapes
-  Stylolites

ACCESSORIES AND FRACTURE

-  Disseminated Pyrite
-  Organic fragments
-  Calcite cementation



Condensed section

